Polymeric Chain-Assemblies of Metal Complexes with Mixed Azido-Carboxylato Bridges; Synthesis and Spectral Studies

Riyadh M. Ahmed

Taki A. Hamdan *Ahmed T. Numan*

Mohamad J. Al-Jeboori

(2013Ac)

Dedication

To my beloved father with respect

To my eyes…..mother

To my brothers and sisters

With love

Summary

The research on coordination polymers chemistry based on organic-metal framework with bridging ligands has accelerated during the past two decades. It is an interested hot topic in the synthetic inorganic chemistry, which allowed the fabrication of a variety of interested materials. These materials have shown a range of applications including light harvesting and magnetic properties.

The thesis is divided in three chapters. The first chapter gives a general introduction on the development of self-assembled polymeric species based on transition metal. It is also covered a summary of the literature review on the current state of the art on self-assembled coordination ploymers. Furthermore, it includes a description on various relevant topics such as the magnetic properties of macro- and micromolecules, spin crossover in transition metal compounds (SCO), the involvement of various bridging systems in the formation of self-assembled species, and highlight current examples in the synthesis of coordination polymer compounds. The uses and applications of current organic ligand systems and their metal complexes have been included in this chapter. It also includes the aim and the objectives of this investigation.

Chapter 2 represents the experimental section. It is stated material used in this work, physical measurements carried out (including spectroscopic techniques), abbreviation and chemical structures of the prepared ligands and the synthesis procedures for ligands and their metal complexes.

This work covers the preparation of five bidentate ligands capable to form polymeric structures upon complexation with metal ions; namely bis(N-carboxylatomethyl)-4,4`-dipyridinium) ($L^1$), bis(N-carboxylato)-4,4`-dipyridinium) (L^2), bis(N-carboxylatoethyl)-4,4`-dipyridinium) ($L^3$), bis(N- carboxylatopropyl)-4,4`-dipyridinium) (L^4) and 1,3-bis(N-carboxymethyl-4-pyridino)propane (L^5). Two types of ligands; one with spacer and others without were synthesised in this work.

Ligands were prepared using two methods procedures. A variety of polymeric complexes were synthesised by by heating 1 mmol of each ligand with 1 mmol of metal chloride and 2 mmol of sodium azide using a mixture of water / ethanol (4:6 v/v). Polymeric complexes of the general formula $[Cr_2(L^n)(N_3)_4]Cl_2.nH_2O$, $[M_2(L^n)(N_3)_4].H_2O$ and $Na_2[Ag_2(L^n)(N_3)_4].H_2O$, where $M^{(II)}$ = Mn, Fe, Co, Ni, Cu, Zn and Cd; $L^n = L^1$-L^5, are reported.

Chapter 3 describes results and discussion in which all the ligands and transition metal complexes synthesised in this investigation, were characterised comprehensively by elemental microanalysis (C.H.N), Atomic Absorption (A.A), thermal analysis, chloride content, molar conductance, melting point, IR, UV-Vis, magnetic susceptibility, ^{1}H-, ^{13}C- and DEPT ^{13}C- NMR and mass spectroscopy. The U.V-Vis spectra of complexes were used to elucidate the spatial arrangements of the ligand around metal ion. The complexes are air-stable solids, soluble in DMSO but not in other common organic solvents, this may be related to their polymeric structures. The molar conductivity values of complexes, except Cr(III) and Ag(I) complexes, were consistent with their nonelectrolytes, while Cr and Ag complexes gave 1:2 electrolytes, respectively. Theoretical approaches were used to confirm the coordination mode of the carboxylato moiety upon complex formation. This was based on using IR and magnetic moment measurements data. Based on the above analyses, the mode of bonding and overall suggested structure of the complexes for L^1 is shown below:

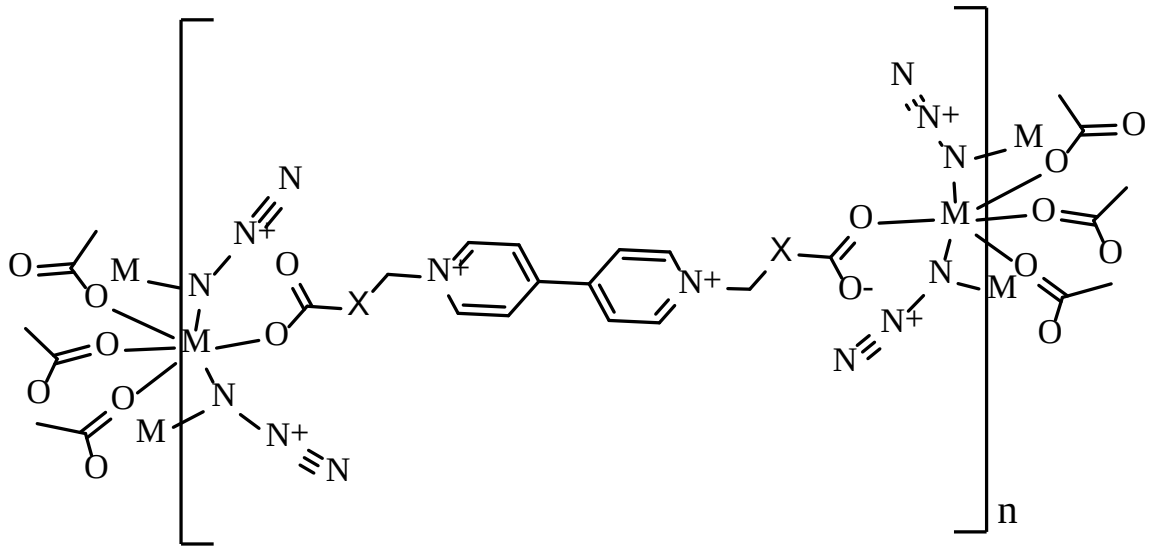

X= CH_2 = L^1

X=CH_2CH_2 = L^2

Where M= Cr^{III}, Mn^{II}, Fe^{II}, Co^{II}, Ni^{II}, Cu^{II}, Zn^{II}, Cd^{II}, Ag^{I}

Keywords; Polymeric complexes; Zwitterionic polydentate ligands; Structural study, theoretical treatment

List of contents

List of Table

List of Figures

List of Scheme

List of Abbreviation

1D	One dimensional
2D	two dimensional
3D	three dimensional
MOF	Metal organic framework
FM	Ferromagnetic
AF	Anti-ferromagnetic
EO	End-on
EE	End to End
SCMs	Single molecule chain magnets
XD	Diamagnetic molar susceptibility
Xp	Paramagnetic molar susceptibility
TIP	Temperature independent paramagnetism
TC	Curie temperature
TN	Neel temperature
LS	Low spin
HS	High spin
Bmdt	N,N-bis(4-methoxy benoyl)-diethylenetriamine
DMF	N,N-dimethyl formamide
Mebta	1-mehylbenzotriazole
Pyz	Pyrazine
Pyzc	Pyrazine-2-carboxylate
Bpa	1,2-bis-(4-pyridyl)ethane
Prz	Piperazine
MIDC	2-methylimidazole-4,5-dicarboxylic acid
TGA	Thermal gravimetric analysis
FTIR	Fourier transform infrared
SPM NPs	Super paramagnetic nanoparticles
MRI	Magnetic resonance imaging
MTX	Methotrexate
SCO	Spin crossover
MCE	Magneto calorimetric effect

Chapter One

INTRODUCTION

(1.1) **General Introduction**

The development of self-assembled polymeric species based on transition metal compounds and multidentate ligands are of current interest, due to their potential applications in supramolecular and environmental chemistry and medicine[1-5.]. One approach in supramolecular chemistry has been to develop coordination polymers with unique properties. The nature of the metal and the coordination fashion of the ligands has been facilitated to develop different synthetic strategies in design and synthesis of supramolecular structures with potential applications in photochemistry, molecular magnetism[6-8], catalysis[9-11], optoelectronic devices and clean energy including gas sorption and carbon capture[12-14].

The development in the design and synthesis of molecular magnetic materials has become an interested field in creating a number of new magnets. In particular, the developments of low-dimensional magnetic features one-dimensional (1D), or two-dimensional (2D), such as metamagnetism, bridge the gap between paramagnetism and three-dimensional (3D) long-range magnetic ordering[15-17]. Coordination chemistry provides an effective approach to design and prepare these low-dimensional magnetic systems when magnetic transition metal ions are assembled into coordination polymers by employing suitable ligands. The key to design such materials is to select short bridging ligands that can effectively mediate the magnetic coupling and construct novel structures[18]. The most used short bridging ligands include the cyanide, dicyanamide, carboxylate and azide.

The carboxylate ligands are interesting versatile species that have been used in the development of several directions in coordination chemistry. These approaches cover the preparation of building blocks of metal organic framework (MOFs) and to study the phenomenon of the antiferromagnetic interaction. The characteristic porous properties of the MOFs compounds allowed them to be used in the applications of

hydrogen storage systems and carbon capture. On other hand, azide species is widely used in the coordination chemistry. The azide moiety can link metal ions in different fashion including a bridging mode. Depending on the coordination mode, complexes with particular structures and magnetic properties of the azido species are reported[19, 20]. It is well documented that the magnetic exchange mediated *via* an azido bridge can be ferro- or antiferromagnetic, depending on the bridging mode and bonding parameters. The structures and thus the magnetic properties of metal azido systems are sensitive to the coligands employed in the system.

Because on these facts, the design of self-assembled polymeric species containing mixed azido and carboxylato bridges are an interested area of research. In this work, we have explored the influence of using the combination of azido and zwitterionic dicarboxylato bridges ligands on the structures and magnetic properties of polymeric self-assembled species. Moreover, the impact of varying the length of the carboxylate ligands and introducing a spacer, the flexible with easy bend or rotational, are used for the design and construction of the self-assembled species[21, 22].

(1.2) Introduction

The current expansion in the number of porous coordination polymers reported has been fuelled primarily through a combination of new organic linker design and the realisation of many possible modes from the connection of these units by metals and metal clusters[23-27]

These interesting materials have a range of applications including light harvesting and magnetic properties. The design and synthesis of magnetic coordination polymers with peculiar structure and potential application have become a focus of intense research activities in the fields of coordination and material chemistry[28]. The key to designing such material is based on the type of the bridging ligand that can effectively mediate the magnetic interactions and construct novel structures[29]. Self-assembly of coordination polymers is influenced by medium, pH, temperature, the nature of metal ions, coordination geometry, stereochemistry, and number of coordination donors provided by ligands[30-32]. A designed synthesis of electro-conductive materials, in particular, has been a great challenge in coordination polymers, both for fundamental interests as a d-π system[33] and for applications in new optoelectronic devices such as electroluminescent devices, thin-film transistors, and solar cells. However, only a few studies on the carrier transport properties of electro-conductive coordination polymers[34] have been conducted due to synthetic challenges. The field of molecular magnetism has attracted much attention and seen great progress in recent years[35]. The systems studied so far consist of extended coordination networks or discrete polynuclear aggregates, in which paramagnetic metal ions are held together by short bridging ligands allowing for sufficiently strong magnetic exchange[36-38]. As a bridging ligand, an azido anion displaying multiple bridging modes and various magnetic exchange pathways between metal ions has been well used in the preparation of molecular magnetic materials[39]. These include

one (1D)-, two dimensional- (2D), or three-dimensional (3D) species with specific topologies[40, 41].

In recent years, the metal azido derivatives have provided several excellent structures and magnetic properties such as ferromagnetic with bridging azido moiety in the end-on fashion (FM EO,) chains[42, 43], anti-ferromagnetic with bridging azido moiety in the end-to-end fashion (AF EE) chains[44], and alternating (FM/AF) systems[45] due to alternating EE/EO bridges. 2D layers with EE bridges, AF coupling[46] and also alternating EE/EO systems[47] which magnetically show alternating FM/AF coupling have been characterised. Regular 3D AF compounds have also been described with only EE azido bridges[48].

Furthermore, the carboxylate group can also efficiently transmit magnetic exchange. Therefore, combining azide and carboxylate moieties in one system is an interesting approach for constructing new materials and modulating magnetic behaviours. It has been observed that the simultaneous azide and carboxylate bridges in some systems can transmit FM interactions between neighbouring metal ions[49-51]. The observations are particularly interesting for the design of molecular ferromagnets and single molecule/chain magnets (SCMs), perhaps because of the mismatch between azide and dianionic dicarboxylates in the competition to bind metal ions and to compensate the charge of the metal ions. Magnetic properties of these polymers strongly depend on the geometry and electronic structure of both metal centres and organic carboxylate bridge[52]. The employment of neutral dicarboxylates as ligands and / or combining to 4,4`-dipyridine and 4,4`-trimethlendipyridine has the potential coordination sites involving both nitrogen of dipyridine and the carboxylate oxygen[53]. It can coordinate in a variety of coordination modes[54, 55], and provide several possibilities in creating supramolecular architectures through hydrogen bonds and π- π interactions; it has been widely used to synthesise mononuclear[56], dinuclear[57-59], trinuclear[60,61], and coordination polymeric compounds[62-64]. Most of these compounds were prepared using hydrothermal methods[55, 56], but several were synthesised by conventional solution methods[65]. Recently, many metal azide clusters

(usually with co-bridges), including a few single-molecule magnets, have been reported[66, 67]. Metal complexes with supramolecular features in the structure have recently aroused much interest as materials with potentially new electronic, optical, magnetic, or catalytic properties. Coordination polymers have intriguing structures and wide potential applications as functional materials[68-72].

(1.3) Magnetic properties of macro- and micromolecules

Over the years, the family of compounds that exhibited magnetic behaviour continuously grew and many of the earlier magnetic materials are based on oxides[73]. During the last two decades or so, many new compounds that exhibit exotic magnetic behaviours are reported. These include, single molecule magnets[74], purely organic magnets[75], dilute semiconductor[76], etc. Along with these discoveries, some important magnetic phenomena, *viz*. magnetic frustration[77], spin chirality[78], spin-crossover[79], etc. are explored. In addition, there is a constant demand to discover materials that would combine magnetism along with other properties such as conductivity, ferroelectricity, etc. and such solids are classified as multiferroic materials[80].

Diamagnetism is a property of all compounds that, arises with the interaction of paired electrons with an applied magnetic field. These compounds are weakly repelled by the applied field due to the orbital motion of electrons induced by the external field which creates an opposing magnetic field. When these materials are subjected to a magnetic field, they reduce the density of the field lines around them or, for a non homogenous field, move to regions of lower field strength (Figure 1.1)[81].

Diamagnetic molar susceptibilities (χ_D) are negative and typically range from -1 to 100 × 10^{-6} emu/mol. They are also independent of field strength and temperature[81]. Paramagnetism is exhibited by materials containing unpaired electrons which are weakly attracted to an externally applied magnetic field. When

placed in a magnetic field, these materials concentrate the density of magnetic field lines around them or, in the case of a non-homogenous field, move to regions of higher field strength, Figure (1. 1).

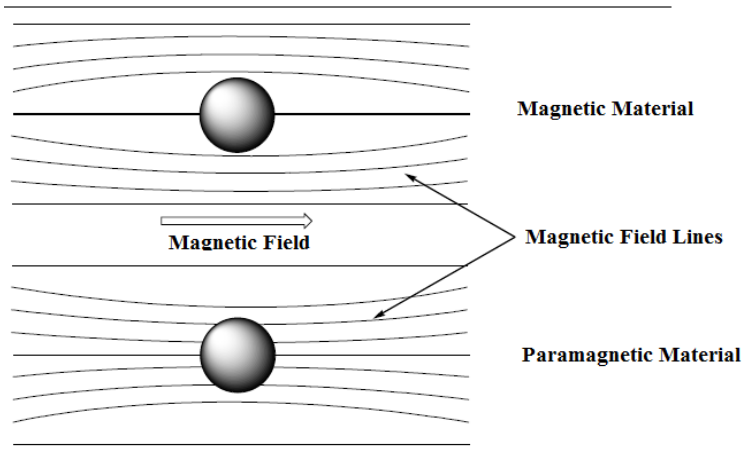

Figure (1. 1) Symbolic illustration of how diamagnetic and paramagnetic materials interact with an applied magnetic field

In the presence of an external field, the individual spins align with the applied field; however, the individual spins become disordered and do not interact with each other magnetically when the external field is removed, Figure (1. 2).

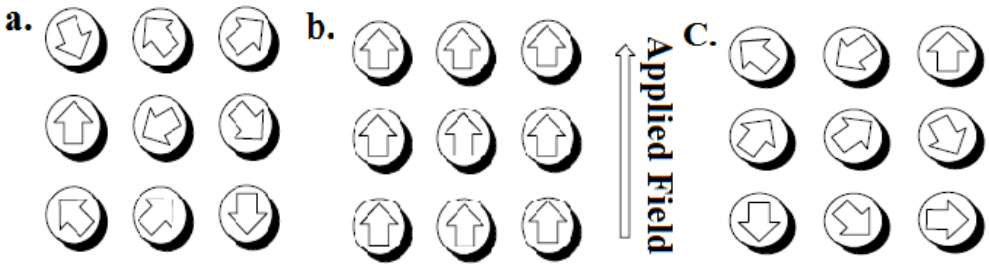

Figure (1. 2): (a) Individual spins randomly oriented in the absence of an external magnetic field; (b) when a strong enough external magnetic field is applied; (c) when the external field is removed, the individual spins return to a random orientation with no interaction.

Paramagnetic molar susceptibilities (χ_P) are positive and typically temperature dependent. Temperature independent paramagnetism (TIP) may exist in systems where there is a mixing of the ground (singlet) state with excited states that are not thermally populated. However, being approximately 10^{-4} emu/mol, TIP is significantly smaller than temperature dependent paramagnetism at low temperatures[81].

Recently, a new class of solids have been prepared by combining the coordination constraints of the central metal atoms and the functionality of the organic ligands and are known as metal–organic framework (MOF) compounds[82, 83]. These compounds offer reasonable thermal stability (typically ~400°C) and porosity[82, 84]. When the central metal ion is a transition metal, preferably the 3d series, it might be expected to observe magnetic behaviour that combines the porous nature of the solid. A magnetic porous solid could find interesting applications including carbon capture and air separation[85].

The interaction of spins with neighbouring spins in a cooperative fashion where the direction of one spin influences the directions of its neighbouring spins represent a short-ranged and only important between nearest neighbours. However, in bulk they can lead to long-range magnetic ordering without an applied field below a certain critical temperature. A few basic types of bulk magnetic properties will be defined, including ferromagnetism, antiferromagnetism and spin crossover.

(1.3.1) Ferromagnetic materials

In ferromagnetic materials the spins align in the same direction below a certain critical temperature in the absence of an external magnetic field. In this type of material, the individual spins are ferromagnetically coupled to their neighbouring spins meaning that the direction of one spin favours the parallel alignment of the neighbouring spin(s). A ferromagnet consists of spins that are all aligned parallel,

Figure (1.3 a, b). Above the critical temperature of ferromagnetic materials, called the Curie temperature (*TC*), they typically behave as paramagnets since the surrounding thermal energy is strong enough to overcome the strength of the ferromagnetic coupling[81].

(1.3.2) Antiferromagnetic materials

In antiferromagnetic materials, the spins of unpaired electrons align in an antiparallel fashion in the absence of an external magnetic field and below a certain critical temperature called the Néel temperature (*TN*) Figure (1.3c). In antiferromagnets, the direction of an individual spin causes neighbouring spin(s) to align in an antiparallel direction. This is referred to as antiferromagnetic coupling. Above the *TN*, antiferromagnets typically behave as paramagnets, like ferromagnetic materials[81].

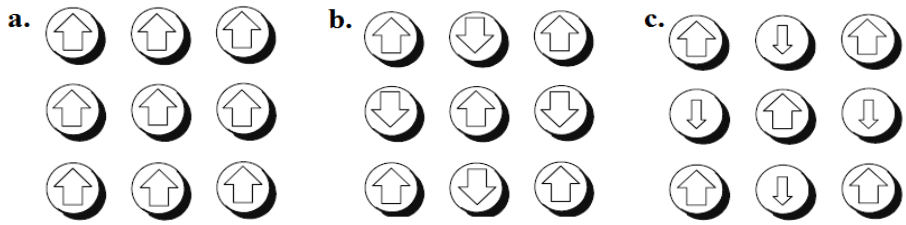

Figure (1.3) (a) (b) Ferromagnetic, (c) antiferromagnetic

(1.4) Spin crossover in transition metal compounds (SCO)

Spin-crossover compounds represent unique class of materials with potential applications in optical switches, sensors or memory devices[86-88] involving transition metal ions linked with organic ligands[89]. These systems show a sharp transition triggered by variation of temperature, pressure or by light irradiation between a low-spin (LS) ground state and a high-spin (HS) excited state with a thermal hysteresis

loop[90]. Spin crossover can be induced photochmically in solution, any d-d transition, the resultant excited electronic state only has lifetime around 10^2 ns [91]. The magnetic isomers of these compounds do not have different chemical structures. They reflect the ability of the same molecule to adopt one of two different electronic states, with different distribution of electronic in frontierd orbitals. The high spin state contains the maximum possible number of unpaired d-electrons, and is favoured in ligand field Δ_{oct} that is weaker than the energy required overcoming the electronic repulsion between pairs of electrons in the same d-orbital (the pairing energy). The converse is true for the low spin state. In an intermediate ligand field, the energy difference between these two states can be so small that an external stimulus will induce a transition from one to the other. Most commonly this will be change in temperature, occurring at a point where the higher vibration and configuration entropy of the high spin state overcomes the more favourable enthalpy of the stronger M-L bonds in the low spin form[92]. In addition, to their different magnetic moments, the spin states for the particular metal compounds can often be distinguished from their crystallographic M-L bond lengths, which can be up to 10% shorter in the low spin form[93]. The spin crossover occurs when the individual spin in the material switch cooperatively, rather than independently of each other. Spin crossover in solution proceeds gradually with changing temperature, typically occurring over a temperature range spanning 150 K. A much greater variety of thermal; spin-transitions is occurred in the solid state, ranging from gradual to abrupt transitions that are complete within a temperature range of 1 or 2 K [94]. Discontinuous or incomplete transitions are also well-known, where fractions of the spin centres in a solid undergo spin crossover under different conditions from each other. Discontinuities in spin-crossover can reflect crystallographic phase changes, or order/disorder phenomena in the crystal, but are most common in materials containing two or more unique spin sites, which undergo spin crossover (or not) independently of each other. Particularly important shapes are dinuclear iron (II) molecules, whose iron atoms may undergo spin-crossover simultaneously (i.e. high/high → low/low[95] or consecutively (high/high → high/low

→ low/low)[96] on cooling. Alternatively, the compound may stop half-way (high/high → high/low)[97].

The great sensitivity of the electronic properties of spin-crossover compounds to relatively minor and very diverse external stimuli makes them potential candidates for a number of practical applications within molecule-based materials[98,99], for instance as molecular switches or information storage devices[100]. As a consequence of the energy splitting of their d orbitals in a ligand field[101], into the t_2g and *eg* sets, octahedral coordination compounds of transition metal ions with electronic configurations d^4 to d^7 may exist in either the high-spin (HS) or the low-spin (LS) state, Figure (1. 4) illustrates the iron(II) and iron(III) cases[102]. This spin state is influenced by the nature of the ligand field surrounding the metal ion. In weak fields, HS is the ground state, corresponding to the highest possible spin multiplicity; therefore, the d electrons are distributed over the; t_2g and *eg* sets. On the contrary, strong fields stabilise the LS state with minimum multiplicity; in this case, the t_2g set is completely occupied before electrons are added to the *eg* set, Figure (1. 4). The energy gap between these orbitals varies subject to the ligands used to generate the metal coordination compounds. If the appropriate energy gap is achieved, *i.e.* when favourable ligand field strength is realised[103,104], then the compound may pass from one configuration to the other (spin crossover) by the application of an external stimulus, like temperature, pressure, or light[105].

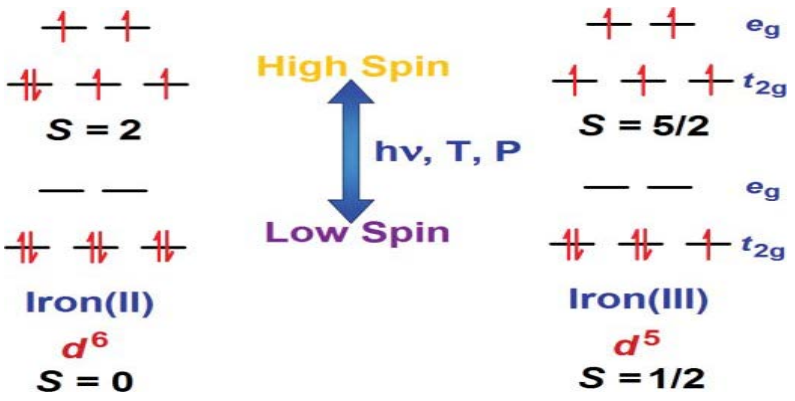

Where hν = light, T = temperature, P = pressure

Figure (1.4) Schematic representation of the two possible spin states for iron(II) and iron(III) coordination compounds in an octahedral environment

(1.5) Bridging systems

(1.5.1) Azido bridging

It is well-known that an azido anion can link metal ions in μ-1,1 (end-on, EO), μ-1,3 (end-to-end, EE), μ-1,1,3, μ-1,1,1 or still other modes, yielding various discrete, species with specific topologies, Figure (1. 5):[40.41]

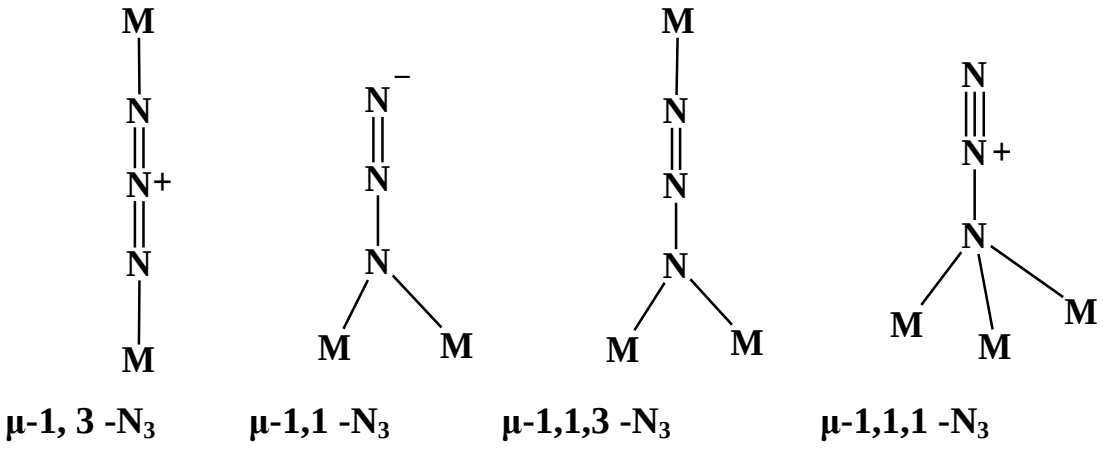

μ-1, 3 -N_3 **μ-1,1 -N_3** **μ-1,1,3 -N_3** **μ-1,1,1 -N_3**

Figure (1. 5) Structures of μ-1,3 (end-end,), μ-1,1 (end-on), μ-1,1,3, μ-1,1,1

In 2006 Liu and co-workers[106] reported the synthesis and characterisation of a new compound $[Ni(\mu\text{-}N_3)(bmdt)(N_3)]_n(DMF)_n$ (bmdt =*N*,*N*□-bis(4-methoxylbenzyl)-diethylenetriamine, DMF=*N*,*N*-dimethylformamide). The complex was characterised by X-ray structure and magnetic properties. The structure of the complex contains infinite 1D Ni^{2+} chains bridged by single EE N_3^- with isolated solvent DMF molecules among the chains; Figure (1. 6). There is only one unique Ni^{2+} ion in the structure, coordinated by six nitrogen atoms, three of which are from the ligand (bmdt) and the rest from two bridging *trans* azides and one terminal azide. The coordination environment of Ni can be considered as a tetragonally compressed octahedron.

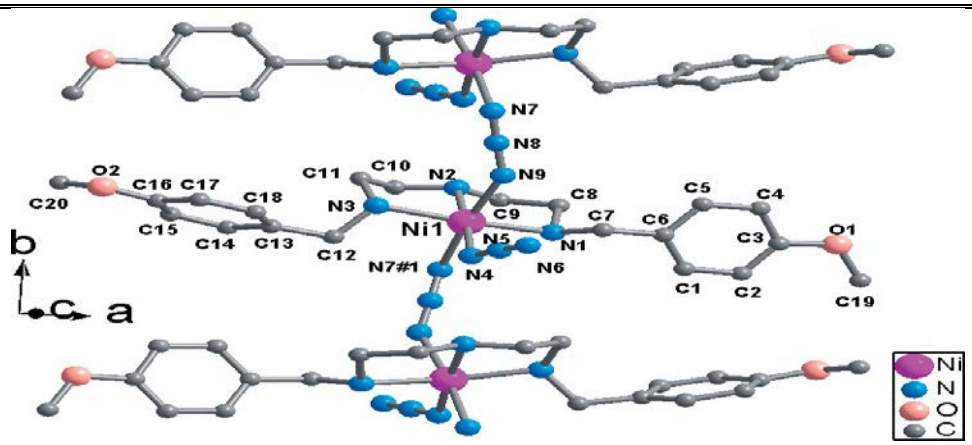

Figure (1. 6) Crystal structure of $[Ni(\mu\text{-}N_3)(bmdt)(N_3)]_n(DMF)_n$

In 2009 Boudalis and co-workers[107] reported new polymeric compounds contain a trinuclear copper clusters $[Cu_3(N_3)_6(DMF)_2]_n$ (1) and $[Cu_3(N_3)_2(Mebta)]n$ (2) (where; Mebta = 1-methylbenzotriazole). The reaction of $Cu(ClO_4)\cdot 2H_2O$ with two equivalents of NaN_3 in DMF gave complex 1 in a 2D coordination polymer possessing µ1,1,1 and µ 1,1,3 azido ligands. The coordination spheres about Cu in (1), Figure (1. 7), and (2) are highly elongated octahedral, due to the Jahn-Teller effect. Based on the Cu^{II}_3 repeating unit, the complexes contain 1D ferromagnetic chain.

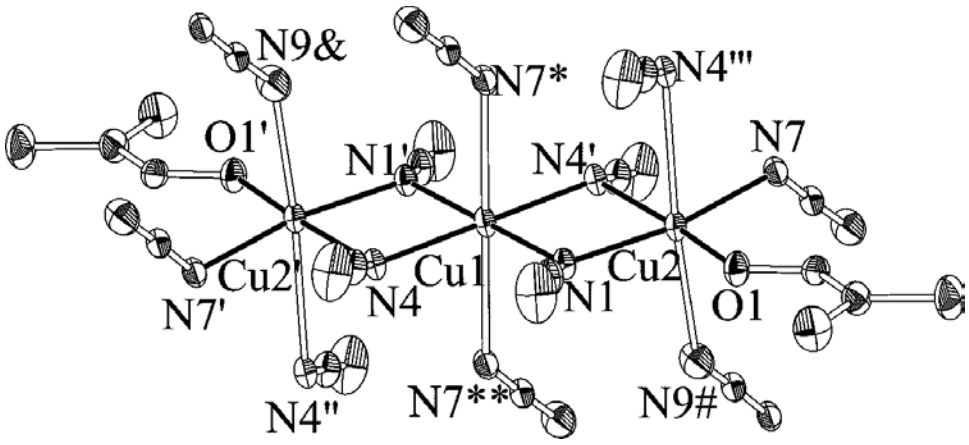

Figure (1. 7) Crystal structure of $[Cu_3(N_3)_6(DMF)_2]_n$

In 2009 Papaefstathiou and co-workers[108] reported the formation of the hexanuclear cluster $[Cu_6(O_2CPh)_4(N_3)_2\{(py)_2\ CO_2\}_2\{(py)_2C(OH)O\}_2]$ (1), and the coordination polymers $[Cu_4(O_2CPh)_2(N_3)_4\{(py)_2C(OMe)O\}_2]_n$ (2) and $[Cu_2(O_2CPh)(N_3)_2\{(py)_2C(OMe)O\}]_n$ (3) from the reaction of the combination of di-2-pyridyl ketone $(py)_2CO$: $PhCO_2^-$:N_3^- ligands in Cu^{II} ion solution. The structural type (cluster versus polymer) depends on the reaction solvent. Cluster 1 is antiferromagnetically coupled with an S = 0 ground state. These complexes were characterised by single crystal X-ray, elemental analysis, and magnetic susceptibility and FTIR spectroscopy. The coordination about Cu in (1), Figure (1. 8), is slightly to moderately square pyramidal; the coordination polyhedron of Cu in (2) is very distorted and can be considered either as a square pyramid or as a trigonal bipyramid.

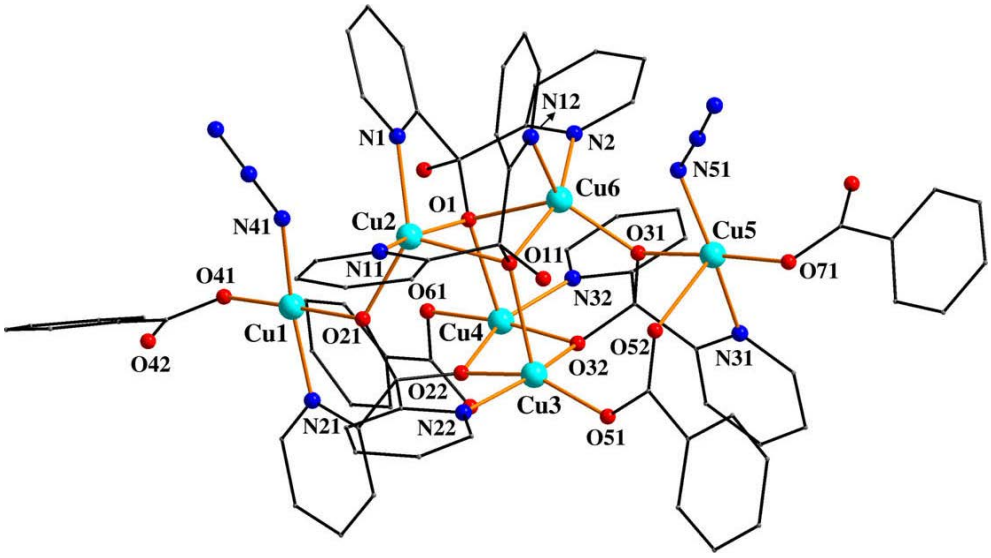

Figure (1.8) Molecular structure of $[Cu_6(O_2CPh)_4(N_3)_2\{(py)_2CO_2\}_2\ \{(py)_2C(OH)O\}_2]$

In 2010 Bu *et al.*[109] reported the synthesis of new manganese complexes from the reactions of Mn^{II} ions with azido ligands in the presence of nicotinic/isonicotinic acids. Two manganese(II) azido coordination polymers, $[Mn_3(L^1)_2(N_3)_4]_n.nH_2O$ (1) and $[Mn_2(L^2)(N_3)_3]_n$ (2), where L^1 = nicotinate and L^2 = isonicotinate, were reported. The X-ray molecular structure of (1) consists of 2D azido-Mn^{II} planes, while complex (2) consists of a 3D azido-Mn^{II} structure with L^2 as the co-ligand. Magnetic

susceptibility measurements reveal dominant antiferromagnetic coupling existing in 1 and 2. The environment around the Mn^{II} atom in 1 is octahedral; Figure (1. 9).

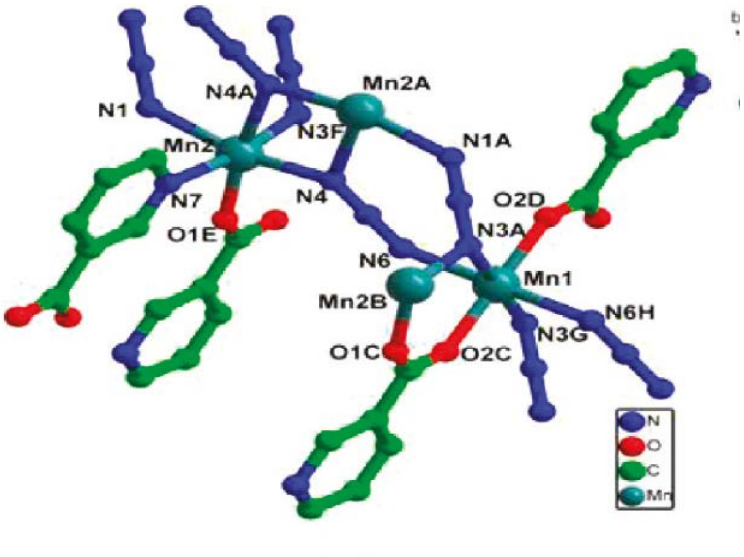

Figure(1. 9) X-ray crystallography of $[Mn_3(L^1)_2(N_3)_4]_n.nH_2O$

Saha *et al.*[110] reported the fabrication of Cu-polymer complex. The reaction of ethylenediamine with $Cu(NO_3)_2.3H_2O$ and an excess of NaN_3 in a mole ratio 1:2:4 lead to the formation of copper-azido based polymer $[Cu_4(N_3)_8(en)_2]_n$ (1), which has been characterised by elemental analyses, IR spectroscopy, X-ray single-crystal and variable temperature magnetic study. X-ray crystal structure determination of 1 reveals that the structure consists of 1D chains of a centrosymmetric tetranuclear copper(II)-azido cluster, connected through double azido end-to-end bridges. Two different coordination spheres around Cu ions are observed, Figure (1. 10). The Cu2 possesses an octahedral coordination environment, while Cu1 possesses a distorted square pyramidal coordination environment. Variable temperature magnetic studies (between 2 and 300 K) suggest dominant antiferromagnetic interactions in this complex.

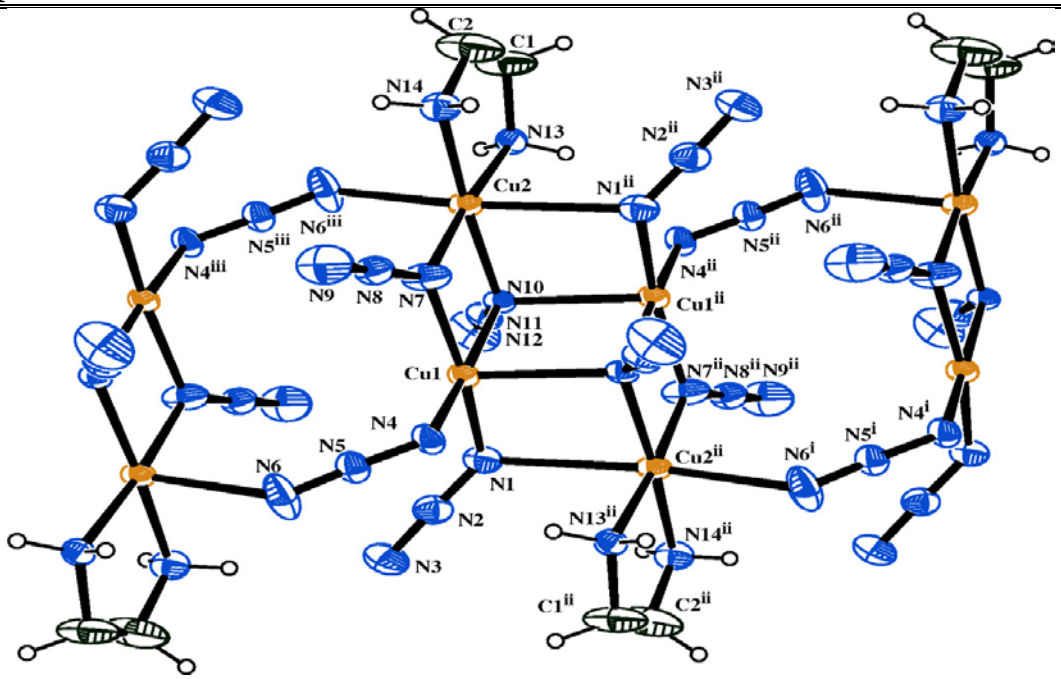

Figure(1. 10) Crystal structure of $[Cu_4(N_3)_8(en)_2]_n$

In 2010 Mukherjee *et al.*[111] reported the crystal structures and magnetic properties of five transition metal–azido complexes with two anionic [pyrazine-2-carboxylat (pyzc) and *p*-amino- benzoate (paba)], two neutral [pyrazine (pyz) and pyridine (py)] co-ligands. All complexes were synthesised by solvothermal methods. $[Co_2(pyzc)_2(N_3)_2(H_2O)_2]_n$ (1) complex is a 1D, Figure (1. 11), while $[MnNa(pyzc)(N_3)_2(H_2O)_2]_n$ (2) complex is a 3D and $[Mn_2(paba)_2(N_3)_2(H_2O)_2]_n$ (3) is a 2D sheet. Complexes found to be antiferromagnetically coupled. The coordination environment of compound 1, 2 and 3 is octahedral, but elongated octahedral for 4 and 5.

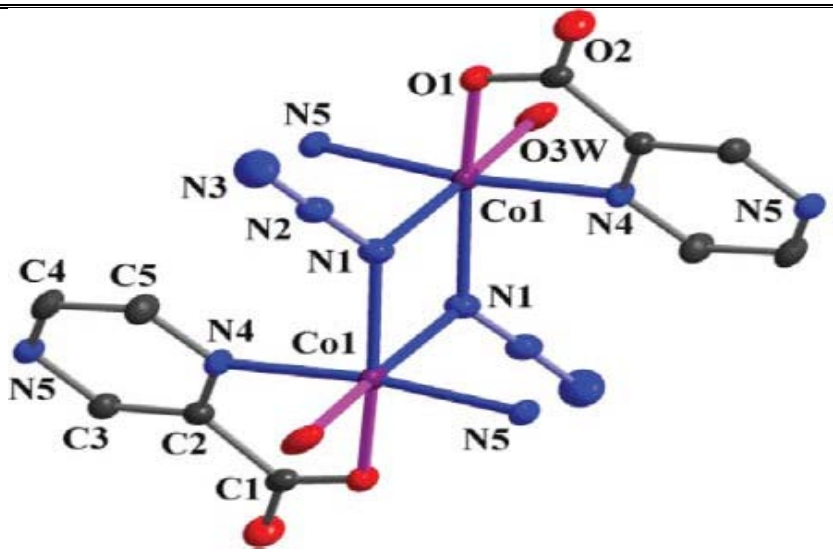

Figure (1.11) Crystal structure of $[Co_2(pyzc)_2(N_3)_2(H_2O)_2]_n$ (1)

In 2011 Chen and co-workers[(112)] prepared a linear Cu^{II} coordination polymer $[CuCl_2Cu(N_3)_2L]$ (where; L = 2-[(4-phenyl-5H-1, 2, 3-triazole) methyl]pyridine). The crystal structure of the complex is found that the Cu^{II} cations are bridged with four types of ligand or anions, 1,2,3-triazole group in L, two different end-on azides and a tri-coordinated chloride anion, Figure (1. 12). The Cu^{II} centres exhibit two different coordination geometries in the Cu^{II} complex. One Cu^{II} cation adopts a distorted octahedral geometry and the other adopts a distorted square pyramidal geometry.

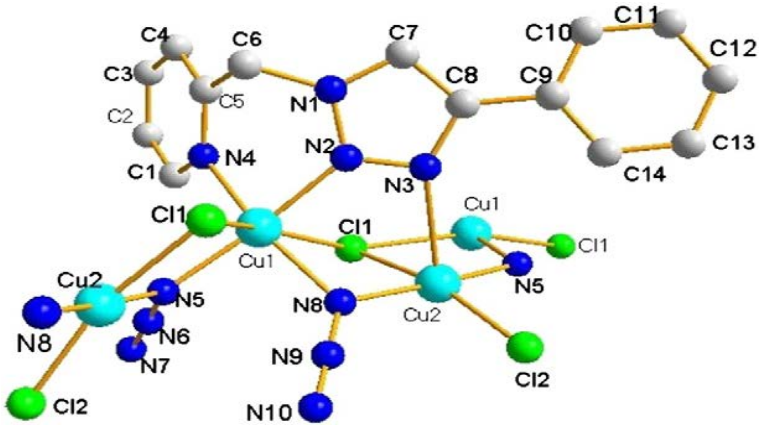

Figure (1. 12) Crystal structure of $[CuCl_2Cu(N_3)_2L]$

In 2011 Liu and co-workers[113] reported the preparation of a 3D nitrate-bridging heterometal-azido inorganic polymer, $[Cd_7Na_4(NO_3)_{12}(N_3)_6]$, from the reaction of 3-amino-1,2,4-triazole, $Cd(NO_3)_2$ and NaN_3. The complex was characterised by elemental analysis, single crystal X-ray, fluorescence and FTIR spectroscopy. The shape of the complex was face octahedrons; Figure (1. 13).

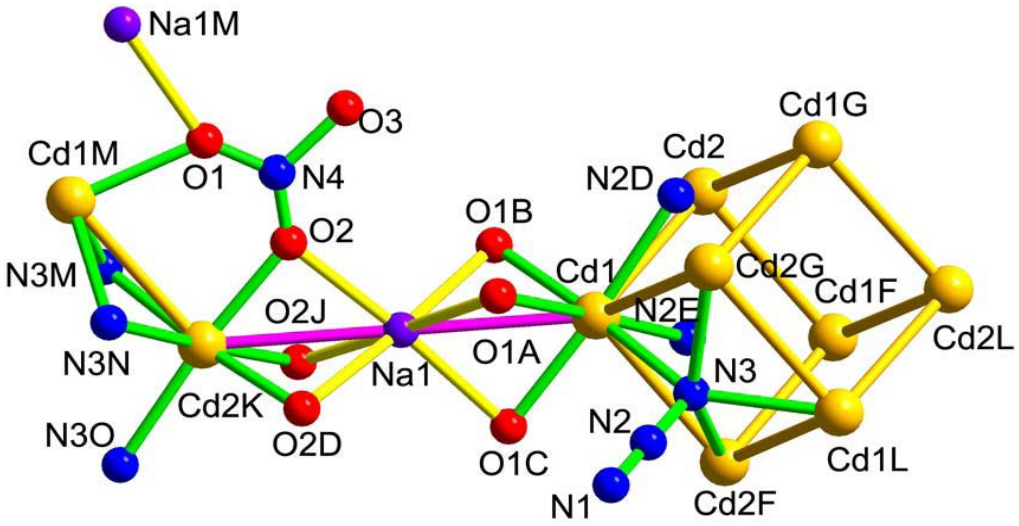

Figure (1. 13) X-ray crystallography of $[Cd_7Na_4(NO_3)_{12}(N_3)_6]$

In 2011 Cortes and co-workers[114] prepared and characterised two compounds $[Co(NCO)_2(bpa)]$ (**1**) and $Cu(N_3)_2(bpa)]$ (**2**) with cyanate and azido moieties, where bpa= 1,2-bis(4-pyridyl)ethane. These compounds were synthesised from the reaction of KNCO, $Co(NO_3)_2.6H_2O$ with 1,2-bis(4-pyridyl)ethane for (1), and using NaN_3 instead of KNCO in (2). These compounds were characterised by X-ray diffraction measurements, FT-IR and UV−Vis spectroscopies, thermogravimetric studies, electron spin resonance (ESR) spectroscopy, and magnetic measurements. Compound **1** shows a one-dimensional (1D) structure with tetrahedral coordination sphere. Compound **2** shows a two-dimensional (2D) structure with octahedral geometry, Figure (1. 14).

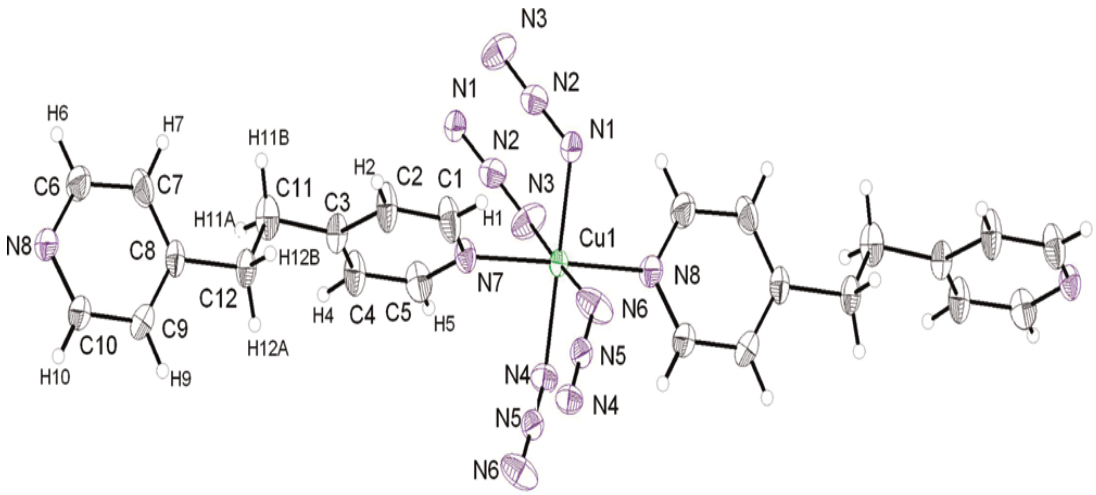

Figure (1. 14) Crystal structure of $[Cu(N_3)_2(bpa)]$

In 2011 Sakai and co-workers[115] reported the preparation of Cu^{II} polymer complexes of the general formula $[Cu_3(Him)_4(im)_2(N_3)_4]_n$ by using the Cu^{II}-imidazole (Him) complex $[Cu(Him)_4Cl]Cl$ as the starting material. X-ray analysis revealed that it possesses an in-bridged linear-chain structure consisting of alternating dinuclear units with a symmetric end-on azido-bridged $[Cu(\mu1,1\text{-}N_3)_2Cu]^{2+}$ core and mononuclear units. The Cu^{II} atoms adopt square pyramidal geometries; Figure (1. 15).

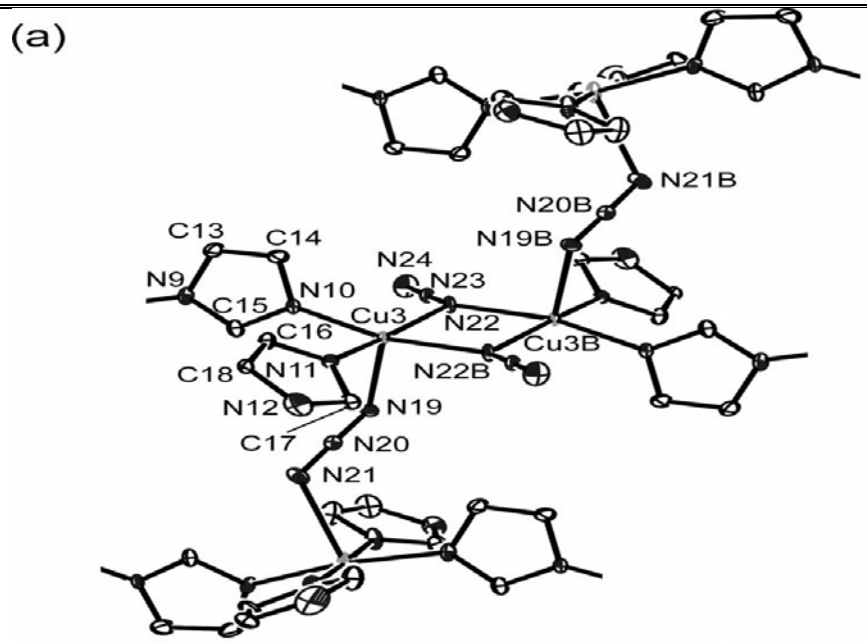

Figure (1. 15) Crystal structure of $[Cu_3(Him)_4(im)_2(N_3)_4]_n$

In 2012 Gao and co-workers[116] reported the fabrication of the Co(II) coordination polymer $[Co_2(N_3)_4(TPOM)]_n$ (where TPOM= tetrakis(4-pyridyloxymethylene)methane) from the reaction of $Co(ClO_4)_2.6H_2O$, NaN_3 and TPOM in a mixed solvent of ethanol and water. The complex exhibits a three dimentional framework in which the Co (II) chains with alternating double (EO) and (EE) azido bridges are linked by the tetrapyridyl ligand in a bowl-shaped conformation. The complex was characterised by X-ray crystallography Figure (1.16), variable temperature magnetic susceptibility and IR spectroscopy. Magnetic studies demonstrated the alternating double (EO) and double (EE) azido bridges induced ferro- and antiferromagnetic interaction. The Co atom adopts octahedral geometry.

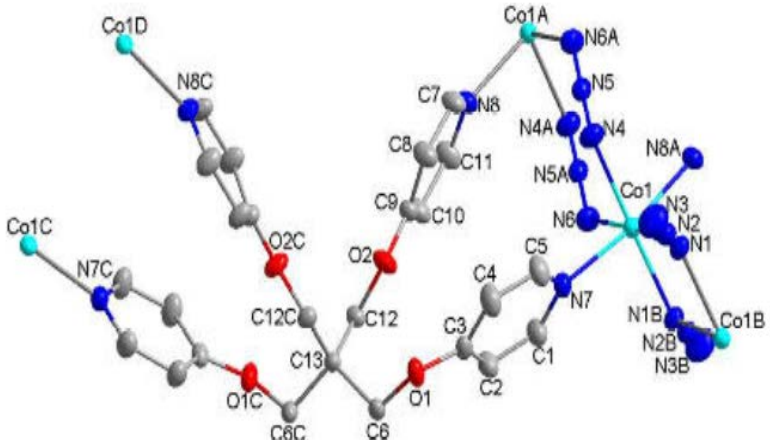

Figure (1. 16) Coordination environment about Co(II) in $[Co_2(N_3)_4(TPOM)]_n$

(1.5.2.) Carboxylate and another bridging moieties

It is well known that the shorter and more conjugated the binding bridges between the metal centres are, the more efficient the magnetic interactions and overlap between them. It is preferable to have bridges such as M–O–C–O–M or M–O–M while using the carboxylates as the linker between the metal centres. For compounds having –M–O–M– connectivity, the M–O–M angle becomes an important parameter in the magnetic behaviour. According to the Goodenough and Kanamori postulations[(117)], for ideal ferromagnetic exchange, the M–O–M angle is 90° (parallel) coupling and the Weiss constant θ is positive values. For antiferromagnetic exchange it is 180° (antiparallel) coupling and the Weiss constant θ is negative. The exchanges M–O–M, generally, occur though the 2p orbital of the oxygen and the outer d orbitals of the transition metal (d_M–p_O–d_M) with appropriate site and spin symmetry of the respective orbitals. In carboxylato bridges (O–C–O), the exchanges occur *via* the 2p orbitals of the oxygen, 2p orbitals of the carbon and the metal d orbitals (d_M–p_O–p_C–p_O–d_M) with similar symmetry consideration of the participating orbitals. In addition, the exchanges through the carboxylato bridges also may depend on the bridging modes of the carboxylate oxygens with the transition metal within the compound. The most commonly observed bridging modes of the

carbxylate oxygen in these structures are *syn–syn*, *syn–anti*, and *anti–anti* arrangements. It has been observed that the carboxylate group with *syn–syn* and *anti–anti* bridging modes exhibit relatively stronger interaction compared to the *syn–anti* mode. Since the metal d orbitals are delocalised towards the oxygen 2p orbitals of the carboxylate bridges, the oxygen 2p orbitals would be more favourably oriented to have the maximum overlap through the *syn–syn* and *anti–anti* modes rather than in the *syn–anti* mode. In addition, the oxygen 2p orbitals also overlap with the same carbon 2p orbital through the *syn–syn* and the *anti–anti* bridging modes and with different carbon 2p orbitals in the *syn–anti* bridging mode. This would result in an overlap that may not be strong for the *syn–anti* arrangement[(118)].

In 2007 Lu *et al.*[(119)] reported the preparation of Zn complex $[Zn_6(IDC)_4(OH)_2(Hprz)_2]_n$ from the hydrothermal reaction of $Zn(NO_3)_2.6H_2O$, H_3IDC and Hprz, (where; IDC= imidazole-4,5-dicarboxylate, Hprz = piperazine), and water under 180 °C for 2 days to give pale-yellow needle-shaped crystals of Zn complex. The complex was characterised by single crystal X-ray which shows each Zn^{2+} has a five-coordinated sphere in a slightly distorted trigonal-bipyramidal coordination environment, Figure (1. 17).

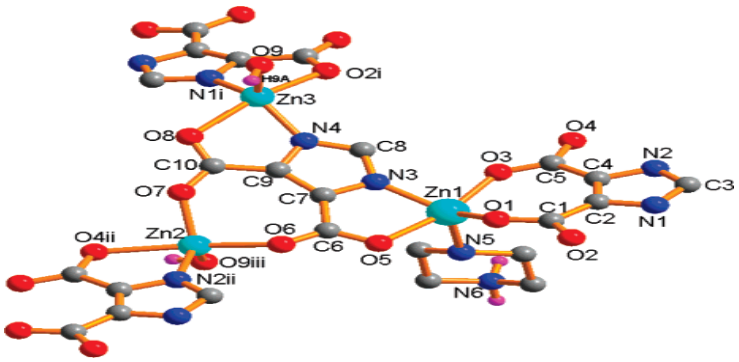

Figure (1. 17) X-ray crystallography of $[Zn_6(IDC)_4(OH)_2(Hprz)_2]_n$

Song and co-workers[(120)] synthesised and characterised a range of complexes based on the reaction of 2-methyl-imidazole-4,5-dicarboxylic acid (H_3MIDC) with different salts (ZnII and MnII). The $[Zn(H_2MIDC)_2(H_2O)_2]$ (1) complex is a 0-D

constructed by H_2MIDC^- and Zn centres, Figure (1. 18). However, $[Mn(HMIDC)(H_2O)_2]$ H_2O (2) complex displays a polymeric 1-D chiral chain structure constructed by $HMIDC^{-2}$ and Mn centres connected into a 3-D supramolecular framework with a 1-D channel. The complex $[Zn_3(MIDC)_2(H_2O)_2(DMF)_2]_{.0.5}$ H_2O (3) shows a 2-D puckered structure composed of $MIDC^{3-}$ and Zn. These compounds were characterized by IR, C.H.N, X-ray, TGA and fluorescence. The geometry of these compounds is octahedral.

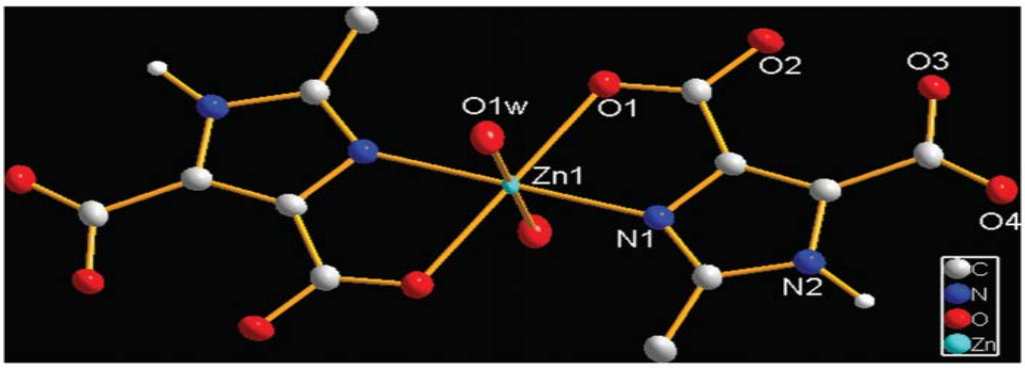

Figure (1. 18) Crystal structure of $[Zn(H_2MIDC)_2$ $(H_2O)_2]$(1)

In 2010 Okubo and co-workers[(121)] reported the synthesis and characterisation of mixed-valence Cu^I-Cu^{II} coordination polymers with one dimensional, infinite-chain structures, $[Cu^I_2Cu^{II}X_2(Hm\text{-}dtc)_2(CH_3CN)_2]_n$, where: $Hmdtc^-$ = hexamethylene dithiocarbamate; X = Br- (1), I^- (2), from the reaction of $CHCl_3$ solution of $Cu^{II}(Hm\text{-}dtc)_2$ with a mixture of acetone/acetonitrile solution of $CuBr.S(CH_3)_2$ in compound (1) and using copper fluoride in (2). These compounds were characterised by X-ray diffraction. Complex (1) consists of a mononuclear copper (II) unit $Cu^{II}(Hm\text{-}dtc)_2$ and dinuclear copper(I) units $Cu^I_2(CH_3CN)_2X_2$, Figure (1. 19). Magnetic studies revealed that these complexes have a relatively strong antiferromagnetic interaction. The coordination environment of Cu atoms in these complexes is square planar for mononuclear and tetrahedral for dinuclear.

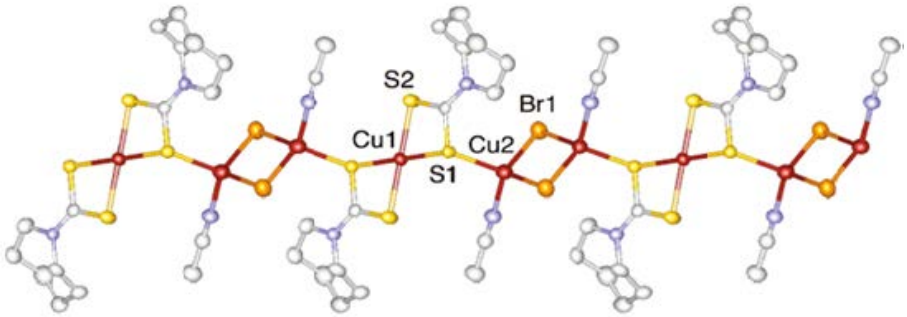

Figure (1. 19) X-ray crystallography of $[Cu^{I}_{2}Cu^{II}Br_{2}(Hm\text{-}dtc)_{2}(CH_{3}CN)_{2}]_{n}$(1)

In 2010 Miao Du and co-workers[122] reported the synthesis of coordination polymer of the general formula $[Co_{3}(pybz)_{2}(pico)_{2}]_{n}$ (1) (where; pybz=4-(pyridin-4-yl)benzoate, pico = 3-hydroxypicolinate), contains 2D $[Co_{3}(pico)_{2}]_{n}^{+2n}$ layers, which are further cross-pillared by exo tridentate bridging pybz ligands to form a three-dimensional structure. The bulk magnetic behaviour of 1 exhibits ferromagnetic long-range ordering below 2.6 K. The coordination environment of each Co1 and Co2 is octahedral, Figure(1. 20).

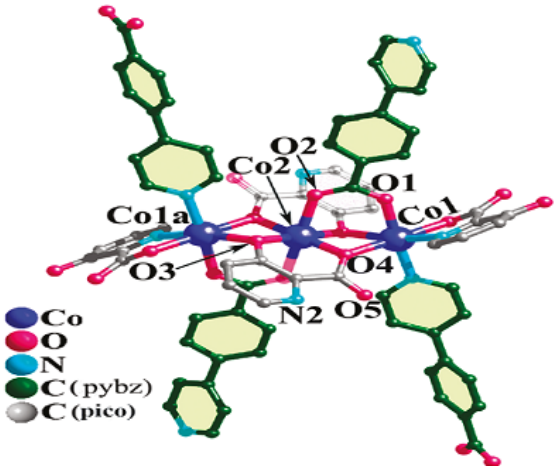

Figure (1. 20) Crystal structure of$[Co_{3}(pybz)_{2}(pico)_{2}]_{n}$

In 2011 Lv *et al.*[123] reported the formation of two coordination polymers, namely $[M(cpna)(phen)(H_{2}O)]_{n}$ (M = Ni, 1; Cd, 2, H_{2}cpna = 5-(2-

carboxylphenyl)nicotic acid, phen = 1,10-phenanthroline), under hydrothermally condition. X-ray single crystal diffraction studies show that the two complexes are isostructural polymers. They have 1D chain structures, which are further extended into 3D metal–organic supramolecular frameworks by p–p stacking interactions. Magnetic studies for complex 1 show antiferromagnetic coupling between the adjacent Ni^{II} centres. The complexes revealed octahedral geometries about metal centre, Figure (1. 21).

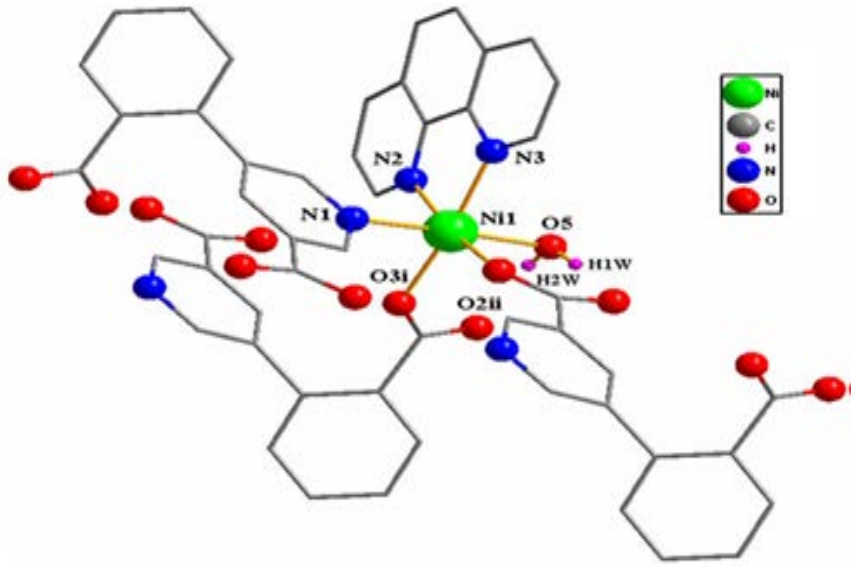

Figure (1. 21) X-ray crystallography of $[Ni(cpna)(phen)(H_2O)]_n$

Liu and co-workers[(124)] reported the formation of polymer complexes. The reaction of 2 equiv. amount of copper(II) nitrate hexahydrate with 1 equiv. of 5-methyl-1-pyridin-2-yl-1H-pyrazole-3-carboxylic acid (PyPzCA) in presence of triethyl amine as a base to give a 1D coordination polymeric compound $[Cu_2(PyPzCA)_2(H_2O)_3(NO_3)]NO_3.H_2O$ (1). Complex $[Cu(PymPzCA)].2H_2O.NEt_3$ (2) was prepared by using 1-(4,6-dimethyl-pyrimidin-2-yl)-5-methyl-1H-pyrazole-3-carboxylic acid PymPzCA instead of PyPzCA. In 1, both of the copper atoms (Cu1 and Cu2) adopted distorted square pyramidal geometry; Figure (1. 22). While in 2, the central copper atom has distorted trigonal bipyramidal geometry. These

complexes were characterised by X-ray crystallography, elemental analysis, magnetic susceptibility measurement and FTIR spectroscopy.

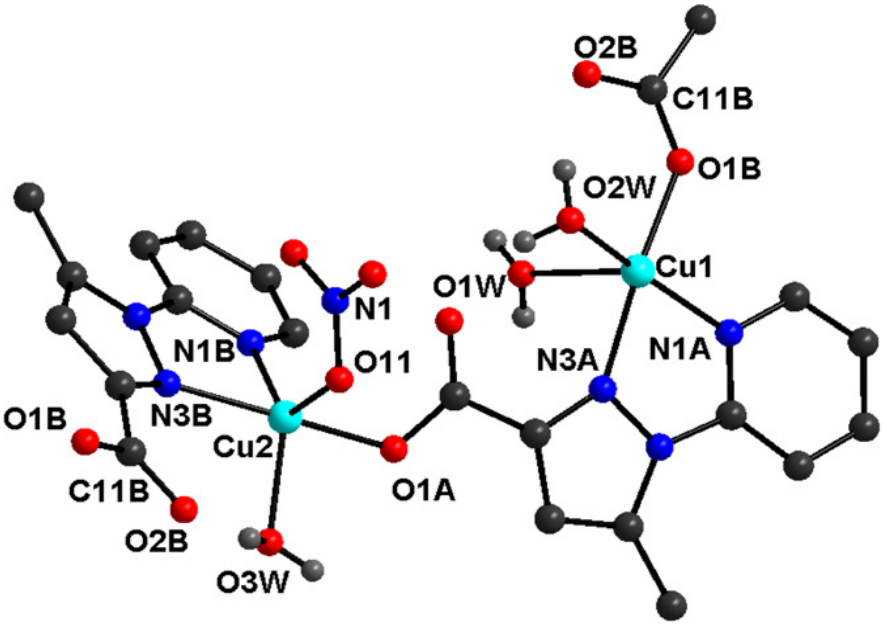

Figure (1. 22) X-ray crystallography of $[Cu_2(PyPzCA)_2\ (H_2O)_3(NO_3)]NO_3.H_2O$(1)

In 2011 Zheng and co-workers[125] reported the synthesis and characterisation of the supramolecular complexes, $[Zn(dpds)(C_6H_5COO)_2]_n$ (1), $[Zn(dpds)(C_7H_7COO)_2]_n$(2), and $[\{Zn(dpds)[C_6H_4(COO)_2]\}.H_2O]_n$ (3) (dpds=4,4¯-dipyridyldisulfide, C_6H_5COOH= benzoic acid, C_7H_7COOH = m-methylbenzoic acid, $C_6H_4(COOH)_2$ = phthalic acid). The $[Zn(C_6H_5COO)_2]$ moieties in 1 are connected by dpds to generate a 1-D helical chain. In 2, the $[Zn(C_7H_7COO)_2]$ moieties are bridged by two dpds ligands of different chiralities to form a discrete chiral macrocycle chair-like structure. The ZnN_2O_2 tetrahedral in 3 is alternately linked by a pair of dpds and phthalate ligands to form a 1-D double-stranded chain, which is assembled *via* (S …S) weak interactions into a 2-D layer. The resulting 2-D layers are inclined parallel into 3-D supramolecular architecture. The coordination environment of Zn in 1 is tetrahedrel, in 2 is regular octahedral, while in 3 is distorted tetrahedral; Figure (1. 23).

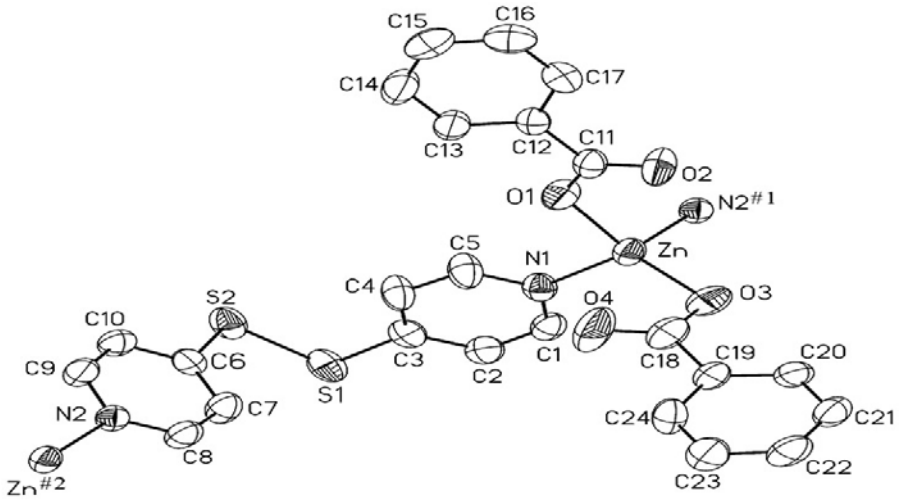

Figure (1. 23) X-ray crystallography of $[Zn(dpds)(C_6H_5COO)_2]_n$

In 2012 Yao *et al.*[126] synthesised Cd-complex of the general formula $[Cd(OH\text{-}BDC)(bpe)_{1.5}]_n$ (where; BDC = 5-hydroxyisophthalic acid, bpe = 1,2-bis(4-pyridyl)ethane) from the reaction of $Cd(NO_3)_2.4H_2O$ with HO-H2BDC and bpe in a mixed solvent of water and ethanol (V/V=5:1) to form a 2-D complex. This 2-D double layer motif is further interlocked with the neighbouring ones in the parallel fashion, to give a 3-D complex. The Cd (II) ion is seven coordinated and can be described as pentagonal bipyramid geometry, Figure (1. 24).

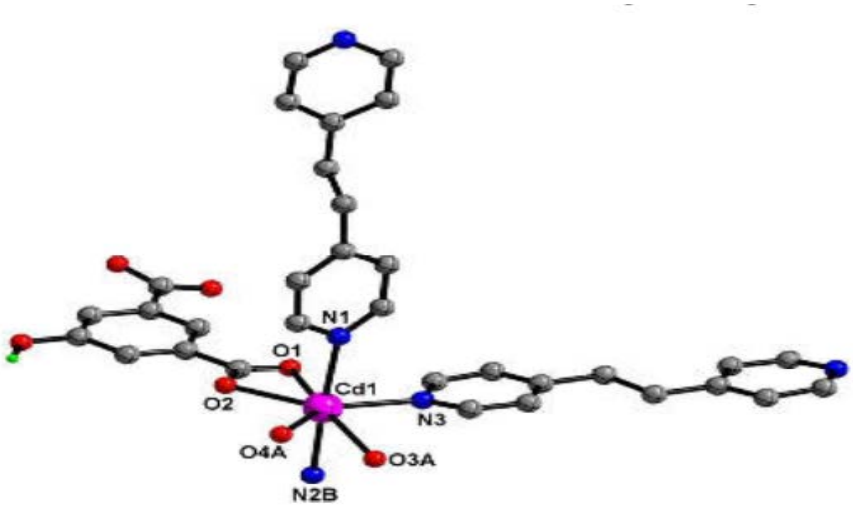

Figure (1. 24) X-ray crystal structure of 2-D Cd(II) complex

In 2012 Kumar *et al.*[127] reported the synthesis and characterisation of [Co(II)(1,4-benzenedicarboxylate)$_2$(pyridine)$_2$(water)$_2$] complex from the reaction of $Co(NO_3)_2.6H_2O$ with pyridine and 1,4-benzenedicarboxylic acid in a mole ratio of 1:4:2. The X-ray reveals that the Co(II) complex consists of 1D polymeric chain. The Co(II) atom adopts octahedral geometry, Figure (1. 25).

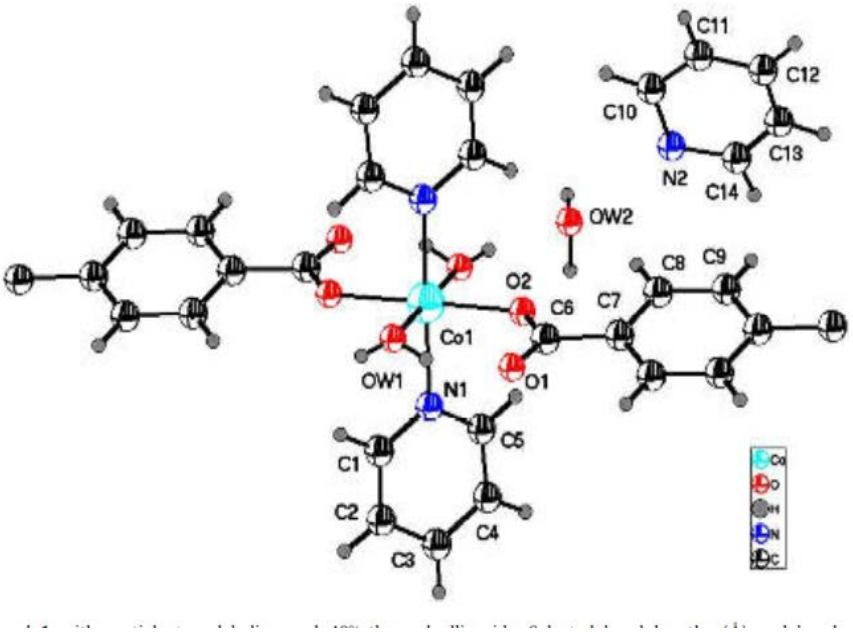

Figure (1. 25) Molecular crystal structure of Co(II) complex

In 2012 Du *et al.*[128] worked on the formation of two new compounds $[C_{48}H_{32}Cd_2N_8O_{16}]$(1) and $[C_{17}H_{13}CdN_3O_5]$(2) from the similar reaction condition but different solvent media. These compounds were synthesised from the reaction of [4,4$^-$-bis(3,3$^-$-dicyano)pyridine] (pydcy) with $Cd(NO_3)_2.6H_2O$. The X-ray diffraction reveals that cyanogens motifes of ligand was hydrolysed to carboxylic acid through *in situ* ligand reaction (Hpydca$^-$, pydca^{2-}, pydca$^-$= 4,4$^-$-bis(3,3$^-$-dicarboxyl) pyridine. Compound 1 form dimeric carboxylate bridged, while compound 2 gives a 3D framework. In the complexes, the geometry about Cd is a distorted octahedral; Figure (1. 26).

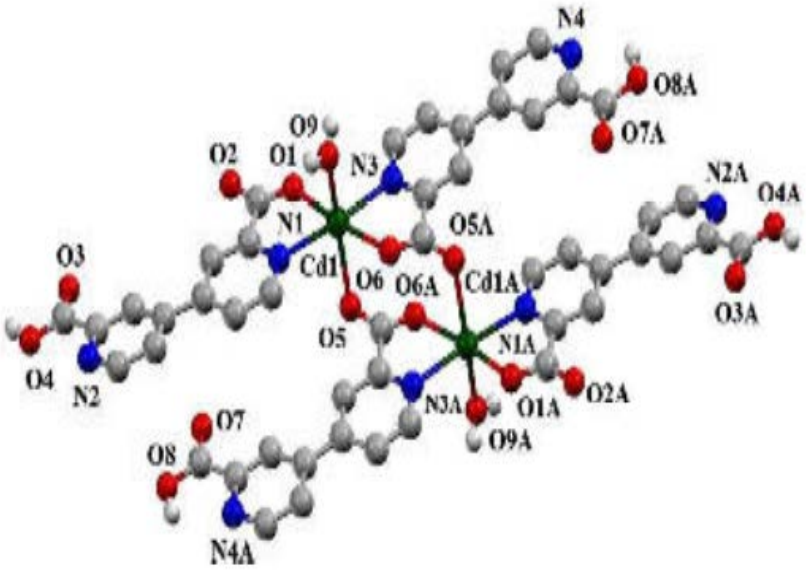

Figure (1. 26) The coordination environment of the Cd(II) ion in complex 1

In 2012 Jiao *et al.*[(129)] reported the formation of two cobalt(II) coordination polymers, namely $[Co_{1.5}(PhCOO)_3(bbbm)_{1.5}(H_2O)]n$ (1) and [Co(chdc)-(bbbm)]n (2) (bbbm = 1,10- (1,4-butanediyl)bis -1H- benzimidazole, H_2chdc = 1,4-cyclohexanedicarboxylic acid), by hydrothermal reaction of cobalt acetate tetrahydrate with the corresponding acid, bbbm ligand and sodium hydroxide at a molar ratio of 1:1:1:2. These complexes were characterised by single crystal X-ray, TGA and FTIR spectrophotometer. The cobalt(II) centres display different environments, with trigonal–bipyramidal and octahedral geometries in 1, Figure(1. 27), and a tetrahedral geometry in 2. The 1D linear chains of complex 1 and ladder-like chains of complex 2 are bridged by bbbm in bis-monodentate coordination mode; the variation of the carboxylate co-ligand effectively tunes the resulting framework architecture.

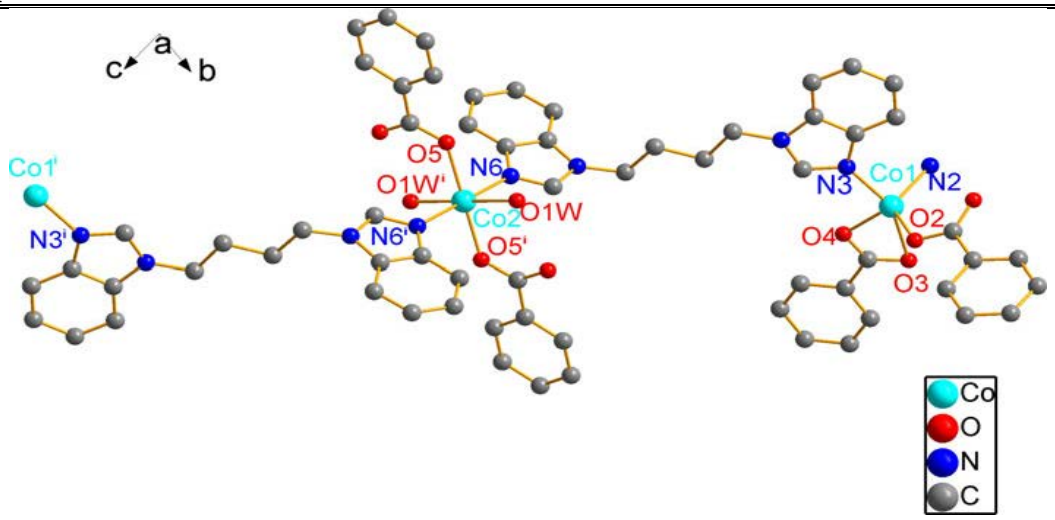

Figure (1. 27) X-ray structure of complex 1

In 2012 Roesky *et al.*[130] reported the synthesis of three polymeric complexes of lead with the general formula $[Pb\{(\eta6\text{-}C_6H_5COO)Cr(CO)_3\}_2bpe]_n$ (**1**), $[Pb\{(\eta6\text{-}C_6H_5COO)Cr(CO)_3\}_2(1,10\text{-phen})]$ (**2**) and $[Pb\{(\eta6\text{-}C_6H_5COO)Cr(CO)_3\}_2(2,2\text{-bipy})]$ (**3**), from the reaction of $[\{\eta6\text{-}C_6H_5COOH\}\text{-}Cr(CO)_3]$ with lead(II) acetate in the presence of *trans*-1,2- bis(4-pyridyl)ethene, 1,10- phenanthroline, and 2,2`-bipyridine, which gave a one-dimensional coordination polymer and mononuclear complexes. These compounds were characterised by X-ray single crystal, elemental analysis, ^1H, ^{13}C NMR, TGA and IR spectroscopy. The environment structure around Pb atom is square pyramidal. Figure (1. 28) represents the molecular structure of (1).

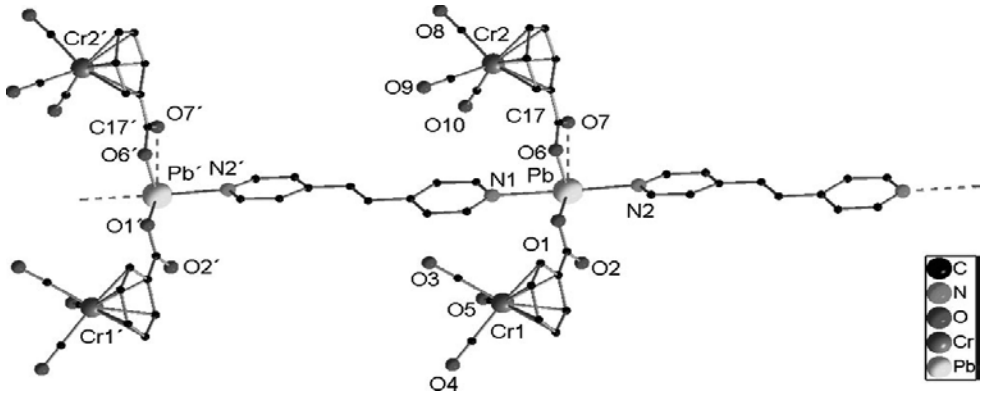

Figure (1. 28) Molecular structure of complex (1)

In 2012 Corbella and co-workers[131] obtained a range of tetranuclear Mn^{III} compounds by assembling two dinuclear units, $[\{Mn(L)(NN)\}_2(\mu\text{-}O)]^{4+}$ with aliphatic dicarboxylate ligands; succinato, glutarato and adipato, and N,N = 2,2`-bipyridine (bpy) or 1,10-phenanthroline (phen). Complexes of the general formula $[\{Mn(L)(NN)\}_4(\mu\text{-}Cm)_2(\mu\text{-}O)_2]X_4$ [X = ClO_4, N,N = bpy and Cm = C_4 (**1**), C_5 (**2**) and C_6 (**3**); X = ClO_4, NN = phen and Cm = C_4 (**4**), C_5 (**5**) and C_6 (**6**); X = NO_3, NN =bpy and Cm = C_5 (**7**)] are reported. Compound **4** shows a dominant ferromagnetic coupling, while the rest display antiferromagnetic couplings. The molecular structure shows the Mn atom adopts octahedral geometry; Figure (1. 29) represents the X-ray crystal structure of (1).

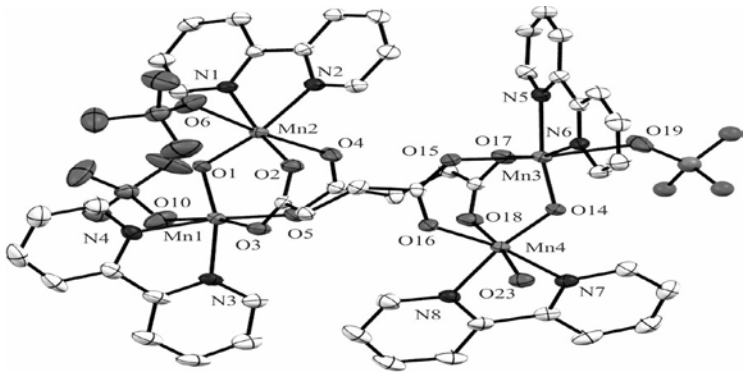

Figure (1. 29) X-ray crystallography of complex (1)

(1.6) Uses and applications

Organic compounds based on pyrdinium core including carboxylate derivatives and their metal complexes, including magnetic complexes, are of particular interest due to their wide applications in agriculture, medicine, catalysis, luminescence, optical devices and energy.

(1.6.1) In agriculture

Mixtures of diquat and paraquat–quaternary ammonium herbicides are widely used to control crop and aquatic weeds. The structures of these herbicides are shown below; Figure (1. 30)[132].

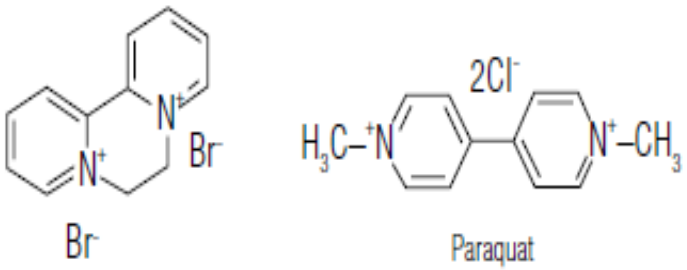

Figure (1. 30) The chemical structure of 1,1` -dimethyl-4,4'-bipyridinium and its dichloride salt

Paraquat (1,1`-dimethyl-4,4'-bipyridinium) and its dichloride salt (1,1`, dimethyl-4, 4`-bipyridinium dichloride) are broad-spectrum contact plant killers and herbage desiccants that were introduced commercially during the past 25 years. Today, they rank among the most widely used herbicides globally and are frequently used in combination with other herbicides. The recommended paraquat field application rates for terrestrial weed control, and for aquatic weed control.

(1.6.2) In biomedical

The super paramagnetic nanoparticles (SPM NPs) have been considered as attractive magnetic probes for biological imaging and therapeutic applications[133,134]. In normal biological conditions, these SPM NPs are not subject to strong magnetic interactions in the dispersion due to the randomisation of their magnetisation and are readily stabilised in physiological conditions. Under an external magnetic field, however, they exhibit a magnetic signal far exceeding that from any of the known biomolecules and cells. This makes SPM NPs readily identified by a magnetic sensing device from the ocean of biomolecules[135].

For SPM NPs to be useful for biomedical applications, they should be first stabilised against the absorption of plasma proteins and non-specific uptake by reticuloendothelial system (RES), like macrophage cells[136]. NPs coupled with these molecules tend to be recognised by these cells and endocytosed for internalisation,

achieving target-specific binding[135]. The cancer detection sensitivity by ferrite NPs are further evaluated. The $MnFe_2O_4$ NPs were coupled with the cancer-targeting Herceptin, an antibody specifically binding to the HER2/neu marker over-expressed on the surface of breast and ovarian cancers[137].

Magnetic nanoparticles have been extensively studied for their diverse biomedical applications such as magnetic resonance imaging (MRI) contrast agents, hyperthermia, targeted drug delivery, biosensing, and protein separation[138,139]. In particular, their use as MRI contrast agents has received considerable attention. MRI has several advantages over other imaging modalities, including high spatial resolution, excellent soft tissue contrast, and non-usage of radioisotopes or X-rays. However, it usually provides poor anatomic descriptions because of its inherent low sensitivity, which hampers the visualization of subtle changes in tissues[140]. Unlike gadolinium, iron is one of the most abundant metallic elements in living organisms and is essential for various biological processes, including oxygen transport by hemoglobin and cellular respiration by redox enzymes. Iron oxide nanoparticles are known to be biologically well tolerated and benign[140].

On targeted delivery, SPM NPs have distinct advantages over the other polymer based delivery systems: (1) the pathway of the drug can be readily tracked in the biological systems through SPM NPs by MRI; (2) the drug-NPs can be guided or held in place by an external magnetic field; and (3) under an alternate magnetic field, the SPM NPs act as a heater and can trigger controlled drug release[141]. Therapeutic drugs are normally coupled to SPM NPs *via* a covalent bond. Hydrophobic drugs can also be adsorbed onto NP surface to be stored in the NP coating layer to preserve their activity[142]. Ideally, the drug-NPs are introduced in the biological systems and concentrated in the targeted area by an active targeting. Drug release can proceed by simple diffusion or through enzymatic activity or the changes in physiological conditions such as pH or temperature[143]. Methotrexate (MTX), a chemotherapeutic drug that can target many cancer cells whose surfaces are over expressed by folate receptors, can be conjugated with Fe_3O_4 NPs through an amide bond[144].

The notable changes of the SCO behaviour under applied pressure[145] may be exploited in pressure sensors when remote sensing of pressure through observation of a colour change is required. Although currently limited to low temperature ranges, memory effects in SCO compounds may ultimately play a role in holographic devices[146,147]**.** Indeed, due to the large difference in the Fe–donor atom distances observed for the HS and LS states[148] the refractive index of an iron SCO system is expected to be substantially different in the two spin states, therefore inducing unusual photo-refractive properties which may be utilized to generate phase holograms[149, 150]**.**

One peculiar feature of magnetic materials is the temperature change following a variation of the applied magnetic field in adiabatic conditions. Magnetocalometric effect (MCE) which results in a temperature drop during an adiabatic magnetasation , is a valid alternative to gas decompression for cooling. The entropy change of a magnetic system once it is exposed to a magnetic field that in general, polarized the magnetic moment, thus reducing the degrees of freedom of the system. When the field is brought to zero, the magnetic contributions to the entropy increase. If the process of demagnetization occurs with out any heat flow from the environment to the magnetic system, that is, in adiabatic conditions, a drop in temperature of the magnetic system occurs. The ferromagnetic materials that are mainly based on lanthanide alloys or, more recently, on manganites, are investigated for cooling around room temperature, while paramagnetic demagnetization is used for cryogenic temperatures[151]**.**

(1.6.3) Miscellaneous

MOFs with the luminescence properties[2] have potential applications in sensor devices[152]. The development of optical sensors for oxygen is important in biology, industry. The determination of oxygen concentration can help to clarify the function

of oxygen in biological systems as well as in many cell culture applications[153]. MOF materials provide a nitro oxide (NO) therapeutic substrate with tunable physical and chemical properties[154]. MOF substrates are [155] indeed viable NO donor materials. These NO donor MOF materials have increased storage capacity over previous NO donors[156].

Supramolecular polymer gels are used to elucidate the structures at different length scales, and to explore their promise in applications as diverse as tissue scaffolds for regenerative tissue engineering, hybrid materials or novel electronic materials[157,158].

It is well documented that MOF materials provide a range of porous materials for the applications of clean energy, including hydrogen storage and carbon capture[159].

(1.7) Aim of the work

During the past years, intense research work has been focused on the design and fabrication of flexible ligand-based complexes. This is because of their intriguing framework connectivity and potential applications in the fields of magnetic, ion exchange, porous, luminescence and optical devices. Moreover, metal organic framework complexes is used in biomedicine because of the activation towards disease, especially killing of cancer cell without damaging normal cells because some types of cancer cells were more sensitive to temperature excess of 41ºC. Therefore, the aim of this work could summarise as follows:

- Synthesis of five ligands, including three new ligands (L^2-L^4), of pyridyl-based containing carboxylato moieties with and without spacer.
- Preparation of polymeric metal complexes of these ligands with some metal ions *via* self-assembly approach.
- Study the magnetic properties of these polymeric complexes which can be used in the field of;

    - Biomedicine and biosensing applications, in particular iron complexes.
    - Industrial applications, this will focus on the uses of copper, manganese, cobalt and nickel complexes.

    - Study the stereochemistry and the possible structures of the prepared complexes.

Chapter Two

EXPERIMENTAL PART

(2) Experimental

(2.1) Materials

All reagents used in this work and their suppliers are listed in Table (2-1), and used as received without further purification.

Table (2.1); Chemicals used in this work and their suppliers

Material	Company source of supply	Purity %
4,4`-dipyridine	B.D.H	99
Trimethylene 4,4`-dipyridine	Aldrich	98
Ethyl chloroacetate	Aldrich	99
Ethyl chloroformate	Aldrich	98
Ethyl-3-chloropropionate	Aldrich	98
Ethyl-4-chlorobutyrate	Aldrich	98
Chromium(III) chloride.$6H_2O$	Merck	99
Manganese(II) chloride.$4H_2O$	Merck	99
Iron(II) chloride.$4H_2O$	Fluka	98
Cobalt(II)chloride.$6H_2O$	RieDel-DeHaen	99
Nickel(II) chloride.$6H_2O$	Fluka	99
Copper(II) chloride.$2H_2O$	Merck	99
Zinc(II) chloride	Aldrich	99
Cadmium(II) chloride.$2H_2O$	B.D.H	99
Silver nitrate	B.D.H	98
Sodium azide	B.D.H	99
Silver oxide	Merck	99
Acetone	RieDel-DeHaen	99

Continued Table (2-1)		
HCl (37%)	RieDel-DeHaen	----
DMSO	Fluka	99
DMF	Fluka	99
CCl_4	Aldrich	99
Ethanol	RieDel-DeHaen	99
Methanol	RieDel-DeHaen	99
Triethylamine	Aldrich	98

(2.2) Physical measurements

The following measurements were used to characterise the ligands and their metal complexes;

(2.2.1) Melting points

Melting points of compounds were obtained on an Electro-thermal Stuart melting point SMP40.

(2.2.2) Infrared spectra (FTIR)

Infrared spectra were recorded as KBr discs using a Shimadzu 8400s FT-IR spectrophotometer in the range 4000-400 cm^{-1}.

(2.2.3) Electronic spectra

Electronic spectra were measured from 200-900 nm for 10^{-3} M solutions in DMSO at 25 ºC with (UV-Vis) spectrophotometer type Shimadzu 1800, using quartz cell of 1.0 cm length.

(2.2.4) Metal analysis

Metals content of complexes were determined using a Shimadzu (A.A) 680G atomic absorption spectrophotometer.

(2.2.5) Elemental microanalysis

Elemental analyses (C, H and N) for selected compounds were carried out on a Heraeus instrument (Vario EL), at the University of at Manchester Metropolitan (MMU) and Imperial College London (IC), U.K.

(2.2.6) Chloride contents

Chloride content for complexes were determined using potentiometer titration method on a 686-titro processor-665 Dosimat-Metrohm Swiss.

(2.2.7) Conductivity measurements

Electrical conductivity measurements of the complexes were made with DMSO solutions at 25 ºC using a Eutech Instruments Con. 150 digital conductivity meter.

(2.2.8) Mass spectra

Mass spectra for ligands and some metal complexes were obtained by positive Electron-Impact (EI), accurate Electrospray (ES) and Matrix Assisted Laser Desorption Ionisation Time of Flight MS (MALDI-TOF MS) was recorded on a VG autospec micromass spectrometer on BRUKER DALTONICS. The spectra were recorded at the EPSRC Swansea Mass Spectroscopy Facility, U.K.

(2.2.9) ^{1}H, ^{13}C and DEPT Nuclear magnetic resonance spectra (NMR)

^{1}H, ^{13}C and DEPT NMR spectra for the ligands and some complexes were acquired in DMSO-d_6 solution using a Jeol-400 MHz spectrometer with tetramethylsilane (TMS) as an internal standard for ^{1}H NMR analysis. The samples were recorded at MMU and IC, U.K.

(2.2.10) Thermal gravimetric analysis

Thermogravimetric analysis was carried out using a Perkin-Elmer 7 Series thermal analyzer. The measurement was conducted under nitrogen atmosphere at a heating rate 20 ˚C/min. The samples were recorded at MMU and IC, U.K.

(2.2.11) Magnetic moment measurement

Magnetic moments at room temperature were measured with a magnetic susceptibility balance (Johnson Matthey Catalytic System Division). The samples were recorded at MMU and IC, U.K.

(2.2.12) Proposed molecular structure

The molecular structures of the complexes were generated using CS 2006 Chem 3D Ultra Molecular Modelling and Analysis Program [(160)].

(2.2.13) Molecular modelling

3D molecular modelling of the proposed structure of the complexes was performed using CS Chem 3D Ultra Molecular Modelling and Analysis Program[(160)]. It is an interactive graphics program that allows rapid structure building, geometry optimization with minimum energy and molecular display. It is well known program and has the ability to handle transition metal complexes[(161)]. The correct stereochemistry was assured through the manipulation and modification of the molecular coordinates to obtain reasonable low energy molecular geometries.

(2.3) Abbreviation of the ligands

Table (2.2) describes the suggested abbreviation, structures and nomenclature of the synthesised ligands.

Table (2.2); Structure and nomenclature of the ligands

L^1	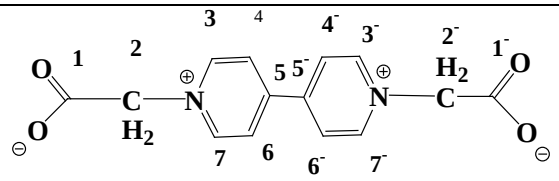	bis(N-carboxylatomethyl) 4,4`-dipyridinium)
L^2	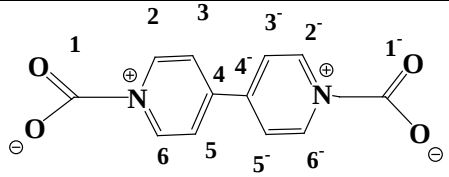	Bis(N-carboxylato)-4,4`-dipyridinium)
L^3	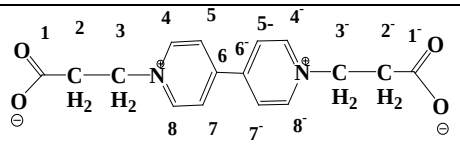	Bis(N-carboxylatoethyl)-4,4`-dipyridinium)
L^4	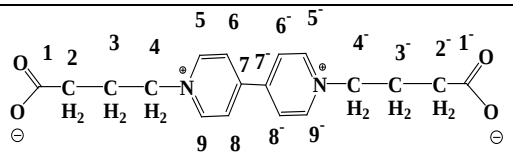	bis(N- carboxylatopropyl)-4,4`-dipyridinium)
L^5	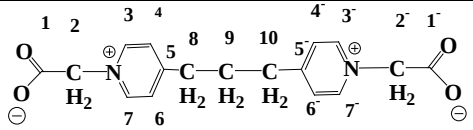	1,3-bis(N-carboxymethyl-4-pyridino)propane

(2.4) Synthesis

Two types of ligands; one with spacer and others without were synthesised in this work. Ligands were prepared using two methods procedures reported by Mao *et al*[162a] and Phillips *et al*[162b]. Using the quantities or recrystallisation mixture reported in Mao *et al*[162] procedure, pure ligands of L^1 and L^5 could not be obtained, as checked by NMR. However, modifications were implemented to obtain the pure ligands.

(2.4.1) Synthesis of the ligands without spacer

(2.4.1.1) Synthesis of the ligands using first method

(2.4.1.1.1) Synthesis of the ligand L^1

An excess of ethyl chloroacetate (up to 5 equivalents) was added slowly to a mixture of 4,4`-bipyridine (2 g, 12 mmol) dissolved in acetone (25 mL). The resulting solution was allowed to reflux for a three day. After the acetone was removed under reduced pressure a green residue was left, and then a mixture of HCl/water (50 mL, 5% w/v) was added. The resulting mixture was heated under reflux for 24 h to give a yellow solution. Removal of solvent afforded a yellow powdery product; yield (2.13 g, 61%). The product was then dissolved in (50 mL) of water, and silver(I) oxide (1.5g, 0.0065 mmol) was added, with stirring, to remove the chloride ions. The white precipitate was filtered off, and the filtrate was then dried to yield a brownish solid, which was recrystallised from water/acetone (1:5, v/v) to give L^1 ligand as a brownish solid; yield (1.61 g, 46%).

(2.4.1.1.2) Synthesis of the ligand L^2

The method used to prepare L^2 was analogous to the procedure given for the L^1, but ethyl chloroformate was used in place of ethyl chloroacetate. The quantities of other reagents used were adjusted accordingly, and an identical work-up procedure

was used to give a yellow solid (2.24g, 72%), and after treating with silver(I) oxide a pale yellow powder was collected; yield (1.62 g, 52%).

(2.4.1.1.3) Synthesis of the ligand L^3

The method used to prepare L^3 was analogous to the procedure given for the L^1, but ethyl-3-chloropropionate was used in place of ethyl chloroacetate. The quantities of other reagents used were adjusted accordingly, and an identical work-up was used to give a yellow solid (2.24g, 58%). After addition of silver (I) oxide a pale yellow powder was collected; yield (1.7 g, 44%).

(2.4.1.1.4) Synthesis of the ligand L^4

The method used to prepare L^4 was analogous to the procedure given for L^1, but ethyl-4-chlorobutyrate was used in place of ethyl- chloroacetate. The quantities of other reagents used were adjusted accordingly, and an identical work up method was used to give a yellow powder (2.19 g, 52%). After treating with silver(I) oxide, a dark yellow powder was collected; yield (1.75 g, 41%).

(2.4.1.2) Synthesis of the ligands with spacer

(2. 4.1.2.1) Synthesis of the ligand L^5

An excess of ethyl chloroacetate (up to 5 equivalents) was added slowly to a mixture of 4,4`-trimethylenebipyridine (2.0 g, 1.01 mmol) dissolved in acetone (25 mL). The resulting solution was heated at reflux for 72 h. After the removal of acetone under reduced pressure a green residue was left, and then a mixture of HCl/water (50 mL, 5% w/v) was added. The resulting mixture was heated under reflux for 24 h to give a yellow solution. Removal of solvent under reduced pressure afforded yellow solids (2.12 g, 66%). The product was then dissolved in water (50 mL), and silver(I) oxide (1.5g, 0.0065 mmol) was added, with stirring, to remove chloride ions. The white precipitate was filtered off, and the filtrate was then allowed to dryness to yield a brownish solid, which was recrystallised from water/acetone (1:5, v/v) to give L^5 ligand as a brownish solid; yield (1.81g, 57%).

(2.4.1.3) Synthesis of the ligands using second method

(2.4.1.3.1) Preparation of L^3

The ligand was prepared adopting a conventional method reported in [162b] and as follows:

(2.4.1.3.1.1) Synthesis of NC_6H_4-$C_6H_4NCH_2CH_2CO_2 \cdot 3H_2O$ (1)

3-Bromopropanoic acid (1.40 g, 0.91 mmol) was stirred with 4,4`-bipyridine (1.42 g, 0.91 mmol) in CH_2Cl_2 (15 mL) for 2 days. The resulting precipitate was filtered, washed with CH_2Cl_2 (2×5 mL), and dried in vacuo. The precipitate was recharged in CH_2Cl_2 (20 mL) and stirred with triethylamine (5 mL) for 10 h. The precipitate was filtered, washed with CH_2Cl_2 (2×5 mL), and dried in vacuo to yield a yellow powder, which was redissolved in water (5 mL) and allowed to slow evaporation at RT to give the title compound. Yield: 57%.

(2.4.1.3.1.2) Synthesis of $[(C_6H_4N\ CH_2CH_2CO_2)_2H]Br \cdot 2H_2O$ (2)

3-Bromopropanoic acid (0.18 g, 0.11 mmol) was added to a mixture of **1** (0.25 g, 0.11 mmol) in CH_2Cl_2 (15 mL). The mixture was allowed to stir at 30 °C for 5 days. The resulting precipitate was filtered, washed with CH_2Cl_2 (3×5 mL), and dried in vacuo to yield a white powder. The powder was dissolved in water (5 mL) and evaporated at RT to give the title compound. Yield: 0.24 g (73%), m.p. = 242-244 °C.

(2.4.1.3.3) Preparation of L^4

The method used was analogous to that procedure given for L^1, but with 4-bromobutanoic acid (2.14 g, 2 mmol) in place of 3-bromopropanoic acid. The

quantities of the other reagents were adjusted accordingly, and an identical work-up gave L^2 as a dark yellow solid. Yield: 1.43 g (68%), m.p 266-268 °C.

(2.5) Synthesis complexes

(2.5.1) Synthesis of L^1 complexes

(2.5.1.1) Synthesis of $[Cr_2(L^1)(N_3)_4]Cl_2.H_2O$

A mixture of $CrCl_3.6H_2O$ (0.14 g, 0.55 mmol), L^1 (0.15 g, 0.55 mmol), and NaN_3 (0.071 g, 1.00 mmol) in water/ethanol (50 mL, 4:6 v/v) was stirred for 30 min at room temperature, and then the mixture was refluxed for 30 min. Slow evaporation of the solution at room temperature yielded green crystals of Cr(III) complex within two weeks, Yield: (0.253 g, 73%).

(2.5.1.2) Synthesis of $[Mn_2(L^1)(N_3)_4].H_2O$, $[Fe_2(L^1)(N_3)_4].H_2O$, $[Co_2(L^1)(N_3)_4].H_2O$, $[Ni_2(L^1)(N_3)_4].H_2O$, $[Cu_2(L^1)(N_3)_4].H_2O$, $[Zn_2(L^1)(N_3)_4].H_2O$, $[Cd_2(L^1)(N_3)_4].H_2O$, $Na_2[Ag_2(L^1)(N_3)_4].H_2O$ complexes

A similar method to that mentioned in preparation of $[Cr_2(L^1)(N_3)_4]$ $Cl_2.H_2O$**,** complex was used to prepare other L^1 complexes with (Mn(II), Fe(II), Co(II), Ni(II), Cu(II), Zn(II), Cd(II) and Ag(I)) ions. Table (2.3) shows some physical properties of the prepared complexes.

Table (2.3); colours, yields, melting points and metal salts quantities of L^1-complexes

Ion	Weight of metal salt g	Weight of complex (g)	Yield (%)	Colour	m.p. ºC
Cr^{III}	0.14	0.253	73	Green	Dec 340
Mn^{II}	0.10	0.231	74	Pale yellow	Dec 350
Fe^{II}	0.10	0.207	66	Brown	Dec 350
Co^{II}	0.12	0.221	70	Blue	Dec 330

Ni^{II}	0.13	0.231	73	Green	Dec 340
Continued Table (2-3)					
Cu^{II}	0.09	0.224	70	Green	Dec 313
Zn^{II}	0.07	0.214	66	Yellow	Dec 317
Cd^{II}	0.12	0.266	71	white	Dec 302
Ag^{I}	0.09	0.203	51	white	182

Dec=decomposed

(2.5.2) Synthesis of L^2-L^5 complexes

(2.5.2.1) Synthesis of $[Cr_2(L^n)(N_3)_4]Cl_2.H_2O$

A mixture of $CrCl_3$. $6H_2O$ (0.16 g, 0.61 mmol), L^2 (0.15 g, 0.61 mmol), and NaN_3 (0.07 g, 1.2 mmol) in water/ethanol (50 mL, 4:6 v/v) was stirred for 30 min at room temperature, then he mixture was refluxed for 30 min. Slow evaporation of the solution at room temperature yielded green crystals of Cr(III) complex within two weeks, washed with washed with (10 mL) mixture of water/ethanol, (5 mL) of diethyl ether, and then dried under vaccu. Yield: (0.211g, 57%)

(2.5.2.2) Synthesis of $[Mn_2(L^n)(N_3)_4].H_2O$, $[Fe_2(L^n)(N_3)_4]$, $[Co_2(L^n)(N_3)_4].H_2O$, $[Ni_2(L^n)(N_3)_4].H_2O$, $[Cu_2(L^n)(N_3)_4].H_2O$, $[Zn_2(L^n)(N_3)_4].H_2O$, $[Cd_2(L^n)(N_3)_4]$, $Na_2[Ag_2(L^n)(N_3)_4].H_2O$ complexes

A similar method to that mentioned in preparation of $[Cr_2(L^2)\ (N_3)_4]Cl_2.H_2O$ complex was used to prepare other L^2 complexes with (Mn(II), Fe(II), Co(II), Ni(II), Cu(II), Zn(II), Cd(II) and Ag(I)) ions. Table (2.4) shows some physical properties of the prepared complexes.

Table (2.4); colours, yields, melting points and metal salts quantities of L^2 complexes

Ion	Weight of metal salt (g)	Weight of complex (g)	Yield (%)	Colour	m.p. °C
Cr^{III}	0.16	0.211	57	Green	Dec 343

Mn^{II}	0.12	0.229	69	Pale yellow	Dec 327
Continued Table (2-4)					
Fe^{II}	0.12	0.237	74	Yellow	Dec 304
Co^{II}	0.14	0.254	76	Blue	Dec 326
Ni^{II}	0.14	0.265	80	Green	Dec 322
Cu^{II}	0.10	0.204	60	Green	Dec 315
Zn^{II}	0.08	0.206	60	Pale yellow	Dec 293
Cd^{II}	0.13	0.237	61	White	Dec 283
Ag^{I}	0.10	0.219	52	White	189

Table (2.5); colours, yields, melting points and metal salts quantities of L^3-complexes

Ion	**Weight of metal salt (g)**	**Weight of complex(g)**	**Yield (%)**	**Colour**	**m.p. ºC**
Cr^{III}	0.13	0.217	66	Green	Dec 346
Mn^{II}	0.09	0.213	70	Pale brown	Dec 327
Fe^{II}	0.09	0.241	81	brown	Dec 206
Co^{II}	0.11	0.201	67	Gray	Dec 329
Ni^{II}	0.11	0.213	71	Green	Dec 322
Cu^{II}	0.08	0.223	75	Green	Dec 325
Zn^{II}	0.06	0.249	81	Pale yellow	Dec 303
Cd^{II}	0.11	0.257	73	White	Dec 319
Ag^{I}	0.08	0.275	74	White	183

Table (2.6); Colours, yields, melting points and metal salts quantities of L^4 complexes

Ion	Weight of metal salt (g)	Weight of complex(g)	Yield (%)	Colour	m.p. ºC
Cr^{III}	0.12	0.217	69	Green	Dec 267
Mn^{II}	0.09	0.213	75	Pale yellow	Dec 244
Fe^{II}	0.09	0.207	74	Brown	Dec 233
Co^{II}	0.10	0.241	83	Blue	Dec 330
Ni^{II}	0.10	0.229	79	Green	Dec 293
Cu^{II}	0.07	0.212	72	Green	Dec 229
Zn^{II}	0.06	0.210	73	White	253
Cd^{II}	0.10	0.228	69	White	Dec 309
Ag^{I}	0.07	0.216	61	White	197

Table (2.7); Colours, yields, melting points and metal salts quantities of L^5 complexes

Ion	Weight of metal salt (g)	Weight of complex (g)	Yield (%)	Colour	m.p. ºC
Cr^{III}	0.12	0.211	65	Green	Dec 316
Mn^{II}	0.09	0.217	74	Yellow	Dec 326
Fe^{II}	0.09	0.232	79	Brown	Dec 315
Co^{II}	0.11	0.211	71	Blue	Dec 308
Ni^{II}	0.11	0.217	74	Green	Dec 330

Cu^{II}	0.08	0.218	73	Green	Dec 328
Continued Table (2-7)					
Zn^{II}	0.06	0.202	67	Pale yellow	193
Cd^{II}	0.11	0.216	62	White	223
Ag^{I}	0.08	0.219	60	White	183

Chapter Three

RESULTS AND DISCUSSION

(3) Results and discussion

(3.1) Recent development in metal-organic polymers with azido-carboxylato bridges

In 2010 while this work was in progress, a paper was published by Gao and co-workers[163] which showed that a similar type of dicarboxylatopyrdinium ligands, namely 1,2-bis(*N*-carboxymethyl-4-pyridinio)ethane was prepared in analogous fashion, and could be effectively used with the azido moiety at the preparation of Mn(II), Co(II) and Ni(II) complexes, Figure (3. 1). However, it made no mention of the synthesis of complexes of other metal ions or the synthesis of ligands L^2 – L^4. Moreover, Mao *et al*[162] and Gao *et al*. papers were based on X-ray crystal structures, IR, CHN and variable temperature magnetic moment measurements. There is no reported data in these two references or references reported within regarding the full characterisation of L^1 and L^5 ligands, or complexes, such as; NMR, thermal analysis, UV-Vis and theoretical studies to predict coordination mode of COO^- moiety using magnetic measurements and IR data.

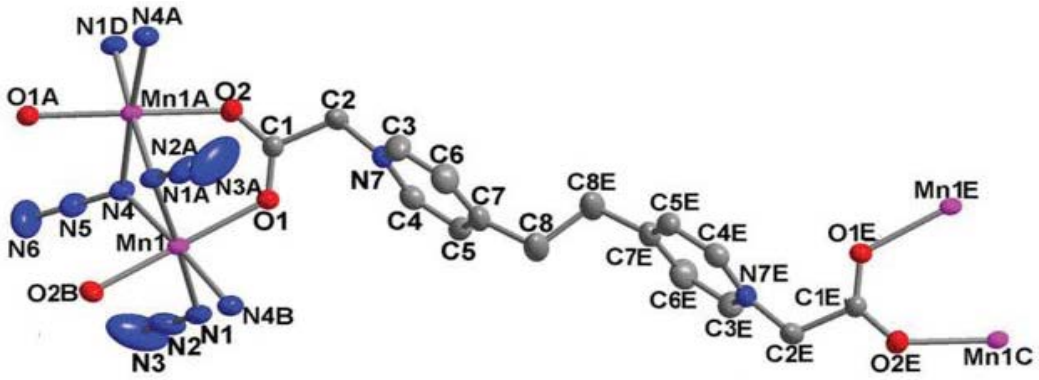

Figure (3. 1) X-ray crystallography of$[Mn_2(bcpe)(N_3)_4]\cdot H_2O$

(3.2) Synthesis and characterisation of the ligands

Ligands with spacer and others without were synthesised in this projet. Ligands were prepared using two procedures that reported by Mao *et al*[162] and Phillips *et al*[162b]. In the latter method, ligands were prepared in two steps. Similar analytical and spectroscopic data were obtained by using Mao *et*[162] *al* or Phillips *et al*[162] procedures. In Mao *et al* approach[162], the reaction of one equivalent of 4,4`-

dipyridine with five equivalents of the appropriate ethyl chlorocarboxylate precursor (Scheme (3. 1)) afforded the ligands in moderate yield. The ligands were characterised by elemental analysis (Table (3.1)), IR, UV-Vis, mass spectroscopy, and ^{1}H-, ^{13}C- and DEPT-NMR spectroscopy. Table (3. 2) represents the solubility of ligands in different solvents.

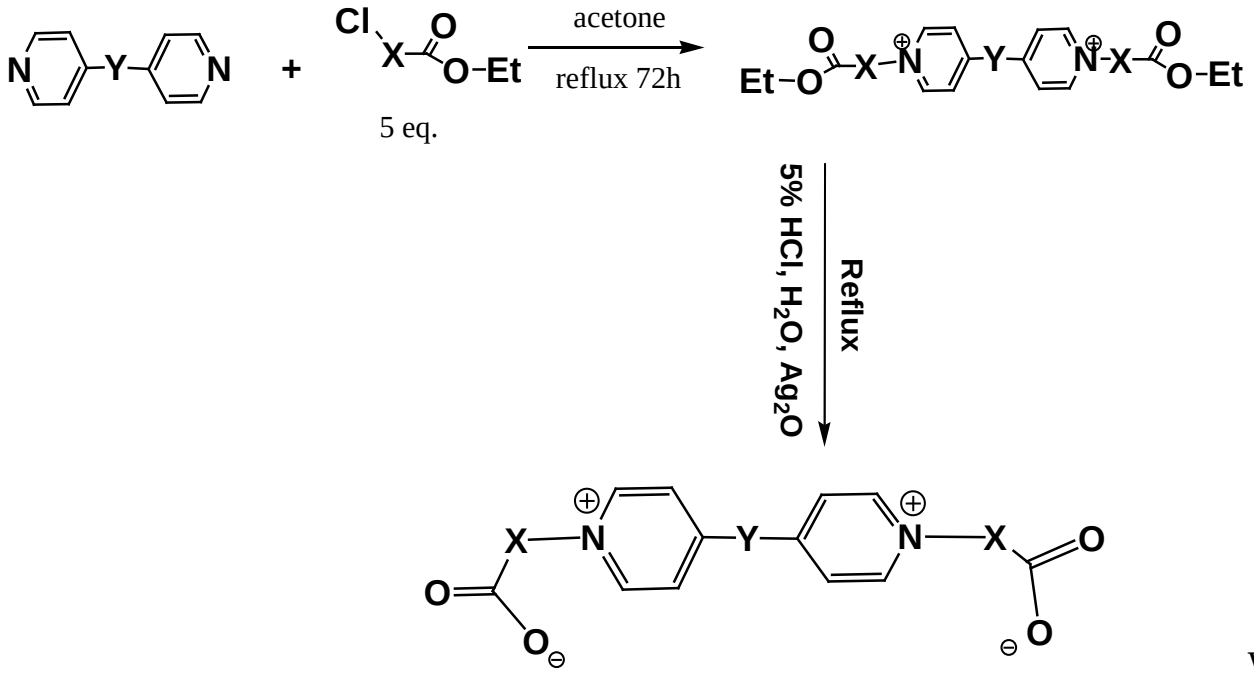

W

Where:
X = CH_2; Y = 0; L^1; bis(N-carboxylatomethyl)-4,4`-dipyridinium)
X = 0; Y = 0; L^2; bis(N-carboxylato)-4,4`-dipyridinium)
X = CH_2CH_2; Y = 0; L^3; Bis(N-carboxylatoethyl)-4,4`-dipyridinium)
X = $CH_2CH_2CH_2$; Y = 0; L^4; bis(N- carboxylatopropyl)-4,4`-dipyridinium)
X = CH_2; Y = $CH_2CH_2CH_2$; L^5; 1,3-bis(N-carboxymethyl-4 pyridino)propane

Scheme (3. 1): Synthesis route of ligands.

Table (3. 1): Microelemental analysis data and some physical properties for the ligands.

Compound	Empirical Formula	M.W	Yield(%)	Colour	Microanalysis found (calc)%		
					C	H	N
L^1	$C_{14}H_{12}N_2O_4$	272.26	46	Brown	61.63 (61.76)	4.43 (4.44)	10.27 (10.29)
L^2	$C_{12}H_8N_2O_4$	244.20	52	Pale yellow	58.92 (59.02)	3.23 (3.30)	11.33 (11.47)
L^3	$C_{16}H_{16}N_2O_4$	300.31	44	Pale yellow	63.97 (63.99)	5.26 (5.37)	9.38 (9.33)
L^4	$C_{18}H_{20}N_2O_4$	328.36	41	Dark yellow	65.23 (65.84)	5.93 (6.14)	8.27 (8.53)
L^5	$C_{17}H_{18}N_2O_4$	314.34	57	Brown	64.78 (64.96)	5.57 (5.77)	8.73 (8.91)

(calc) = calculated

Table (3. 2): The solubility of the ligands in different solvents.

Compound	H_2O	MeOH	EtOH	DMF	DMSO	CCl_4
L^1	+	-	-	+	+	-
L^2	+	-	-	+	+	-
L^3	+	-	-	+	+	-
L^4	+	-	-	+	+	-
L^5	+	-	-	+	+	-

Soluble (+), Insoluble (-)

(3.3) IR Spectral data for the ligands without spacer

(3.3.1) IR Spectrum of bis(N-carboxylatomethyl)-4,4`-dipyridinium) L^1

The IR spectrum of bis(N-carboxylatomethyl)-4,4`-dipyridinium) $L^1$ , Figure (3. 4) is compared with the IR spectra of the starting materials 4,4`-dipyridine Figure (3. 3) and ethyl chloroacetate Figure (3. 2), respectively. The spectrum of L^1 shows no band around 1759 cm^{-1} which attribute to **ν**(C=O) stretching in comparison with the ethyl chloroacetate spectrum. The new bands at 1634 and 1468 cm^{-1} can be attributed to $\nu_{as}(COO^-)$ and $\nu_s(COO^-)$ stretching, respectively of carboxylato moiety[164,165]. The IR spectrum reveals the two carboxylato moieties are equivalent in the solid state. However, in solution of L^1 these groups appear nonequivalent. The band at 1611 cm^{-1} is attributed to **ν**(C=N) of pyridine in 4,4`-dipyridyl[166]. The band at 1593 cm^{-1} can be assigned to **ν**(C=C) of aromatic ring[167]. IR spectrum shows bands at 1373 and 1231 cm^{-1} may be due to $\delta(CH_2)$ and **ν**(C-N), respectively[168].

(3.3.2) IR Spectra of ligands L^2-L^4

The IR spectra for ligands L^2 – L^4 are shown in Figures (3.6, 3.8, and 3.10). The spectra show bands similar to that of L^1 and similar reasoning could be used to interpret the spectra. The assignment of the bands are summarised in Table (3-3).

Table (3-3): Infrared spectral data (wave number) cm^{-1} of the ligands.

Compound	ν_{ar}C-H	ν_{ali} C-H	ν_{as}COO	νC=N	νC=C	ν_sCOO	δ CH_2	νC-N	$\Delta(\nu_{as}-\nu_s)$
L^1	3038	2913	1634	1611	1593	1468	1373	1231	166
L^2	3046	2903	1630	1620	1595	1458		1223	172
L^3	3048	2851	1632	1597	1578	1458	1359	1218	174
L^4	3055 3009	2913	1614	1603	1568	1416	1343	1223	198

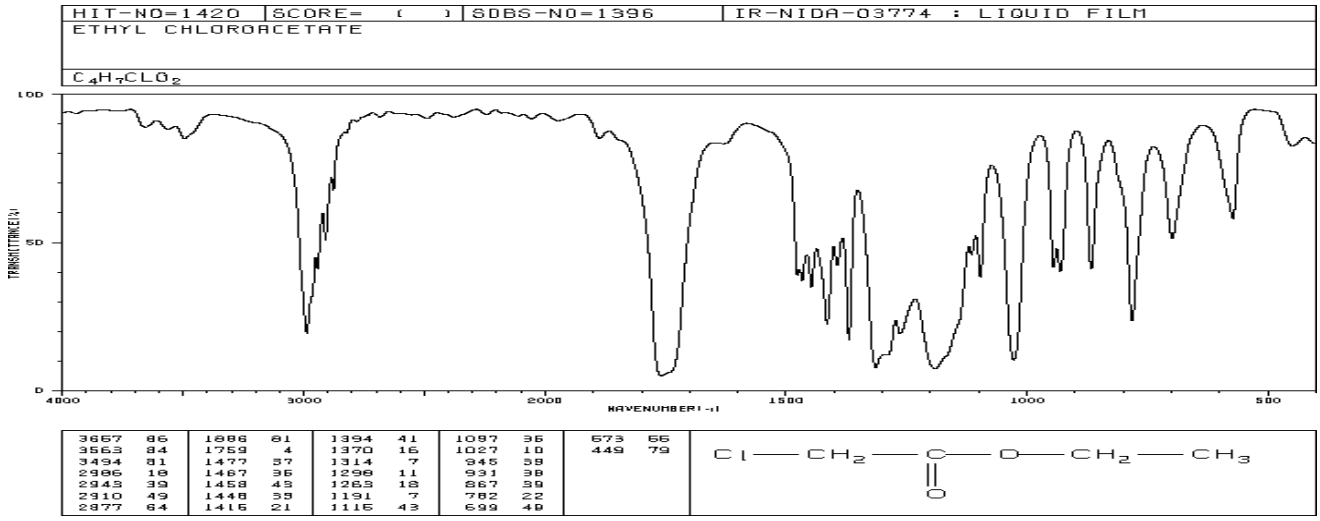

Figure (3. 2) IR spectrum of ethyl chloroacetate

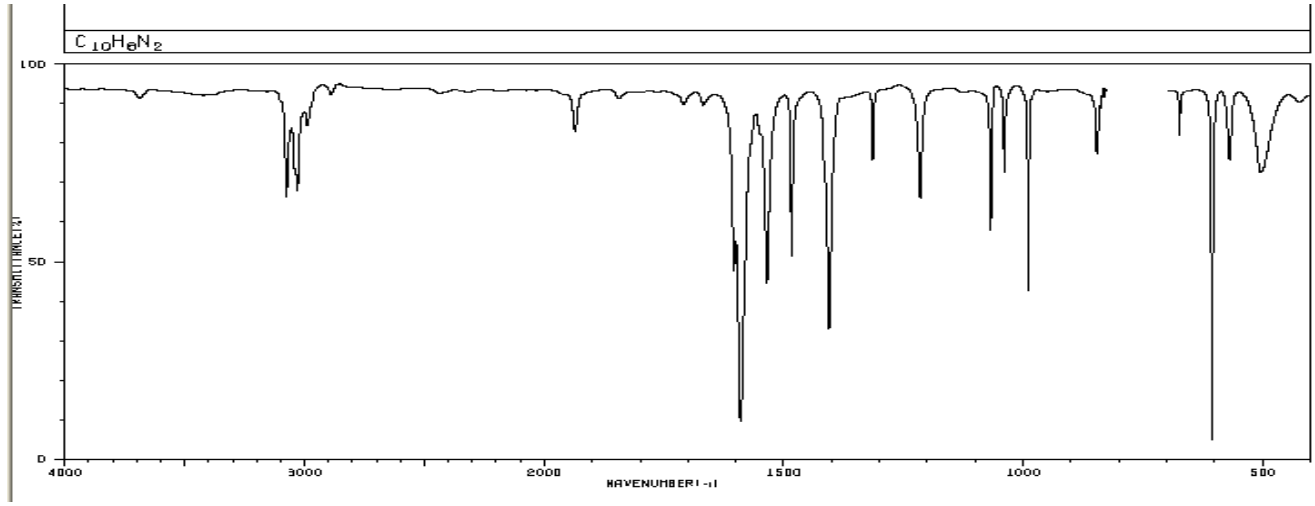

Figure (3. 3) IR spectrum of 4,4`-dipyridyl

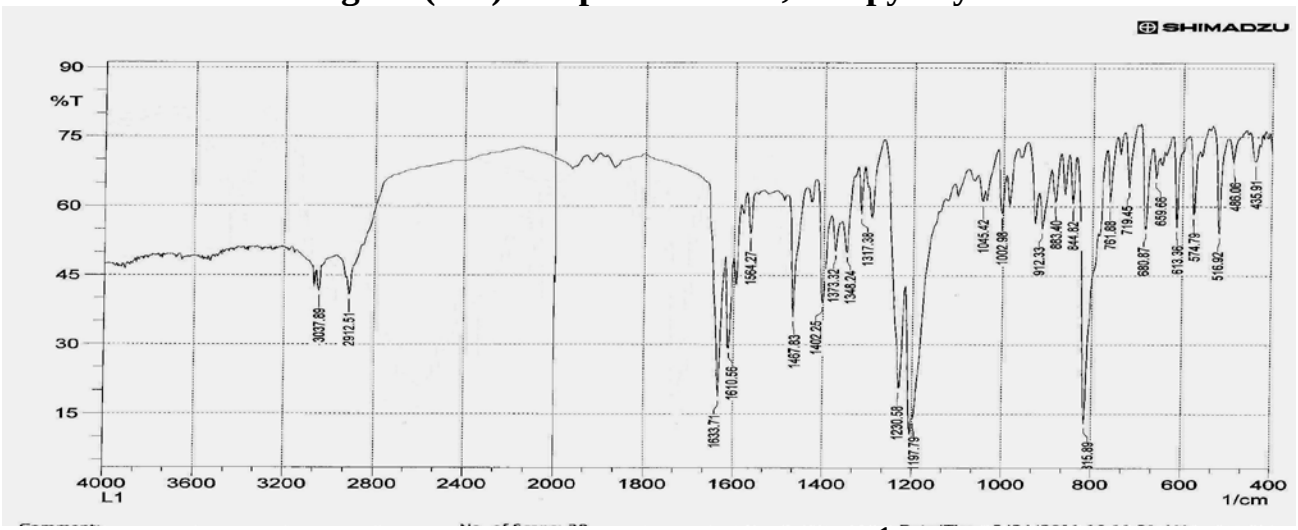

Figure (3. 4) IR spectrum of L^1

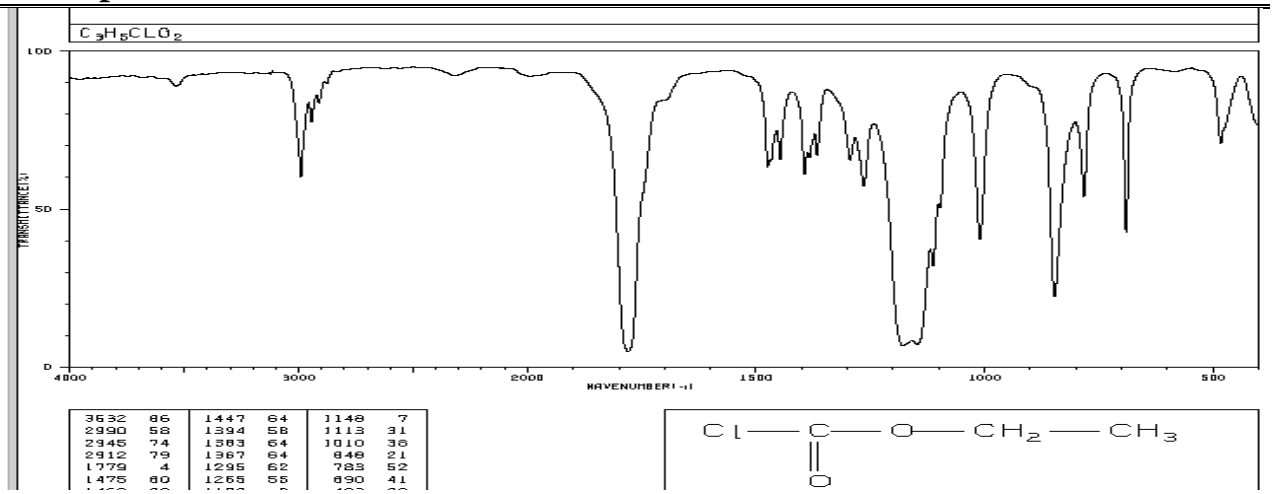

Figure (3. 5) IR spectrum of ethyl chloroformate

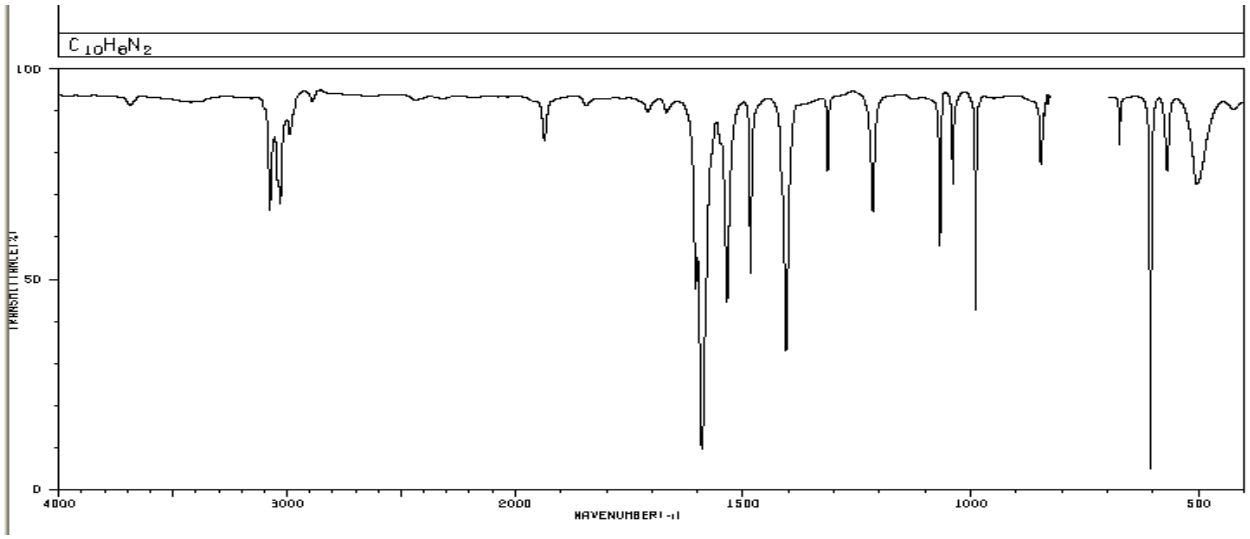

Figure (3. 3) IR spectrum of 4,4`-dipyridyl

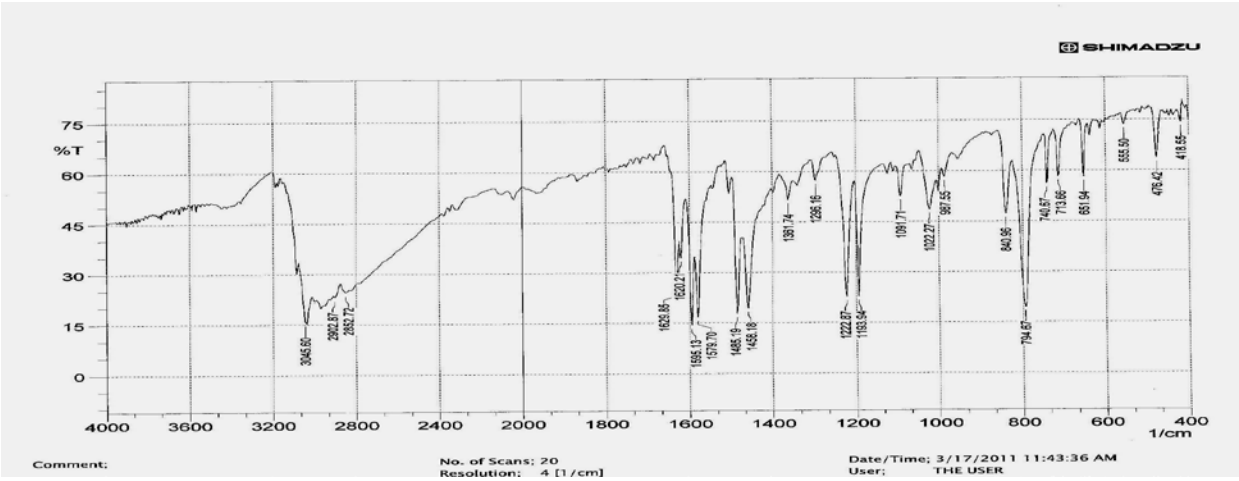

Figure (3. 6) IR spectrum of L^2

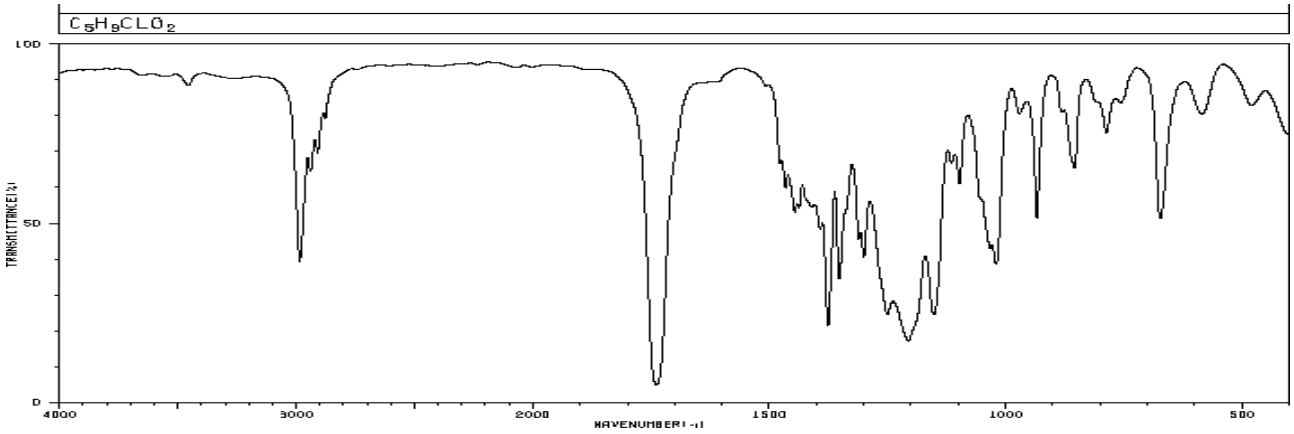

Figure (3.7)IR spectrum of ethyl chloropropionate.

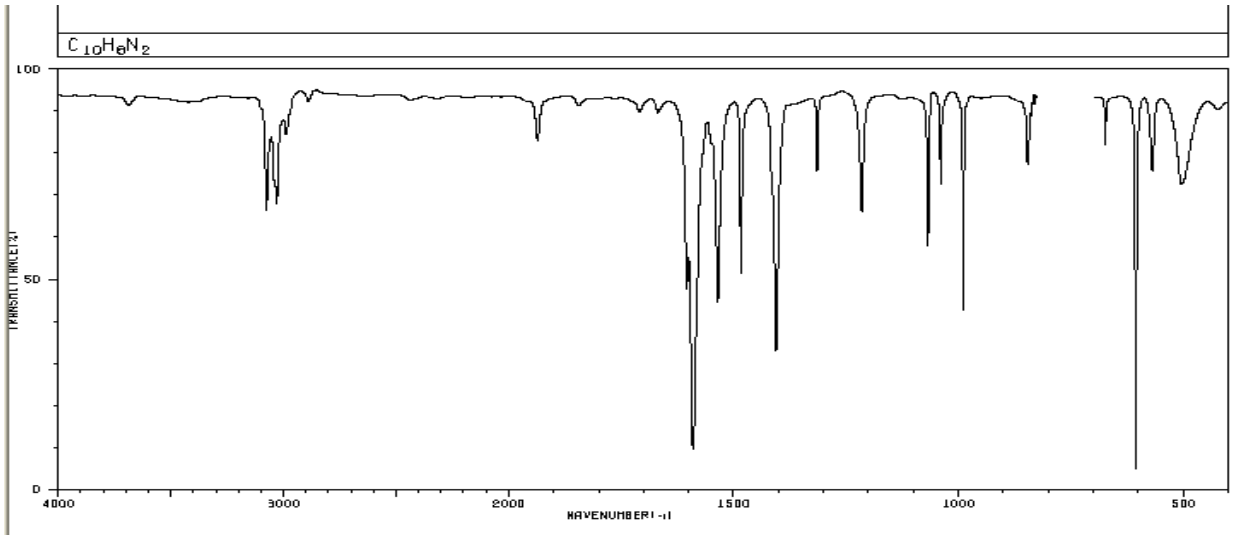

Figure (3. 3) IR spectrum of 4,4`-dipyridyl

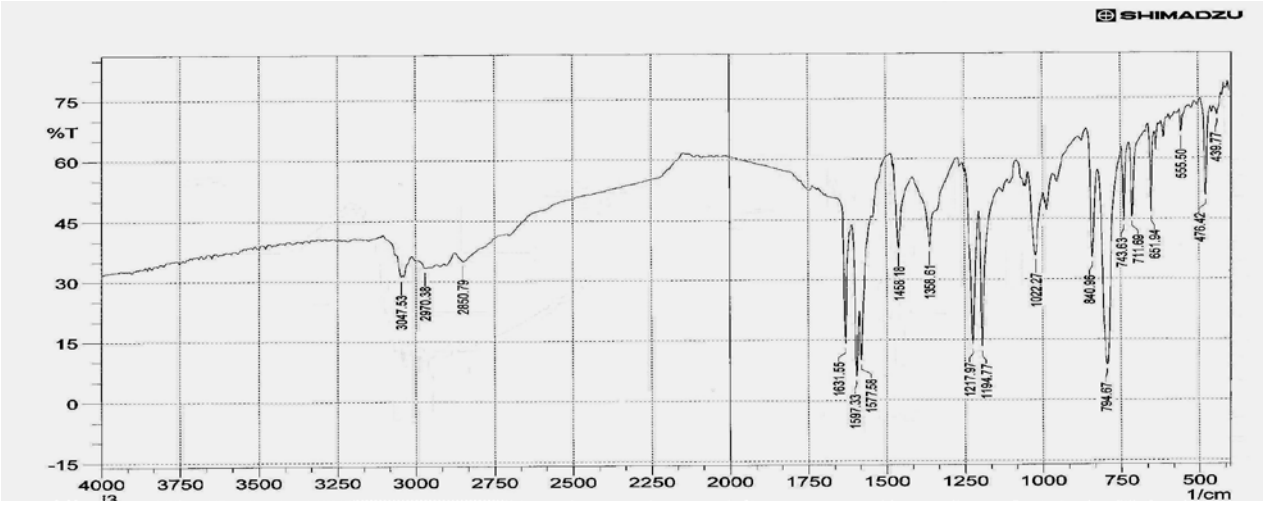

Figure (3. 8) IR spectrum of L^3

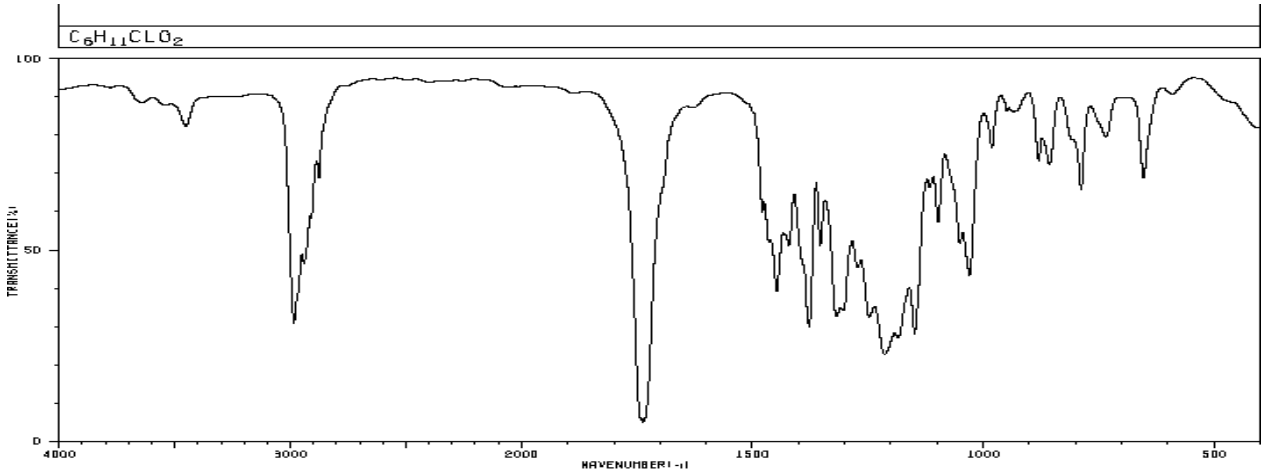

Figure (3. 9) IR spectrum of ethyl chlorobutyrate

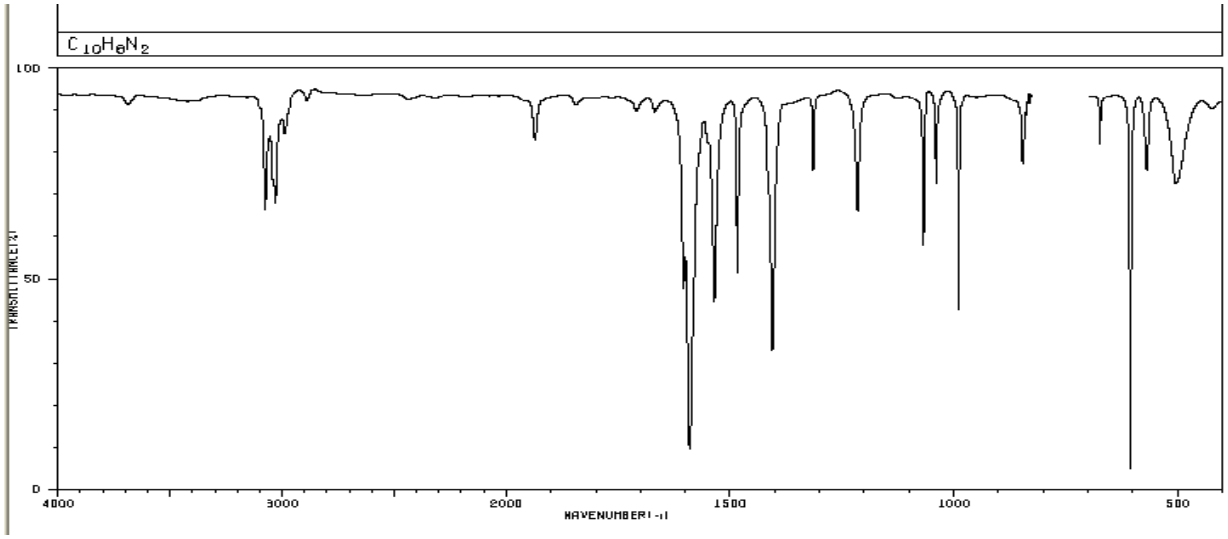

Figure (3. 3) IR spectrum of 4,4`-dipyridyl

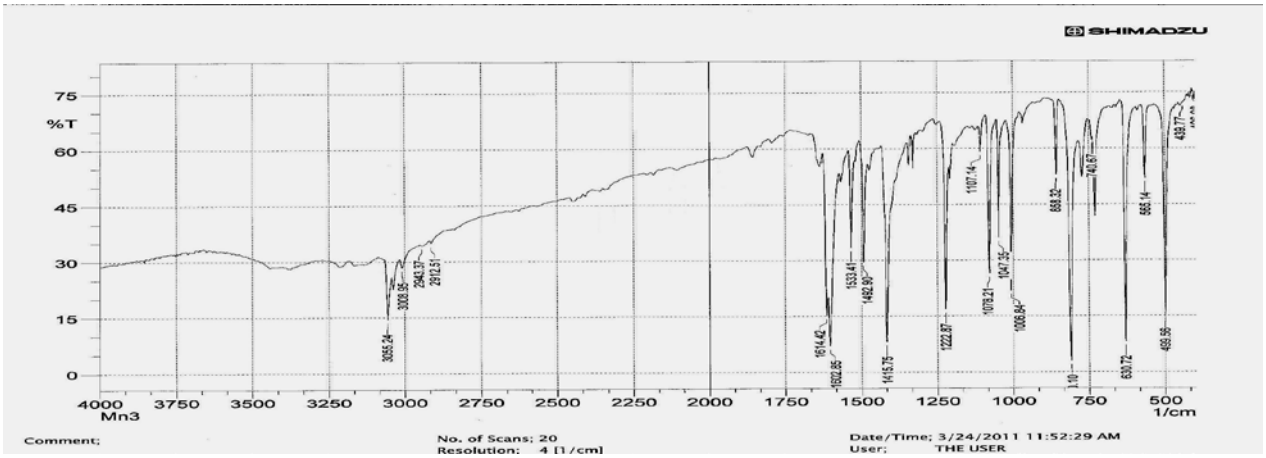

Figure 1(3. 10) IR spectrum of L^4

(3.4) IR Spectral data for the ligands with spacer

(3.4.1) IR spectrum of 1,3-bis(N-carboxymethyl-4-pyridino)propane L^5

The IR spectrum of 1,3-bis(N-carboxymethyl-4-pyridino)propane L^5, Figure (3. 12) is compared with IR spectra of starting materials trimethylen-4,4-dipyridine Figure (3. 11) and ethyl chloroacetate Figure (3-2), respectively. The spectrum of L^5 shows no band around 1759 cm^{-1} could attribute to ν_{as}(C=O) stretching in comparison with ethyl chloroacetate spectrum. The new band at 1643 can be attributed to ν_{as}(COO) stretching of carboxylate[164, 169]. The band at 1618 cm^{-1} attributed to stretching of ν(C=N) stretching[166], which shifted to higher frequency compared with trimethylen-4,4-dipyridyl. The band at 1572 cm^{-1} can be attributed to ν(C=C) stretching of aromatic ring[167], this band was shifted to higher frequency. The band at 1429 can be attributed to ν_s(COO) stretching[164]. The band at (1472 and 1387cm^{-1}) can be attributed to $\delta(CH_2)$ stretching[168]. The band at 1194 cm^{-1} attributed to ν(C-N) stretching[168]. The above result are syummarisd in Table (3. 4).

Table (3. 4): Infrared spectral data (wave number) cm^{-1} of the ligand L^5.

compound	ν_{ar} C-H	ν_{ali} C-H	ν_{as}COO	νC=N	νC=C	ν_sCOO	δ CH_2	ν C-N	$\Delta(\nu_{as}-\nu)$
L^5	3049	2936	1643	1618	1572	1429	1472 1387	1194	214

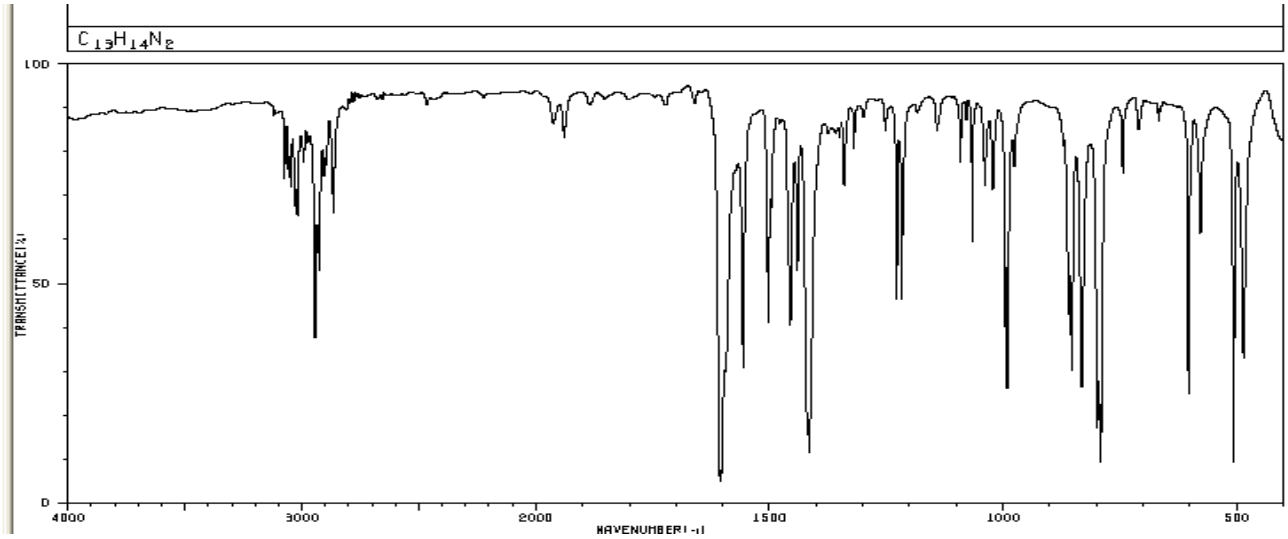

Figure (3. 11) IR spectrum of trimethylen-4,4`-dipyridine

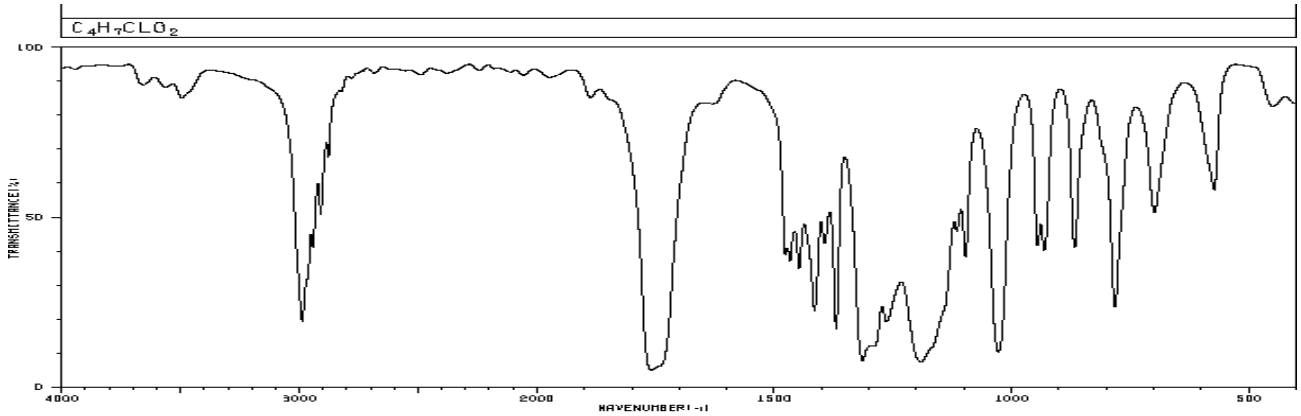

Figure (3. 2) IR spectrum of ethyl chloroacetate

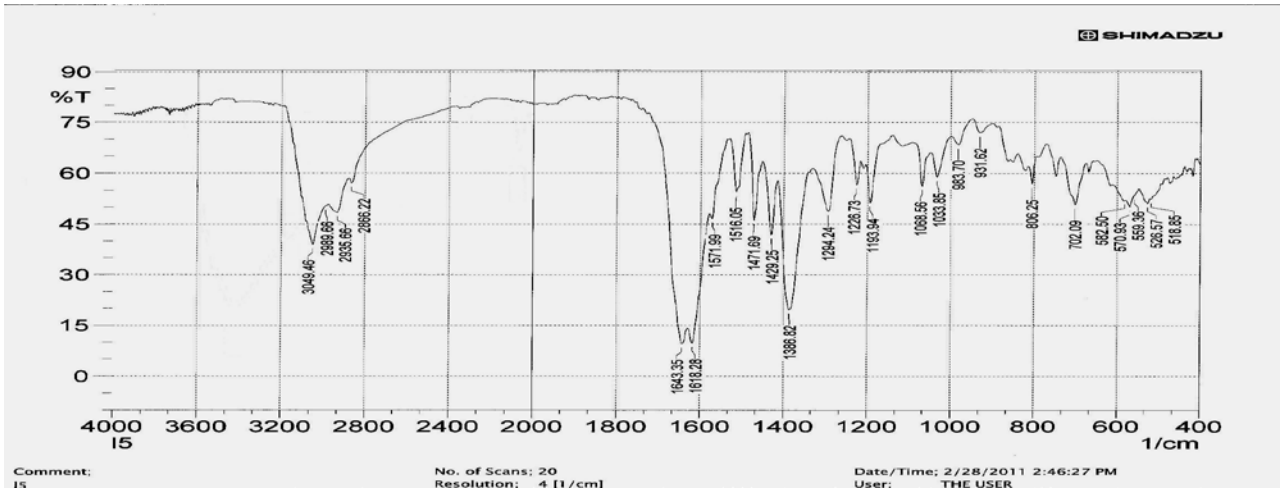

Figure (3. 12) IR spectrum of L^5

(3.5) UV-Vis Spectra of the ligands

(3.5.1) UV-Vis spectra of the ligands with and with out spacer

(3.5.1.1) UV-Vis spectrum of L^1

The UV-Vis spectrum of L^1 , Figure (3. 13) shows one absorption peak at (268 nm) (37313 cm^{-1}) (ε_{max}= 1130 $molar^{-1}$ cm^{-1}) assigned to ($\pi \rightarrow \pi^*$) transition, Table (3-5).

(3.5.1.2) UV-Vis spectrum of L^2

The UV-Vis spectrum of L^2 , Figure (3. 14) shows one absorption peak at (261 nm) (38314 cm^{-1}) (ε_{max} = 2119 $molar^{-1}$ cm^{-1}) assigned to ($\pi \rightarrow \pi^*$) transition, Table (3-5).

(3.5.1.3) UV-Vis spectrum of L^3

The UV-Vis spectrum of L^3, Figure (3. 15) shows one absorption peak at (279 nm) (35842 cm^{-1}) (ε_{max}= 2046 $molar^{-1}$ cm^{-1}) assigned to ($\pi \rightarrow \pi^*$) transition, Table (3-5).

(3.5.1.4) UV-Vis spectrum of L^4

The UV-Vis spectrum of L^4, Figure (3. 16) shows one absorption peak at (267 nm) (37453 cm^{-1}) (ε_{max}= 1531 $molar^{-1}$ cm^{-1}) assigned to ($\pi \rightarrow \pi^*$) transition, Table (3. 5).

(3.5.2) UV-Vis spectrum of L^5

The UV-Vis spectrum of L^5, Figure (3. 17) shows one absorption peak at (261 nm) (38314 cm^{-1}) (ε_{max}= 1680 $molar^{-1}$ cm^{-1}) assigned to the overlap of ($\pi \rightarrow \pi^*$)

transition, while the peak at (357 nm) (28011 cm^{-1}) (ε_{max}= 36 $molar^{-1}$ cm^{-1}) can be assigned to (n $\rightarrow \pi^*$) Table (3. 5).

Table (3. 5) Electronic spectral data for the ligands

Compound	Band Position λ_{nm}	Wave number (cm^{-1})	Extinction coefficient ε_{max} ($dm^3\ mol^{-1}\ cm^{-1}$)	Assignment
L^1	268	37313	1130	$\pi \rightarrow \pi^*$
L^2	261	38314	2119	$\pi \rightarrow \pi^*$
L^3	279	35842	2046	$\pi \rightarrow \pi^*$
L^4	267	37453	1531	$\pi \rightarrow \pi^*$
L^5	261 357	38314 28011	1680 36	$\pi \rightarrow \pi^*$ n $\rightarrow \pi^*$

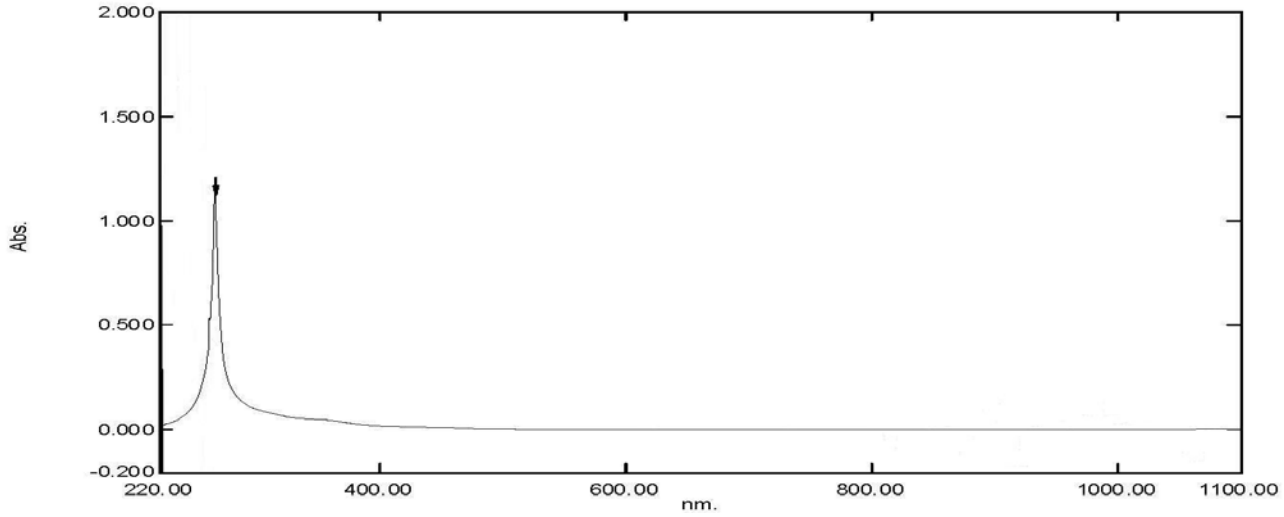

Figure (3. 13) Electronic spectrum of L^1

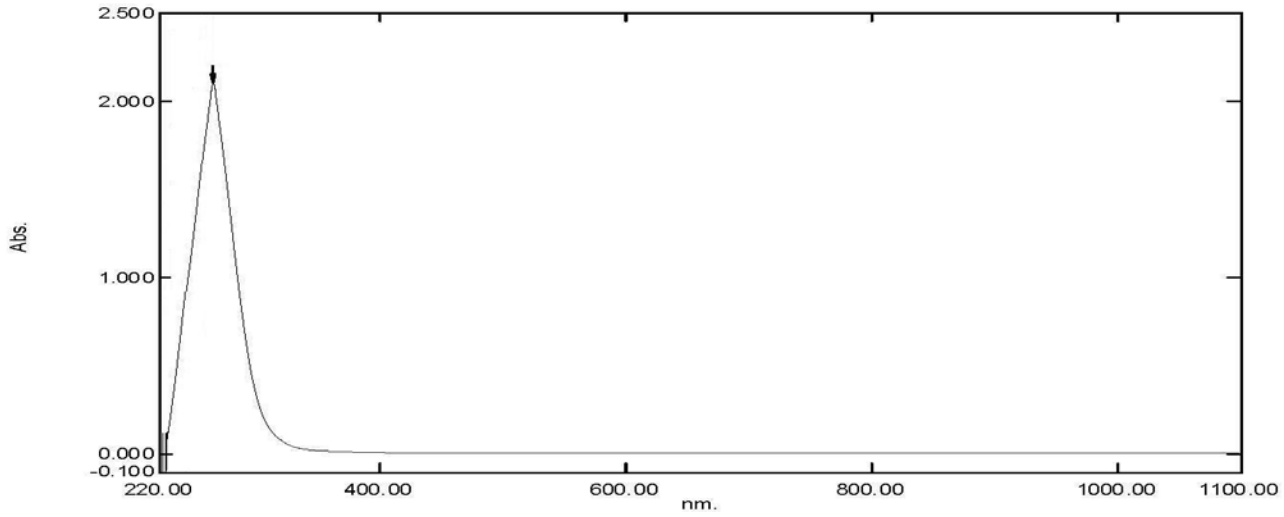

Figure(3. 14) Electronic spectrum of L^2

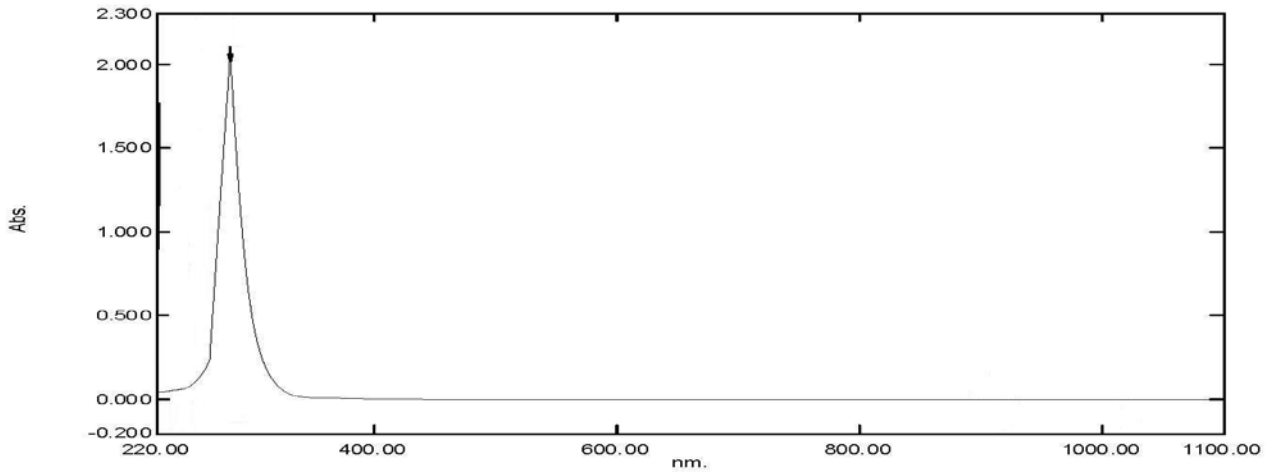

Figure (3-15) Electronic spectrum of L^3

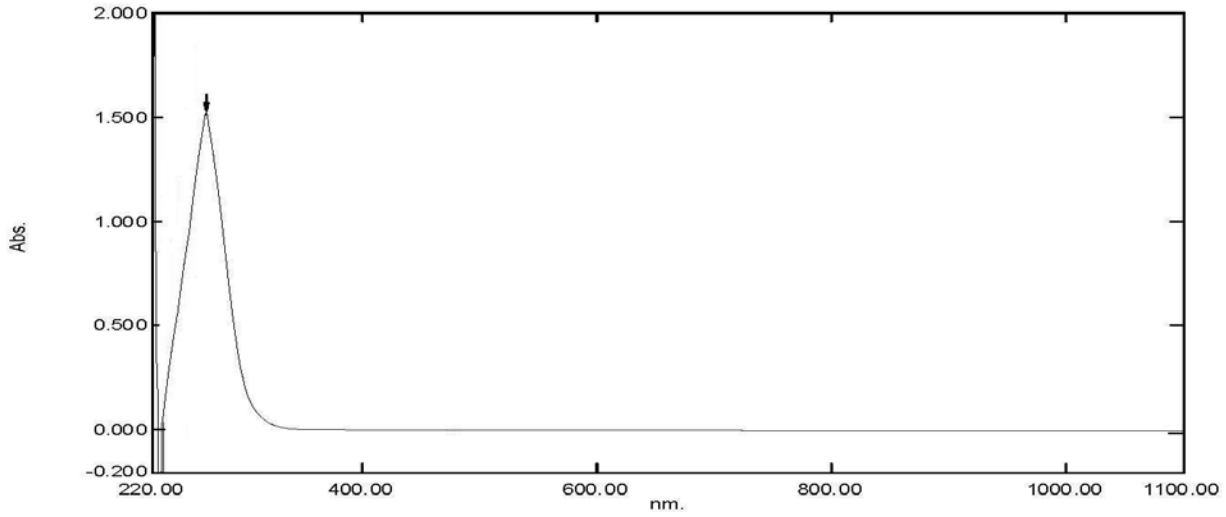

Figure (3. 16) Electronic spectrum of L^4

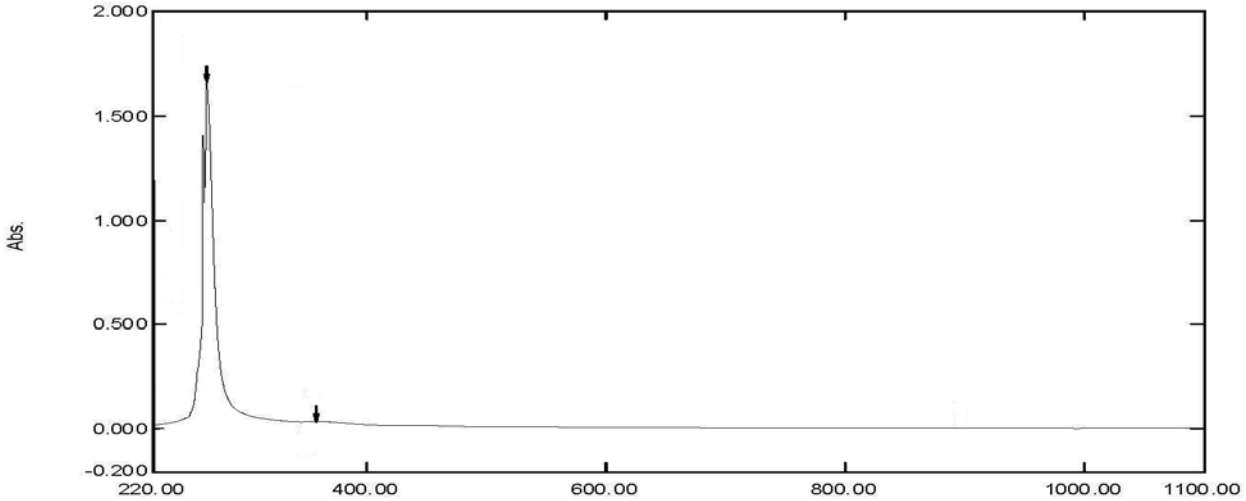

Figure(3. 17) Electronic spectrum of L^5

(3.6) ^{1}H, ^{13}C and DEPT NMR spectra for the ligands without spacer

The ^{1}H, ^{13}C and DEPT NMR analysis was used to characterise the structure of ligands. The samples were recorded in DMSO-d6 solutions.

(3.6.1) ^{1}H ^{13}C NMR spectra for the ligand L^{1}

(3.6.1.1) ^{1}H NMR spectrum for the ligand L^{1}

Analysis of the ^{1}H NMR spectrum for L^{1} in DMSO-d_6, shows two conformational isomers Figure (3. 18). Isomer A shows chemical shift at δ = 5.72 ppm equivalent to 4 protons which assigned to ($C_{2,\ 2}$-*H*). This peak is shifted downfield, in comparison with that in the ethyl chloroacetate, due to its attachment to the nitrogen atom, electron withdrawing group, and therefore the (CH_2) group is deshielded and appeared at a higher chemical shift. The signals at (δ = 8.71-8.73 ppm, 4H, d, J_{HH} = 6.87 Hz) attributed to ($C_{4,\ 4}$; $_{6,\ 6}$-*H*). The chemical shifts of ($C_{3,\ 3}$; $_{7,\ 7}$-*H*) protons appear as a doublet at (9.23-9.25 ppm, 4H, d, J_{HH} = 7.33 Hz). Isomer B displays chemical shift at 5.78 ppm equivalent to 4 H which assigned to ($C_{2,\ 2}$-*H*) protons. Peaks at δ = 8.63-8.65 ppm (1H, d, J_{HH} = 6.87 Hz), and δ = 8.85-8.87 ppm (3H, d, J_{HH} = 7.33 Hz) were assigned to ($C_{4,\ 4}$; $_{6,\ 6}$-*H*) protons. The signals at δ = 8.78-8.79 ppm (3H, d, J_{HH} = 6.87 Hz) and at δ = 9.18-9.20 ppm (1H, d, J_{HH} = 6.87 Hz) assigned to ($C_{3,\ 3}$; $_{7,\ 7}$-*H*) protons. The appearance of two isomers is perhaps due to the ease of rotation of the chelating portion of the molecule and/or the ease of rotation of the two pyridyl molecules; slow rotation could give one or two conformations that are not symmetrical. The results are summarised in Table (3. 6).

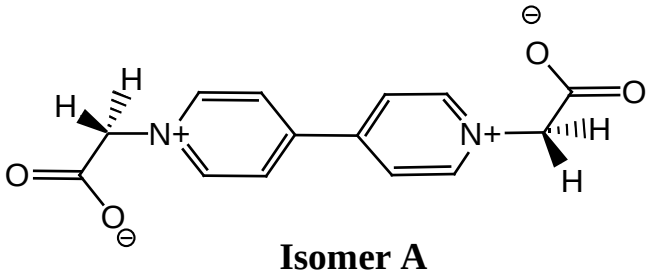

Isomer A

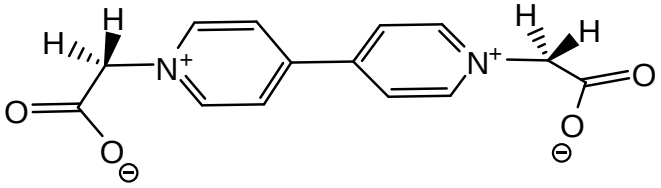

Isomer B

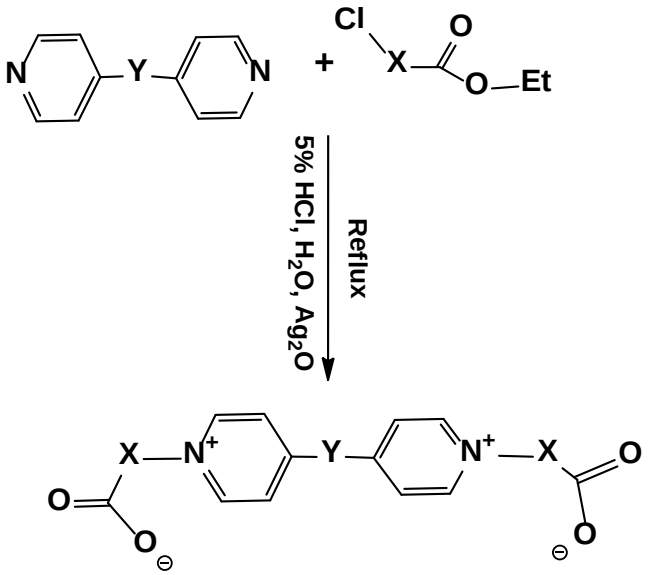

Where:
X = 0; Y = 0; L^2
X = CH_2; Y = 0; L^1
X = CH_2CH_2; Y = 0; L^3
X = $CH_2CH_2CH_2$; Y = 0; L^4
X = CH_2; Y = $CH_2CH_2CH_2$; L^5

Scheme(3.2) Structure of carboxylate *syn-syn* and *syn-anti*

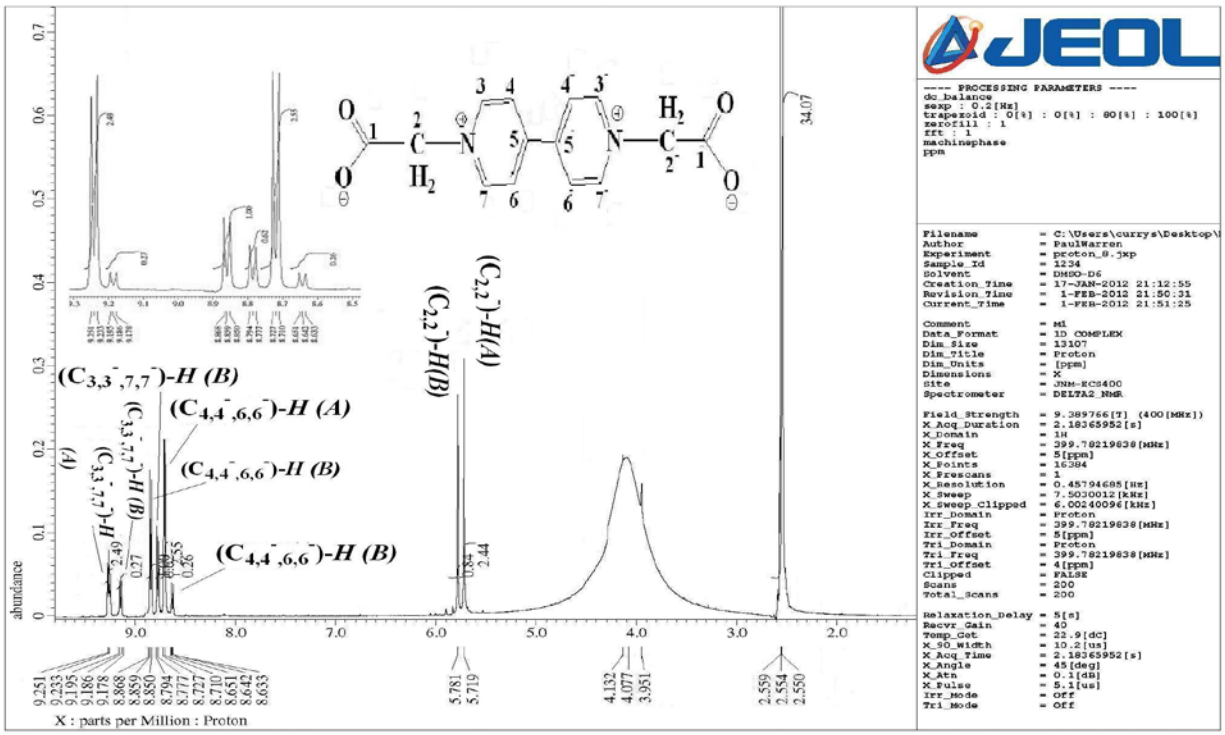

Figure (3. 18) ^{1}H NMR spectrum in DMSO-d6 of L^{1}

(3.6.1.2) ^{13}C NMR spectrum for the ligand L^{1}

^{13}C NMR spectrum of L^{1}, Figure (3. 19), shows the chemical shifts of ($C_{2,\,2}$`) are nonequivalent and appear at 60.01 and 60.92 ppm. This is due to the presence of two isomers in solution, A and B. The chemical shift at 126.59 and 126.80 ppm assigned to ($C_{4,\,4}$`; $_{6,\,6}$`). Signals related to ($C_{3,\,3}$`; $_{7,\,7}$`) were detected at 144.01 and 149.02. Chemical shifts at 152.73 and 152.76 ppm were attributed to ($C_{5,\,5}$`) indicating the two signals are nonequivalent. The chemical shift of the C=O of the carboxylate moiety appears as expected downfield at 174.35 and 169.09 ppm. The results are summarised in Table (3. 7).

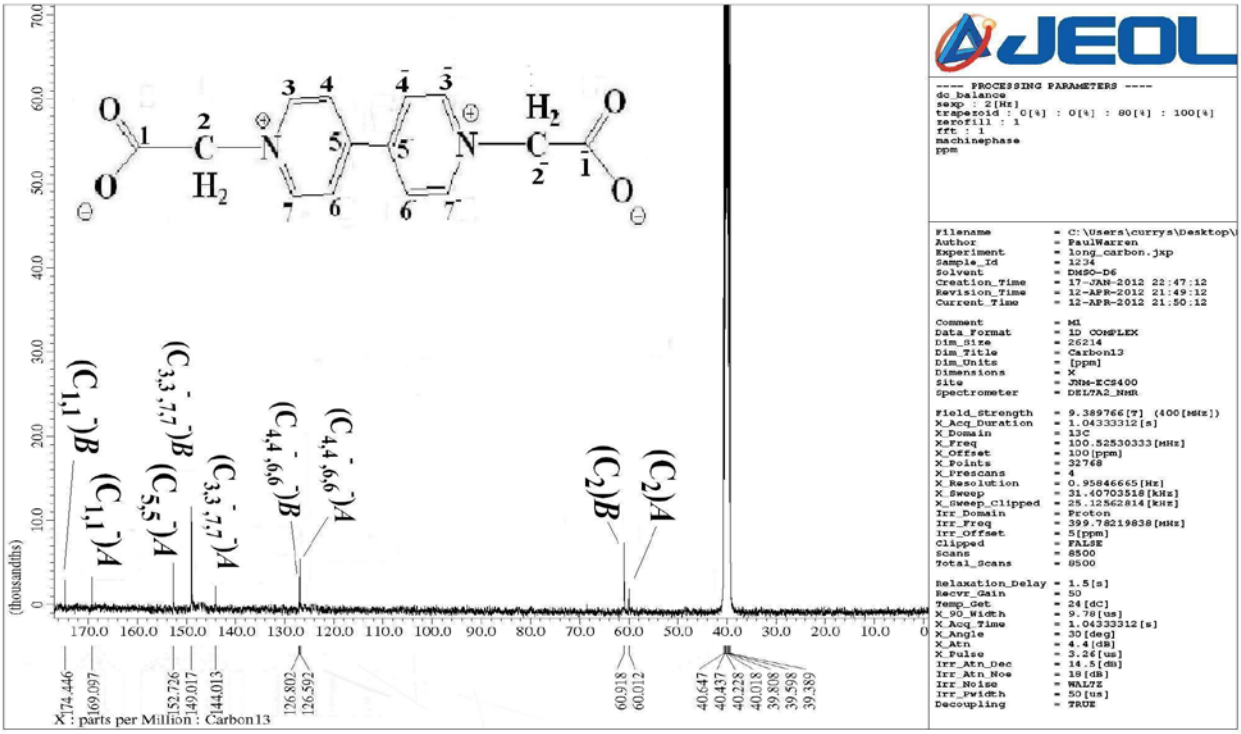

Figure (3. 19) ^{13}C NMR spectrum in DMSO-d6 of L^1

(3.6.1.3) DEPT ^{13}C-NMR

DEPT (Distortionless Enhancement of Polarisation Transfer) is one of NMR technique which can be used to identify the number of attached proton. In a DEPT experiment, a sequence of pulses with various delay times are used to create the DEPT spectrum where (-CH_3) and (-CH) peaks will enhance in the positive direction (up) and appear as normal. The (-CH_2) peaks enhance in the negative direction (down) and appear inverted. Quaternary carbon is not usually seen. This way the number of H attached to C can usually be deduced(170).

DEPT ^{13}C NMR spectrum for the ligand L^1

DEPT ^{13}C NMR spectrum for L^1, Figure (3. 20), reveals the ($C_{2,\ 2}$) are nonequivalent and appear as two signals at 60.01 and 60.92 ppm. These peaks were enhanced in the negative direction (down), and therefore assigned to (-CH_2)

group. Signals at chemical shifts 126.59; 126.80 and 144.0; 149.02 ppm were assigned to ($C_{4,\ 4'}$; $_{6,\ 6'}$) and ($C_{3,3'}$; $_{7,\ 7'}$), respectively. These signals enhance in the positive direction (up), and therefore assigned to (-CH). No signals in the range 150 -170 ppm, may assign for ($C_{5,\ 5'}$) and ($C_{1,\ 1'}$) are detected[130].

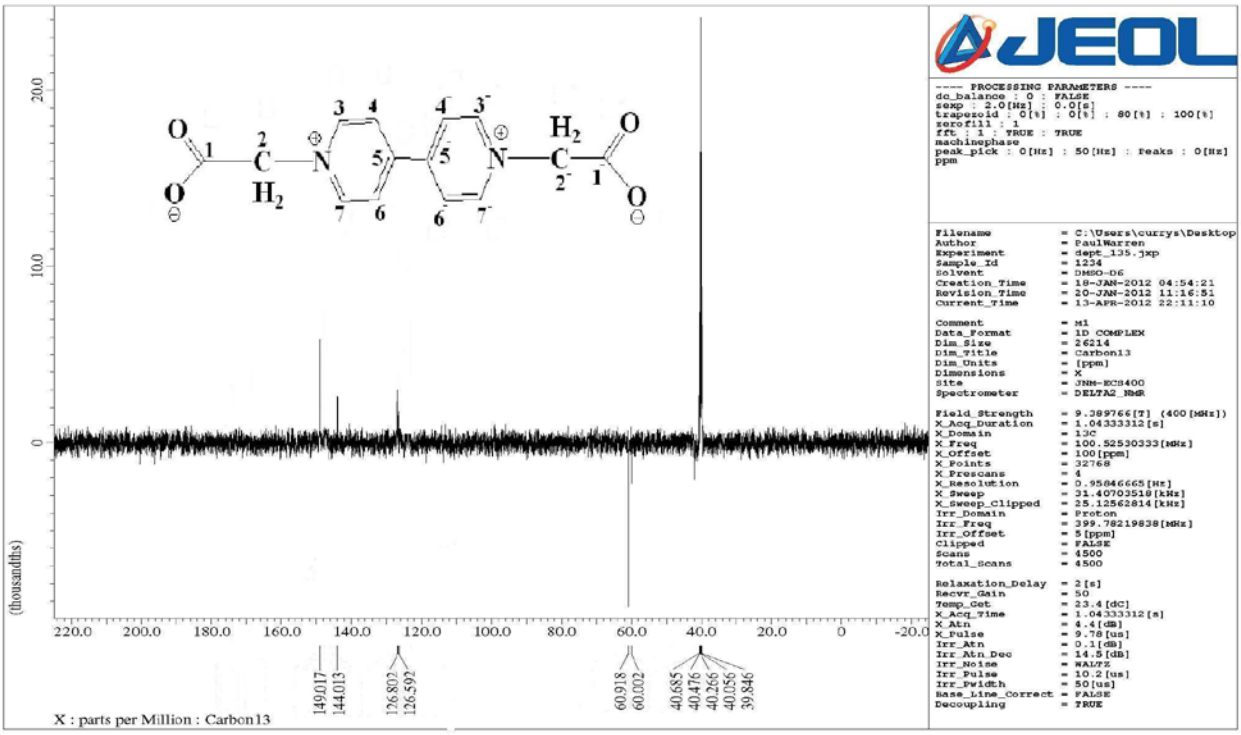

Figure (3. 20) DEPT ^{13}C NMR spectrum in DMSO-d6 of L^1

(3.6.2) ^{1}H , ^{13}C NMR spectra for the ligand L^2

(3.6.2.1) ^{1}H NMR spectrum for the ligand L^2

Analysis of the ^{1}H NMR spectrum for L^2, Figure (3. 21) shows chemical shift at δ = 9.05-9.06 ppm(4H, d, J_{HH}=6.0 Hz) attributed to ($C_{3,\ 3'}$; $_{5,\ 5'}$-*H*) protons. The signals of ($C_{2,\ 2'}$, $_{6,\ 6'}$-*H*) protons appear as a doublet at δ=9.10 - 9.12 ppm (4H, d, J_{HH}=6.0 Hz) . The results are summarised in Table (3. 6)[130].

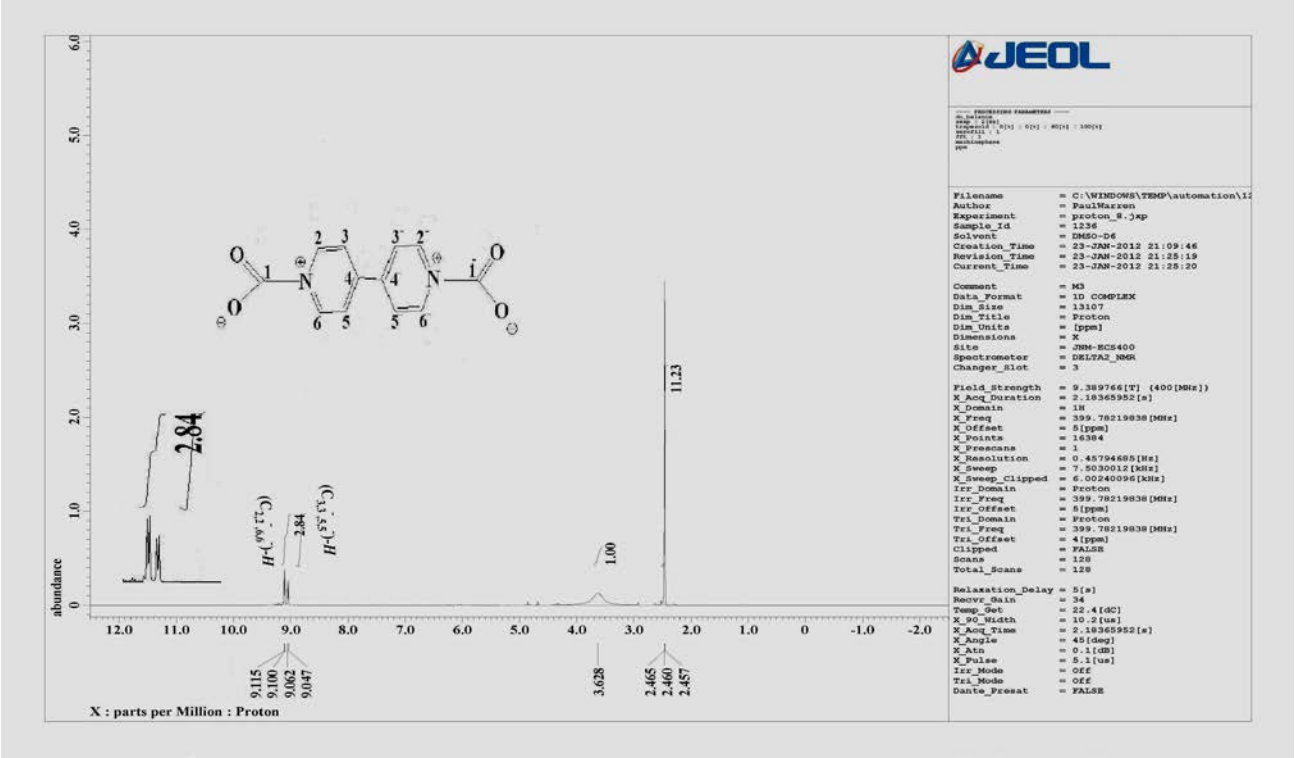

Figure (3. 21) ^{1}H NMR spectrum in DMSO-d6 of L^{2}

(3.6.2.2) ^{13}C NMR spectrum for the ligand L^{2}

The ^{13}C NMR spectrum for L^{2}, Figure (3. 22), shows chemical shift at δ = 125.46 ppm assigned to ($C_{3,3^{-};\ 5,5^{-}}$). Signals related to ($C_{2,2^{-};\ 6,6^{-}}$) were equivalent and detected at δ =150.90 ppm. Chemical shifts at δ =151.52 and 151.56 ppm, were attributed to ($C_{4,4^{-}}$). The chemical shift of the C=O of the

carboxylate moiety appears as expected downfield at δ=173.01 ppm. The results are summarised in Table (3. 7).

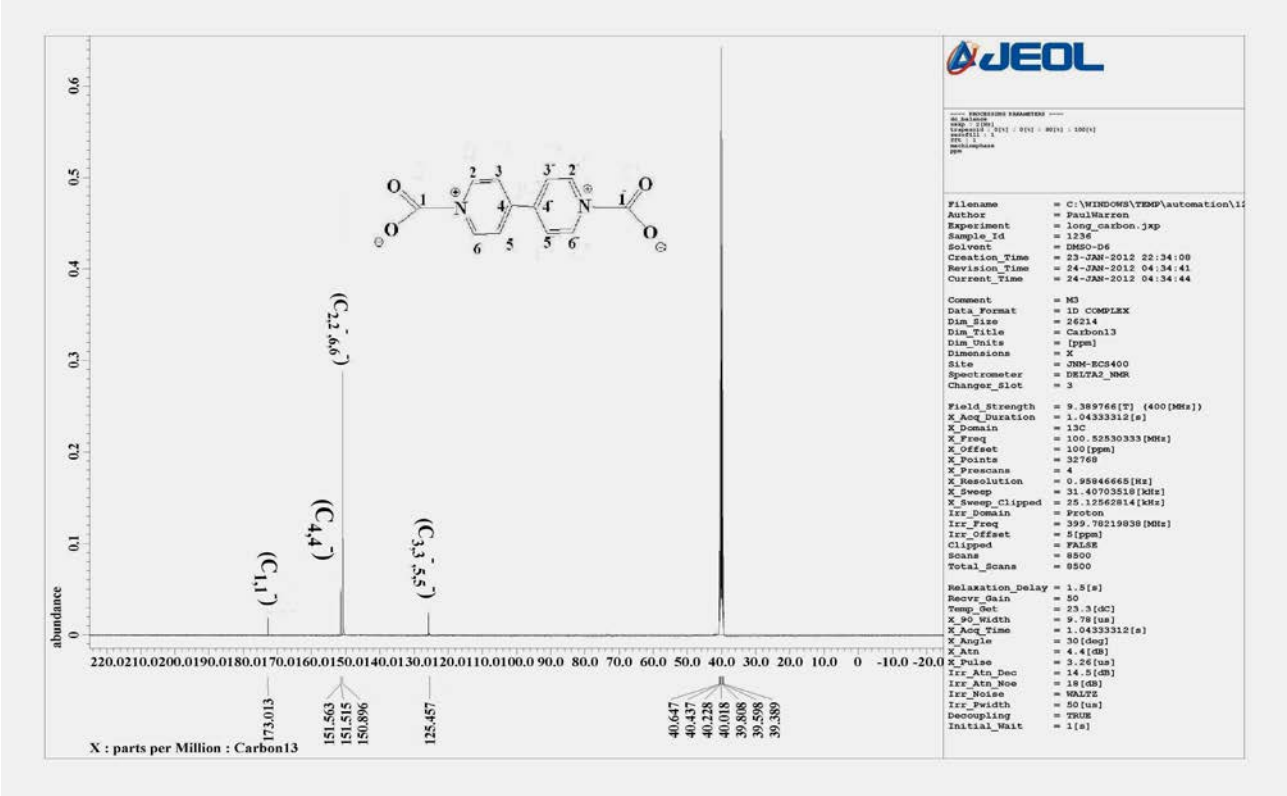

Figure (3. 22) ^{13}C NMR spectrum in DMSO-d6 of L^2

(3.6.2.3) DEPT ^{13}C NMR spectrum for the ligand L^2

DEPT ^{13}C NMR spectrum for L^2, Figure (3. 23), shows that all signals enhance in the positive direction (up), and therefore assigned to (-CH). No signals in the range 150- 175 ppm, may be assigned for ($C_{5,\ 5}^-$) and ($C_{1,\ 1}^-$) are detected. These signals are related to a quaternary carbon which is not usually seen in the spectrum.

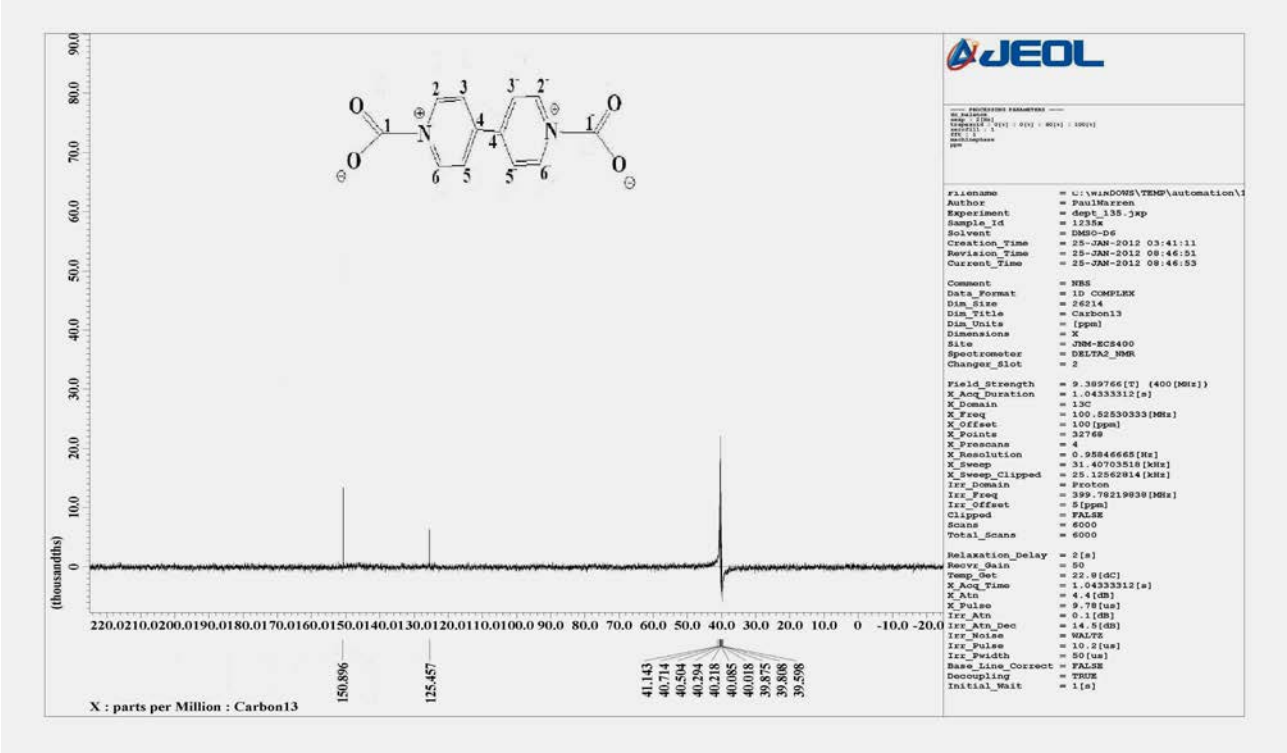

Figure(3. 23) DEPT ^{13}C NMR spectrum in DMSO-d6 of L^2

(3.6.3) ^{1}H, ^{13}C NMR spectra for the ligand L^3

(3.6.3.1) ^{1}H NMR spectrum for the ligand L^3

The ^{1}H NMR spectrum for L^3 is shown in Figure (3. 24). The spectrum shows chemical shift at δ = 2.31-2.33 (4H, t, J_{HH}=8 Hz) equivalent to 4 protons which assigned to ($C_{2,\ 2}$-*H*) protons. This signal is shifted to upfield due the attachment to electron withdrawing group, and therefore the (-CH_2) group is shielded and appeared at lower chemical shift. The signal at δ = 4.71-4.72 ppm(4H, t, J_{HH}= 6.8 Hz) equivalent to 4 protons assigned to ($C_{3,\ 3}$-*H*) protons. This peak is shifted to downfield due to its attachment to the nitrogen atom, electron withdrawing group, and therefore the (-CH_2) group is deshielded and appeared at higher chemical shift. The chemical shift of ($C_{5,\ 5}$; $_{7,\ 7}$-*H*) protons appeared as a doublet at δ=8.60-8.62 ppm(4H, d, J_{HH}=7.33 Hz). The signal at δ=9.13 -9.134 ppm (4H, d, J_{HH}=6.87 Hz) attributed to ($C_{4,}$

$_{4}^{-}$; $_{8,}$ $_{8}^{-}$ –*H*) protons. The results are summarised in Table (3. 6).

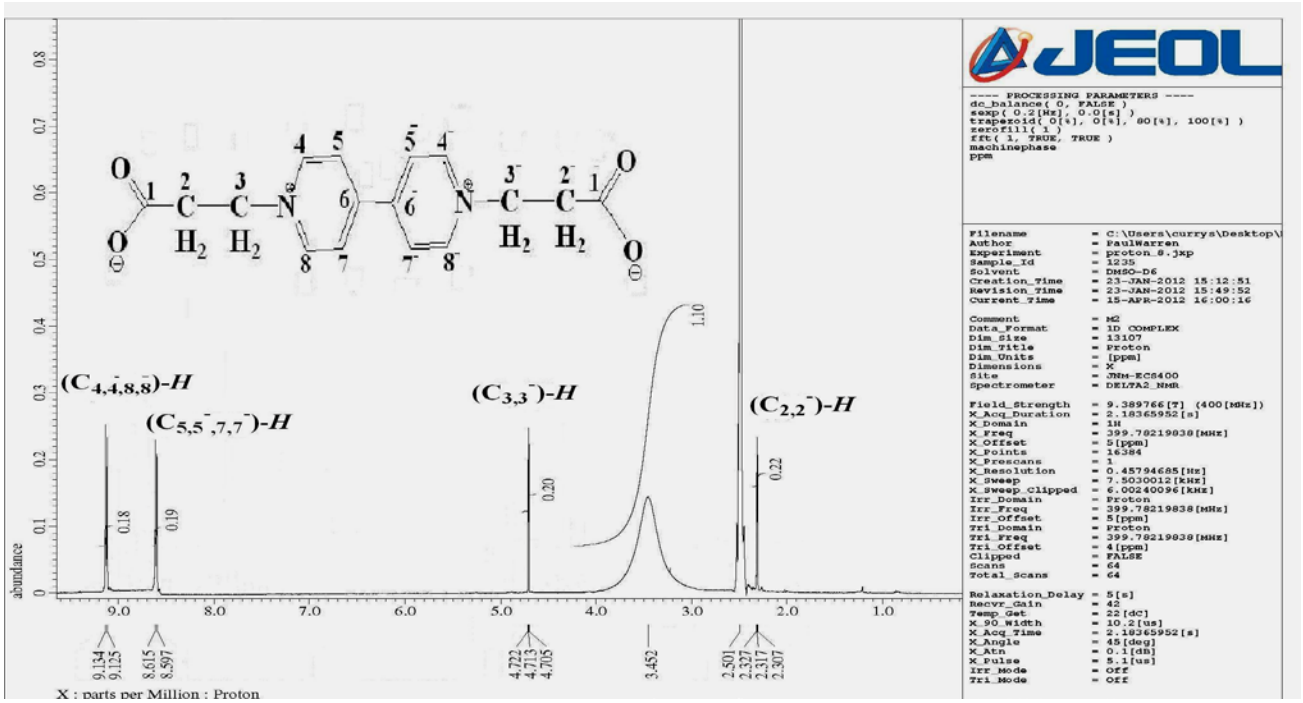

Figure (3. 24) ^{1}H NMR spectrum in DMSO-d6 of L^{3}

(3.6.3.2) ^{13}C NMR spectrum for the ligand L^{3}

The ^{13}C NMR spectrum for L^{3}, Figure (3. 25) shows chemical shift at δ= 29.99 ppm assigned to ($C_{2,\ 2}^{-}$). The signal related to ($C_{3,\ 3}$) was detected at δ=58.69 ppm. Chemical shifts at δ = 124.93; 125.24 and 145.70 ppm, were attributed to ($C_{5,\ 5}^{-}$; $_{7,\ 7}^{-}$ and ($C_{4,\ 4}^{-}$; $_{8,\ 8}^{-}$). The signal at δ=153.60 ppm assigned to ($C_{6,6}^{-}$).The chemical shift of the C=O of the carboxylate moiety appears, as expected, downfield at δ = 177.00 ppm. The results are summarised in Table (3. 7).

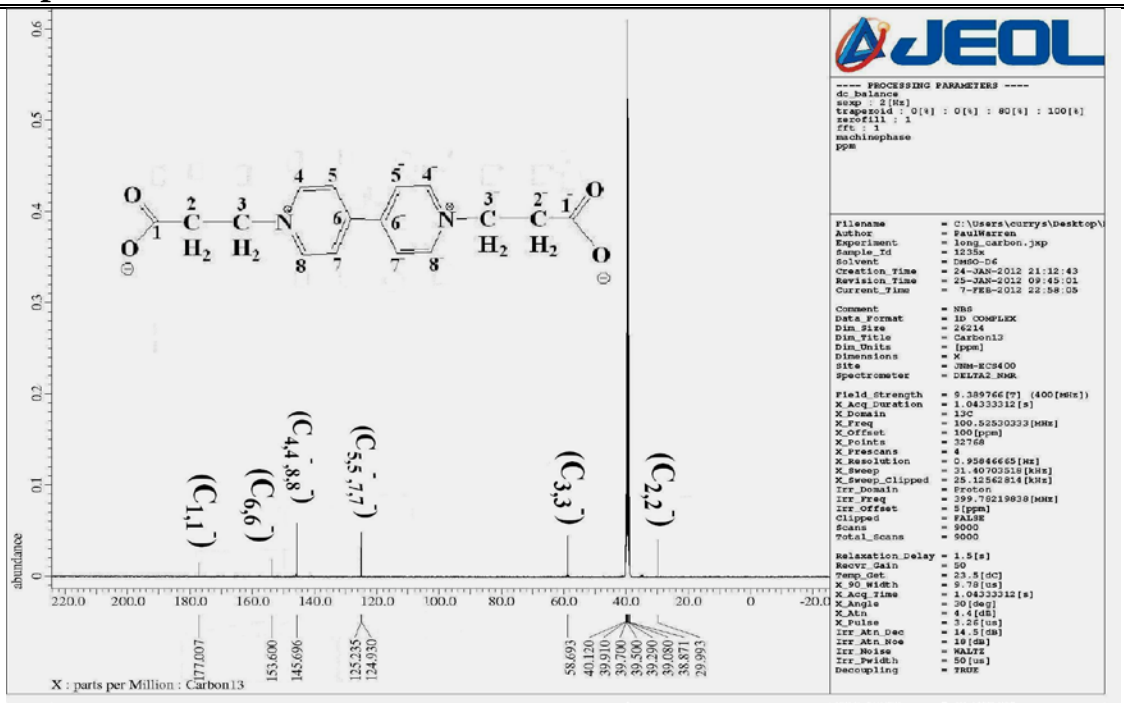

Figure (3. 25) ^{13}C NMR spectrum in DMSO-d6 of L^3

(3.6.3.3) DEPT ^{13}C NMR spectrum for the ligand L^3

DEPT ^{13}C NMR spectrum for L^3, Figure (3. 26), shows two signals at δ =29.99 and 58.69 ppm, attributed to (C_2, $_2$) and (C_3, $_3$), respectively. These peaks were enhanced in the negative direction (down), and therefore assigned to (-CH_2) group. Signals at chemical shift δ =124.93 and 145.70 ppm were assigned to ($C_{5,5}$; $_{7,7}$) and ($C_{4,4}$; $_{8,8}$), respectively. These signals enhanced in the positive direction (up), and therefore assigned to (-CH). No signals in the range of 153- 177 ppm may be assigned to ($C_{6,6}$) and ($C_{1,1}$) are detected. These signals are related to a quaternary carbon which is not usually seen in the spectrum..

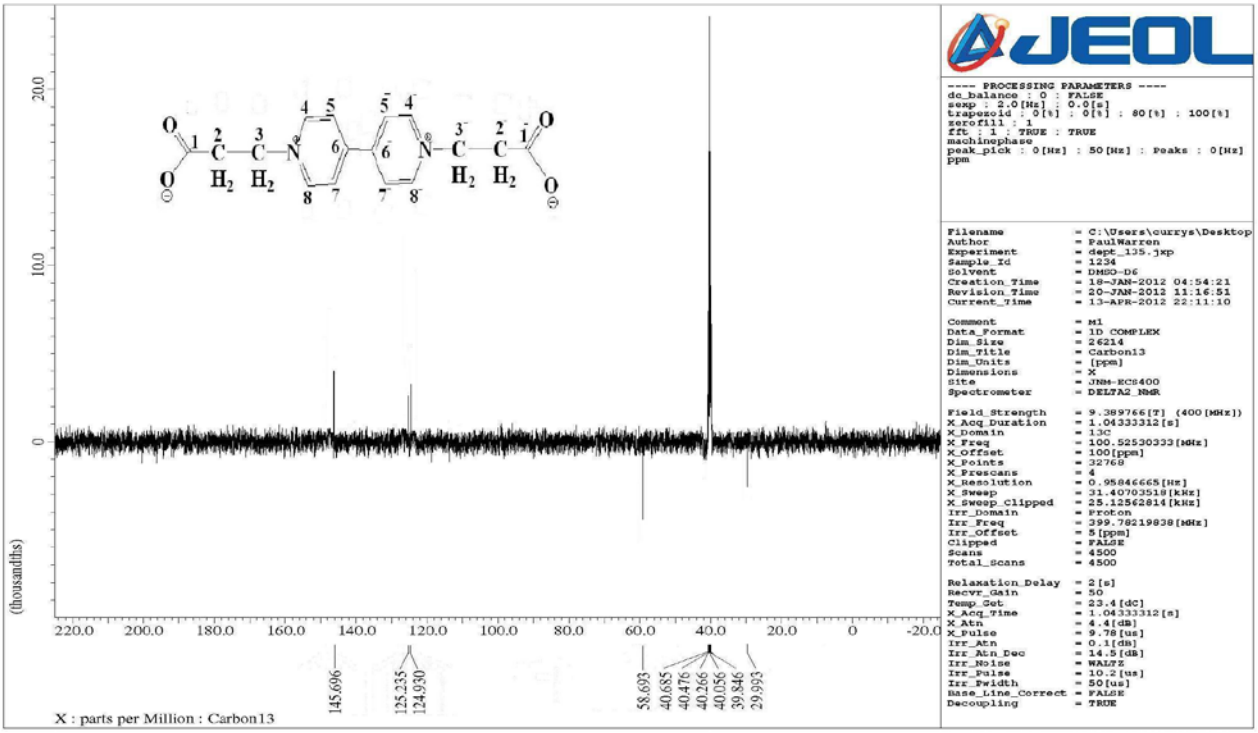

Figure(3. 26) Dept ^{13}C NMR spectrum in DMSO-d6 of L^{3}

(3.6.4) ^{1}H, ^{13}C NMR spectra for the ligand L^{4}

(3.6.4.1) ^{1}H NMR spectrum for the ligand L^{4}

The ^{1}H NMR spectrum for L^{4} is shown in Figure (3. 27). The spectrum displays chemical shift at δ = 2.16-2.23 ppm (4H, t, J_{HH}=7.33 Hz) and δ = 2.36-2.49 ppm (4H, t, J_{HH}=7.33 Hz) assigned to ($C_{3,3}$-*H*) and ($C_{2,2}$-*H*) protons, respectively, and each equivalent to 4 protons. These signals are shifted upfield due to the fact that, in each of the pyridinium portion the carboxylate group is almost co-planar with the CH_2 group and the pyridinium molecue. This can lead to the increase of the electron density, shifting the electron charge density from the carboxylate group, on the (CH_2) group and appeared at upfield position. The signal at chemical shift 4.68-4.72 ppm(4H, t, J_{HH}= 14.4 Hz) equivalent to 4 protons assigned to ($C_{4,4}$-*H*). This peak is

shifted to downfield and can be explain according to above explanation. Other chemical shifts are summarised in Table (3. 6).

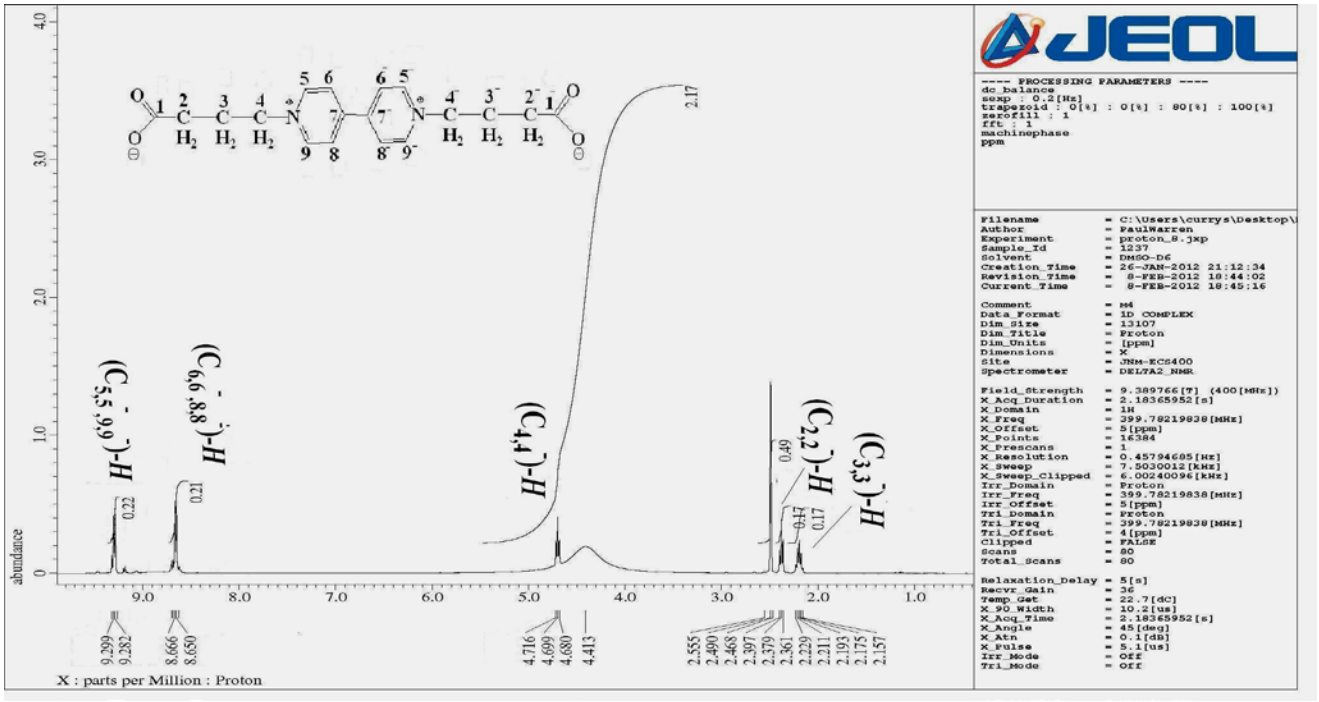

Figure (3. 27) ^{1}H NMR spectrum in DMSO-d6 of L^4

(3.6.4.2) ^{13}C NMR spectrum for the ligand L^4

The ^{13}C NMR spectrum for L^4, Figure (3. 28) shows chemical shift at δ = 26.08, δ=30.23 and 59.77 ppm assigned to ($C_{3,\ 3}^{-}$), ($C_{2,\ 2}^{-}$) and ($C_{4,\ 4}^{-}$), reapectively. The chemical shifts at δ = 125.69, 145.93 and 152.17 ppm attributed to ($C_{6,\ 6}^{-}$; $_{8,\ 8}^{-}$). ($C_{5,\ 5}^{-}$; $_{9,\ 9}^{-}$) and ($C_{7,\ 7}^{-}$), respectively. The chemical shift of the C=O of the carboxylate moiety appears as expected downfield at δ = 173.38 ppm. The results are summarised in Table (3. 7).

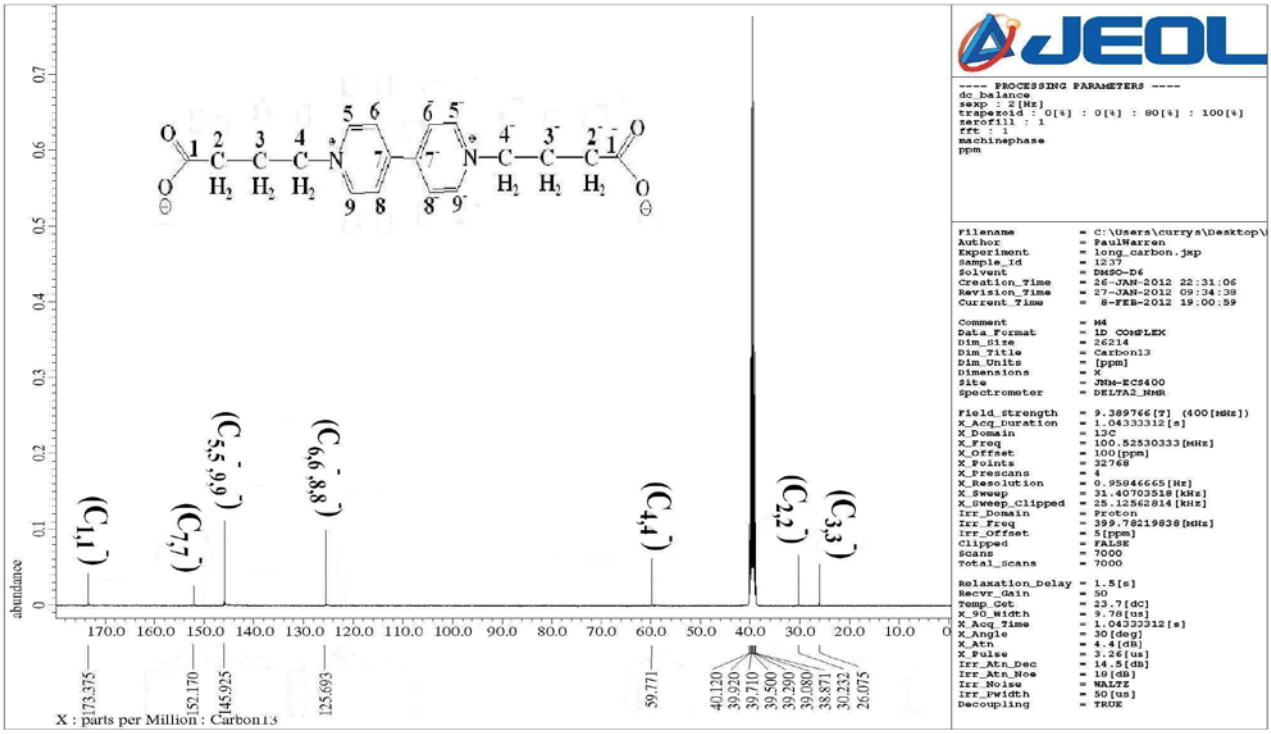

Figure (3. 28) ^{13}C NMR spectrum in DMSO-d6 of L^4

(3.6.4.3) DEPT ^{13}C NMR spectrum for the ligand L^4

DEPT ^{13}C NMR spectrum for L^4, Figure (3. 29) shows three signals at δ = 26.08, 30.23 and 59.77 ppm assigned to ($C_{3,\ 3}^{-}$), ($C_{2,2}^{-}$) and ($C_{4,\ 4}^{-}$), respectively. These peaks were enhanced in the negative direction (down), and therefore assigned to (-CH_2) group. The other signals in the range 125-145 ppm, are assigned to ($C_{6,\ 6}^{-}$; $_{8,\ 8}^{-}$) and ($C_{5,\ 5}^{-}$; $_{9,\ 9}^{-}$), respectively. These signals enhanced in the positive direction (up), and therefore assigned to (-CH). No signals around chemical shifts 152.0 and 170.0 ppm may assign for ($C_{7,7}^{-}$)and ($C_{1,1}^{-}$) are detected. These signals are related to a quaternary carbon which is not shown in the spectrum.

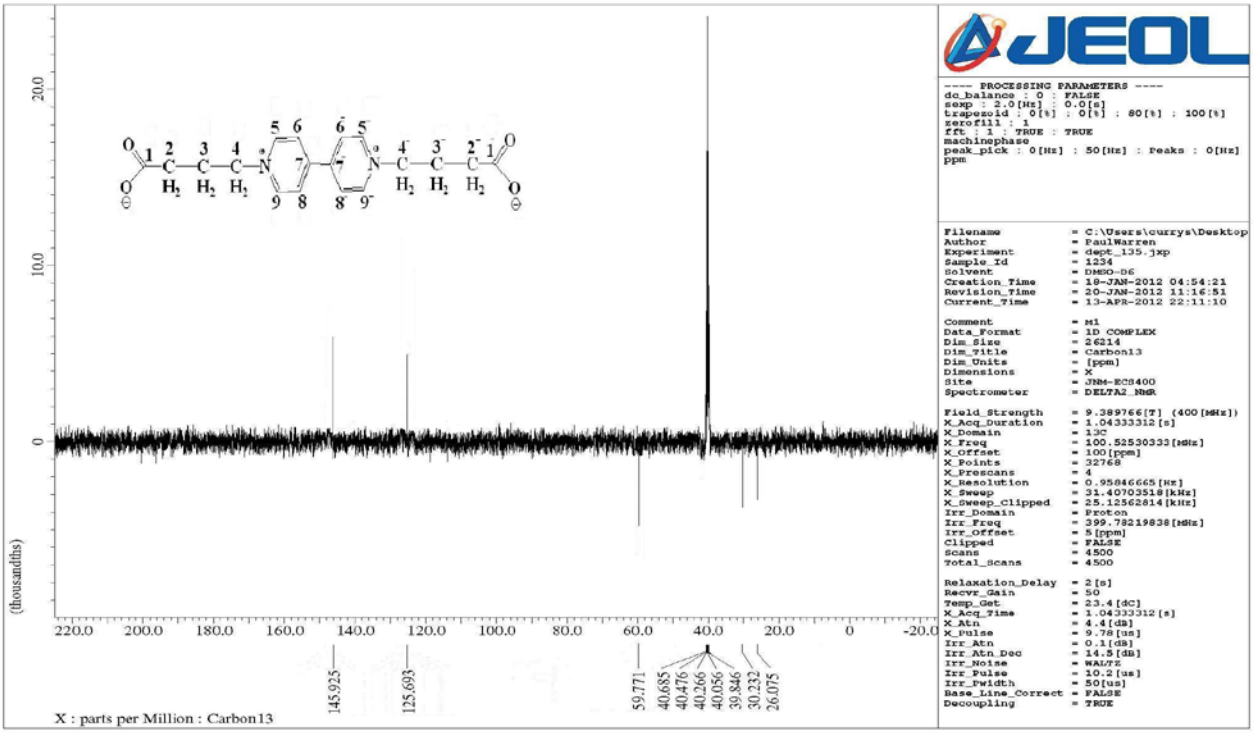

Figure(3. 29) DEPT ^{13}C NMR spectrum in DMSO-d_6 of L^4

(3-7) ^{1}H, ^{13}C NMR spectra for the ligands with spacer

(3.7.1) ^{1}H, ^{13}C NMR spectra for the ligand L^5

(3.7.1.1) ^{1}H NMR spectrum for the ligand L^5

The ^{1}H NMR spectrum for L^5, Figure (3. 30) shows chemical shift at δ =1.90-2.14 ppm (2H, m) assigned to (C_9-*H*) protons. The signal at δ = 2.70-2.73 ppm (2H, t, J_{HH}= 12.8 Hz) and at δ =2.89-2.92 ppm (2H, t, J_{HH}= 9.6 Hz) assigned to ($C_{8,\ 10}$-*H*) proton. The appearance of two signals is perhaps due to the ease of rotation of the chelating portion of the molecule and/or the ease of rotation of the two pyridyl molecules. These signals are shifted to upfield due to not contact to electron withdrawing group, and therefore the (-CH_2) group is shielding and appeared at lower chemical shift. The chemical shift at δ = 4.27-4.30 ppm (4H d, J_{HH}= 11.2 Hz) assigned to ($C_{2,\ 2'}$-*H*) protons. The

signal at δ = 7.49 - 7.53 ppm (4H, d, J_{HH}= 16 Hz) attributed to ($C_{4,4'}$; $_{6,6'}$-*H*) protons. The chemical shifts of ($C_{3,3'}$; $_{7,7'}$-*H*) protons appear as a doublet at δ 8.61 -8.62 ppm (4H, d, J_{HH}=4.4 Hz). The results are summarised in Table (3. 6).

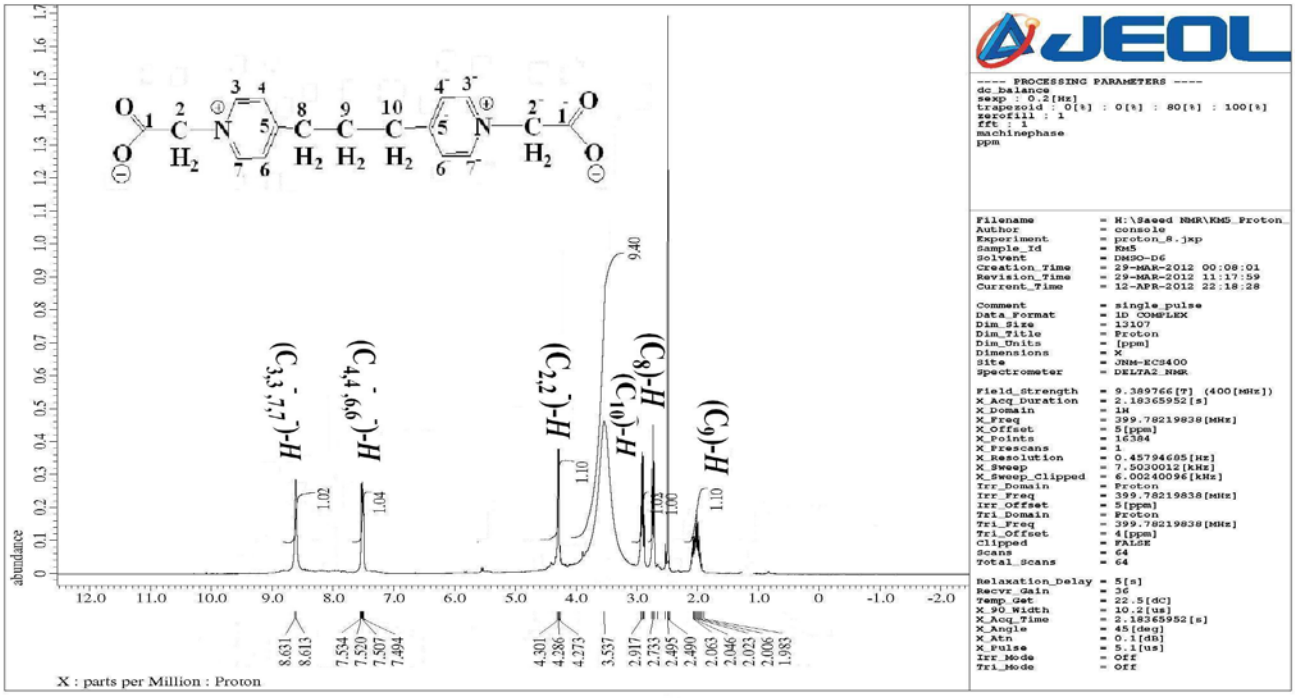

Figure (3. 30) ^{1}H NMR spectrum in DMSO-d6 of L^{5}

(3.7.1.2) ^{13}C NMR spectrum in DMSO-d6 for the ligand L^{5}

The ^{13}C NMR spectrum for L^{5}, Figure (3. 31), shows chemical shift at δ = 29.23 ppm assigned to (C_9). Signal related to ($C_{8,10}$) was detected at δ = 33.83 ppm. The signal at δ = 59.49 ppm assigned to ($C_{2,2'}$). Chemical shifts could be attributed to ($C_{4,4'}$; $_{6,6'}$) appear at δ =125.72 and 127.85 ppm,. The appearance of two signals indicating that the two (CH_2) groups ($C_{8,10}$) are non-equivalent. The signal related to ($C_{3,3'}$; $_{7,7'}$) and ($C_{5,5'}$) were detected at δ = 146.73 ppm. Other chemical shifts are summarised in Table (3. 7).

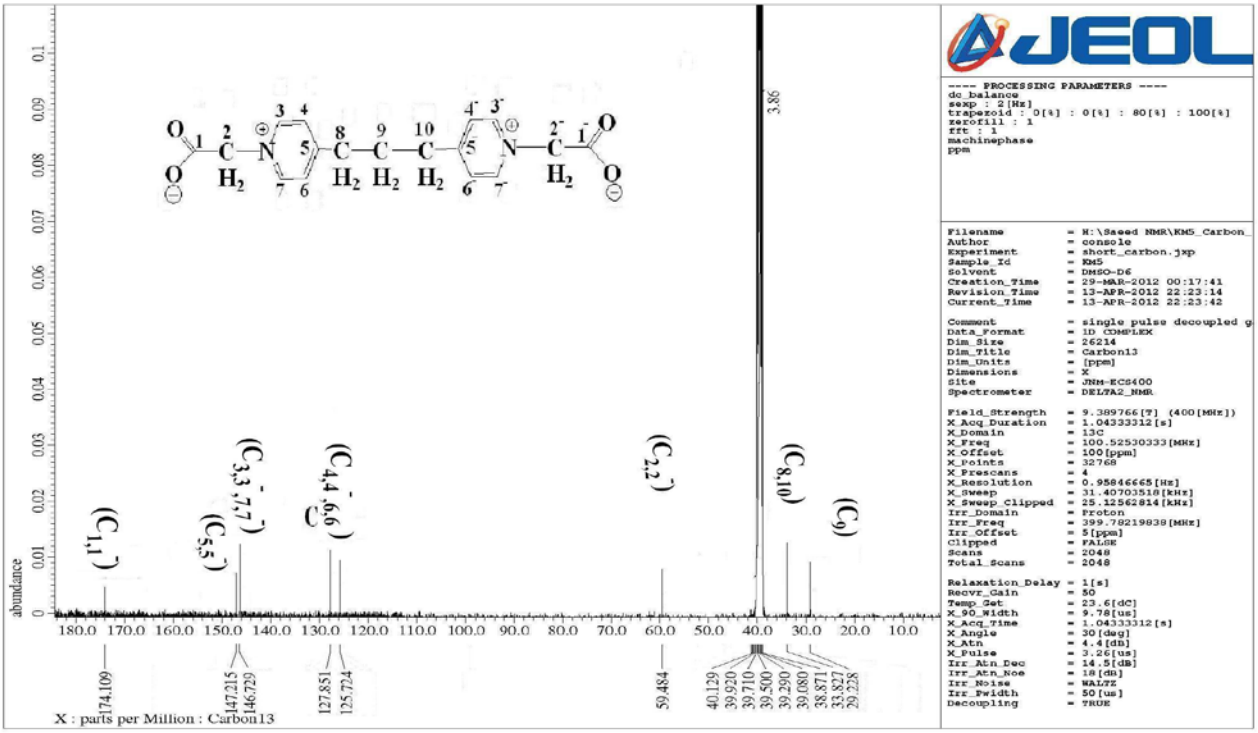

Figure (3. 31) ^{13}C NMR spectrum in DMSO-d_6 of L^5

(3.7.1.3) DEPT ^{13}C NMR spectrum for the ligand L^5

DEPT ^{13}C NMR spectrum for L^5, Figure (3. 32), shows signals enhanced in the negative direction (down), and therefore assigned to ($-CH_2$) group. The signals that were enhanced in the positive direction (up), were assigned to (-CH). No signals around chemical shifts 150 and 170 ppm may assign for ($C_{(5,5')}$ and $C_{(1,1')}$) are detected. These signals are related to a quaternary carbon which is not seen in the spectrum.

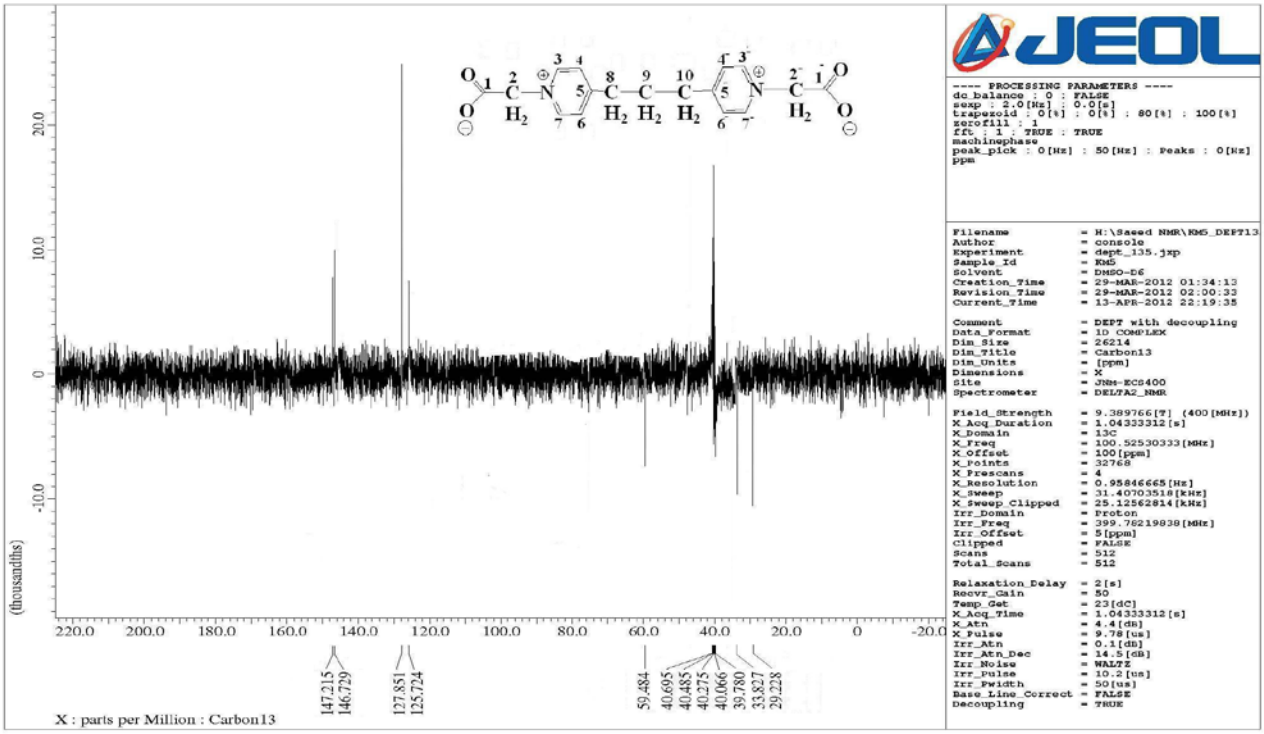

Figure (3. 32) DEPT ^{13}C NMR spectrum in DMSO-d_6 of L^5

Table (3. 6) ^{1}H NMR data for the ligands measured in DMSO-d6 and chemical shift in p.p.m (δ)

Compound	Func. group	δ (P.P.M)
L^1 isomer A	**$C_{(2,2')}$-H**	**5.72, 4H**
	$C_{(4,4';6,6')}$-H	**8.71-8.73, d,4H, J_{HH}= 6.87 Hz**
	$C_{(3,3';7,7')}$-H	**9.23-9.25, d,4H, J_{HH}=7.33 Hz**
Isomer B	**$C_{(2,2')}$-H**	**5.78,4H**
	$C_{(4,4';6,6')}$-H	**8.63-8.65,1H,d, J_{HH}=6.87 Hz**
	$C_{(3,3';7,7')}$-H	**8.78-8.79,d,3H, J_{HH}=6.87 Hz**
	$C_{(4,4';6,6')}$-H	**8.85-8.87,d, 4H, J_{HH}=7.33 Hz**
	$C_{(3,3';7,7')}$-H	**9.18-9.20,d,1H, J_{HH}=6.87 Hz**
L^2	**$C_{(3,3';5,5')}$-H**	**9.05-9.06,d, 4H, J_{HH}=5.95 Hz**
	$C_{(2,2';6,6')}$-H	**9.10-9.12, d, 4H, J_{HH}= 6.87 Hz**
L^3	**$C_{(2,2')}$-H**	**2.31-2.33,t, *4H*, J_{HH}=8 Hz**
	$C_{(3,3')}$-H	**4.71-4.72,t,4H, J_{HH}=6.8 Hz**
	$C_{(5,5';7,7')}$-H	**8.60-8.62,d, 4H, J_{HH}=7.33 Hz**
	$C_{(4,4';8,8')}$-H	**9.12-9.13,d,4H, J_{HH}=6.87 Hz**
L^4	**$C_{(3,3')}$-H**	**2.16-2.23,m,4H, J_{HH}= 7.33Hz**
	$C_{(2,2')}$-H	**2.36-2.49, t, 4H, J_{HH}=7.33 Hz**
	$C_{(4,4')}$-H	**4.68-4.72,t, 4H, J_{HH}=14.4 Hz**
	$C_{(6,6';8,8')}$-H	**8.65-8.67, d, 4H, J_{HH}=6.41 Hz**
	$C_{(5,5';9,9')}$-H	**9.28- 9.30, d, 4H, J_{HH}=6.87 Hz**

L^5	**$C_{(9)}$-H**	**1.90-2.14,m,4H, J_{HH}= 94 Hz**
	$C_{(8)}$-H	**2.70-2.73, t, 4H, J_{HH}=12.8Hz**
	$C_{(10)}$-H	**2.89-2.920, t, 4H, J_{HH}=9.6 Hz**
	$C_{(2, 2')}$-H	**4.27-4.30, t, 4H, J_{HH}=11.2 Hz**
	$C_{(4, 4' ; 6, 6')}$-H	**7.49-7.53, d, 4H, J_{HH}=16 Hz**
	$C_{(3, 3' ; 7, 7')}$-H	**8.61-8.62, d, 4H, J_{HH}=4.4 Hz**

Table (3. 7) ^{13}C NMR data for the ligands measured in DMSO-d6 and chemical shift in p.p.m (δ)

Compound	Func. Group	δ (P.P.M)
L^1 isomer 1	**$C_{(2, 2')}$**	**60.01**
	$C_{(4, 4' ; 6, 6')}$	**126.59**
	$C_{(3, 3' ; 7, 7')}$	**144.01**
	$C_{(5, 5')}$	**152.76**
	$C_{(1, 1')}$	**169.09**
Isomer 2	**$C_{(2, 2')}$**	**60.92**
	$C_{(4, 4' ; 6, 6')}$	**126.80**
	$C_{(3, 3; 7, 7')}$	149.02
	$C_{(5, 5')}$	152.73
	$C_{(1, 1')}$	174.35
L^2	**$C_{(3, 3' ; 5, 5')}$**	**125.46**
	$C_{(2, 2' ; 6, 6')}$	**150.90**
	$C_{(4)}$	**151.52**
		151.56
	$C_{(1)}$	**173.01**

L^3	$C_{(2,2)}$	29.99
	$C_{(3,3)}$	58.69
	$C_{(5,5;7,7)}$	124.93
	$C_{(5,5;7,7)}$	125.24
	$C_{(4,4;8,8)}$	145.70
	$C_{(6,6)}$	153.60
	$C_{(1,1)}$	177.00
L^4	$C_{(3,3)}$	26.08
	$C_{(2,2)}$	30.23
	$C_{(4,4)}$	59.77
	$C_{(6,6;8,8)}$	125.69
	$C_{(5,5;9,9)}$	145.93
	$C_{(7,7)}$	152.17
	$C_{(1,1)}$	173.38
L^5	$C_{(9)}$	29.23
	$C_{(8,10)}$	33.83
	$C_{(2,2)}$	59.49
	$C_{(4,4;6,6)}$	125.72
		127.85
	$C_{(3,3;7,7)}$	146.73
	$C_{(5,5)}$	147.22
	$C_{(1,1)}$	174.11

(3.8) Mass Spectra for the ligands

(3.8.1) Mass spectrum of L^1

The high resolution electrospray (+) mass spectrum of L^1 is presented in Figure (3. 33). The molecular ion peak for the ligand is observed at m/z = 273.0871 $(M)^+$ (24 %) for $C_{14}H_{12}N_2O_4$, requires =273.0870. The other peaks detected at m/z =243 (42 %), 215 (100 %), 185 (5 %) and 157 (50 %) correspond to $[M\text{-}CH_2O]^+$, $[M\text{-}(CH_2O+CO)]^+$, $[M\text{-}(CH_2O+CO+CH_2O)]^+$ and $[M\text{-}(CH_2O+CO+CH_2O+CO)]^+$, respectively. The peak at m/z = 429 (10%) corresponds to $[M\text{-}(CH_2O+CO)_2]^+$. The accurate electrospray mass of the ligand, observed and theoretical, is presented in Figure (3.34). The fragmentation pattern of the molecular ion of L^1 is shown in Scheme (3. 3).

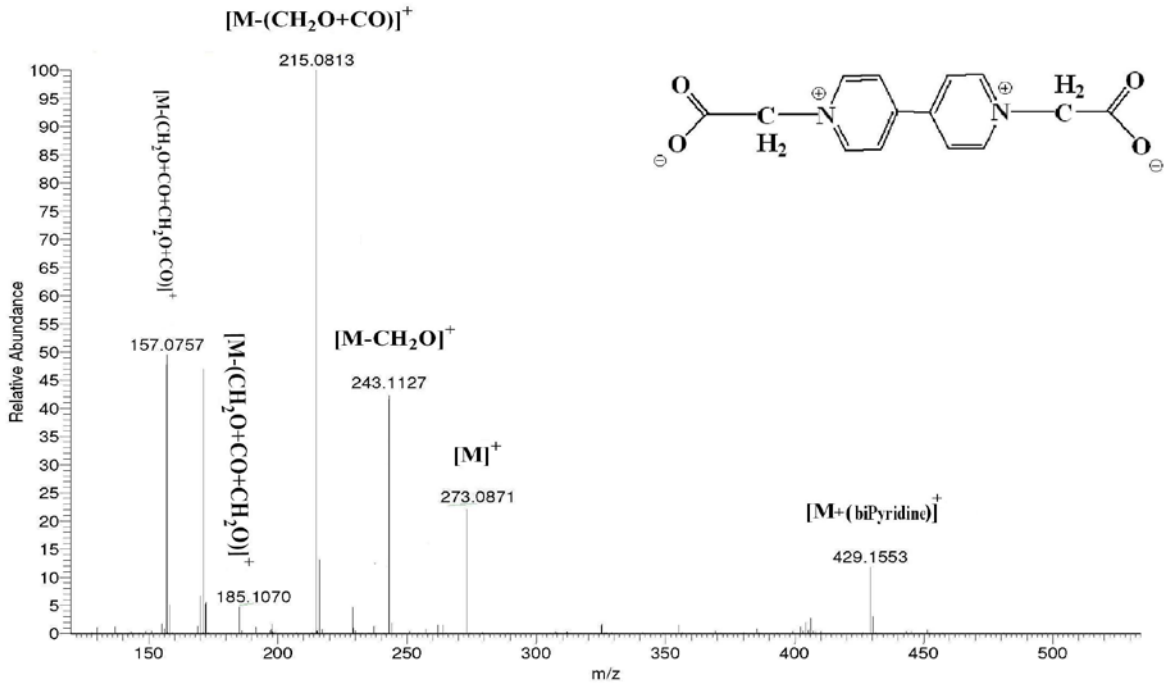

Figure (3. 33) ES (+) mass spectrum of L^1

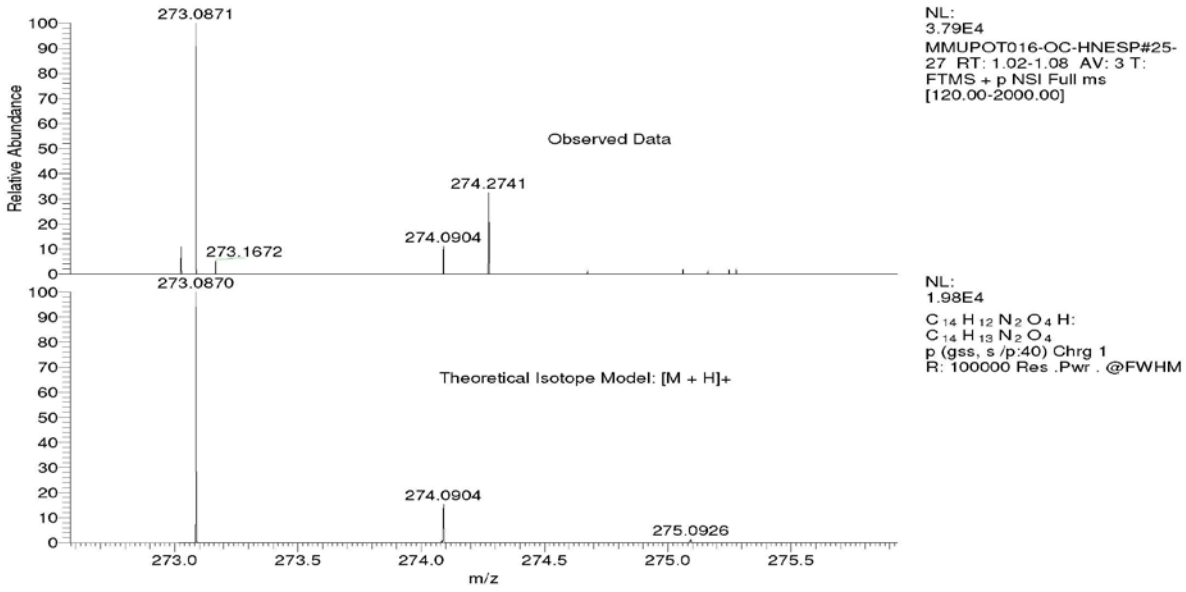

Figure (3. 34)The accurate ES (+) mass spectrum of L^1

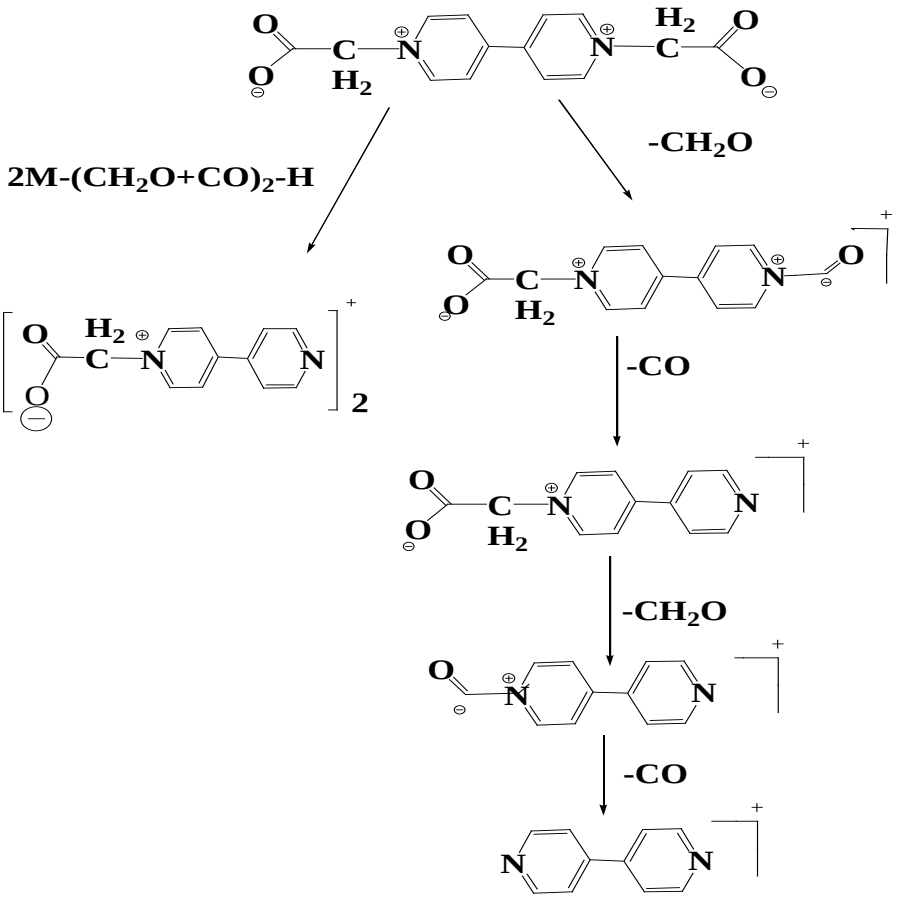

Scheme (3. 3) The fragmentation pattern of L^1

(3.8.2) The mass spectrum of L^2

The EI (+) mass spectrum of L^2 is presented in Figure (3. 35). The molecular ion peak for the ligand is observed at m/z = 244.8 ($M^{+)}$ (25%) for ($C_{12}H_8N_2O_4$) requires =244.20). The peak detected at m/z=156.0 (100%) correspond to $[M-2CO_2]^+$. Peaks detected at 128 (10%) and 42 (8%) are assigned to $[M-(2CO_2+N_2)]^+$. The fragmentation pattern of the molecular structure is shown in Scheme (3. 4).

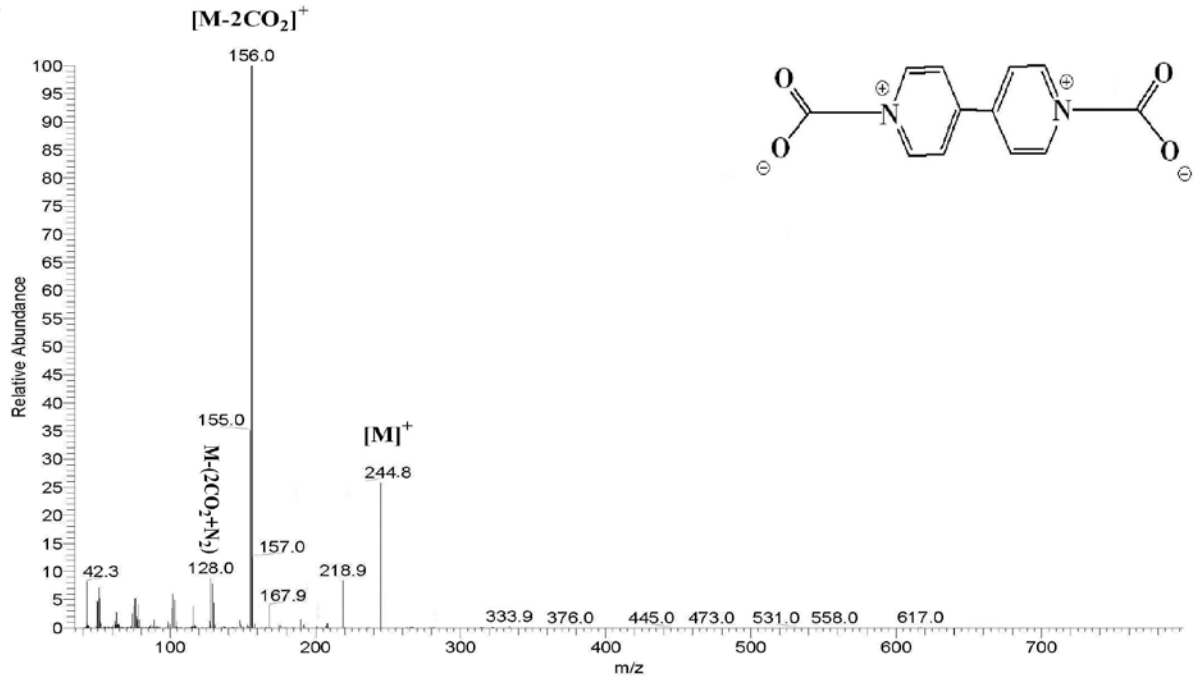

Figure (3. 35) EI (+) mass spectrum of L^2

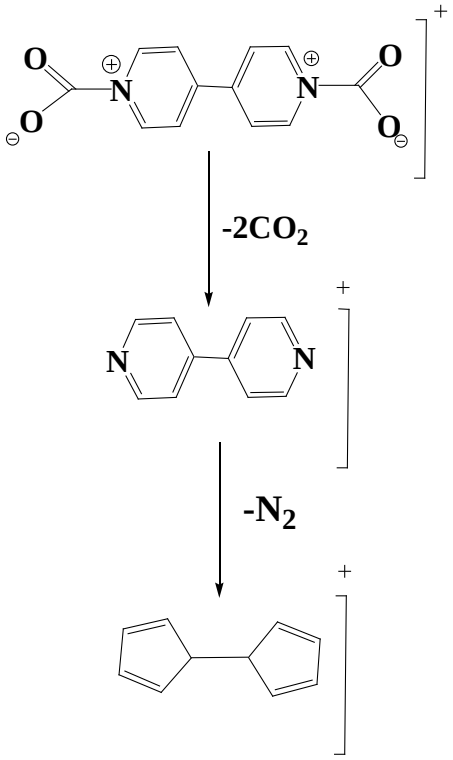

Scheme (3. 4) The fragmentation pattern of L^2

(3.8.3) The mass spectrum of L^3

The high resolution electrospray (+) mass spectrum of L^3 is presented in Figure (3. 36). The molecular ion peak for the ligand is observed at m/z = 301.1184 $(M)^+$ (5%) for $(C_{16}H_{16}N_2O_4)$, requires = 301.1183. The other peaks detected at m/z=257 (32%), 229 (68%), and 157 (100%) correspond to $[M\text{-}CO_2]^+$, $[M\text{-}(CO_2 + CH_2CH_2)]^+$, and $(M\text{-}(CO_2+CH_2CH_2+CH_2CH_2CO_2)]^+$, respectively. The accurate electrospray mass of the ligand, observed and calculated data, is presented in Figure (3.37). The fragmentation pattern of the molecular ion is shown in Scheme (3. 5).

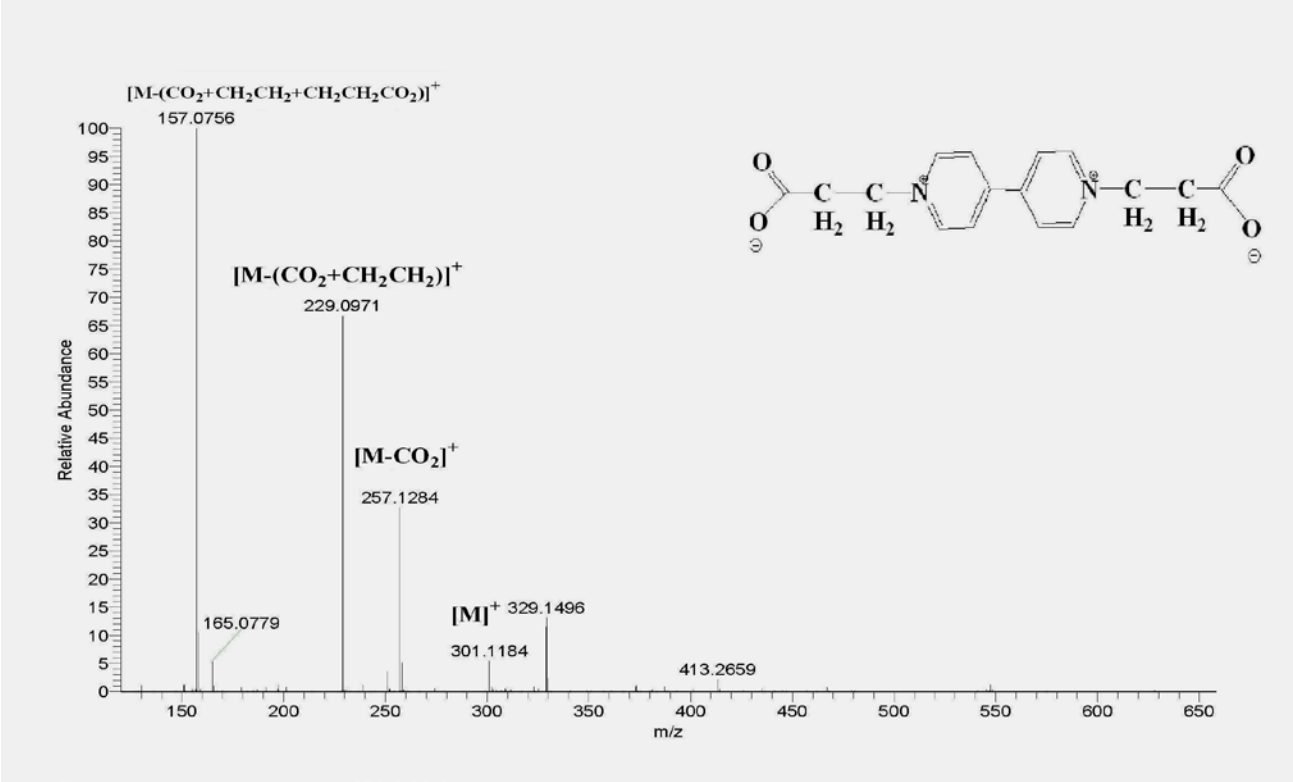

Figure (3. 36) ES (+) mass spectrum of L^3

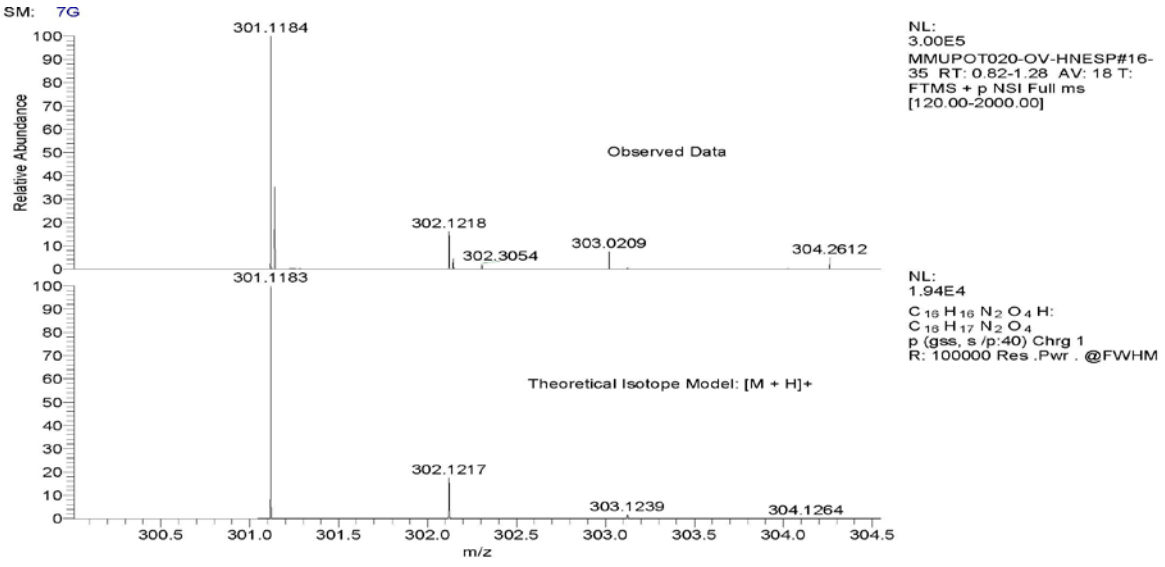

Figure (3. 37)The accurate ES (+) mass spectrum of L^3

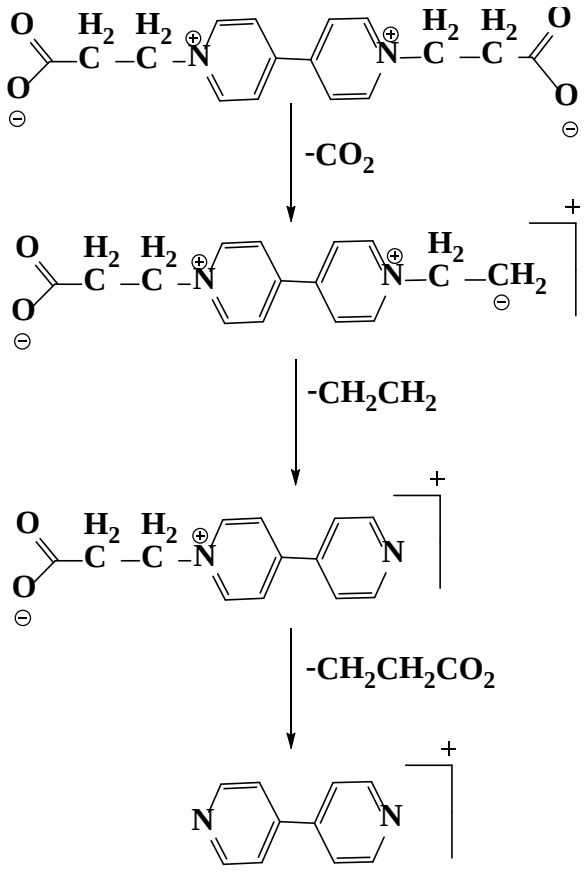

Scheme (3. 5) The fragmentation pattern of L^3

(3.8.4) The mass spectrum of L^4

The EI (+) mass spectrum of L^4 is presented in Figure (3. 38). The molecular ion peak for the ligand is observed at m/z = 328.7 $(M)^+$ (13%). The other peaks detected at m/z=284.5 (5%), 242.4 (3%), 198.2 (5%), 156 (100%) and 128 (8%) correspond to $[M\text{-}CO_2]^+$, $[M\text{-}(CO_2+(CH_2)_3)]^+$, $[M\text{-}(CO_2+(CH_2)_3+CO_2)]^+$, $[M\text{-}(CO_2+(CH_2)_3+CO_2+(CH_2)_3]^+$, and $[M\text{-}(CO_2+(CH_2)_3+CO_2+(CH_2)_3+N_2)]^+$, respectively. The fragmentation pattern of the molecular ion is shown in Scheme (3. 6).

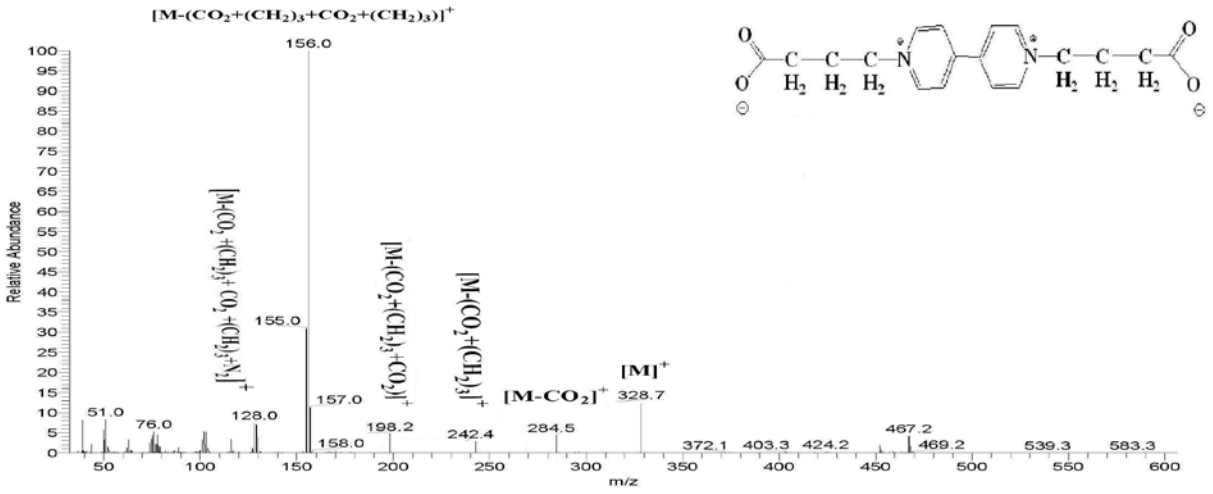

Figure (3. 38) ES (+) mass spectrum of L^4

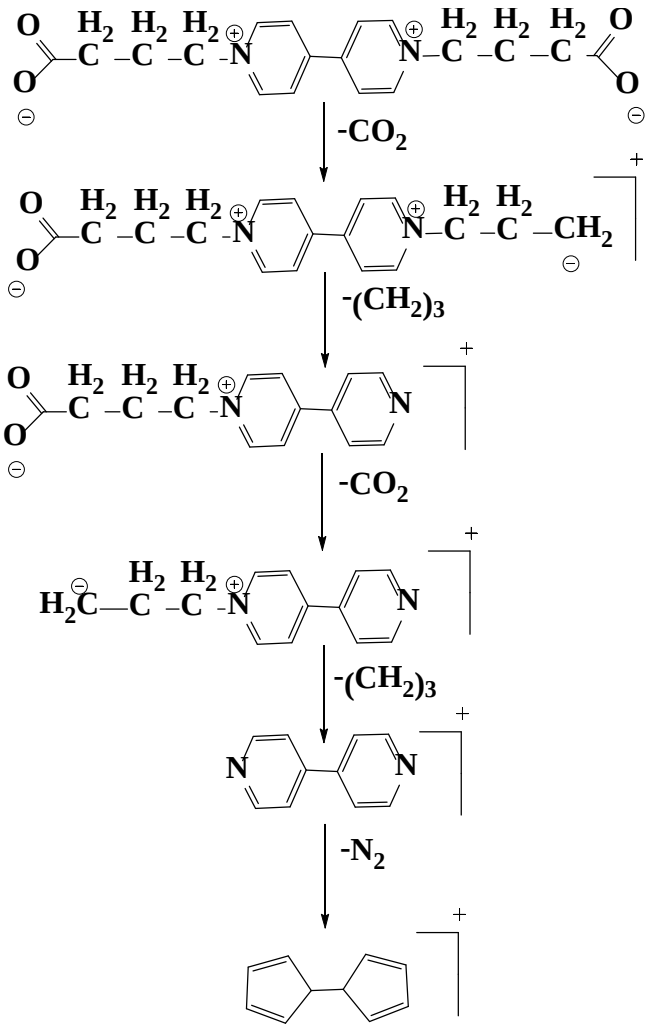

Scheme (3. 6) The fragmentation pattern of L^4

(3.8.5) The mass spectrum of L^5

The high resolution electrospray (+) mass spectrum of L^5 is presented in Figure (3. 39). The molecular ion peak for the ligand is observed at m/z= =315.1 $(M+1)^+$ (5%) for $(C_{17}H_{18}N_2O_4+H)^+$, requires =315.13). The other peaks detected at m/z= 271 (10%), 213 (7%) and 198 (47%) correspond to $[M-CO_2]^+$, $[M-(CO_2+CH_2CO_2)]^+$, $[M-(CO_2+CH_2CO_2+CH_3)]^+$, respectively. The fragmentation pattern of the molecular ion is shown in Scheme (3. 7).

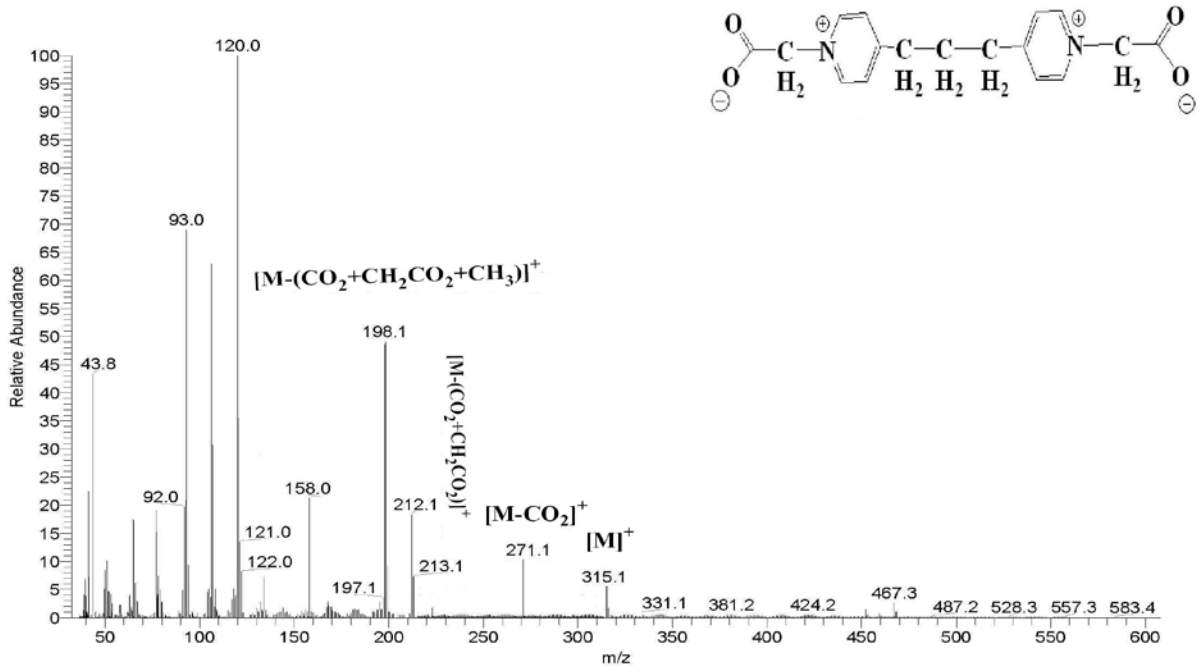

Figure (3. 39) ES (+) mass spectrum of L^5

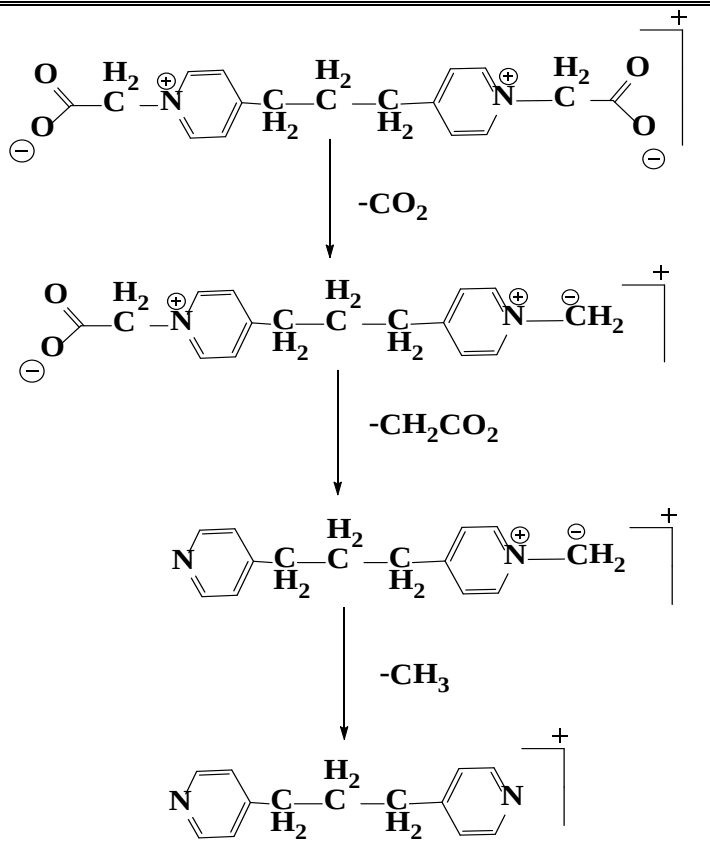

Scheme (3. 7) The fragmentation pattern of L^5

(3.9) Synthesis and characterisation of the complexes

Complexes of the ligands with selected metal ions, Cr^{III} , Mn^{II}, Fe^{II}, Co^{II}, Ni^{II}, Cu^{II}, Zn^{II}, Cd^{II} and Ag^{I}, were synthesised by a similar method, Scheme (3. 8). The complexes were prepared by heating 1 mmol of each ligand with 1 mmol of metal chloride and 1 mmol of sodium azide using a mixture of water/ethanol (4:6 v/v). Polymeric complexes of the general formula $[Cr_2(L^n)(N_3)_4]Cl_2.nH_2O$, $[M_2(L^n)(N_3)_4].nH_2O$ and $Na_2[Ag_2(L^n)(N_3)_4].nH_2O$, where M = Mn(II), Fe(II) Co(II), Ni(II) Cu(II), Zn(II) and Cd(II), $L^n = L^1$-L^5, are reported.

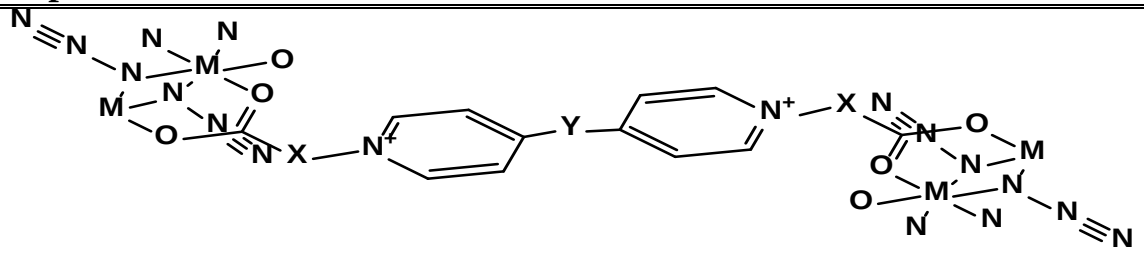

Where:
X = 0; Y = 0; L^2
X = CH_2; Y = 0; L^1
X = CH_2CH_2; Y = 0; L^3
X = $CH_2CH_2CH_2$; Y = 0; L^4
X = CH_2; Y = $CH_2CH_2CH_2$; L^5
M = Mn(II), Fe(II) Co(II), Ni(II) Cu(II), Zn(II) and Cd(II)

Scheme (3-8) Proposed structures of complexes

These complexes were characterised by elemental microanalysis (C.H.N), A.A, thermal analysis, chloride content, conductance, melting point, IR, UV-Vis, magnetic susceptibility, ^{1}H- ^{13}C- and DEPT ^{13}C- NMR and mass spectroscopy. Microanalysis (CHN), metal and chloride analyses are in good agreement with the calculated values, Tables (3. 9, 3.11, 3.13, 3.15, 3.17).

The solubility of complexes in different solvents are shown in Tables (3. 8, 3. 10, 3. 12, 3. 14, 3.16).

Table (3. 8) The solubility of L^1 complexes in different solvents

Complex	H_2O	MeOH	EtOH	CCl_4	C_6H_6	DMF	DMSO
Cr(III)	+	-	-	-	-	÷	+
Mn (II)	÷	-	-	-	-	÷	+
Fe(II)	+	-	-	-	-	÷	+
Co(II)	-	-	-	-	-	÷	+
Ni(II)	÷	-	-	-	-	+	+
Cu(II)	-	-	-	-	-	÷	+
Zn(II)	-	-	-	-	-	÷	+
Cd(II)	-	-	-	-	-	+	+
Ag(I)	+	-	-	-	-	÷	+

(÷) sparingly, (+) soluble, (-) insoluble

Table (3. 9) Microanalysis results and some physical properties of L^1 complexes

Formula	Colour	M.P °C	M.W	Yield%	Micro analysis found (calc)%				
					C	H	N	Metal	Cl
$C_{14}H_{14}Cl_2Cr_2N_{14}O_5$	Green	Dec 340	633.25	73	26.89 (26.55)	2.21 (2.23)	31.02 (30.97)	17.93 (16.42)	12.23 (11.20)
$C_{14}H_{14}Mn_2N_{14}O_5$	Pale yellow	Dec 350	568.23	74	29.16 (29.59)	2.31 (2.48)	35.64 (34.51)	19.17 (19.34)	0.71
$C_{14}H_{14}Fe_2N_{14}O_5$	Brown	Dec 350	570.04	66	28.99 (29.50)	2.35 (2.48)	35.52 (34.40)	19.86 (19.59)	0.77
$C_{14}H_{14}Co_2N_{14}O_5$	blue	Dec 330	576.22	70				19.83 (20.46)	0.09
$C_{14}H_{14}Ni_2N_{14}O_5$	Green	Dec 340	575.74	73	28.13 (29.21)	2.29 (2.45)	35.16 (34.06)	20.31 (20.39)	0.2
$C_{14}H_{14}Cu_2N_{14}O_5$	Green	Dec 313	585.44	70	27.83 (28.72)	2.37 (2.41)	34.56 (33.49)	21.99 (21.71)	0.51
$C_{14}H_{14}Zn_2N_{14}O_5$	yellow	Dec 317	589.13	66				21.52 (22.20)	0.41
$C_{14}H_{14}Cd_2N_{14}O_5$	white	Dec 302	683.17	71				31.42 (32.91)	0.82
$C_{14}H_{14}Na_2Ag_2N_{14}O_5$	white	182	720.07	51				30.93 (29.96)	0.54

(Calculated)

Table (3. 10) The solubility of L^2 complexes in different solvents

Complex	H_2O	MeOH	EtOH	CCl_4	C_6H_6	DMF	DMSO
Cr(III)	+	-	-	-	-	+	+
Mn (II)	-	-	-	-	-	÷	+
Fe(II)	+	-	-	-	-	+	+
Co(II)	-	-	-	-	-	÷	+
Ni(II)	÷	-	-	-	-	÷	+
Cu(II)	-	-	-	-	-	÷	+
Zn(II)	÷	-	-	-	-	÷	+
Cd(II)	-	-	-	-	-	÷	+
Ag(I)	-	÷	÷	-	-	÷	+

(÷) sparingly, (+) soluble, (-) insoluble

Table (3. 11) Microanalysis results and some physical properties of L^2 complexes

Formula	Colour	M.P C	M.W	Yield%	Micro analysis found (calc)%				
					C	H	N	Metal	Cl
$C_{12}H_{10}Cl_2Cr_2N_{14}O_5$	Green	Dec 343	605.20	57	22.63 (23.82)	1.47 (1.67)	33.98 (32.40)	18.65 (17.18)	12.14 (11.72)
$C_{12}H_{10}Mn_2N_{14}O_5$	Pale yellow	Dec 327	540.18	69	25.12 (26.68)	1.72 (1.87)	37.55 (36.30)	20.77 (20.34)	0.67
$C_{12}H_8Fe_2N_{14}O_4$	Yellow	Dec 304	523.99	74	26.64 (27.51)	1.33 (1.54)	37.42 (37.42)	21.19 (21.32)	0.72
$C_{12}H_{10}Co_2N_{14}O_5$	Blue	Dec 326	548.17	76				21.58 (21.50)	0.81
$C_{12}H_{10}Ni_2N_{14}O_5$	Green	Dec 322	547.69	80	25.21 (26.32)	1.75 (1.84)	34.02 (35.80)	21.81 (21.43)	0.13
$C_{12}H_{10}Cu_2N_{14}O_5$	Green	Dec 315	557.39	60	24.17 (25.86)	1.89 (1.81)	36.36 (35.18)	23.23 (22.80)	0.55
$C_{12}H_{10}Zn_2N_{14}O_5$	pale yellow	Dec 293	561.08	60				22.17 (23.31)	0.47
$C_{12}H_8Cd_2N_{14}O_4$	White	Dec 283	637.12	61				31.32 (33.83)	1.02
$C_{12}H_{10}Na_2Ag_2N_{14}O_5$	White	189	692.02	52				31.98 (31.18)	0.28

(Calculated)

Table (3. 12) The solubility of L^3 complexes in different solvents

Complex	H_2O	MeOH	EtOH	CCl_4	C_6H_6	DMF	DMSO
Cr(III)	-	-	-	-	-	÷	+
Mn (II)	-	-	-	-	-	÷	+
Fe(II)	-	-	-	-	-	÷	+
Co(II)	-	-	-	-	-	÷	+
Ni(II)	-	-	-	-	-	÷	+
Cu(II)	-	-	-	-	-	÷	+
Zn(II)	-	-	-	-	-	÷	+
Cd(II)	-	-	-	-	-	÷	+
Ag(I)	-	-	-	-	-	÷	+

(÷) sparingly, (+) soluble, (-) insoluble

Table (3. 13) Microanalysis results and some physical properties of L^3 complexes

Formula	Colour	M.P C	M.W	Yield%	Micro analysis found (calc)%				
					C	H	N	Metal	Cl
$C_{16}H_{18}Cl_2Cr_2N_{14}O_5$	Green	Dec 346	661.30	68	27.88 (29.06)	2.81 (2.74)	28.26 (29.65)	14.63 (15.73)	10.05 (10.72)
$C_{16}H_{20}Mn_2N_{14}O_6$	Pale brown	Dec 327	614.30	69	31.17 (31.28)	3.19 (3.28)	33.91 (31.92)	18.91 (17.89)	0.61
$C_{16}H_{18}Fe_2N_{14}O_5$	brown	Dec 206	598.10	88	31.36 (32.13)	2.84 (3.03)	33.80 (32.79)	18.98 (18.67)	1.40
$C_{16}H_{18}Co_2N_{14}O_5$	Blue	Dec 329	604.27	68				18.73 (19.51)	0.70
$C_{16}H_{18}Ni_2N_{14}O_5$	Green	Dec 322	603.79	76	30.81 (31.83)	2.95 (3.00)	33.48 (32.48)	19.54 (19.44)	1.02
$C_{16}H_{16}Cu_2N_{14}O_4$	Green	Dec 325	595.48	74	32.65 (32.27)	2.56 (2.71)	32.93 (32.93)	21.03 (21.34)	1.15
$C_{16}H_{18}Zn_2N_{14}O_5$	pale yellow	Dec 303	617.19	78				21.17 (21.19)	0.32
$C_{16}H_{18}Cd_2N_{14}O_5$	White	Dec 319	711.23	68				30.76 (31.61)	0.42
$C_{16}H_{18}Na_2Ag_2N_{14}O_5$	White	183	748.12	61				27.82 (28.84)	0.43

(Calculated)

Table (3. 14) The solubility of L^4 complexes in different solvents

Complex	H_2O	MeOH	EtOH	CCl_4	C_6H_6	DMF	DMSO
Cr(III)	÷	-	-	-	-	÷	+
Mn (II)	-	-	-	-	-	÷	+
Fe(II)	-	÷	÷	-	-	÷	+
Co(II)	-	-	-	-	-	÷	+
Ni(II)	-	-	-	-	-	÷	+
Cu(II)	÷	-	-	-	-	+	+
Zn(II)	-	-	-	-	-	÷	+
Cd(II)	÷	-	-	-	-	÷	+
Ag(I)	-	÷	÷	-	-	+	+

(÷) sparingly, (+) soluble, (-) insoluble

Table (3. 15) Microanalysis results and some physical properties of L^4 complexes

Formula	Colour	M.P C	M.W	Yield%	Micro analysis found (calc)%				
					C	H	N	Metal	Cl
$C_{18}H_{22}Cl_2Cr_2N_{14}O_5$	Green	Dec 267	689.36	69	30.94 (31.36)	3.15 (3.22)	27.66 (28.45)	14.16 (15.09)	11.42 (10.29)
$C_{18}H_{22}Mn_2N_{14}O_5$	Pale yellow	Dec 244	624.33	75	33.67 (34.63)	3.31 (3.55)	32.34 (31.41)	17.94 (17.60)	0.52
$C_{18}H_{20}Fe_2N_{14}O_4$	Brown	Dec 233	608.13	74	33.57 (35.55)	3.18 (3.31)	32.12 (32.25)	17.61 (18.37)	1.61
$C_{18}H_{22}Co_2N_{14}O_5$	Blue	Dec 330	632.33	83				17.96 (18.64)	0.72
$C_{18}H_{22}Ni_2N_{14}O_5$	Green	Dec 293	631.85	79	33.06 (34.22)	3.32 (3.51)	31.95 (31.04)	18.92 (18.58)	0.52
$C_{18}H_{22}Cu_2N_{14}O_5$	Green	Dec 229	641.55	72	32.43 (33.70)	3.26 (3.46)	31.45 (30.57)	20.03 (19.81)	0.37
$C_{18}H_{20}Zn_2N_{14}O_4$	White	253	627.22	73				21.38 (20.85)	1.19
$C_{18}H_{20}Cd_2N_{14}O_4$	White	Dec 309	721.27	62				29.96 (31.17)	0.14
$C_{18}H_{22}Na_2Ag_2N_{14}O_5$	White	197	776.17	61				27.49 (27.79)	0.93

(Calculated)

Table (3. 16) The solubility of L^5 complexes in different solvents

Complex	H_2O	MeOH	EtOH	CCl4	C6H6	DMF	DMSO
Cr(III)	+	-	-	-	-	÷	+
Mn (II)	÷	-	-	-	-	÷	+
Fe(II)	÷	-	-	-	-	÷	+
Co(II)	-	-	-	-	-	÷	+
Ni(II)	-	-	-	-	-	÷	+
Cu(II)	÷	-	-	-	-	+	+
Zn(II)	÷	-	-	-	-	÷	+
Cd(II)	÷	-	-	-	-	+	+
Ag(I)	+	-	-	-	-	÷	+

(÷) sparingly, (+) soluble, (-) insoluble

Table (3. 17) Microanalysis results and some physical properties of L^5 complexes

Formula	Colour	M.P C	M.W	Yield%	Micro analysis found (calc)%				
					C	H	N	Metal	Cl
$C_{17}H_{20}Cl_2Cr_2N_{14}O_5$	Green	Dec 316	675.33	65	31.68 (30.23)	2.76 (2.99)	28.46 (29.04)	14.02 (15.40)	10.24 (10.50)
$C_{17}H_{20}Mn_2N_{14}O_5$	yellow	Dec 326	610.31	74	31.96 (33.46)	3.15 (3.30)	30.12 (32.13)	18.16 (18.00)	0.72
$C_{17}H_{20}Fe_2N_{14}O_5$	Brown	Dec 315	612.12	79	31.85 (33.36)	3.03 (3.29)	31.01 (32.04)	18.33 (18.25)	0.83
$C_{17}H_{20}Co_2N_{14}O_5$	Blue	Dec 308	618.30	71				18.77 (19.06)	0.64
$C_{17}H_{20}Ni_2N_{14}O_5$	Green	Dec 330	617.82	74	33.99 (33.05)	3.14 (3.26)	30.69 (31.74)	19.12 (19.00)	0.51
$C_{17}H_{20}Cu_2N_{14}O_5$	Green	Dec 328	627.52	73	31.12 (32.54)	3.07 (3.21)	29.17 (31.25)	19.57 (20.25)	0.07
$C_{17}H_{20}Zn_2N_{14}O_5$	pale yellow	193	631.21	67				18.76 (20.72)	0.81
$C_{17}H_{20}Cd_2N_{14}O_5$	White	223	725.25	62				28.32 31.00)	0.89
$C_{17}H_{20}Na_2Ag_2N_{14}O_5$	White	183	762.15	60				27.64 (28.31)	0.68

(Calculated)

(3.10) IR Spectral data for the complexes

(3.10.1) IR spectral data for L^1 complexes

The structurally important IR absorption frequencies of the prepared complexes with L^1 are presented in Table (3.18). The IR spectrum of $[Cr_2(L^1)(N_3)_4]Cl_2.H_2O$, Figure (3.40), exhibits bands related to the carboxylato moiety at 1620 and 1406 cm^{-1}, which are assigned to anti-symmetric $\nu_{as}(COO^-)$ and symmetric $\nu_s(COO^-)$ modes, respectively[170]. The shift of these bands to lower wave numbers by 14 and 62 cm^{-1}, for the anti- and symmetric modes, respectively compared with that in the free L^1 ligand can be attributed to delocalisation of metal electron density (t_2g) to the π-system of the ligand, and indicating the involvement of the carboxylato group in coordination with the Cr(III) ion. The stretching vibration anti-symmetric $\nu_{as}(COO^-)$ and symmetric $\nu_s(COO^-)$ modes, should be helping in elucidating the structure of the complexes. The $\Delta(\nu_{as}- \nu_s)$ value of (216 cm^{-1}) is consistent with carboxylato bridge coordination fashion with the metal atoms in the *syn-syn* mode [171]. The spectrum shows bands at 1603 and 1584 cm^{-1} assigned to ν(C=N) and ν(C=C) stretching, respectively[172]. These bands are shifted to lower frequency in comparison with that in the free ligand, due to complex formation. The band at 2868 and 3065 cm^{-1} are assigned to $\nu(C\text{-}H)_{aro}$ and $\nu(CH_2)$ stretches[172], respectively. The spectrum exhibited new bands which are not observed in the spectrum of the ligand. These bands are located at 2037 and 1368 cm^{-1}, which are attributed to $\nu_{as}(N_3)$ and $\nu_s(N_3)$ stretches, respectively[173]. These values suggest azido bridging mode with metal ion with $N_{(}\mu_{1,1)}$ fashion (see Figure 1. 5, page 12) [173]. Band at 1225 cm^{-1} attributed to ν(C-N) stretching[168]. In the low-frequency region, spectrum of the Cr(III) complex showed new bands which are not present in the spectrum of the ligand. These bands are located at 550, 588 and 436, 499

cm^{-1}, which are attributed to ν(Cr−O) and ν(Cr−N), respectively[174]. Additional broad band observed around 3462 cm^{-1} is assigned to hydrated water molecule in the complex[166].

The IR spectrum of the $[Mn_2(L^1)(N_3)_4].H_2O$ complex, Figure (3. 41), showed strong bands at 1602 and 1404 cm^{-1}, which can be attributed to anti-symmetric $\nu_{as}(COO^-)$ and symmetric $\nu_s(COO^-)$ modes, respectively of the carboxylato moiety[175]. These bands are shifted to lower wave numbers by 32 and 64 cm^{-1} compared with that in the free L^1 ligand. This can be attributed to delocalisation of metal electron density (t_2g) to the π-system of the ligand, and confirming the involvement of the carboxylato group in coordination with the Mn(II) ion. The Δ (ν_{as} - ν_s) value of (198 cm^{-1}) is in a good agreement with previous studies of carboxylato bridge coordination fashion with metal atoms in the *syn-syn* mode[171]. The new bands at 2038 and 1338 cm^{-1} may be attributed to $\nu_{as}(N_3)$ and $\nu_s(N_3)$ stretches, respectively[176]. These values suggest an EO azido bridge mode with metal ion, $N_{(}\mu_{1,1)}$ fashion, (see Figure 1.5)[176]. The spectrum showed new bands at 548, 579 and 442, 467 cm^{-1} which are attributed to ν(Mn−O) and ν(Mn−N)[174]. Broad band observed around 3422 cm^{-1} is assigned to hydrated water molecule in the complex[177].

The IR spectra of $[Fe_2(L^1)(N_3)_4].H_2O$, $[Co_2(L^1)(N_3)_4].H_2O$, $[Ni_2(L^1)(N_3)_4].H_2O$, $[Cu_2(L^1)(N_3)_4].H_2O$, $[Zn_2(L^1)(N_3)_4].H_2O$, $[Cd_2(L^1)(N_3)_4].H_2O$ and $Na_2[Ag_2(L^1)(N_3)_4]H_2O$, Figures (3.42 to 3. 48) exhibit similar trend to that of the $[Mn_2(L^1)(N_3)_4].H_2O$ complex and same reasoning could be used to interpret the spectra. All complexes show *syn-syn* modes, except Co(II)- complex which shows the mode of *syn-anti*. The $\Delta(\nu_{as}$- $\nu_s)$ value of (165 cm^{-1}) confirming carboxylato bridge coordination fashion

with Co(II) ion in the *syn-anti* mode. This is in a good agreement with previous studies of *syn-anti* carboxylato bridge coordination mode[177].

The appearance of *v*(M−O) at frequency higher than that of *v*(M−N) due to the larger dipole moment change for the M-O bond compared to the M-N bond[178, 179]. Furthermore, the appearance of more than one value for M-O and M-N may indicate the formation of more than one dimension structure upon coordination, and indicating the polymer structure of the complexes.

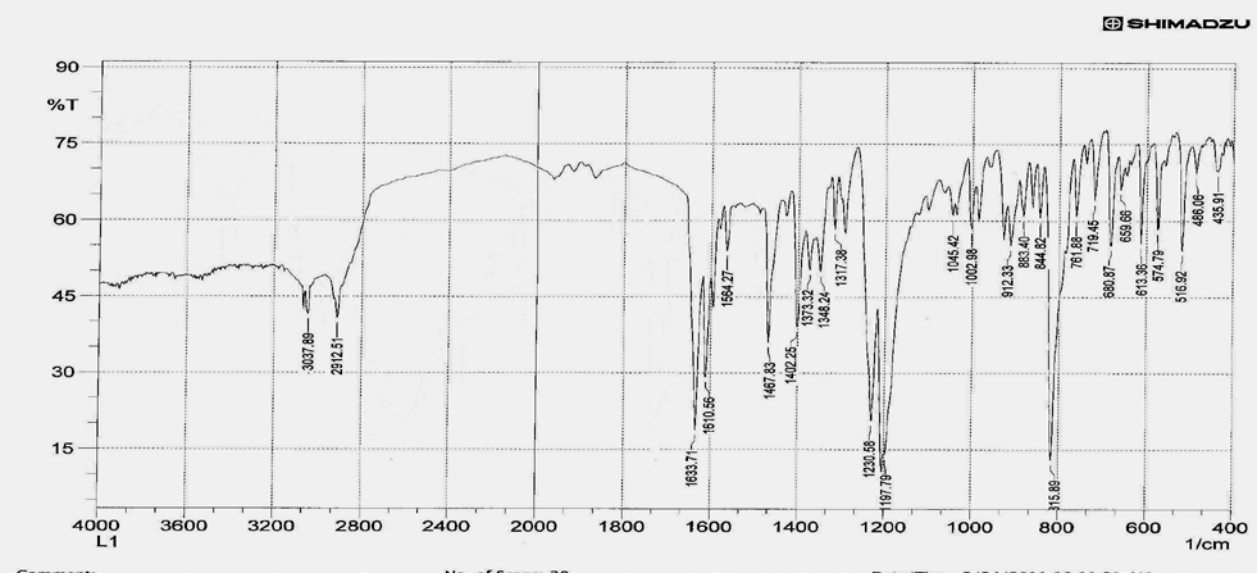

Figure (3. 4) IR spectrum of L^1

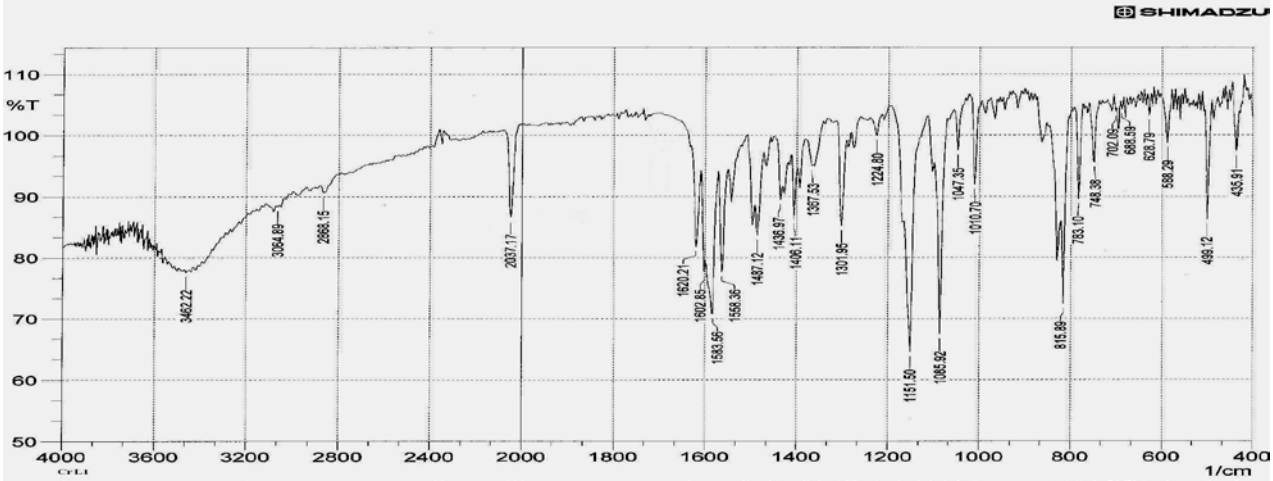

Figure (3. 40) IR spectrum of $[Cr_2(L^1)(N_3)_4]Cl_2.H_2O$

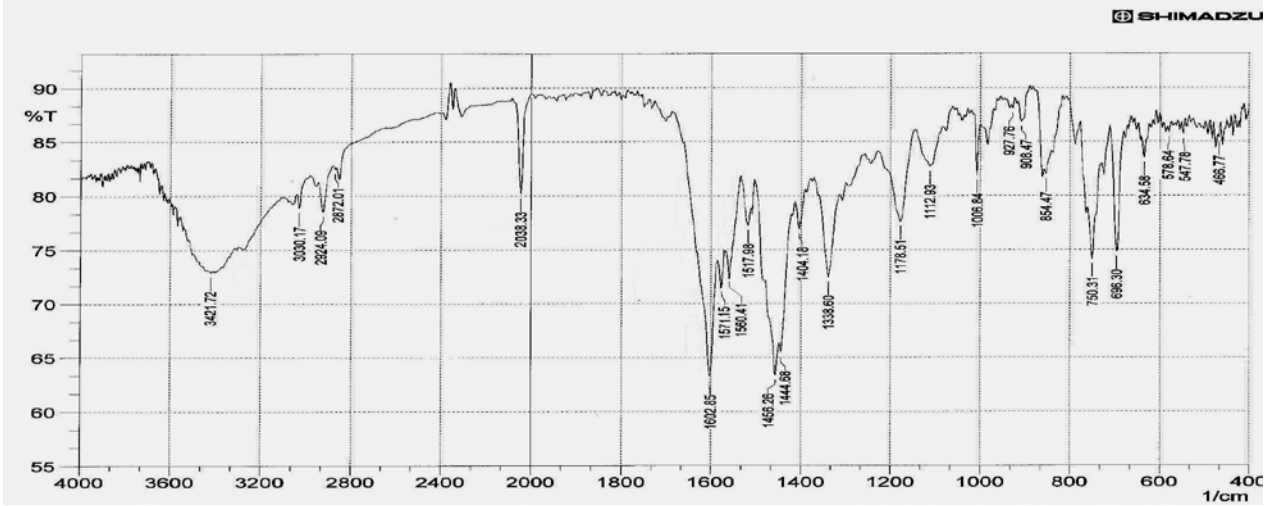

Figure (3. 41) IR spectrum of $[Mn_2(L^1)(N_3)_4]H_2O$

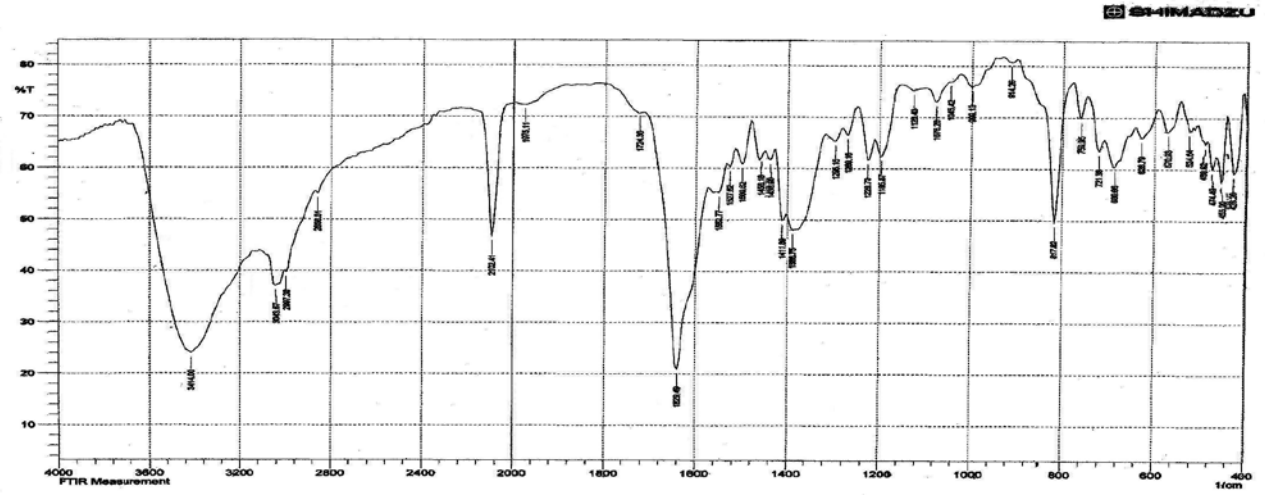

Figure (3. 42) IR spectrum of $[Fe_2(L^1(N_3)_4]H_2O$

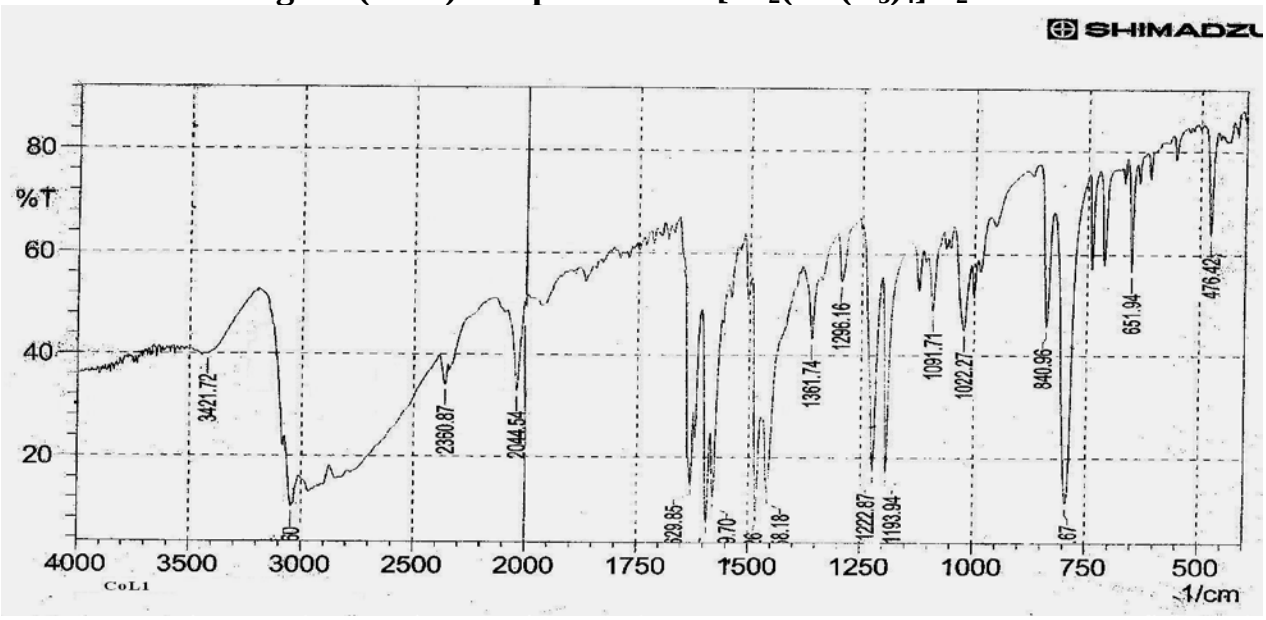

Figure (3. 43) IR spectrum of $[Co_2(L^1)(N_3)_4].H_2O$

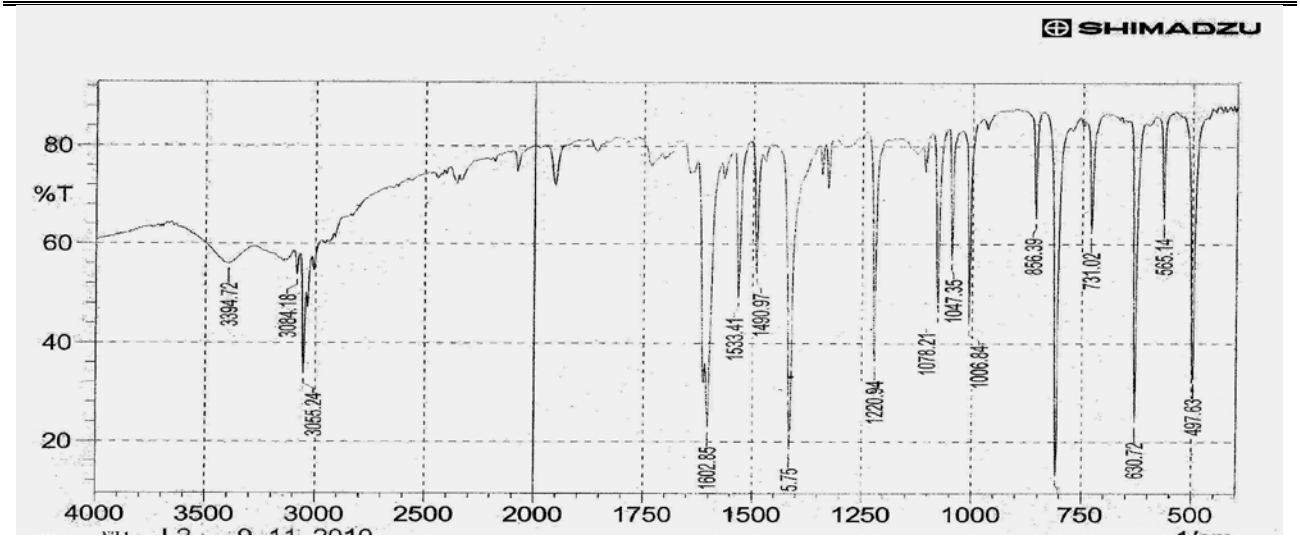

Figure (3. 44) IR spectrum of $[Ni_2(L^1)(N_3)_4].H_2O$

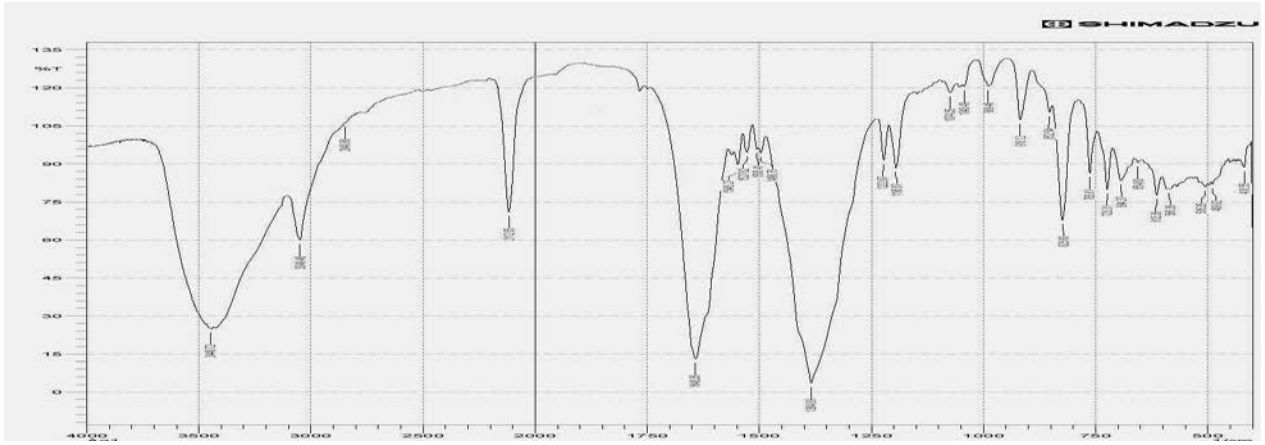

Figure (3. 45) IR spectrum of $[Cu_2(L^1)(N_3)_4].H_2O$

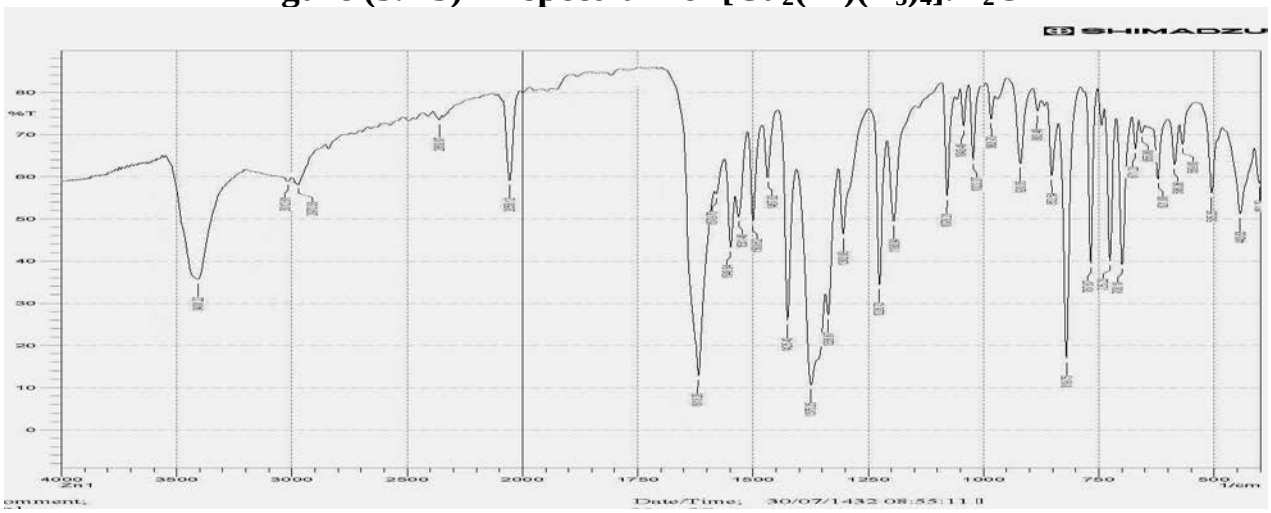

Figure (3. 46) IR spectrum of $[Zn_2(L^1)(N_3)_4].H_2O$

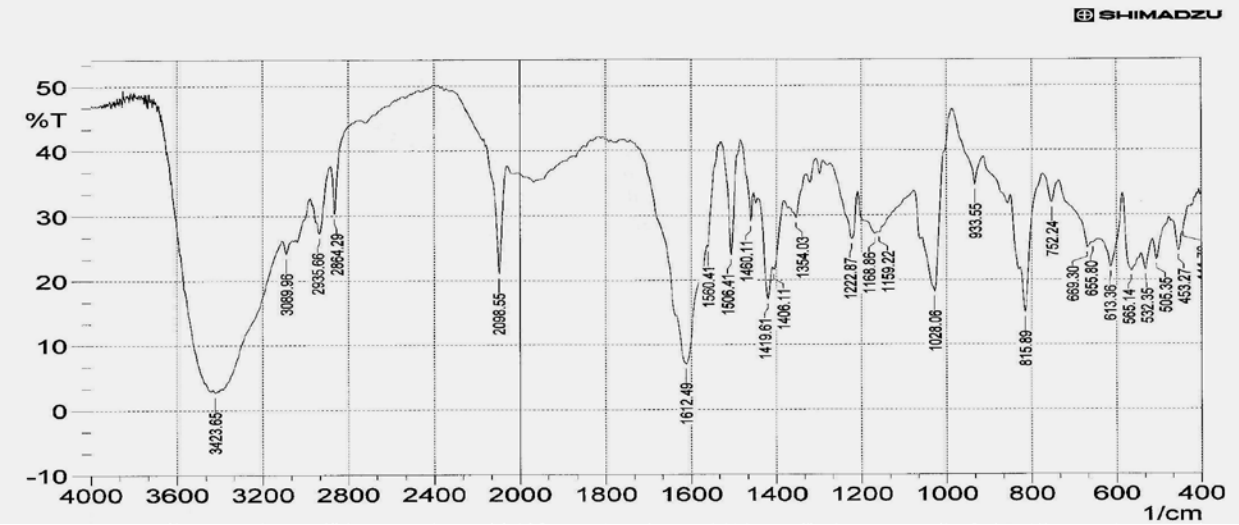

Figure (3. 47) IR spectrum of $[Cd_2(L^1)(N_3)_4].H_2O$

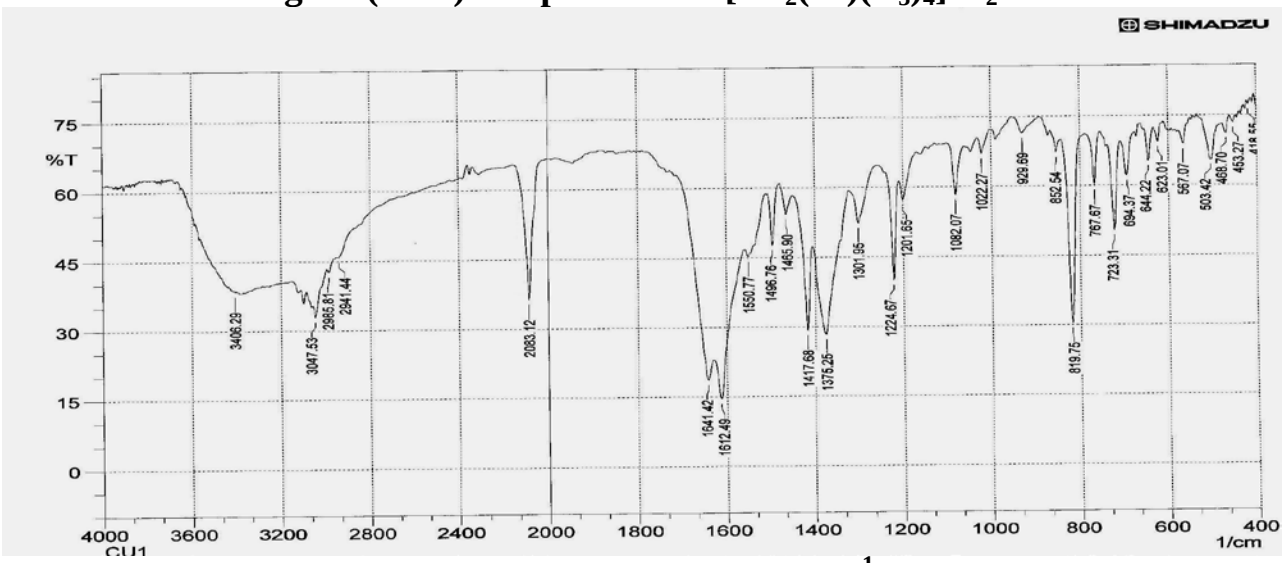

Figure (3. 48) IR spectrum of $Na_2[Ag_2(L^1)(N_3)_4].H_2O$

Table (3. 18) Infrared spectral data (wave number) cm^{-1} of L^1 complexes

Complex	νO-H	ν_{ar}C-H	νCH_2	$\nu_{as}N_3$	ν_{as}COO	νC=N	νC=C	ν_sCOO	δO-H	ν_sN_3	νC-N	$\delta_{O.O.P}$	νM-O	νM-N	$\Delta(\nu_{as}-\nu)$
L^1	-	3038	2913	-	1634	1611	1593	1468	-	-	1231		-	-	166
$[Cr_2(L^1)(N_3)_4]Cl_2.H_2O$	3462	3065	2868	2037	1620	1603	1584 1436	1406	1558	1368	1225	816 689	550 588	436 499	206
$[Mn_2(L^1)(N_3)_4]H_2O$	3422	3030	2872	2038	1603	1560	1560	1404	1518	1338	1179	812 646	548 579	442 467	199
$[Fe_2(L^1)(N_3)_4]H_2O$	3414	3044	2859	2102	1629	1553	1528 1456	1412	1501	1298	1229	818	525	428 455	217
$[Co_2(L^1)(N_3)_4]H_2O$	3422	3046	2830	2045	1623	1593	1580	1458		1362	1223	841 652	541 600	413 27 476	165
$[Ni_2(L^1)(N_3)_4]H_2O$	3395	3084 3055		2078	1603	1613	1533	1416	1491	1317	1221	856 731	563 498	467 498	187
$[Cu_2(L^1)(N_3)_4]H_2O$	3449	3053	2849	2112	1612	1643	1546	1418	1528	Over-lap	1223	918 655	505 586	419 453	194
$[Zn_2(L^1)(N_3)_4].H_2O$	3408	3012	2849	2056	1618	1580	1549 1468	1425	1531	1367	1227	920 671	569	444	193
$[Cd_2(L^1)(N_3)_4]H_2O$	3424	3090	2864	2099	1612	1628	1540	1406	1506	1354	1223	934 673	505 532 565	401 453	206
$Na_2[Ag_2(L^1)(N_3)_4]H_2O$	3406	3048	2941	2083	1612	1641	1641 1466	1418	1551	1302	1225	820 644	503 567	419 453	194

Where: ar = aromatic; s = symmetric; as = antisymmetric; o.o.p = out of plane.

(3.10.2) IR Spectral data for L^2 complexes

The IR spectral data of L^2 complexes are presented in Table (3.19). In general, the bands of (COO^{-}) moiety in complexes were abruptly decreased, which proves the metal-carboxylate binding. The IR spectrum of $[Cr_2(L^2)(N_3)_4]Cl_2.H_2O$ complex, Figure (3.49), displays characteristic strong bands which may be responsible of the anti-symmetric $v_{as}(COO^{-})$ and symmetric $v_s(COO^{-})$ modes, of the carboxylato moiety which located at 1626 and 1418 cm^{-1}, respectively[180]. The shift of these bands to lower wave numbers by 4 and 40 cm^{-1} compared with that in the free L^2 ligand can be due to delocalisation of metal electron density (t_2g) to the π-system of the ligand, and indicating the involvement of the (COO^{-}) in coordination with the Cr(III) ion. The $\Delta(v_{as}- v_s)$ value of (208 cm^{-1}) is in a good agreement with carboxylato bridge coordination fashion with the metal atoms in the *syn-syn* mode[171]. The spectrum shows bands of v(C=N) and v(C=C) stretching at 1616 and 1593 cm^{-1}, respectively[166, 167]. The shift of these bands to lower frequencies, compared with that in the free ligand, may be due to complex formation. The spectrum shows new bands at 2091 and 1339 cm^{-1}, which are attributed to $v_{as}(N_3)$ and $v_s(N_3)$ stretches, respectively[173, 176]. These values is in agreement with the suggest azido bridge mode with metal ion with $N_{(\mu\text{-}1,1)}$ fashion (see Figure 1. 5)[176]. The band at 1225 cm^{-1} assigned to v(C-N) stretching. In the low-frequency region, spectrum of the Cr(III) complex showed new bands which are not present in the spectrum of the ligand. These bands are located at 500, 517, 596 and 419, 436 cm^{-1} which are attributed to v(Cr−O) and v(Cr−N), respectively[174]. Additional broad band observed around 3385 cm^{-1} is assigned to hydrated water molecule in the complex[177].

The essential infrared data of $[Mn_2(L^2)(N_3)_4].H_2O$ complex, Table (3.19), Figure(3.50) displays bands of the carboxylato moiety at 1614 and 1416

cm^{-1}, which may be assigned to anti-symmetric $\nu_{as}(COO^{-})$ and symmetric $\nu_s(COO^{-})$ modes, respectively[181]. The shifting of these bands to lower wave numbers by 16 and 42 cm^{-1} compared with that in the free L^2 ligand can be attributed to delocalisation of metal electron density (t_2g) to the π-system of the ligand, and indicating the involvement of the carboxylato group in coordination with the Mn(II) ion. The $\Delta(\nu_{as}- \nu_s)$ value of (198 cm^{-1}) is consistent with carboxylato bridging coordination fashion with the metal atoms in the *syn-syn* mode[171]. The $\nu_{as}(N_3)$ and $\nu_s(N_3)$ vibrations of the azide group appear as strong bands at 2081 and 1329 cm^{-1}, respectively [176]. The appearance of these bands in this position indicated the azido bridging mode with metal ion with $N_{(}\mu_{-1,1)}$ fashion (see Figure 1.5)[176]. While the bands at 500, 561 and 431, 442 cm^{-1} are attributed to ν(Mn−O) and ν(Mn−N), respectively[178, 179].

The IR spectrum of the $[Fe_2(L^2)(N_3)_4]$ complex, Figure (3.51) shows two absorption peaks at 1601 and 1410 cm^{-1}, which can be assigned to the anti-symmetric $\nu_{as}(COO^{-})$ and symmetric $\nu_s(COO^{-})$ modes, respectively[180]. The shift of these bands can be explained by the same method that used in the interpretation of Mn (II) complex. The $\Delta(\nu_{as}- \nu_s)$ value of (191 cm^{-1}) refers to the carboxylato bridge coordination fashion with the metal atoms in the *syn-syn* mode[171]. Bands detected at 552, 627 and 417, 436, 488 cm^{-1} are attributed to ν(Fe−O) and ν(Fe−N), respectively[174]. Additional broad band observed around 3381 cm^{-1} is assigned to hydrated water molecule in the complex [177]. Other bands are summarised in Table (3.19).

The IR spectra of $[Co_2(L^2)(N_3)_4]H_2O$, $[Ni_2(L^2)(N_3)_4]H_2O$, $[Cu_2(L^2)(N_3)_4]H_2O$, $[Zn_2(L^2)(N_3)_4]H_2O$, $[Cd_2(L^2)(N_3)_4]$ and $Na_2[Ag_2(L^2)(N_3)_4]$ H_2O, Figures (3.52 to 3.57), show similar pattern to that of $[Cr_2(L^2)(N_3)_4]Cl_2.H_2O$ complex and same reasoning could be used to interpret the spectra.

The prepared complexes showed both $\nu_{as}(COO^{-})$ and $\nu_s(COO^{-})$ frequencies is changed in the same direction, indicating that the coordination of the carboxylate

moiety is bridging bidentate. This is because the bond orders of both C-O bonds would change by the same amount. This result is in accord with data reported by Hamed and co-workers[182]. All complexes show the coordination fashion of the carboxylato group with the metal atoms in the *syn-syn* mode.

The appearance of ν(M−O) at frequency higher than that of ν(M−N) due to the larger dipole moment change for the M-O bond compared to the M-N bond[178, 179]. Furthermore, the appearance of more than one value for M-O and M-N may indicate the formation of more than one dimension structure upon coordination, and indicating the polymer structure of the complexes.

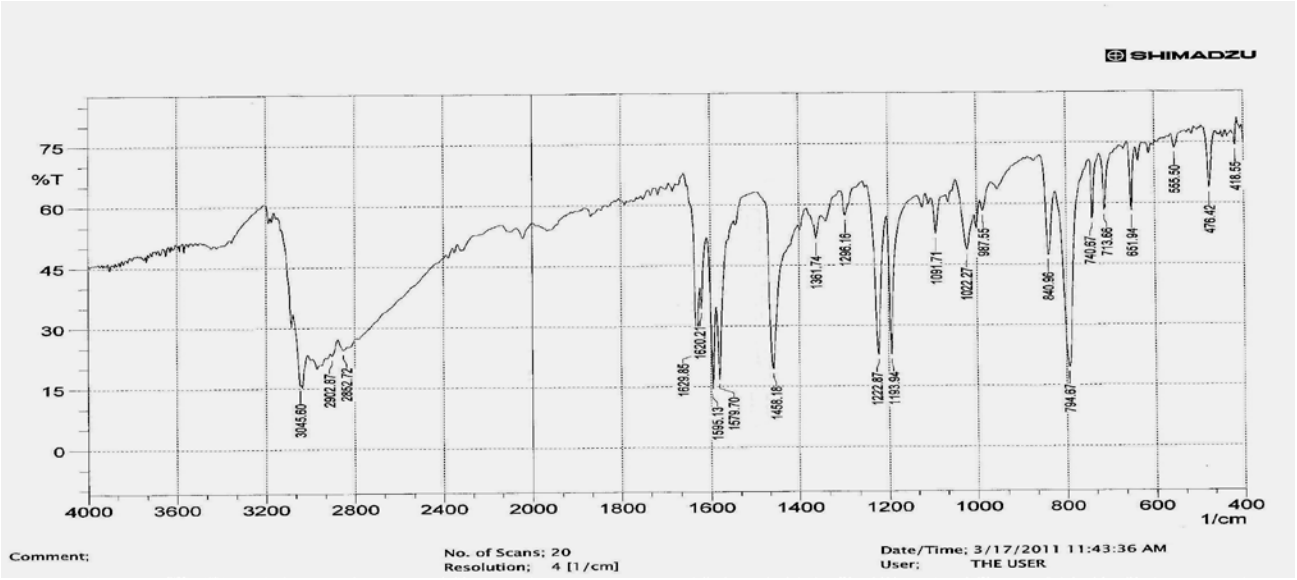

Figure (3.6) IR spectrum of L^2

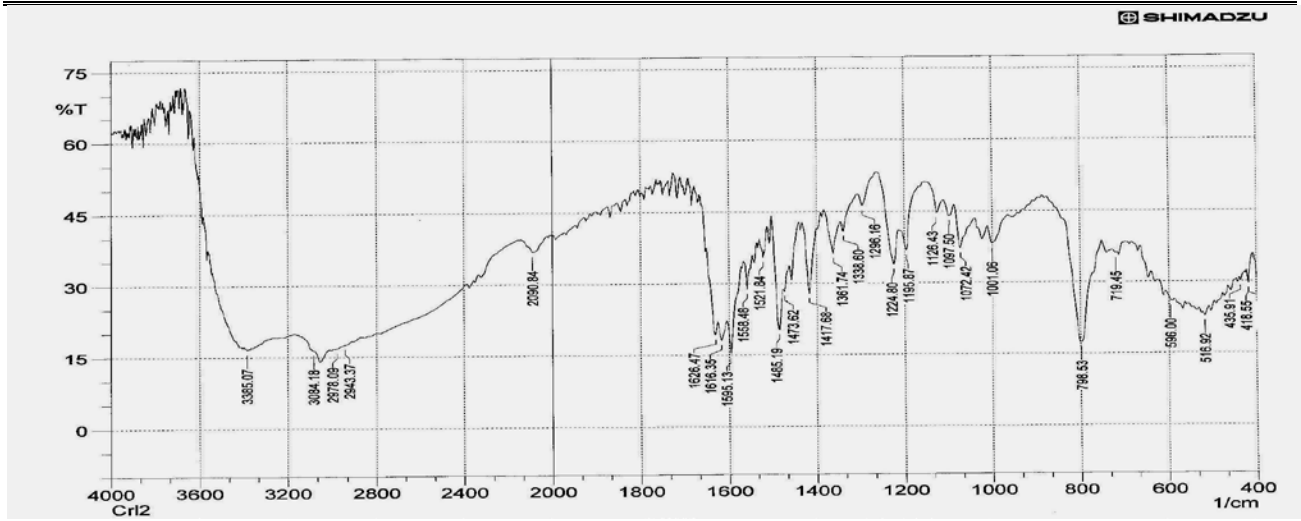

Figure (3.49) IR spectrum of $[Cr_2(L^2)(N_3)_4]Cl_2.H_2O$

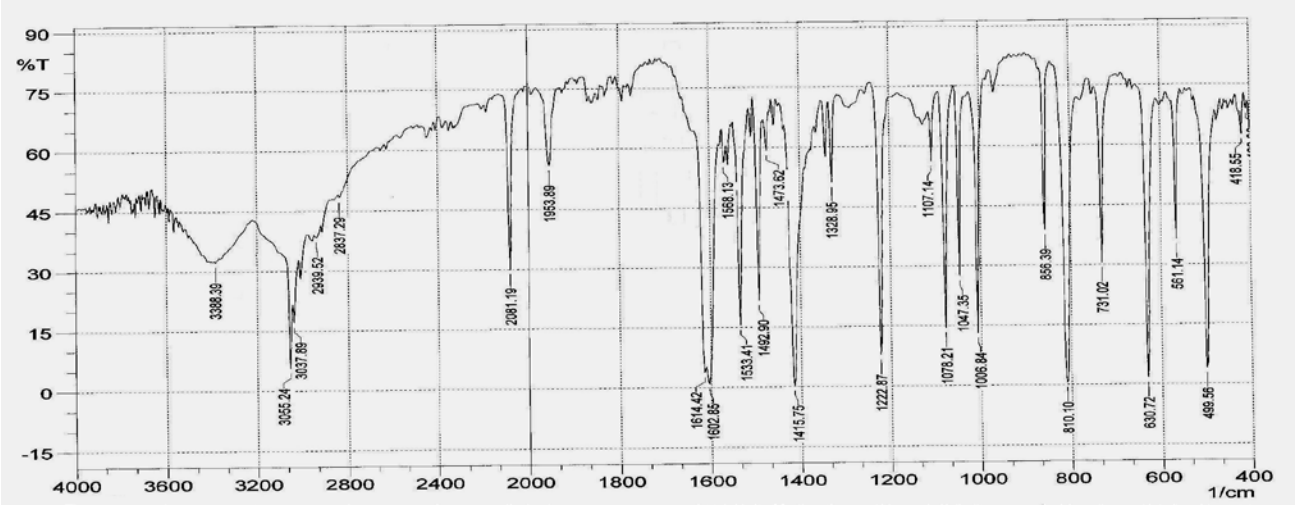

Figure (3.50) IR spectrum of $[Mn_2(L^2)(N_3)_4].H_2O$

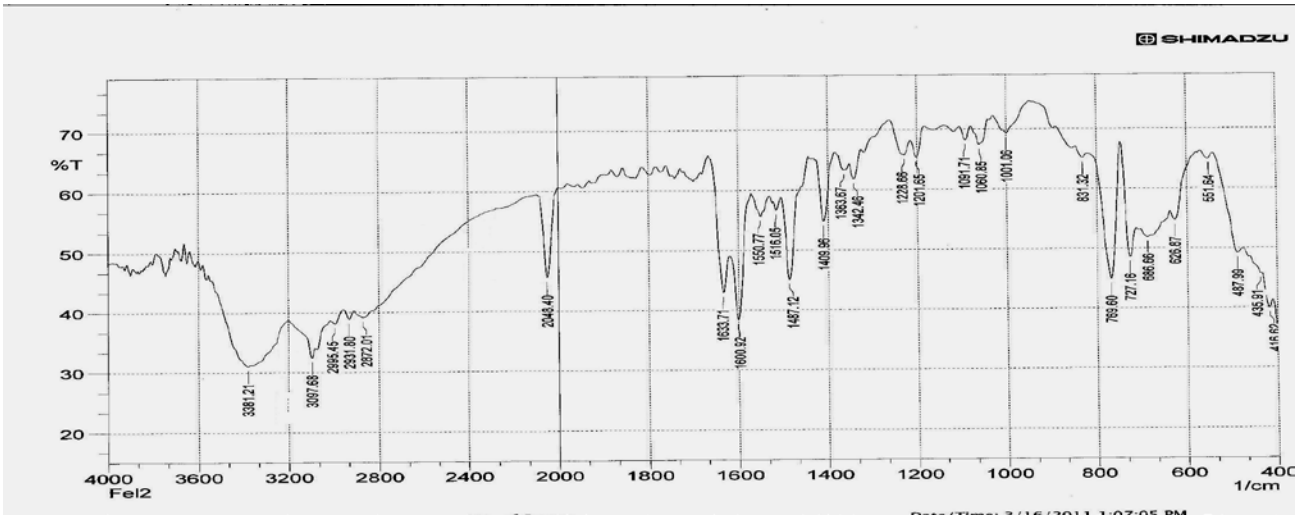

Figure (3.51) IR spectrum of $[Fe_2(L^2)(N_3)_4]$

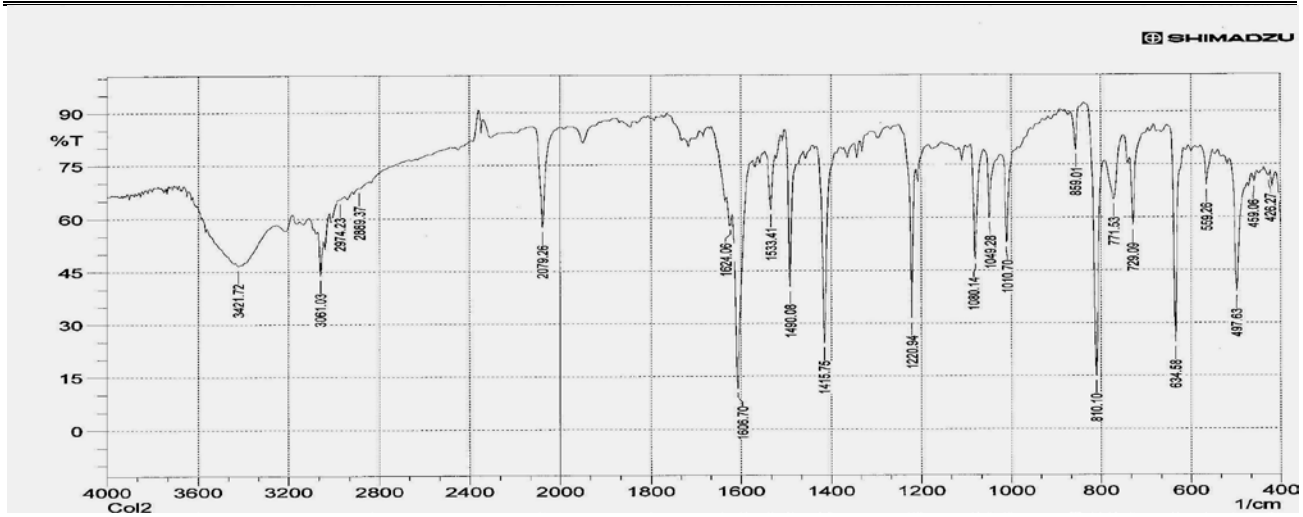

Figure (3.52) IR spectrum of $[Co_2(L^2)(N_3)_4].H_2O$

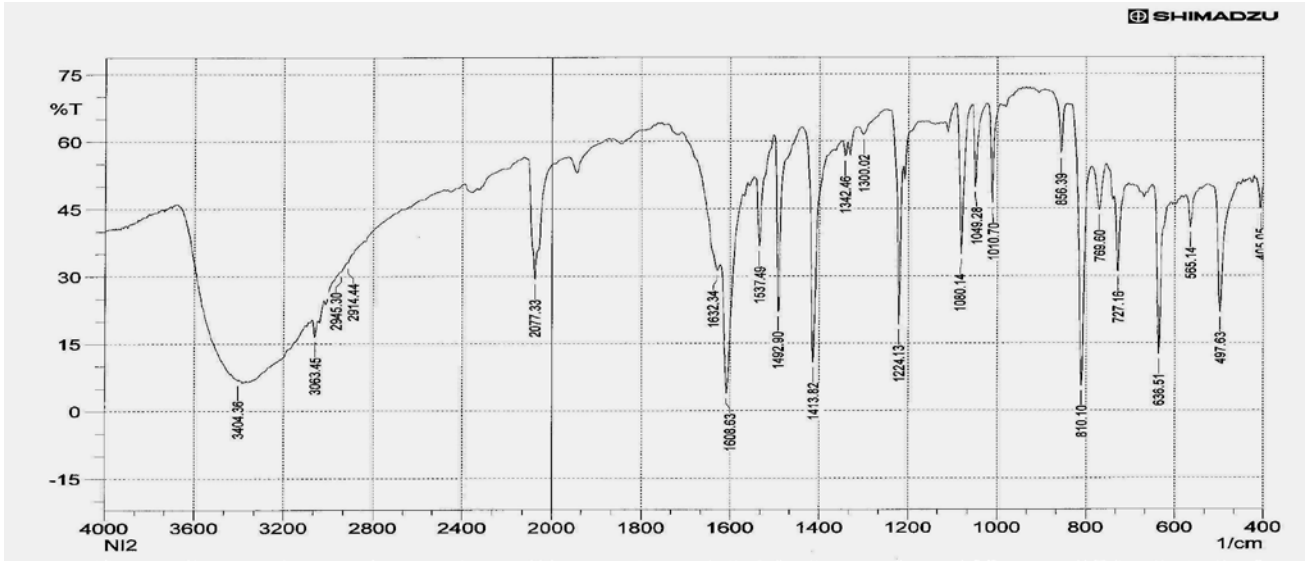

Figure (3.53) IR spectrum of $[Ni_2(L^2)(N_3)_4]H_2O$

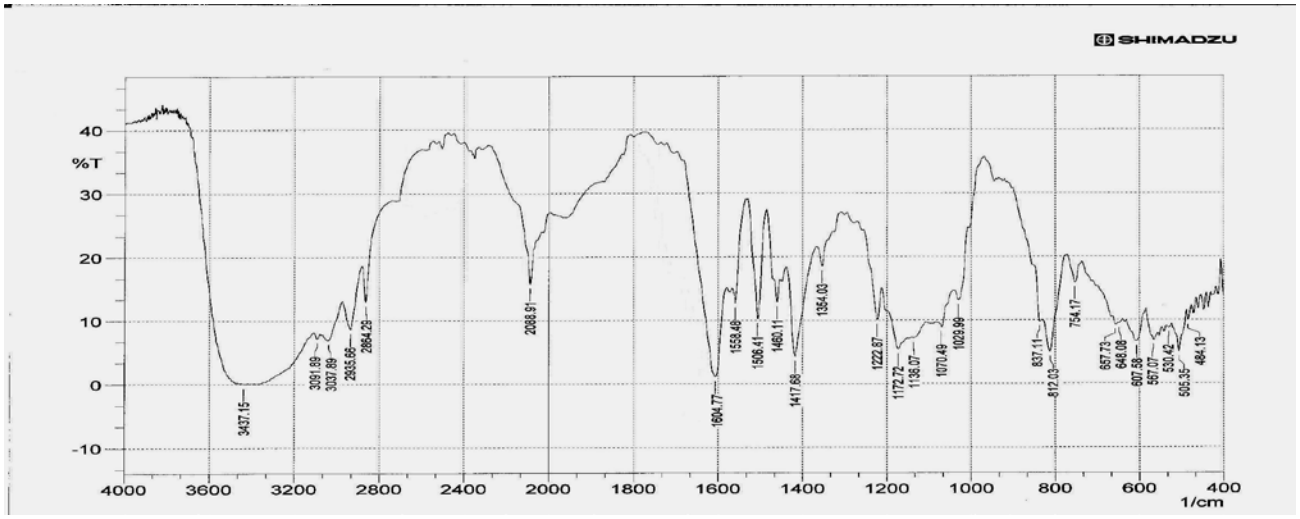

Figure (3.54) IR spectrum of $[Cu_2(L^2)(N_3)_4].H_2O$

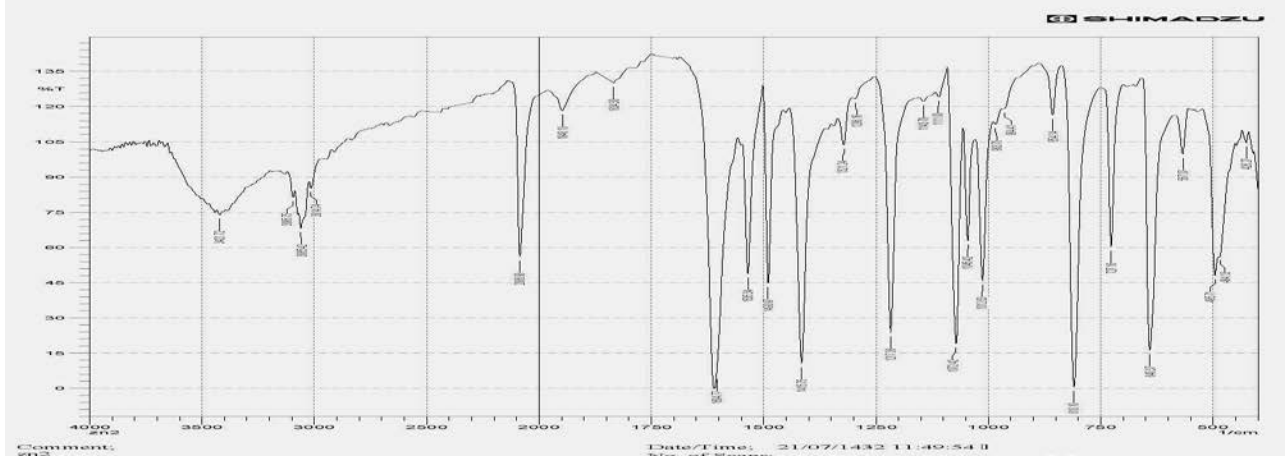

Figure (3. 55) IR spectrum of $[Zn_2(L^2)(N_3)_4].H_2O$

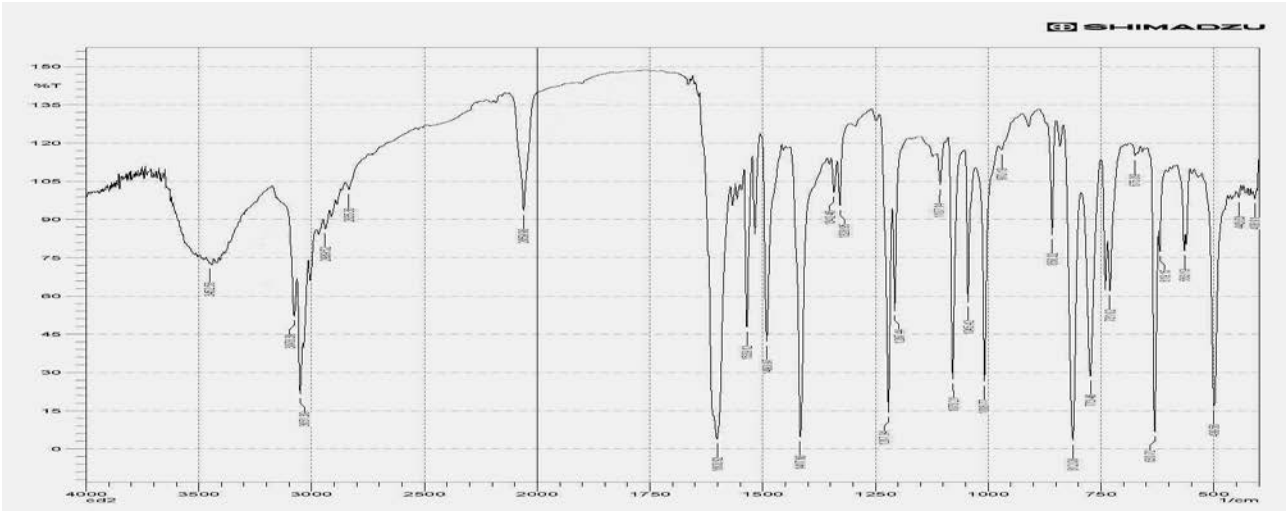

Figure (3. 56) IR spectrum of $[Cd_2(L^2)(N_3)_4]$

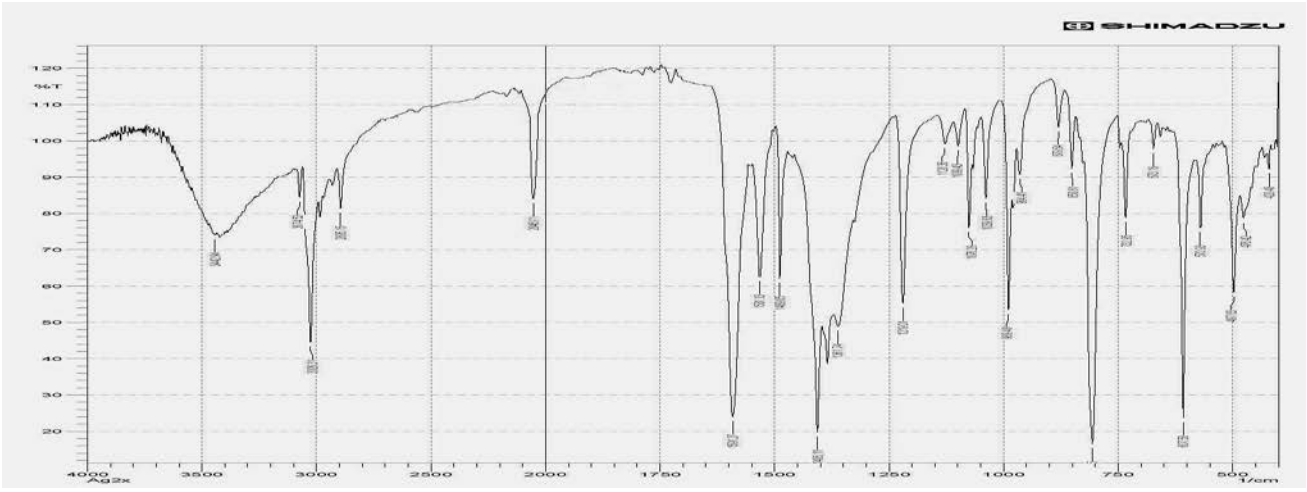

Figure (3. 57) IR spectrum of $Na_2[Ag_2(L^2)(N_3)_4]H_2O$

Table (3. 19) Infrared spectral data (wave number) cm^{-1} of L^2 complexes

Complex	νO-H	ν_{ar}C-H	νCH_2	$\nu_{as}N_3$	ν_{as}COO	νC=N	νC=C	ν_sCOO	δO-H	ν_sN_3	νC-N	$\delta_{O.O.P}$	νM-O	νM-N	$\Delta(\nu_{as}-\nu)$
L^2	-	3046	2903	-	1630	1620	1595	1458	-	-	1223		-	-	172
$[Cr_2(L^2)(N_3)_4]Cl_2.H_2O$	3385	3084 3058	2943	2091	1626	1616	1593 1474	1418	1558	1339	1225	799	517 576	419 436	208
$[Mn_2(L^2)(N_3)_4]H_2O$	3388	3055 3038	2837	2081	1614	1603	1568 1474	1416	1533	1329	1223	856 731	500 561	431 442	198
$[Fe_2(L^2)(N_3)_4]$	3381	3098	2872	2048	1601	1634	1551 1487	1410	1516	1342	1229	831 687	552 627	417 436 488	191
$[Co_2(L^2)(N_3)_4]H_2O$	3422	3061	2889	2079	1607	1624	1624	1416	1533	1319	1221	859 635	498 559	426 459	191
$[Ni_2(L^2)(N_3)_4]H_2O$	3404	3063	2914	2077	1609	1632	1632	1414	1537	1342	1224	856 637	498 565	405	195
$[Cu_2(L^2)(N_3)_4]H_2O$	3437	3092 3038	2864	2089	1605	1558	1558	1418	1506	1354	1223	851 646	505 530 567	441 452 484	187
$[Zn_2(L^2)(N_3)_4]H_2O$	3422	3096 3065 3015	2911	2087	1605	1535	1535	1416	1491	1321	1217	854 640	567 496	426 484	189
$[Cd_2(L^2)(N_3)_4]$	3453	3078 3051	2835	2060	1601	1563	1552	1418	1539	1329	1218	858 675	500 563	406 444	183
$Na_2[Ag_2(L^2)(N_3)_4]H_2O$	3443	3075 3026	2895	2046	1591	1531	1531	1406	1489	1326	1219	880 673	498 571	420 476	185

Where: ar = aromatic; s = symmetric; as = antisymmetric; o.o.p = out of plane.

(3.10.3) IR Spectral data for L^3 complexes

The IR spectral data of L^3 complexes are presented in Table (3. 20). The IR spectrum of the $[Cr_2(L^3)(N_3)_4]Cl_2.H_2O$ complex, Figure (3. 58), shows the characteristic carboxylato stretching frequency anti-symmetric $\nu_{as}(COO^-)$ and symmetric $\nu_s(COO^-)$ modes at 1620 and 1420 cm^{-1}, respectively[170]. The shift of these bands to lower wave numbers by 12 and 38 cm^{-1} compared with that in the free L^3 ligand can be attributed to delocalisation of metal electron density (t_2g) to the π-system of the ligand, and indicating the involvement of the carboxylato moiety in coordination with the Cr(III) ion. The vibration stretching modes $\nu_{as}(COO^-)$ and ν_s (COO^-) should help in elucidating the structure of the complex. The $\Delta(\nu_{as}- \nu_s)$ value of (200 cm^{-1}) is consistent with carboxylato bridging coordination fashion with the metal atoms in the *syn-syn* mode[171, 183]. Bands assigned to ν(C=N) and ν(C=C) stretching, were appeared at 1616 and 1595 cm^{-1}, respectively[172]. These bands are shifted to higher frequency in comparison with that in the free ligand, due to complex formation. The band at 3062, 3044 and 2862 cm^{-1} are assigned to $\nu(C-H)_{aromatic}$ and $\nu(CH_2)$ stretches, respectively[168]. The spectrum exhibited new band which are not present in the spectrum of the ligand. This band is located at 2068 cm^{-1} and may be assigned to asymmetric stretching mode of the azide $\nu_{as}(N_3)$. The appearance of a shoulder at 2114 cm^{-1} may imply to the involvement of the azido group[184] to interact through different layers in the polymeric complex. This could be occurred with the assistance of the hydrated water molecule by forming a hydrogen bond between the azido moiety and H_2O *via* N(μ-3) fashion. Therefore the azido group adopts N(μ-1,1,3) fashion (see Figure 1-5)[185]. The multiple bands are indicative of multiple bridging modes of the azido ligand, while the band at 1335 cm^{-1} can be assigned to symmetric vibration $\nu_s(N_3)$ stretching. (see Figure 1. 5)[176]. The band at 1223 cm^{-1} attributed to ν(C-N) stretching[168]. In the low-frequency

region, spectrum of the Cr(III) complex showed new bands which are not present in the spectrum of the ligand. These bands are located at 536, 562 and 424, 440 cm^{-1}, which are attributed to ν(Cr−O) and ν(Cr−N), respectively[174]. Additional broad band observed around 3414 is assigned to hydrated water molecule in the complex[166]. The appearance of ν(Cr−O) at frequency higher than that of ν(Cr−N) is due to the larger dipole moment change for the M-O bond compared to the M-N bond[178, 179]. Furthermore, the appearance of more than one value for M-O and M-N may reflect the impact of stacking of complex molecules in the polymeric structure.

The FTIR data of the $[Fe_2(L^3)(N_3)_4].H_2O$, complex is summarised in Table (3. 20) and is shown in Figure (3. 60). The spectrum shows bands related to the carboxylato moiety. These bands are detected at 1617 and 1400 cm^{-1}, which assigned to anti-symmetric $\nu_{as}(COO^-)$ and symmetric $\nu_s(COO^-)$ modes, respectively[181]. These bands are shifted to lower wave numbers by 15 and 58 cm^{-1} in comparison with that in the free L^3 ligand, The shift of these bands can be explained by using same reasoning used in the interpretation of Cr(lll) complex. The difference between $\nu_{as}(COO^-)$ and $\nu_s(COO^-)$ is currently employed to determine the corresponding mode of the caboxylate group. The $\Delta(\nu_{as}- \nu_s)$ value of (217 cm^{-1}) is in agreement with carboxylato bridging coordination fashion with the metal atoms in the *syn-syn* mode[171]. The stretching of $\nu_{as}(N_3)$ and $\nu_s(N_3)$ azido group are observed at 2064 and 1346 cm^{-1}, respectively[173] suggesting the EO bridging mode with metal ion with $N_{(\mu\text{-}1,1)}$ fashion (see Figure 1. 5) [176]. The bands at 536, 563 and 406, 436 cm^{-1}, are attributed to ν(Fe−O) and ν(Fe−N), respectively[174]. Additional broad band observed around 3439 cm^{-1} is assigned to hydrated water molecule present in the complex[177]. The appearance of ν(Fe−O) at frequency higher than that of ν(Fe−N) due to the larger dipole moment change for the M-O bond compared to the M-N bond[178, 179]. Furthermore, the appearance of more than one value for M-O and M-N

may indicate the formation of more than one dimension structure upon coordination, and indicating the polymer structure of the complexes.

The IR spectrum of the $[Ni_2(L^3)(N_3)_4].H_2O$ complex with L^3 is shown in Figure (3. 62), Table (3. 20). The spectrum exhibits similar bands to that in the Fe(II) complex, except the azido group showed two bands, one is shoulder, of the $\nu_{as}(N_3)$ one detected at 2060 cm^{-1}. The appearance of a shoulder at 2091cm^{-1} may imply to the involvement of the azido group[184] to interact with other species through different layers in the polymeric complex. This could be occurred with the assistance of the hydrated water molecule by forming a hydrogen bond between the azido moiety and H_2O *via* N(μ-3) fashion. Therefore the azido group adopts N(μ-1,1,3) fashion (see Figure 1.5)[185]. The multiple peaks are indicative of multiple bridging modes of the azido ligand. The band at (1344 cm^{-1}) may be assigned to symmetric stretching mode of the azido $\nu_s(N_3)$[173].

The IR spectra of $[Mn_2(L^3)(N_3)_4].2H_2O$, $[Co_2(L^3)(N_3)_4].H_2O$, $[Cu_2(L^3)(N_3)_4]$, $[Zn_2(L^3)(N_3)_4].H_2O$ and $[Cd_2(L^3)(N_3)_4].H_2O$ and $Na_2[Ag_2(L^3)(N_3)_4].H_2O$, Figures (3. 59, 3. 61, 3. 63 to 3. 66), exhibit similar trend to that of the $[Ni_2(L^3)(N_3)_4].H_2O$ complex and same reasoning could be used to interpret the spectra.

The prepared complexes showed both $\nu_{as}(COO^-)$ and $\nu_s(COO^-)$ frequencies is changed in the same direction, indicating that the coordination of the carboxylato moiety is bridging bidentate. This is because the bond orders of both C-O bonds would change by the same amount. This result is in accord with data reported by Hamed and co-workers[183]. In all complexes the coordination mode of the carboxylato group is *syn-syn*, except Ag^I complex which shows the *syn-anti* mode. The Δ (ν_{as}- ν_{as}) value of (166 cm^{-1}) confirming the carboxylato bridge coordination fashion with Ag(I) ion in the *syn-anti* mode. This is in a good agreement with previous studies of *syn-anti* carboxylato bridge coordination mode[177].

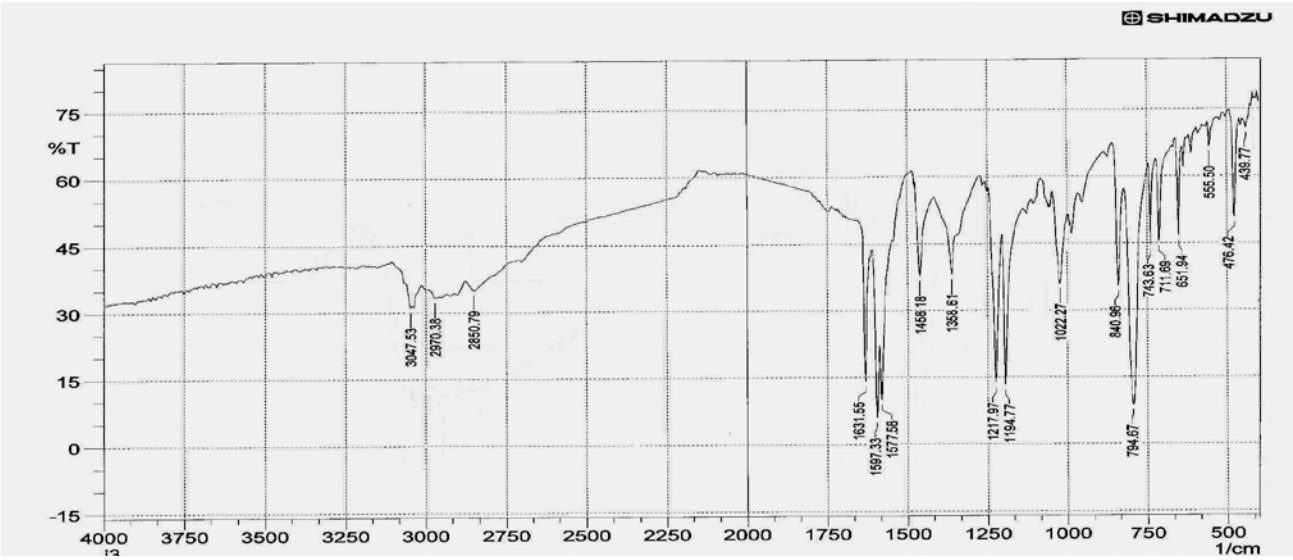

Figure (3. 8) IR spectrum of L^3

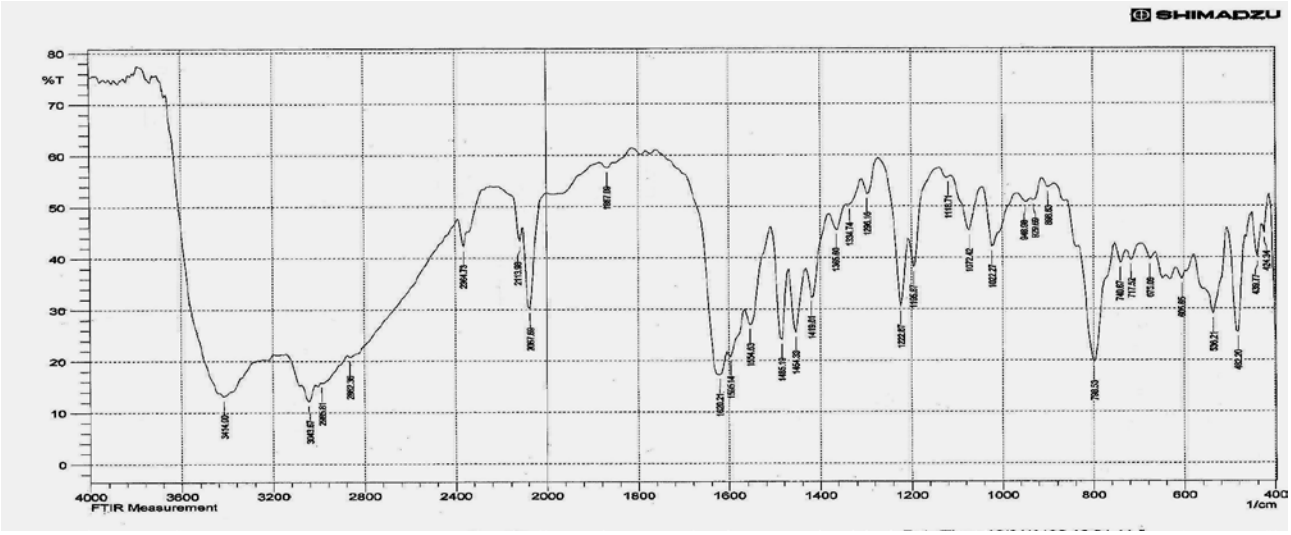

Figure (3. 58) IR spectrum of $[Cr_2(L^3)(N_3)_4]Cl_2.H_2O$

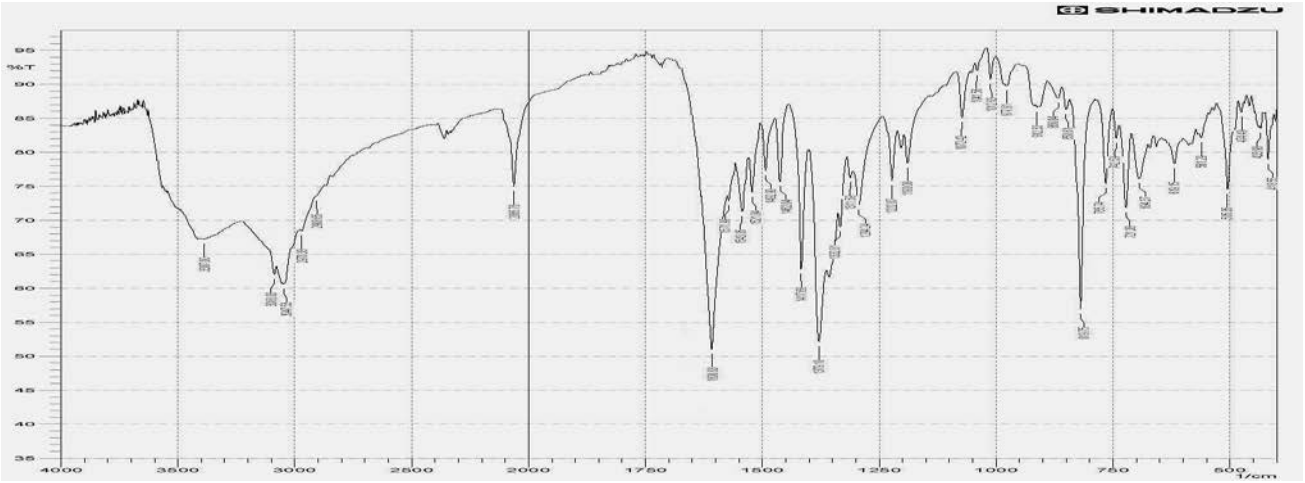

Figure (3. 59) IR spectrum of $[Mn_2(L^3)(N_3)_4].2H_2O$

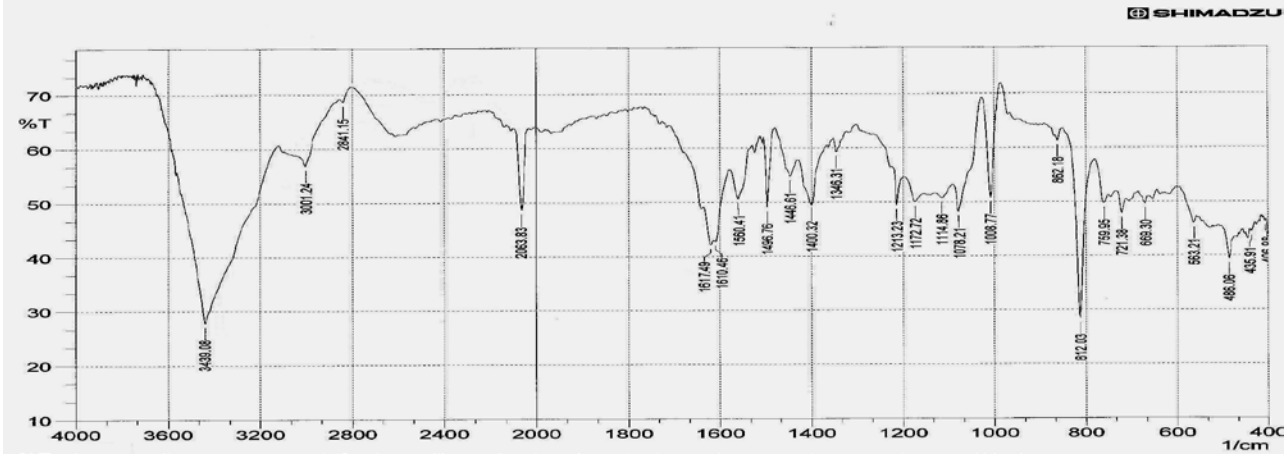

Figure (3. 60) IR spectrum of $[Fe_2(L^3)(N_3)_4].H_2O$

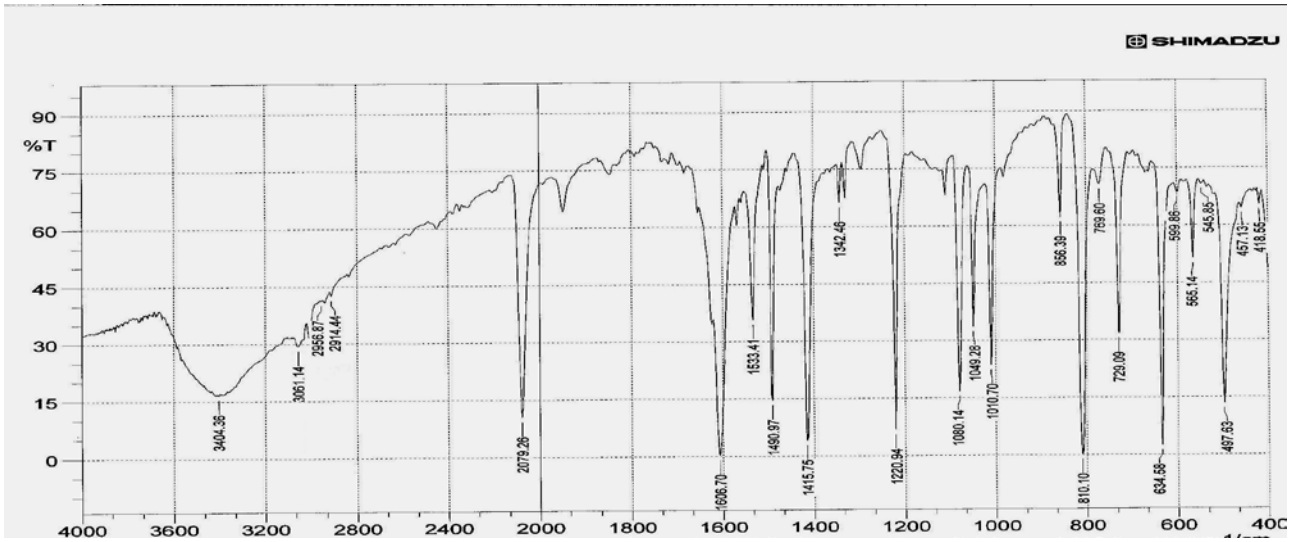

Figure (3. 61) IR spectrum of $[Co_2(L^3)(N_3)_4].H_2O$

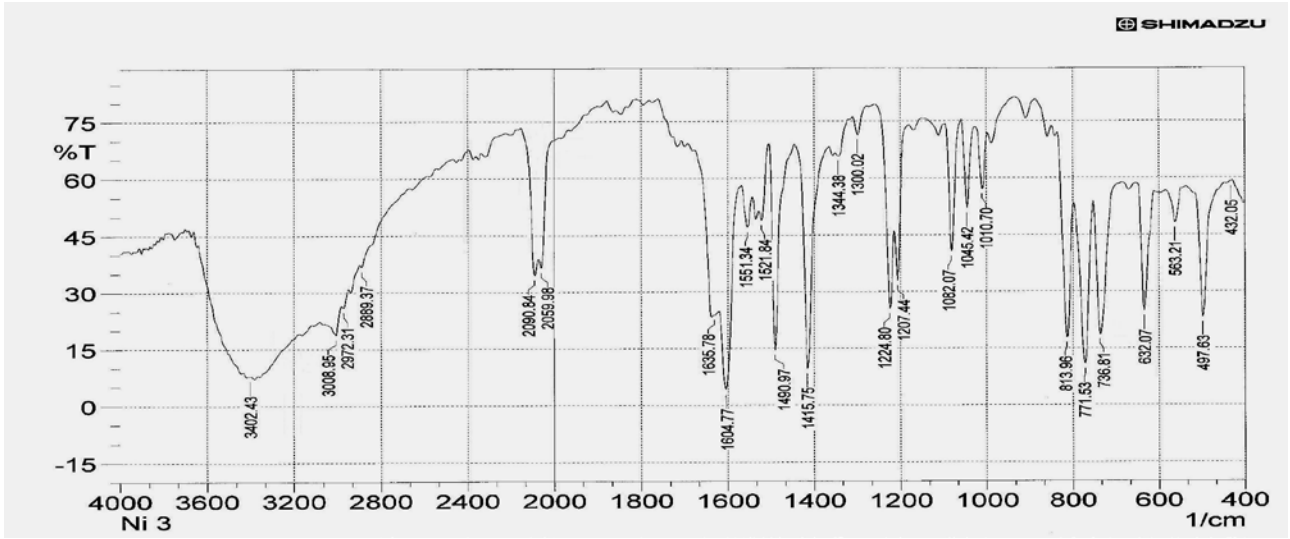

Figure (3. 62) IR spectrum of $[Ni_2(L^3)(N_3)_4].H_2O$

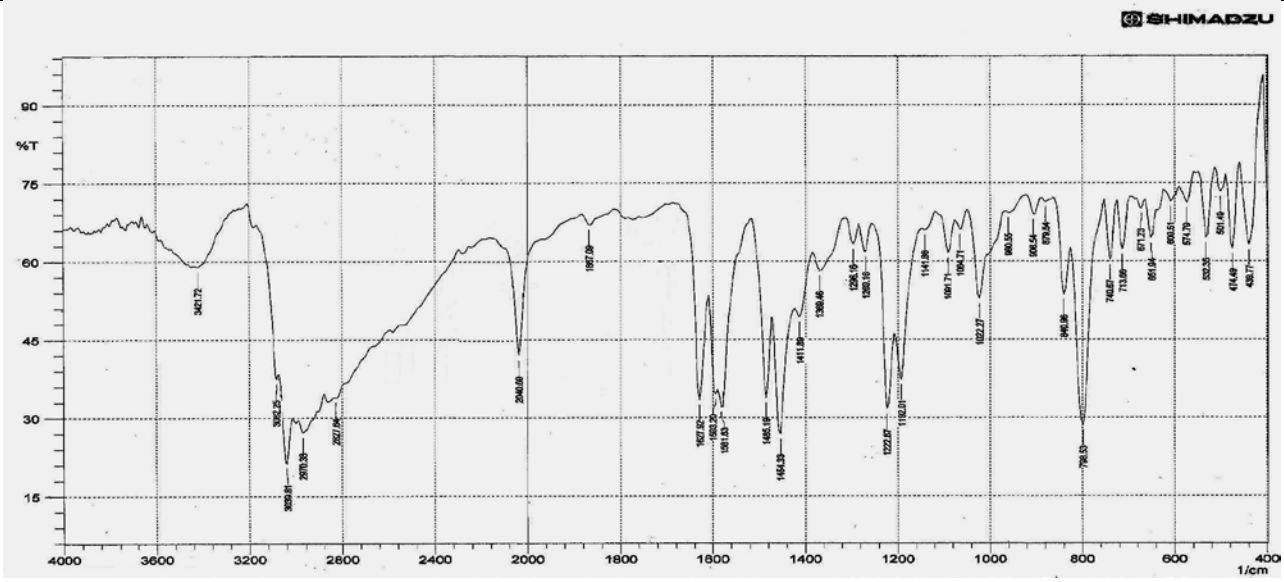

Figure (3. 63) IR spectrum of $[Cu_2(L^3)(N_3)_4]$

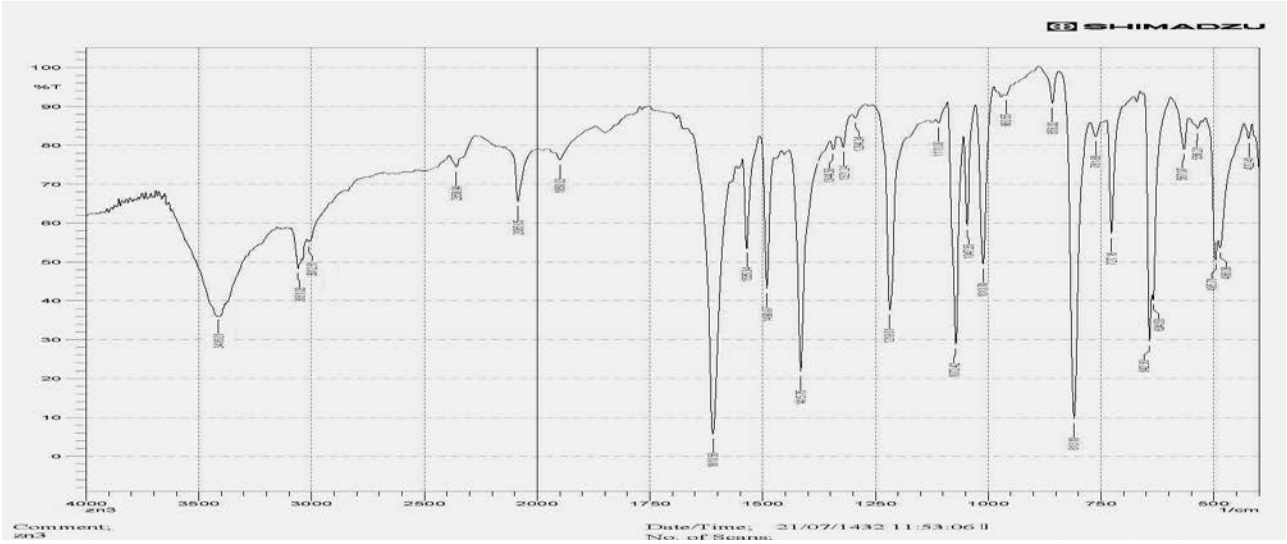

Figure (3. 64) IR spectrum of $[Zn_2(L^3)(N_3)_4].H_2O$

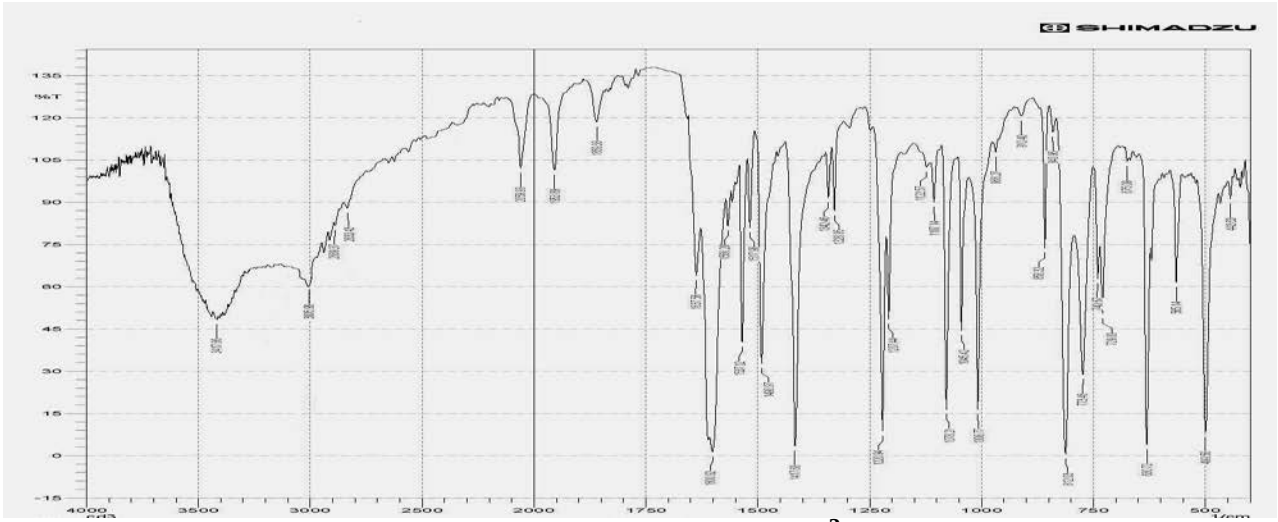

Figure (3. 65) IR spectrum of $[Cd_2(L^3)(N_3)_4].H_2O$

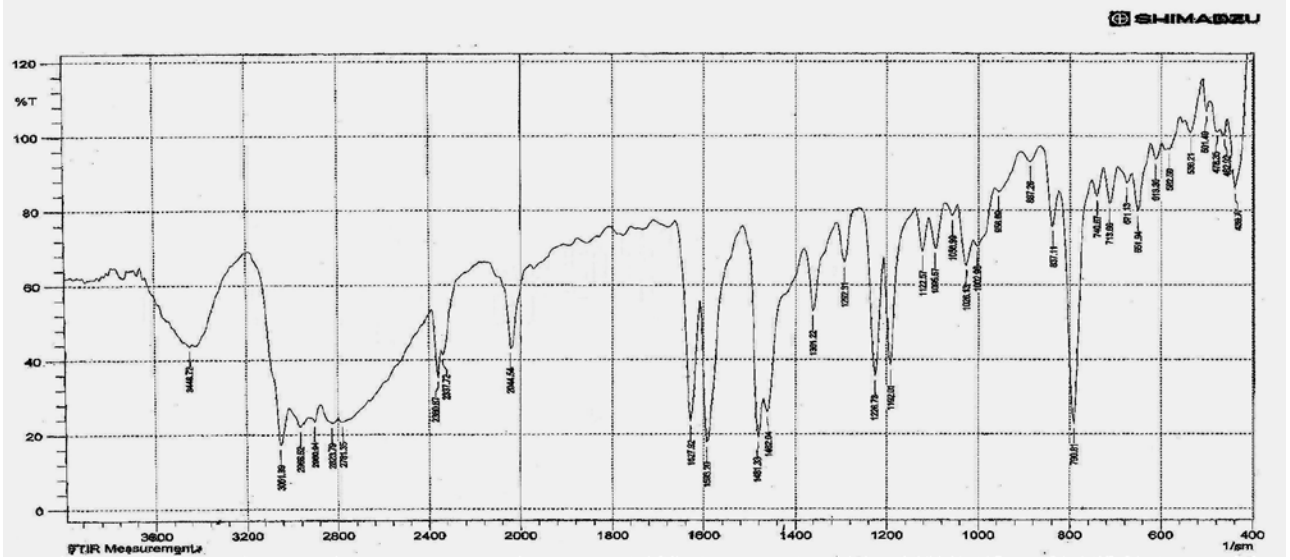

Figure (3. 66) IR spectrum of $Na_2[Ag_2(L^3)(N_3)_4].H_2O$

Table (3. 20)Infrared spectral data (wave number) cm^{-1} of L^3 complexes

Complex	ν O-H	ν_{ar} C-H	νCH_2	$\nu_{as}N_3$	$\nu_{as}COO$	νC=N	νC=C	ν_sCOO	δO-H	ν_sN_3	νC-N	δ O.O.P	νM-O	νM-N	$\Delta(\nu_{as}-\nu)$
L^3	-	3048	2851	-	1632	1597	1578	1458	-	-	1218		-	-	174
$[Cr_2(L^3)(N_3)_4]Cl_2.H_2O$	3414	3062 3044	2862	2114 2068	1620	1595	1595 1454	1420	1555	1335	1223	949 675	536 562	424 440	200
$[Mn_2(L^3)(N_3)_4].2H_2O$	3387	3088 3048	2909	2066	1609	1572	1543 1462	1418	1522	1333	1223	978 694	505 561	419 434	191
$[Fe_2(L^3)(N_3)_4].H_2O$	3439	3001	2841	2064	1617	1610	1610 1447	1400	1560	1346	1213	862 669	536 563	406 436	217
$[Co_2(L^3)(N_3)_4].H_2O$	3404	3061	2914	2079	1607	1570	1570	1416	1533	1342	1221	856 635	546 565	419 457	191
$[Ni_2(L^3)(N_3)_4].H_2O$	3402	3009	2889	2091 2060	1605	1636	1551	1416	1522	1344	1225	814 632	498 563	432	189
$[Cu_2(L^3)(N_3)_4]$	3422	3082 3040	2828	2041	1628	1593	1582 1458	1412	1485	1369	1223	937 644	501 532 574	440 474	216
$[Zn_2(L^3)(N_3)_4].H_2O$	3416	3013	2846	2085	1611	1533	1533	1416	1491	1344	1219	961 642	536 567	422 486	195
$[Cd_2(L^3)(N_3)_4].H_2O$	3418	3006	2833	2060	1601	1638	1560	1418	1537	1329	1221	968 675	500 565	444 463	183
$Na_2[Ag_2(L^3)(N_3)_4].H_2O$	3449	3061	2824	2045	1628	1593	1593	1462	1482	1361	1227	957 671	501 583	478 483	166

Where: ar = aromatic; s = symmetric; as = antisymmetric; o.o.p = out of plane.

(3.10.4) IR Spectral data for L^4 complexes

The structurally important IR absorption frequencies of the $[Cr_2(L^4)(N_3)_4]Cl_2.H_2O$ complex with L^4 is shown in Figure (3. 67), Table (3. 21). The IR spectrum shows the bands of anti-symmetric $\nu_{as}(COO^-)$ and symmetric $\nu_s(COO^-)$ modes, of the carboxylato moiety at 1593 and 1412 cm^{-1}, respectively[167]. The shift of these bands compared with that in the free L^4 ligand can be attributed to delocalisation of metal electron density (t_2g) to the π-system of the ligand, and indicating the involvement of the carboxylato in coordination with the Cr(III) ion. The $\Delta(\nu_{as}- \nu_s)$ value of (181 cm^{-1}) is consistent with carboxylato bridging coordination fashion with the metal atoms in the *syn-syn* mode[171]. The spectrum shows bands at 1628 and 1582 cm^{-1} assigned to ν(C=N) and ν(C=C) stretching, respectively[172]. The shift of the former and the latter to higher frequency, compared with that in the free ligand, is due to complex formation. The band at 3082, 3040 and 2828 cm^{-1} are assigned to $\nu(C\text{-}H)_{aromatic}$ and $\nu(CH_2)$ stretches, respectively[168]. The intense band located at 2047 cm^{-1} may attribute to asymmetric stretching mode of the azido $\nu_{as}(N_3)$. The appearance of a shoulder at 2106 cm^{-1} may imply to the involvement of the azido group[184] to connect different layers in the polymeric complex. This could be occurred with the assistance of the hydrated water molecule by forming a hydrogen bond between the azido moiety and H_2O via N(μ-3) fashion. Therefore the azido group adopts N(μ-1,1,3) fashion (see Figure 1. 5)[185]. The multiple peaks are indicative of multiple bridging modes of the azido ligand. The band at 1369 cm^{-1} is assigned to symmetric vibration $\nu_s(N_3)$ stretch[176]. In the low-frequency region, spectrum of the Cr(III) complex showed new bands which are not observed in the spectrum of the ligand.

These bands are located at 532 and 575 and 440,474 cm^{-1}, which are attributed to ν(Cr−O) and ν(Cr−N), respectively[174]. Additional broad band observed around 3421 cm^{-1} is assigned to hydrated water molecule in the complex[166].

The IR spectra of $[Mn_2(L^4)(N_3)_4].H_2O$, $[Fe_2(L^4)(N_3)_4]$, $[Co_2(L^4)(N_3)_4]$ $.H_2O$, $[Ni_2(L^4)(N_3)_4].H_2O$, $[Cu_2(L^4)(N_3)_4].H_2O$, $[Zn_2(L^4)(N_3)_4]$, $[Cd_2(L^4)$ $(N_3)_4]$ and $Na_2[Ag_2(L^4)(N_3)_4].H_2O$ Figures (3. 68 to 3. 75) show a similar pattern to that of $[Cr_2(L^4)(N_3)_4]Cl_2.H_2O$ complex and same reasoning could be used to interpret the spectra.

The prepared complexes showed both $v_{as}(COO^{-})$ and $v_{as}(COO^{-})$ frequencies is changed in the same direction, indicating that the coordination of the carboxylate moiety is bridging bidentate. This is because the bond orders of both C-O bonds would change by the same amount. This result is in a good agreement with the data reported by E-Hamed and co-workers[182]. All the complexes shows the *syn-syn* mode of the carboxylate group.

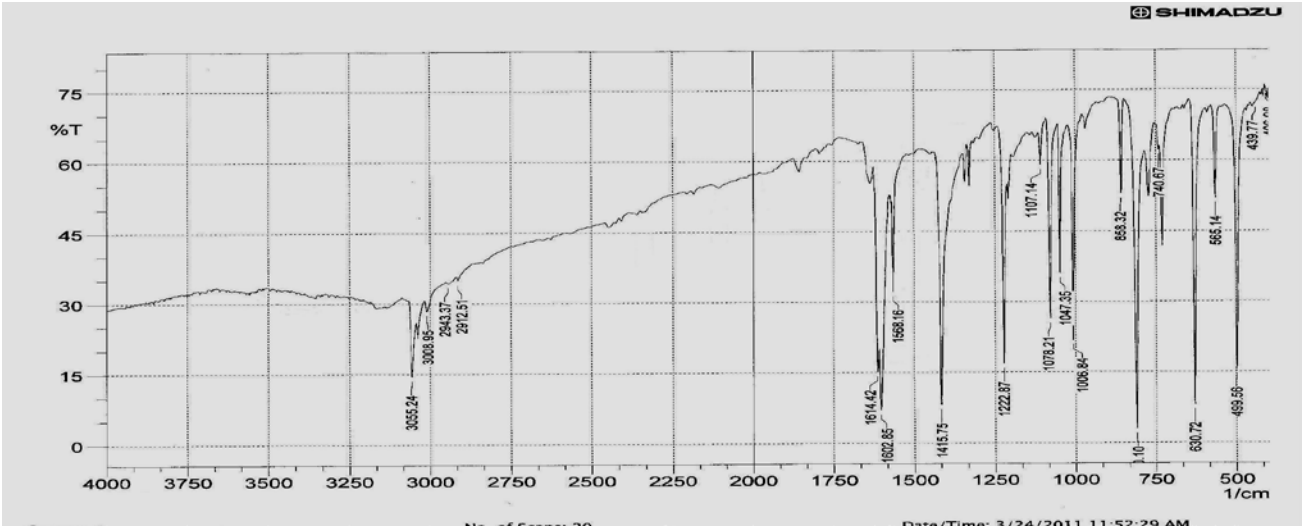

Figure (3. 10) IR spectrum of L^4

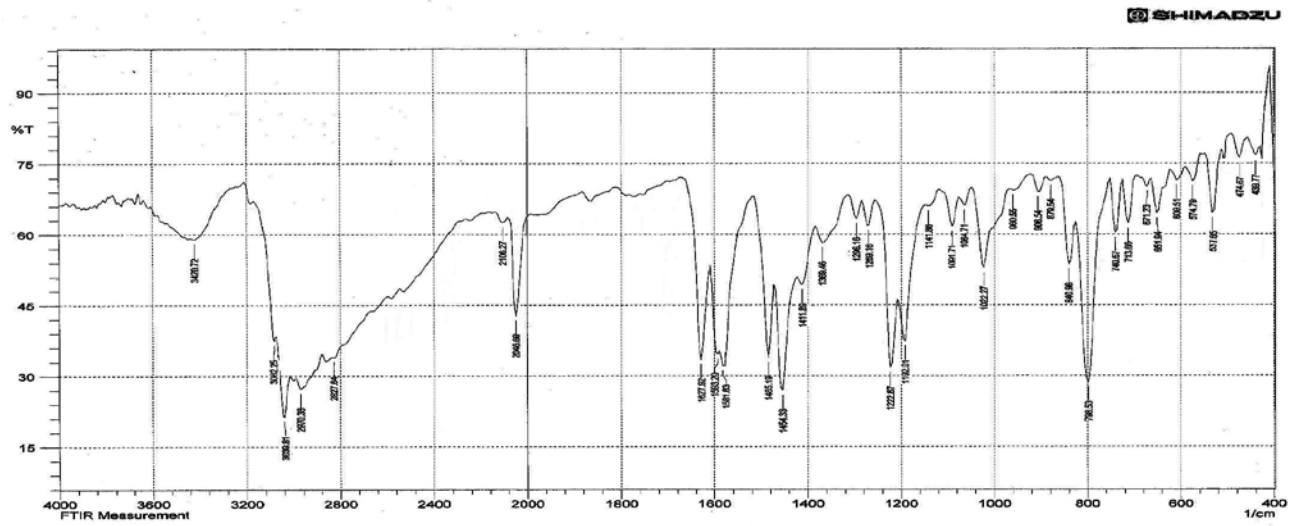

Figure (3. 67) IR spectrum of $[Cr_2(L^4)(N_3)_4]Cl_2.H_2O$

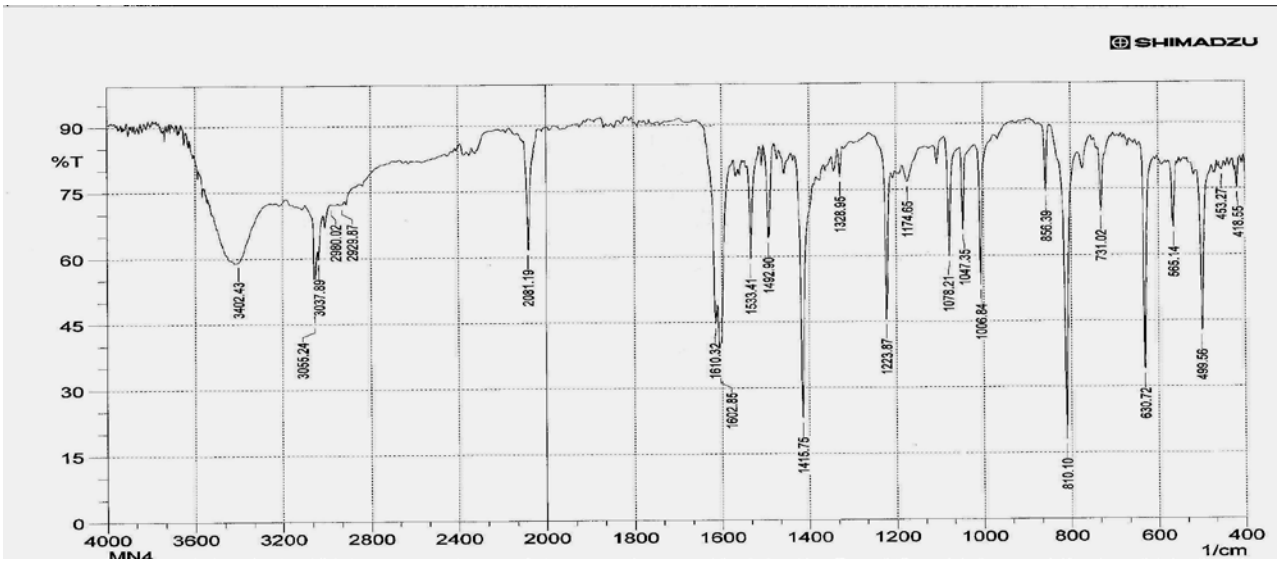

Figure (3. 68) IR spectrum of $[Mn_2(L^4)(N_3)_4].H_2O$

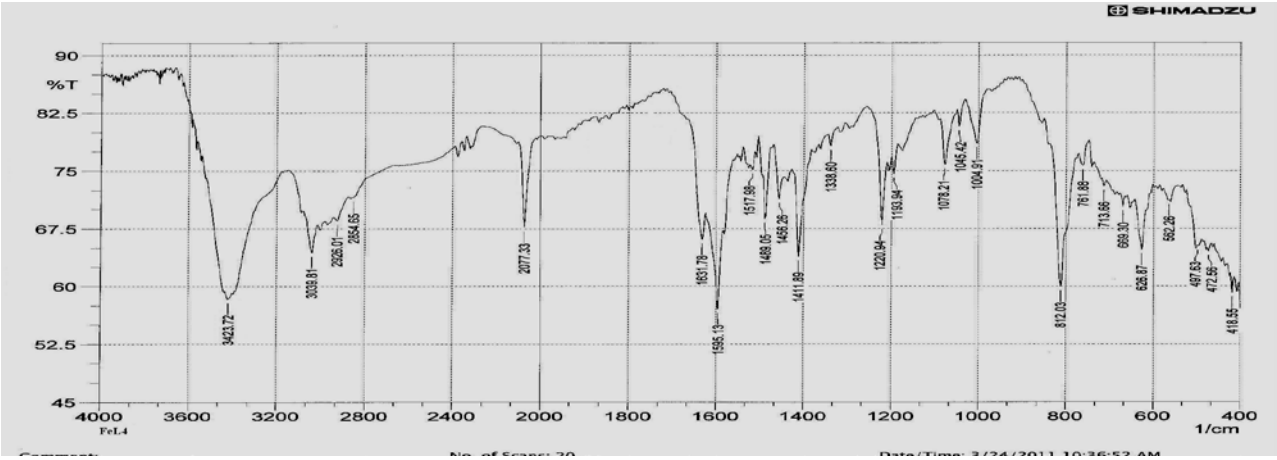

Figure (3. 69) IR spectrum of $[Fe_2(L^4)(N_3)_4]$

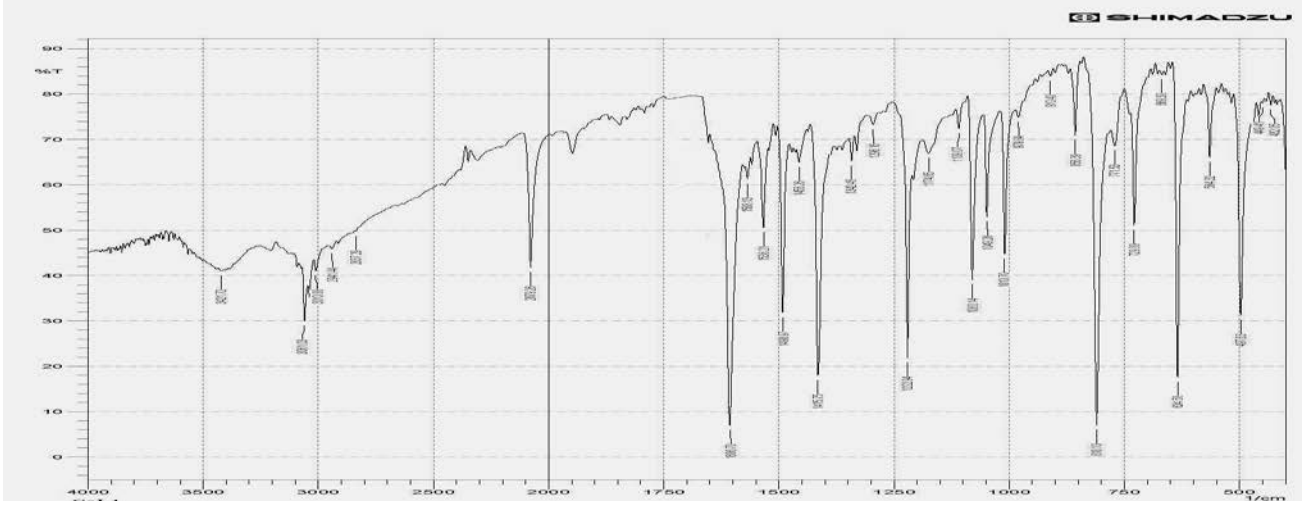

Figure (3. 70) IR spectrum of $[Co_2(L^4)(N_3)_4].H_2O$

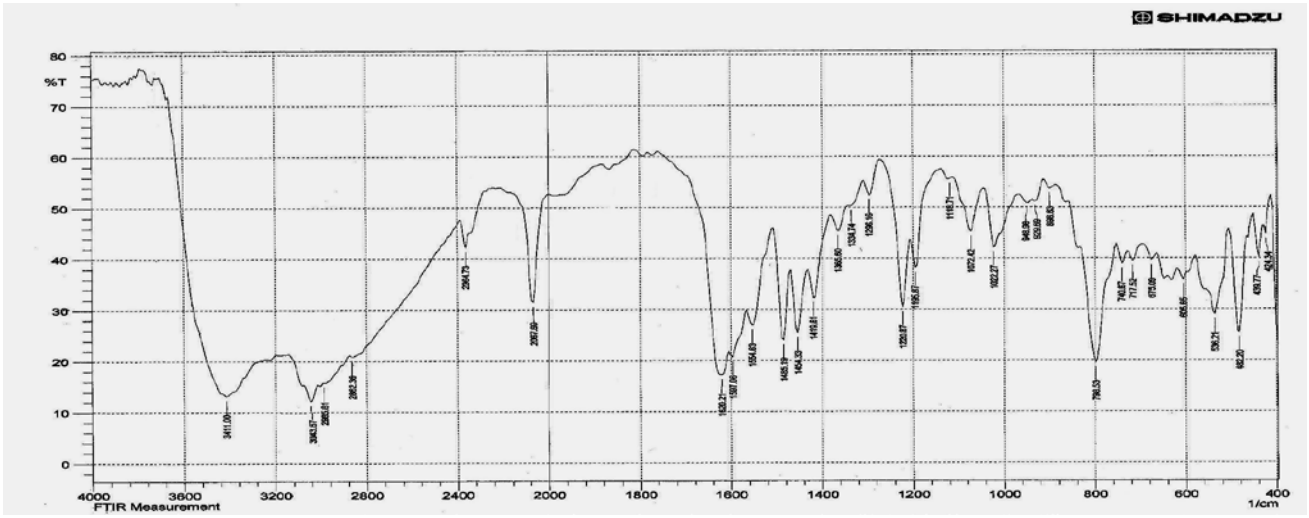

Figure (3. 71) IR spectrum of $[Ni_2(L^4)(N_3)_4].H_2O$

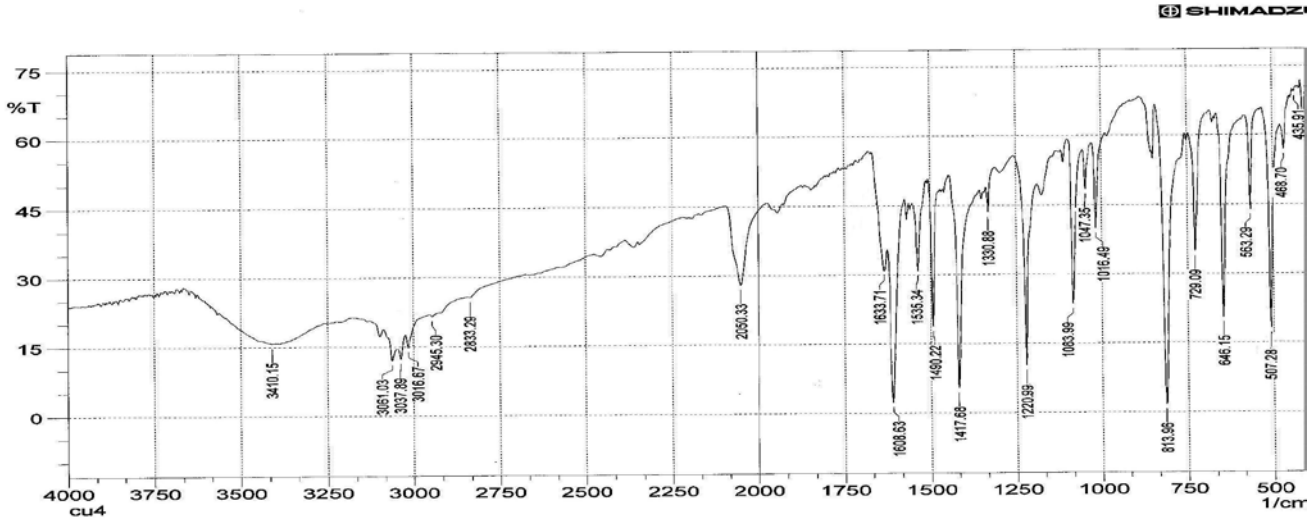

Figure (3. 72) IR spectrum of $[Cu_2(L^4)(N_3)_4].H_2O$

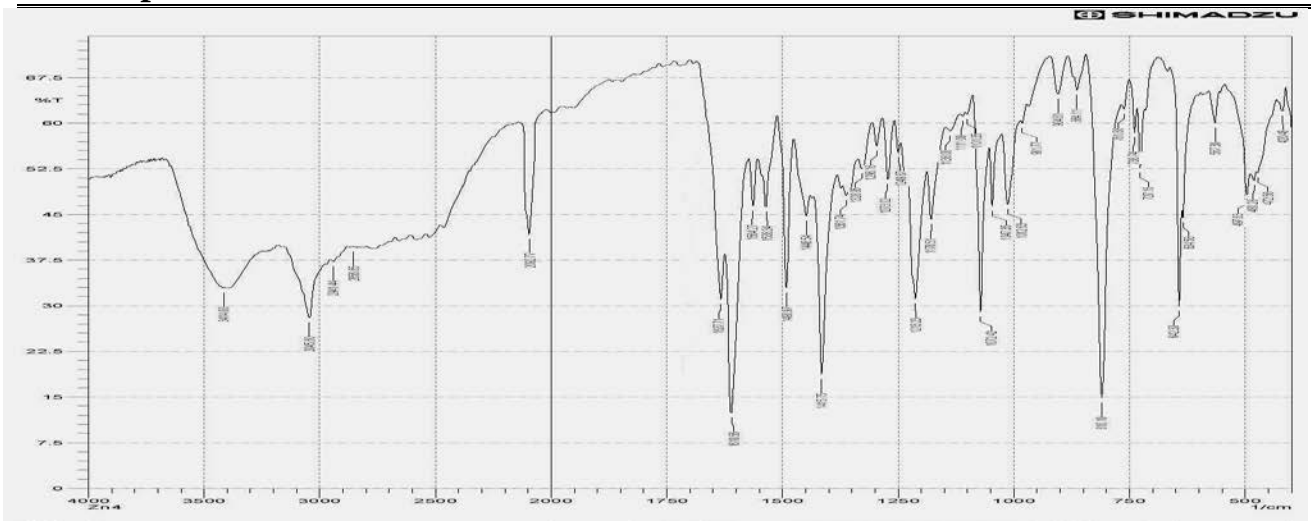

Figure (3. 73) IR spectrum of $[Zn_2(L^4)(N_3)_4]$

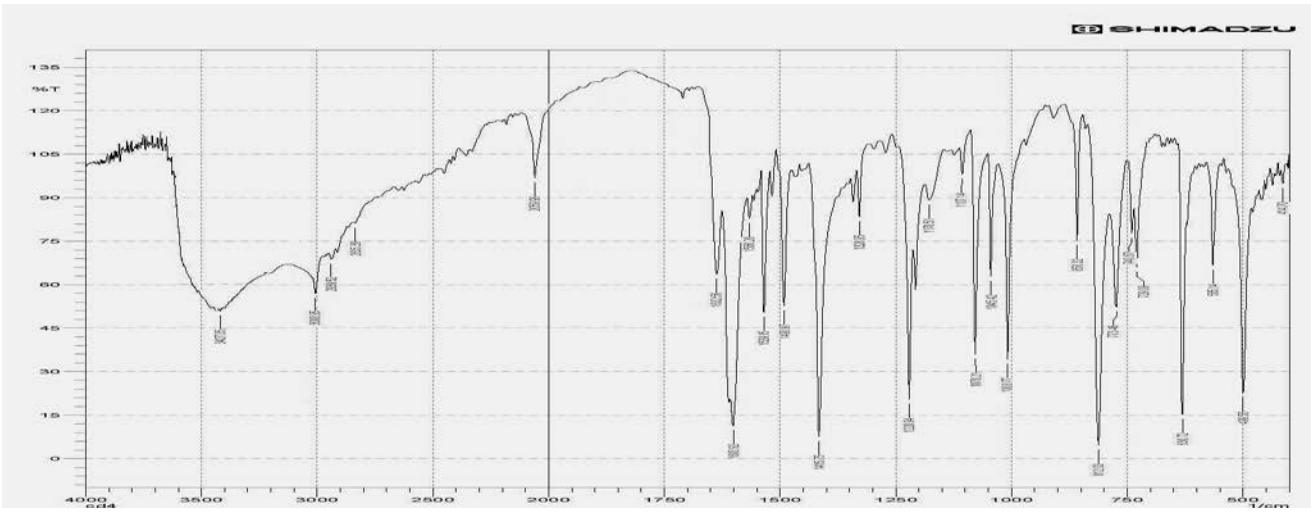

Figure (3. 74) IR spectrum of $[Cd_2(L^4)(N_3)_4]$

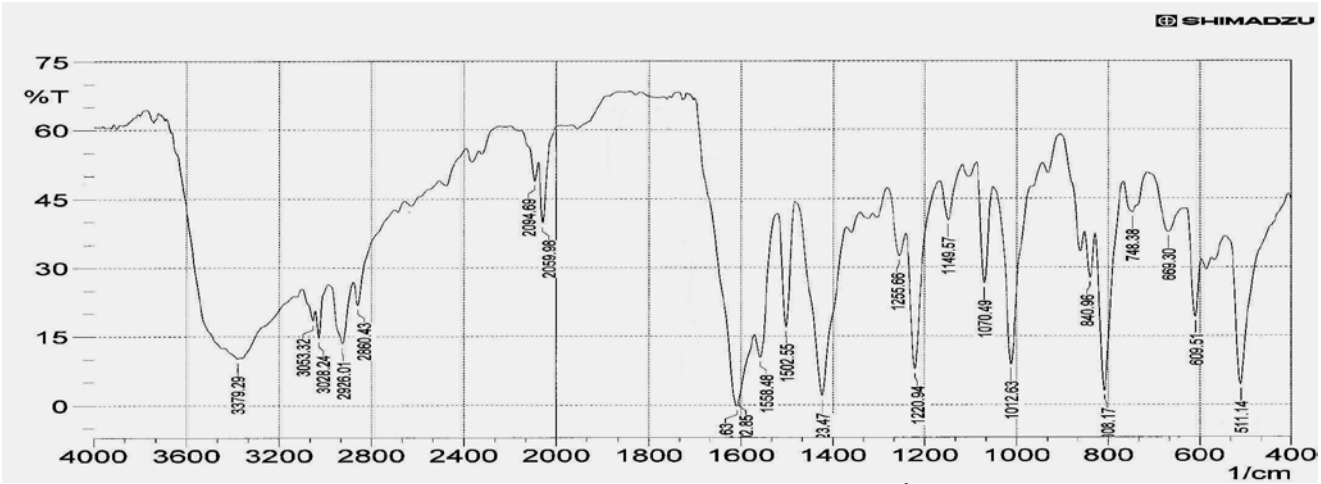

Figure (3. 75) IR spectrum of $Na_2[Ag_2(L^4)(N_3)_4].H_2O$

Table (3. 21)Infrared spectral data (wave number) cm^{-1} of L^4 complexes

Complex	ν O-H	ν_{ar}C-H	νCH$_2$	$\nu_{as}N_3$	ν_{as}COO	νC=N	νC=C	ν_sCOO	δO-H	ν_sN_3	νC-N	$\delta_{O.O.P}$	νM-O	νM-N	$\Delta(\nu_{as}-\nu_s)$
L^4	-	3055 3009	2913	-	1614	1603	1568	1416	-	-	1223		-	-	198
$[Cr_2(L^4)(N_3)_4]Cl_2.H_2O$	3421	3082 3040	2828	2106 2047	1593	1628	1582 1454	1412	1485	1369	1223	961 652	532 575	440 474	181
$[Mn_2(L^4)(N_3)_4].H_2O$	3402	3055 3038	2930	2081	1610	1603	1603 1456	1416	1533	1329	1224	856 631	565	419 453	194
$[Fe_2(L^4)(N_3)_4]$	3424	3040	2855	2077	1595	1632	1632 1456	1412	1518	1339	1221	812 669	498 562	419 473	183
$[Co_2(L^4)(N_3)_4].H_2O$	3422	3061 3011	2837	2079	1607	1568	1568 1456	1416	1536	1342	1223	810 635	507 564	432 449	191
$[Ni_2(L^4)(N_3)_4].H_2O$	3414	3044	2862	2068	1620	1597	1597 1454	1420	1555	1335	1221	949 675	536 606	424 440	200
$[Cu_2(L^4)(N_3)_4].H_2O$	3410	3061 3038 3017	2833	2050	1609	1634	1535	1418	1490	1331	1221	814 646	507 563	436 469	191
$[Zn_2(L^4)(N_3)_4]$	3414	3046	2857	2093	1611	1638	1564	1416	1538	1329	1213	981 642	498 567	420 473	195
$[Cd_2(L^4)(N_3)_4]$	3427	3009	2835	2060	1601	1633	1566	1416	1539	1329	1221	858 631	565	415 441	185
$Na_2[Ag_2(L^4)(N_3)_4].H_2O$	3380	3053 3028	2860	2095 2060	1609	1593	1593	1423	1493	1318	1221	856 669	511 561	426	186

Where: ar = aromatic; s = symmetric; as = antisymmetric; o.o.p = out of plane.

(3.10.5) IR Spectral data for L^5 complexes

The essential infrared data of complexes with L^5 are presented in Table (3. 22). The IR spectrum of $[Cr_2(L^5)(N_3)_4]Cl_2.H_2O$, Figure (3. 76), shows the characteristic bands of the carboxylato moiety at 1601 and 1398 cm^{-1}, which are assigned to anti-symmetric $\nu_{as}(COO^-)$ and symmetric $\nu_s(COO^-)$ modes, respectively[181]. The shift of these bands to lower wave numbers by 42 and 31 cm^{-1} compared with that in the free L^5 ligand can be attributed to delocalisation of metal electron density (t_2g) to the π-system of the ligand, and confirming the involvement of the ($-COO^-$) in coordination with the Cr(III) ion. The $\Delta(\nu_{as}- \nu_s)$ value of (203 cm^{-1}) is consistent with carboxylato bridge coordination fashion with the metal atoms in the *syn-syn* mode[171]. The spectrum shows bands at 1582 and 1564 cm^{-1} assigned to ν(C=N) and ν(C=C) stretching, respectively[166, 167]. These bands are shifted to lower and higher frequency for the former and the latter, respectively in comparison with that in the free ligand, due to complex formation. The intense new bands at 2043 and 1319 cm^{-1}, are attributed to $\nu_{as}(N_3)$ and $\nu_s(N_3)$ stretches, respectively[173]. These values suggest azido bridge mode with metal ion with $N_{(\mu\text{-}1,1)}$ fashion (see Figure 1.5)[173]. The band at 1198 cm^{-1} attributed to ν(C-N) stretching. The spectrum of the Cr(III) complex shows new bands located at 530, 565 and 467, 494 cm^{-1}, which are attributed to ν(Cr−O) and ν(Cr−N), respectively[174, 186]. Additional broad band observed around 3422 cm^{-1} is assigned to hydrated water molecule in the complex[177].

The IR spectra of $[Mn_2(L^5)(N_3)_4]H_2O$, $[Fe_2(L^5)(N_3)_4]H_2O$, $[Co_2(L^5)(N_3)_4]H_2O$, $[Ni_2(L^5)(N_3)_4]H_2O$, $[Cu_2(L^5)(N_3)_4]$ and $[Zn_2(L^5)(N_3)_4]H_2O$, Figures (3. 76 to 3. 81), show similar IR pattern to that of $[Cr_2(L^5)(N_3)_4]Cl_2H_2O$ complex and same reasoning could be used to interpret the spectra.

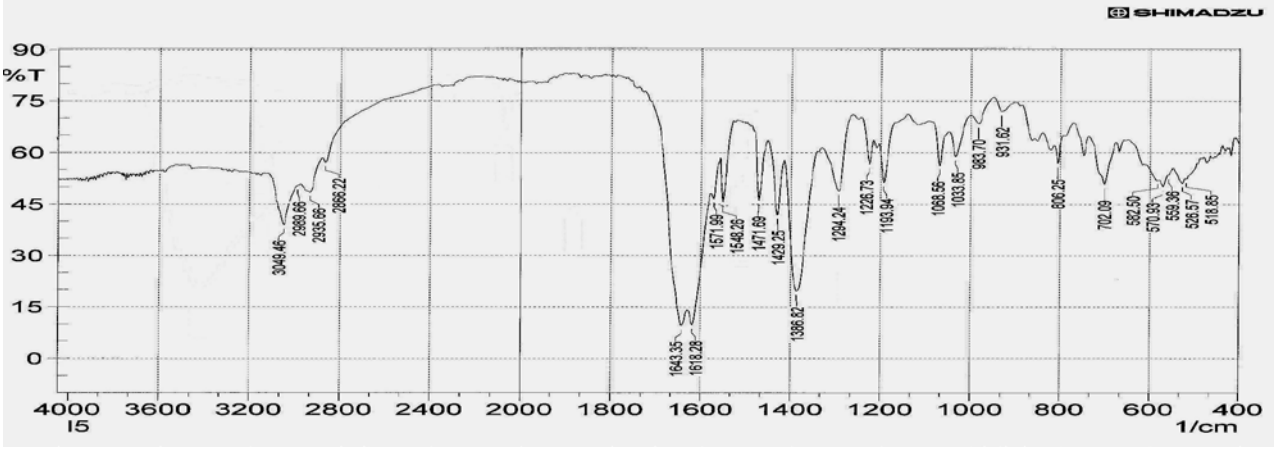

Figure (3. 12)IR spectrum of L^5

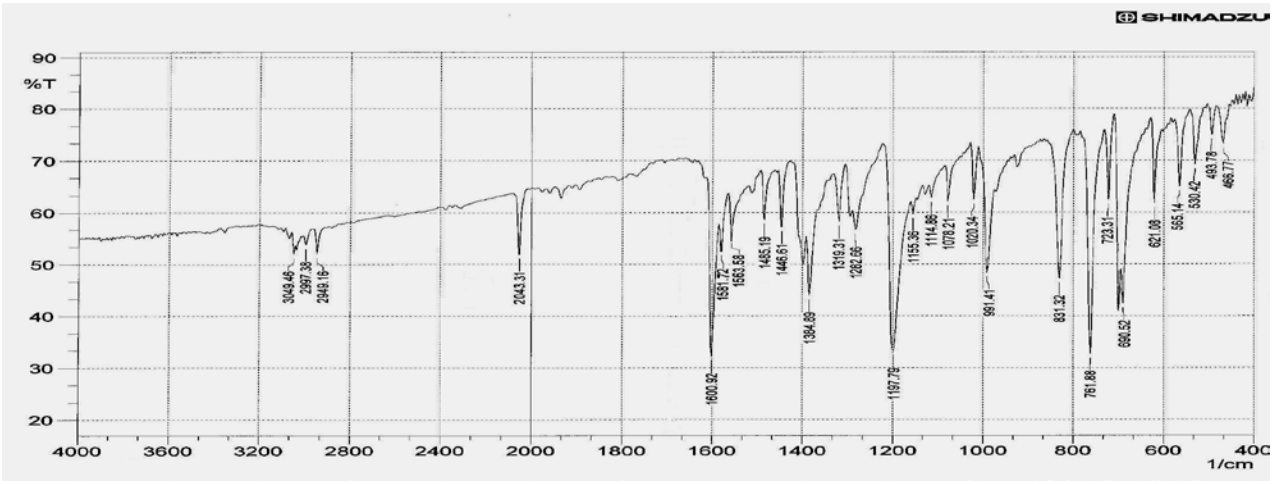

Figure (3. 76) IR spectrum of $[Cr_2(L^5)(N_3)_4]Cl_2.H_2O$

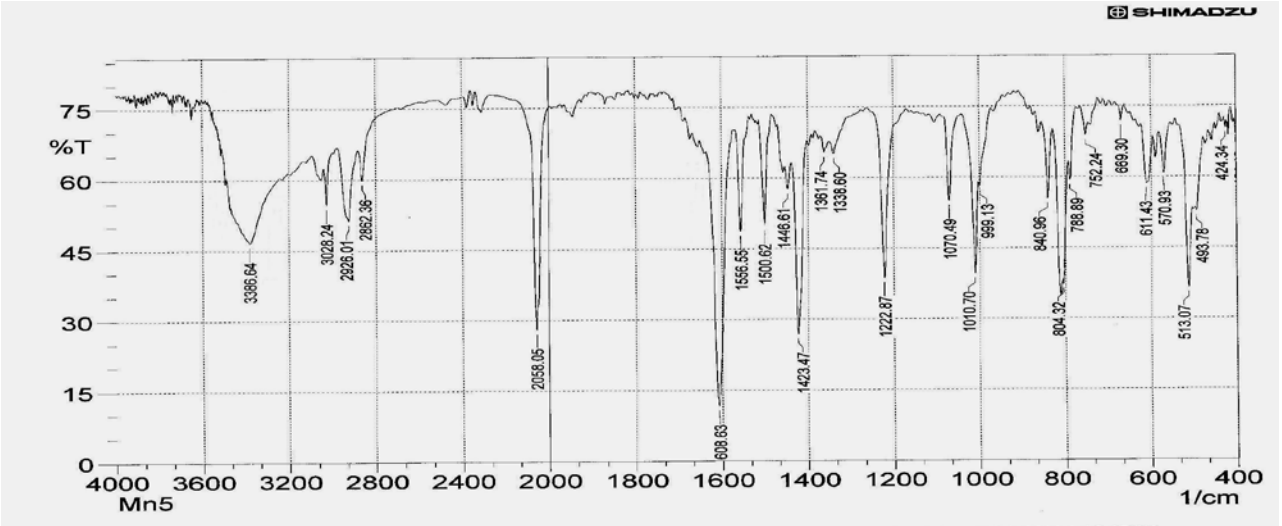

Figure (3. 77) IR spectrum of $[Mn_2(L^5)(N_3)_4].H_2O$

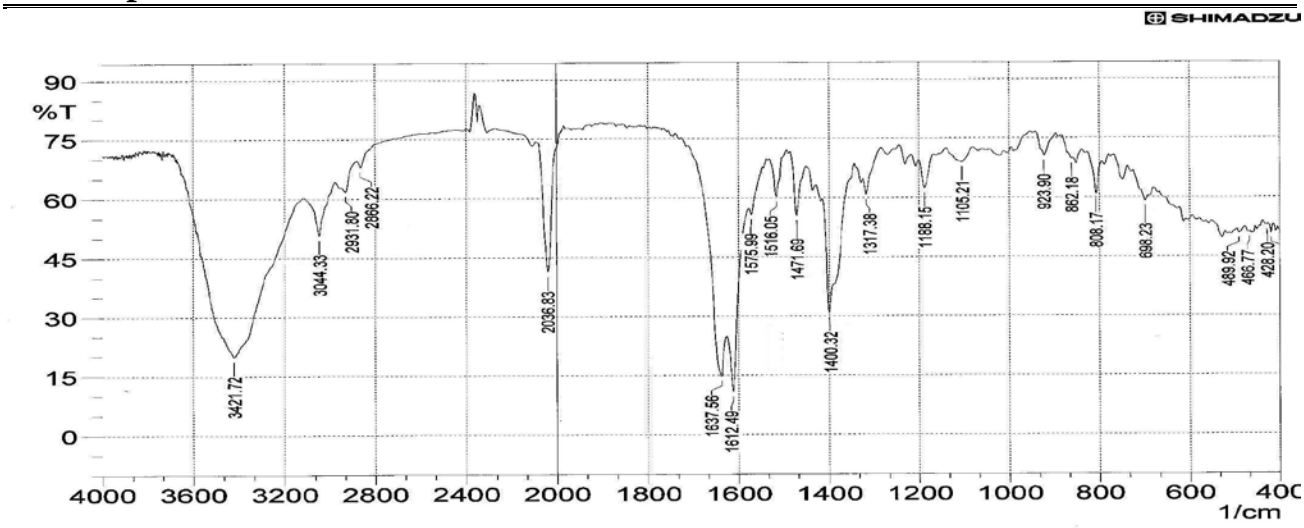

Figure (3. 78) IR spectrum of $[Fe_2(L^5)(N_3)_4].H_2O$

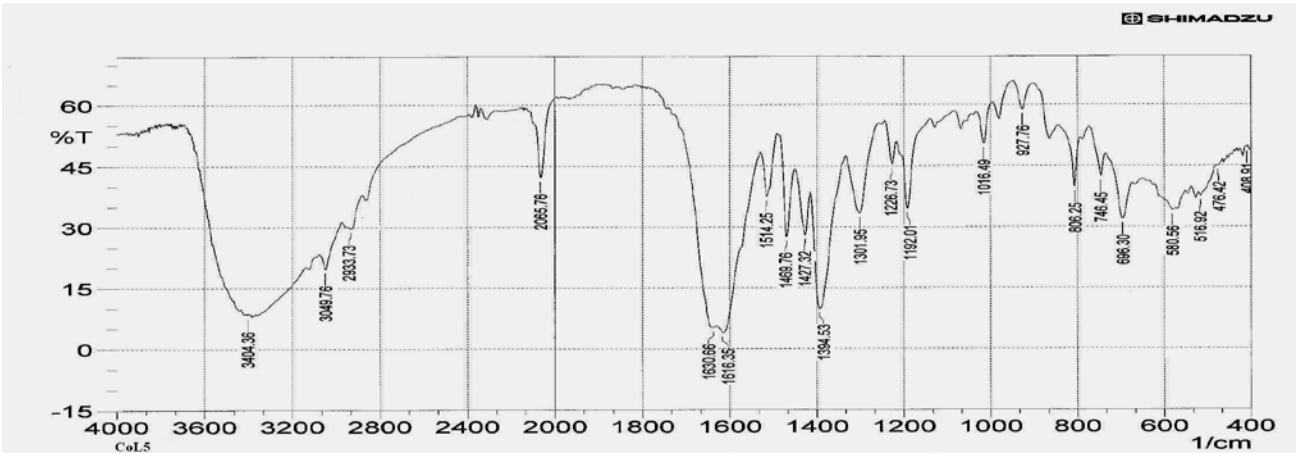

Figure (3. 79) IR spectrum of $[Co_2(L^5)(N_3)_4].H_2O$

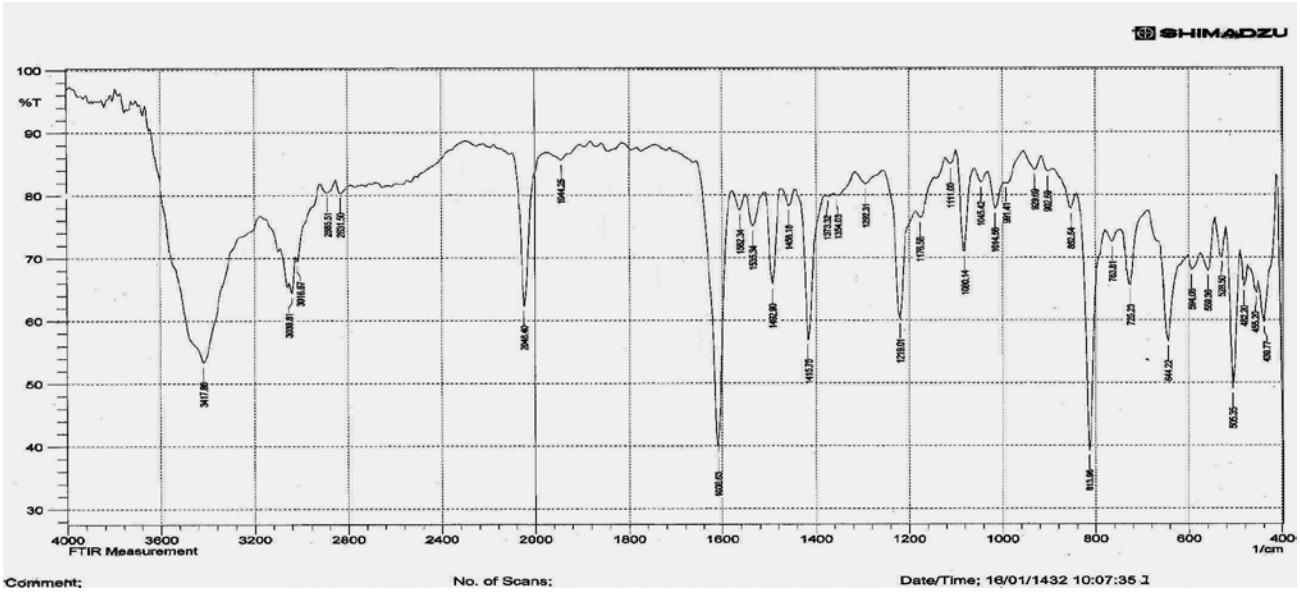

Figure (3. 80) IR spectrum of $[Ni_2(L^5)(N_3)_4].H_2O$

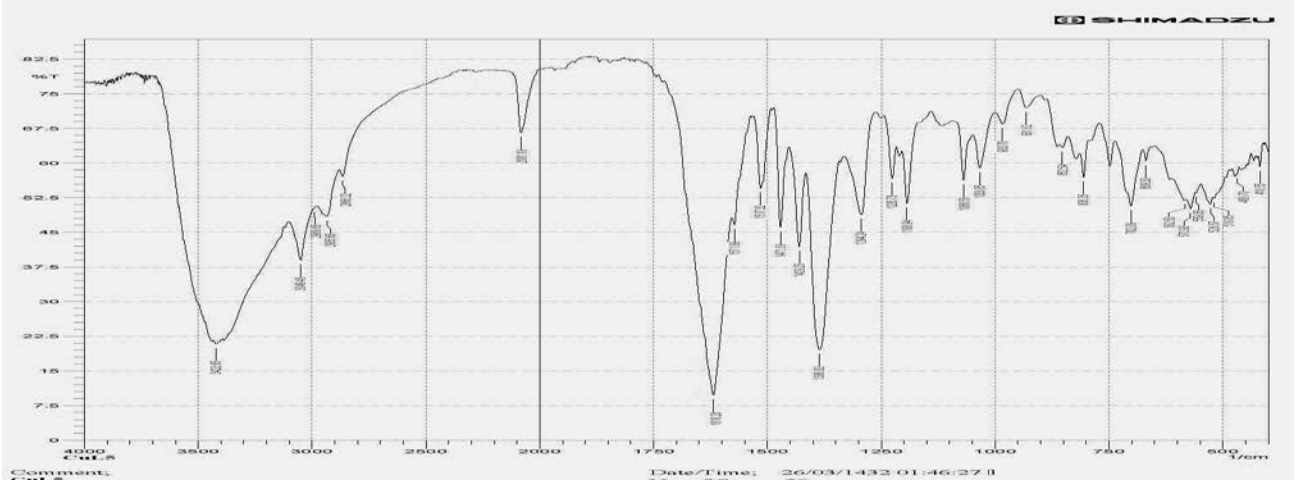

Figure (3. 81) IR spectrum of $[Cu_2(L^5)(N_3)_4].H_2O$

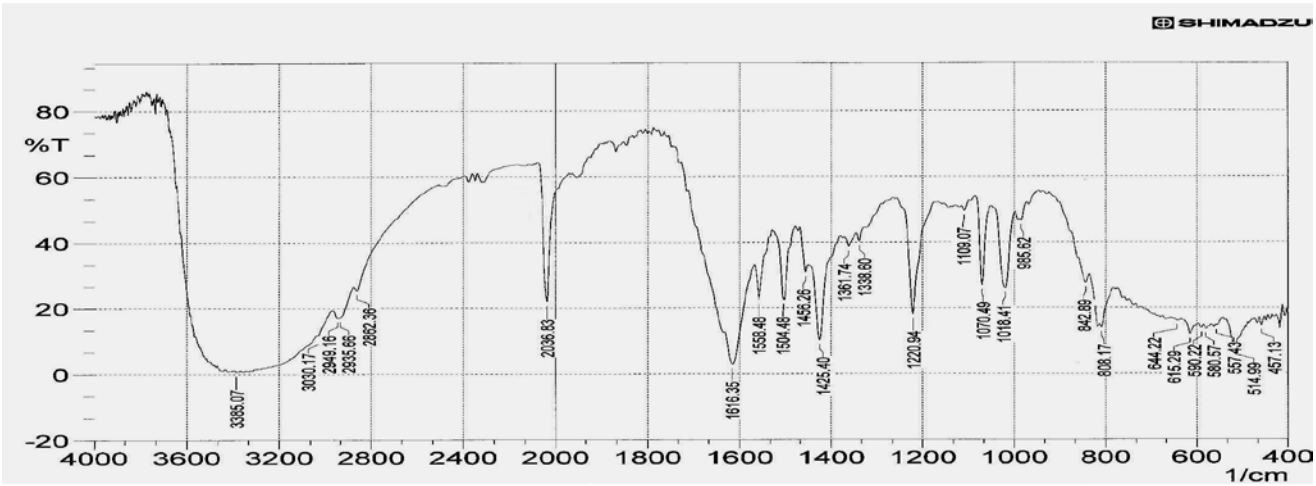

Figure (3. 82) IR spectrum of $[Zn_2(L^5)(N_3)_4].H_2O$

The IR spectrum of $[Cd_2(L^5)(N_3)_4].H_2O$ complex, Figure (3. 83), shows characteristic frequencies of the ligand with the appropriate shift, indicating the coordination to metal atom. The spectrum shows bands of the anti-symmetric $\nu_{as}(COO^-)$ and symmetric $\nu_s(COO^-)$ modes, of $(-COO^-)$ moiety at 1614 and 1433 cm^{-1}, respectively[167]. The shift of the former band to lower wave numbers by 29 cm^{-1} and the latter band to higher wave number by 4 cm^{-1} compared with that in the free L^5 ligand can be attributed to delocalisation of metal electron density (t_2g) to the π-system of the ligand, and indicating the involvement of the (COO^-) group in coordination with the Cd(II) ion. The stretching vibration modes $\nu_{as}(COO^-)$ and symmetric $\nu_s(COO^-)$ of the carboxylate group should help in elucidating the structure of the complex. The $\Delta(\nu_{as}-\nu_s)$ value of (181 cm^{-1}) is consistent with carboxylato

bridge coordination mode with the metal atoms in the *syn-syn* mode[171]. The spectrum shows band at 1641and 1576 cm^{-1} assigned to ν(C=N) and ν(C=C) stretching, respectively[166, 167]. These bands are shifted to higher frequency in comparison with that in the free ligand, due to complex formation. The intense bands located at 2064 and 1344 cm^{-1}, are attributed to $\nu_{as}(N_3)$ and $\nu_s(N_3)$ stretches, respectively[176]. The appearance of a shoulder at 2104 cm^{-1} may imply to the involvement of the azido[184] to connect different layers in the polymeric complex. This could be occurred with the assistance of the hydrated water molecule by forming a hydrogen bond between the azido moiety and H_2O via N(μ-3) fashion. Therefore the azido group adopts N(μ-1,1,3) fashion (see Figure 1. 5)[185]. The multiple peaks are indicative of multiple bridging modes of the azido ligand. Spectrum of the Cd (II) complex showed new bands which are not present in the spectrum of the ligand. These bands are located at 575, 430 and 455 cm^{-1}, respectively, which are attributed to ν(Cd−O) and ν(Cd−N)[174, 186]. Additional broad band observed around 3439 cm^{-1} is assigned to hydrated water molecule in the complex[177].

The IR spectrum of $Na_2[Ag_2(L^5)(N_3)_4].H_2O$, Figure (3. 84) shows a similar IR pattern to that of $[Cd_2(L^5)(N_3)_4]$ H_2O complex which shows two bands for the azido group and same reasoning could be used to interpret the spectra.

The prepared complexes showed both $\nu_{as}(COO^-)$ and $\nu_s(COO^-)$ frequencies is changed in the same direction, indicating that the coordination of the carboxylate moiety is bridging bidentate. This is because the bond orders of both C-O bonds would change by the same amount. This result is in accord with data reported by E-Hamed and co-workers [183].

The appearance of ν(M−O) at frequency higher than that of ν(M−N) due to the larger dipole moment change for the M-O bond compared to the M-N bond[178, 179]. Furthermore, the appearance of more than one value for M-O and M-N may indicate the formation of more than one dimension structure upon coordination, and indicating the polymer structure of the complexes.

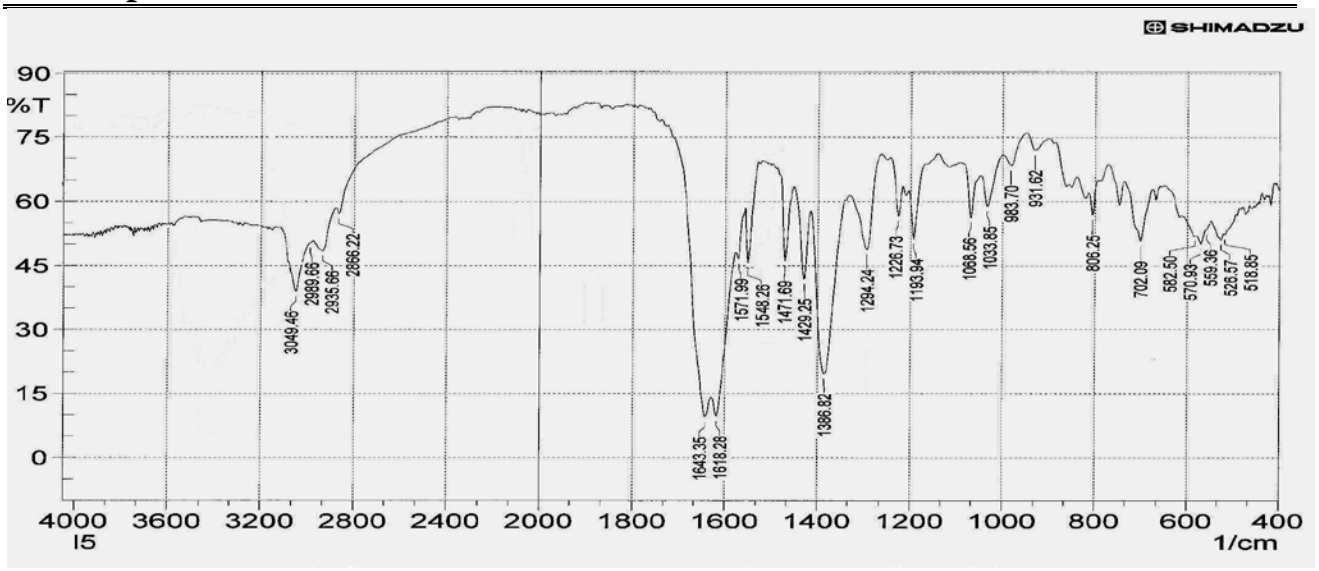

Figure (3. 12)IR spectrum of L^5

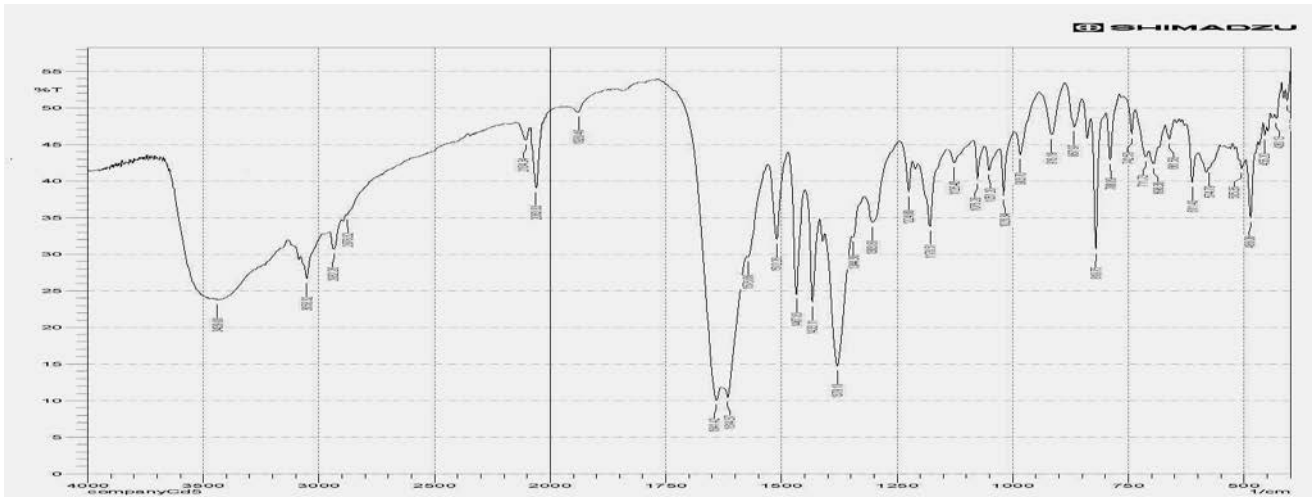

Figure (3. 83) IR spectrum of $[Cd_2(L^5)(N_3)_4].H_2O$

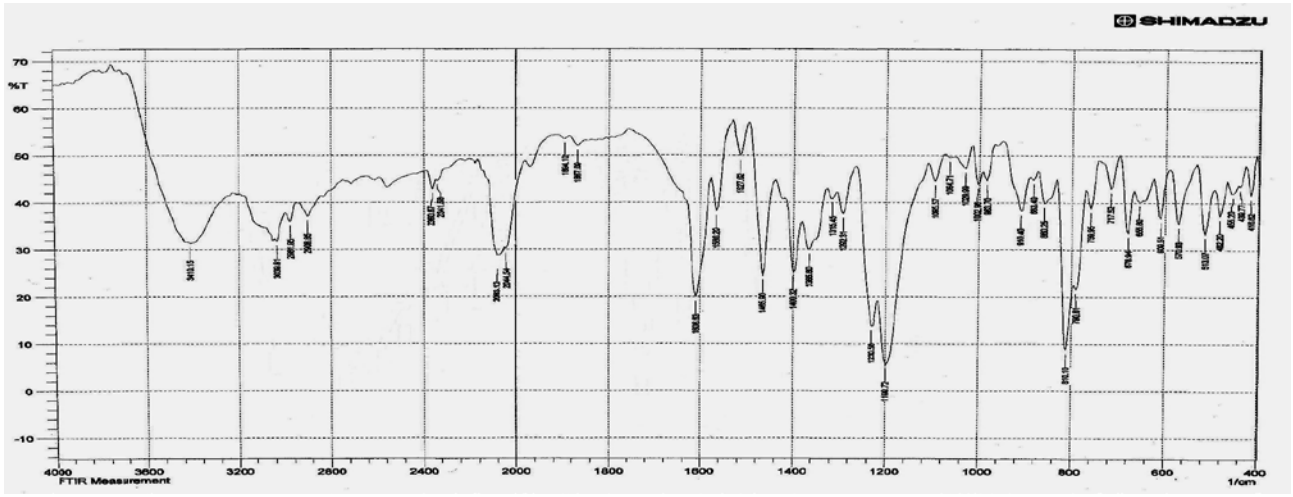

Figure (3. 84) IR spectrum of $Na_2[Ag_2(L^5)(N_3)_4].H_2O$

Table (3. 22)Infrared spectral data (wave number) cm^{-1} of L^5 complexes

Complex	νO-H	ν_{ar}C-H	νCH_2	$\nu_{as}N_3$	ν_{as}COO	νC=N	νC=C	ν_sCOO	δO-H	$\nu_s N_3$	νC-N	$\delta_{O.O.P}$	νM-O	νM-N	$\Delta(\nu_{as}-\nu)$
L^5	-	3049	2936	-	1643	1618	1572	1429	-	-	1194		-	-	214
$[Cr_2(L^5)(N_3)_4]Cl_2.H_2O$	-	3049	2949	2043	1601	1582	1564 1485	1398	1517	1319	1198	951 704	530 565	467 494	203
$[Mn_2(L^5)(N_3)_4]H_2O$	3387	3028	2862	2058	1609	1557	1557 1446	1423	1501	1339	1223	841 669	513 571	417 424	186
$[Fe_2(L^5)(N_3)_4]H_2O$	3422	3044	2866	2037	1612	1638	1576	1400	1516	1317	1188	924 668	540 604	428 467	212
$[Co_2(L^5)(N_3)_4]H_2O$	3404	3050	2934	2066	1616	1631	1631 1470	1394	1514	1302	1192	928 696	517 581	409 476	222
$[Ni_2(L^5)(N_3)_4]H_2O$	3418	3040 3017	2832	2048	1609	1562	1562 1458	1416	1535	1354	1219	930 644	529 559	440 455	193
$[Cu_2(L^5)(N_3)_4]H_2O$	3424	3049	2936	2081	1618	1572	1572 1472	1429	1517	1294	1194	984 669	527 559 571	419 469	189
$[Zn_2(L^5)(N_3)_4]H_2O$	3385	3030	2862	2037	1616	1558	1558	1425	1504	1334	1221	982 665	515 557 580	417 457	191
$[Cd_2(L^5)(N_3)_4]H_2O$	3439	3058	2879	2104 2064	1614	1641	1576 1468	1433	1512	1344	1179	916 662	505 575	430 455	181
$Na_2[Ag_2(L^5)(N_3)_4]H_2O$	3410	3040	2909	2083 2045	1609	1588	1588 1466	1400	1528	1315	1221	984 656	513 571	419 455	209

Where: ar = aromatic; s = symmetric; as = antisymmetric; o.o.p = out of plane.

(3.11) UV-Vis Spectral data for complexes

(3.11.1) UV-Vis Spectral data for L^1 complexes

The electronic spectra of the complexes of L^1 exhibited various extents of bathochromic shift of the bands related to the ligand field $\pi \rightarrow \pi^*$ transition, except for that of the Cu(II), Cd(II) and Ag(I) complexes which showed a hypsochromic shift (see Table 3. 23). Bands in the range of 373-379 nm related to the charge transfer transitions(CT) were observed in the spectra of the Mn(II), Fe(II), Co(II) complexes.

The electronic spectrum of the $[Cr_2(L^1)(N_3)_4]Cl_2.H_2O$ complex, Figure (3.85) displayed two additional bands at 405 and 604 nm, due to $^4A_2g^{(F)} \rightarrow {}^4T_2g^{(F)}$ (ν_2) and $^4A_2g^{(F)} \rightarrow {}^4T_1g^{(F)}$ (ν_1) transitions, respectively. These bands attributed to the spin allowed d–d transitions[187], indicating octahedral geometry around the Cr(III) atom[188]. The spectrum of the $[Mn_2(L^1)(N_3)_4]H_2O$ complex, Figure (3.86) showed the intraligand $\pi \rightarrow \pi^*$ transition and the charge transfer transition at 379 nm. The additional bands in the d-d region assignable to $^6A_1g^{(s)} \rightarrow {}^4T_1g^{(G}$ were attributed to spin forbidden transitions in an octahedral geometry[189, 190].

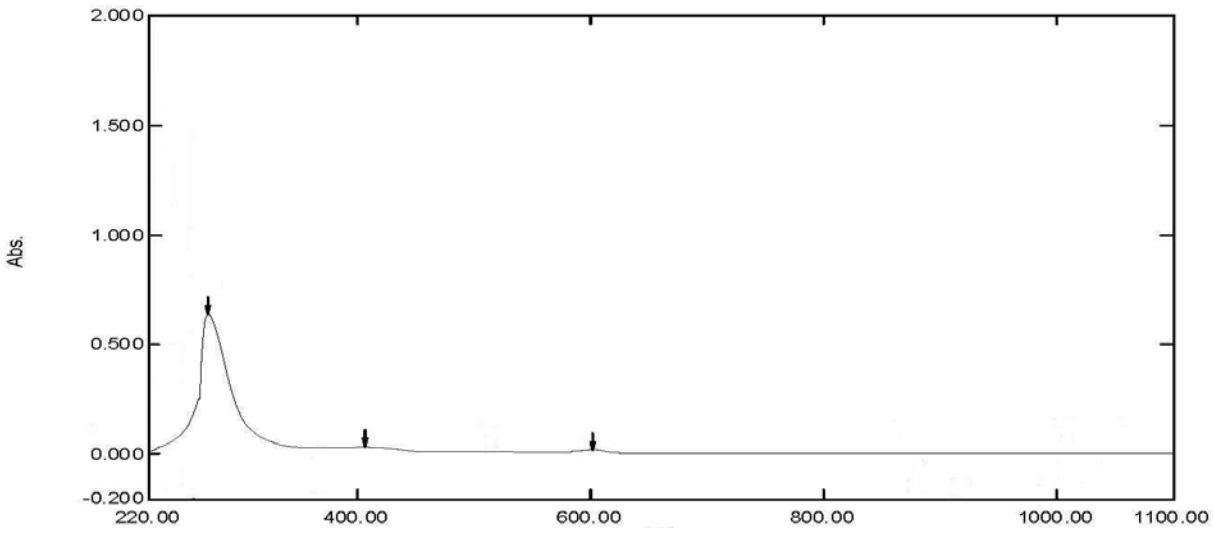

Figure(3. 85) Electronic spectrum of $[Cr_2(L^1)(N_3)_4]Cl_2.H_2O$ complex

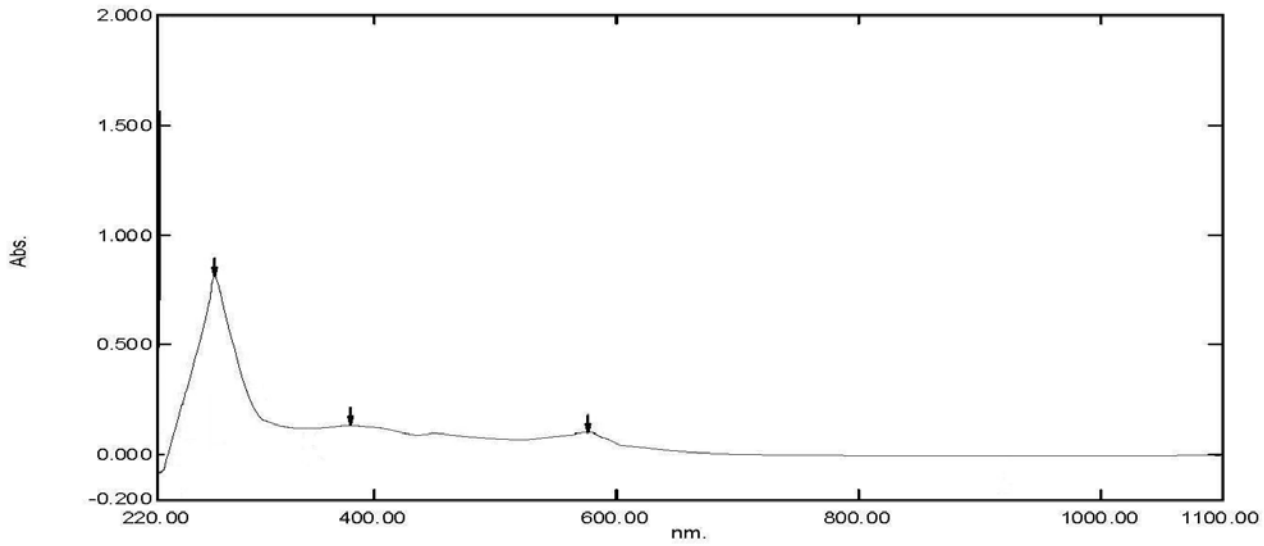

Figure (3. 86) Electronic spectrum of $[Mn_2(L^1)(N_3)_4]H_2O$ complex

The spectrum of the $[Fe_2(L^1)(N_3)_4]H_2O$ complex, Figure (3-87) showed the intra-ligand $\pi \rightarrow \pi^*$ transition and the charge transfer transition at 273 and 379 nm, respectively. The two additional bands in the visible region at 500 nm assignable $^5T_2g \rightarrow {}^5Eg$, was attributed to spin forbidden in an octahedral geometry[191-193].

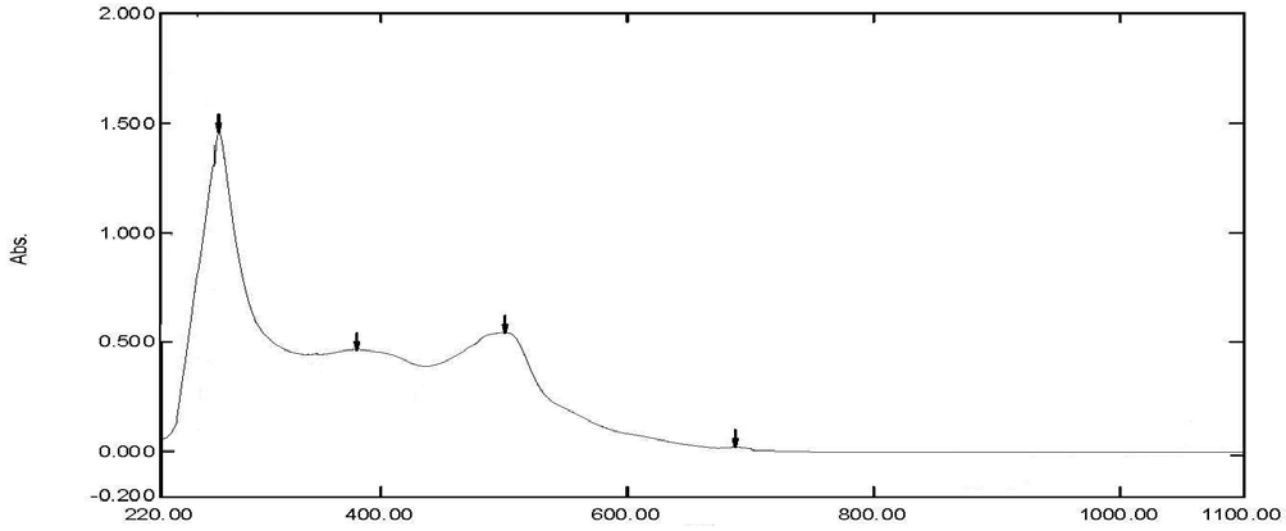

Figure (3. 87) Electronic spectrum of $[Fe_2(L^1)(N_3)_4]H_2O$ complex

The electronic spectra of $[Co_2(L^1)(N_3)_4]H_2O$, $[Ni_2(L^1)(N_3)_4]H_2O$ and $[Cu_2(L^1)(N_3)_4]H_2O$ complexes, Figures (3.88 to 3.90) showed the

intraligand $\pi \rightarrow \pi^*$ and charge transfer transitions (see Table 3.23). The Co-complex displays additional bands in the d-d region due to $^4T_1g^{(F)} \rightarrow {}^4A_2g^{(F)}$, characteristic for octahedral geometry around Co atom[192, 193]. The d-d band in the Ni-complex at 639 assigned to $^3A_2g \rightarrow {}^3T_1g^{(F)}$, while band at 737 nm is assignable to the combination of $^3A_2g \rightarrow {}^3T_2g^{(F)}$,, indicating an octahedral geometry about Ni atom[189, 194]. Band in the Cu spectrum at 674 nm attributed to d-d transition type $^2Eg \rightarrow {}^2T_2g$, confirming octahedral geometries about Cu atom.[189, 190, 192].

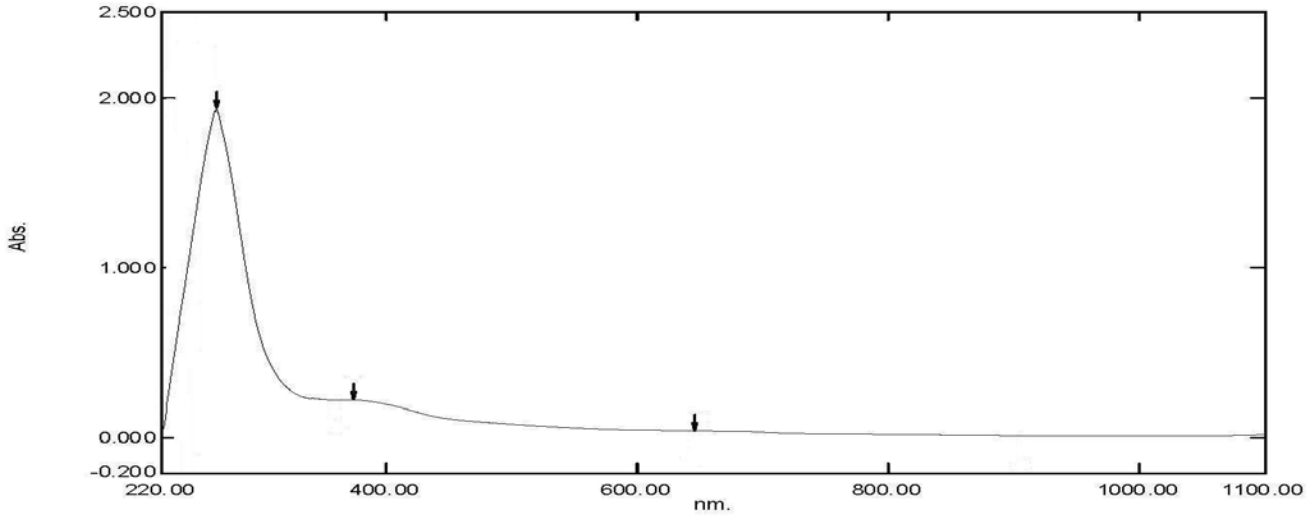

Figure (3. 88) Electronic spectrum of $[Co_2(L^1)(N_3)_4]H_2O$ complex

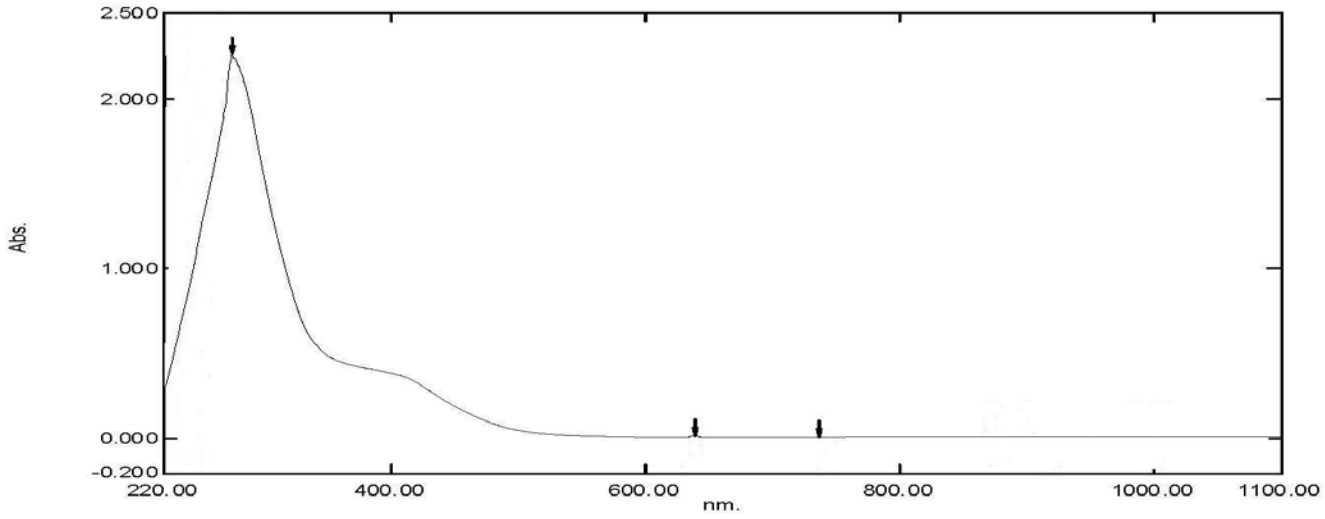

Figure (3. 89) Electronic spectrum of $[Ni_2(L^1)(N_3)_4]H_2O$ complex

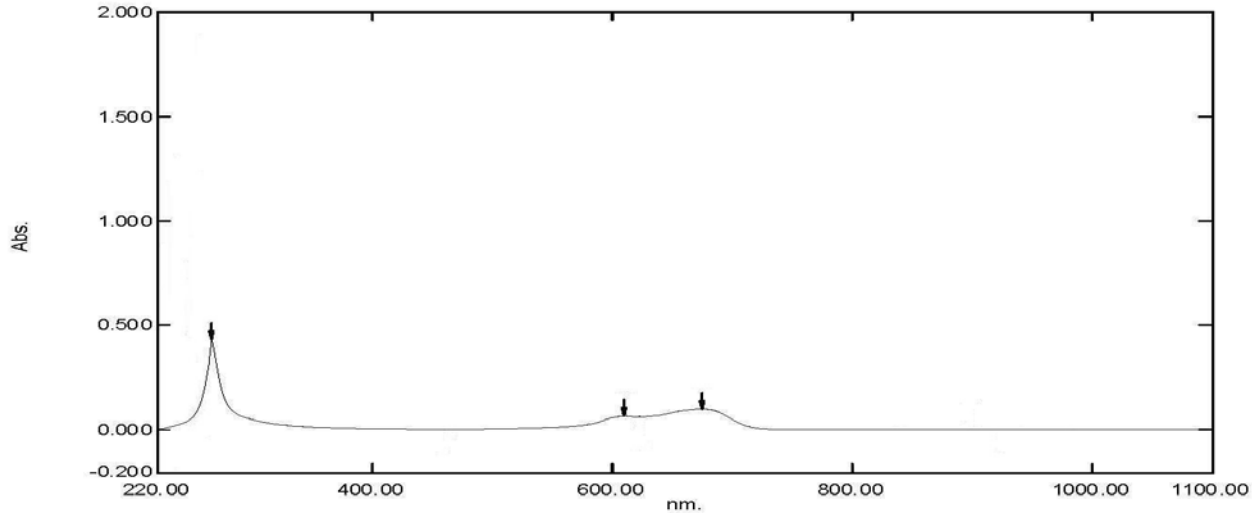

Figure (3. 90) Electronic spectrum of $[Cu_2(L^1)(N_3)_4]H_2O$ complex

The electronic spectra of the $[Zn_2(L^1)(N_3)_4]H_2O$, $[Cd_2(L^1)(N_3)_4]H_2O$ and $Na_2[Ag_2(L^1)(N_3)_4]H_2O$ complexes, Figures (3.91 to 3.93) exhibited bands at 272; 386, 264; 362 and 267; 307 nm, respectively which were assigned to the ligand field $\pi\rightarrow\pi^*$and $n\rightarrow\pi^*$charge transfer transitions, respectively[192, 195].

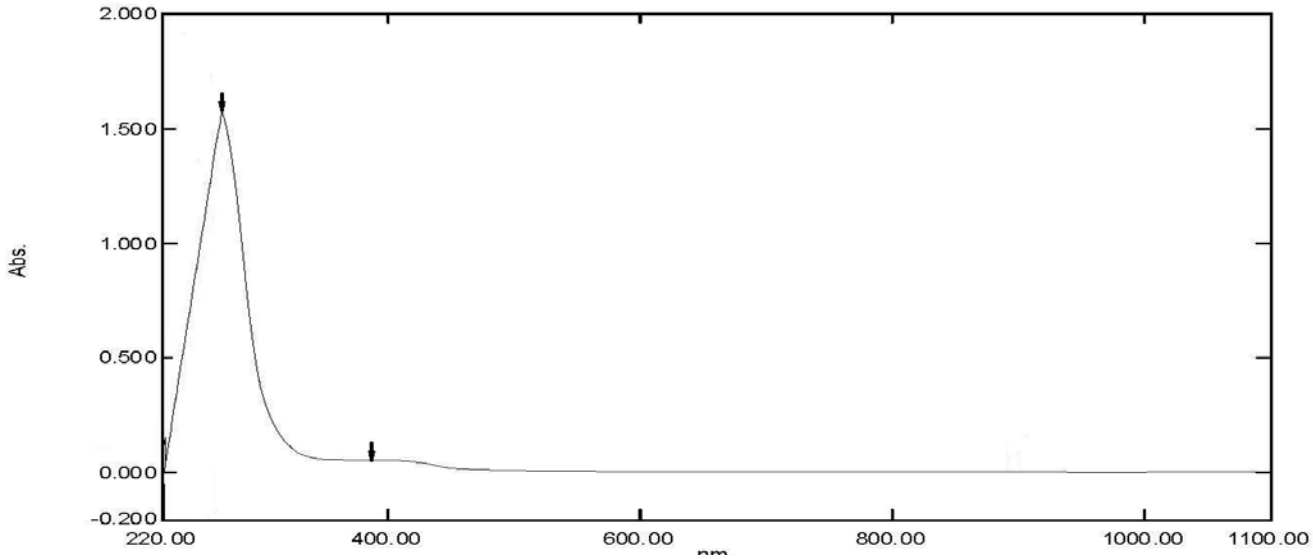

Figure (3. 91) Electronic spectrum of $[Zn_2(L^1)(N_3)_4]H_2O$ complex

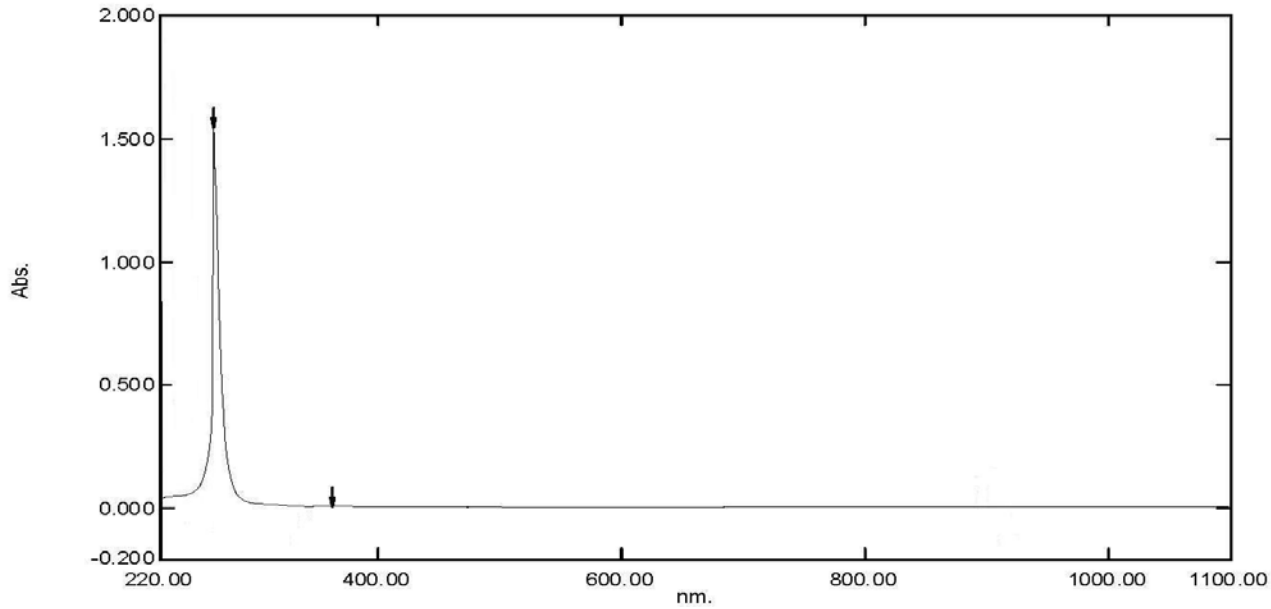

Figure (3. 92) Electronic spectrum of $[Cd_2(L^1)(N_3)_4]H_2O$ complex

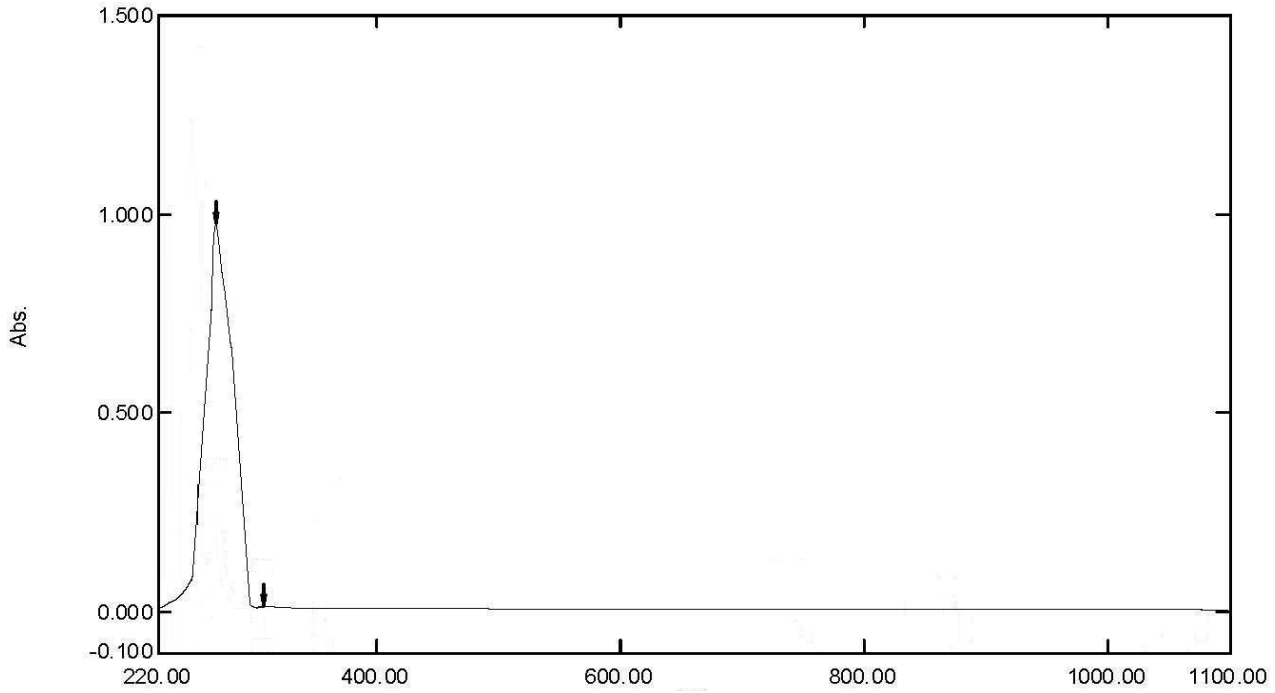

Figure (3. 93) Electronic spectrum of $Na_2[Ag_2(L^1)(N_3)_4]H_2O$ complex

Table (3. 23)UV-Vis spectral data of L^1 complexes in DMSO solutions

Compound	Band Position λ_{nm}	Wave number (cm^{-1})	Extinction coefficient ε_{max} ($dm^3\ mol^{-1}\ cm^{-1}$)	Assignment
L^1	268	37313	1130	$\pi\rightarrow\pi^*$
$[Cr_2(L^1)(N_3)_4]Cl_2.H_2O$	271 405 604	36900 24691 16556	639 32 15	Intra-ligand $\pi\rightarrow\pi^*$ $^4A_2g^{(F)} \rightarrow {}^4T_2g^{(F)}$ (ν_2) $^4A_2g^{(F)} \rightarrow {}^4T_2g^{(F)}$ (ν_1)
$[Mn_2(L^1)(N_3)_4]H_2O$	277 379 576	36101 26385 1736	850 259 62	Intra-ligand $\pi\rightarrow\pi^*$ C.T $^6A_1g^{(S)} \rightarrow {}^4T_1g^{(G)}$
$[Fe_2(L^1)(N_3)_4]H_2O$	273 379 500	36630 26385 20000	1460 467 545	Intra-ligand $\pi\rightarrow\pi^*$ C.T $^5T_2g \rightarrow {}^5Eg$
$[Co_2(L^1)(N_3)_4]H_2O$	263 373 652	38023 26810 15337	1931 222 39	Intra-ligand $\pi\rightarrow\pi^*$ C.T $^4T_1g^{(F)} \rightarrow {}^4A_2g^{(F)}$
$[Ni_2(L^1)(N_3)_4]H_2O$	278 639 737	35971 15640 13569	2257 4 8	Intra-ligand $\pi\rightarrow\pi^*$ $^3A_2g \rightarrow {}^3T_1g^{(F)}$ $^3A_2g \rightarrow {}^3T_2g^{(F)}$
$[Cu_2(L^1)(N_3)_4]H_2O$	268 674	37313 14837	450 20	Intra-ligand $\pi\rightarrow\pi^*$ $^2Eg \rightarrow {}^2T_2g$
$[Zn_2(L^1)(N_3)_4]H_2O$	272 386	36764 25907	1579 57	Intra-ligand $\pi\rightarrow\pi^*$ $n \rightarrow\pi^*$
$[Cd_2(L^1)(N_3)_4]H_2O$	264 362	37879 27624	1547 11	Intra-ligand $\pi\rightarrow\pi^*$ $n \rightarrow\pi^*$
$Na_2[Ag_2(L^1)(N_3)_4]\ H_2O$	267 307	37453 32573	981 12	Intra-ligand $\pi\rightarrow\pi^*$ $n \rightarrow\pi^*$

(3.11.2) UV-Vis Spectral data for L^2 complexes

The electronic spectra of the complexes of L^2 exhibited various extents of bathochromic shift of the bands related to the intra-ligand $\pi \rightarrow \pi^*$ transition, except for that of the Co(II) complex which showed a hypsochromic shift (see Table 3.24). Band in the range of 372 nm related to the charge transfer transitions(CT) were observed in the spectra of the Ag(I) complex.

The electronic spectrum of the green $[Cr_2(L^2)(N_3)_4]Cl_2.H_2O$ complex, Figure (3.94) displayed two additional bands centered at 611 and 674 nm due to $^4A_2g^{(F)} \rightarrow {}^4T_1g^{(F)}$ (ν_1), $^4A_2g^{(F)} \rightarrow {}^4T_2g^{(F)}$ (ν_2) transitions, which could be attributed to the spin allowed d–d transitions[187, 189]. These data indicate a distorted octahedral geometry around the Cr(III) atom[187, 189]. The spectrum of the pale yellow $[Mn_2(L^2)(N_3)_4]H_2O$ complex, Figure (3.95) showed the intraligand $\pi \rightarrow \pi^*$ transition 268 nm. The additional bands in the d-d region at 658 nm is assignable to spin forbidden transition type $^6A_1g \rightarrow {}^4T_1g^{(G)}$, indicating a distorted octahedral geometry around Mn atom [189, 190].

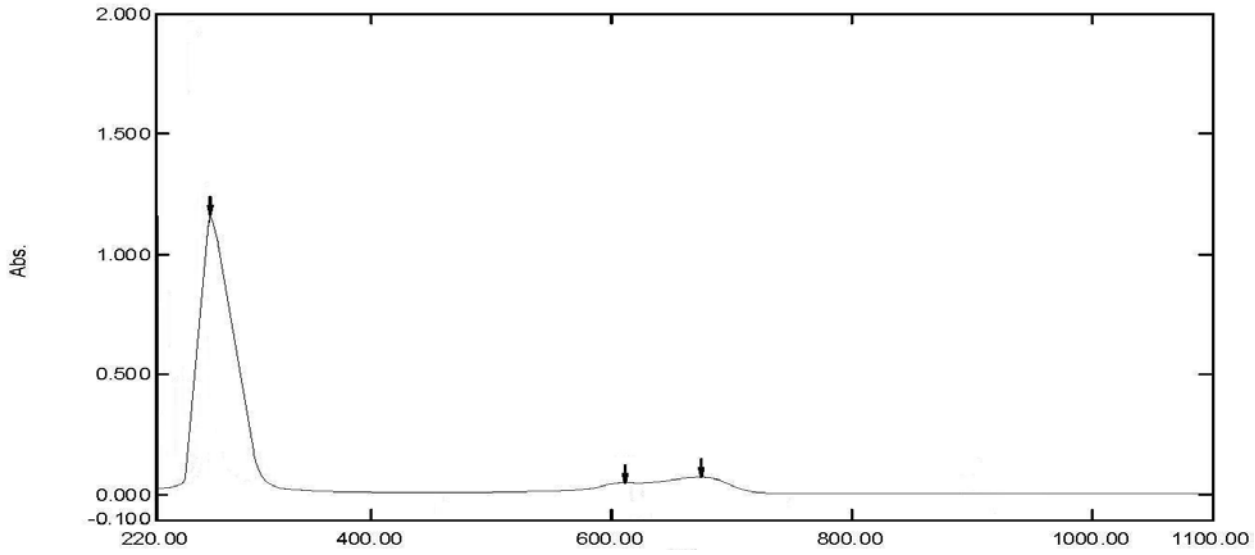

Figure (3.94) Electronic spectrum of $[Cr_2(L^2)(N_3)_4]Cl_2.H_2O$ complex

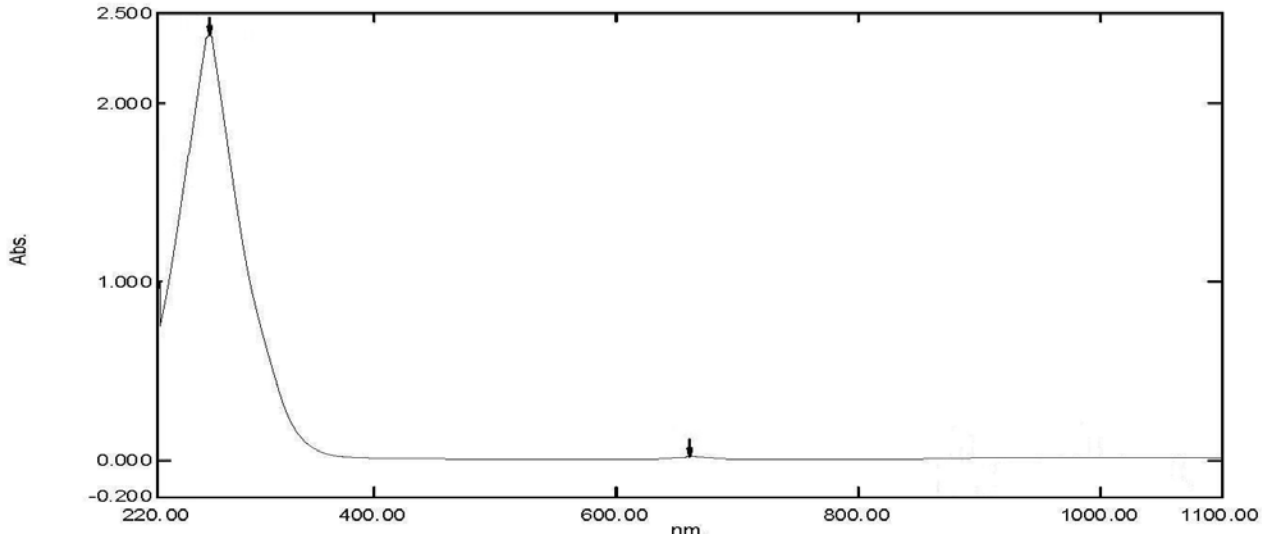

Figure (3.95) Electronic spectrum of $[Mn_2(L^2)(N_3)_4].H_2O$ complex

The electronic spectra of $[Fe_2(L^2)(N_3)_4]$, $[Co_2(L^2)(N_3)_4].H_2O$, $[Ni_2(L^2)(N_3)_4]$ $.H_2O$ and $[Cu_2(L^2)\ (N_3)_4].H_2O$, Figures (3.96 to 3.99) show bands similar to that mentioned in the L^1 complexes. The absorption data of the complexes are summarised in Table (3.24). These data confirm octahedral configuration for all the complexes[191-194].

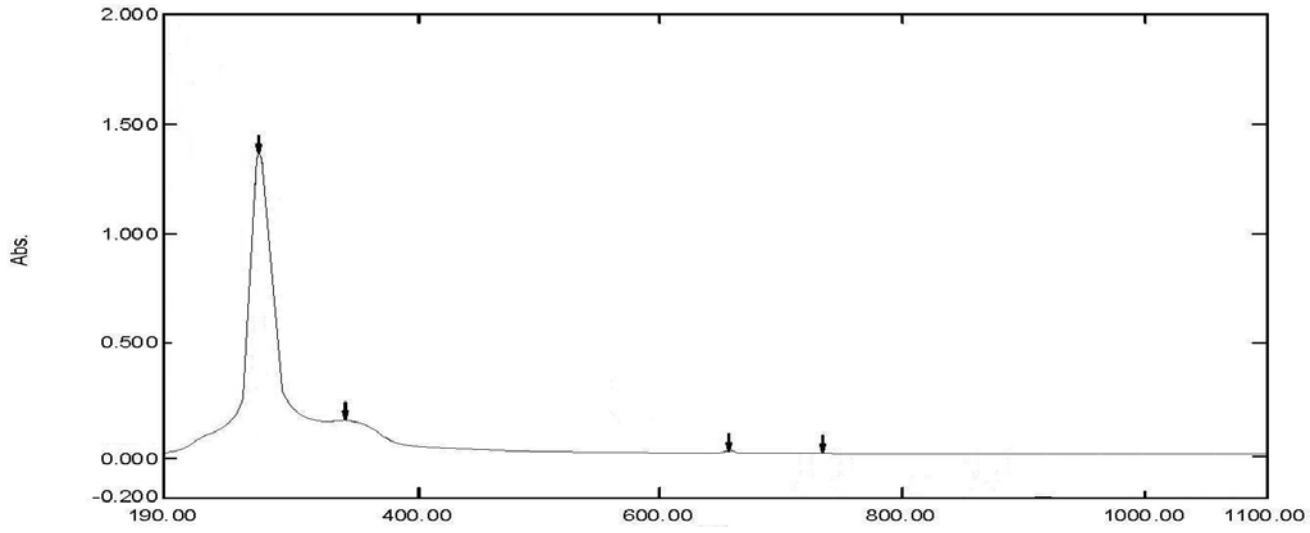

Figure (3. 96) Electronic spectrum of $[Fe_2(L^2)(N_3)_4]$ complex

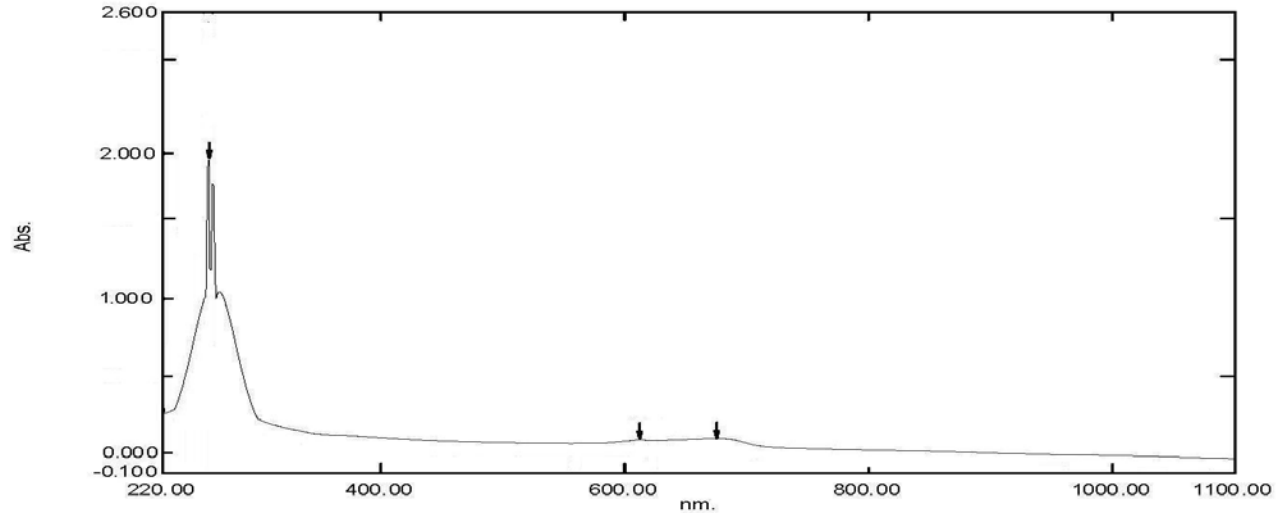

Figure (3. 97) Electronic spectrum of $[Co_2(L^2)(N_3)_4].H_2O$ complex

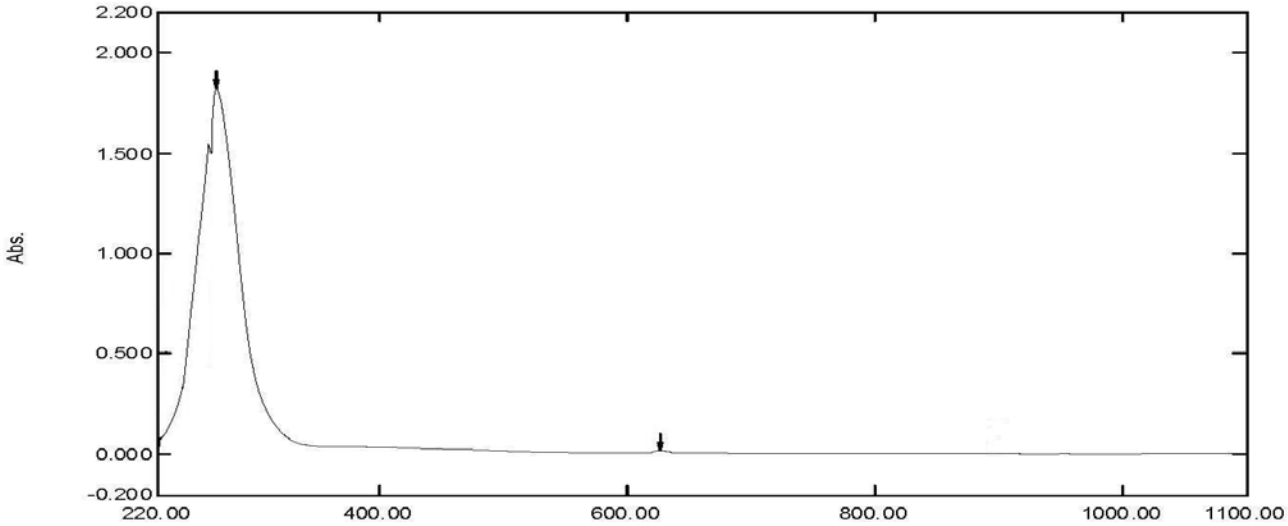

Figure (3. 98) Electronic spectrum of $[Ni_2(L^2)(N_3)_4].H_2O$ complex

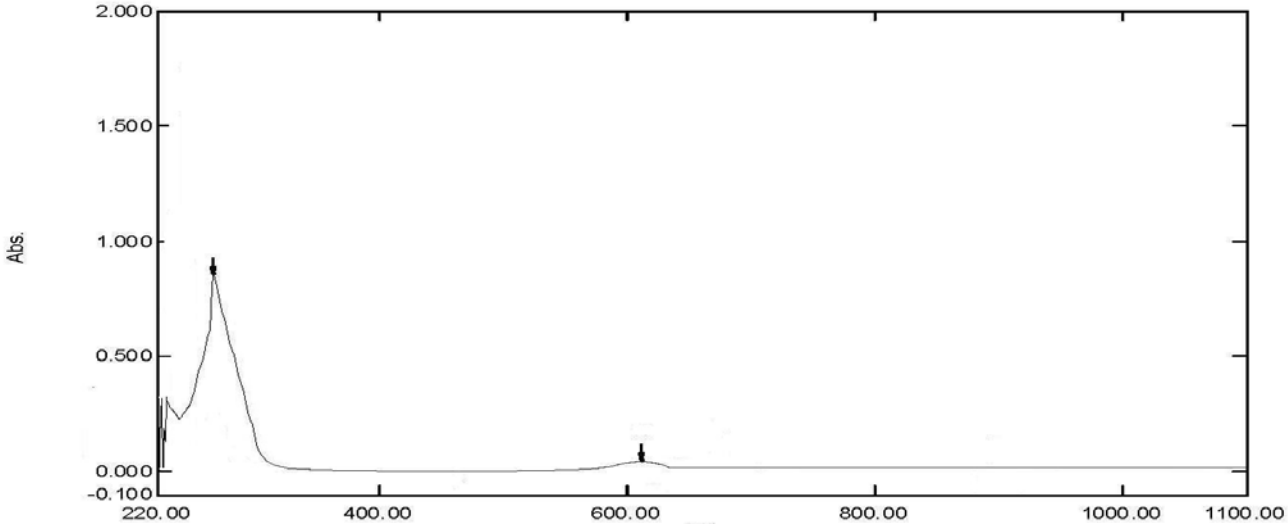

Figure (3. 99) Electronic spectrum of $[Cu_2(L^2)(N_3)_4].H_2O$ complex

The electronic spectra of the pale yellow $[Zn_2(L^2)(N_3)_4]H_2O$, white $[Cd_2(L^2)(N_3)_4]$ and $Na_2[Ag_2(L^2)(N_3)_4]H_2O$ complexes, Figures (3. 100 to 3. 102), exhibited bands at 263, 262 and 265 nm, respectively which assigned to the intraligand $\pi \rightarrow \pi^*$ transition. The $Na_2[Ag_2(L^2)(N_3)_4]H_2O$ complex displays a charge transfer band centred at 372 nm. All these characteristic bands observed in the UV region confirm the octahedral geometry about metal centre[192, 195].

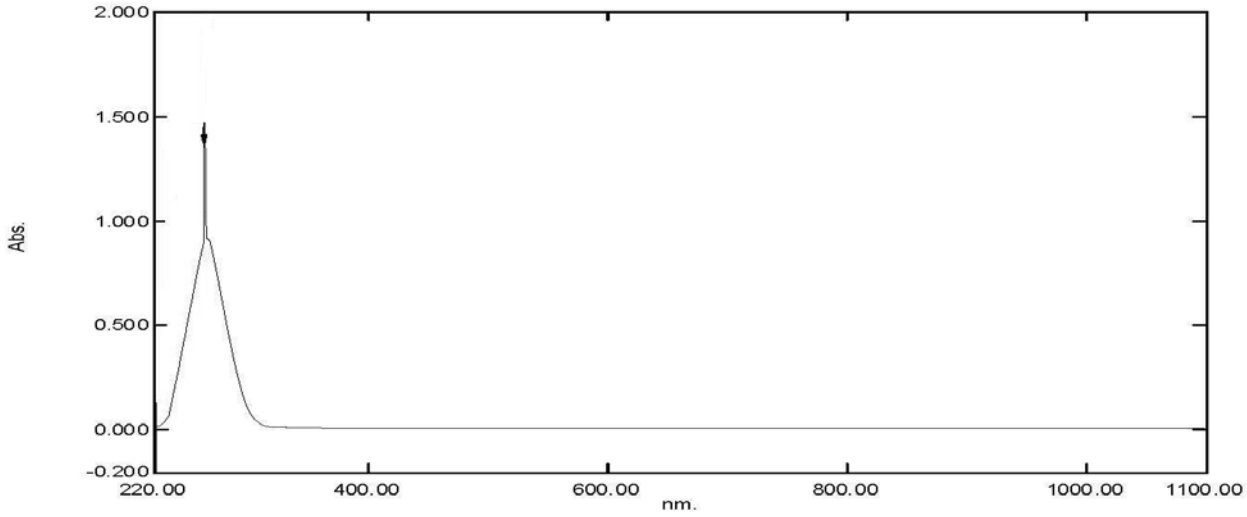

Figure (3. 100) Electronic spectrum of $[Zn_2(L^2)(N_3)_4].H_2O$ complex

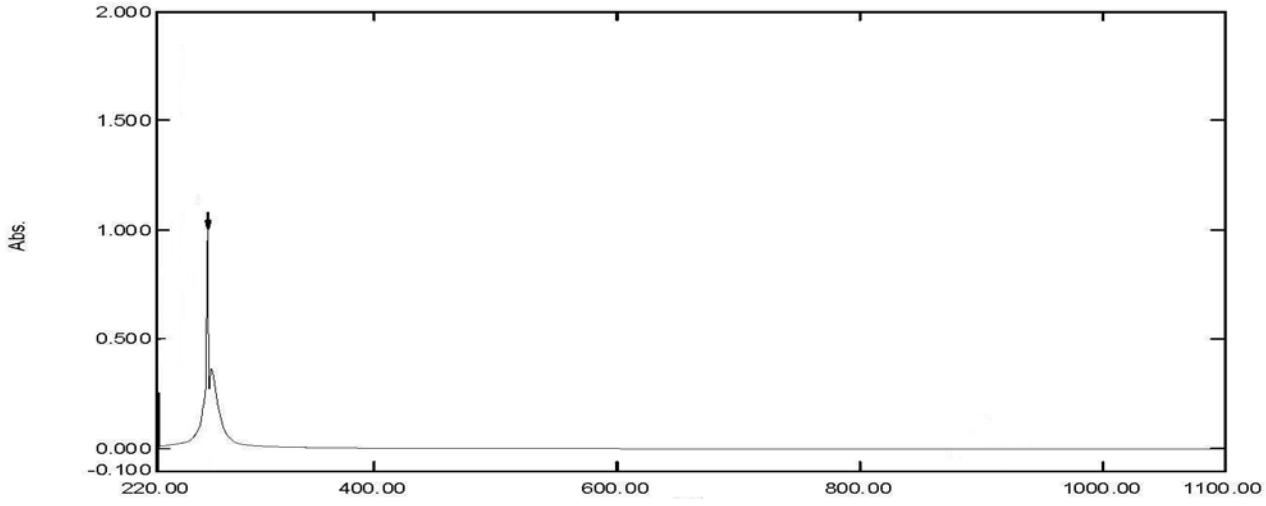

Figure (3. 101) Electronic spectrum of $[Cd_2(L^2)(N_3)_4]$ complex

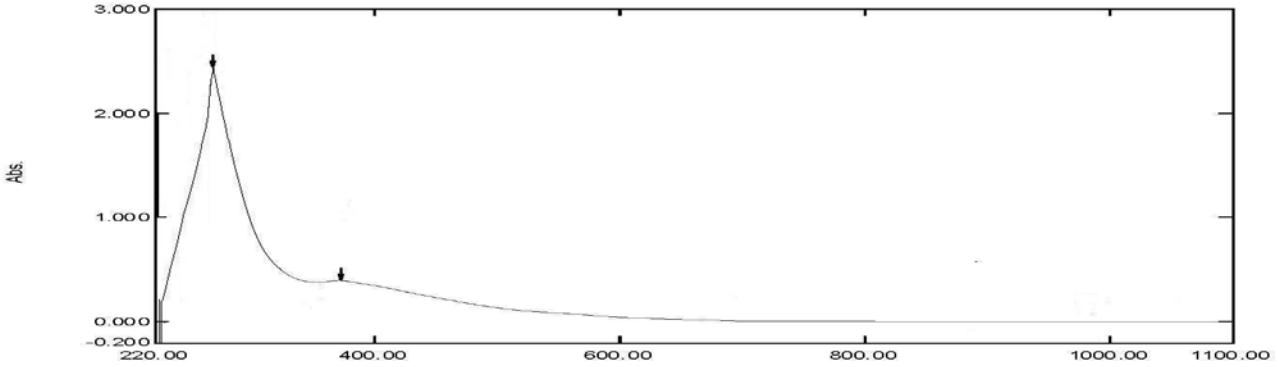

Figure (3. 102) Electronic spectrum of $Na_2[Ag_2(L^2)(N_3)_4].H_2O$ complex

Table (3.24) UV-Vis spectral data of L^2 complexes in DMSO solutions

Compound	Band Position λ_{nm}	Wave number (cm^{-1})	Extinction coefficient ε_{max} ($dm^3\ mol^{-1}\ cm^{-1}$)	Assignment
L^2	261	38314	2119	$\pi\rightarrow\pi^*$
$[Cr_2(L^2)(N_3)_4]Cl_2.H_2O$	264 611 674	37879 16367 14837	1163 52 75	Intra-ligand $\pi\rightarrow\pi^*$ $^4A_2g^{(F)} \rightarrow {}^4T_1g^{(F)}$ (ν_1) $^4A_2g^{(F)} \rightarrow {}^4T_2g^{(F)}$ (ν_2)
$[Mn_2(L^2)(N_3)_4]H_2O$	268 658	37313 15198	2333 23	Intra-ligand $\pi\rightarrow\pi^*$ $^6A_1g \rightarrow {}^4T_1g^{(G)}$
$[Fe_2(L^2)(N_3)_4]$	269 340 657	37175 29412 15221	1371 148 31	Intra-ligand $\pi\rightarrow\pi^*$ C.T $^5T_2g \rightarrow {}^5Eg$
$[Co_2(L^2)(N_3)_4]H_2O$	259 263 674	38616 38023 14837	1941 1808 91	L.F Intra-ligand $\pi\rightarrow\pi^*$ $^4T_1g^{(F)} \rightarrow {}^4A_2g^{(F)}$
$[Ni_2(L^2)(N_3)_4]H_2O$	268 626	37313 15974	1821 4	Intra-ligand $\pi\rightarrow\pi^*$ $^3A_2g \rightarrow {}^3T_1g^{(F)}$
$[Cu_2(L^2)(N_3)_4]H_2O$	265 611	37736 16367	837 42	Intra-ligand $\pi\rightarrow\pi^*$ $^2Eg \rightarrow {}^2T_2g$
$[Zn_2(L^2)(N_3)_4]H_2O$	263	38023	1370	Intra-ligand $\pi\rightarrow\pi^*$
$[Cd_2(L^2)(N_3)_4]$	262	38168	1006	Intra-ligand $\pi\rightarrow\pi^*$
$Na_2[Ag_2(L^2)(N_3)_4].H_2O$	265 372	37736 26882	2449 392	Intra-ligand $\pi\rightarrow\pi^*$ C.T

(3.11.3) UV-Vis Spectral data for L^3 complexes

The electronic spectra of the complexes of L^3 exhibited various extents of hypsochromic shift (see Table 3. 25). Bands in the range of 303-362 nm related to the charge transfer transitions (CT) were observed in the spectra of the Mn(II), Fe(II), Co(II) and Ni(II) complexes.

The electronic spectrum of the green $[Cr_2(L^3)(N_3)_4]Cl_2.H_2O$ complex, Figure (3. 103) showed two additional bands at 467 and 756 nm due to $^4A_2g \rightarrow {}^4T_1g^{(F)}$ (ν_1) and $^4A_2g^{(F)} \rightarrow {}^4T_2g^{(F)}$ (ν_2) transitions, respectively. These bands attributed to the spin allowed d–d transitions[187, 188]. These data are in a good agreement with a distorted octahedral geometry about Cr(III) atom[187, 188]. The spectrum of the brown $[Mn_2(L^3)(N_3)_4].2H_2O$ complex, Figure (3. 104) showed band in the d-d region at 643 nm assigned to spin forbidden type $^6A_1g \rightarrow {}^4T_1g^{(G)}$. This band confirms a distorted octahedral geometry around Mn centre[189, 190].

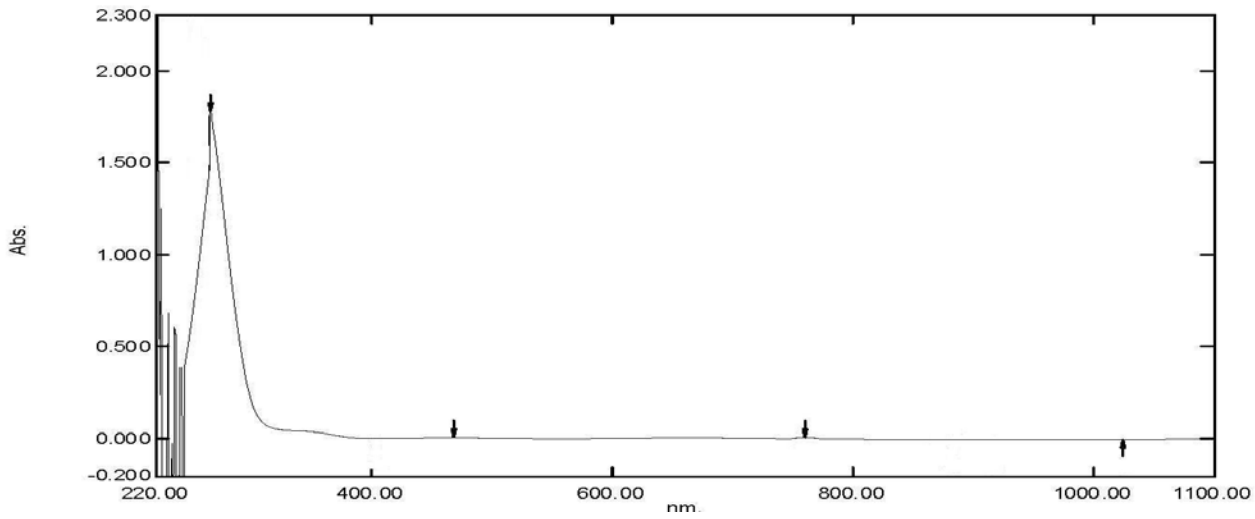

Figure (3. 103) Electronic spectrum of $[Cr_2(L^3)(N_3)_4]Cl_2.H_2O$ complex

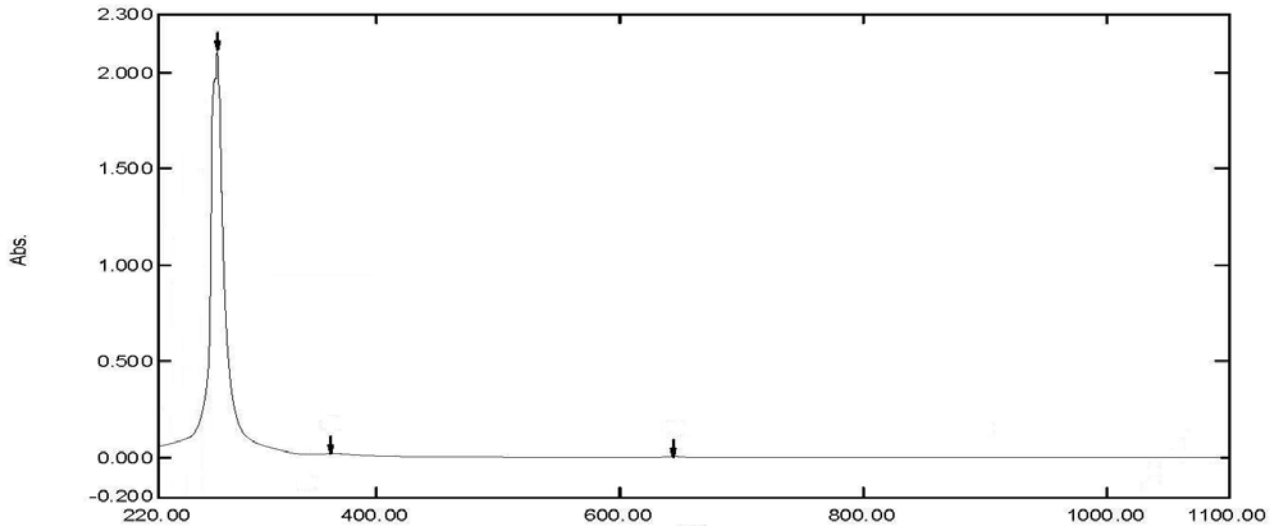

Figure (3. 104) Electronic spectrum of $[Mn_2(L^3)(N_3)_4].2H_2O$ complex

The electronic spectra of $[Fe_2(L^3)(N_3)_4]H_2O$, $[Co_2(L^3)(N_3)_4]H_2O$, $[Ni_2(L^3)(N_3)_4]H_2O$ and $[Cu_2(L^3)(N_3)_4]$, Figures (3. 105 to 3. 108), show bands similar to that mentioned in the UV-Vis spectra of L^1 complexes. The absorption data are summarised in Table (3. 25). These data confirm distorted octahedral geometries about metal centres[191-194].

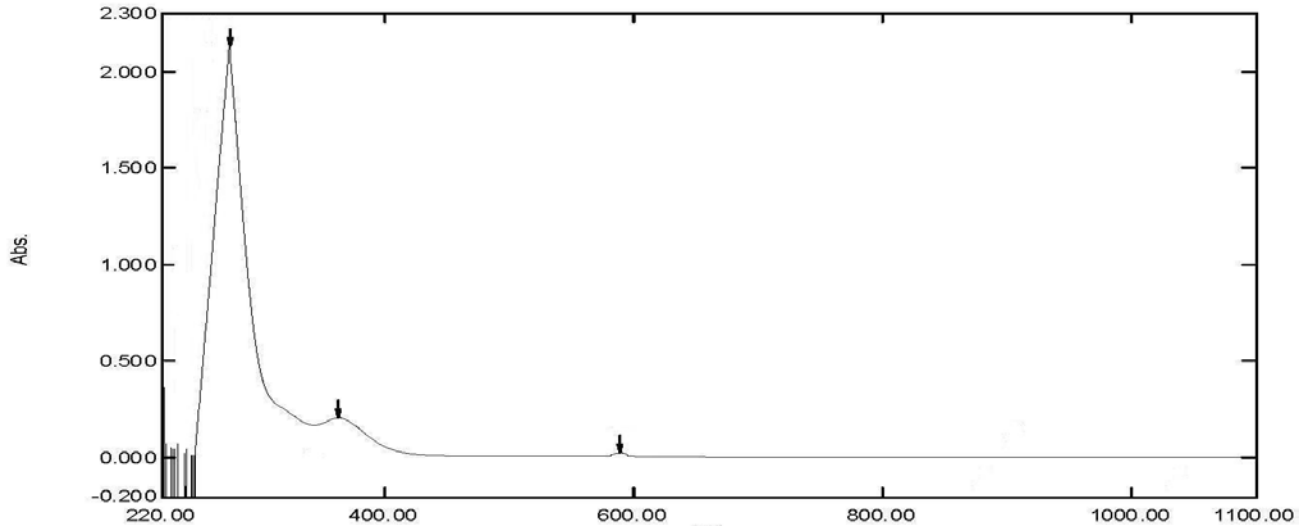

Figure (3. 105) Electronic spectrum of $[Fe_2(L^3)(N_3)_4].H_2O$ complex

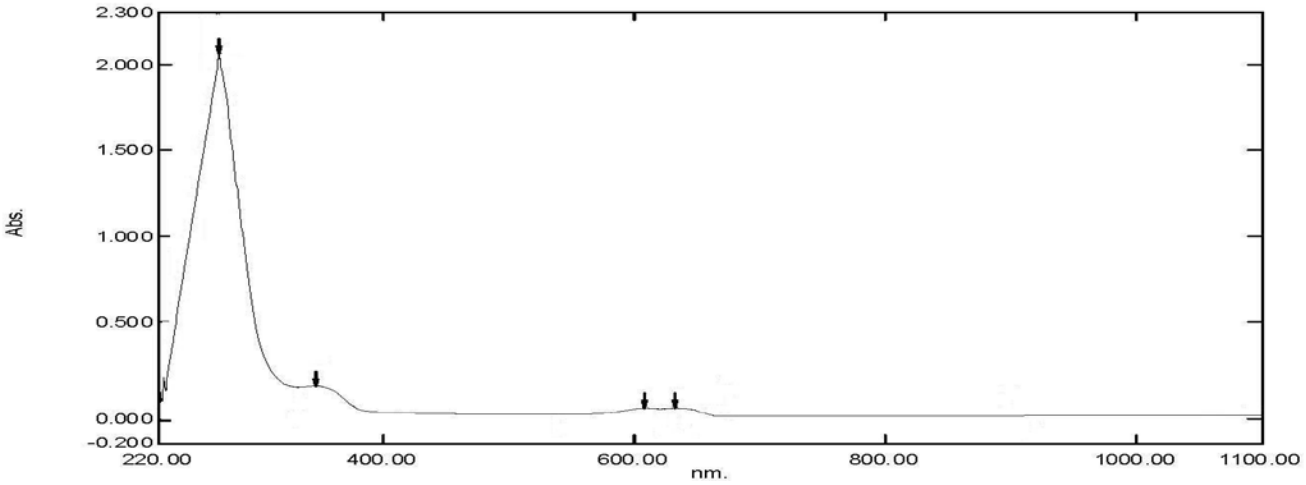

Figure (3. 106) Electronic spectrum of $[Co_2(L^3)(N_3)_4].H_2O$ complex

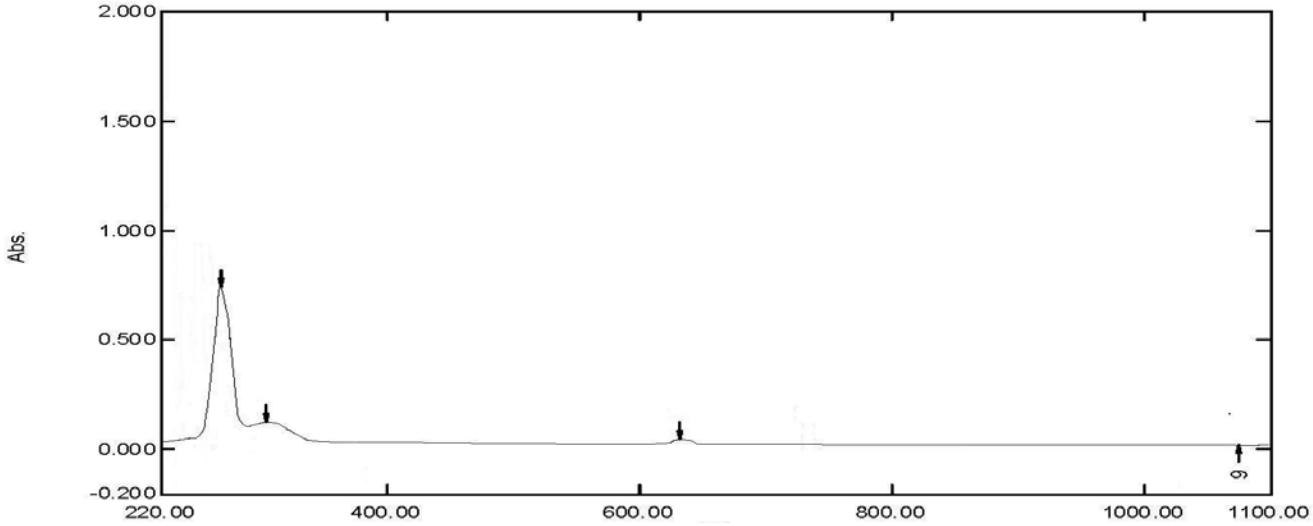

Figure (3. 107) Electronic spectrum of $[Ni_2(L^3)(N_3)_4].H_2O$ complex

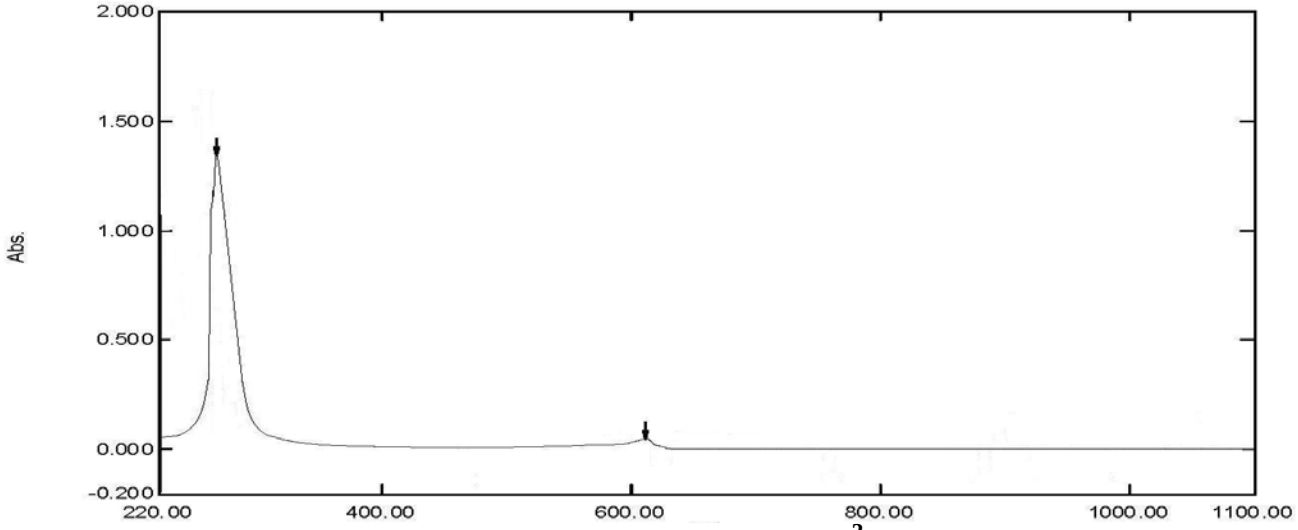

Figure (3. 108) Electronic spectrum of $[Cu_2(L^3)(N_3)_4]$ complex

The electronic spectra of the $[Zn_2(L^3)(N_3)_4].H_2O$, $[Cd_2(L^3)(N_3)_4].H_2O$ and $Na_2[Ag_2(L^3)(N_3)_4].H_2O$ complexes, Figures (3. 109 to 3. 111), exhibited bands at 266, 265 and 264 nm, respectively which assigned to the intra-ligand Intra-ligand $\pi \rightarrow \pi^*$. The spectra show no bands in the visible region, indicating a d^{10} configuration about metal atom[192, 195].

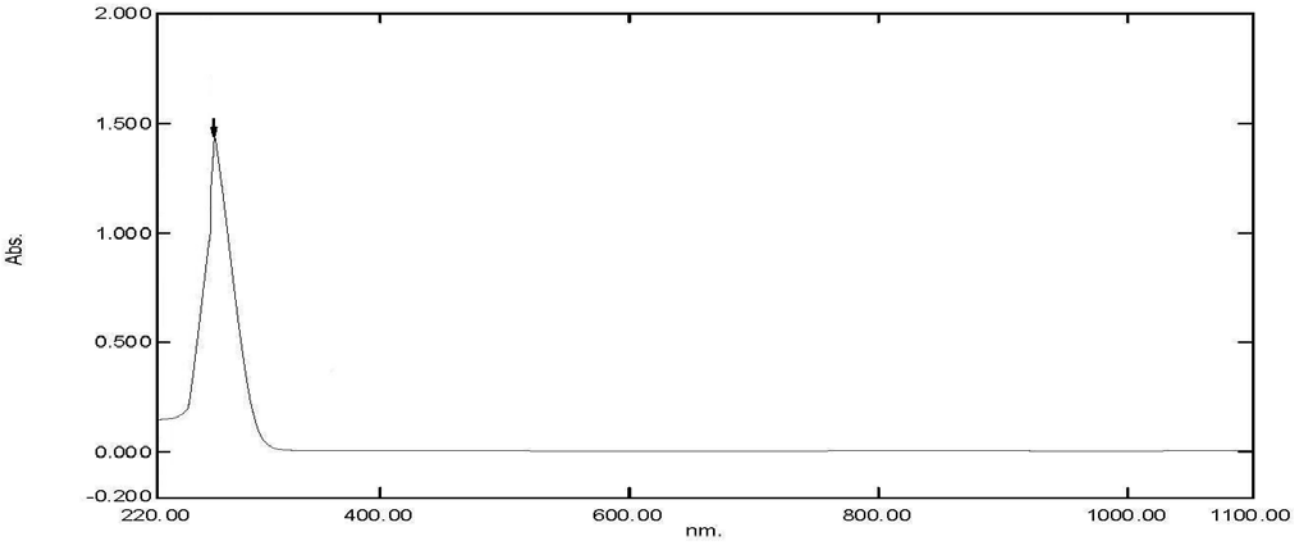

Figure (3. 109) Electronic spectrum of $[Zn_2(L^3)(N_3)_4].H_2O$ complex

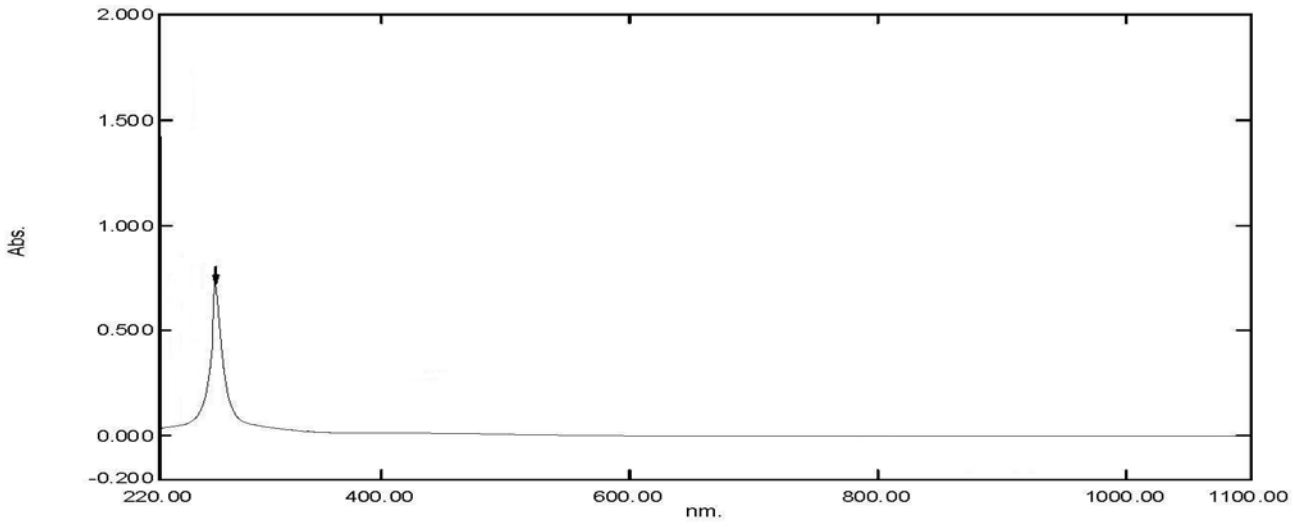

Figure (3. 110) Electronic spectrum of $[Cd_2(L^3)(N_3)_4].H_2O$ complex

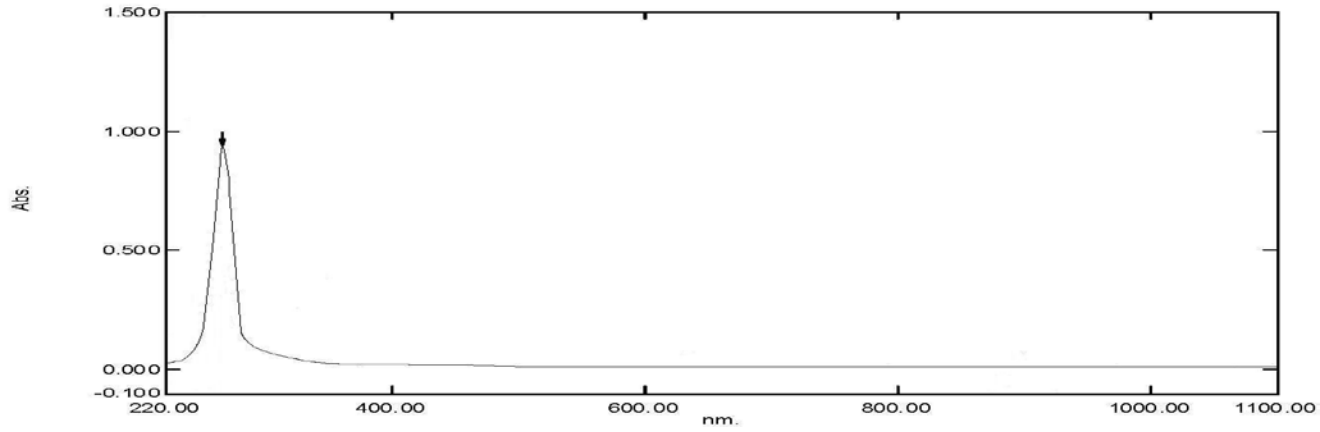

Figure(3. 111) Electronic spectrum of $Na_2[Ag_2(L^3)(N_3)_4].H_2O$ complex

Table (3. 25) UV-Vis spectral data of L^3 complexes in DMSO solutions

Compound	Band Position λ_{nm}	Wave number (cm^{-1})	Extinction coefficient ε_{max} ($dm^3\ mol^{-1}\ cm^{-1}$)	Assignment
L^3	279	35842	2046	$\pi\rightarrow\pi^*$
$[Cr_2(L^3)(N_3)_4]Cl_2.H_2O$	263 467 756	38023 21413 13228	1785 4 1	Intra-ligand $\pi\rightarrow\pi^*$ $^4A_2g \rightarrow {}^4T_1g^{(F)}(\nu_1)$ $^4A_2g^{(F)} \rightarrow {}^4T_2g^{(F)}(\nu_2)$
$[Mn_2(L^3)(N_3)_4].2H_2O$	268 362 643	37313 27624 15552	2150 21 1	Intra-ligand $\pi\rightarrow\pi^*$ $n\rightarrow\pi^*$ $^6A_1g\rightarrow {}^4T_1g^{(G)}$
$[Fe_2(L^3)(N_3)_4].H_2O$	272 362 586	36764 27624 17065	2144 206 21	L.F C.T $^5T_2g \rightarrow {}^5Eg$
$[Co_2(L^3)(N_3)_4].H_2O$	270 346 633	37037 28901 15798	2036 129 61	L.F C.T $^4T_1g^{(F)} \rightarrow {}^4A_2g^{(F)}$
$[Ni_2(L^3)(N_3)_4].H_2O$	266 303 633	37594 33003 15798	758 124 53	L.F C.T $^3A_2g \rightarrow {}^3T_1g^{(F)}$
$[Cu_2(L^3)(N_3)_4]$	268 611	37313 16367	1350 50	Intra-ligand $\pi\rightarrow\pi^*$ $^2Eg \rightarrow {}^2T_2g$
$[Zn_2(L^3)(N_3)_4].H_2O$	266	37594	1443	Intra-ligand $\pi\rightarrow\pi^*$
$[Cd_2(L^3)(N_3)_4].H_2O$	265	37736	723	Intra-ligand $\pi\rightarrow\pi^*$
$Na_2[Ag_2(L^3)(N_3)_4].H_2O$	264	37879	9350	Intra-ligand $\pi\rightarrow\pi^*$

(3.11.4) UV-Vis Spectral data for L^4 complexes

The electronic spectra of the complexes of L^4 exhibited various extents of bathochromic shift of the bands related to the intra-ligand $\pi \rightarrow \pi^*$ transition, except for that of the Mn(II), Co(II) and Ag(I) complexes which showed a hypsochromic shift (see Table 3. 26). The spectrum of the $[Mn(L^4)(N_3)_4]H_2O$ complex displays band centred at 376 nm related to the charge transfer transition (CT).

The electronic spectrum of the green $[Cr_2(L^4)(N_3)_4]Cl_2.H_2O$ complex, Figure (3. 112) exhibit two additional bands at 462 and 670 nm due to $^4A_2g^{(F)} \rightarrow {}^4T_1g^{(F)}$ (ν_1) and $^4A_2g^{(F)} \rightarrow {}^4T_2g^{(F)}$ (ν_2) transitions, respectively. These bands attributed to the spin allowed d–d transitions[187, 188]. These data indicate a distorted octahedral geometry around the Cr(III) atom[187, 188]. The spectrum of the $[Mn_2(L^4)(N_3)_4].H_2O$ complex, Figure (3. 113) showed two bands in the d-d region centred at 459 and 552 nm, which are assignable to $^6A_1g^{(F)} \rightarrow {}^4T_2g^{(G)}$ and $^6A_1g^{(S)} \rightarrow {}^4T_1g^{(G)}$ in a distorted octahedral configuration[189, 190].

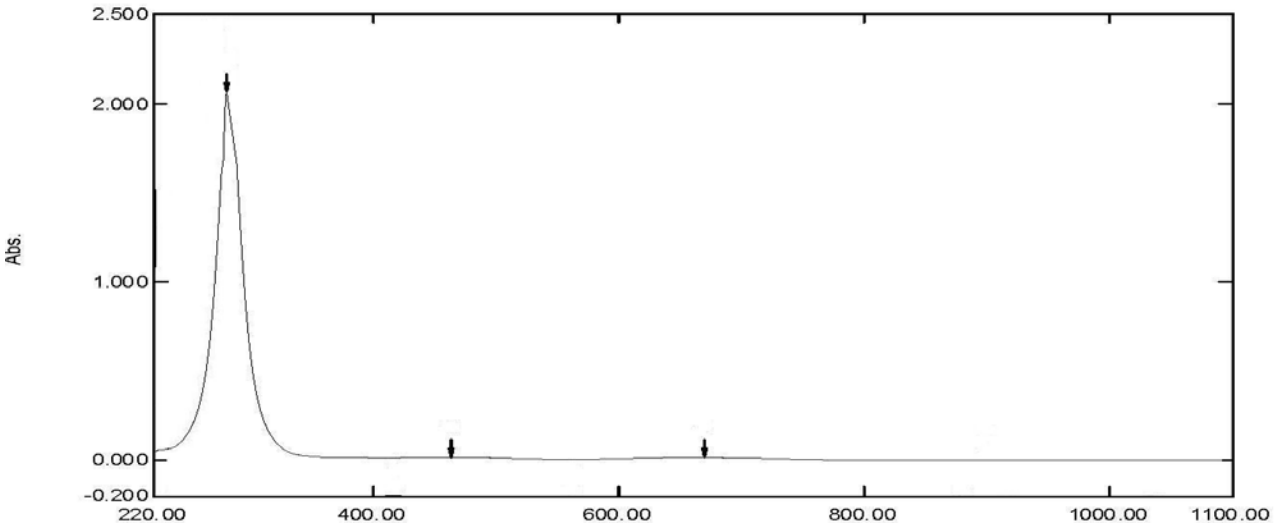

Figure (3. 112) Electronic spectrum of $[Cr_2(L^4)(N_3)_4]Cl_2.H_2O$ complex

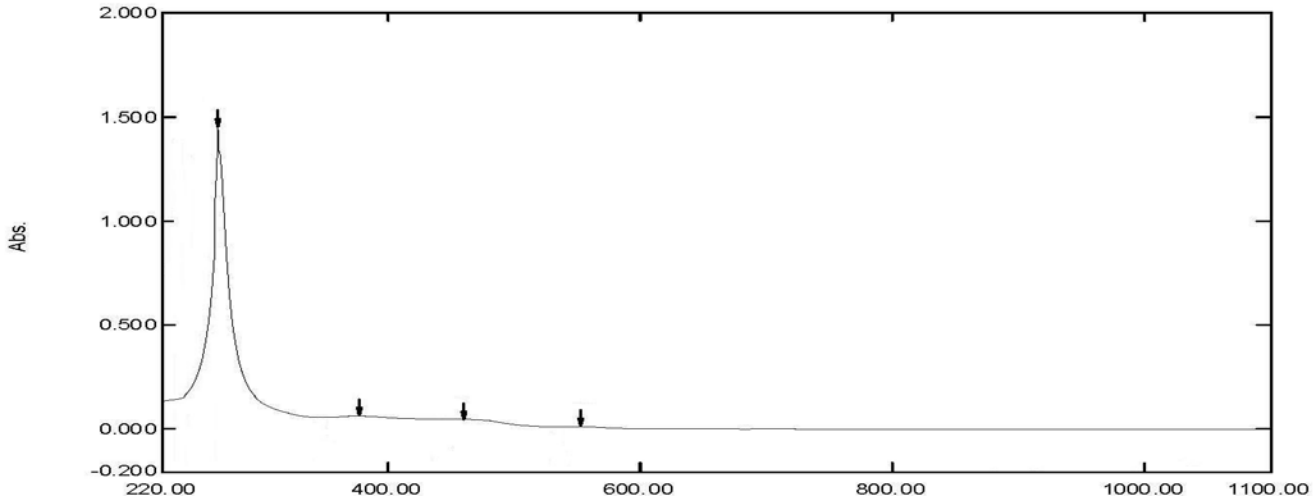

Figure (3. 113) Electronic spectrum of $[Mn_2(L^4)(N_3)_4].H_2O$ complex

The electronic spectra of $[Fe_2(L^4)(N_3)_4]$, $[Co_2(L^4)(N_3)_4]H_2O$, $[Ni_2(L^4)(N_3)_4]H_2O$ and $[Cu_2(L^4)(N_3)_4]H_2O$, Figures (3. 114 to 3. 117), show bands similar to that mentioned in the electronic spectra of the L^1 complexes. The absorption bands of the complexes are summarised in Table (3. 26). These data confirm octahedral geometries about metal centres[191-194].

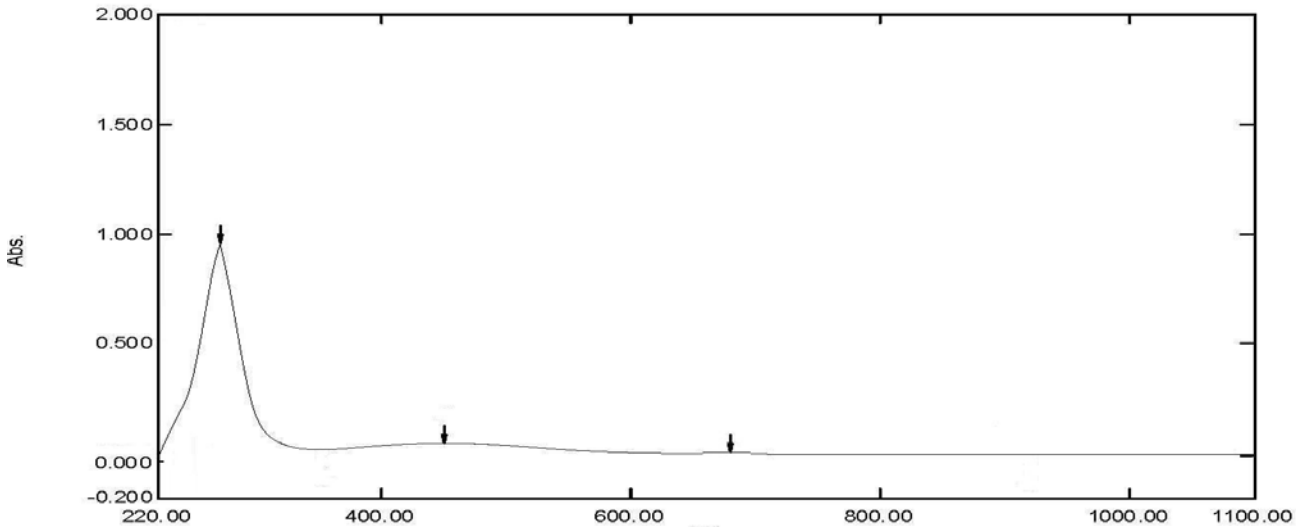

Figure (3. 114) Electronic spectrum of $[Fe_2(L^4)(N_3)_4]$ complex

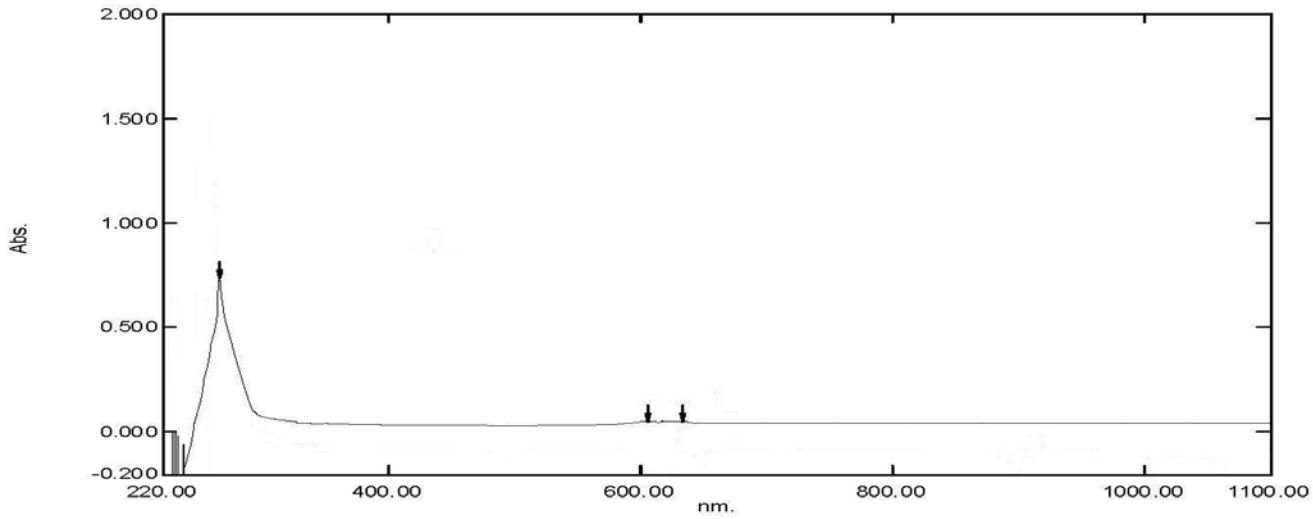

Figure (3. 115) Electronic spectrum of $[Co_2(L^4)(N_3)_4]H_2O$ complex

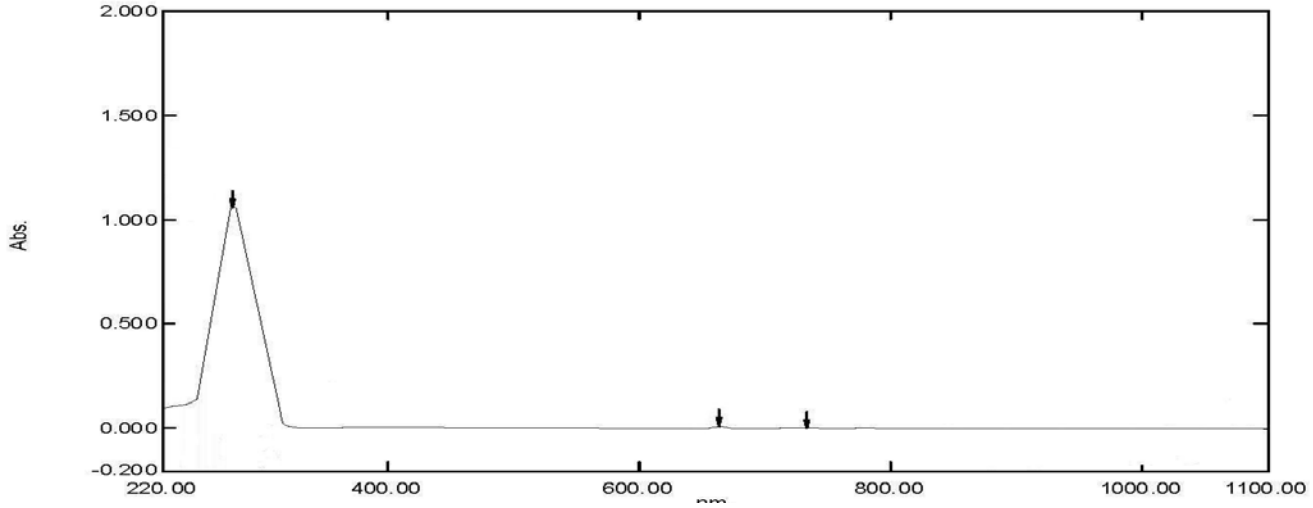

Figure (3. 116) Electronic spectrum of $[Ni_2(L^4)(N_3)_4]H_2O$ complex

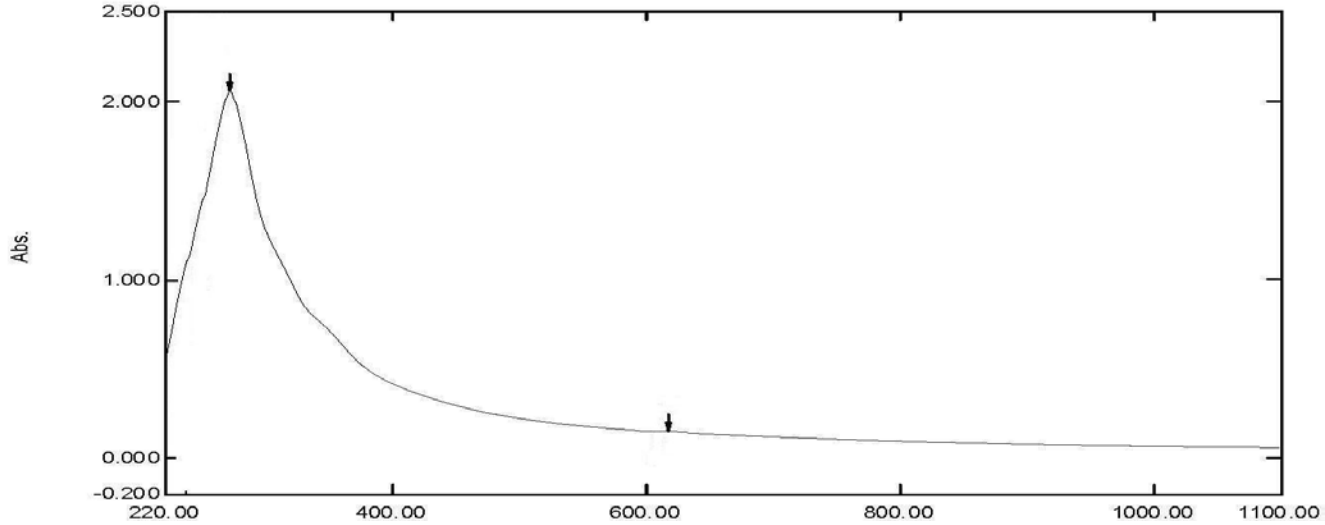

Figure (3. 117) Electronic spectrum of $[Cu_2(L^4)(N_3)_4]H_2O$ complex

The electronic spectra of the $[Zn_2(L^4)(N_3)_4]$, $[Cd_2(L^4)(N_3)_4]$ and $Na_2[Ag_2(L^4)(N_3)_4].H_2O$ complexes, Figures (3. 118 to 3. 120), display bands at 268, 267, and 266 nm assigned to the intraligand $\pi \rightarrow \pi^*$ transitions. The electronic spectra exhibit no bands in the visible region confirming the d^{10} configuration about metal atom[192, 195].

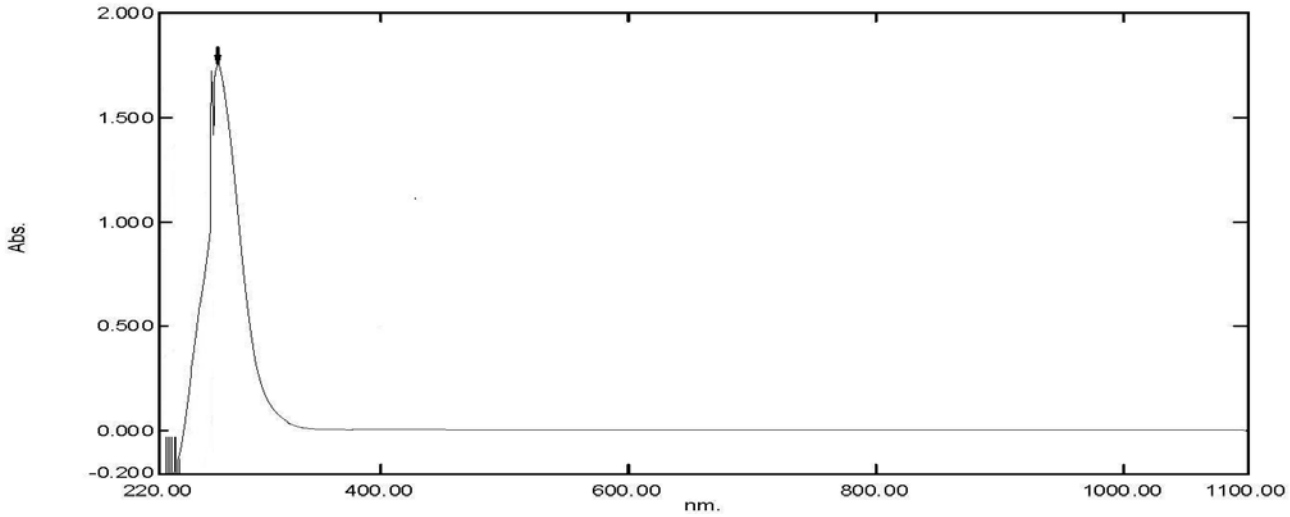

Figure(3. 118) Electronic spectrum of $[Zn_2(L^4)(N_3)_4]$ complex

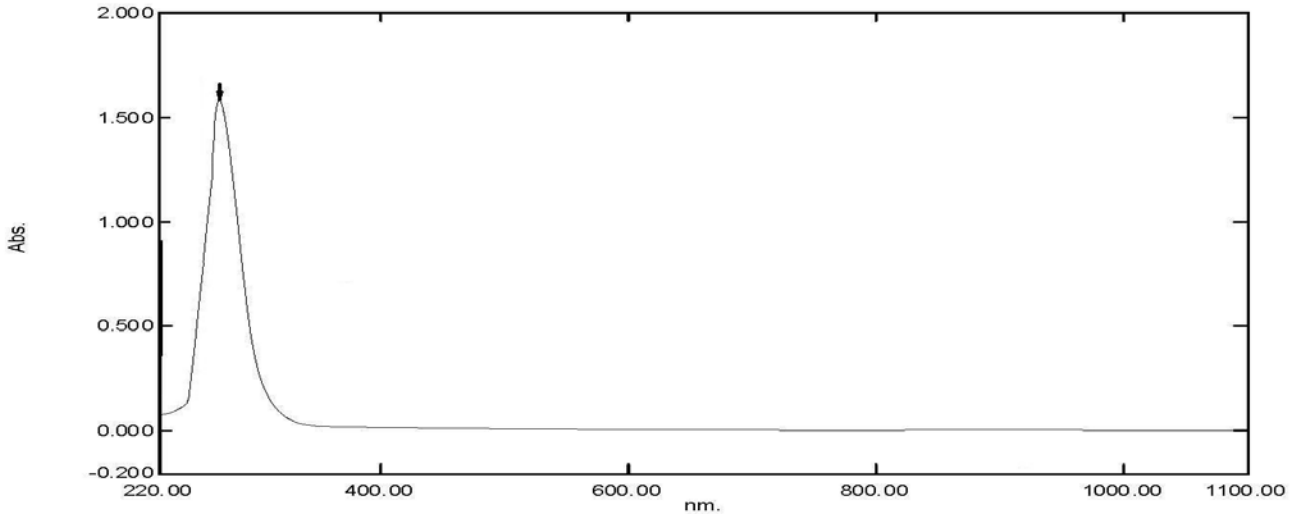

Figure (3. 119) Electronic spectrum of $[Cd_2(L^4)(N_3)_4]$ complex

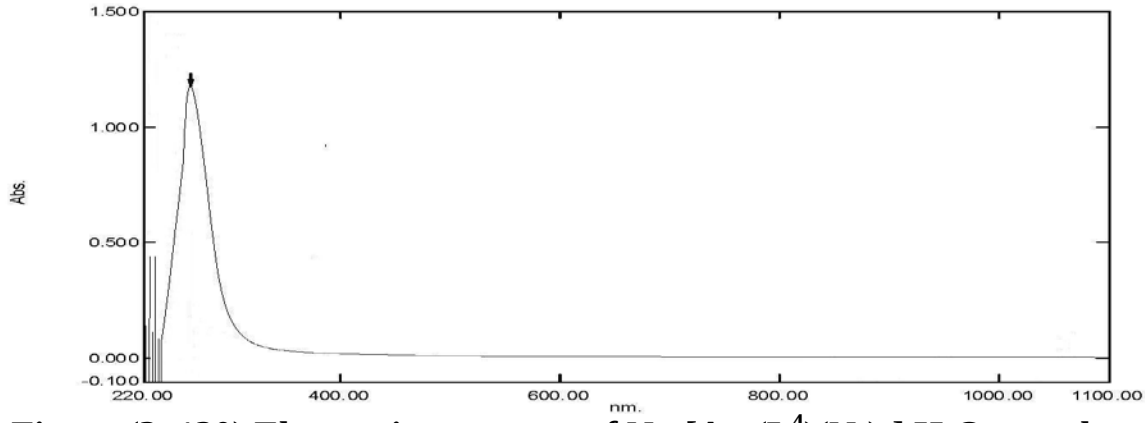

Figure (3. 120) Electronic spectrum of $Na_2[Ag_2(L^4)(N_3)_4]$ H_2O complex

Table (3. 26) UV-Vis spectral data of L^4 complexes in DMSO solutions

Compound	Band Position λ_{nm}	Wave number (cm^{-1})	Extinction coefficient ε_{max} ($dm^3\ mol^{-1}\ cm^{-1}$)	Assignment
L^4	267	37453	1531	$\pi\rightarrow\pi^*$
$[Cr_2(L^4)(N_3)_4]Cl_2.H_2O$	287 462 670	34843 21645 149258	2062 15 13	Intra-ligand $\pi\rightarrow\pi^*$ $^4A_2g \rightarrow {}^4T_1g^{(F)}$ (ν_1) $^4A_2g^{(F)} \rightarrow {}^4T_2g^{(F)}$ (ν_2)
$[Mn_2(L^4)(N_3)_4].H_2O$	264 376 459 552	37879 26596 21786 18116	1455 64 48 13	Intra-ligand $\pi\rightarrow\pi^*$ C.T $^6A_1g^{(F)} \rightarrow {}^4T_2g^{(G)}$ $^6A_1g^{(S)} \rightarrow {}^4T_1g^{(G)}$
$[Fe_2(L^4)(N_3)_4]$	269 450 675	37175 22222 14815	970 91 45	Intra-ligand $\pi\rightarrow\pi^*$ C.T $^5T_2g\rightarrow {}^5Eg$
$[Co_2(L^4)(N_3)_4].H_2O$	263 607	38023 16474	663 50	Intra-ligand $\pi\rightarrow\pi^*$ $^4T_1g^{(F)} \rightarrow {}^4A_2g^{(F)}$
$[Ni_2(L^4)(N_3)_4].H_2O$	276 662 734	36232 15106 13624	1053 9 7	Intra-ligand $\pi\rightarrow\pi^*$ $^3A_2g \rightarrow {}^3T_1g^{(F)}$ $^3A_2g \rightarrow {}^3T_2g^{(F)}$
$[Cu_2(L^4)(N_3)_4].H_2O$	270 622	37037 16077	2087 150	Intra-ligand $\pi\rightarrow\pi^*$ $^2Eg \rightarrow {}^2T_2g$
$[Zn_2(L^4)(N_3)_4]$	268	37313	1744	Intra-ligand $\pi\rightarrow\pi^*$
$[Cd_2(L^4)(N_3)_4]$	269	37175	1603	Intra-ligand $\pi\rightarrow\pi^*$
$Na_2[Ag_2(L^4)(N_3)_4].H_2O$	266	37594	1172	Intra-ligand $\pi\rightarrow\pi^*$

(3.11.5) UV-Vis Spectral data for L^5 complexes

The electronic spectra of the complexes of L^5 exhibited various extents of bathochromic shift of the bands related to the intraligand $\pi \rightarrow \pi^*$ transition, except for that of the Co(II), Cu(II) and Cd(II) complexes which showed a hypsochromic shift (see Table 3. 27). Bands in the range of 315-436 nm related to the charge transfer transitions (CT) were observed in the spectra of the Mn(II) and Fe(II) complexes.

The electronic spectrum of the green $[Cr_2(L^5)(N_3)_4]Cl_2.H_2O$ complex, Figure (3. 121) displayed band in the visible region at 637 nm, attributed to the spin allowed d–d transition[187, 188]. This band is assignable to $^4A_2g^{(F)} \rightarrow {}^4T_2g^{(F)}$ transition, indicating a distorted octahedral geometry around the Cr(III) atom[187, 188]. The spectrum of the $[Mn_2(L^5)(N_3)_4]H_2O$ complex, Figure (3. 122) showed the intra-ligand $\pi \rightarrow \pi^*$ transition and the charge transfer transition at 339 nm. The additional bands in the d-d region at 401, 437 and 637 nm are attributed to $^6A_2g \rightarrow {}^4A_1g$, ^4Eg, $^6A_1g \rightarrow {}^4T_2g^{(G)}$ and $^6A_1g \rightarrow {}^4T_1g^{(G)}$ transitions, respectively. These spin forbidden transitions confirm the distorted octahedral geometry about metal centre[189, 190].

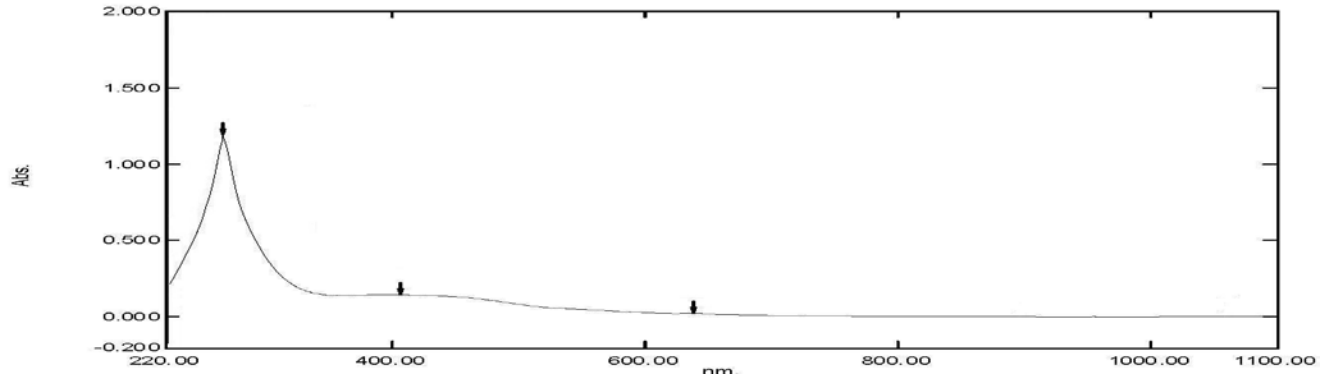

Figure (3. 121) Electronic spectrum of $[Cr_2(L^5)(N_3)_4]Cl_2.H_2O$ complex

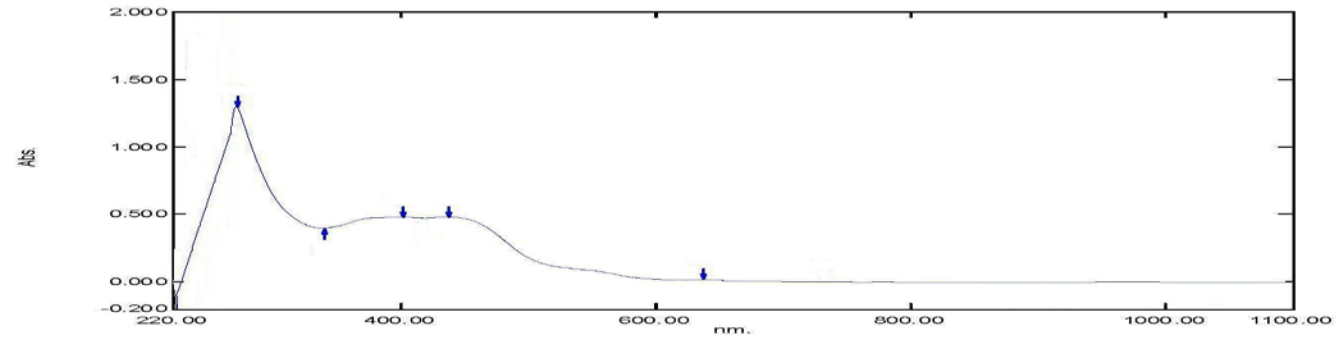

Figure (3. 122) Electronic spectrum of $[Mn_2(L^5)(N_3)_4]H_2O$ complex

The electronic spectra of $[Fe_2(L^5)(N_3)_4]H_2O$, $[Co_2(L^5)(N_3)_4]H_2O$, $[Ni_2(L^5)(N_3)_4]H_2O$ and $[Cu_2(L^5)(N_3)_4]H_2O$, Figures (3. 123 to 3. 126), show bands similar to that mentioned in the electronic spectra of the L^1 complexes. The absorption bands of the complexes are summarised in Table (3. 27). These data confirm octahedral geometries about metal centres[191-194].

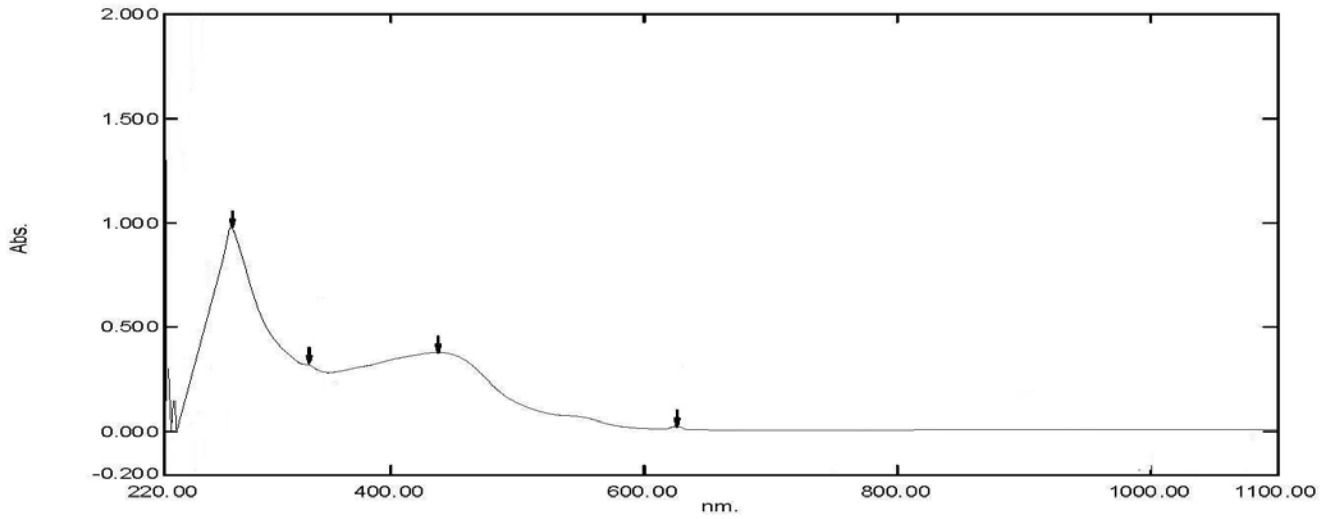

Figure (3. 123) Electronic spectrum of $[Fe_2(L^5)(N_3)_4].H_2O$ complex

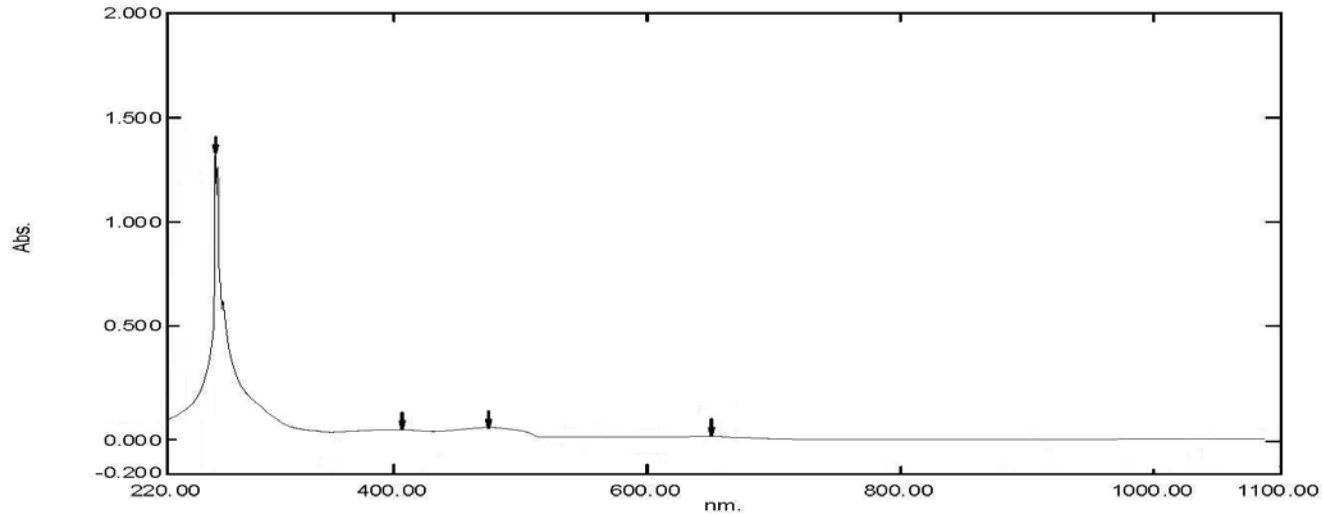

Figure (3. 124) Electronic spectrum of $[Co_2(L^5)(N_3)_4]H_2O$ complex

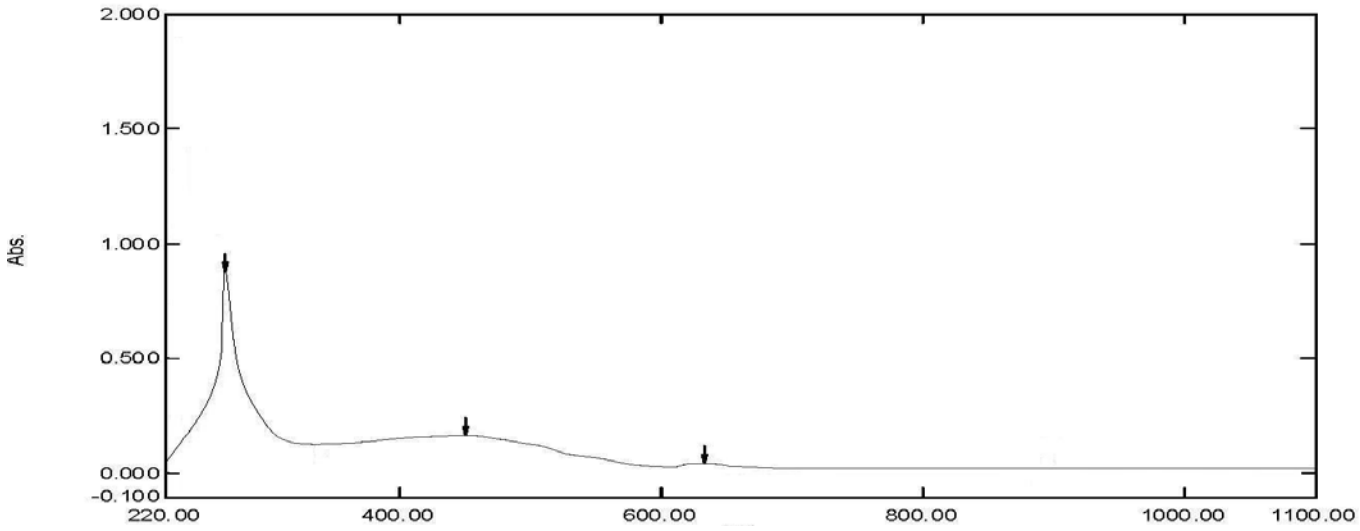

Figure (3. 125) Electronic spectrum of $[Ni_2(L^5)(N_3)_4]H_2O$ complex

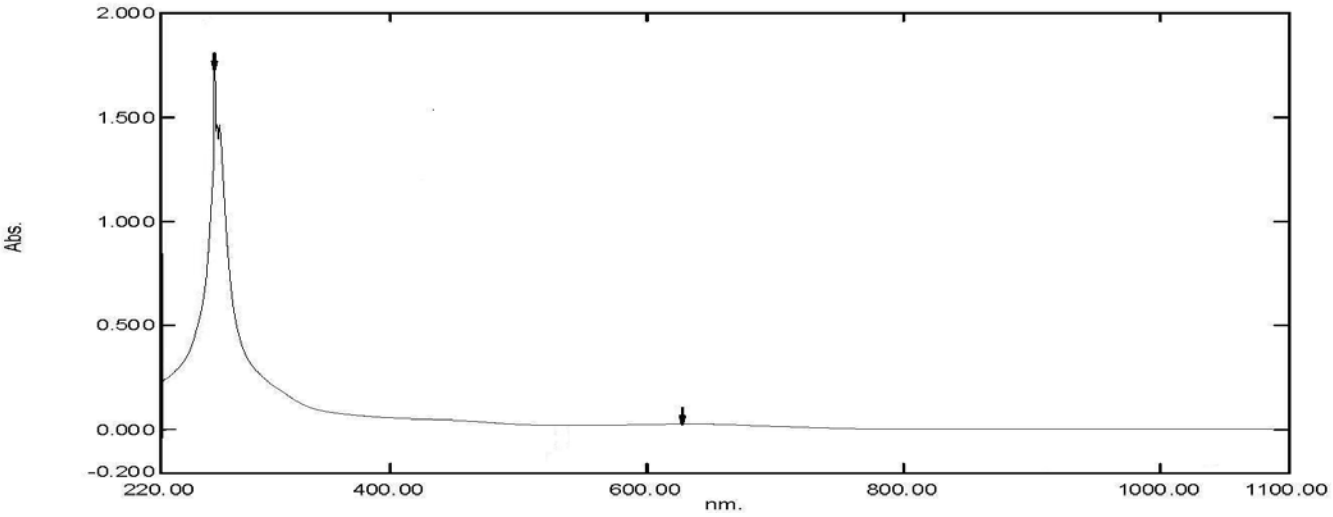

Figure (3. 126) Electronic spectrum of $[Cu_2(L^5)(N_3)_4]H_2O$ complex

The electronic spectra of the $[Zn_2(L^5)(N_3)_4]H_2O$, $[Cd_2(L^5)(N_3)_4]H_2O$ and $Na_2[Ag_2(L^5)(N_3)_4]H_2O$ complexes, Figures (3. 127. to 3. 129), exhibited bands centred at 263, 261 and 266 nm assigned to the intra-ligand $\pi \rightarrow \pi^*$. The electronic spectra display no bands in the d-d region, indicating a d^{10} configuration about the metal atom[192, 195].

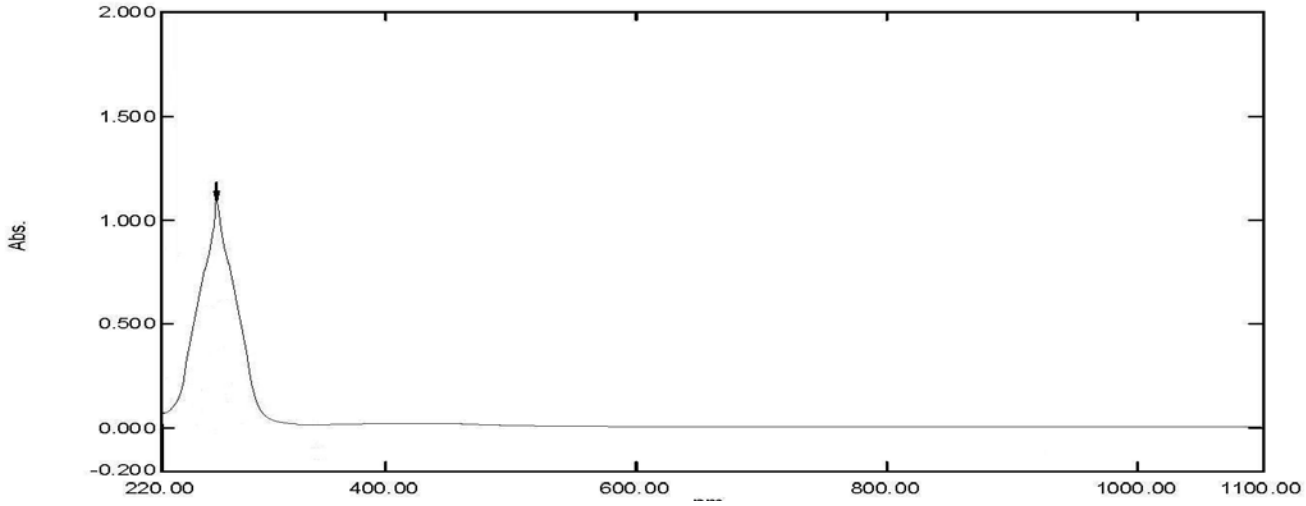

Figure (3. 127) Electronic spectrum of $[Zn_2(L^5)(N_3)_4]H_2O$ complex

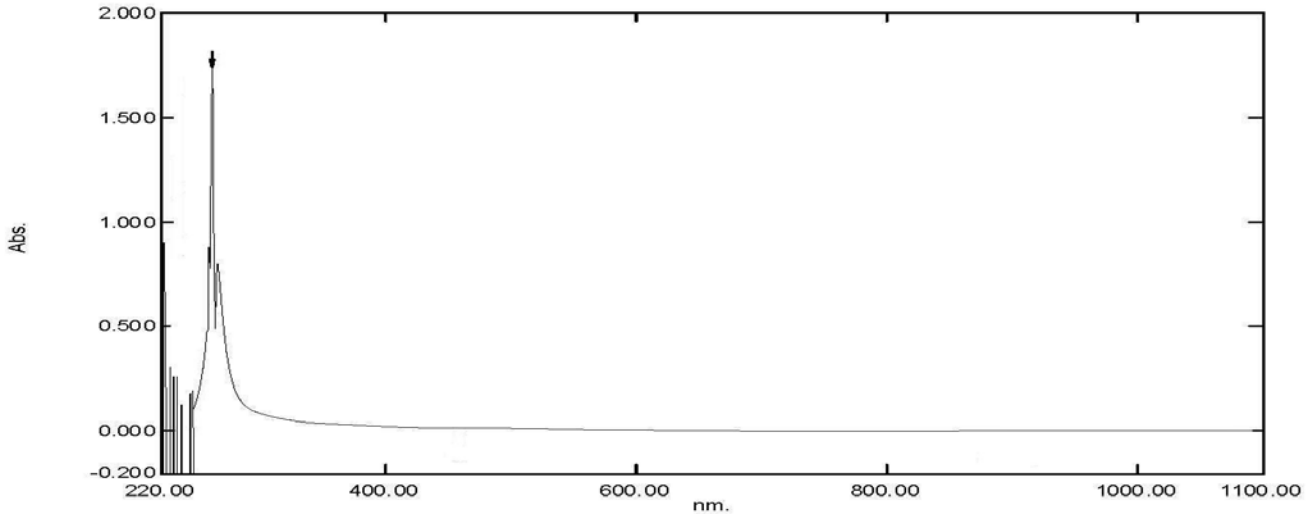

Figure (3. 128) Electronic spectrum of $[Cd_2(L^5)(N_3)_4]H_2O$ complex

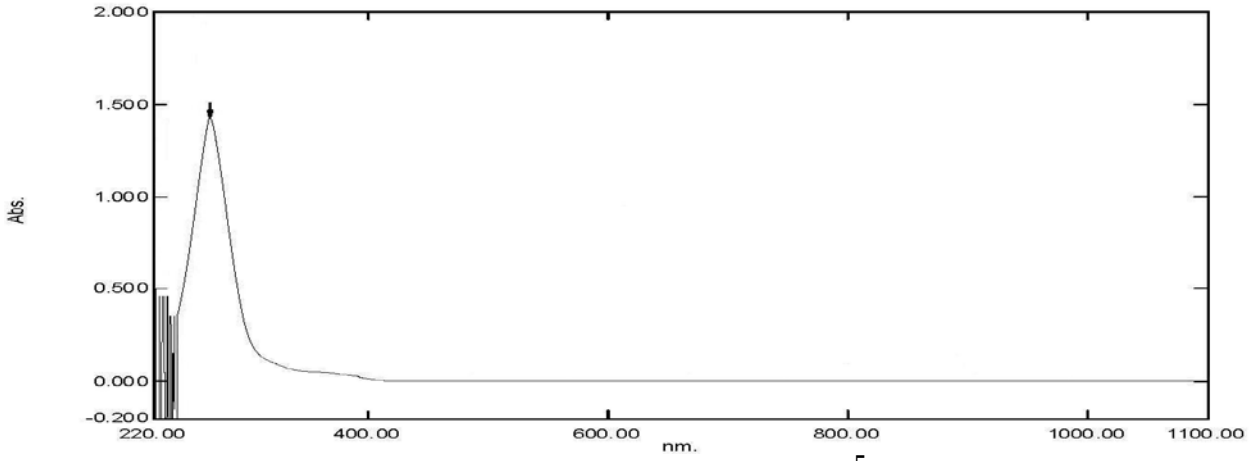

Figure (3. 129) Electronic spectrum of $Na_2[Ag_2(L^5)(N_3)_4]H_2O$ complex

Table (3. 27) UV-Vis spectral data of L^5 complexes in DMSO solutions

Compound	Band Position λ_{nm}	Wave number (cm^{-1})	Extinction coefficient ε_{max} ($dm^3\ mol^{-1}\ cm^{-1}$)	Assignment
L^5	261 357	38314 28011	1680 36	л→л*
$[Cr_2(L^5)(N_3)_4]Cl_2.H_2O$	269 356 637	37175 28090 15699	1201 159 21	Intra-ligand π→π* $^4A_2g^{(F)} \rightarrow {}^4T_1g^{(F)}$ (v1) $^4A_2g^{(F)} \rightarrow {}^4T_2g^{(F)}$
$[Mn_2(L^5)\ (N_3)_4].H_2O$	269 339 401 437 637	37175 29499 24938 22883 15699	1310 339 478 479 31	Intra-ligand π→π* C.T $^6A_2g \rightarrow {}^4A_1g, {}^4Eg$ $^6A_1g \rightarrow {}^4T_2g^{(G)}$ $^6A_1g \rightarrow {}^4T_1g^{(G)}$
$[Fe_2(L^5)\ (N_3)_4].H_2O$	270 315 436 626	37037 31746 22936 15974	983 381 283 21	Intraligand C.T C.T $^5T_2g \rightarrow {}^5Eg$
$[Co_2(L^5)\ (N_3)_4].H_2O$	257 474 649	38911 21097 15408	1339 57 18	Intra-ligand π→π* $^4T_1g^{(F)} \rightarrow {}^4A_2g^{(F)}$ $^4T_1g^{(F)} \rightarrow {}^4T_2g^{(F)}$
$[Ni_2(L^5)\ (N_3)_4].H_2O$	266 450 632	37594 22222 15823	880 165 47	Intra-ligand π→π* $^3A_2g \rightarrow {}^1T_1g^{(P)}$ $^3A_2g \rightarrow {}^3T_1g^{(F)}$
$[Cu_2(L^5)\ (N_3)_4].H_2O$	259 627	38616 15949	1739 21	Intra-ligand π→π* $^2Eg \rightarrow {}^2T_2g$
$[Zn_2(L^5)\ (N_3)_4].H_2O$	263	38023	1127	Intra-ligand π→π*
$[Cd_2(L^5)\ (N_3)_4].H_2O$	259	38616	1659	Intra-ligand π→π*
$Na_2[Ag_2(L^5)\ (N_3)_4].H_2O$	266	37594	1423	Intra-ligand π→π*

(3.12) ^{1}H, ^{13}C and DEPT ^{13}C NMR spectra for the complexes

(3.12.1) ^{1}H, ^{13}C NMR spectra for $[Cd_2(L^1)(N_3)_4].H_2O$ complex

In solution, the complex exhibits two conformation forms: the A form and the B form. In the NMR we observed the presence of double signals related to the two forms.

(3.12.1.1) ^{1}H NMR spectrum for $[Cd_2(L^1)(N_3)_4].H_2O$

The ^{1}H NMR spectrum for $[Cd_2(L^1)(N_3)_4].H_2O$ in DMSO-d6 is shown in Figure (3.130). The complex exhibits two conformational isomers A and B in a ratio about 2:1, respectively. This is based on the integration of the detected signals in the spectrum. Isomer A shows chemical shift at δ =5.00 ppm equivalent to 4 protons which assigned to ($C_{2,\ 2}$-*H*). This peak is shifted to upfield position compared with that observed in the free ligand. This may be due to the fact that, upon complexation, in each of the pyridinium portion the carboxylato moiety is almost co-planar with the CH_2 group and the pyridinium molecue. This can lead to the increase of the electron density, shifting the electron charge density from the carboxylato moiety, on the (CH_2) group allowing it to appear at upfield position. The signal at (δ = 8.54-8.56 ppm, 4H, d, J_{HH} = 6.8 Hz) attributed to ($C_{4,\ 4}$; $_{6,\ 6}$-*H*). The chemical shifts of ($C_{3,\ 3}$; $_{7,\ 7}$-*H*) protons appear as a doublet at (9.00-9.02 ppm, 4H, d, J_{HH} = 6.8 Hz). These signals are shifted to upfield. This may due to the co-planar alignment occurred between the carboxylato, CH_2 and the aromatic groups. On other hand, isomer B displays chemical shift at 5.08 ppm equivalent to 4H which assigned to ($C_{2,\ 2}$-*H*) protons. Peaks at δ = 8.62-8.64 ppm (4H, d, J_{HH} = 8.00 Hz) assigned to ($C_{4,\ 4}$; $_{6,\ 6}$-*H*) protons. The signals at δ = 9.17-9.19 ppm (4H, d, J_{HH} = 8.00 Hz) attributed to ($C_{3,\ 3}$; $_{7,\ 7}$-*H*) protons. The above

reasoning can be used to explain shifts occurred in isomer B. The appearance of two isomers is perhaps due to the ease of rotation of the chelating portion of the molecule and/or the ease of rotation of the two pyridinium molecules; slow rotation could give one or two conformations that are not symmetrical. The results are summarised in Table (3.28).

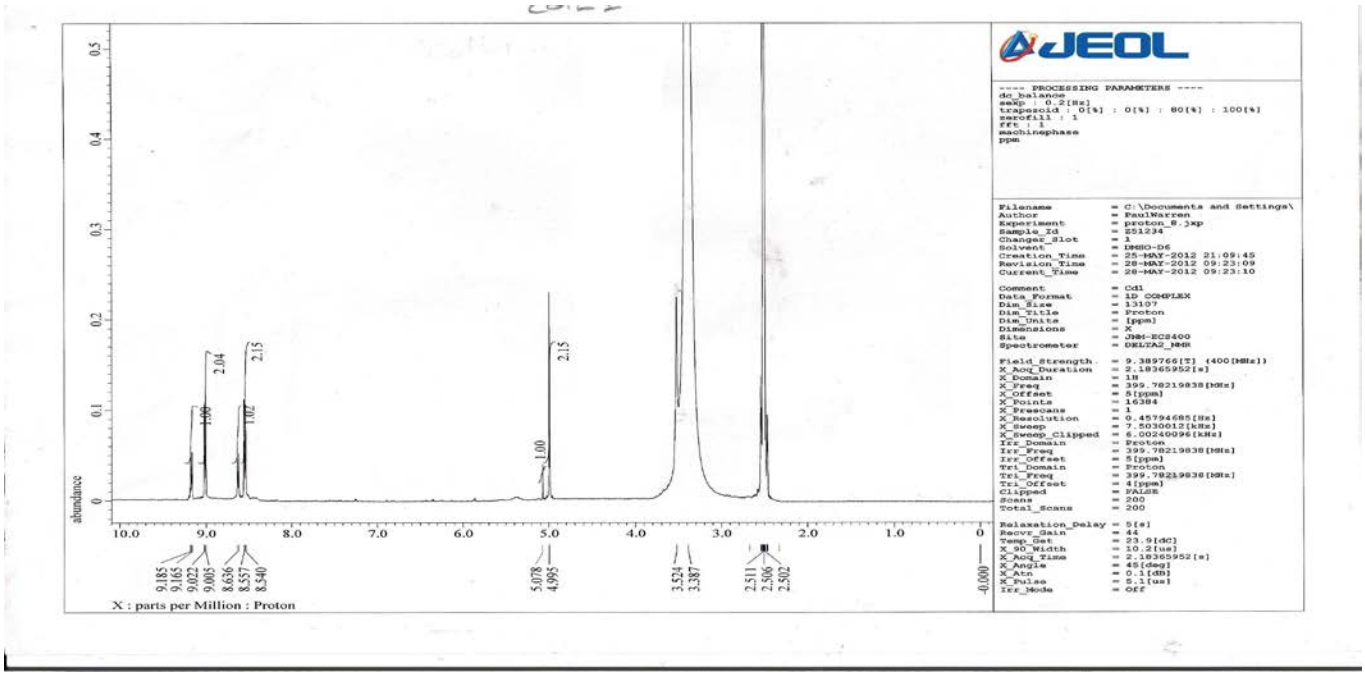

Figure (3. 130) ^{1}H NMR spectrum in DMSO-d6 of $[Cd_2(L^1)(N_3)_4].H_2O$

(3.12.1.2) ^{13}C NMR spectrum for $[Cd_2(L^1)(N_3)_4].H_2O$

The ^{13}C NMR spectrum of $[Cd_2(L^1)(N_3)_4].H_2O$ in DMSO-d6, Figure (3.131) shows the chemical shifts of ($C_{2,\ 2`}$) are nonequivalent and appear at 64.30 and 69.43 ppm. This is due to the presence of two isomers in solution, A and B. The chemical shift at 138.25 and 141.35 ppm assigned to ($C_{4,\ 4`;\ 6,\ 6`}$). Signals related to ($C_{3,\ 3`;\ 7,\ 7`}$) were detected at 151.48 and 151.53. Chemical shifts at 164.93 and 165.64 ppm were attributed to ($C_{5,\ 5`}$) indicating the two signals are nonequivalent. The chemical shift of the C=O of the carboxylate moiety appears as expected downfield at 177.86 and 183.82 ppm. The shift of these signals to downfield is due to the electron deshielding of the carboxylato group upon complex formation. The results are summarised in Table (3. 29).

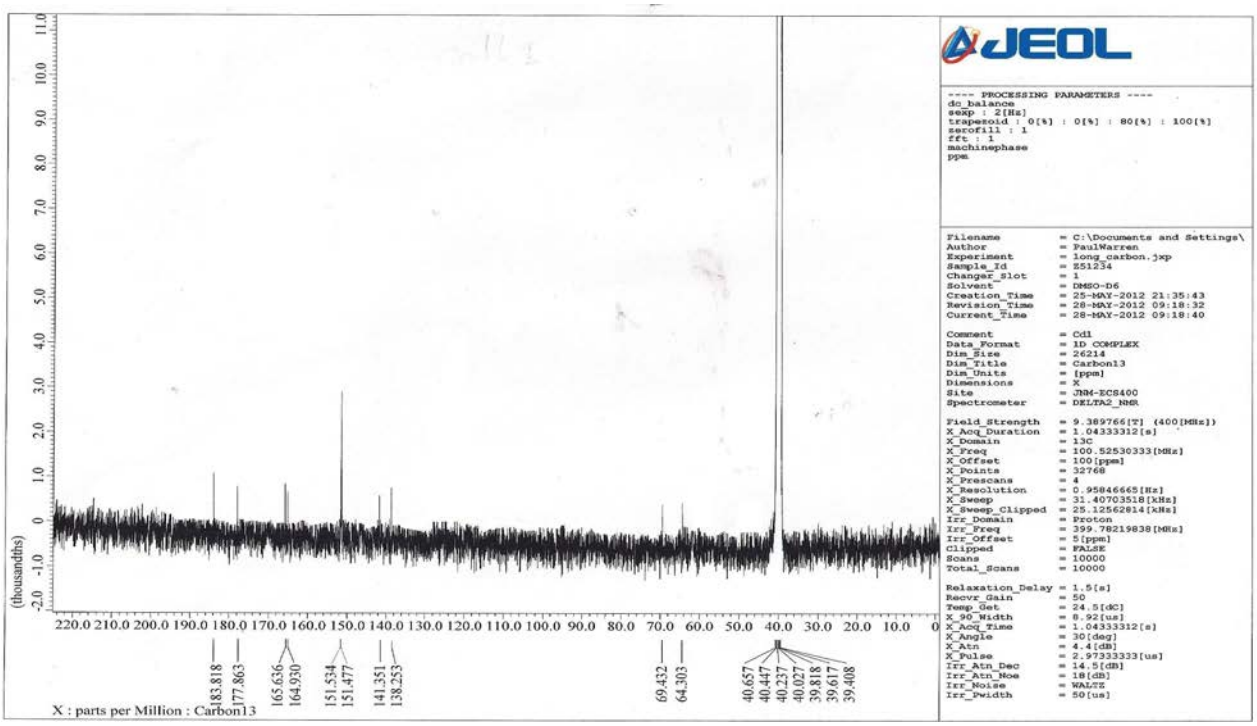

Figure (3. 131) ^{13}C NMR spectrum in DMSO-d6 of $[Cd_2(L^1)(N_3)_4]\ .H_2O$

(3.12.1.3) DEPT ^{13}C NMR spectrum for $[Cd_2(L^1)(N_3)_4].H_2O$

The DEPT ^{13}C NMR spectrum for $[Cd_2(L^1)(N_3)_4]$, Figure (3. 132) reveals the ($C_{2,\ 2}^{-}$) are nonequivalent and appear as two signals at 64.30 and 69.43 ppm, indicating the present of two isomers A and B. These peaks were enhanced, as expected, in the negative direction (down), and therefore assigned to ($-CH_2$) group. Signals at chemical shifts 138.25; 141.35 and 151.48; 151.53 ppm were assigned to ($C_{4,\ 4}^{-}$; $_{6,\ 6}^{-}$) and ($C_{3,3}^{-}$; $_{7,\ 7}^{-}$), respectively. These signals enhance in the positive direction (up), and therefore assigned to (-CH). No signals in the range 177-183 ppm, may assign for ($C_{5,\ 5}^{-}$) and ($C_{1,\ 1}^{-}$) are detected, quaternary carbons.

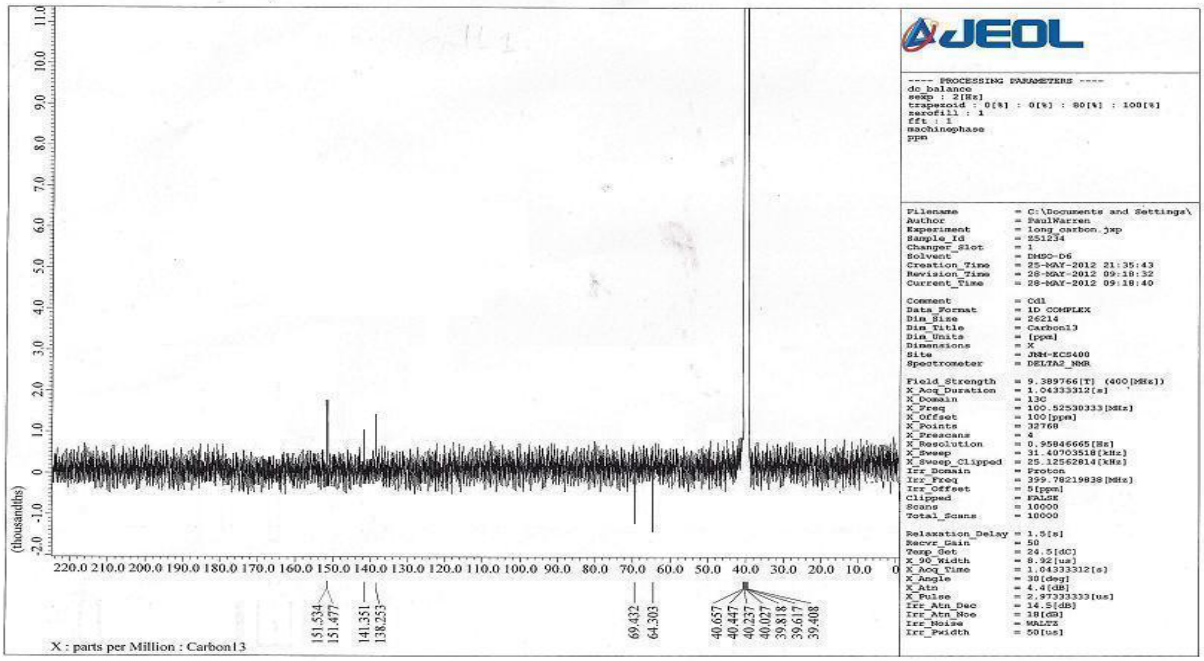

Figure (3. 132) DEPT ^{13}C NMR spectrum of $[Cd_2(L^1)(N_3)_4].H_2O$ in DMSO-d6

(3-12.2) ^{1}H, ^{13}C NMR spectra for $[Zn_2(L^2)(N_3)_4].H_2O$ Complex

(3.12.2.1) ^{1}H NMR spectrum for $[Zn_2(L^2)(N_3)_4].H_2O$

The ^{1}H NMR spectrum for $[Zn_2(L^2)(N_3)_4].H_2O$ in DMSO-d6 is shown in Figure (3. 133). The spectrum displays one set of signals indicatating the present of one isomer in solution. The spectrum shows chemical shift at δ = 9.13-9.15 ppm (4H, d, J_{HH} = 7.2 Hz) attributed to ($C_{3,3'}$; $_{5,5'}$-*H*) protons. The signals of ($C_{2,2'}$, $_{6,6'}$-*H*) protons appear as a doublet at δ = 9.21-9.22 ppm (4H, d, J_{HH} = 4.8 Hz). These signals are shifted to downfield compared to that detected in the free ligand. This may be due to the redistribution of the negative charge of the carboxylato moiety, upon complexation, to the nitrogen atom resulting in the shielding of the aromatic group. The results are summarised in Table (3. 28).

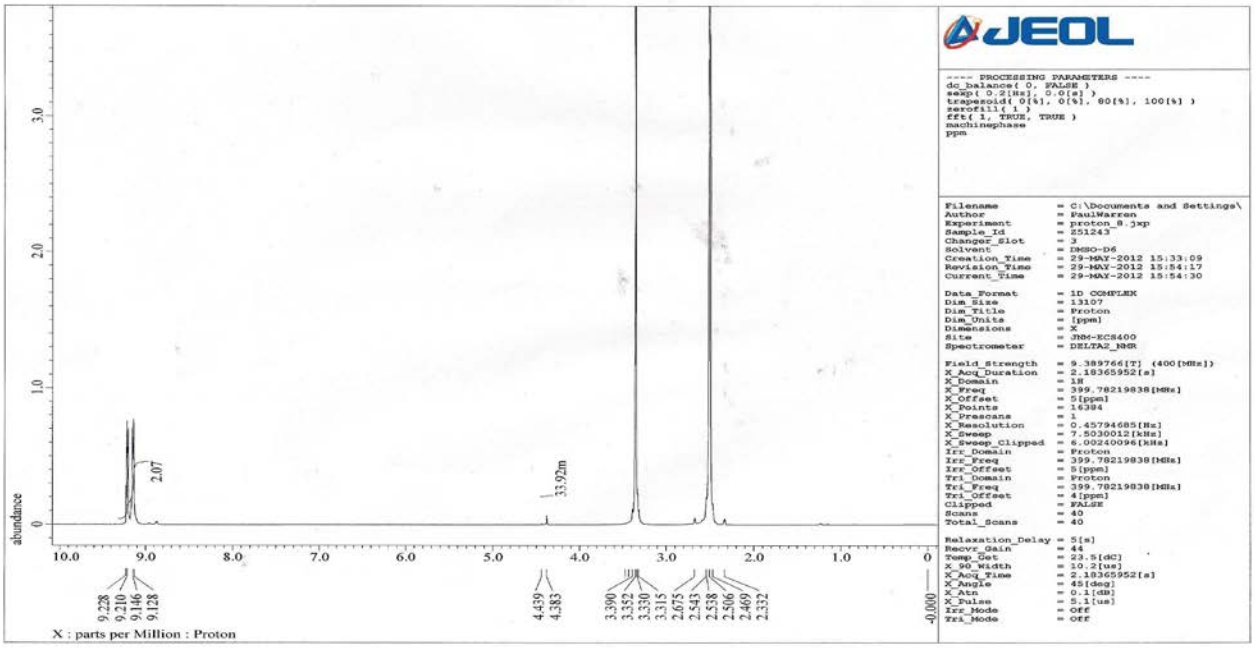

Figure (3. 133) ^{1}H NMR spectrum in DMSO-d6 for $[Zn_2(L^2)(N_3)_4]\ .H_2O$

(3.12.2.2) ^{13}C NMR spectrum for $[Zn_2(L^2)(N_3)_4].H_2O$

As in the ^{1}H NMR, the ^{13}C NMR for the complex shows one set of signals. The ^{13}C NMR spectrum for $[Zn_2(L^2)(N_3)_4].H_2O$ in DMSO-d6 , Figure (3. 134) shows chemical shift at δ=130.02 ppm assigned to ($C_{3,3'; 5,5'}$). Signals related to ($C_{2,2'; 6,6'}$) are equivalent and detected at δ =157.99 ppm. Chemical shift at δ =162.02 ppm, attributed to ($C_{4,4'}$). The chemical shift of the C=O of the carboxylato moiety appears as expected downfield at δ=181.99 ppm. These signals are shifted to downfield due to complex formation. The results are summarised in Table (3. 29).

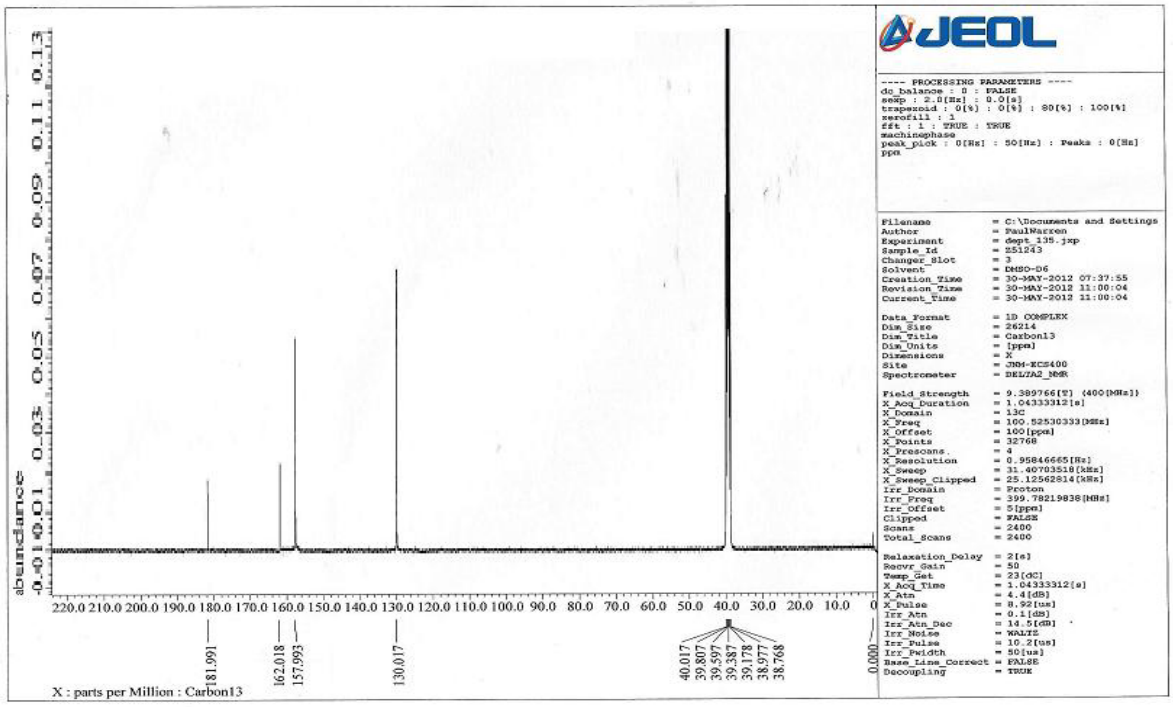

Figure (3. 134) ^{13}C NMR spectrum in DMSO-d6 for $[Zn_2(L^2)(N_3)_4]$ .H_2O

(3-12.3) ^{1}H, ^{13}C NMR spectra for $[Cd_2(L^4)(N_3)_4].H_2O$

(3.12.3.1) ^{1}H NMR spectrum for $[Cd_2(L^4)(N_3)_4].H_2O$

The ^{1}H NMR spectrum for $[Cd(L^4)(N_3)_4].H_2O$, Figure(3-135) displays chemical shifts at δ = 2.15-2.22 ppm (4H) and δ = 2.35-2.38 ppm (4H, t, J_{HH}=14.4 Hz) assigned to ($C_{3,3}$-*H*) and ($C_{2,2}$-*H*) protons, respectively, and each is equivalent to 4 protons. The latter signal is shifted to upfield due to the fact that, upon complexation, in each of the pyridinium portion the carboxylato group is almost co-planar with the CH_2 group and the pyridinium molecue. This can lead to the increase of the electron density, shifting the electron charge density from the carboxylato group, on the (CH_2) group and appeared at upfield position. Therefore the (-CH_2) group is shielded and appeared at lower chemical shift. These signals show a slight change in the chemical shifts values compared with that in the free ligand. This may be related to a weak interaction, upon complexation, between the ligand and metal

ion. The signal at chemical shift 4.65-4.68 ppm (4H, t, J_{HH}= 14.4 Hz) equivalent to 4 protons assigned to ($C_{4,\ 4}$-*H*). This peak is shifted to downfield and can be explained using similar explanation as above. The signal at chemical shift 8.72-8.75 ppm (4H, t, J_{HH}= 12.0 Hz) equivalent to 4 protons assigned to ($C_{6,\ 6}$, $_{8,\ 8}$-*H*). The signal at chemical shift 9.22-9.24 ppm (4H, d, J_{HH}= 7.2 Hz) equivalent to 4 protons assigned to ($C_{5,\ 5}$, $_{9,\ 9}$-*H*). These signals are shifted to downfield compared with that in the free ligand. This may be due to the co-planar between the pyridinium and the carboxylato anion groups and lead to increase of the electron density over the pyridinium group. Chemical shifts are summarised in Table (3. 28).

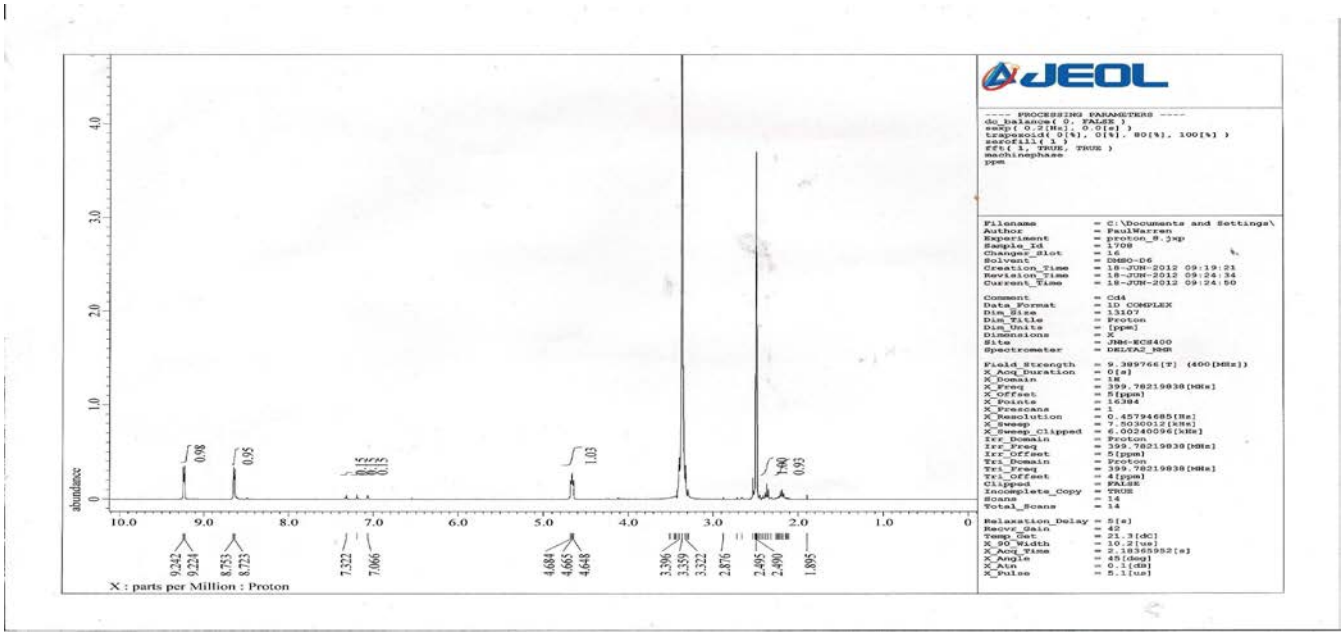

Figure (3. 135) ^{1}H NMR spectrum in DMSO-d_6 for $[Cd_2(L^4)(N_3)_4].H_2O$

(3.12.3.2) ^{13}C NMR spectrum for $[Cd_2(L^4)(N_3)_4].H_2O$

The ^{13}C NMR spectrum for $[Cd_2(L^4)(N_3)_4]$.**H_2O**, Figure (3. 136) shows chemical shifts at δ = 29.34, δ=33.99 and 65.52 ppm, assigned to (C_3, $_3$), (C_2, $_2$) and (C_4, $_4$), respectively. Signals at 129.99, 150.57and 156.05 ppm, were attributed to ($C_{6,\ 6}$; $_{8,\ 8}$), ($C_{5,\ 5}$; $_{9,\ 9}$) and ($C_{7,\ 7}$), respectively. The chemical shift of C=O group of the carboxylato moiety appears as expected downfield at δ = 178.11 ppm. The results are summarised in Table (3. 29).

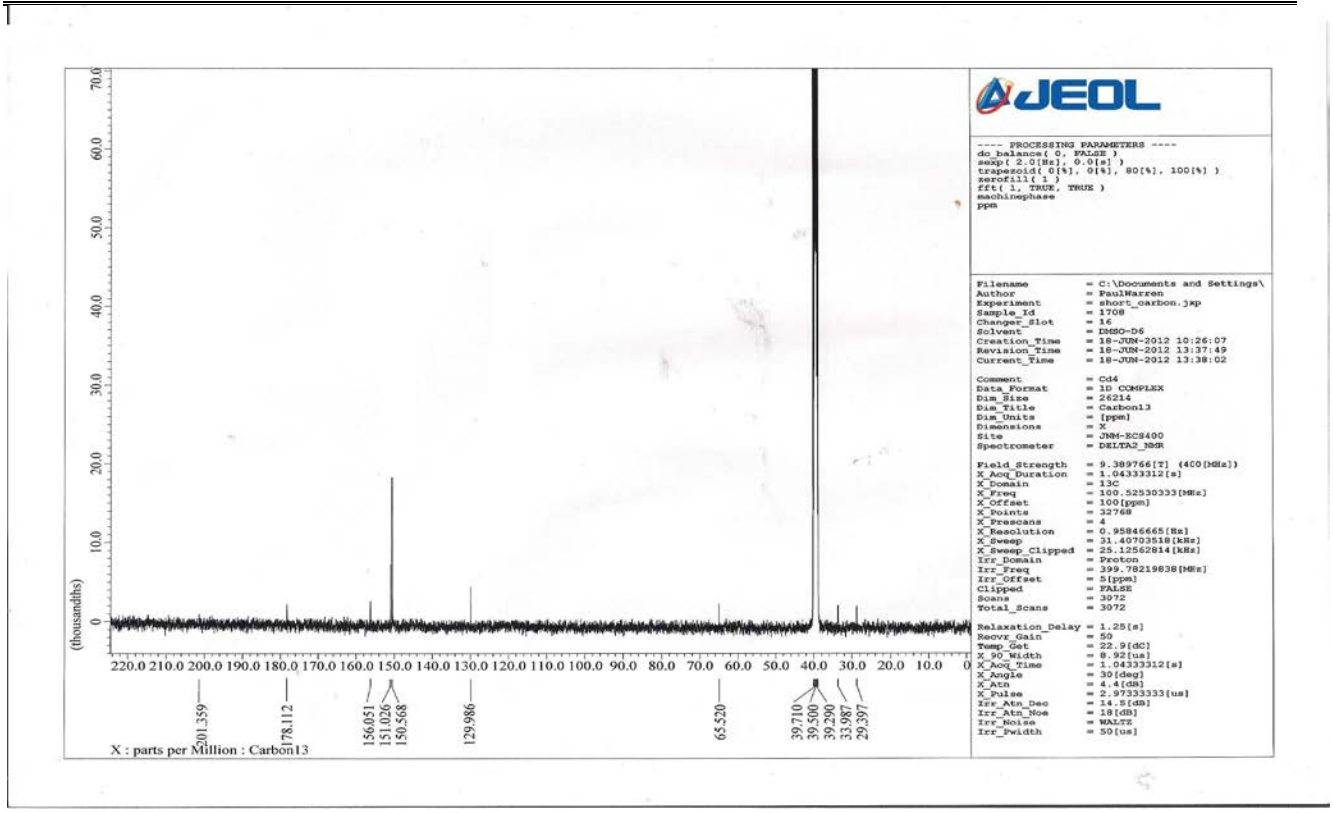

Figure (3. 136) ^{13}C NMR spectrum in DMSO-d6 for $[Cd_2(L^4)(N_3)_4].H_2O$

Table (3-28) ^{1}H NMR data for the complexes measured in DMSO-d6 and chemical shift in p.p.m (δ)

Compound	Func. Group	δ (P.P.M)
CdL[1]		
isomer A	**$C_{(2,2')}$-H**	**5.00, 4H**
	$C_{(4,4';6,6')}$-H	**8.54-8.56, d, 4H, J_{HH}= 6.8 Hz**
	$C_{(3,3';7,7')}$-H	**9.00-9.02, d, 4H, J_{HH}=6.8 Hz**
Isomer B	**$C_{(2,2')}$-H**	**5.08,4H**
	$C_{(4,4';6,6')}$-H	**8.62-8.64,1H,d, J_{HH}=8.0 Hz**
	$C_{(3,3';7,7')}$-H	**9.17-9.19,d,4H, J_{HH}=8.0 Hz**
ZnL[2]	**$C_{(3,3';5,5')}$-H**	**9.13-9.15,d, 4H, J_{HH}=7.2 Hz**
	$C_{(2,2';6,6')}$-H	**9.21-9.23, d, 4H, J_{HH}= 7.2 Hz**
CdL[4]	**$C_{(3,3')}$-H**	**2.15-2.22,m,4H, J_{HH}= 27.2 Hz**
	$C_{(2,2')}$-H	**2.35-2.38, t, 4H, J_{HH}=14.4 Hz**
	$C_{(4,4')}$-H	**4.65-4.68, t, 4H, J_{HH}=14.4 Hz**
	$C_{(6,6';8,8')}$-H	**8.72-8.75, d, 4H, J_{HH}=12.0 Hz**
	$C_{(5,5';9,9')}$-H	**9.22- 9.24, d, 4H, J_{HH}=7.2 Hz**

Table (3-29) ^{13}C NMR data for the complexes measured in DMSO-d6 and chemical shift in p.p.m (δ)

Compound	Func. Group	δ (P.P.M)
CdL^1 isomer 1	**$C_{(2,2')}$**	**64.30**
	$C_{(4,4';6,6')}$	**138.25**
	$C_{(3,3';7,7')}$	**151.48**
	$C_{(5,5')}$	**164.93**
	$C_{(1,1')}$	**177.86**
Isomer 2	**$C_{(2,2')}$**	**69.43**
	$C_{(4,4';6,6')}$	**141.35**
	$C_{(3,3;7,7')}$	151.53
	$C_{(5,5')}$	165.64
	$C_{(1,1')}$	183.82
ZnL^2	**$C_{(3,3';5,5')}$**	**130.02**
	$C_{(2,2';6,6')}$	**157.99**
	$C_{(4)}$	**162.02**
	$C_{(1)}$	**181.99**
CdL^4	**$C_{(3,3')}$**	**29.34**
	$C_{(2,2')}$	**33.99**
	$C_{(4,4')}$	**65.52**
	$C_{(6,6';8,8')}$	**129.99**
	$C_{(5,5';9,9')}$	**150.57**
	$C_{(7,7')}$	**156.05**
	$C_{(1,1')}$	**178.11**

(3.13) Mass spectra of the complexes

(3.13.1) Mass spectrum of $[Cd_2(L^1)(N_3)_4].H_2O$

The high resolution electrospray (+) mass spectrum of CdL^1 is presented in Figure (3. 137). The molecular ion peak for the complex is observed at m/z = 641.42 $(M\text{-}N_3)^+$ (63 %) for $C_{14}H_{14}Cd_2N_{14}O_5$, requires =683.17. The other peaks detected at m/z =613.14 (40 %), 579.13 (22 %), 581.10(19 %) , 598.13 (16 %) and 571.10 The fragmentation pattern of the molecular ion of $[Cd_2(L^1)(N_3)_4].H_2O$ is shown in Scheme (3. 9).

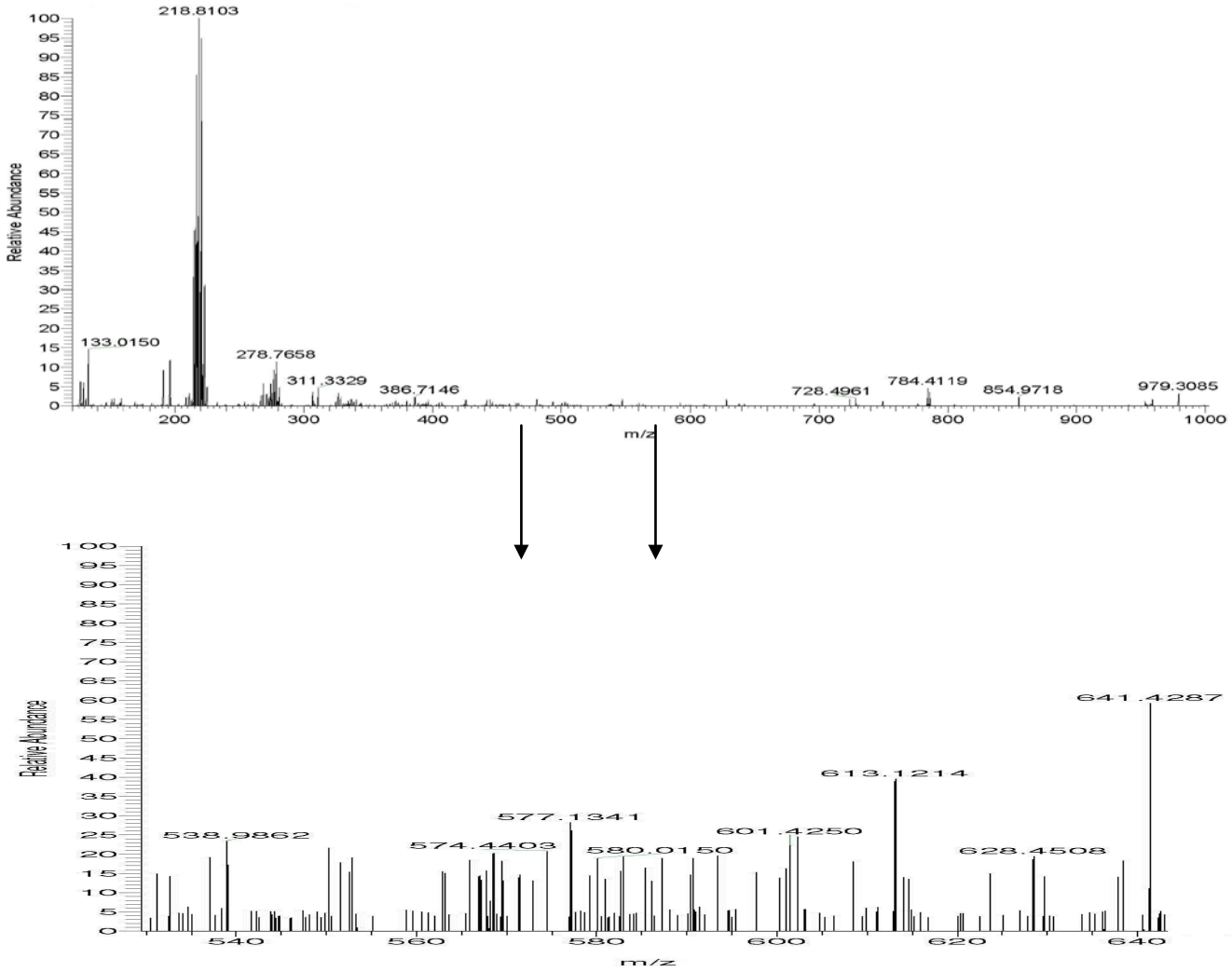

Figure (3.137) ES (+) mass spectrum of $[Cd_2(L^1)(N_3)_4].H_2O$

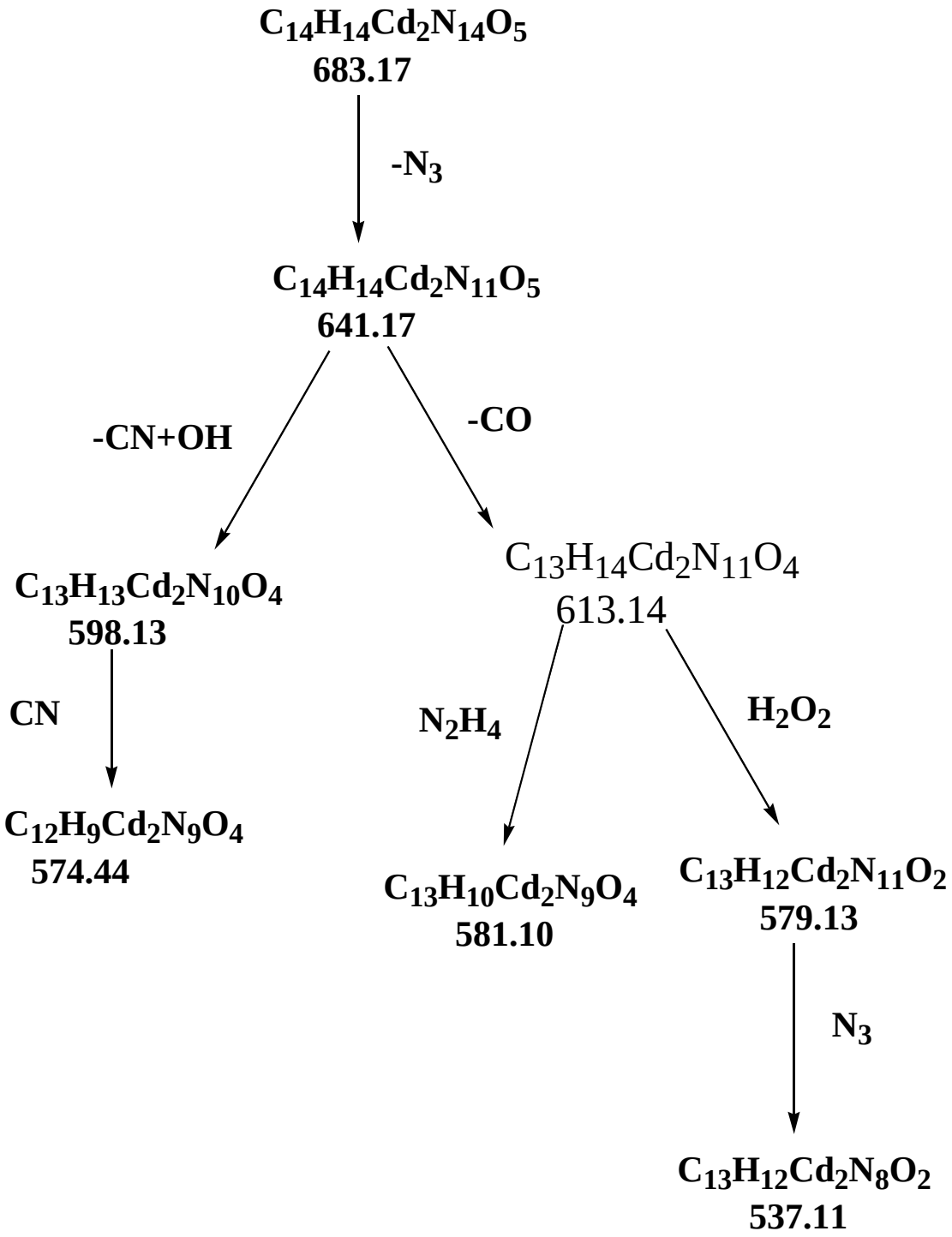

Scheme (3.9) The fragmentation pattern of $[Cd_2(L^1)(N_3)_4].H_2O$

(3.13.2) Mass spectrum of $[Ni_2(L^1)(N_3)_4].H_2O$

The high resolution electrospray (+) mass spectrum of NiL^1 is presented in Figure (3. 138). The exact molecular ion peak for the complex is observed at m/z = 574.11 $(M)^+$ (9 %) for $C_{14}H_{14}Ni_2N_{14}O_5$, requires =574.0. The other peaks detected at m/z =485.94 (9 %), 410.22 (16 %), 324.18(8 %) , 270.15 (3 %), 243.14 (100 %), 215.13 (9 %), 185.13(13 %) and 145.08 (51%). The fragmentation pattern of the molecular ion of $[Ni_2(L^1)(N_3)_4].H_2O$ is shown in Scheme (3. 10).

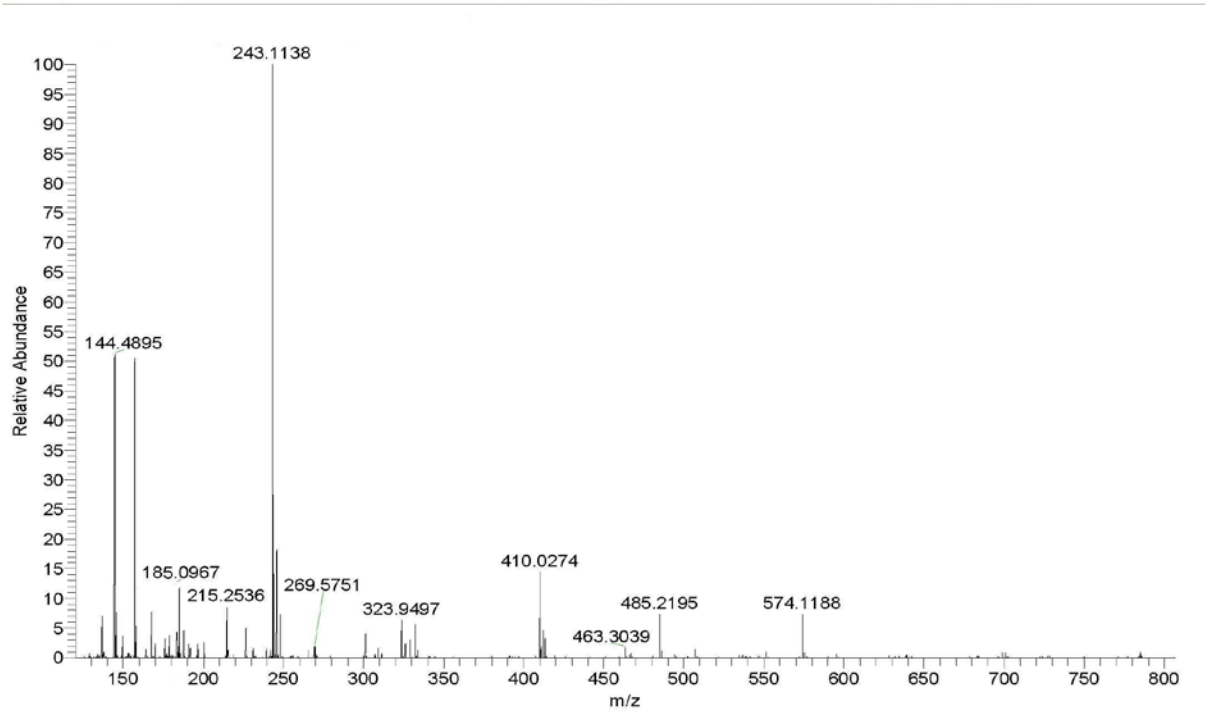

Figure (3.138) ES (+) mass spectrum of $[Ni_2(L^1)(N_3)_4].H_2O$

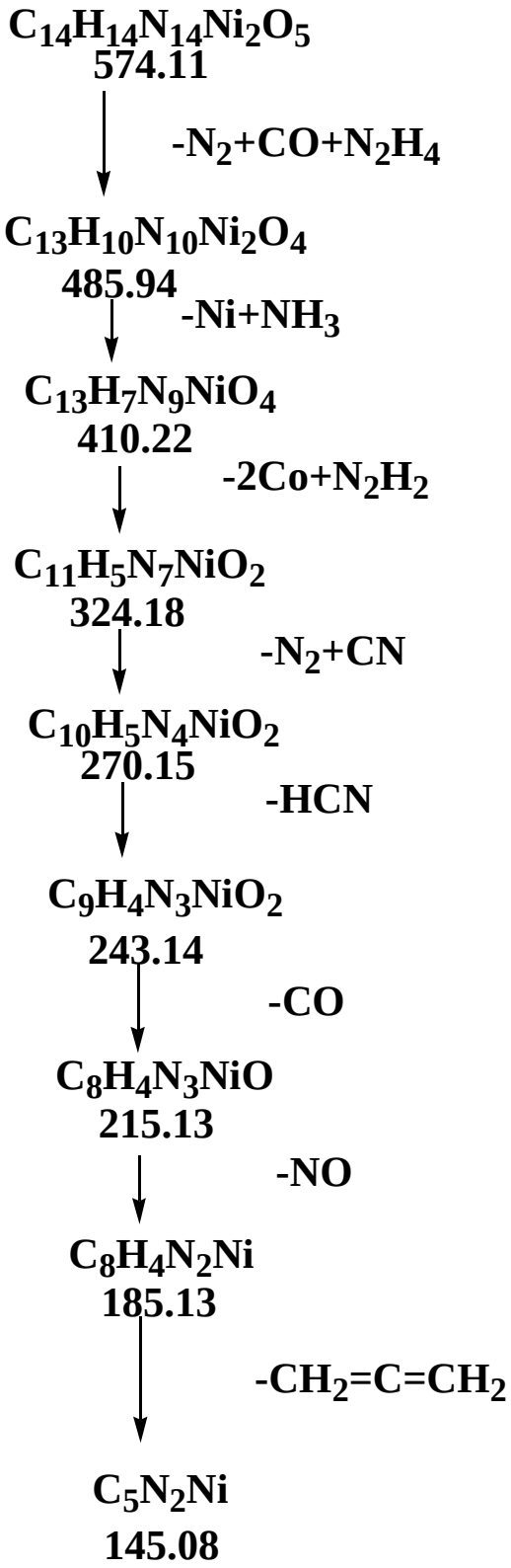

Scheme(3.10) The fragmentation pattern of $[Ni_2(L^1)(N_3)_4].H_2O$

(3.13.3) Mass spectrum of $[Cd_2(L^2)(N_3)_4]$

The high resolution electrospray (+) mass spectrum of $[Cd_2(L^2)(N_3)_4]$ is presented in Figure (3. 139). The exact molecular ion peak for the complex is observed at m/z = 638.43 $(M+1)^+$ (16 %) for $C_{12}H_8Cd_2N_{14}O_4$, requires =637.12. The other peaks detected at m/z =537.39 (73 %), 413.26 (94 %), 301.14 (76 %) and 172.09 (100 %). The fragmentation pattern of the molecular ion of $[Cd_2(L^2)(N_3)_4]$ is shown in Scheme (3. 11).

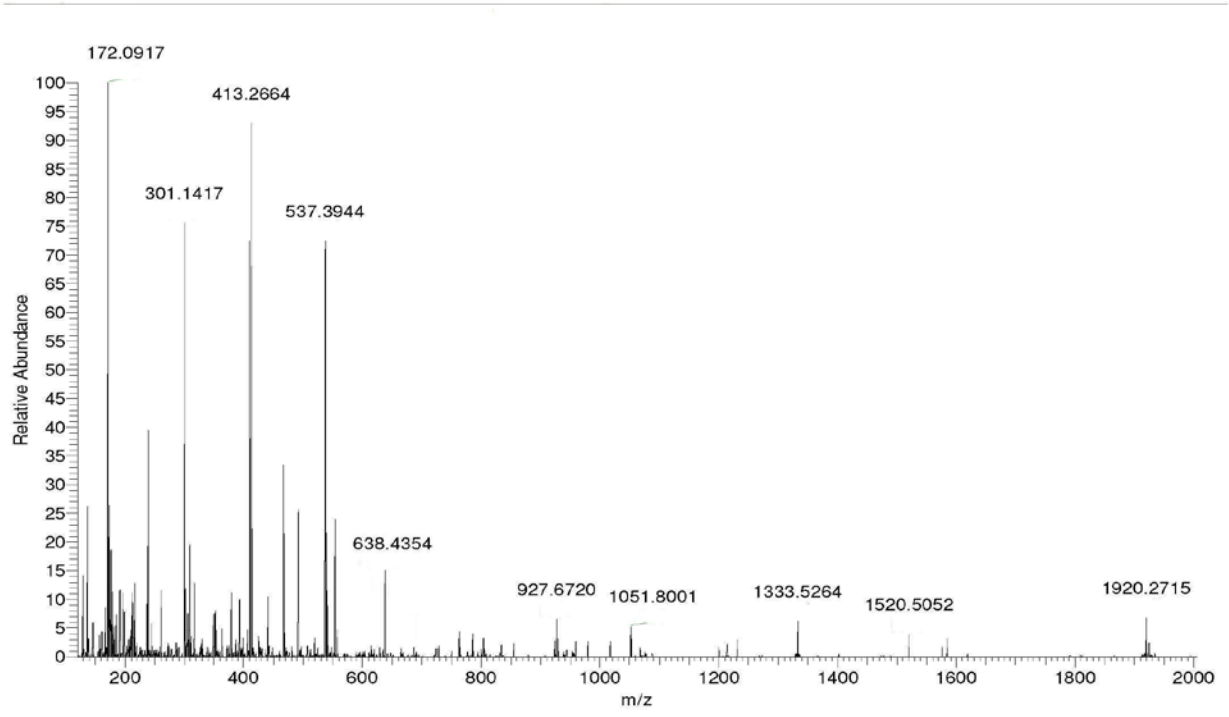

Figure (3.139) ES (+) mass spectrum of $[Cd_2(L^2)(N_3)_4]$

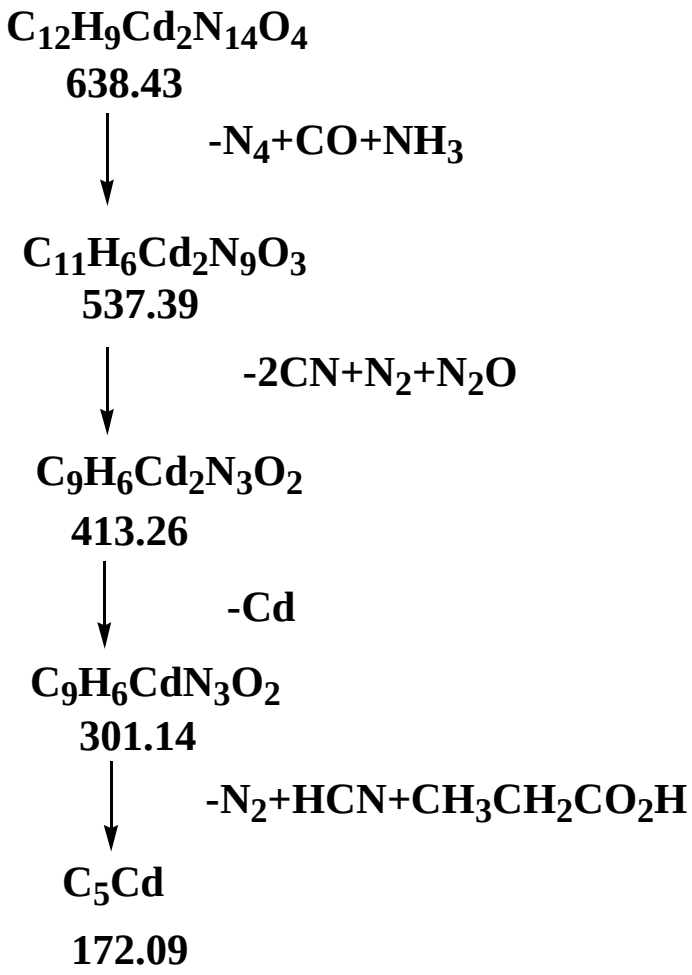

Scheme(3.11) The fragmentation pattern of $[Cd_2(L^2)(N_3)_4]$

(3.13.4) Mass spectrum of $[Co_2(L^3)(N_3)_4].H_2O$

The high resolution electrospray (+) mass spectrum of CoL^3 is presented in Figure (3. 140). The exact molecular ion peak for the complex is observed at m/z = 604.86 $(M)^+$ (7 %) for $C_{16}H_{18}Co_2N_{14}O_5$, requires =604.27. The other peaks detected at m/z =444.73 (5 %), 418.72 (10 %), 352.64(56 %) , 336.65 (100 %),

284.60 (6 %) and 202.56 (4 %). The fragmentation pattern of the molecular ion of $[Co_2(L^3)(N_3)_4].H_2O$ is shown in Scheme (3. 12).

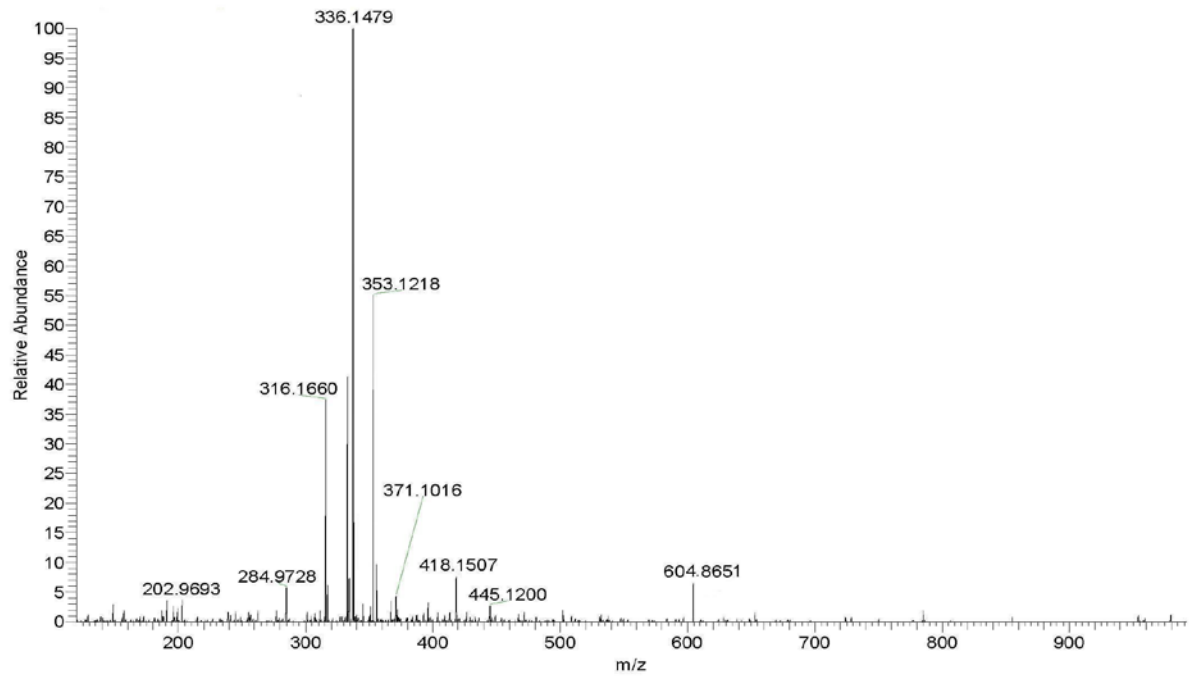

Figure (3.140) ES (+) mass spectrum of $[Co_2(L^3)(N_3)_4].H_2O$

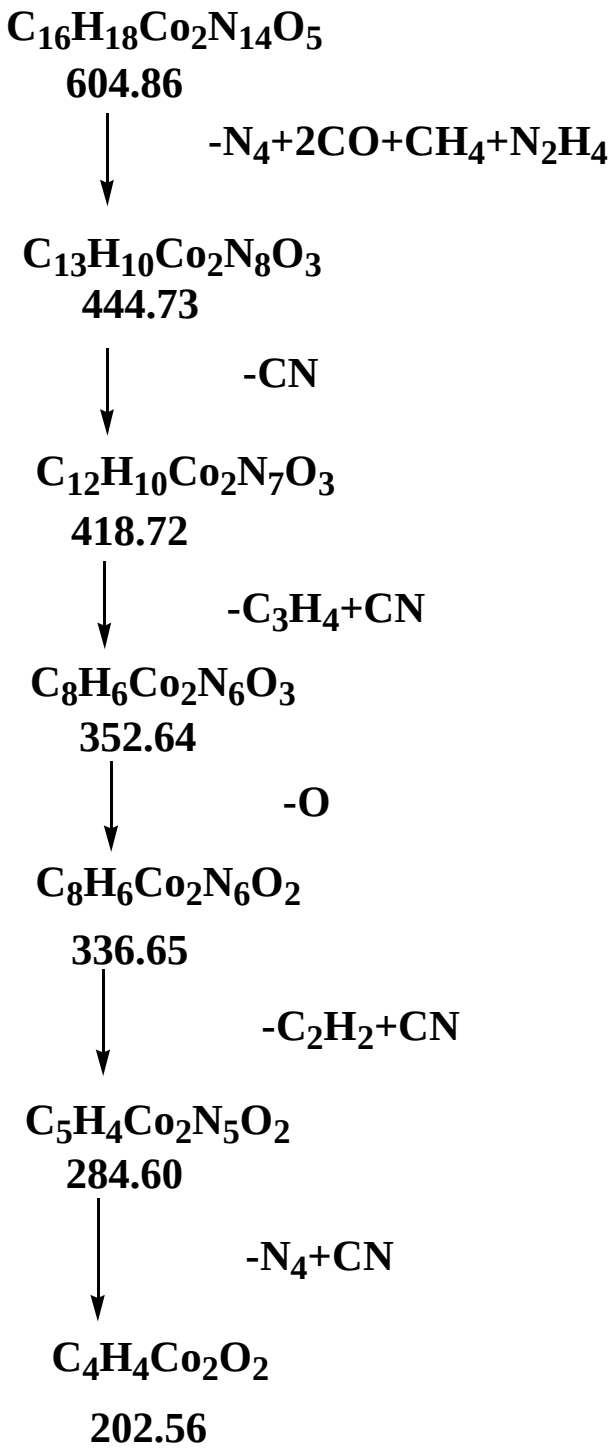

Scheme(3.12) The fragmentation pattern of $[Co_2(L^3)(N_3)_4].H_2O$

(3.13.5) Mass spectrum of $[Zn_2(L^3)(N_3)_4].H_2O$

The high resolution electrospray (+) mass spectrum of ZnL^3 is presented in Figure (3. 141). The exact molecular ion peak for the complex is observed at m/z = 617.53 $(M)^+$ (7 %) for $C_{16}H_{18}Zn_2N_{14}O_5$, requires =617.19. The other peaks detected at m/z =545.42 (3 %), 405.00 (6 %), 332.98 (8 %) , 229.09 (24 %), 187.99 (44 %) and 157.07 (100 %). The fragmentation pattern of the molecular ion of $[Zn_2(L^3)(N_3)_4].H_2O$ is shown in Scheme (3. 13).

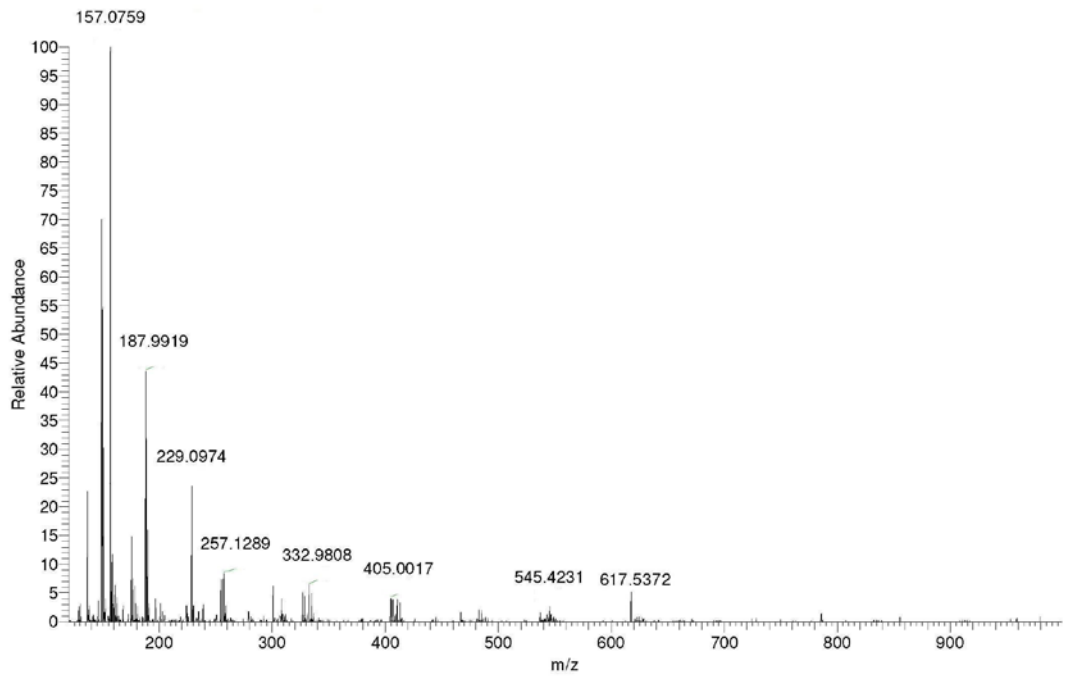

Figure (3.141) ES (+) mass spectrum of $[Zn_2(L^3)(N_3)_4].H_2O$

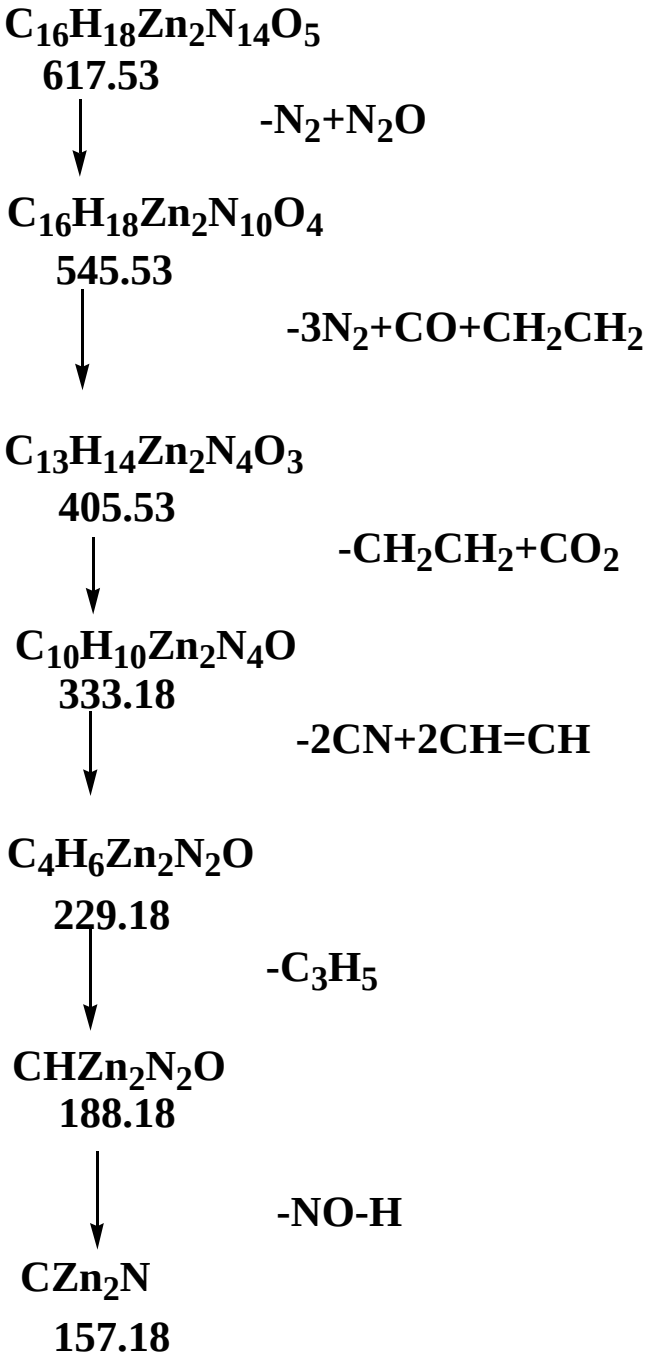

Scheme(3.13) The fragmentation pattern of $[Zn_2(L^3)(N_3)_4].H_2O$

(3.13.6) Mass spectrum of $[Mn_2(L^4)(N_3)_4].H_2O$

The high resolution electrospray (+) mass spectrum of $[Mn_2(L^4)(N_3)_4].H_2O$ is presented in Figure (3. 142). The exact molecular ion peak for the complex is observed at m/z = 624.23 $(M)^+$ (4 %) for $C_{18}H_{22}Mn_2N_{14}O_5$, requires =624.33. The other peaks detected at m/z =594.23 (7 %), 532.20 (13 %), 515.17(3 %) , 445.12 (28 %), 371.09 (40 %), 302.02 (100 %) and 198.92 (16 %). The fragmentation pattern of the molecular ion of $[Mn_2(L^4)(N_3)_4].H_2O$ is shown in Scheme (3. 14).

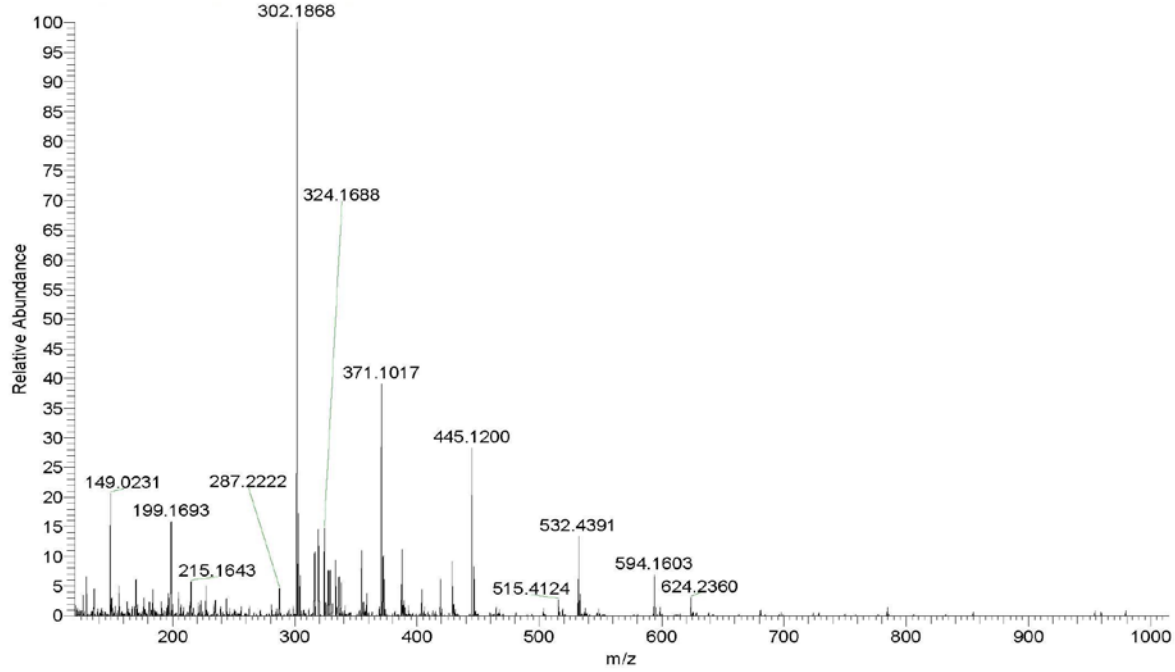

Figure (3.142) ES (+) mass spectrum of $[Mn_2(L^4)(N_3)_4].H_2O$

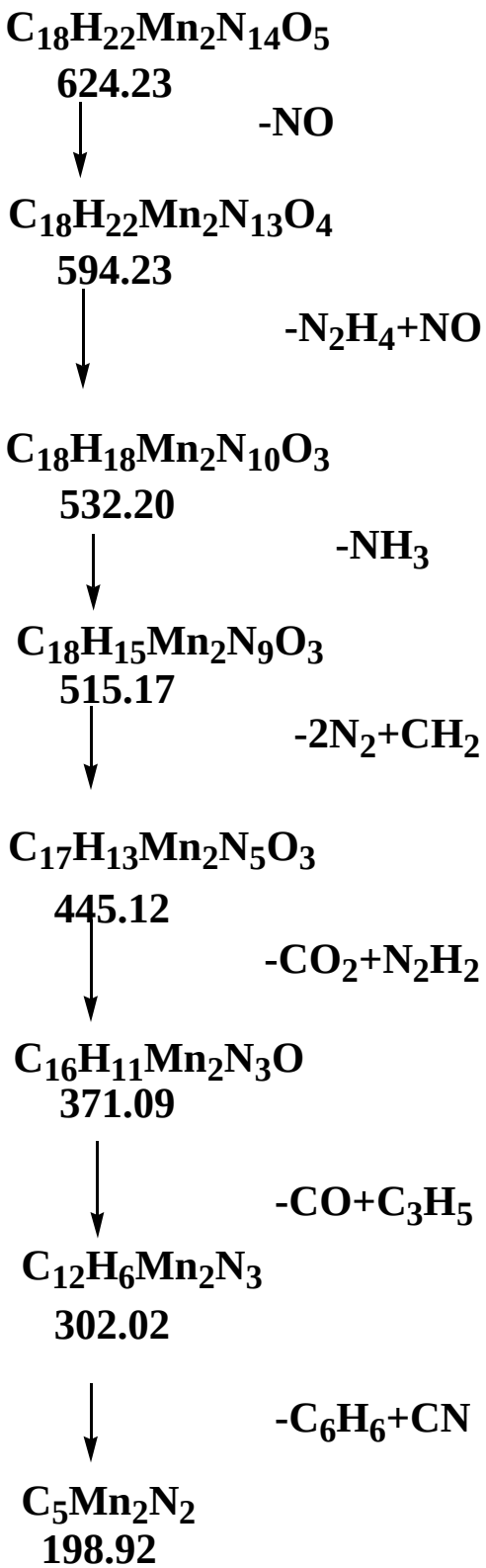

Scheme(3.14) The fragmentation pattern of $[Mn_2(L^4)(N_3)_4].H_2O$

(3.14) Thermal decomposition study

Thermal decomposition data for selected ligands and some of their metal complexes are summarised in Table (3. 26). Analysis curves (TG/DTG, DTA and DSC) of compounds are studied and interpreted as follows.

(3.14.1) Thermal decomposition of $[Mn_2(L^1)(N_3)_4].H_2O$ complex

The TGA thermal analysis curve for $[Mn_2(L^1)(N_3)_4].H_2O$ complex is shown in Figure (3. 143). The sample decomposes at the 74-406 ºC range with temperature of maximum rate of weight loss. The associated endothermic peaks over the temperature 74 ºC and 191 ºC indicate the loss of (H_2O+O_2) corresponds to hydrated water and adsorped oxygen molecule (the adsorption of O_2 is possible since the complex represents MOF molecule) and nitrogen with ammonia molecules (N_2+NH_3), respectively. These correspond well with weight loss data of H_2O+O_2 (obs. = 0.50000 mg; calc. = 0.4841 mg, 8.80%) and N_2+NH_3 (obs. = 0.4676 mg; calc. = 0.4359 mg, 7.92%) molecules. The third step occurs from 339 ºC corresponding to the loss of (N_2H_4) molecules representing weight loss (obs. = 0.3335; calc. = 0.3101 mg, 5.63%). The fourth steps from 369 ºC corresponding to the loss of ($3N_2$) representing weight loss (obs. = 0.8223mg; calc. = 0.8133 mg, 14.78%)[196]. The fifth step occurs over the temperature 393 ºC corresponding to the loss of (CO_2) molecules representing weight loss (obs. = 0.4109 mg and calc. = 0.4259 mg, 7.74%)[197]. The sixth steps at 435 ºC corresponding to the loss (N_3H_5) representing weight loss (obs. = 0.4667 mg; calc. = 0.4554 mg, 8.27%). The final weight (obs.= 1.6665 mg; calc. = 2.5845 mg, 42.72%) represents metallic and carbon residue are the final product. is much less than the expected weight related to ($Mn_2C_{13}H$) indicating the partial sublimation.

The decomposition of the complex in 74-113ºC is indicated by an endothermic process at 85 ºC , while the decomposition in the 191-213 ºC range is indicated by

an endothermic peak at 210 ºC. The DSC analysis Figure (3. 144) show peaks at the 185 ºC, 280 ºC and 393 ºC refer to exothermic decomposition process. The peak at the 91 ºC range refers to endothermic decomposition process. The endothermic may signify the metal-ligand bond breaking and the exothermic may indicate oxidation or combustion of the organic ligand in the atmosphere of air.

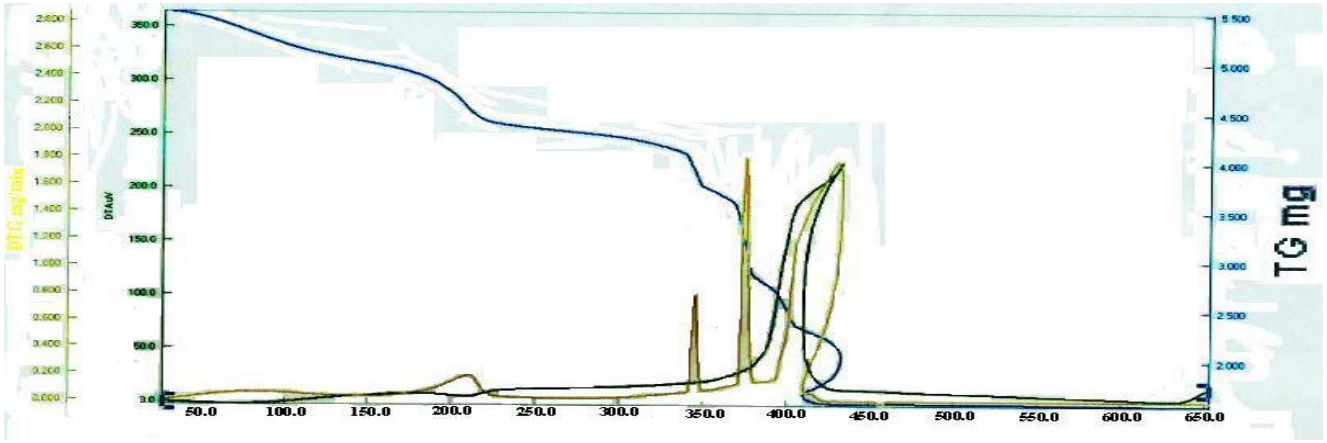

Figure (3.143) TGA, DTG and DTA thermograms of $[Mn_2(L^1)(N_3)_4].H_2O$ complex in nitrogen at the heating of 20°C min^{-1}

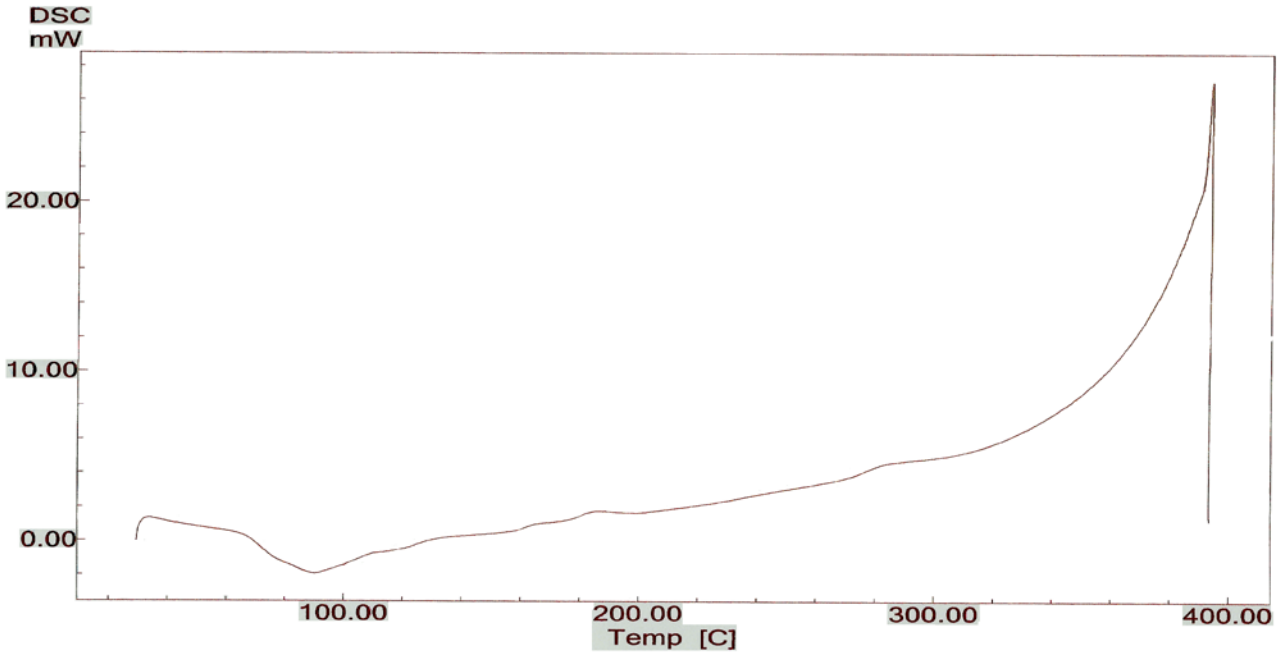

Figure (3.144) DSC thermogram of $[Mn_2(L^1)(N_3)_4].H_2O$ complex in nitrogen at the heating of 20°C min^{-1}

(3.14.2) Thermal decomposition of $[Mn_2(L^2)(N_3)_4].H_2O$ complex

The TGA thermal analysis curve for $[Mn_2(L^2)(N_3)_4].H_2O$ complex is shown in Figure (3. 145). The complex found to be stable up to 50 ºC as shown by the TG curve. It decomposes in two endothermic steps, from 50 to 200 ºC. The complex undergoes rapid decomposition and weight loss initially at rate of (obs. = 0.1502 mg and calc. = 0.1444 mg, 5.55%) (DTG peak centred at 57 and 81 ºC) related to losing (NO) molecule. The second decomposition refer to the loss of ($6N_2 + H_2O + 2CO +$ NO) molecules representing weight loss (obs. = 1.2954 mg and calc. = 1.3097 mg, 50.37%), (DTG 104 and 181ºC). The final weight of the compound observed with 1.0546 mg (calc.=1.1453 mg, 44.05%) related to ($Mn_2 + C_{10}H_8$)[196]. The decomposition of the complex in the 50-59 range ºC is indicated by an endothermic at 56 ºC. The decomposition in the 112-200 ºC range is indicated by endothermic peaks at 113, 178 and 188 ºC. The DSC analysis Figure (3.146) shows peaks at 113 and 245 ºC refer to endothermic process, while the peak at 396 ºC refers to an exothermic decomposition process. The endothermic may signify the metal-ligand bond breaking and the exothermic may indicate the oxidation or combustion of the organic ligand in the atmosphere of air.

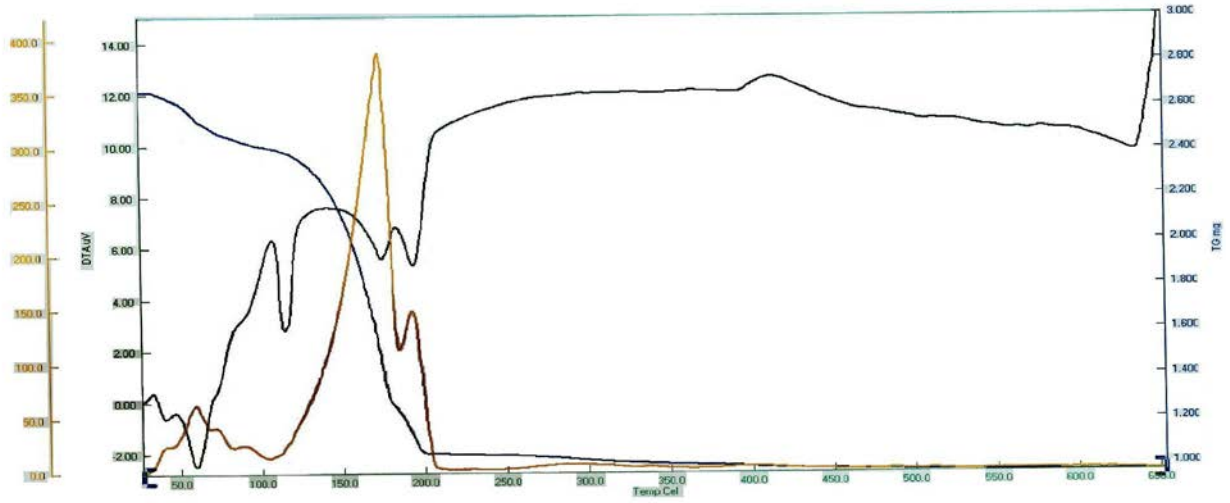

Figure (3.145) TGA, DTG and DTA thermograms of $[Mn_2(L^2)(N_3)_4].H_2O$ complex in nitrogen at the heating of 20 °C min^{-1}

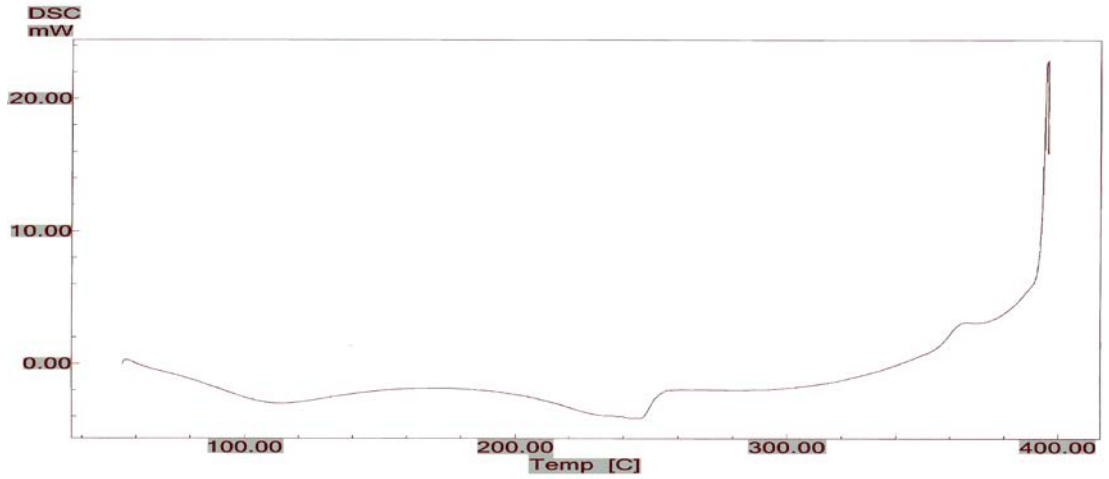

Figure (3-146) DSC thermogram of $[Mn_2(L^2)(N_3)_4].H_2O$ complex in nitrogen at the heating of 20 °C min^{-1}

(3.14.3) Thermal decomposition of $[Fe_2(L^2)(N_3)_4]$complex

The TGA thermal analysis curve for $[Fe_2(L^2)(N_3)_4]$ complex is shown in Figure (3.147). The sample decomposes into two endothermic peaks over the temperature range of 93-765 ºC. The first step occurs from 93 ºC corresponding to the loss of (NO) molecules with mass loss 1.1394 mg, 5.22% (calc. = 1.2474 mg, 5.72%). The second step at 449 ºC is related to the loss of (2CO) fragments and representing weight loss (obs. = 2.1981 mg, 10.08% ; calc. = 2.3290 mg, 10.69%)[197]. The third step occurs around 668 ºC corresponding to the loss of $(3N_2 + N_2O)$ molecules showing weight loss of 5.1805 mg, 23.77% (calc. = 5.3235 mg, 24.43%). The final weight of the residue observed at 13.1669 mg, 60.44% (calc. = 12.8514 mg, 59.48%) related to (dipyridyl + N_3+ Fe_2)[196]. The decomposition of the complex at 93-247 ºC is indicated by endothermic peaks at 117, 166 and 258 ºC. The decomposition at 449.38-548 ºC is indicated by an endothermic peak at 355ºC. The endothermic peak may signify the metal-ligand bond breaking and the exothermic one may indicate the oxidation or combustion of the organic ligand in the atmosphere of air.

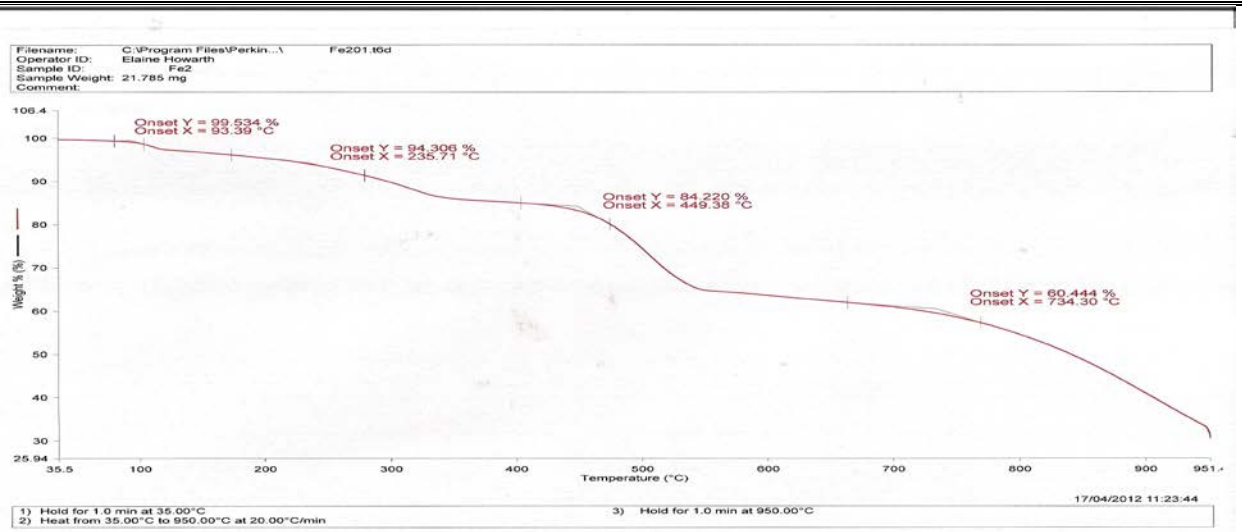

Figure (3. 147) TGA thermogram of $[Fe_2(L^2)(N_3)_4]$ complex in nitrogen at the heating at heating 20 ºC min^{-1}

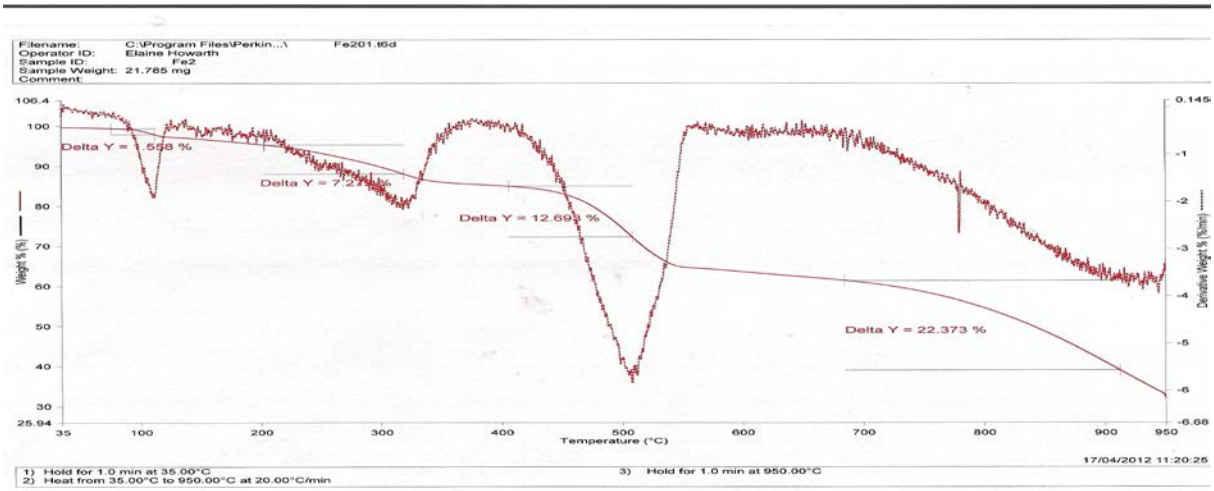

Figure (3. 148) TG-DTG thermograms of $[Fe_2(L^2)(N_3)_4]$ complex in nitrogen at the heating of 20 °C min^{-1}

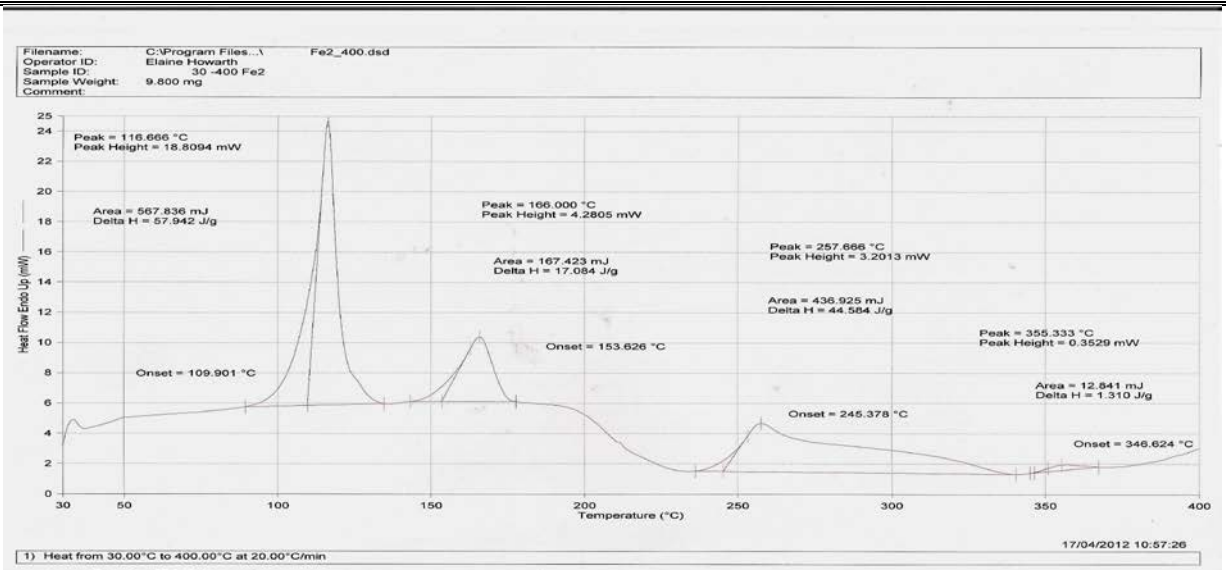

Figure (3. 149) DSC thermogram of $[Fe_2(L^2)(N_3)_4]$ complex in nitrogen at the heating of 20 °C min^{-1}

(3.14.4) Thermal decomposition of $[Cd_2(L^2)(N_3)_4]$complex

The complex $[Cd_2(L^2)(N_3)_4]$ is found to be stable up-to 200 ºC as shown by the TG curve, Figure (3.150). The complex undergoes a rapid decomposition and weight loss initially at first step (obs. = 0.0844 mg, 2.63%; calc. = 0.0857 mg, 2.67%) due to losing of (NH_3) molecule. The second step with weight loss of 1.3577 mg, 42.31% (calc.= 1.4108 mg, 43.97%) may related to the detached of ($6N_2$+4CO) molecules. This was represented by DTG peaks centred at 442 and 449 ºC. The final weight of the residue observed at 1.7691 mg, 57.30% (calc. = 1.9886 mg, 61.97%) is related to (Cd_2N+dipyridyl)[196]. The DSC analysis Figure(3-152), shows endothermic peaks at 119, 167, 196 and 213 ºC. The peak at 371 ºC refers to an exothermic decomposition process. The endothermic may signify the metal-ligand bond breaking and the exothermic may indicate the oxidation or combustion of the organic ligand in the atmosphere of air.

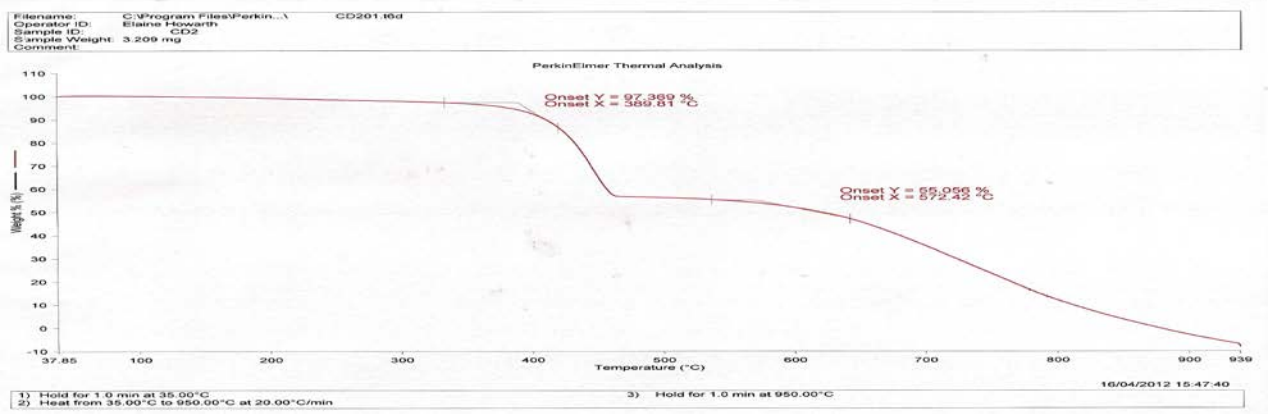

Figure (3. 150) TGA thermogram of $[Cd_2(L^2)(N_3)_4]$ complex in nitrogen at the heating of 20 °C min^{-1}

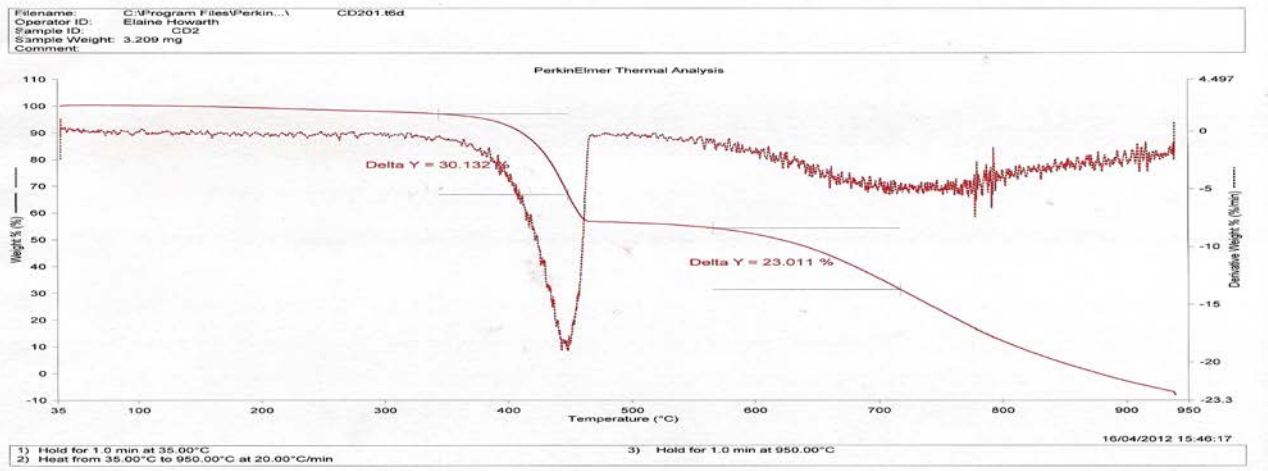

Figure (3. 151) TG-DTG thermograms of $[Cd_2(L^2)(N_3)_4]$ complex in nitrogen at the heating of 20 °C min^{-1}

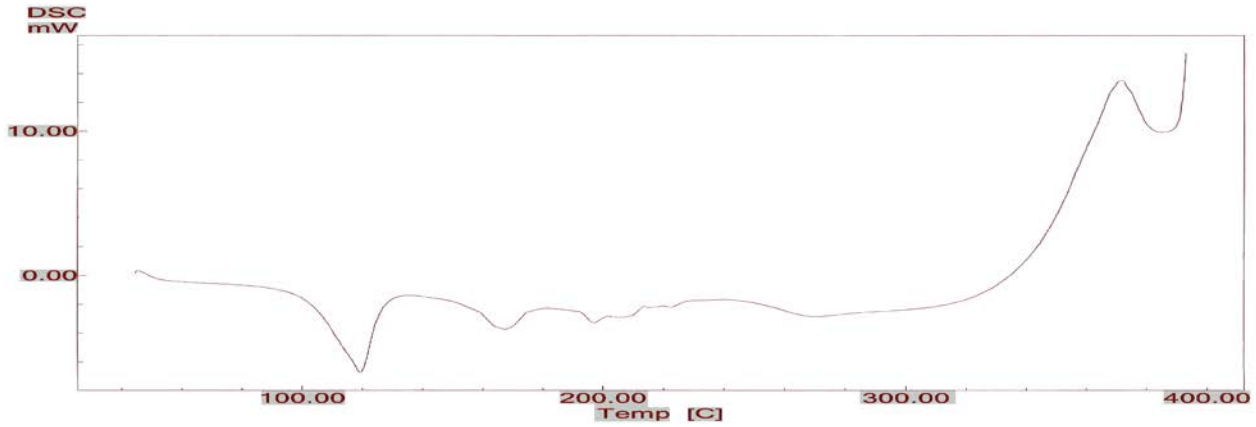

Figure (3. 152) DSC thermogram of $[Cd_2(L^2)(N_3)_4]$ complex in nitrogen at the heating of 20 °C min^{-1}

(3.14.5) Thermal decomposition of $[Mn_2(L^3)(N_3)_4].2H_2O$ complex

The TGA thermal analysis curve for $[Mn_2(L^3)(N_3)_4].2H_2O$ complex is shown in Figure(3.153). The sample decomposes in three endothermic steps over the range of temperature 51-450 ºC. The first step occurs from 161 ºC corresponding to the loss of ($2H_2O$ + NO) molecules with weight loss of 0.8104 mg (calc. = 0.8690 mg, 10.75%). The second step from 240 ºC represents the loss of ($2N_2$) molecules with weight loss of 0.8332 mg (calc. = 0.7372 mg, 9.12%). The third step occurs from 343 ºC corresponding to the loss of (CO) molecules with the loss of 0.3753 mg (calc. = 0.3685 mg, 4.55%)[196]. The fourth step from 375ºC relates to the loss of ($(CH_2CH_2)_2$+$2N_2O$ +HCN) with mass loss of 2.2334 mg (calc.= 2.2522 mg, 27.86%). The weight of the compound observed at 3.2085 mg is much less than that calculated weight at 3.8541 mg, 22.44% representing the (Mn_2N_2+dipyridyl-H) residue[197]. This could be due to partial sublimation process upon thermal analysis. The decomposition of the complex in the range of 51-129 and 200-243 ºC is indicated by endothermic peaks at 88 and 215 ºC, respectively. The decomposition in the range of 400-450 ºC is indicated by an exothermic peak at 431 ºC. The DSC analysis Figure (3.154), shows peaks at 117 and 236 ºC refer to an endothermic reaction. Peaks at 347 and 392 ºC refer to the exothermic decomposition process. The endothermic may signify the metal-ligand bond breaking and the exothermic may indicate the oxidation or combustion of the organic ligand in the atmosphere of air.

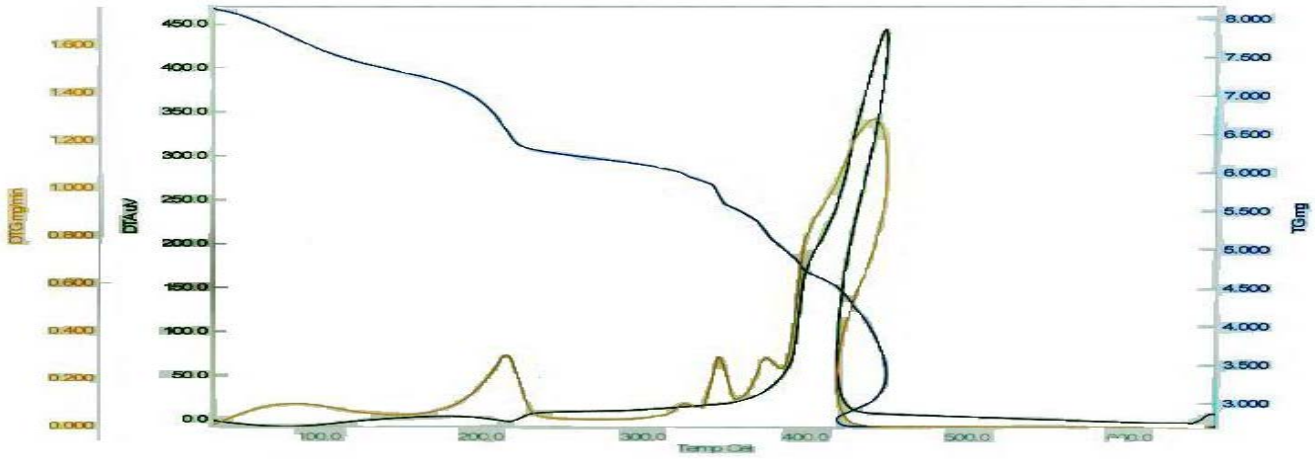

Figure (3.153) TGA,DTG and DTA thermograms of $[Mn_2(L^3)(N_3)_4].2H_2O$ complex in nitrogen at the heating of 20 °C min^{-1}

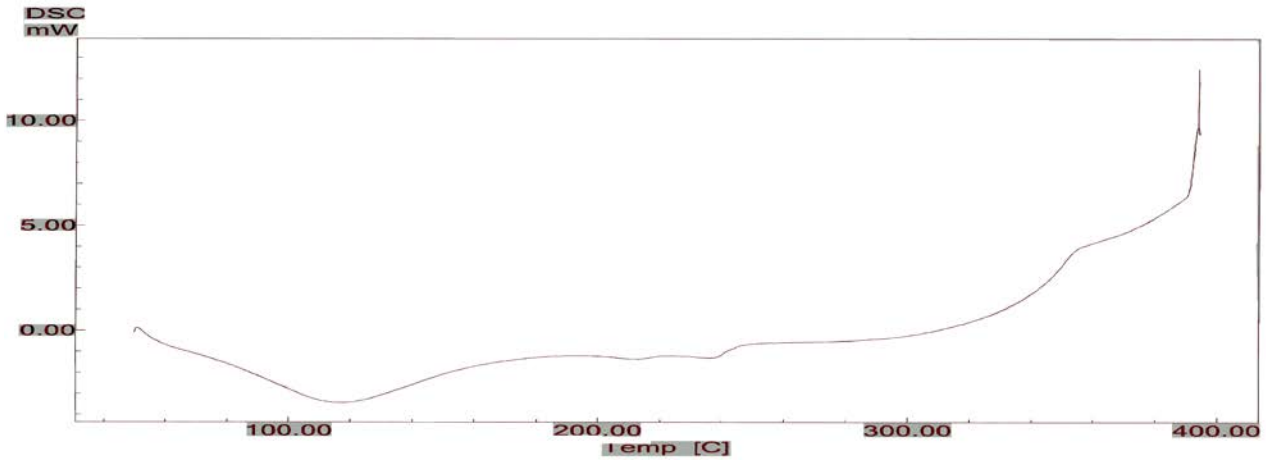

Figure (3.154) DSC of $[Mn_2(L^3)(N_3)_4].2H_2O$ complex in nitrogen at the heating of 20 °C min^{-1}

(3.14.6) Thermal decomposition of $[Fe_2(L^3)(N_3)_4].H_2O$ complex

The complex $[Fe_2(L^3)(N_3)_4].H_2O$ is found to be stable upto 72 ºC as shown by the TG curve, Figure (3.155). The sample decomposes in three endothermic peaks over the temperature range of 72-400 ºC. The decomposition and weight loss initially at rate of (obs. = 0.1430 mg; calc. = 0.1498 mg, 3.01%), (DTG peak centred at 75 and 107 ºC) is due to the losing of (H_2O) molecule. The second step occurs from 139 ºC corresponding to the loss of (CO) with weight loss of 0.2200 mg (calc. = 0.2330 mg, 4.68%). The third step shows weight loss of 1.6400 mg (calc. = 1.6562 mg, 28.60%),

(DTG 261 and 309 ºC) attributed to the losing of ($2N_2$+$3N_2O$+HCN) residue. The final weight of the compound shows weight of 2.6800 mg (calc. = 2.7971 mg, 53.96%) related to the residue of (Fe_2N+dipyridyl-H) + $(CH_2CH_2)_2$][197]. The decomposition of the complex in the range of 72-111ºC is indicated by endothermic peaks at 71 and 111 ºC. Other decomposition endothermic peaks are detected at 139 and 147 ºC. The decomposition in the range of 259-400 ºC is indicated by endothermic and exothermic peaks at 282; 339 and 400 ºC, respectively. The endothermic may signify the metal-ligand bond breaking. The DSC analysis Figure (3.156) shows peaks at 102, 112, and 305 ºC refer to endothermic peaks. Peak detected at 392 ºC refers to an exothermic decomposition process. The endothermic may signify the metal-ligand bond breaking and the exothermic may indicate the oxidation or combustion of the organic ligand in the atmosphere of air.

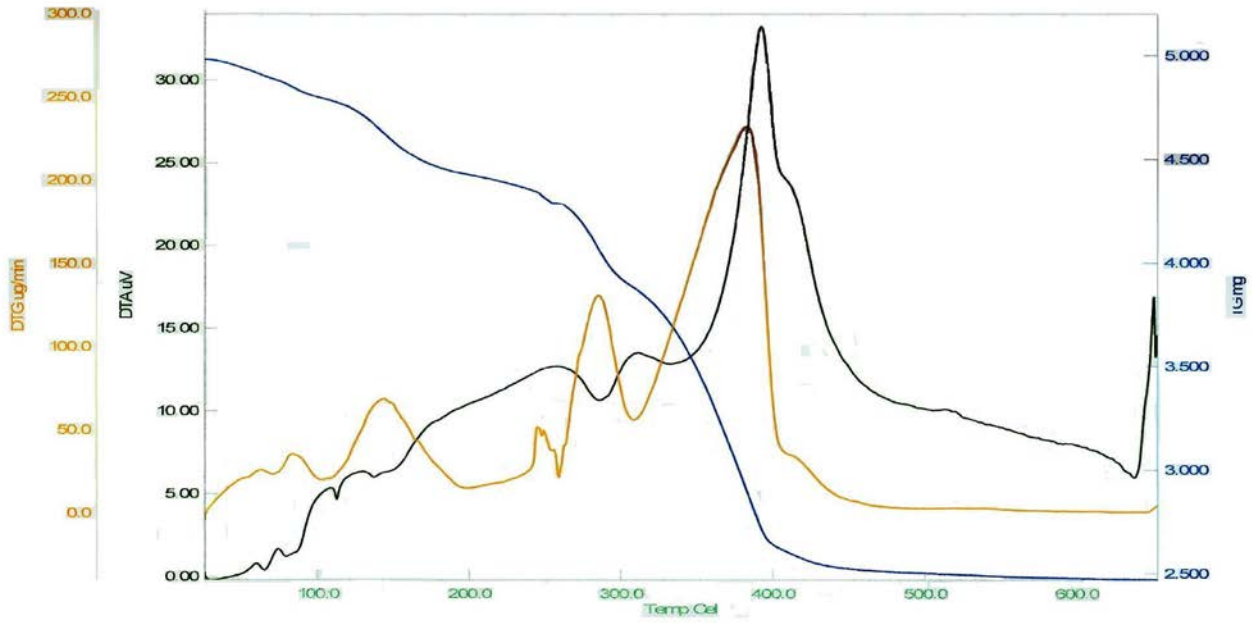

Figure (3. 155) TGA, DTG and DTA thermograms of $[Fe_2(L^3)(N_3)_4].H_2O$ complex in nitrogen at the heating of 20 °C min^{-1}

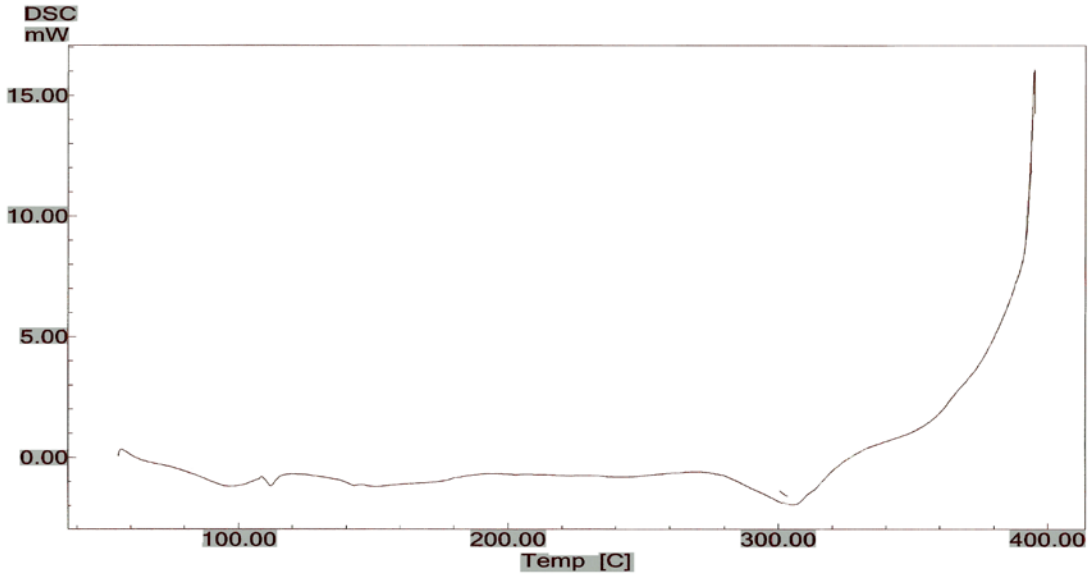

Figure (3. 156) DSC thermogram of $[Fe_2(L^3)(N_3)_4].H_2O$ complex in nitrogen at the heating of 20 °C min^{-1}

(3.14.7) Thermal decomposition of $[Zn_2(L^3)(N_3)_4].H_2O$ complex

The TGA thermal analysis curve for $[Zn_2(L^3)(N_3)_4].H_2O$ complex is shown in Figure (3. 157). The sample decomposes in two endothermic decomposition processes over the temperature range 145-593ºC. The first step occurs from 220 ºC with weight loss of 0.1683 mg, 2.69% (calc. = 0.1725 mg, 2.75%) corresponding to the loss of (NH_3). The second and third steps from 382-593 ºC corresponding to the loss of (3CO) with weight loss of 0.8938 mg, 14.28% (calc. = 0.8516 mg, 13.61%) and to the losing of ($6N_2$+CH_2CH_2+HCN) fragments with weight loss of 2.1936 mg, 35.07% (calc. = 2.2615 mg, 36.15%), respectively. The final weight of the compound observed at 2.8317 mg, 47.99% (calc = 2.7855 mg, 44.39%) related to the (Zn_2O+$C_{10}H_8$) residue[196, 197].

The decomposition of the complex in the 145-225˚C range is indicated by endothermic processes at 103 and 206 ºC. The decomposition in the 382-472 ºC range is indicated by an endothermic decompositon at 268˚C. The endothermic process may signify the metal-ligand bond breaking.

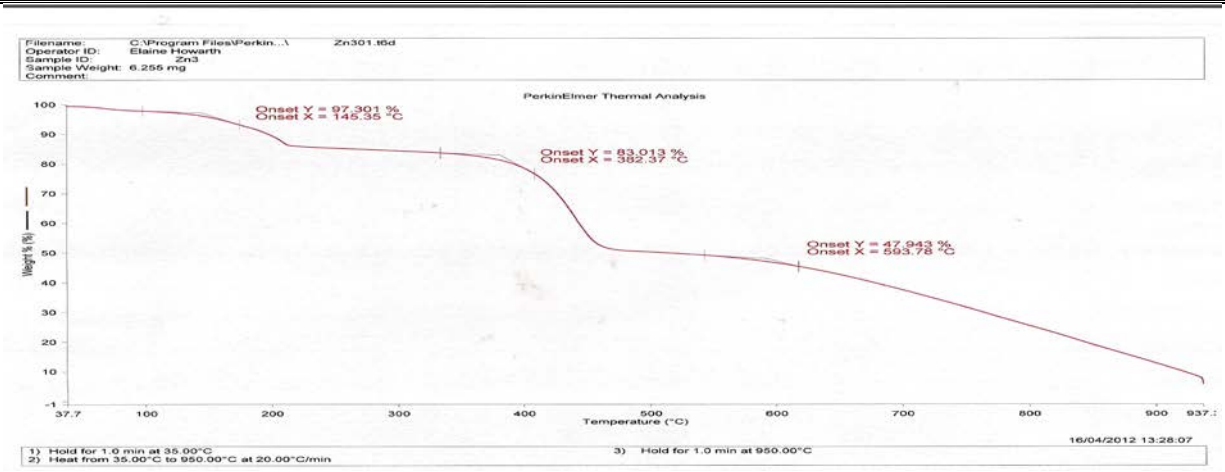

Figure (3. 157) TGA thermogram of $[Zn_2(L^3)(N_3)_4].H_2O$ complex in nitrogen at the heating of 20 °C min^{-1}

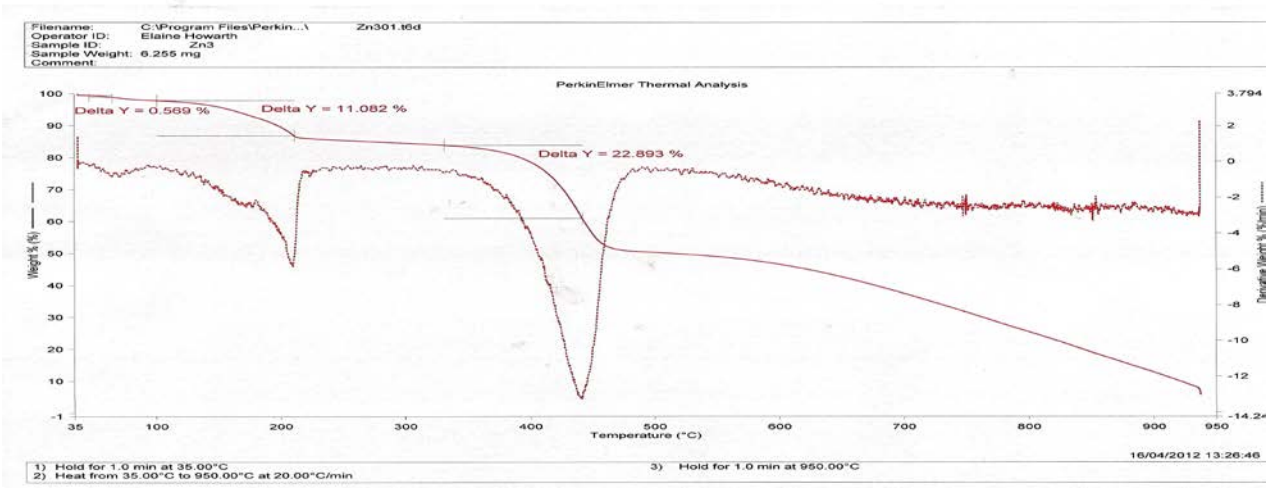

Figure (3. 158) TGA-DTG thermograms of $[Zn_2(L^3)(N_3)_4].H_2O$ complex in nitrogen at the heating of 20 °C min^{-1}

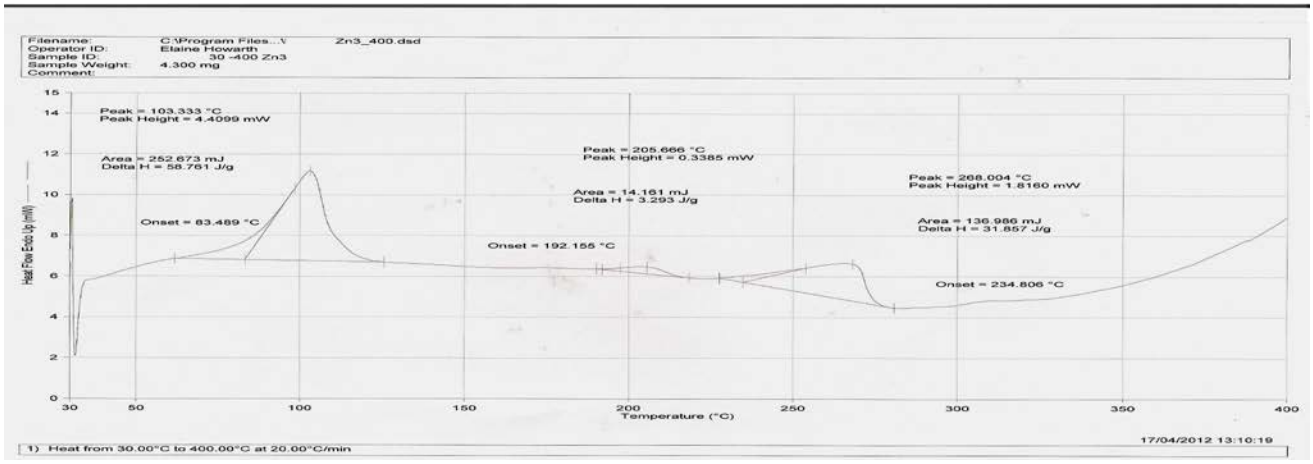

Figure (3. 159) DSC thermogram of $[Zn_2(L^3)(N_3)_4].H_2O$ complex in nitrogen at the heating of 20 °C min^{-1}

(3.14.8) Thermal decomposition of L^4 complex

The TGA thermal analysis curve for L^4 ligand is shown in Figure (3. 160). The sample decomposes into two endothermic decomposition processes with peaks detected over in the 186-618 ºC range. The first step occurs at 186 ˚C with weight loss of 3.6196 mg, 80.94% (calc. = 3.6545 mg, 81.71%), is related to the loss of (dipyridyl+4CO) fragments. The second step from 461ºC corresponding to the loss of ($2CH_4$) molecules, showed a weight loss of 0.4405 mg, 9.85% (calc. = 0.4374 mg, 9.78%)[196]. The decomposition of the complex in the 1856-275 mg is indicated by endothermic peaks at 262 and 276 ˚C. The endothermic decomposition process may signify the metal-ligand bond breaking. The differences in the calculated in observed of the residue weight may be related to the sublimation upon thermal decomposition.

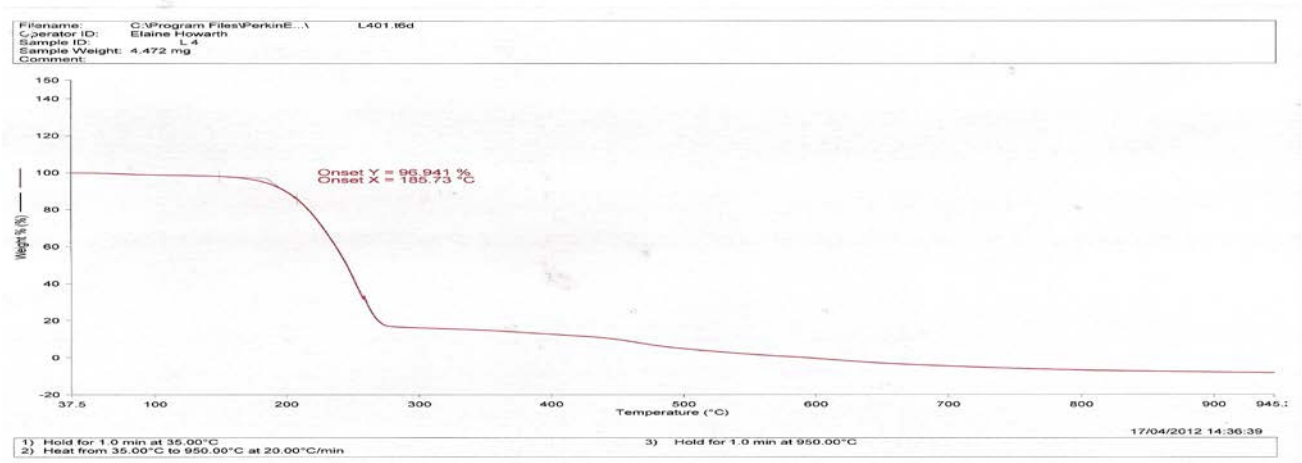

Figure (3. 160) TGA thermogram of L^4 ligand in nitrogen at the heating of 20 °C min^{-1}

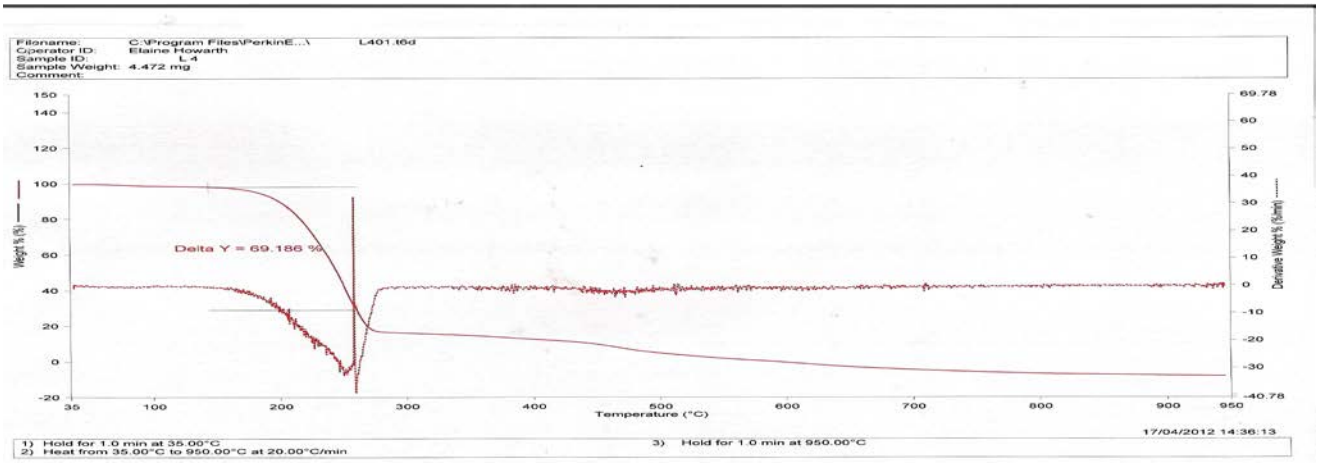

Figure (3. 161) TG-DTG thermograms of L^4 ligand in nitrogen at the heating of 20 °C min^{-1}

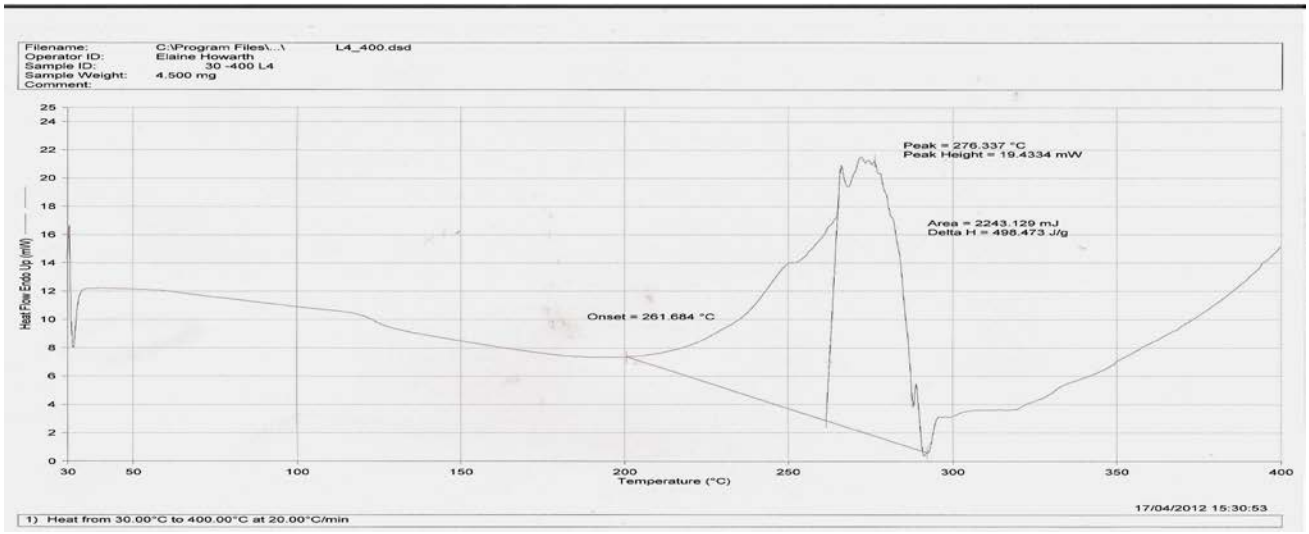

Figure (3. 162) DSC thermogram of L^4 ligand in nitrogen at the heating of 20 °C min^{-1}

(3.14.9) Thermal decomposition of $[Mn_2(L^4)(N_3)_4].H_2O$ complex

The TGA thermal analysis curve for $[Mn_2(L^4)(N_3)_4].H_2O$ complex is shown in Figure(3. 163). The sample decomposes in four endothermic peaks over the temperature range of 55-484 ºC. The first decomposition shows weight loss of 0.6365 mg (calc. = 0.5763 mg, 7.37%), which is due to losing of (H_2O+CO) molecules. The second step with weight loss of 0.1820 mg (calc. = 0.2132 mg, 2.72%) shows a peak in the DTG in the 150 ºC range. The third and forth steps in the 278-484 ºC range, show weight loss of 1.3648 mg (calc. = 1.4031 mg, 17.94%) and at 2.8459 mg (calc.= 2.8431 mg, 33.80%), corresponding to the loss of ($2N_2$+2CO), and (dipyridyl+(N_2O) +HCN) molecules, respectively. The final weight of the residue observed at 2.6360 mg (calc at 2.7801 mg, 35.55%), is related to the residue of $(Mn_2N_4(CH_2CH_2)_2)$[197]. The decomposition of the complex in the 55-108 ºC range is indicated by an endothermic decomposition peak at 91 ºC, while the decomposition about 444-484 ºC is showed by an exothermic peak at 469 ºC. The endothermic decomposition process may signify the metal-ligand bond breaking and the exothermic decomposition process may indicate the oxidation or combustion of the organic ligand in the atmosphere of air. The DSC analysis Figure (3. 164), displays peaks at

383 and 389 ºC indicating exothermic decomposition process. The exothermic may refer to the oxidation or combustion process of the organic ligand in the atmosphere of air.

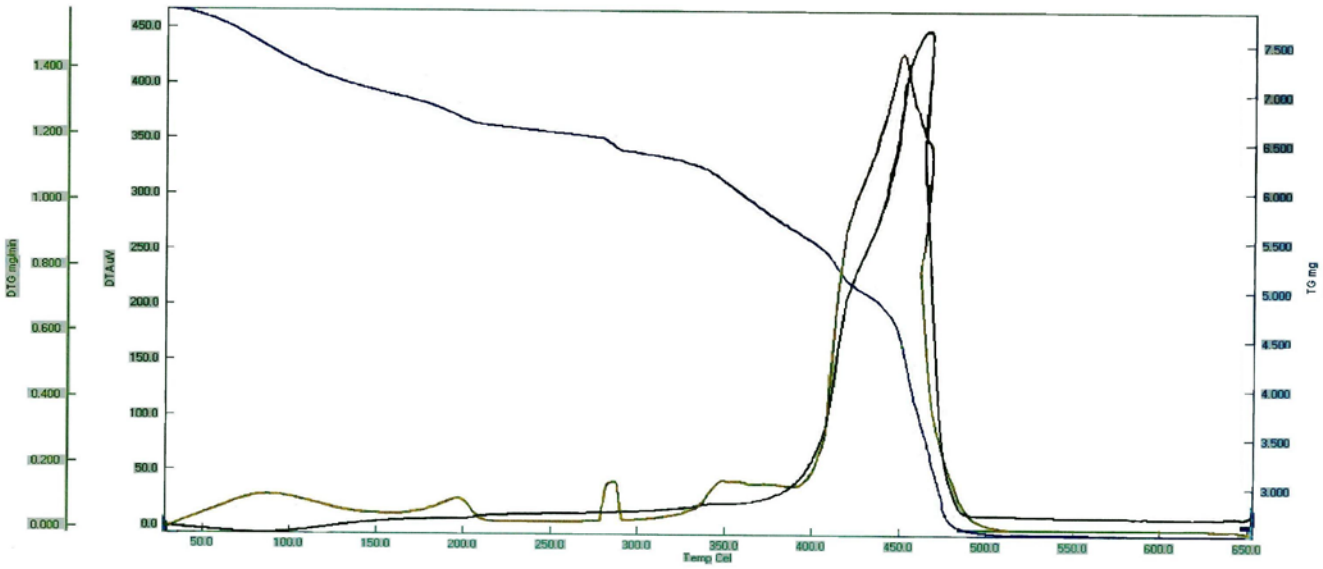

Figure (3. 163) TGA,DTG and DTA thermograms of $[Mn_2(L^4)(N_3)_4].H_2O$ complex in nitrogen at the heating of 20 °C min^{-1}

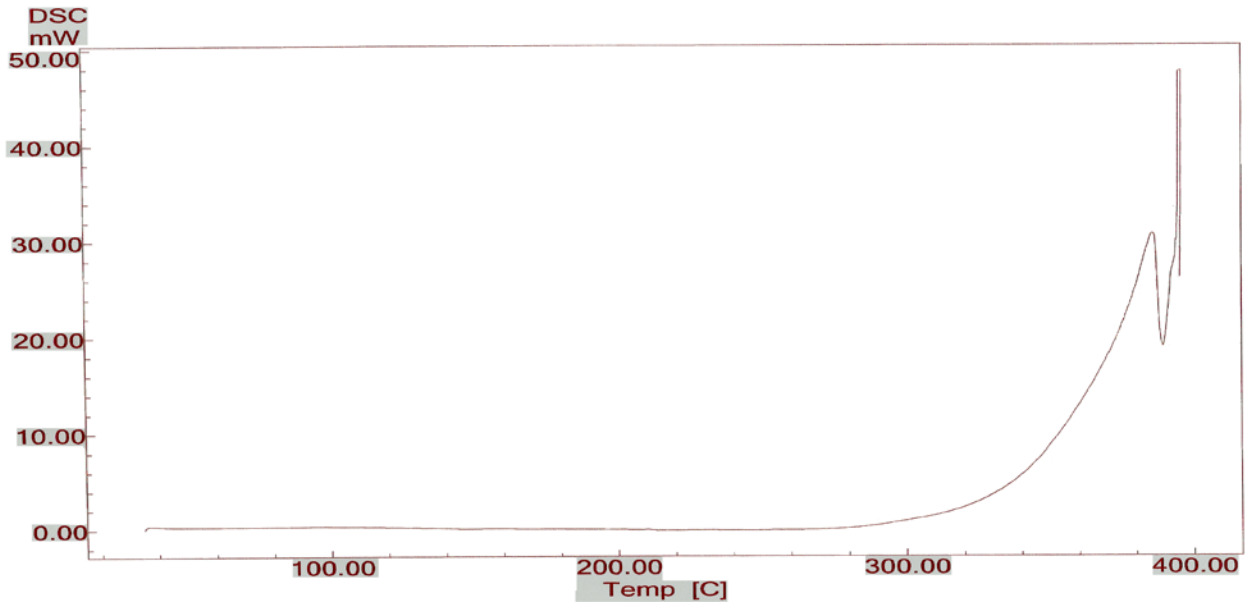

Figure (3-164) DSC thermogram of $[Mn_2(L^4)(N_3)_4].H_2O$ complex in nitrogen at the heating of 20 °C min^{-1}

(3.14.10) Thermal decomposition of $[Fe_2(L^4)(N_3)_4]$ complex

The TGA thermal analysis curve for $[Fe_2(L^4)(N_3)_4]$ complex is shown in Figure (3-165). The sample decomposes into two endothermic peaks over the temperature range of 131.95- 798.66 ºC. The first step occurs in the 131.95-207 ºC range, is corresponding to the loss of (dipyridyl+$6N_2$+$(CH_2CH_2)_2$+$2(CO_2)$) molecules and indicated by the weight loss of 1.1077 mg, 78.55% (calc. = 1.0855 mg, 76.98%). The other weight loss of 0.3251 mg, 23.06% (calc. = 0.3226 mg, 23.30%), is detected by the DTG at 329 ºC) due to (Fe_2 + (CH_2CH_2) . The decomposition of the complex in the 132-207 ºC range is indicated by the endothermic and exothermic peaks at 115 and 189 ºC, respectively[197]. The endothermic decomposition may signify the metal-ligand bond breaking and the exothermic may indicated the oxidation or combustion of the organic ligand in the atmosphere of air.

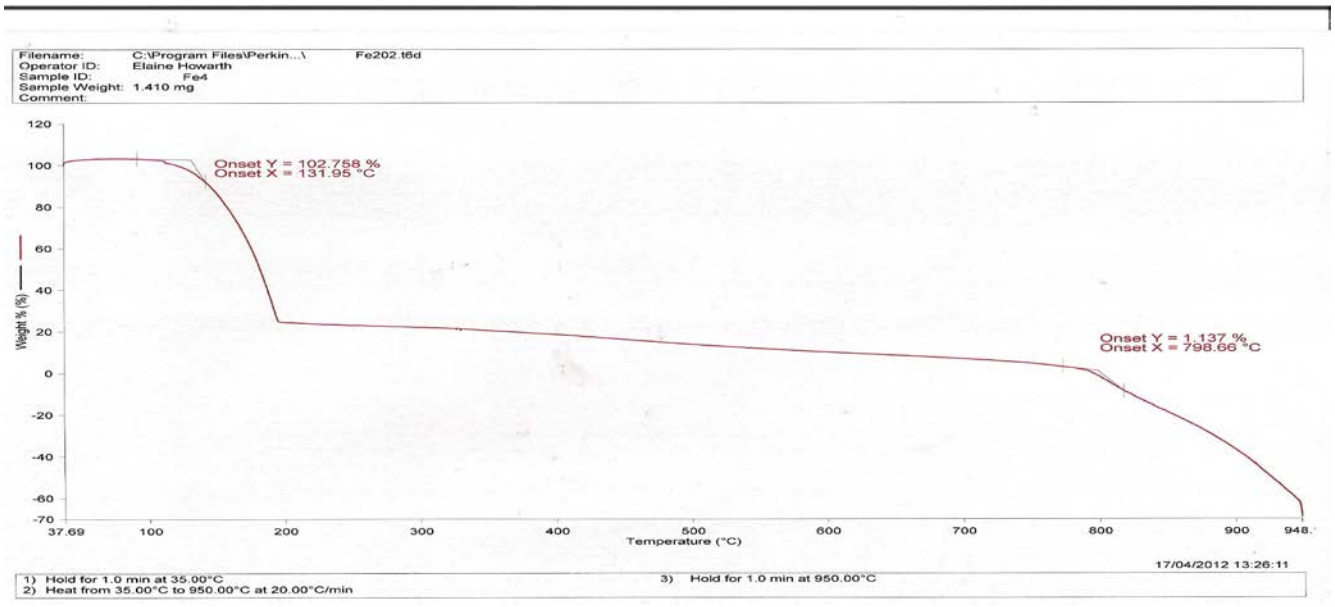

Figure (3. 165) TGA thermogram of $[Fe_2(L^4)(N_3)_4]$ complex in nitrogen at the heating of 20 °C min^{-1}

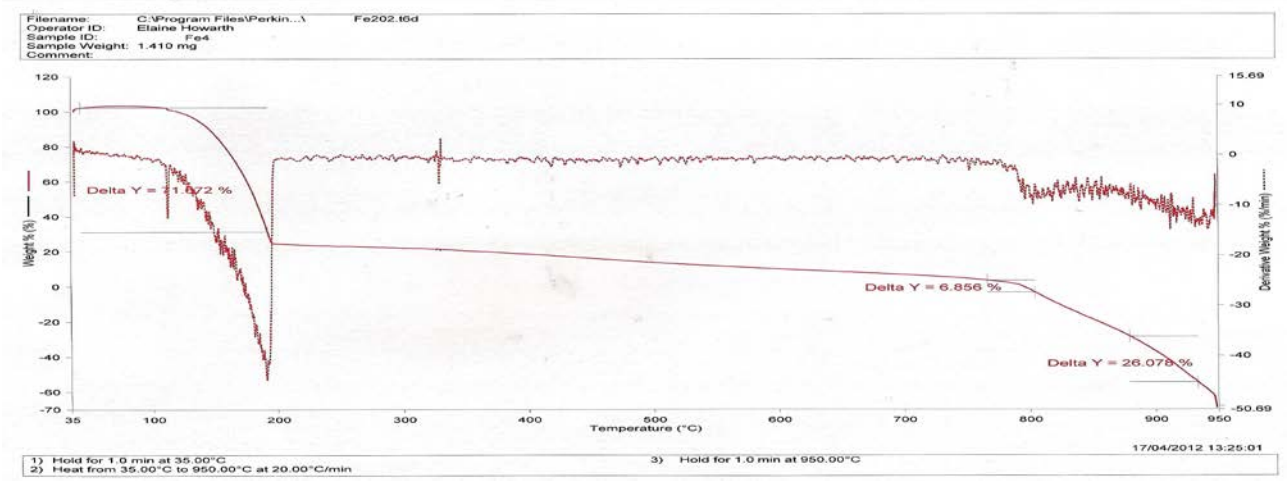

Figure (3. 166) TG-DTG thermograms of $[Fe_2(L^4)(N_3)_4]$ complex in nitrogen at the heating of 20 °C min^{-1}

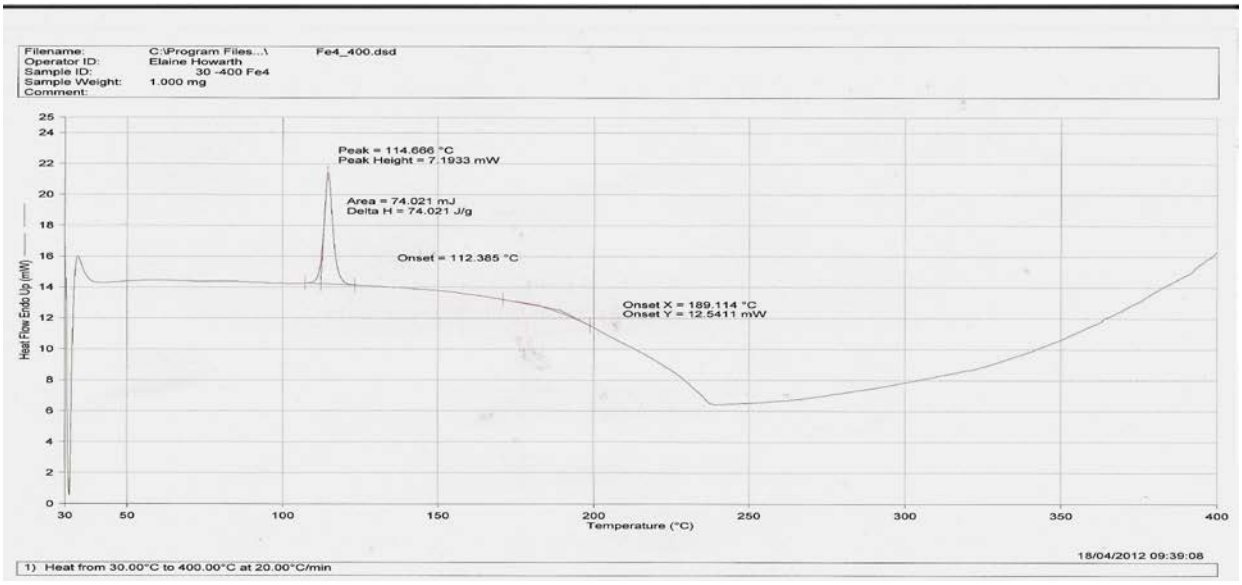

Figure (3. 167) DSC thermogram of $[Fe_2(L^4)(N_3)_4]$ complex in nitrogen at the heating of 20 °C min^{-1}

(3.14.11) Thermal decomposition of $[Zn_2(L^4)(N_3)_4]$ complex

The TGA thermal analysis curve for $[Zn_2(L^4)(N_3)_4]$ complex is shown in Figure(3. 168). The sample decomposes into three endothermic peaks over the temperature range of 103.95- 803.66 ºC. The first decomposition shows weight loss of 0.0752 mg, 2.29% (calc. = 0.0887 mg, 2.71%). The DTG peak centered at 248 ºC can be attributed to the losing of (NH_3) molecule. The second step shows weight loss

of 0.6259 mg, 19.14% (calc.=0.5841 mg, 17.86%), the DTG detected in the 428 ºC, is due to the losing of the (4CO) fragment. The third step with the weight loss of 1.4293 mg, 43.70% (calc. = 1.4862 mg, 45.45%) is assigned to (dipyridyl+4N_2+NH_3). The final weight of the residue observed at 1.1396 mg, 34.85% (calc. = 1.1256 mg, 34.25%) is related to (Zn_2N_2+C_4H_6) residue[(197)]. The decomposition of the complex in the 201-275 ºC range is indicated by endothermic peaks at 163 and 277 ºC. The endothermic decomposition peaks may signify the metal-ligand bond breaking.

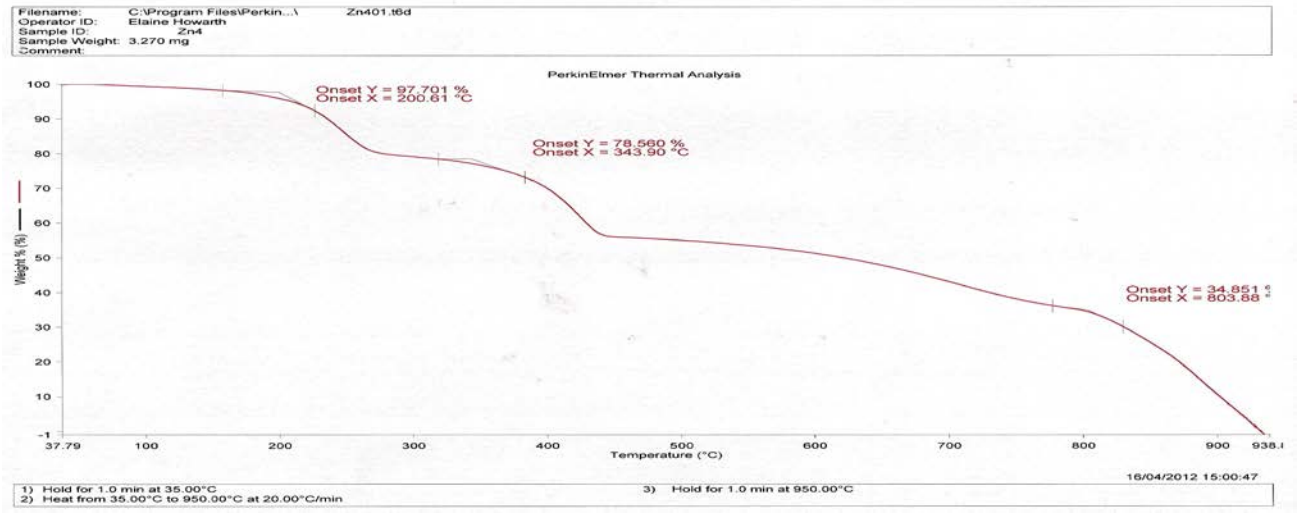

Figure (3. 168) TGA thermogram of $[Zn_2(L^4)(N_3)_4]$ complex in nitrogen at the heating of 20 °C min^{-1}

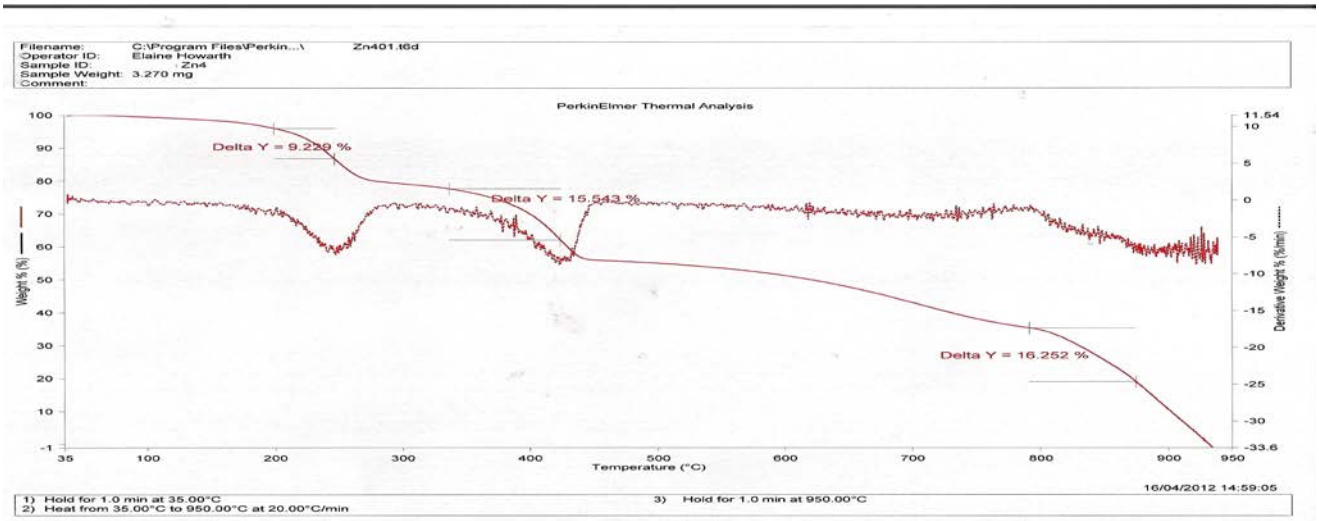

Figure (3-169) TG-DTG thermograms of $[Zn_2(L^4)(N_3)_4]$ complex in nitrogen at the heating of 20 °C min^{-1}

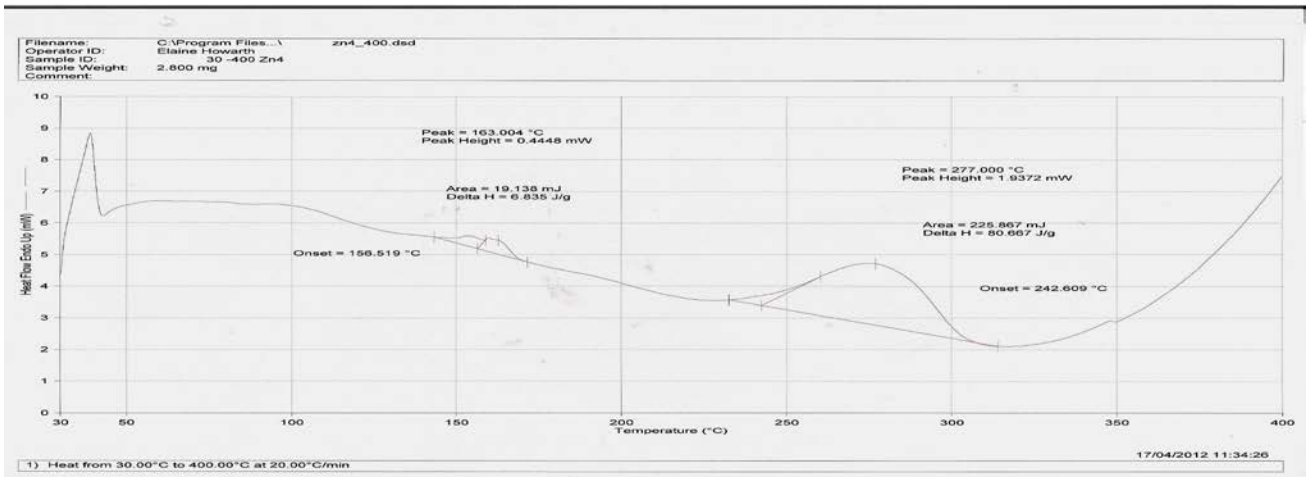

Figure (3. 170) DSC thermogram of $[Zn_2(L^4)(N_3)_4]$ complex in nitrogen at the heating of 20 °C min^{-1}

(3.14.12) Thermal decomposition of $[Cd_2(L^4)(N_3)_4]$ complex

The TGA thermal analysis curve for $[Cd_2(L^4)(N_3)_4]$ complex is shown in Figure (3. 171). The sample decomposes into three endothermic peaks over the temperature range of 190-600ºC. The first step occurs from 190 ºC corresponding to the loss of (NO) molecule. This was indicated from the weight loss of 0.1490 mg, 4.34% (calc. = 0.1425 mg, 4.16%) upon decomposition process. The second and third steps in the 407-600 ºC range is corresponding; to the loss of ($2CO+N_2O$) molecule with the weight loss of 0.4834 mg, 14.10% (calc .= 0.4751 mg, 13.86%), and the loss of (dipyridyl+$2N_2$+N_2H_4) fragment with weight loss of 1.1645 mg, 33.99% (calc.=1.1593 mg, 33.83%), respectively. The final weight of residue observed at 1.6291 mg, 47.55% (calc. = 1.6480 mg, 48.10%) is assigned to (Cd_2N_3+C_6H_8)[196, 197]. The decomposition of the complex in the 190-249 ºC range is indicated by an endothermic peak at 264ºC. The endothermic decomposition process may signify the metal-ligand bond breaking.

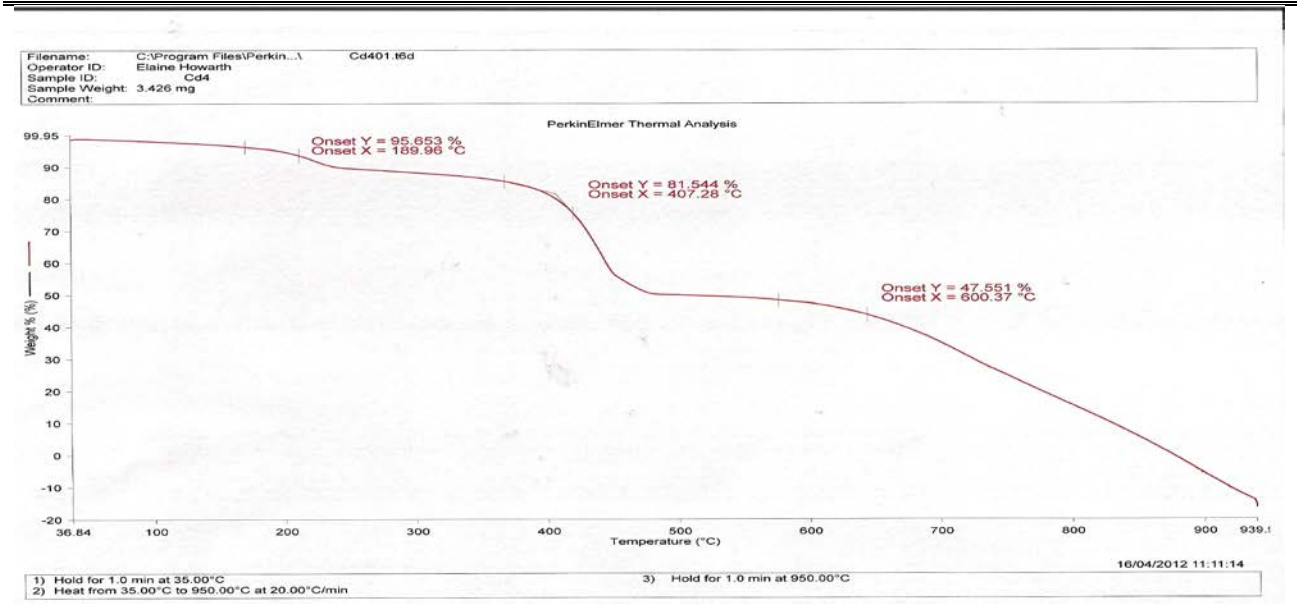

Figure (3. 171) TGA thermogram of $[Cd_2(L^4)(N_3)_4]$ complex in nitrogen at the heating of 20 °C min^{-1}

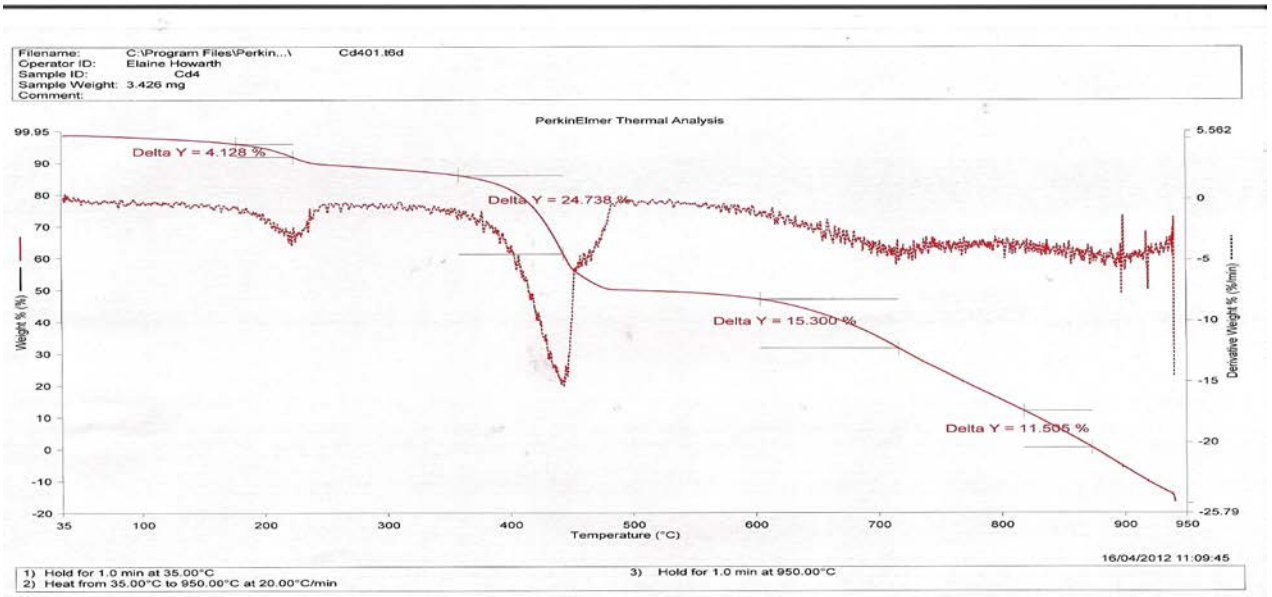

Figure (3. 172) TG-DTG thermograms of $[Cd_2(L^4)(N_3)_4]$ complex in nitrogen at the heating of 20 °C min^{-1}

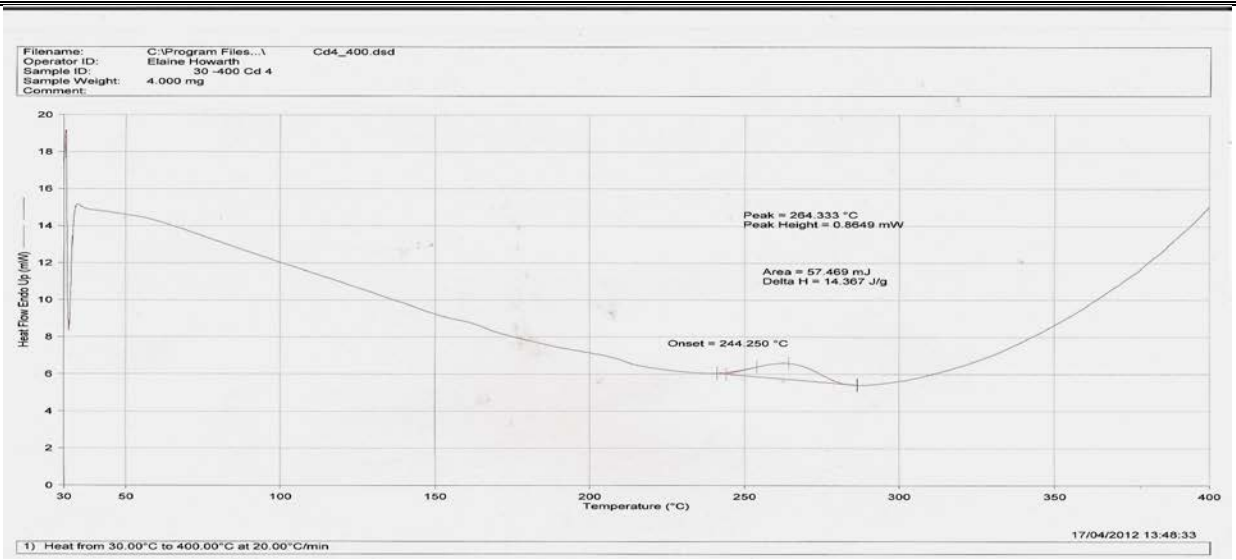

Figure (3. 173) DSC thermogram of $[Cd_2(L^4)(N_3)_4]$ complex in nitrogen at the heating of 20 °C min^{-1}

(3.14.13) Thermal decomposition of $[Cu_2(L^5)(N_3)_4].H_2O$ complex

The TGA thermal analysis curve for $[Cu_2(L^5)(N_3)_4].H_2O$ complex is shown in Figure (3. 174). The sample decomposes in four endothermic peaks over the temperature range of 76-566 ºC. The first decomposition with weight loss of 0.4319 mg calc. = 0.4978 mg, 7.33%), the DTG peak is centered at 76 ºC, is due to losing of (H_2O+CO) molecule. The second and third steps show weight loss of 0.5908 mg (calc.=0.6490 mg, 9.56%), the DTG peaks centered at 129 and 161 ºC, is related to losing of (2NO). The other step with weight loss of 0.7896 mg (calc. = 0.9088 mg, 13.39%), the DTG peaks centered at 200, 271, 321 and 429 ºC, assigned to losing of ($3N_2$). The final step shows weight loss of 0.7951 mg (calc. = 0.7682 mg, 11.32%), the DTG peak is centered at 535 ºC), is assigned to the losing of (N_2O+HCN) molecule. The final weight (obs.=4.000, calc.=3.9716, 58.39%) The decomposition of the complex in the 70-88 mg/min range is indicated by an endothermic peak at 76 ºC. The decomposition of the complex in the 129-189 ºC range is indicated by an endothermic decomposition process at 161 ºC. The decomposition in the 193-429 ºC range is indicated by endothermic peaks at 200 and 407 ºC. The complex shows other

decomposition process in the 472-566 ºC range, indicating an exothermic process, which observed at 493 ºC. The endothermic decomposition process may signify the metal-ligand bond breaking. The DSC thermogram analysis, Figure (3. 175), shows peaks at 82, 183, and 335 ºC, indicating endothermic decomposition process. The peaks at 163 and 393 ºC are referred to exothermic process. The endothermic may signify the metal-ligand bond breaking and the exothermic may indicate the oxidation or combustion of the organic ligand in the atmosphere of air.

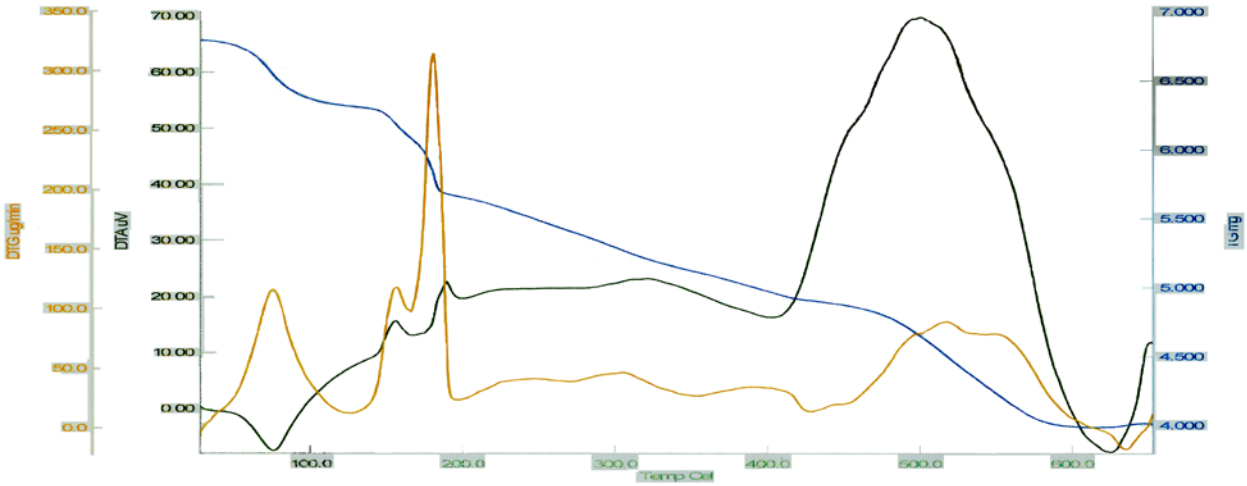

Figure (3. 174) TGA,DTG and DTA thermograms of $[Cu_2(L^5)(N_3)_4].H_2O$ complex in nitrogen at the heating of 20 °C min^{-1}

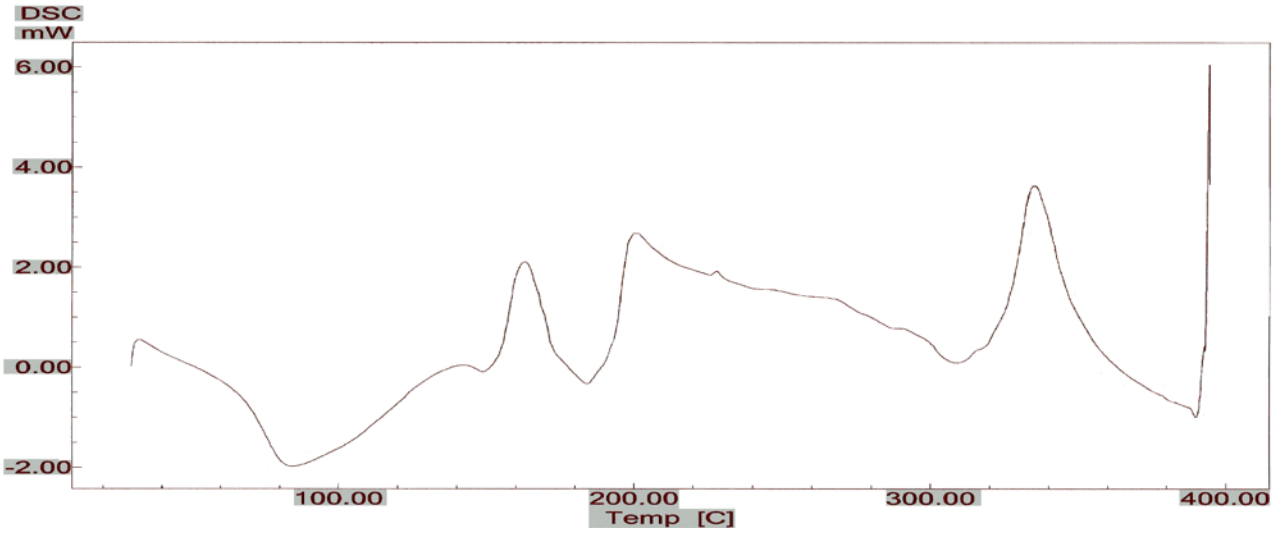

Figure (3. 175) DSC thermogram of $[Cu_2(L^5)(N_3)_4].H_2O$ complex in nitrogen at the heating of 20 °C min^{-1}

Table (3-30) TG/DTG/DTA data for ligands and metal complexes

Compound	Stable up to °C	Stage	Decomposition Temperature Initial-Final (°C)	Nature of Transformation/Intermediate Formed % mass found (calc.)	Nature of DSC peak and Temp. °C	DTG peak Temp. °C
MnL1	74	1	74-113	0.5000(0.4841)	85	
		2	191-213	0.4676(0.4359)	210	
		3	339-350	0.3335(0.3101)		
		4	369-385	0.8223(0.8133)		
		5	393-406	0.4109(0.4259)	435 Exo	
MnL2	50	1	50-59	0.1502(0.1444)	56 Endo	57 and 81
		2	112-200	1.2954(1.3097)	113,178 and 188 Endo	104 and 181
FeL2	93	1	93-247	1.1394(1.2474)	116.666 Endo 166 Endo 258 Endo	110
		2	449-548	2.1981(2.3290)	355.333 Endo	312, 510
		3	668-765	5.1805(5.3235)	-	777
CdL2	390	1	200-300	0.0844 (0.0857)	-	-
		2	390-475	1.3577 (1.4108)	-	442 and 449

Continued Table (3. 30)						
MnL3	51	1	51-129	0.8104 (0.8690)	88 Endo	161
		2	200-243	0.8332 (0.7372)	215 Endo	240
		3	322-354	0.3753 (0.3685)		343
		4	400-450	2.2334 (2.2522)	431 Exo	368, 375
FeL3	70	1	72-111	0.1430 (0.1498)	71, 111 Endo	75, 107
		2	139-173	0.2200 (0.2330)	139, 147 Endo	214
		3	259-400	1.6400 (1.6562)	282, 339 Endo 400 Exo	261 309
ZnL3	145	1	145-225	0.1683 (0.1725)	103.333 Endo 205.666 Endo	220
		2	382-472	0.8938 (0.8516)	268.004 Endo	439
		3	557-594	2.1936 (2.2615)		-
L4	186	1	186-275	3.6196 (3.6545)	261.684 Endo	-
		2	461-618	0.4405 (0.4374)	276.337 Endo	250
MnL4	55	1	55-108	0.6365 (0.5763)	91	-
		2	188-209	0.1820 (0.2132)	-	150
		3	278-419	1.3648 (1.4031)	-	250,338
		4	444-484	2.8459 (2.8431)	469 Exo	440
FeL4	132	1	132-207	1.1077 (1.0855)	114 Endo 189 Exo	189
		2	247-799	0.3251(0.3226)	-	329
ZnL4	103	1	103-125	0.0752 (0.0887)		-
		2	201-275	0.6259 (0.5841)	163 and 277 Endo	248
		3	600-804	1.4293 (1.4862)	-	428
CdL4	190	1	190-249	0.1490 (0.1425)	264 Endo	215
		2	407-486	0.4834 (0.4751)	-	442
		3	586-600	1.1645 (1.1593)	-	719
CuL5	70	1	70-88	0.4319 (0.4978)	76 Endo	-
		2	129-189	0.5908 (0.6490)	161 Endo	129, 161
		3	193-429	0.7896 (0.9088)	200, 407 Endo	200, 271, 321, 429
		4	472-566	0.7951 (0.7682)	493 Exo	535

Exo=exothermic, Endo=endothermic

(3.15) Magnetic moment properties

Coordination chemistry provides an effective approach to design and prepare molecular magnetic materials. One approach in this field is the preparation of low dimensional magnetic systems in which magnetic transition metal ions are assembled into coordination polymers by employing suitable ligands. Two types of ligands, the short bridging ligands and coligands, are used to fulfil these requirements. The short bridging ones can mediate effectively near-neighbour magnetic interactions and the auxiliary ones or coligands tuning the final structures as well as the secondary magnetic interactions in the materials. Within this in mind, we have explored the use of a range of ligands with neutral inner-salt dicarboxylato group and azido moiety to prepare complexes. Carboxylate ligands may bind to metal ions with various coordination modes, allowing for varied magnetic interactions. Furthermore, the carboxylato group may coexist with the azido group to bridge adjacent metal centres, giving rise to mixed-bridged complexes. N_3^- has proved to be very versatile by displaying remarkable diversities in both magnetism and crystal engineering. This is due to the fact that azide can link metal ions in different coordination modes, resulting in polymeric materials of low dimensionalities (chains or layers).

(3.15.1) Magnetic Moment Measurements

In this work, magnetic susceptibility measurements were conducted with an Evans balance. In these experiments a modified form of the Guoy balance method, using a microscale apparatus devised by D. F. Evans and manufactured by Johnson-Matthey, Figure (3. 176).

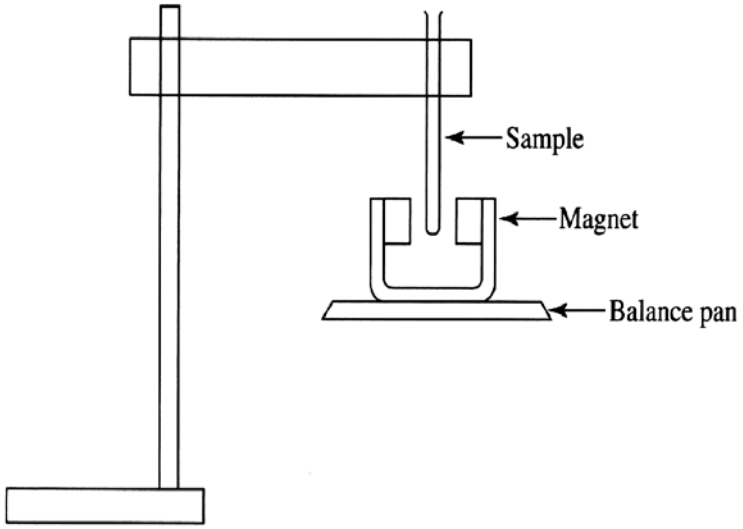

Figure (3. 176) Schematic diagram of Evans's balance

In this balance, a moveable magnet attached to a torsion balance detects the force created by diamagnetic and paramagnetic moments in the sample. Diamagnetic behaviour makes the magnet move down. However, paramagnetic moment makes the magnet move up.

(3.15.1.1) Evans balance susceptibility calculation

The gram susceptibility of the sample is given by Equation (3. 1);

$$\chi_g = \frac{C_{Bal} \times L \times (R - Ro)}{m \times 10^9} \qquad \textbf{(3. 1)}$$

Where:

χ_g = mass magnetic susceptibility

Ro = reading from the digital display when the empty sample tube is in place in the balance

R = reading from the digital display when the sample (in the sample tube) is in place in the balance

m = sample mass in grams

***L*=** sample length in centimetres

C_{Bal} = balance calibration constant

The molar magnetic susceptibility, χ_M, is obtained from the mass magnetic susceptibility by multiplying by the molecular weight of the sample.

$$\chi_M = M\chi_g$$

χ_M = molar magnetic susceptibility

M = molecular weight of the sample in units of g/mol

Diamagnetic corrections need to be applied to this measured molar magnetic susceptibility. The diamagnetic contributions arise from core paired electrons (metal ion), ligand electron pairs, and counter ion electron pairs.

$$\chi_P = \chi_M - \chi_D$$

Where: χ_D = {χ_D(core) + χ_D(ligand) + χ_D (counter ion)}

The diamagnetic correction factors are tabulated values, called Pascal's constants[(210)].

The magnetic moment value is obtained by using Equation (3. 2).

$$\mu = 2.83 (\chi_P T)^{1/2} \qquad (3.\ 2)$$

Where T = temperature at the time of the measurements in Kelvin.

(3.15.1.2) Worked examples for the calculation of magnetic moment, μ

(3.15.1.3) $[Cr_2(L^1)(N_3)_4]Cl_2.H_2O$.

This complex has been used as an example for L^1 complexes for the calculation method of the magnetic susceptibility measurements of the complexes:

$$\chi_g = \frac{C_{Bal} \times L \times (R-Ro)}{m \times 10^9}$$

C_{Bal} is a constant = 0.9324

$$\chi_g = \frac{0.9324 \times 1.5 \times \{671-(-33)\}}{(\text{mass of tube and sample-mass of tube}) \times 10^9}$$

$$\chi_g = \frac{984.6144}{54700000}$$

$=1.80\times10^{-5}$

Pascal's constants Tables (3.31 to 3.33) are used to determine the diamagnetic correction factor χ_D as follows:(210)

Table (3. 31) Values of χ_D for cations

Cation	χ_D/(1x10^{-6} emu mol^{-1})
Cr^{+3}	-12
Mn^{+2}	-14
Fe^{+2}	-13
Co^{+2}	-12
Ni^{+2}	-12
Cu^{+2}	-11
Ag^{+1}	-28

Table (3. 32) Values of χ_D for atoms in covalent species

Atom	χ_D/(1x10^{-6} emu mol^{-1})
C_{ring}	-6.24
N_{ring}	-4.61
H	-2.93
CO_2^-	-2.0700
Cl^-	-23.4
K^+	-18.5
C	-6
N	-5.57
H_2O	-13

Table (3. 33) Values of λ_i for specific bond types

Bond	λ_i / ($1x10^{-6}$ emu mol^{-1})
C-N	-13
Pyridine	0.5
Ar-Ar	-0.5
C=O	-6.3
C-C	0.8
N=N	1.85

χ_D = [10 χ_D (Cring) + 2 χ_D (N ring) + 12 χ_D (H) + 2 χ_D (CO2) + 2λ(C-N) + 2λ(py) + λ(Ar-Ar) + 2 λ(C=O) + 12 χ_D (N) + 8 λ(N=N) + 2 χ_D (C) + 2 λ(C-C)] $\times 10^{-6}$

χ_D = 10(– 6.24) + 2(– 4.61) + 12 (– 2.93) + 2(– 2.0700) + 2(– 13) + 2(0.5) + (– 0.5) + 2(6.3) + 12(–5.57) + 8(1.85) + 2(– 6) + 2 (0.8)] $\times 10^{-6}$ emu mol^{-1}

χ_D = – 62.4 – 9.22 – 35.166 – 4.1400 – 26 + 1 – 0.5 + 12.6000 – 66.8400 + 14.800 – 12 + 1.6] $\times 10^{-6}$ emu mol^{-1}

= - 0.00018266

χ_D = [{ χ_D (ligand) and azide} + χ_D(core) + χ_D (counter ion)]

χ_D for complex CrL1 = – 0.00018266 - (0.000022 for Cr) + (χ_D (Cl) + (χ_D (H_2O)

= – 0.00018266 – (0.000022 for Cr) + (– 0.0000201) + (– 0.000023.4) + (– 0.000013)

= – 0.000244666 emu mol^{-1}

$\chi_M = M\chi_g$

= 633.25 × 0.0000180 emu mol^{-1}

= 0.0113985 emu mol^{-1}

$\chi_P = \chi_M - \chi_D$

= 0.0113985 + 0.000244666

$= 0.011643166$ emu mol^{-1}

$\chi_P T = 0.011643166 \times 294K$

$= 3.423090804$ emu K mol^{-1}

$\mu = 2.83 (\chi_A T)^{1/2}$

$= 2.83 (3.423090804)^{1/2}$

$= 5.233041795\ \mu_B$ (for two metal ions)

$= 2.616520898\ \mu_B$ (for one metal ion)

(3.15.1.4) $[Mn_2(L^2)(N_3)_4].H_2O$.

This complex has been used as an example for L^2 complexes for the calculation method of the magnetic susceptibility measurements of the complexes:

$$\chi_g = \frac{0.9324 \times 1.3 \times \{589-(-23)\}}{(\text{mass of tube and sample-mass of tube}) \times 10^9}$$

C_{Bal} is constant = 0.9324

$$\chi_g = \frac{741.8174}{66400000}$$

$= 1.12 \times 10^{-5}$

$\chi_D = 10\ \chi_D (C_{ring}) + 2\ \chi_D (N_{ring}) + 8\ \chi_D (H) + 2\ \chi_D (CO_2) + 2\lambda(C\text{-}N) + 2\lambda(py) + \lambda(Ar\text{-}Ar) + 2\ \lambda(C{=}O) + 12\ \chi_D (N) + 8\ \lambda(N{=}N)$

$\chi_{D\,=}$ 10(– 6.24) + 2(– 4.61) + 8 (– 2.93) + 2(– 2.0700) + 2(– 13) + 2(0.5) + (– 0.5) + 2(6.3) + 12(– 5.57) + 8(1.85)] × 10^{-6} emu mol^{-1}

χ_D = – 62.4 – 9.22 – 23.4400 –4.1400 – 26 + 1 - 0.5 + 12.6000 –66.8400 + 14.800] ×10^{-6} emu mol^{-1}

= – 0.00017894 emu mol^{-1}

χ_D = [χ_D {(ligand) + (azide)} + χ_D(core) + χ_D (counter ion)]

χ_D for MnL2 = – 0.00017894 + (– 0.000028 for Mn) + (– 0.000013) for H_2O

= – 0.00021994 emu mol^{-1}

$\chi_{M\,=}$ $M\chi_g$

= 540.18 × 0.0000112

= 0.006050016 emu mol^{-1}

$\chi_{P\,=}$ χ_M − χ_D

= 0.006050016 + 0.00021994

= 0.006269956 emu mol^{-1}

$\chi_P T$ = 0.006269956 × 294 K

= 1.843367064 emu K mol^{-1}

$\mu = 2.83\ (\chi_A\, T)^{1/2}$

= $2.83(1.843367064)^{1/2}$

= 3.840174021 μ_B (for two metal ions)

= 1.920870105 μ_B (for one metal ion)

(3.15.1.5) [$Co_2(L^3)(N_3)_4$].H_2O.

This complex has been used as an example for L^3 complexes for the calculation method of the magnetic susceptibility measurements of the complexes

$$\chi_g = \frac{0.9324\times2.5\times\{502-(-31)\}}{(\text{mass of tube and sample-mass of tube})\times10^9}$$

C_{Bal} is constant = 0.9324

$$\chi_g = \frac{1242.4230}{147000000}$$

$= 8.5\times10^{-6}$

$\chi_D = 10\,\chi_D(C_{ring}) + 2\,\chi_D(N_{ring}) + 16\,\chi_D(H) + 2\,\chi_D(CO_2) + 2\lambda(C\text{-}N) + 2\lambda(py) + \lambda(Ar\text{-}Ar) + 2\,\lambda(C{=}O) + 12\,\chi_D(N) + 8\,\lambda(N{=}N) + 4\,\chi_D(C) + 4\,\lambda(C\text{-}C)]$

$\chi_D = 10(-6.24) + 2(-4.61) + 16(-2.93) + 2(-2.0700) + 2(-13) + 2(0.5) + (-0.5) + 2(6.3) + 12(-5.57) + 8(1.85) + 4(-6) + 4(0.8)]\times10^{-6}$ emu mol^{-1}

$= -62.4-9.22 - 46.8800 - 4.1400 - 26 + 1 - 0.5 + 12.6 - 66.8400 + 14.800 - 24 + 3.2$

$= -0.00020838$ emu mol^{-1}

$\chi_D = [\{\chi_D(\text{ligand and azide}\} + \chi_D(\text{core}) + \chi_D(\text{counter ion})]$

χ_D for CoL3 = – 0.00020838 – (0.000024 for Co) + (-0.000013) for H_2O

$= -0.00024538$ emu mol^{-1}

$\chi_M = M\chi_g$

$= 604.27 \times 0.0000085$

$= 0.005136295$ emu mol^{-1}

$\chi_P = \chi_M - \chi_D$

= 0.005136295 + 0.00024538

= 0.005381675 emu mol^{-1}

$\chi_P T = 0.005381675 \times 294K$

= 1.58221245 emu K mol^{-1}

$\mu = 2.83 (\chi_A T)^{1/2}$
$\mu = 2.83 (1.58221245)^{1/2}$

= 3.557766097 μ_B (for two metal ions)
= 1.778883049 μ_B (for one metal ion)

(3.15.1.6) $[Ni_2(L^4)(N_3)_4].H_2O$.

This complex has been used as an example for L^4 complexes for the calculation method of the magnetic susceptibility measurements of the complexes

$$\chi_g = \frac{0.9324 \times 3 \times \{150-(-58)\}}{(\text{mass of tube and sample-mass of tube}) \times 10^9}$$

C_{Bal} is constant = 0.9324

$$\chi_g = \frac{581.8176}{87600000}$$

= 6.6×10^{-6}

χ_D = 10 χ_D (Cring) + 2 χ_D (N ring) + 20 χ_D (H) + 2 χ_D (CO_2) + 2λ(C-N) + 2λ(py) + λ(Ar-Ar) + 2 λ(C=O) + 12 χ_D (N) + 8 λ(N=N) + 6 χ_D (C) + 6 λ(C-C)] $\times 10^{-6}$

χ_D = 10(– 6.24) + 2(– 4.61) + 20 (– 2.93) + 2(– 2.0700) + 2(– 13) + 2(0.5) + (– 0.5) + 2(6.3) + 12(– 5.57) + 8(1.85) + 6 (– 6) + 6 (0.8)] $\times 10^{-6}$ emu mol^{-1}

= [62.4 – 9.22 – 58.600 – 4.1400 – 26 + 1 – 0.5 + 12.6 – 66.8400 + 14.800 – 36 + 4.800] $\times 10^{-6}$ emu mol^{-1}

= – 0.0002305 emu mol^{-1}

χ_D = [{ χ_D (ligand) and azide} + χ_D(core) + χ_D (counter ion)]

χ_D for NiL4= – 0.00031794 + (– 0.000024 for Ni) + (– 0.000013) for H_2O

= – 0.0002675 emu mol^{-1}

$\chi_M = M\chi_g$

= 631.85×0.0000066
= 0.00417021 emu mol^{-1}

$\chi_P = \chi_M - \chi_D$

= 0.00417021 + 0.0002675

= 0.00443771 emu mol^{-1}

$\chi_P T$ =0.00443771 × 294K

= 1.30468674 emu K mol^{-1}

$\mu = 2.83 (\chi_A T)^{1/2}$

$\mu = 2.83 (1.30468674)^{1/2}$

= 3.230711055 μ_B (for two metal ions)

= 1.615355775 μ_B (for one metal ion)

(3.15.1.7) $[Fe_2(L^5)(N_3)_4].H_2O$.

This complex has been used as an example for L^5 complexes for the calculation method of the magnetic susceptibility measurements of the complexes

$$\chi_g = \frac{0.9324\times1.2\times\{737-(-29)\}}{(\text{mass of tube and sample-mass of tube})\times10^9}$$

C_{Bal} is constant = 0.9324

$$\chi_g = \frac{409.5101}{55000000}$$

$= 7.4 \times 10^{-6}$

$\chi_D = 10\,\chi_D(C_{ring}) + 2\,\chi_D(N_{ring}) + 18\,\chi_D(H) + 2\,\chi_D(CO_2) + 2\,\lambda(C\text{-}N) + 2\lambda(py) + \lambda(Ar\text{-}Ar) + 2\,\lambda(C{=}O) + 12\,\chi_D(N) + 8\,\lambda(N{=}N) + 5\,\chi_D(C) + 2\,\lambda(C\text{-}C) + 4\,\lambda(C\text{-}C)] \times 10^{-6}$

$\chi_D = 10(-6.24) + 2(-4.61) + 18(-2.93) + 2(-2.0700) + 2(-13) + 2(0.5) + (-0.5) + 2(6.3) + 12(-5.57) + 8(1.85) + 5(-6) + 4(0.8)] \times 10^{-6}$ emu mol^{-1}

$= 62.4 - 9.22 - 52.7400 - 4.1400 - 26 + 1 - 0.5 + 12.6 - 66.8400 + 14.800 - 30 + 3.2] \times 10^{-6}$ emu mol^{-1}

$\chi_D = -0.00022024$ emu mol^{-1}

$\chi_D = [\{\chi_D(\text{ligand and azide}\} + \chi_D(\text{core}) + \chi_D(\text{counter ion})]$

χ_D for FeL5$= -0.00022024 + (-0.000026$ for Fe$) + (-0.000013)$ for H_2O

$= -0.00025924$ emu mol^{-1}

$\chi_M = M\chi_g$

= 612.12 × 0.0000074

= 0.004529688 emu mol^{-1}

$\chi_P = \chi_M - \chi_D$

=0.004529688 + 0.00025924

=0.004788928 emu mol^{-1}

$\chi_P T$ = 0.004788928 × 294 K

= 1.407944832 emu K mol^{-1}

$\mu = 2.83 (\chi_A T)^{1/2}$

$\mu = 2.83 (1.407944832)^{1/2}$

= 3.356122503 μ_B (for two metal ions)

= 1.678061252 μ_B (for one metal ion)

Table (3. 34) Calculation of magnetic moment measurements for L^1-L^5 complexes

Complex	*Ro*	*R*	Mass of tube	Mass of (tube + sample)	Length in cm	χ_g	μ_{eff} per atom
$[Cr_2^{III}(L^1)(N_3)_4]Cl_2.H_2O$	-33	671	2.6805	2.7352	1.5	1.80×10^{-5}	2.6165
$[Mn_2^{II}(L^1))(N_3)_4].H_2O$	-54	380	2.7013	2.7298	1.0	1.42×10^{-5}	2.2086
$[Fe_2^{II}(L^1))(N_3)_4].H_2O$	-22	561	2.7467	2.8160	2.5	1.93×10^{-5}	2.5693
$[Co_2^{II}(L^1))(N_3)_4].H_2O$	-61	275	2.7455	2.7749	1	1.07×10^{-5}	1.9382
$[Ni_2^{II}(L^1))(N_3)_4].H_2O$	-60	147	2.5939	2.6698	2.5	6.4×10^{-6}	1.5158
$[Cu_2^{II}(L^1))(N_3)_4].H_2O$	-53	-16	2.7027	2.7956	3.0	1.1×10^{-6}	0.7132
$Na_2[Ag_2^{I}(L^1)(N_3)_4].H_2O$	-54	-57	2.7014	2.7688	2.5	1.2×10^{-6}	0.8317
$[Mn_2^{II}(L^2))(N_3)_4].H_2O$	-23	589	2.6802	2.7466	1.3	1.12×10^{-5}	1.9208

Continued Table (3-34)							
$[Fe_2^{II}(L^2)\ )(N_3)_4]$	-58	781	2.5930	2.7096	3.0	2.01×10^{-5}	2.5126
$[Co_2^{II}(L^2))(N_3)_4].H_2O$	-32	1018	2.8429	2.8798	1	2.65×10^{-5}	2.9442
$[Cu_2^{II}(L^2))(N_3)_4].H_2O$	-31	109	2.8361	2.9673	2.21	2.2×10^{-6}	0.9202
$[Cr_2^{III}(L^3)(N_3)_4]Cl_2.H_2O$	-51	182	2.7045	2.7480	3	1.5×10^{-5}	2.4473
$[Mn_2^{II}(L^3)(N_3)_4].2H_2O$	-58	247	2.7478	2.7818	3	2.51×10^{-5}	3.0352
$[Fe_2^{II}(L^3)\ )(N_3)_4].H_2O$	-58	-23	2.5946	2.6634	3	1.4×10^{-6}	0.7986
$[Co_2^{II}(L^3\ )(N_3)_4].H_2O$	-31	502	2.8199	2.9669	2.5	8.5×10^{-6}	1.7788
$[Ni_2^{II}(L^3)(N_3)_4].H_2O$	-52	144	2.7032	2.7887	3	6.412×10^{-6}	1.5536
$[Cu_2^{II}(L^3)\ )(N_3)_4]$	-58	22	2.5951	2.6704	3	3×10^{-6}	1.0889
$[Cr_2^{III}(L^4)(N_3)_4]Cl_2.H_2O$	-61	242	2.7450	2.8510	3	8×10^{-6}	1.8473
$[Mn_2^{II}(L^4)(N_3)_4].H_2O$	-23	981	2.6800	2.7302	1.2	2.24×10^{-5}	2.8975
$[Co_2^{II}(L^4)(N_3)_4].H_2O$	-31	511	2.8360	2.8753	0.7	9×10^{-6}	1.8717
$[Ni_2^{II}(L^4)\ (N_3)_4].H_2O$	-58	150	2.5930	2.6806	3	6.6×10^{-6}	1.6153
$[Cu_2^{II}(L^4)(N_3)_4].H_2O$	-60	-27	2.6996	2.7497	2.7	1.7×10^{-6}	0.8929
$[Cr_2^{III}(L^5)(N_3)_4]Cl_2.H_2O$	-59	274	2.6989	2.7300	1.2	1.2×10^{-5}	2.2251
$[Mn_2^{II}(L^5)(N_3)_4].H_2O$	-56	283	2.5932	2.7309	2.2	5×10^{-6}	1.3956
$[Fe_2^{II}(L^5)(N_3)_4].H_2O$	-29	737	2.8362	2.8912	1.2	7.4×10^{-6}	1.6780
$[Co_2^{II}(L^5)(N_3)_4].H_2O$	-31	607	2.8240	2.9363	1.9	1.01×10^{-5}	1.9553
$[Cu_2^{II}(L^5)(N_3)_4].H_2O$	-60	-15	2.6989	2.7300	3.3	4.5×10^{-6}	1.3455

(3.15.2) Magnetic properties of complexes; experimental and modelling calculated values

In this work, room temperature magnetic moment of the mixed-(azido, carboxylato)-bridged complexes was investigated. Since the nature of the donor atoms and the bridging groups in all the complexes are the same. It would be very interesting to compare the magnetic properties of the same M(II)-complexes based on the increasing of the chain length of the caboxylate segment and the introduction of the spacer in the ligand.

Polynuclear metal carboxylates[198] of the 4,4`-dipyridine are good candidates for the investigation of magnetic exchange interaction between adjacent metal ions. It is well known that the carboxylate group can bridge metal ions to give rise to a variety of polynuclear transition metal complexes, ranging from discrete entities to three-dimensional systems[199, 200]. Carboxylate group can adopt many types of bridging conformations, the most important being triatomic, *syn-syn*, *syn-anti*, *anti-anti* and monoatomic (see scheme 3.15, page 247)[201]. The *syn-syn* conformation mediates the antiferromagnetic exchange pathway between the metal centers and resulted in a low-dimensional feature, while the *syn-anti* favors the ferromagnetic exchange interaction with some exceptions in both cases. On the other hand, the magnetic exchange mediated *via* an azido bridge can be ferro- or antiferromagnetic, depending on the bridging mode and bonding parameters.

The experimental magnetic moment values of the complexes are shown in Tables (3. 34).

The magnetic moment values at (294 K) of the $[Cr_2^{III}(L^n)(N_3)_4]Cl_2.H_2O$ complexes show values in the range of 1.84-2.61 B.M, Table (3. 34) which are lower than the total spin-only values, Table (3. 35) indicating a high spin octahedral geometry around $[Cr_2^{III}(L^n)(N_3)_4]Cl_2.H_2O$ complexes[202]. The lowering of these magnetic moments indicates a dominant antiferromagnetic interaction in all complexes. This may due to the fact that the *syn-syn* carboxylate bridges provide a

small metal-metal distance and results in a good overlap of the magnetic orbitals, an antiferromagnetic coupling is always induced[203]. For the EO azido bridge, previous theoretical studies on $[Cr_2^{III}(L^4)(N_3)_4]Cl_2.H_2O$ complexes[163] have indicated that the main factor controlling the exchange should be the M-N-M bridging angle *Φ*: a crossover between ferro- and antiferromagnetic interactions occurs at *Φ* 98°, and the ferromagnetic interaction increases from *Φ* 98°, with the maximum ferromagnetic interaction appearing at *Φ* 114°. In the octahedral $[Cr_2^{III}(L^n)(N_3)_4]Cl_2.H_2O$ complexes, the predicted *Φ* values obtained from the modelling of the complexes using Chemoffice programme are around (85.1-102.5°) Table (3. 36). This value is within the range of bond angles mentioned above, for a crossover between ferro- and antiferromagnetic interactions. Therefore, intrachain antiferromagnetic coupling might be promoted by EO azido bridges. Moreover, cooperative effect of the *syn-syn* carboxylate and EO azido bridges results in a strong antiferromagnetic coupling between the Cr atoms. The low magnetic moment values behavior and the insolubility of these complexes in most common organic solvents, soluble only in a hot DMSO, could refer to the formation of a polymeric structure of these complexes.

The magnetic moment measurements of the $[Mn_2^{II}(L^n)(N_3)_4].nH_2O$ complexes show values in the range of 1.39-3.03 B.M, Tabl3 (3. 34). The μ_{eff} value of all complexes, are much lower than the spin only value, Table (3. 35). This is attributed to the strong antiferromagnetic coupling interaction through the bridged-mixed ligands. This behavior could refer to the formation of a polymeric structure in these complexes. The carboxylate groups are in the *syn-syn* bridging mode, and assuming that the antiferromagnetic behavior is mainly due to intrachain exchange interactions through the carboxylato bridge.[196]. $[Mn_2^{II}(L^n)(N_3)_4].nH_2O$ complexes show increase in the μ_{eff} values as the length of the carboxylate CH_2-segment are increased and as follows: $MnL^2 < MnL^1 < MnL^3 > MnL^4$. An exceptional trend is observed in the MnL^4 complex, which shows a lower μ_{eff} value.

According to the predicted structural data generated by the Chemoffice program, the system can magnetically be treated as an infinite uniform chain in which

magnetic coupling is mediated through a triple bridge (a two EO azido and a *syn-syn* carboxylato)[(203)]. The decrease of magnetic moment for all complexes may be attributed to the saturation effect or to presence of interchain antiferromagnetic interactions. Structurally, these compounds are isomorphic and contain almost identical chains in which neighboring metal ions are triply linked by two EO azido bridges and *syn-syn* carboxylato bridge, with only minor differences in bond parameters. Magnetically, $[Mn_2^{II}(L^n)(N_3)_4].nH_2O$ compounds display antiferromagnetic coupling through the triple bridges. It is well established that the *syn-syn* carboxylato bridge is a universal antiferromagnetic pathway because it induces a good overlap of magnetic orbitals[(204)]. The incorporation of cabboxylato bridge lead to decrease of the Φ for the two azido bridges, and according the Mn-N-Mn bridging angle Φ might be the key factor for the crossover between ferro- and antiferromagnetic interactions. In the $[Mn_2^{II}(L^n)(N_3)_4].nH_2O$ complexes, the predicted Φ values of the modelling complexes using Chemoffice programme are about (94.3-99.3°), Table (3. 36) and thus the azido bridge is expected to promote antiferromagnetic exchange. The observed antiferromagnetic interaction suggest that the antiferromagnetic pathway through the carboxylato overtakes the antiferromagnetic one through the azido[(203)].

The magnetic moment measurement of $[Fe_2^{II}(L^n)(N_3)_4].H_2O$ complexes show values in the range of 0.79-2.56 B.M**,** Table **(**3.34**).** The μ_{eff} values for all complexes are much lower than the spin only value, Table (3.35), indicating a high spin octahedral geometry around Fe^{II} atom. The lowering of these magnetic moments is due to antiferromagnetic phenomena. The predicted Φ values of the modelling complexes using Chemoffice programme for Fe are about (88.1-99.7°), Table (3.36) and thus the azido bridge is expected to promote antiferromagnetic exchange.

The carboxylato groups are in the *syn-syn* bridging mode, and assuming that the antiferromagnetic interactions are mainly due to intrachain exchange interactions through the carboxylato bridge[(196)]. The observed antiferromagnetic interaction

suggest that the antiferromagnetic pathway through the carboxylato overtakes the antiferromagnetic one through the azido[203].

The magnetic moment measurements for $[Co_2^{II}(L^n)(N_3)_4].H_2O$ complexes show values in the range of 1.77-2.94 B.M, Table (3. 34). The μ_{eff} values of all complexes are much lower than the spin only value, Table (3. 35). This is attributed to the strong antiferromagnetic coupling interaction through nitrogen atoms of the azido moieties. This behavior could refer to the formation of a polymeric structure in these complexes. The predicted *Φ* values of the modelling complexes using Chemoffice programme for Co are about (87.9- 93.1°), Table (3.36) and thus the azido bridge is expected to promote antiferromagnetic exchange. The carboxylato groups are in the *syn-syn* bridging mode, and assuming that the antiferromagnetic interactions are mainly due to intrachain exchange interactions through the carboxylato bridge[196]. The $[Co_2^{II}(L^n)(N_3)_4].H_2O$ complexes show antiferromagnetic exchange interaction, because the ligands are expected to saturate the coordination sites around the metal ions, preferring six-coordinate complexes via self assembly, through the carboxylato and azido groups, leading to a polymeric structure bearing a mixed carboxylato-azido bridges[196]. The magnetic behaviors of the complexes based on the CH_2-aliphatic chain attached to the carboxylato moiety are as follows: CoL2 > CoL1 > CoL3 < CoL4. These values indicate that the increase of the chain length has a positive influence on the antiferromagnetic behavior. The complex $[Co_2^{II}(L^5)(N_3)_4].H_2O$ shows value similar to that of CoL^1, which indicate that no effect with add the spacer.

The magnetic moment measurements for $[Ni_2^{II}(L^n)(N_3)_4].H_2O$ complexes show values in the range of 1.51-1.61 B.M, Table (3. 34). The μ_{eff} values of all complexes are much lower than the spin only value, Table (3. 35). The lowering of these magnetic moments is due to antiferromagnetic coupling interaction through the nitrogen atoms of the azido moieties. The carboxylato groups are in the *syn-syn* bridging mode, and assuming that the antiferromagnetic interactions are mainly due to intrachain exchange interactions through the carboxylato bridge. [196]. The

predicted *Φ* values of the modelling complexes using Chemoffice programme for Ni are about (86.6-90 °), Table (3. 36) and thus the azido bridge is expected to promote antiferromagnetic exchange. The following order can be see NiL1<NiL3<NiL4. It is well known that, magnetic exchange interactions are mainly propagated by the bridging of RCOO- group in which an antiferromagnetic (AF) coupling transmits can be achieved upon *syn-syn* carboxylato bridge mood[205-207]. The experimental magnetic values of the complexes presented in this work indicate a dominated intermolecular antiferromagnetic interaction between adjacent Ni atom through the end-on azido exchange bridge. This pattern is in agreement with moderate antiferromagnetic coupling reported in literature[208, 209].

The magnetic moment measurements of $[Cu_2^{II}(L^n))(N_3)_4].nH_2O$ complexes show values in the range of 0.71-1.34 B.M, Table (3. 34). The μ_{eff} values of all complexes are much lower than the spin only value, Table (3. 35), indicating a high spin octahedral geometry around Cu atom. The lowering of these magnetic moments is due to antiferromagnetic coupling via nitrogen atoms of the azido groups and the intrachain exchange interactions through the carboxylato bridge[196]. The predicted *Φ* values of the modelling complexes using Chemoffice programme for Cu are about (87.6-105.5°), Table (3. 36) and thus the azido bridge is expected to promote antiferromagnetic exchange. The obtained data show there is no trend could be followed regarding the relationship between the length of the CH_2 group and the μ_{eff} values. The CuL5 shows value higher to that reported for other $[Cu_2^{II}(L^2))(N_3)_4].H_2O$ complexes, which may related to the introduction of the spacer into the ligand system. On other hand, we may consider that the exchange coupling will be mainly propagated by bridges direct towards the magnetic orbitals which, for Cu^{II} ions in axially elongated octahedral environments, are of $d_{x^2-y^2}$ character. Thus, the main exchange pathways will be within the formed polymeric chains, since inter-chain bridging in only accomplished through axially coordinated azides. These occupy orbitals of dz^2 character, thus the coupling they transmit is expected to be weak, and can be neglected[108, 107]. It is indicate that, the CH_2 spacer groups may play a role in

the enhancement of the overlap between Cu atom and the bridged-moieties orbitals, leading to propagate the antiferromagnetic interaction.

The antiferromagnetic behaviour of the prepared complexes support the formation of a polymeric structure in which, the carboxylato group is adopting the *syn-syn* mode upon complex formation. This is in agreement with the obtained IR data in this work which reveled the carboxylato moiety is adopting the *syn-syn* mode upon complex formation.

Table (3. 35) Values of spin only of the metal ions

Number of unpaired electron	Value of magnetic moment μ_{eff}
1	1.73
2	2.83
3	3.87
4	4.96
5	5.92

Table (3. 36) Values of bond angle Φ (º) of M-N-M

Metal ion	L^1	L^2	L^3	L^4	L^5
Cr^{+3}	102.5	85.1	88.3	86.7	86.9
Mn^{+2}	99.3	94.3	96.7	97.5	96.5
Fe^{+2}	89.9	93.0	88.1	88.2	99.7
Co^{+2}	87.9	93.1	88.1	88.1	88.4
Ni^{+2}	89.6	90.0	89.6	89.6	86.6
Cu^{+2}	89.9	87.6	89.9	105.5	87.7

(3. 16) Theoretical calculations to predict $\Delta(\nu_{as}- \nu_s)$ value and coordination mode of the carboxylato group

The carboxylate group has proved to be very versatile by displaying a range of coordination behaviour upon complex formation. It can display several coordination modes, including ionic, monodentate, bidentate, chelating or bridging, Scheme (3. 15). Infrared spectroscopy (IR) is an important method that can be used to determine the mode of the carboxylate binding, especially when no structural data are available.

Correlation between the COO stretching frequencies and the types of COO coordination has been investigated extensively[164]. In these studies, the mode of the carboxylate binding can be predicted from the asymmetric vibration frequency of the carboxylate, $\nu_{as}(COO^-)$, and the magnitude of the separation between the carboxylate stretches, $\Delta(\nu_{as}- \nu_s)$. These are used as spectroscopic guides to determine the mode of the carboxylate coordination binding inorganic complexes[211, 212] and biomolecules[213]. Deacon and Phillip[214] have observed a correlation between the solid structures and the IR frequencies for a number of divalent metal carboxylates, and have proposed an empirical rule for the correlation between $\Delta(\nu_{as}- \nu_s)$ and the types of coordination of the COO^- group:

$$\Delta(\text{chelating}) < \Delta(\text{bridging}) < \Delta(\text{ionic}) < \Delta(\text{monodentate})$$

where Δ ionic is approximately 160–170 cm^{-1} for acetates[211, 212]. In the bridging coordination, when one divalent metal cation is bound to one of the oxygens of the COO^- group and another divalent metal cation to the other oxygen, the band $\nu_{as}(COO^-)$ is located at the same position as that of the ionic group[214]. However, the range 160–170 cm^{-1} was derived for acetates and in general the comparison of the Δ value of the title complex with the Δ value of the particular sodium salt should be used for the assignment following the guidelines: (i) bidentate chelating coordination occurs when $\Delta (COO^-)_{\text{sodium complex}} << \Delta (COO^-)_{\text{sodium salt}}$; (ii) the bidentate bridging carboxylate exists when $\Delta(COO^-)$ studied complex$\leq \Delta(COO^-)_{\text{sodium salt}}$; (iii) monodentate coordination is characterised by $\Delta(COO^-)_{\text{studied complex}} >> \Delta(COO^-)_{\text{sodium salt}}$. (211, 212, 215)..

The frequency of asymmetric and symmetric vibration depends on the electronic charge density of the C-O bonds in the carboxylato. Therefore, one can suppose that the higher are differences in electronic density of C-O bonds and C-O bond lengths the higher is frequency of the asymmetric vibration and the lower is the frequency of the symmetric vibration [165].

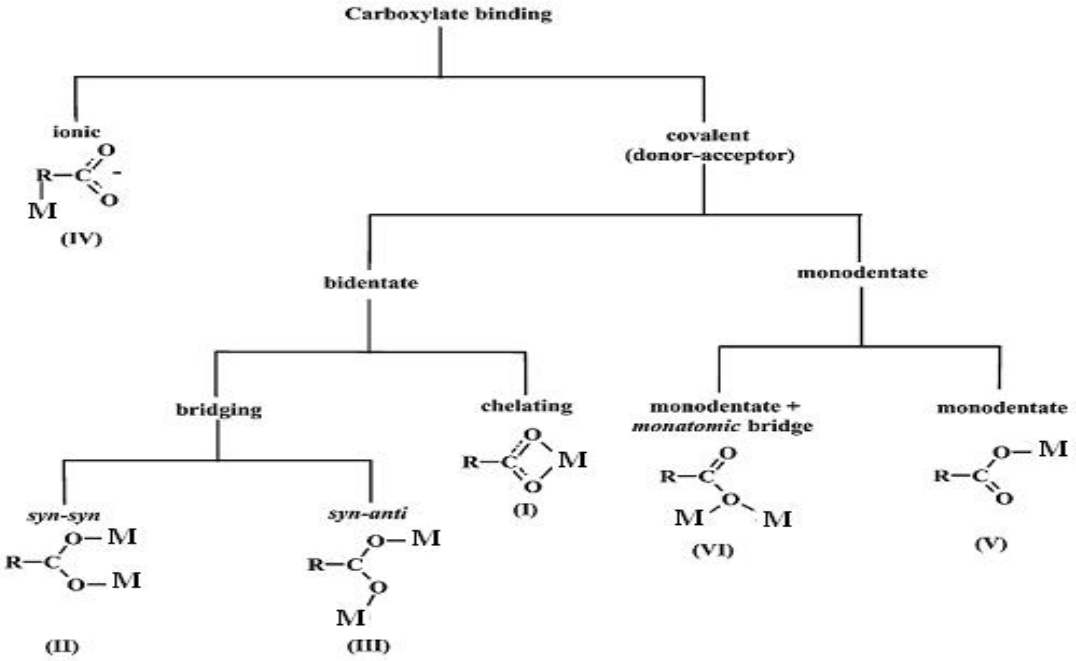

Scheme (3. 15) Carboxylate binding mode for divalent metal ions

Tasumi *et al.* [164] proposed a relation between the values of $\Delta(\nu_{as}- \nu_s)$, in cm^{-1} , and the structure of the carboxylato anion. This was based on a theoretical approach derived from the *Ab initio* molecular orbital calculations of the vibrational frequencies of the carboxylate groups in different compounds [216, 217]:

$$\Delta(\nu_{as}- \nu_{as}) = 1818.1\ \delta r + 16.47(\theta_{OCO} - 120) + 66.8 \qquad (3.\ 3)$$

where δr is the difference between the two CO bond lengths in (Å) and (θ_{OCO}) is the (O-C-O) angle in (°)[164].

The correlation between δr and $\Delta(\nu_{as}- \nu_s)$ is rationalised by examining the vibrational patterns in the (COO^{-}) anti-symmetric and symmetric stretching modes. The correlation between (θOCO) and $\Delta(\nu_{as}- \nu_s)$ is considered to originate mainly from the following two factors. One is the change in the interaction force constant between the stretches of the two CO bonds. As (θ_{OCO}) becomes smaller, this interaction force constant becomes larger. The other factor is the change in the

mixing of the (O-C-O) bond and the (C-C) stretch with the (COO^-) symmetric stretch. The (OCO) bond and the (C-C) stretch are more strongly mixed with the (COO^-) symmetric stretch in a species having a smaller value of (θ_{OCO}). Since the strong mixing of these vibrations raises the frequency of the (COO^-) symmetric stretch, $\Delta(\nu_{as}- \nu_s)$ decreases as (θ_{OCO}) becomes smaller.

(3.16.1) Relationship between the structures and the COO^- stretching frequencies of the carboxylato group

The optimised structures, bond lengths and bond angles, of the carboxylate group for the L^3 and L^5 complexes are shown in Table (3. 37). Molecular modelling of the proposed structures of the complexes was performed using CS Chem 3D Ultra Molecular Modelling and Analysis Program [160]. The optimised structures have been obtained on the assumption that the carboxylato moiety is bound to the metal ion in the bridging mode.

Carboxylate group can adopt many types of bridging conformations, the most important being the *syn-syn*, *syn-anti* and *anti-anti* (see Scheme 3.15).

The aim of this theoretical calculation is; to investigate the applicability of Equation (3-3) in the prediction of the $\Delta(\nu_{as}- \nu_s)$ values of the carboxylato group upon complex formation; and to validate the bridging conformations mode of the carboxylato group upon complex formation, based on the experimental values.

The relationship stated in Equation (3. 3) was applied to calculate the $\Delta(\nu_{as}- \nu_s)$ of the carboxylato group of the L^1 and L^5 metal complexes. Results show there is a difference in the Δ value compared with the experimental one, (see Table 3. 37). $[Fe(L^5)(N_3)_4].H_2O$ complex has been used as an example for L^5 complexes to calculate the $\Delta(\nu_{as}- \nu_s)$ value of the carboxylate group.

The carboxylato ligands in the Fe-complex are not equivalent and the pairs of bridges differ in C–O distances (1.208 and 1.3381 Å), indicating that the (COO^-) group is anti-symmetric, and O–C–O angles (102.096 º and 123.616 º), Scheme (3-16).

Carboxylato 1 Carboxylato 2

Scheme (3. 16) Optimised structures of the carboxylate moieties interacting with Fe^{2+}

The values of the $\Delta(\nu_{as}- \nu_s)$ of the carboxylate groups can be calculated as follows:

$\Delta(\nu_{as}- \nu_s)_1 = 1818.1\ \delta r + 16.47(\theta_{OCO} - 120) + 66.8$ (1)

$= 1818.1(1.338 - 1.208)+16.47(115.044-120)+66.8$

$= 1818.1(0.130) + 16.47(-4.956)+66.8$

$= 236.353-81.625+66.8$

$= 221.52\ cm^{-1}$

$\Delta(\nu_{as}- \nu_s)_2 = 1818.1\ \delta r + 16.47(\theta_{OCO} - 120) + 66.8$ (1)

$= 1818.1(1.338-1.208) + 16.47(115.503 - 120) + 66.8$

$= 1818.1(0.130)+16.47(-4.497) + 66.8$

$= 236.353-74.065 + 66.8$

$= 229.08\ cm^{-1}$

Average = 221.52 + 229.08

= 450.60 ÷ 2

= 225.31 cm^{-1} (calculated value), 212 cm^{-1} (experimental value)

The obtained Δ value of the carboxylato groups indicate that, the (COO^{-}) group is interacting with the Fe^{+2} in the bridging mode. The distances between Fe^{+2} and the two oxygen atoms of the (COO^{-}) group are different by about 0.13 Å. The difference in the bond length refers to the fact that, one of the oxygen atoms interacting to the metal ion stronger than the other one. Contrast to the experimental data, only one value is observed in the spectrum. The existence of two distinct vibration levels may relate to the conjugation effects between pyridyl rings and

carboxylate groups. The non-coplanar orientation between the two pyridyl groups is more favourable than the coplanar orientation, and consequently the electronic charge density in both carboxylato ligands should be different. Therefore two vibrational levels for the non-equivalent carboxylate groups should be expected in line with the two distinct values Δ calc. However, this fact does not agree with the experiment, where only one asymmetric and symmetric stretch was observed. Accordingly, we propose that because the non-equivalent pyridyl-carboxylato parts have the same symmetry, their vibration levels may be also very close. Therefore an interaction may exist between these groups originating to only one pair of the bands $\nu_{as}(COO^{-})$ and $\nu_{s}(COO^{-})$ in the IR spectrum. This assumption agrees well with the calculated and experimental of the Δ value. The calculation gave Δcalc = 225.31 cm^{-1}. The experimental value is very close to the calculated one, Δexp = 212 cm^{-1}. Other complexes that have large differences between the calculated and experimental value in the $\Delta(\nu_{as}- \nu_{s})$ can be attributed to the substantial asymmetric in (COO^{-}) group, which is induced by a stronger interaction with metal ions upon complexation.

Calculation on the other carboxylate ions with large n-alkyl chains may useful information on this problem, because the (COO^{-}) symmetric stretch is more or less mixed with the neighbouring (C-C) stretch, which is likely to be influenced by vibrations of the group bonded to the (C-C) bond or even by those of farther groups.

Table (3. 37) Calculated frequencies (in cm^{-1}) of the COO-symmetric and anti-symmetric stretches of the acetate ion interacting with metal ions

Compound	Bond length1 L1 (Å)	Bond length2 L2 (Å)	L2-L1	Bond angle (°)	$\Delta \nu_{as}$-ν_s	Experimental value	Calculated value
$[Cr_2(L^5)(N_3)_4]Cl_2.H_2O$	1.388	1.208	0.130	115.1308	222.9573	203	222.9573
$[Mn_2(L^5)(N_3)_4].H_2O$	1.3595 1.3592	1.1908 1.2031	0.1687 0.1561	114.927 114.997	289.9612 268.206	186	279.08358
$[Fe_2(L^5)(N_3)_4].H_2O$	1.388 1.388	1.208 1.208	0.13 0.13	115.0448 115.503	221.5409 229.0874	212	225.3141
$[Co_2(L^5)(N_3)_4].H_2O$	1.338 1.3583	1.208 1.2743	0.13 0.084	120.126 116.966	305.2282 169.5504	222	237.38932
$[Ni_2(L^5)(N_3)_4].H_2O$	1.3381 1.338	1.208 1.208	1.1301 0.13	123.6156	362.8837 7.8294	193	185.3565
$[Cu_2(L^5)(N_3)_4].H_2O$	1.338 1.338	1.208 1.208	0.13 0.13	116.579 115.65	246.8091 231.5085	189	239.1588
$[Zn_2(L^5)(N_3)_4].H_2O$	1.338 1.338	1.208 1.208	0.13 0.13	118.76 115.625	282.7302 231.0968	191	256.9134
$[Cd_2(L^5)(N_3)_4].H_2O$	1.3608 1.338	1.2202 1.208	0.1406 0.13	116.97 118.779	272.5208 283.0431	181	277.7819
$Na_2[Ag_2(L^5)(N_3)_4].H_2O$	1.357 1.36	1.2276 1.218	0.1294 0.142	117.109 115.78	254.4474 255.4668	209	254.9570
$[Cr_2(L^3)(N_3)_4]Cl_2.H_2O$	1.355 1.338	1.121 1.233	0.234 0.105	104.93 112.97	244.0325 141.9164	200	192.97445
$[Mn_2(L^3)(N_3)_4].2H_2O$	1.338 1.344	1.251 1.208	0.087 0.136	116.74 114.61	171.2825 225.2883	191	198.2845
$[Fe_2(L^3)(N_3)_4].H_2O$	1.338 1.338	1.208 1.208	0.13 0.13	115.91 114.44	235.7907 211.5798	217	223.68525
$[Co_2(L^3)(N_3)_4].H_2O$	1.359 1.327	1.251 1.221	0.108 0.106	114.78 117.81	177.1814 223.4493	191	200.31535
$[Ni_2(L^3)(N_3)_4].H_2O$	1.344 1.338	1.1197 1.1201	0.2243 0.2179	102.7308 102.738	190.1761 178.6589	189	184.417478
$[Cu_2(L^3)(N_3)_4]$	1.341 1.338	1.208 1.221	0.133 0.117	117.25 114.96	263.3148 196.5089	216	229.91185
$[Zn_2(L^3)(N_3)_4].H_2O$	1.328 1.328	1.201 1.208	0.127 0.130	118.21 113.11	268.2174 189.6747	195	228.94605
$[Cd2(L^3)(N3)4].H_2O$	1.338 1.360	1.228 1.208	0.110 0.152	118.96 112.31	249.6622 216.4969	183	233.07955
$Na_2[Ag_2(L^3)(N_3)_4].H_2O$	1.338 1.3608	1.207 1.208	0.131 0.1528	116.37 111.69	245.185 207.74	166	226.46249

(3.17) Molar conductance measurements

Table (3. 38) displays the molar conductance data of the prepared complexes. Conductance measurement values of all complexes, except Cr^{III} and Ag^{I}, in DMSO lie in the range of 6.36 – 22.74 $\Omega^{-1}cm^2mol^{-1}$. These values are too low to account for any dissociation of the complexes in DMSO, indicating their non electrolytes in nature. Conductivity measurements of Cr^{III} and Ag^{I} complexes lie in the 71.41-78.46 Ω^{-1} cm^2 mol^{-1} range, indicating their 1:2 electrolytic behaviour [218].

Table (3. 38) Molar conductivity measurements in DMSO for the Complexes

No	Compound	$\Lambda_M(\Omega^{-1}cm^2mol^{-1})$	Behaviour
1	$[Cr_2(L^1)(N_3)_4]$ $Cl_2.H_2O$	72.11	1:2
2	$[Mn_2(L^1)(N_3)_4].H_2O$	17.13	non-electrolyte
3	$[Fe_2(L^1)(N_3)_4].H_2O$	14.62	non-electrolyte
4	$[Co_2(L^1)(N_3)_4].H_2O$	16.81	non-electrolyte
5	$[Ni_2(L^1)(N_3)_4].H_2O$	18.21	non-electrolyte
6	$[Cu_2(L^1)(N_3)_4].H_2O$	16.62	non-electrolyte
7	$[Zn_2(L^1)(N_3)_4].H_2O$	14.32	non-electrolyte
8	$[Cd_2(L^1)(N_3)_4].H_2O$	17.13	non-electrolyte
9	$Na_2[Ag_2(L^1)(N_3)_4].H_2O$	76.09	1:2
10	$[Cr_2(L^2)(N_3)_4]Cl_2.H_2O$	78.23	1:2
11	$[Mn_2(L^2)(N_3)_4].H_2O$	18.42	non-electrolyte
12	$[Fe_2(L^2)(N_3)_4]$	16.63	non-electrolyte
13	$[Co_2(L^2)(N_3)_4].H_2O$	12.95	non-electrolyte
14	$[Ni_2(L^2)(N_3)_4].H_2O$	22.74	non-electrolyte
15	$[Cu_2(L^2)(N_3)_4].H_2O$	15.57	non-electrolyte
16	$[Zn_2(L^2)(N_3)_4].H_2O$	6.36	non-electrolyte
17	$[Cd_2(L^2)(N_3)_4]$	13.71	non-electrolyte
18	$Na_2[Ag_2(L^2)(N_3)_4].H_2O$	75.12	1:2
19	$[Cr_2(L^3)(N_3)_4]Cl_2.H_2O$	78.46	1:2
20	$[Mn_2(L^3)(N_3)_4].2H_2O$	18.47	non-electrolyte
21	$[Fe_2(L^3)(N_3)_4].H_2O$	12.67	non-electrolyte
22	$[Co_2(L^3)(N_3)_4].H_2O$	17.13	non-electrolyte
23	$[Ni_2(L^3)(N_3)_4].H_2O$	14.78	non-electrolyte
24	$[Cu_2(L^3)(N_3)_4]$	12.11	non-electrolyte
25	$[Zn_2(L^3)(N_3)_4].H_2O$	18.24	non-electrolyte
26	$[Cd_2(L^3)(N_3)_4].H_2O$	11.54	non-electrolyte
27	$Na_2[Ag_2(L^3)(N_3)_4].H_2O$	71.41	1:2

Continued Table (3. 38)			
28	$[Cr_2(L^4)(N_3)_4]Cl_2.H_2O$	73.01	1:2
29	$[Mn_2(L^4)(N_3)_4].H_2O$	31.52	non-electrolyte
30	$[Fe_2(L^4)(N_3)_4]$	15.64	non-electrolyte
31	$[Co_2(L^4)(N_3)_4].H_2O$	19.82	non-electrolyte
32	$[Ni_2(L^4)(N_3)_4].H_2O$	13.46	non-electrolyte
33	$[Cu_2(L^4)(N_3)_4].H_2O$	18.63	non-electrolyte
34	$[Zn_2(L^4)(N_3)_4]$	17.07	non-electrolyte
35	$[Cd_2(L^4)(N_3)_4]$	17.15	non-electrolyte
36	$Na_2[Ag_2(L^4)(N_3)_4] .H_2O$	73.37	1:2
37	$[Cr_2(L^5)(N_3)_4]Cl_2.H_2O$	76.27	1:2
38	$[Mn_2(L^5)(N_3)_4].H_2O$	18.69	non-electrolyte
39	$[Fe_2(L^5)(N_3)_4].H_2O$	18.19	non-electrolyte
40	$[Co_2(L^5)(N_3)_4].H_2O$	13.32	non-electrolyte
41	$[Ni_2(L^5)(N_3)_4] .H_2O$	11.04	non-electrolyte
42	$[Cu_2(L^5)(N_3)_4].H_2O$	12.78	non-electrolyte
43	$[Zn_2(L^5)(N_3)_4].H_2O$	18.66	non-electrolyte
44	$[Cd_2(L^5)(N_3)_4].H_2O$	13.40	non-electrolyte
45	$Na_2[Ag_2(L^5)(N_3)_4].H_2O$	77.18	1:2

(3.18) Conclusion and proposed molecular structure for complexes

(3.18.1) The proposed molecular structure for $[Cr_2(L^1)(N_3)_4]Cl_2.H_2O$, $[Cr_2(L^2)(N_3)_4]Cl_2.H_2O$, $[Cr_2(L^3)(N_3)_4]Cl_2.H_2O$ and $[Cr_2(L^4)(N_3)_4]Cl_2.H_2O$ complexes

According to the following analytical results:

- **I.R spectra**

The I.R spectra for $[Cr_2(L^n)(N_3)_4]Cl_2.H_2O$ complexes (where n = 1-4), Tables (3. 18) to (3. 21) and Figures (3. 40); (3. 49); (3. 58) and (3. 67), show new bands around 2037-2114 cm^{-1} assigned to $\nu_{as}(N_3)$. Bands about 1593-1626 and 1406-1420 cm^{-1} were attributed to the anti-symmetric $\nu_{as}(COO^-)$ and symmetric $\nu_s(COO^-)$ of the carboxylato groups, respectively. These bands are shifted to lower frequency compared with that in the free ligands, due to delocalisation of electronic density of the metal ion into the π-system of the ligands (HOMO → LUMO). The $\Delta(\nu_{as}- \nu_{as})$ value around (181-208) cm^{-1} consistent with carboxylato bridging coordination fashion with the metal atoms in the *syn-syn* mode. These information are supported by theoretical studies conducted to calculate the $\Delta(\nu_{as}- \nu_s)$ of the acetate group, in which the mode of the carboxylato binding can be predicted from the magnitude of the separation between the carboxylato stretches, $\Delta(\nu_{as}- \nu_s)$. Bands detected about 1335-1369 cm^{-1} attributed to $\nu_s(N_3)$. Bands around 532-588 cm^{-1} were assigned to ν(M-O), while bands about 419-499 cm^{-1} were attributed to ν(M-N). The insolubility behaviour of the complexes in most organic solvent may indicate the formation of polymeric structures.

- **UV-Vis spectra and magnetic moments**

The UV-Vis spectral data for $[Cr_2(L^n)(N_3)_4]Cl_2.H_2O$ complexes (where n = 1-4), Tables (3. 23) to (3. 26) and Figures (3. 85); (3. 94); (3. 103) and (3. 112), display peaks around 263-287 nm assigned to intraligand field in the complexes. Peaks detected at the visible region around 356-467 nm assigned to $^4A_2g^{(F)} \rightarrow {}^4T_1g^{(F)}$ (ν_1), while peaks observed about 604-670 nm assigned to $^4A_2g^{(F)} \rightarrow {}^4T_2g^{(F)}$ (ν_2), indicating

an octahedral geometry about Cr atom. These complexes show magnetic moment values in the range of 1.84-2.61 B.M, Table (3. 34) which are lower than the total spin-only values (see Table 3.35), supported octahedral geometry around Cr atom [(202)]. The lowering of these magnetic moments may suggest dominant antiferromagnetic interactions in all complexes. This may due to the fact that the *syn-syn* carboxylato bridges provide a small metal-metal distance and resulted in a good overlap of the magnetic orbitals, an antiferromagnetic coupling is always induced[(203)]. For the EO azido bridge, previous theoretical studies on metal complexes [(163)] indicated that the main factor controlling the exchange should be the M-N-M bridging angle *Φ*: a crossover between ferro- and antiferromagnetic interactions occurs at *Φ* 98°, and the antiferromagnetic interaction increases below *Φ* 98°. The maximum ferromagnetic interaction appears at *Φ* 114°.

- **Conductivity measurements**

The molar conductance of complexes in DMSO lie in the range 72.11 – 78.46 $\Omega^{-1}cm^2mol^{-1}$, Table (3. 38), indicating their electrolyte nature with a 1:2 ratio[(218)].

- **Elemental microanalysis**

The elemental microanalysis (C.H.N) along with metal analysis (A.A), and chloride content results for the complexes Tables (3. 9), (3. 11), (3. 13) and (3. 15) are in good agreement with the calculated values. These data supported the formation of complexes and helped in verifying the suggested formula of the complexes. These data predicated a six coordinate environment about Cr atom in the $[Cr_2(L^n)(N_3)_4]Cl_2.H_2O$ complexes, where n = 1-4.

- **^{1}H- ^{13}C- and DEPT ^{13}C NMR**

The ^{1}H- ^{13}C- and DEPT ^{13}C NMR spectroscopy of diamagnetic complexes were used to confirm the formation of the complexes. The ^{1}H-, ^{13}C- and DEPT ^{13}C-NMR spectra of the ligands in DMSO-d6 displayed signals corresponding to the various proton and carbon nuclei consistent with the proposed structural formula. The NMR

data of complexes in DMSO-d6 showed peaks of coordinated ligand, shifted downfield, indicating the formation of the complexes.

- **Mass spectrum**

The mass spectra of the ligands were also consistent with the proposed structural formula. The positive mass spectrum for selected complexes showed several peaks corresponding to successive fragmentation of the molecule.

- **Thermal gravimetric analysis**

This technique was used to show thermal stability and chemical composition of compounds, which helped in the characterisation of complexes.

- **Molecular modelling**

3D molecular modelling of the proposed structure of the complexes was performed using CS Chem 3D Ultra Molecular Modelling and Analysis Program[160]. This interactive graphics program allows rapid structure building, geometry optimisation with minimum energy and molecular display. Bond lengths and bond angles of the suggested structure are shown in Table (3.39). Figure (3.177) depicts a general polymeric structure for the complexes. The proposed octahedral monomeric structure for $[Cr_2(L^1)(N_3)_4]Cl_2.H_2O$ complex is shown in Figure (3.178).

(3.18.2) The proposed molecular structure for $[Mn_2(L^1)(N_3)_4]H_2O$, $[Mn_2(L^2)(N_3)_4]H_2O$, $[Mn_2(L^3)(N_3)_4]2H_2O$, $[Mn_2(L^4)(N_3)_4]H_2O$, $[Fe_2(L^1)(N_3)_4]H_2O$, $[Fe_2(L^2)(N_3)_4]$, $[Fe_2(L^3)(N_3)_4]$, $[Fe_2(L^4)(N_3)_4]$, $[Co(L^1)(N_3)_4]H_2O$, $[Co_2(L^2)(N_3)_4]H_2O$,$[Co_2(L^3)(N_3)_4]H_2O$,$[Co_2(L^4)(N_3)_4]H_2O$, $[Ni_2(L^1)(N_3)_4]H_2O$,$[Ni_2(L^2)(N_3)_4)]H_2O$,$[Ni_2(L^3)(N_3)_4]H_2O$, $[Ni_2(L^4)(N_3)_4]H_2O$, $[Cu_2(L^1)(N_3)_4]H_2O$, $[Cu_2(L^2)(N_3)_4]H_2O$, $[Cu_2(L^3)(N_3)_4]$, $[Cu_2(L^4)(N_3)_4]H_2O$, $[Zn_2(L^1)(N_3)_4]H_2O$,$[Zn_2(L^2)(N_3)_4]H_2O$, $[Zn_2(L^3)(N_3)_4]H_2O$, $[Zn_2(L^4)(N_3)_4]$, $[Cd_2(L^1)(N_3)_4]H_2O$, $[Cd_2(L^2)(N_3)_4]$, $[Cd_2(L^3)(N_3)_4]H_2O$, $[Cd_2(L^4)(N_3)_4]$ complexes: According to the results shown below:

- **I.R spectra**

The I.R spectra for these complexes, Tables (3-18) to (3-21), Figures (3-41), (3. 50), (3. 59), (3. 68), (3. 42), (3. 51), (3.60), (3. 69), (3. 43), (3. 52), (3. 61),

(3. 70), (3. 44), (3. 53), (3. 62) , (3.71), (3. 45), (3. 54), (3. 63), (3. 72), (3. show new bands around 2114-2037 cm^{-1} assigned to $\nu_{as}(N_3)$. Band about 1591-1629 and 1404-1462 cm^{-1} were attributed to the anti-symmetric to $\nu_{as}(COO^{-})$ and symmetric $\nu_s(COO^{-})$ of the carboxylato groups, respectively. These bands are shifted to lower or to higher frequency compared with that in the free ligands, if it shifted to lower frequency due to delocalisation of electronic density of the metal ion into the π-system of the ligands (HOMO-LUMO), while if it shifted to higher due to weak coordination between the metal ion and the ligand. The $\Delta(\nu_{as}- \nu_s)$ value around (183-217) cm^{-1} consistent with carboxylato bridging coordination fashion with the metal atoms in the *syn-syn* mode, except CoL^1 in *syn-anti* mode. These information are supported by theoretical studies conducted to calculate the $\Delta(\nu_{as}- \nu_s)$ of the acetate group, in which the mode of the carboxylato binding can be predicted from the magnitude of the separation between the carboxylato stretches, $\Delta(\nu_{as}- \nu_s)$. Bands detected about 1298-1369 cm^{-1} attributed to $\nu_s(N_3)$.. Bands around 498-627 were assigned to ν(M-O), while bands at 401-499 were attributed to ν(M-N). The insolubility behaviour of the complex in most organic solvent may indicate the formation of polymeric structures.

- **UV-Vis spectra and magnetic momments**

The UV-Vis spectral data for these complexes, Tables (3. 23) to (3. 26), Figures (3. 86), (3. 95), (3. 104), (3. 113), (3. 87), (3. 96), (3. 105), (3. 114), (3. 88), (3. 97), (3. 106), (3. 115), (3. 89), (3. 98), (3. 107), (3. 116), (3. 90), (3. 99), (3. 108), (3. 117), (3. 91), (3. 100), (3. 109), (3. 118) , (3. 92), (3. 101), (3. 110) and (3. 119), display peaks at range 259-278 nm assigned to ligand field and intraligand in these complexes. Peaks detected at the 303-379 nm assigned to charge transfer. Peaks detected at the visible are different from the complexes and all the transition refer to octahedral structures. These complexes show magnetic moment values in the range of 0.71-3.03B.M, Table (3. 34) which are lower than the total spin-only values (see Table 3.35), supported octahedral geometry around Mn atom[(202)]. The lowering of

these magnetic moments may suggest dominant antiferromagnetic interactions in all complexes. The carboxylate groups are in the *syn-syn* bridging mode, and assuming that the antiferromagnetic behavior is mainly due to intrachain exchange interactions through the carboxylato bridge.

- **Conductivity measurements**

The molar conductance of complexes in DMSO lie in the range 6.36–22.74 $\Omega^{-1}cm^2mol^{-1}$, Table (3. 38), indicating their nonelectrolyte.

- **Elemental microanalysis**

The elemental microanalysis (C.H.N) along with metal analysis (A.A), and chloride content results for the complexes, Table (3. 9), (3. 11), (3. 13) and (3. 15) are in good agreement with the calculated values. These data supported the formation of complexes and helped in verifying the suggested formula of the complexes. These data predicted a six coordinate environment about M^{II} atom in the complexes.

- **^{1}H- ^{13}C- and DEPT ^{13}C NMR**
- **Mass spectrum**
- **Thermal gravimetric analysis**
- **Molecular modelling**

3D molecular modelling of the proposed structure of the complexes was performed using CS Chem 3D Ultra Molecular Modelling and Analysis Program[(160)]. This interactive graphics program allows rapid structure building, geometry optimisation with minimum energy and molecular display. Bond lengths and bond angles of the suggested structure are shown in Table (3.40-3.46). Figure (3.174-3.180) depicts a general polymeric structure for the complexes. The proposed octahedral monomeric structure for selected complexes is shown in Figures (3.179-3.185).

(3.18.3) The proposed molecular structure for $Na_2[Ag_2(L^1)(N_3)_4]H_2O$, $Na_2[Ag_2(L^2)(N_3)_4]H_2O$, $Na_2[Ag_2(L^3)(N_3)_4)]H_2O$, $Na_2[Ag_2(L^4)(N_3)_4]H_2O$ complexes:

According to the results shown below:

-

- **I.R spectra**

The I.R spectra for $Na_2[Ag_2(L^n)(N_3)_4]H_2O$ (where n=1-4) complexes, Tables (3. 18) to (3. 21), Figures (3. 48), (3. 57), (3. 66) and (3. 75) show new bands about 2095-2045 cm^{-1} assigned to $\nu_{as}(N_3)$. Bands about 1628-1591 and 1406-1462 cm^{-1} were attributed to the anti-symmetric $\nu_{as}(COO^-)$ and symmetric $\nu_s(COO^-)$ of the carboxylato groups, respectively. These bands are shifted to lower frequency compared with that in the free ligands, due to delocalisation of electronic density of the metal ion into the π-system of the ligands (HOMO-LUMO). The $\Delta(\nu_{as}- \nu_s)$ value around (185-194) cm^{-1} consistent with carboxylato bridging coordination fashion with the metal atoms in the *syn-syn* mode. These information are supported by theoretical studies of IR vibration pf carboxylate group. Bands detected about 1302-1361 cm^{-1} attributed to $\nu_s(N_3)$. Bands at range 498-586 cm^{-1} were assigned to ν(M-O), while bands about 419-483 cm^{-1} were attributed to ν(M-N). The insolubility behaviour of the complexes in most organic solvent may indicate the formation of polymeric structure.

- **UV-Vis spectra and magnetic moments**

The UV-Vis spectral data for $Na_2[Ag_2(L^n)(N_3)_4]H_2O$ (where n=1-4) complexes, Tables (3. 23), (3-24), (3-25) and (3-26), Figure (3. 93), (3. 102), (3. 111) and (3. 120), display peaks at range (264-267) nm assigned to ligand field and intraligand in the complexes. The peaks at range (307-372) nm assigned to charge transfer. The peaks at the visible region are different from the complexes and all the transition refer to octahedral structure. The magnetic moment of Ag^I complexes show small values due to d^{10}.

- **Conductivity measurements**

The molar conductance of $Na_2[Ag_2(L^n)(N_3)_4]H_2O$ (where n=1-4) complexes in DMSO lie in the range 71.41-77.18 $\Omega^{-1}cm^2mol^{-1}$, Table (3. 38), indicating their electrolyte with 1:2 ratio[218].

- **Elemental microanalysis**

The elemental microanalysis (C.H.N) along with metal analysis (A.A), and chloride content results for the complexes Table (3. 9), (3. 11), (3. 13) and (3. 15) are in good agreement with the calculated values. These data supported the formation of complexes and helped in verifying the suggested formula of the complexes. These data predicted a six environment about Ag^I atom in the complexes.

- **Molecular modelling**

3D molecular modelling of the proposed structure of the complexes was performed using CS Chem 3D Ultra Molecular Modelling and Analysis Program[160]. This interactive graphics program allows rapid structure building, geometry optimisation with minimum energy and molecular display. Bond lengths and bond angles of the suggested structure are shown in Table (3.47). Figure (3.181) depicts a general polymeric structure for the complexes. The proposed octahedral monomeric structure for $Na_2[Ag_2(L^1)(N_3)_4]H_2O$ complex is shown in Figure (3.186).

(3.18.4) The proposed molecular structure for $[Cr_2(L^5)(N_3)_4]Cl_2.H_2O$ complexes

According to the results shown below:

- **I.R spectra**

The I.R spectra for $[Cr_2(L^5)(N_3)_4]Cl_2.H_2O$ complex, Tables (3. 22), Figure (3. 76), show new bands at 2043 cm^{-1} assigned to $\nu_{as}(N_3)$. Bands at 1601 and 1398 cm^{-1} were attributed to anti-symmetric $\nu_{as}(COO^-)$ and symmetric $\nu_s(COO^-)$ of carboxylato groups, respectively. These bands are shifted to lower frequency in compared with that in the free ligands, due to delocalisation of electronic densitym of the metal ion into the π-system of the ligands (HOMO-LUMO). The $\Delta(\nu_{as}- \nu_s)$

value around (203) cm^{-1} consistent with carboxylato bridging coordination fashion with the metal atoms in the *syn-syn* mode. These information are supported by theoretical studies of IR vibration pf carboxylate group. Bands detected at 1319 cm^{-1} attributed to $\nu_s(N_3)$. Bands around 530 and 565 cm^{-1} were assigned to ν(M-O), while bands about 467 and 494 cm^{-1} can be attributed to ν(M-N). The insolubility behaviour of the complexes in most organic solvent may indicate the formation of polymeric structure.

UV-Vis spectra and magnetic momments

The UV-Vis spectral data for the complexes $[Cr_2(L^5)(N_3)_4]Cl_2.H_2O$, Table (3. 27), Figure (3. 121), display peak at 269 nm can be assigned to intraligand in the complex. The peaks at the visible region around (356 nm) in assigned to $^4A_2g^{(F)} \rightarrow {}^4T_1g^{(F)}$ (v_1) (calc), while peaks at 637 nm assigned to $^4A_2g^{(F)} \rightarrow {}^4T_2g^{(F)}$ transition in octahedral structure. We can use the same method that used to explanation CrL^1 complex.

- **Conductivity measurements**

The molar conductance of $[Cr_2(L^5)(N_3)_4]Cl_2.H_2O$ complex in DMSO lie in the range 76.27 $\Omega^{-1}cm^2mol^{-1}$, Table (3. 38), indicating their electrolyte with 1:2 ratio[214].

- **Elemental microanalysis**

The elemental microanalysis (C.H.N) along with metal analysis (A.A), and chloride content results for the complex Table (3. 17), is in good agreement with the calculated values. These data supported the formation of complexes and helped in verifying the suggested formula of the complexes. These data predicted a six environment about Cr atom in the complexes.

- **Molecular modelling**

3D molecular modelling of the proposed structure of the complexes was performed using CS Chem 3D Ultra Molecular Modelling and Analysis Program[160]. This interactive graphics program allows rapid structure building, geometry optimisation with minimum energy and molecular display. Bond lengths and bond angles of the suggested structure are shown in Table (3.48). Figure (3.181) depicts a

general polymeric structure for the complexes. The proposed octahedral monomeric structure for $[Cr_2(L^1)(N_3)_4]Cl_2.H_2O$ complex is shown in Figure (3.187).

(3.18.5) The proposed molecular structure for $[Mn_2(L^5)(N_3)_4]H_2O$, $[Fe_2(L^5)(N_3)_4]H_2O$, $[Co_2(L^5)(N_3)_4]H_2O$, $[Ni_2(L^5)(N_3)_4]H_2O$, $[Cu_2(L^5)(N_3)_4]$ H_2O, $[Zn_2(L^5)(N_3)_4]H_2O$, $[Cd_2(L^5)(N_3)_4]H_2O$ complexes:

According to the results shown below:

- **I.R spectra**

The I.R spectra for $[M_2(L^5)(N_3)_4]H_2O$ complexes (where M = Mn, Fe, Co, Ni, Cu, Zn and Cd) complexes, Table (3. 22), Figures (3. 77 to 3. 83), show new bands at 2037-2104 cm^{-1} assigned to $\nu_{as}(N_3)$. Bands about 1609-1618 and 1394-1433 cm^{-1} were attributed to anti-symmetric $\nu_{as}(COO^{-})$ and symmetric $\nu_s(COO^{-})$ of the carboxylato groups, respectively. These bands are shifted to lower frequency compared with that in the free ligands, due to delocalisation of electronic density of the metal ion into the π-system of the ligands (HOMO-LUMO). The $\Delta(\nu_{as}- \nu_s)$ value around (181-222) cm^{-1} consistent with carboxylato bridging coordination fashion with the metal atoms in the *syn-syn* mode. These information are supported by theoretical studies of IR vibration pf carboxylate group. Bands detected about 1302-1354 cm^{-1} attributed to $\nu_s(N_3)$. Bands around 505-604 cm^{-1} were assigned to ν(M-O), while bands about 409-494 cm^{-1} can be attributed to ν(M-N). The insolubility behaviour of the complexes in most organic solvent may indicate the formation of polymeric structure.

UV-Vis spectra and magnetic momments

The UV-Vis spectral data for the complexes $[M_2(L^5)(N_3)_4]H_2O$ complexes (where M = Mn, Fe, Co, Ni, Cu, Zn and Cd), display peaks at 257-270 nm assigned to ligand field and intraligand in the complexes. Peaks detected at 315-405 nm

assigned to charge transfer in these complexes. The peaks at the visible region are different from the complexes and all transition refer to octahedral structure. We can use the same method that used to explanation MnL^1 complex.

- **Conductivity measurements**

The molar conductance of $[M(L^5)(N_3)_4]H_2O$ complexes (where M=Mn, Fe, Co, Ni, Cu, Zn and Cd) complexes, in DMSO lie in the range 11.04-18.69 $\Omega^{-1}cm^2mol^{-1}$, Table (3. 38), indicating their nonelectrolyte.

- **Elemental microanalysis**

The elemental microanalysis (C.H.N) along with metal analysis (A.A), and chloride content results for the complex Table (3. 17), is in good agreement with the calculated values. These data supported the formation of complexes and helped in verifying the suggested formula of the complexes. These data predicted a six environment about Cr atom in the $[M_2(L^5)(N_3)_4]H_2O$ complexes (where M = Mn, Fe, Co, Ni, Cu, Zn and Cd) complexes.

- **Mass spectrum**
- **Thermal gravimetric analysis**
- **Molecular modelling**

3D molecular modelling of the proposed structure of the complexes was performed using CS Chem 3D Ultra Molecular Modelling and Analysis Program(160). This interactive graphics program allows rapid structure building, geometry optimisation with minimum energy and molecular display. Bond lengths and bond angles of the suggested structure are shown in Table (3.49). Figure (3. 183) depicts a general polymeric structure for the complexes. The proposed octahedral monomeric structure for $[Mn_2(L^5)(N_3)_4]H_2O$ complex is shown in Figure (3.188).

(3.18.6) The proposed molecular structure for $Na_2[Ag_2(L^5)(N_3)_4].H_2O$ complex:

According to the results shown below:

- **I.R spectra**

The I.R spectra for $Na_2[Ag_2(L^5)(N_3)_4].H_2O$ complex, Tables (3. 22.), Figure (3-84), show new bands at 2045 and 2083 cm^{-1} assigned to $\nu_{as}(N_3)$. Bands at 1609 and 1400 cm^{-1} were attributed to anti-symmetric $\nu_{as}(COO^{-})$ and symmetric $\nu_s(COO^{-})$ of the carboxylato groups, respectively. These bands are shifted to lower frequency compared with that in the free ligand, due to delocalisation of electronic density of the metal ion into the π-system of the ligands (HOMO-LUMO). The $\Delta(\nu_{as}- \nu_s)$ value around (209) cm^{-1} consistent with carboxylato bridging coordination fashion with the metal atoms in the *syn-syn* mode. These information are supported by theoretical studies of IR vibration of carboxylate group. Bands detected about 1315 cm^{-1} attributed to $\nu_s(N_3)$. Bands around 513 and 571 cm^{-1} were assigned to ν(M-O), while bands at 419 and 455 cm^{-1} can be attributed to ν(M-N). The insolubility behaviour of the complexes in most organic solvent may indicate the formation of polymeric structure.

UV-Vis spectra and magnetic momments

The UV-Vis spectral data for $Na_2[Ag_2(L^5)(N_3)_4].H_2O$ complex, Table (3. 27), display peak at (266) nm assigned to the ligand field in the complex. We can use the same method that used to explanation AgL^1 complex.

- **Conductivity measurements**

The molar conductance of $Na_2[Ag_2(L^5)(N_3)_4].H_2O$ complex in DMSO lie in the range 77.18 $\Omega^{-1}cm^2mol^{-1}$, Table (3.38), indicating their electrolyte nature with a 2:1 ratio.

- **Elemental microanalysis**

The elemental microanalysis (C.H.N) along with metal analysis (A.A), and chloride content results for the complex Table (3. 17), is in good agreement with the calculated values. These data supported the formation of complexes and helped in

verifying the suggested formula of the complexes. These data predicted a six environment about Ag atom in the $Na_2[Ag_2(L^5)(N_3)_4].H_2O$ complex.

- **Molecular modelling**

3D molecular modelling of the proposed structure of the complexes was performed using CS Chem 3D Ultra Molecular Modelling and Analysis Program[(160)]. This interactive graphics program allows rapid structure building, geometry optimisation with minimum energy and molecular display. Bond lengths and bond angles of the suggested structure are shown in Table (3.50). Figure (3.184) depicts a general polymeric structure for the complexes. The proposed octahedral monomeric structure for $Na_2[Ag_2(L^5)(N_3)_4].H_2O$ complex is shown in Figure (3.189).

The proposed structure of all complexes can be draw at following structure Figure (3. 177):

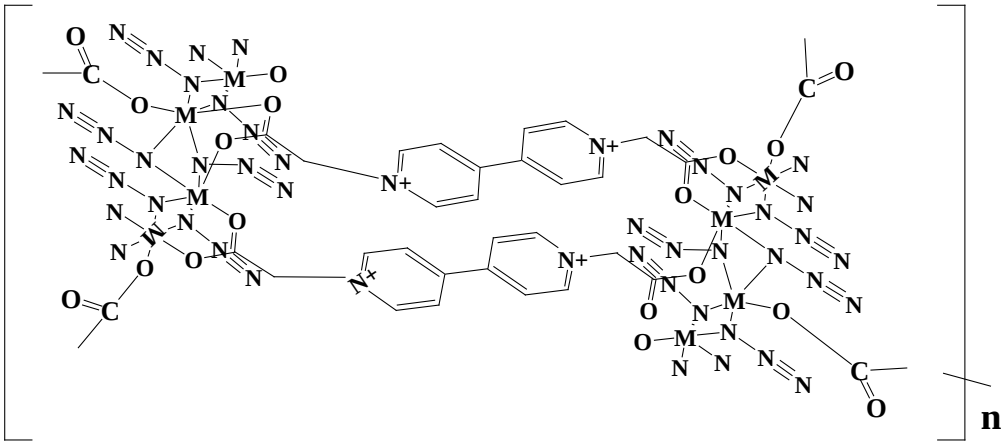

Figure (3. 177) The proposed polymeric structure of complexes

(3-19) **3D molecular modelling and analysis of bonding modes**

Molecular mechanics attempts to reproduce molecular geometries, energies and other features. This is based on adjusting bond lengths, bond angles and torsion angles to equilibrium values that are dependent on the hybridization of an atom and its bonding scheme. In order to obtain estimates of structural details of these complexes and in view the coordination of all complexes; we have optimised the molecular structure of selected complexes of different ligands. For example we have chosen $[Cr^{III}_2(L^1)(N_3)_4]Cl_2.H_2O$ for L^1 complexes as a representative compound (Figure 3.178). The details of bond lengths and bond angles per the 3D molecular structure are given in Tables (3.39). Energy minimisation was repeated several times to find the global minimum [(219)]. The energy minimisation value for octahedral and without restricting the structure for the Cr-complex is almost same i.e, 124.0233 Kcal /mol. The molecular modelling for the modulated Cr(III)-complex indicates the distorted octahedral geometry around Cr(II) ion[(220)]. Energy minimisation of other complexes for different ligands was repeated several times to find the global minimum, (Tables 3.51 to 3.55).

Table (3-39) The calculated bond lengths and bond angles of $[Cr_2(L^1)(N_3)_4]Cl_2.H_2O$

Type of Bond	Bond length (A°)	Type of Bond	Bond angle (°)
Cr_1-O_1	1.861	C_1-O_1-Cr_1	120.531
Cr_1-N_2	1.856	O_1-Cr_1-N_2	167.369
Cr_1-N_4	1.910	O_1-Cr_1-N_4	93.620
Cr_1-N_3	1.912	O_1-Cr_1-N_3	96.618
Cr_1-N_1	1.876	O_1-Cr_1-N_1	87.811
Cr_1-O_2	1.841	O_1-Cr_1-O_2	84.917
C_1-O_1	1.418	N_2-Cr_1-N_4	89.848
N_4-N_6	1.364	N_2-Cr_1-N_3	95.749
N_3-N_5	1.363	N_2-Cr_1-N_1	90.060
		N_2-Cr_1-O_2	82.695
		N_4-Cr1-N3	85.687
		N_4-Cr_1-N_1	173.706
		N_4-Cr_1-O_2	94.744
		N_3-Cr_1-N_1	88.058
		N_3-Cr_1-O_2	178.387
		N_1-Cr_1-O_2	91.488
		Cr_1-N4-N6	117.436
		Cr_1-N_3-N_5	117.052
		Cr_1-N_4-Cr_2	102.501
		Cr_1-N_3-Cr_2	102.292

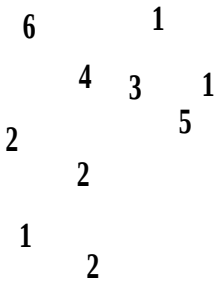

Figure (3-178) The proposed molecular structure of $[Cr_2(L^1)(N_3)_4]Cl_2.H_2O$

Table (3-340) The calculated bond length and bond angle of $[Mn_2(L^1)(N_3)_4].H_2O$

Type of Bond	Bond length (A)	Type of Bond	Bond angle
Mn_1-O_1	1.837	C_1-O_1-Mn_1	118.111
Mn_1-N_2	1.867	O_1-Mn_1-N_2	168.640
Mn_1-N_4	1.881	O_1-Mn_1-N_4	90.341
Mn_1-N_3	1.884	O_1-Mn_1-N_3	93.803
Mn_1-N_1	1.866	O_1-Mn_1-N_1	88.278
Mn_1-O_2	1.830	O_1-Mn_1-O_2	84.435
C_1-O_1	1.407	N_2-Mn1-N_4	93.828
N_4-N_6	1.363	N_2-Mn_1-N_3	97.379
N_3-N_5	1.366	N_2-Mn_1-N_1	89.748
		N_2-Mn_1-O_2	84.578
		N_4-Mn_1-N_3	78.446
		N_4-Mn_1-N_1	168.179
		N_4-Mn_1-O_2	96.919
		N_3-Mn_1-N_1	89.929
		N_3-Mn_1-O_2	175.054
		N_1-Mn_1-O_2	94.632
		Mn_1-N_4-N_6	116.559
		Mn_1-N_3-N_5	115.557
		Mn_1-N_4-Mn_2	99.329
		Mn_1-N_3-Mn_2	99.100

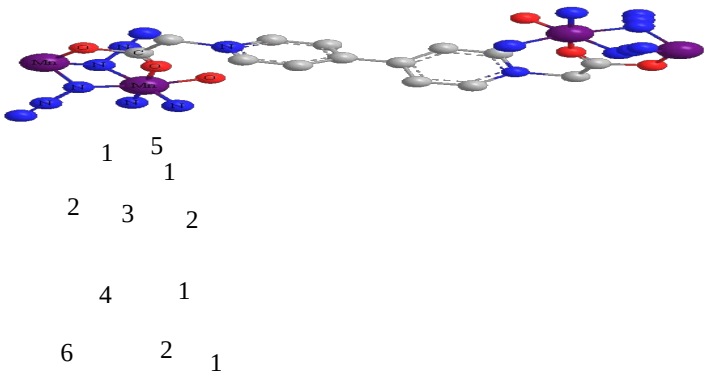

Figure (3-179) The proposed molecular structure of $[Mn_2(L^1)(N_3)_4].H_2O$

Table (3-41) The calculated bond length and bond angle of $[Fe_2(L^2)(N_3)_4]$

Type of Bond	Bond length (A˚)	Type of Bond	Bond angle(˚)
Fe28-O26	1.853	C_1-O_1- Fe_1	112.366
		C_1-Fe_1-N_1	168.397
Fe_1-N_1	1.868	O_1- Fe_1-N_3	101.673
Fe_1-N_3	1.894	O_1-Fe_1-N_4	85.451
Fe_1-N_4	1.889	O_1- Fe_1-N_2	86.711
Fe_1-N_2	1.865	O_1- Fe_1-O_2	86.260
Fe_1-O_2	1.810	N_1- Fe_1-N_3	87.204
N_4-N_6	1.360	N_1- Fe_1-N_4	103.322
N_3-N_5	1.360	N_1- Fe_1-N_2	84.412
C_1-O_1	1.375	N_1- Fe_1-O_2	85.713
		N_3- Fe_1-N_4	82.191
		N_3- Fe_1-N_2	171.595
		N_3- Fe_1-O_2	93.721
		N_4- Fe_1-N_2	99.203
		N_4- Fe_1-O_2	169.819
		N_2- Fe_1-O_2	86.202
		Fe_1-N_3-N_5	116.027
		Fe_1-N_4-N_6	114.957
		Fe_1-N_3- Fe_2	93.016
		Fe_1-N_4- Fe_2	93.099

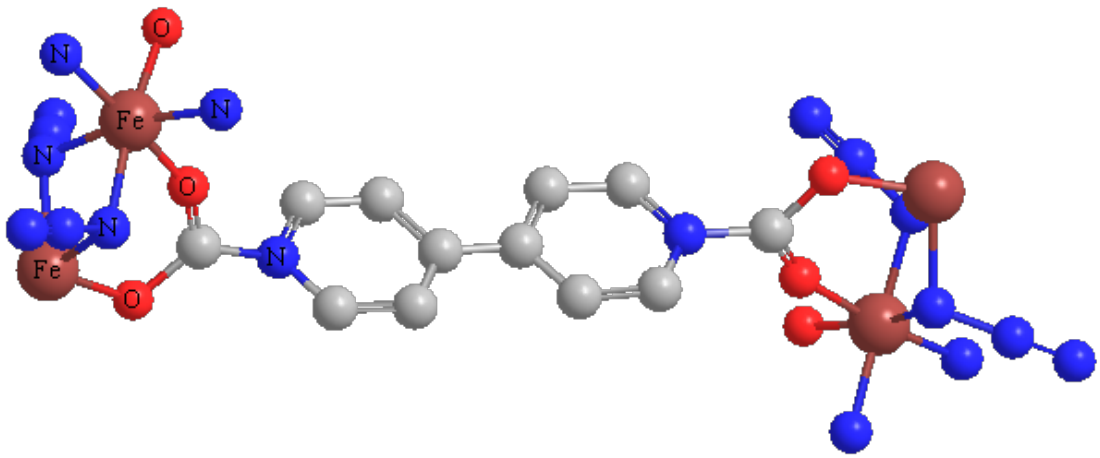

Figure (3-180) The proposed molecular structure of $[Fe_2(L^2)(N_3)_4]$

Table (3-42) The calculated bond length and bond angle of $[Co_2(L^2)(N_3)_4].H_2O$

Type of Bond	Bond length (A˚)	Type of Bond	Bond angle(˚)
Fe28-O26	1.853	C_1-O_1- Co $_1$	114.135
		C_1- Co $_1$-N_1	170.125
Co_1-N_1	1.845	O_1- Co $_1$-N_3	100.458
Co $_1$-N_3	1.859	O_1- Co_1 –N_4	85.968
Co $_1$-N_4	1.885	O_1- Co $_1$-N_2	85.611
Co_1-N_2	1.883	O_1- Co $_1$-O_2	87.666
Co_1-O_2	1.858	N_1- Co_1-N_3	88.659
N_4-N_6	1.359	N_1- Co 1-N_4	99.145
N_3-N_5	1.359	N_1- Co $_1$-N_2	85.632
C_1-O_1	1.375	N1- Co 1-O_2	88.072
		N_3- Co_1-N_4	82.183
		N_3- Co_1-N_2	172.326
		N_3- Co_1-O_2	92.999
		N_4- Co $_1$-N_2	93.651
		N_4- Co_1-O_2	171.179
		N_2- Co_1-O_2	91.936
		Co_1-N_3-N_5	115.936
		Co_1-N4-N_6	115.408
		Co_1-N3- Co_2	93.146
		Co_1-N_4- Co_2	93.174

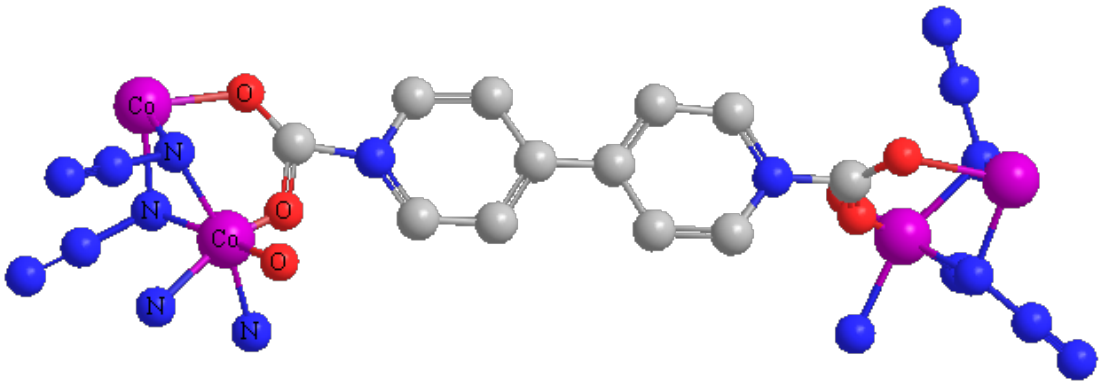

Figure (3-181) The proposed molecular structure of $[Co_2(L^2)\ (N_3)_4].H_2O$

Table (3-43) The calculated bond length and bond angle of $[Ni_2(L^3)(N_3)_4].H_2O$

Type of Bond	Bond length (A°)	Type of Bond	Bond angle(°)
Ni_1-O_1	1.790	C_1-O_1-Ni_1	109.470
Ni_1-N_1	1.826	O_1- Ni_1-N_1	180.00
Ni_1-N_3	1.826	O_1- Ni_1-N_3	89.999
Ni_1-N_4	1.838	O_1- Ni_1-N_4	89.915
Ni_1-N_2	1.826	O_1- Ni_1-N_2	89.993
Ni_1-O_2	1.790	O_1- Ni_1-O_2	89.997
C_1-O_1	1.402	N_1- Ni_1-N_3	90.004
N_3-N_5	1.351	N_1- Ni_1-N_4	90.082
N_4-N_6	1.351	N_1- Ni_1-N_2	90.004
		N_1- Ni_1-O_2	90.004
		N_3- Ni_1-N_4	89.637
		N_3- Ni_1-N_2	104.244
		N_3- Ni_1-O_2	74.103
		N_4- Ni_1-N_2	64.607
		N_4- Ni_1-O_2	163.737
		N_2- Ni_1-O_2	178.355
		Ni_1-N_3-N_5	109.475
		Ni_1-N_4-N_6	109.465
		Ni_1-N_3-Ni_2	90.00
		Ni_1-N_4-Ni_2	89.642

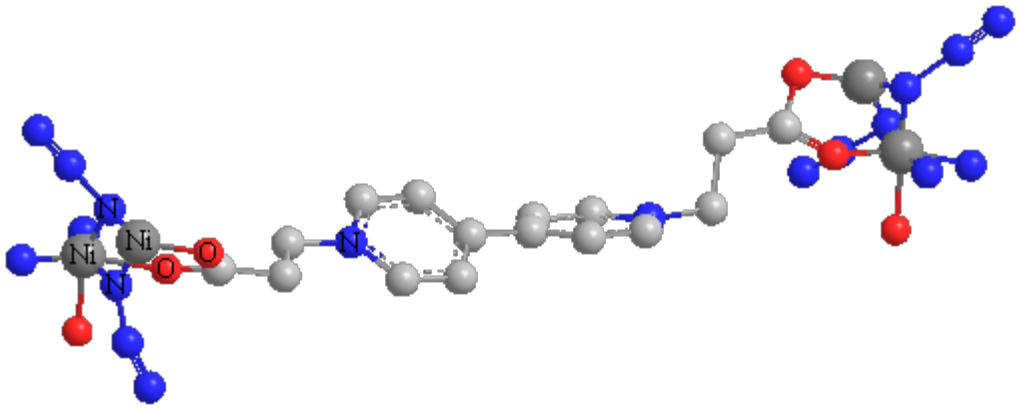

Fig.(3-182) The proposed molecular structure of $[Ni_2(L^3)(N_3)_4].H_2O$

Table (3-44) The calculated bond length and bond angle of $[Zn_2(L^3)(N_3)_4].H_2O$

Type of Bond	Bond length (A°)	Type of Bond	Bond angle (°)
Zn_1-O_1	1.890	C_1-O_1- Zn_1	109.468
Zn_1-N_1	1.926	O_1- Zn_1-N_1	180.00
Zn_1-N_3	1.926	O_1- Zn_1-N_3	90.002
Zn_1-N_4	1.926	O_1- Zn_1-N_4	90.002
Zn_1-N_2	1.926	O_1- Zn_1-N_2	90.002
Zn_1-O_2	1.889	O_1- Zn_1-O_2	90.004
C_1-O_1	1.402	N_1- Zn_1-N_3	89.999
N_3-N_5	1.352	N_1- Zn_1-N_4	90.00
N_4-N_6	1.352	N_1- Zn_1-N_2	90.00
		N_1- Zn_1-O_2	89.993
		N_3- Zn_1-N_4	90.005
		N_3- Zn_1-N_2	76.946
		N_3- Zn_1-O_2	67.089
		N_4- Zn_1-N_2	113.060
		N_4- Zn_1-O_2	157.097
		N_2- Zn1-O_2	144.033
		Zn_1-N3-N_5	109.468
		Zn_1-N_4-N_6	109.474
		Zn1-N3- Zn2	89.995
		Zn1-N4- Zn2	83.148

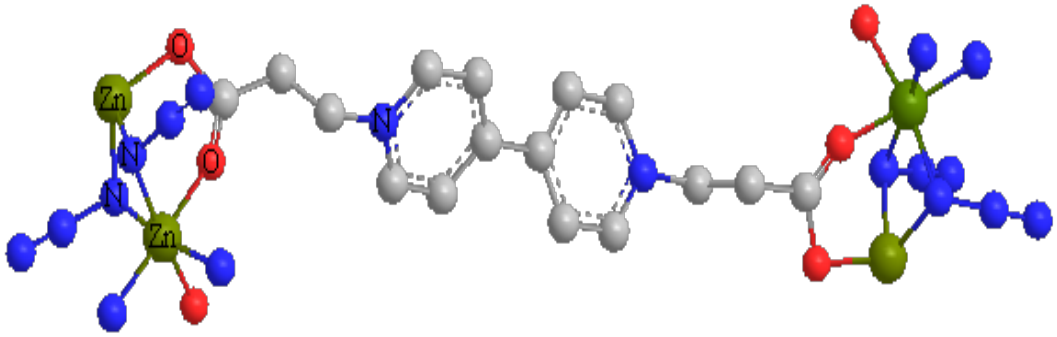

Figure (3-183) The proposed molecular structure of $[Zn_2(L^3)\ (N_3)_4].H_2O$

Table (3-45) The calculated bond length and bond angle of $[Cu_2(L^4)(N_3)_4].H_2O$

Type of Bond	Bond length (A)	Type of Bond	Bond angle
Cu_1-O_1	1.810	C_1-O_1- Cu_1	109.467
Cu_1-N_1	1.845	O_1- Cu_1-N_1	180.00
Cu_1-N_4	1.846	O_1- Cu_1-N_4	89.988
Cu_1-N_3	1.846	O_1- Cu_1-N_3	89.986
Cu_1-N_2	1.846	O_1- Cu_1-N_2	89.988
Cu_1-O_2	1.810	O_1- Cu_1-O_2	89.986
N_3-N_5	1.352	N_1- Cu_1-N_4	90.011
N_4-N_6	1.351	N_1- Cu_1-N_3	90.012
C_1-O_1	1.402	N_1- Cu_1-N_2	90.011
		N_1- Cu_1-O_2	90.011
		N_4- Cu_1-N_3	89.993
		N_4- Cu_1-N_2	9.743
		N_4- Cu_1-O_2	9.717
		N_3- Cu_1-N_2	80.252
		N_3- Cu_1-O_2	80.280
		N_2- Cu_1-O_2	0.000
		Cu_1-N_4-N_6	109.456
		Cu_1-N_3-N_5	109.482
		Cu_1-N_4- Cu_2	105.541
		Cu_1-N3- Cu_2	62.860

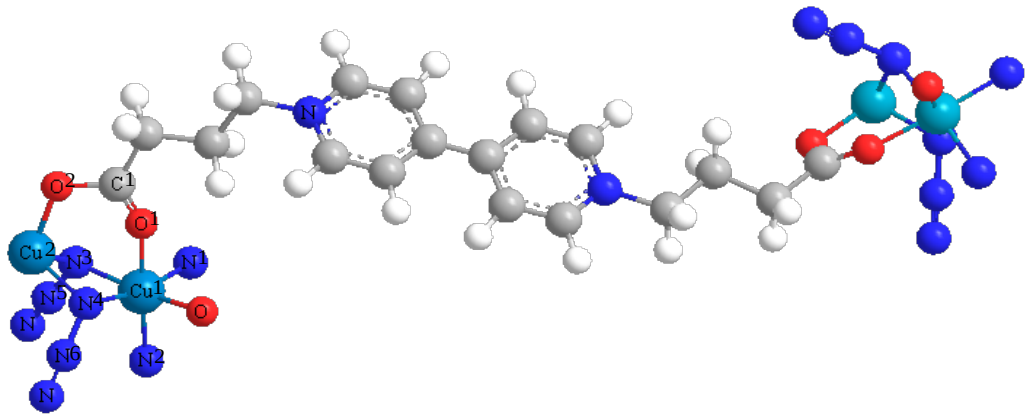

Figure (3-184) The proposed molecular structure of $[Cu_2(L^4)\ (N_3)_4].H_2O$

Table (3-46) The calculated bond length and bond angle of $[Cd_2(L^4)(N_3)_4]$

Type of Bond	Bond length (A˚)	Type of Bond	Bond angle (˚)
Cd_1-O_1	2.120	C_1-O_1- Cd_1	109.465
Cd_1-N_1	2.155	O_1- Cd_1-N_1	180.00
Cd_1-N_4	2.156	O_1- Cd_1-N_4	89.993
Cd_1-N_3	2.156	O_1- Cd_1-N_3	89.993
Cd_1-N_2	2.156	O_1- Cd_1-N_2	89.993
Cd_1-O_2	2.120	O_1- Cd_1-O_2	89.990
N_4-N_6	1.351	N_1- Cd_1-N_4	90.007
N_3-N_5	1.352	N_1- Cd_1-N_3	90.009
C_1-O_1	1.402	N_1- Cd_1-N_2	90.007
		N_1- Cd_1-O_2	90.011
		N_4- Cd_1-N_3	90.00
		N_4- Cd_1-N_2	19.697
		N_4- Cd_1-O_2	19.526
		N_3- Cd_1-N_2	70.301
		N_3- Cd_1-O_2	70.474
		N_2- Cd_1-O_2	0.000
		Cd_1-N_4-N_6	109.447
		Cd_1-N_3-N_5	109.481
		Cd_1-N_4- Cd_2	99.734
		Cd_1-N_3- Cd_2	64.321

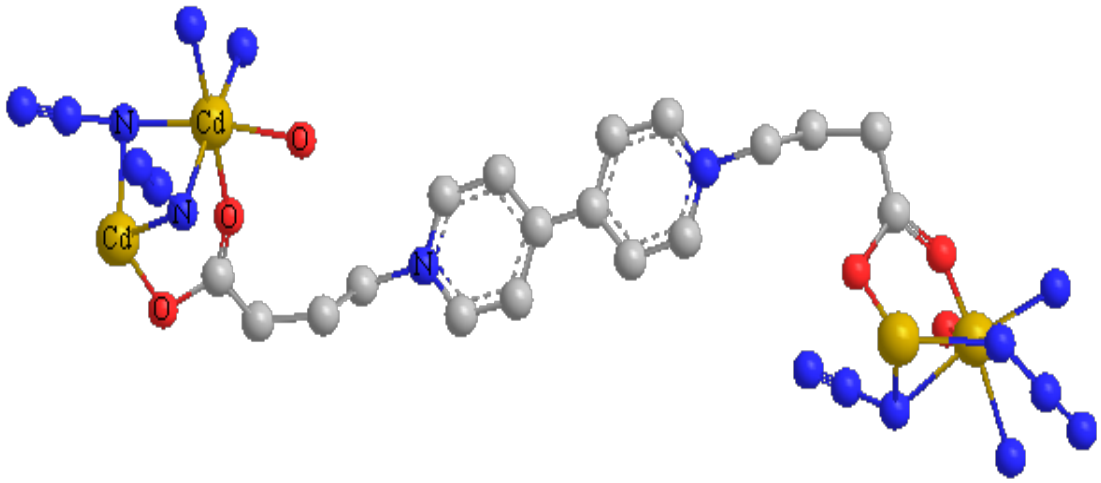

Figure (3-185) The proposed molecular structure of $[Cd_2(L^4)(N_3)_4]$

Table (3-47) The calculated bond length and bond angle of $Na_2[Ag_2(L^1)(N_3)_4].H_2O$

Type of Bond	Bond length (A˚)	Type of Bond	Bond angle(˚)
Ag_1-O_1	1.969	C_1-O_1- Ag_1	107.874
Ag_1-N_1	2.140	O_1-Ag_1-N_1	180.00
Ag_1-N_3	2.140	O_1-Ag_1-N_3	87.875
Ag_1-N_4	2.140	O_1-Ag_1-N_4	89.863
Ag_1-N_2	2.140	O_1-Ag_1-N_2	89.863
Ag_1-O_2	1.9994	O_1-Ag_1-O_2	89.743
N_3-N_5	1.347	N_1-Ag_1-N_3	90.211
N_4-N_6	1.349	N_1-Ag_1-N_4	90.208
C_1-O_1	1.441	N_1-Ag_1-N_2	90.211
		N_1-Ag_1-O_2	90.201
		N_3-Ag_1-N_4	89.786
		N_3-Ag_1-N_2	13.893
		N_3-Ag_1-O_2	162.234
		N_4- Ag_1-N_2	76.408
		N_4-Ag_1-O_2	77.387
		N_2-Ag_1-O_2	16.158
		Ag_1-N_3-N_5	109.214
		Ag_1-N_4-N_6	109.208
		Ag_1-N_3- Ag_2	101.982
		Ag_1-N_4- Ag_2	63.657

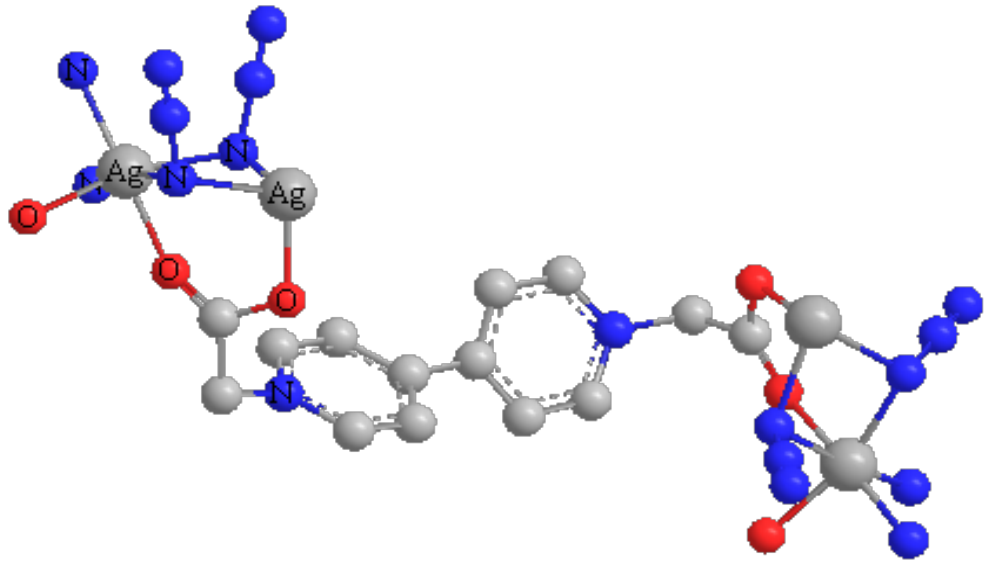

Figure (3-186) The proposed molecular structure of $Na_2[Ag_2(L^1)(N_3)_4].H_2O$

Table (3-48) The calculated bond length and bond angle of $[Cr_2(L^5)(N_3)_4]Cl_2.H_2O$

Type of Bond	Bond length (A˚)	Type of Bond	Bond angle(˚)
Cr_1-O_1	1.864	C_1-O_1- Cr $_1$	120.460
Cr_1-N_1	1.880	O_1- Cr_1-N_1	84.136
Cr_1-N_3	1.913	O_1- Cr_1-N_3	92.189
Cr_1-N_4	1.915	O_1- Cr 1-N_4	96.510
Cr_1-N_2	1.878	O_1- Cr $_1$-N_2	168.247
Cr_1-O_2	1.842	O_1- Cr_1-O_2	87.944
N_3-N_5	1.363	N_1- Cr1-N3	91.929
N_4-N_6	1.364	N_1- Cr_1-N_4	177.390
C_1-O_1	1.420	N_1- Cr_1-N_2	84.783
		N_1- Cr_1-O_2	98.461
		N_3- Cr_1-N_4	85.524
		N_3- Cr_1-N_2	92.093
		N_3- Cr_1-O_2	169.564
		N_4- Cr_1-N_2	94.735
		N_4- Cr_1-O_2	84.094
		N_2- Cr_1-O_2	89.817
		Cr_1-N_3-N_5	117.253
		Cr_1-N_4-N_6	117.833
		Cr_1-N3- Cr_2	86.696
		Cr_1-N_4- Cr_2	86.588

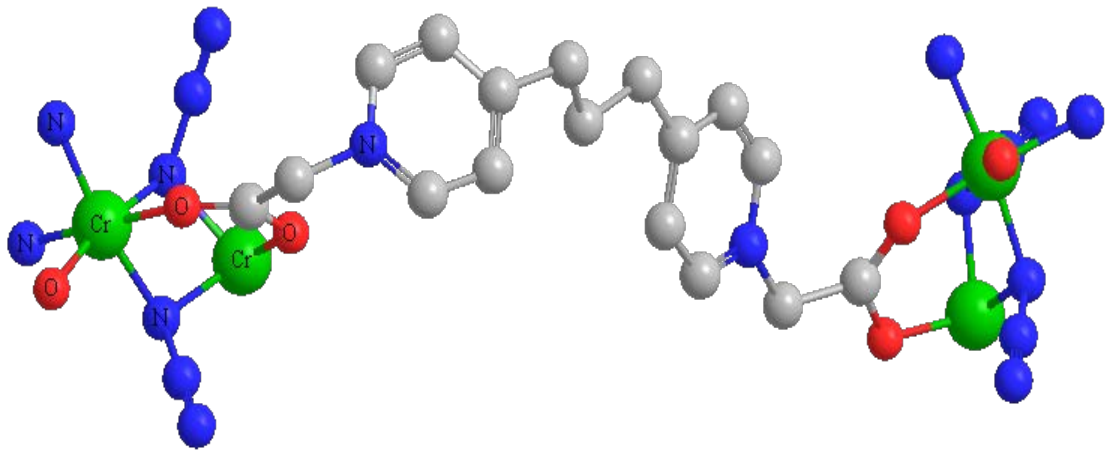

Figure (3-187) The proposed molecular structure of $[Cr_2(L^5)(N_3)_4]Cl_2.H_2O$

Table (3-49) The calculated bond length and bond angle of $[Mn_2(L^5)(N_3)_4].H_2O$

Type of Bond	Bond length (A)	Type of Bond	Bond angle
Mn_1-O_1	1.748	C_1-O_1-Mn_1	114.074
Mn_1-N_2	1.773	O_1-Mn_1-N_2	164.354
Mn_1-N_4	1.821	O_1-Mn_1-N_4	90.027
Mn_1-N_3	1.864	O_1-Mn_1-N_3	93.742
Mn_1-N_1	1.802	O_1-Mn_1-N_1	88.457
Mn_1-O_2	1.801	O_1-Mn_1-O_2	84.875
C_1-O_1	1.396	N_2-Mn1-N_4	92.718
N_4-N_6	1.317	N_2-Mn_1-N_3	95.201
N_3-N_5	1.352	N_2-Mn_1-N_1	87.124
		N_2-Mn_1-O_2	82.365
		N_4-Mn_1-N_3	75.981
		N_4-Mn_1-N_1	165.011
		N_4-Mn_1-O_2	93.714
		N_3-Mn_1-N_1	85.308
		N_3-Mn_1-O_2	172.540
		N_1-Mn_1-O_2	92.367
		Mn_1-N_4-N_6	113.684
		Mn_1-N_3-N_5	112.557
		Mn_1-N_4-Mn_2	96.003
		Mn_1-N_3-Mn_2	97.608

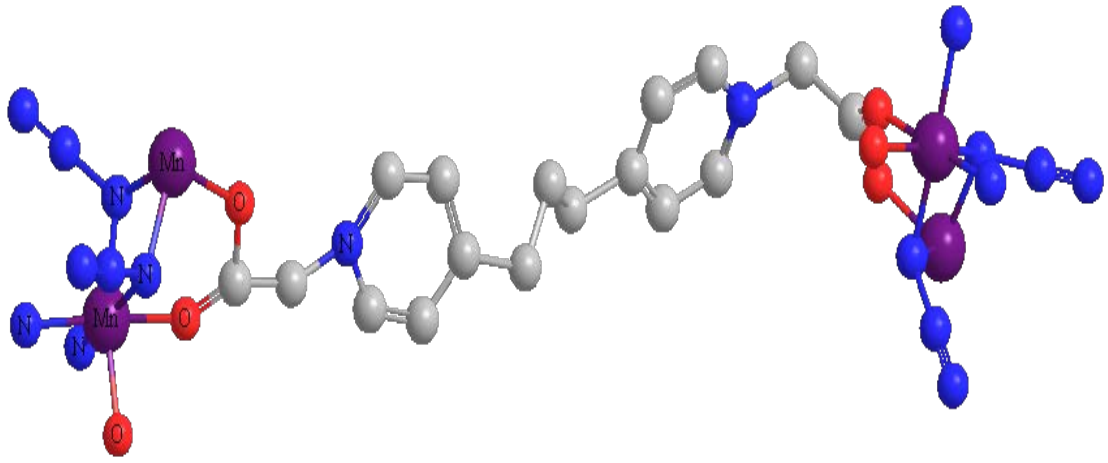

Figure (3-188) The proposed molecular structure of $[Mn_2(L^5)(N_3)_4]$ .H_2O

Table (3-50) The calculated bond length and bond angle of $Na_2[Ag_2(L^5)(N_3)_4].H_2O$

Type of Bond	Bond length (A˚)	Type of Bond	Bond angle(˚)
Ag_1-O_1	1.980	C_1-O_1- Ag_1	109.465
Ag_1-N_1	2.016	O_1-Ag_1-N_1	180
Ag_1-N_3	2.016	O_1-Ag_1-N_3	89.990
Ag_1-N_4	2.016	O_1-Ag_1-N_4	89.992
Ag_1-N_2	2.016	O_1-Ag_1-N_2	89.992
Ag_1-O_2	1.980	O_1-Ag_1-O_2	89.990
N_3-N_5	1.351	N_1-Ag_1-N_3	90.011
N_4-N_6	1.352	N_1-Ag_1-N_4	90.007
C_1-O_1	1.402	N_1-Ag_1-N_2	90.009
		N_1-Ag_1-O_2	90.011
		N_3-Ag_1-N_4	89.999
		N_3-Ag_1-N_2	13.943
		N_3-Ag_1-O_2	162.570
		N_4- Ag_1-N_2	76.056
		N_4-Ag_1-O_2	77.427
		N_2-Ag_1-O_2	16.380
		Ag_1-N_3-N_5	109.475
		Ag_1-N_4-N_6	109.482
		Ag_1-N_3- Ag_2	101.383
		Ag_1-N_4- Ag_2	63.552

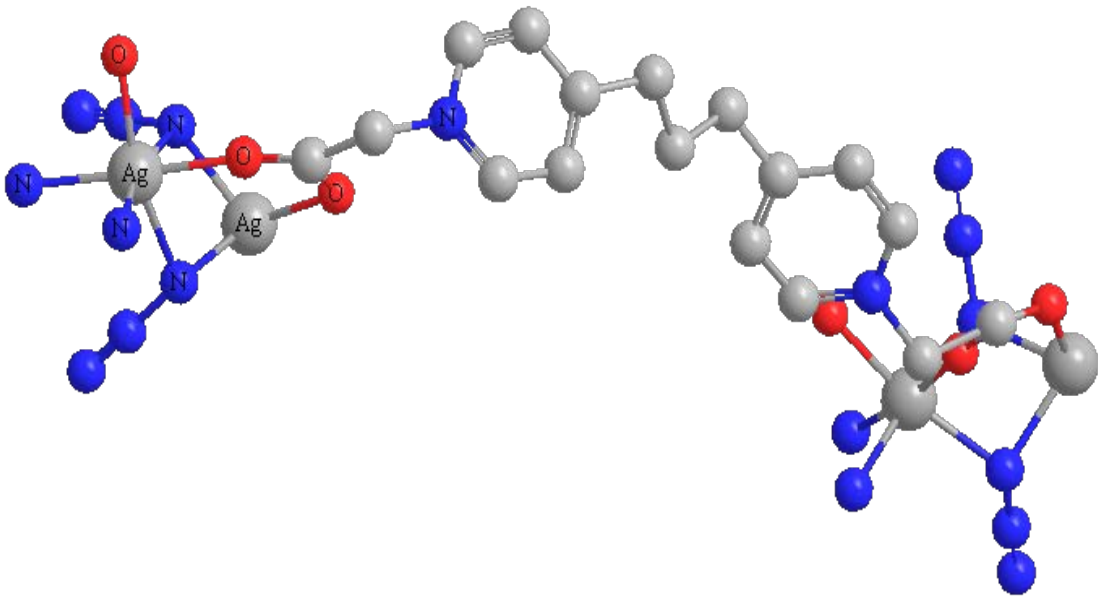

Fig.(3-189) The proposed molecular structure of $Na_2[Ag_2(L^5)(N_3)_4].H_2O$

Table (3-51) Minimisation energy of L^1 complexes in Kcal/mol

Complex	Stretch	Bend	Stretch-Bend	Torsion	Non-1,4 VDW	VDW	Charge/ Charge	Charge /Dipole	Dipole/ Dipole	Total Energy Kcal/mol
L^1	0.4861	4.7461	0.0551	-9.6143	-1.2864	15.4306	-158.3900	-0.1037	-0.0122	-148.6887
$[Cr_2(L^1)(N_3)_4]Cl_2.H_2O$	3.2649	69.8095	0.0024	-5.4058	-7.3521	34.6253	30.7618	-7.6400	5.9572	124.0233
$[Mn_2(L^1)(N_3)_4].H_2O$	3.6282	72.1820	0.1480	-9.2256	-10.2224	33.8643	30.5051	-1.5172	3.1996	122.5619
$[Fe_2(L^1)(N_3)_4].H_2O$	1.8392	68.2980	-0.0025	-5.4869	-4.8244	12.1315	30.7802	-3.3399	3.5634	102.9585
$[Co_2(L^1)(N_3)_4].H_2O$	23.4650	122.5929	-2.1594	-2.8250	-9.2758	50.2437	31.4081	-8.5100	-4.4848	200.4545
$[Ni_2(L^1)(N_3)_4].H_2O$	236.3985	337.2670	2.7842	-5.3427	-0.8550	68.8038	30.7656	-1.2572	-	668.5644
$[Cu_2(L^1)(N_3)_4].H_2O$	3.7886	81.8782	-1.6499	-5.3715	-6.9779	21.1018	30.8082	-4.9467	4.9522	126.5830
$[Zn_2(L^1)(N_3)_4].H_2O$	3.7030	90.7822	-2.8755	-5.4232	-6.9045	19.9947	30.7982	-4.3796	5.7716	131.4667
$[Cd_2(L^1)(N_3)_4].H_2O$	2.8713	74.8387	-2.8390	-5.4499	-6.2927	18.6014	30.8026	-7.1243	6.9262	112.3343
$Na_2[Ag_2(L^1)(N_3)_4].H_2O$	2.6476	60.0234	-1.6488	-5.0402	-7.3825	22.7238	30.8124	-7.8302	5.7121	100.0175

VDW=Van der Waals interaction

Table (3-52) Minimisation energy of L^2 complexes in Kcal/mol

Complex	Stretch	Bend	Stretch -Bend	Torsion	Non-1,4 VDW	VDW	Charge/ Charge	Charge/ Dipole	Dipole/ Dipole	Total Energy Kcal/mol
L^2	0.3309	0.7264	0.0201	-7.6590	-1.5088	6.9558	2.9021	0.5295	0.0244	2.3215
$[Cr_2(L^2)(N_3)_4]Cl_2.H_2O$	3.7499	71.7094	-0.4478	23.7845	-10.1455	41.6571	37.5766	-52.0531	5.7419	121.5729
$[Mn_2(L^2)(N_3)_4].H_2O$	3.6363	73.0147	-0.4606	22.0988	-10.1538	38.2068	36.8856	-50.2051	6.8352	119.8580
$[Fe_2(L^2)(N_3)_4]$	2.0048	65.7376	0.0051	-3.5476	-5.4751	15.7389	32.4396	-0.2230	5.7319	112.4122
$[Co_2(L^2)(N_3)_4].H_2O$	25.2227	118.6664	-2.4998	-4.7989	-6.5427	54.0673	32.4350	2.4493	-1.7222	217.2772
$[Ni_2(L^2)(N_3)_4].H_2O$	239.0974	351.1421	0.0213	50.8687	41.0235	87.3033	63.7946	-202.4981	-	630.7529
$[Cu_2(L^2)(N_3)_4].H_2O$	4.2572	83.1182	-2.1208	23.2851	-8.7616	30.4159	37.3019	-51.5600	5.9116	121.8475
$[Zn_2(L^2)(N_3)_4].H_2O$	4.3293	92.2440	-3.2423	17.6846	-9.7354	27.1037	35.3873	-39.0975	7.6224	132.2965
$[Cd_2(L^2)(N_3)_4]$	3.8590	124.1412	-3.4364	18.3518	-8.2732	29.1650	35.5280	-45.8686	6.5070	159.9739
$Na_2[Ag_2(L^2)(N_3)_4].H_2O$	3.2711	61.4204	-2.1015	18.3360	-9.2465	28.6835	35.5989	-43.7813	7.1757	99.3563

Table (3-53) Minimize energy of L^3 complexes in Kcal/mol

Complex	Stretch	Bend	Stretch-Bend	Torsion	Non-1,4 VDW	VDW	Charge/ Charge	Charge/ Dipole	Dipole/ Dipole	Total Energy Kcal/mol
L^3	0.8610	1.0263	0.1178	-9.4034	9.8269	13.8063	-155.2766	0.9348	-0.0084	-138.1154
$[Cr_2(L^3)(N_3)_4]Cl_2.H_2O$	4.8561	73.9384	0.3791	-11.3613	-5.5453	44.9584	31.6775	7.1326	2.8595	148.8950
$[Mn_2(L^3)(N_3)_4].H_2O$	4.7636	75.3233	0.3615	-10.0061	-5.0164	41.4056	31.6686	8.7909	2.0868	149.3776
$[Fe_2(L^3)(N_3)_4]$	3.4018	71.6066	0.3504	-9.7152	-3.2331	22.3490	31.6943	9.0813	2.7910	128.3262
$[Co_2(L^3)(N_3)_4].H_2O$	27.8664	125.2559	-2.1001	-9.2265	-6.0334	61.1864	31.7999	-16.8022	-4.3950	207.5514
$[Ni_2(L^3)(N_3)_4].H_2O$	238.3848	338.6709	3.3990	-6.2591	-10.8605	84.7271	32.1783	-30.6939	-	649.5465
$[Cu_2(L^3)(N_3)_4]$	5.3182	85.1859	-1.3637	-10.8229	-5.2021	34.4234	31.6901	6.9079	3.9125	150.0493
$[Zn_2(L^3)(N_3)_4].H_2O$	4.3293	92.2440	-3.2423	17.6846	-9.7354	27.1037	35.3873	-39.0975	7.6224	132.2965
$[Cd_2(L^3)(N_3)_4].H_2O$	3.8590	124.1412	-3.4364	18.3518	-8.2732	29.1650	35.5280	-45.8686	6.5070	159.9739
$Na_2[Ag_2(L^3)(N_3)_4].H_2O$	4.2629	64.2175	-1.2687	-10.4598	-3.9894	32.6717	31.6644	8.3923	4.5104	130.0012

VDW= Van der Waals interaction

Table (3-54) Minimisatiion energy of L^4 complexes in Kcal/mol

Complex	Stretch	Bend	Stretch -Bend	Torsion	Non-1,4 VDW	VDW	Charge/ Charge	Charge/ Dipole	Dipole/ Dipole	Total Energy Kcal/mol
L^4	1.2294	4.7412	0.2550	-6.6099	9.6810	14.1818	-167.1188	- 1.4778	0.0267	-145.0912
$[Cr_2(L^4)(N_3)_4]Cl_2.H_2O$	4.9671	73.5914	0.3520	-10.4531	-6.1421	46.3226	31.6710	0.3357	2.4032	143.0476
$[Mn_2(L^4)(N_3)_4].H_2O$	4.9276	76.7671	0.3948	-10.7620	-4.0431	44.2842	31.6703	-1.2548	2.0880	144.0721
$[Fe_2(L^4)(N_3)_4]$	3.5504	71.6926	0.3432	-9.8168	-3.4332	22.9071	31.6688	6.3854	2.1102	125.4075
$[Co_2(L^4)(N_3)_4].H_2O$	27.3119	126.1901	-2.0040	-8.9445	-4.6297	63.4269	31.8157	-8.9943	-4.2798	219.8923
$[Ni_2(L^4)(N_3)_4].H_2O$	236.3112	344.4473	4.5645	10.0352	-10.1944	90.1613	33.6191	-66.7752	-	642.1690
$[Cu_2(L^4)(N_3)_4].H_2O$	5.3182	85.1859	-1.3637	-10.8229	-5.2021	34.4234	31.6901	6.9079	3.9125	150.0493
$[Zn_2(L^4)(N_3)_4]$	69.1472	259.4193	-5.7666	1.7385	12.5127	110.3154	32.7062	-48.7585	4.2804	435.5946
$[Cd_2(L^4)(N_3)_4]$	20.0220	184.3346	-8.1751	12.5286	-5.9878	44.9047	32.4031	-34.8171	6.2935	251.5066
$Na_2[Ag_2(L^4)(N_3)_4].H_2O$	4.2664	63.1307	-1.3007	-9.5034	-7.4315	35.1595	31.7378	-8.0190	4.1383	112.1781

VDW= Van der Waals interaction

Table (3-55) Minimisation energy of L^5 complexes in kcal/mol

Complex	Stretch	Bend	Stretch -Bend	Torsion	Non-1,4 VDW	VDW	Charge/ Charge	Charge/ Dipole	Dipole/ Dipole	Total Energy Kcal/mol
L^5	0.7717	7.8306	0.1343	-3.3142	-2.8047	16.3092	-178.3736	-6.8667	-0.2541	-166.5675
$[Cr_2(L^5)(N_3)_4]Cl_2.H_2O$	4.1129	75.6144	0.2294	-1.7187	-16.5237	44.5656	35.8872	-46.9232	2.6078	97.8517
$[Mn_2(L^5)(N_3)_4].H_2O$	3.9785	77.7057	0.3275	-1.7330	-16.7557	42.2458	35.6757	-45.0317	2.4544	98.8673
$[Fe_2(L^5)(N_3)_4].H_2O$	1.7658	67.5667	-0.0513	-3.0826	-5.2857	10.7706	21.7093	-7.2781	4.1743	90.2890
$[Co_2(L^5)(N_3)_4].H_2O$	25.1511	122.0128	-2.0433	-5.0326	-13.4073	60.4950	23.8613	-7.1058	-4.2356	199.6957
$[Ni_2(L^5)(N_3)_4].H_2O$	237.86015	339.0763	3.2372	-1.5934	-8.7610	81.8857	32.0331	-46.4100	-	637.3280
$[Cu_2(L^5)(N_3)_4].H_2O$	4.7874	86.1395	-1.7042	0.7326	-15.9410	36.8611	29.7212	-34.9466	3.7245	109.3746
$[Zn_2(L^5)(N_3)_4].H_2O$	4.7072	95.4744	-2.6523	-1.7340	-12.3473	30.8917	35.0427	-47.4069	5.5104	107.4860
$[Cd_2(L^5)(N_3)_4].H_2O$	3.9288	124.4754	-2.9252	-1.8594	-12.7812	31.4805	35.0775	-43.3093	4.0064	138.0935
$Na_2[Ag_2(L^5)(N_3)_4].H_2O$	3.5441	60.9903	-1.4971	-6.2516	-11.0694	32.1801	22.1023	-4.7653	4.5075	99.7409

VDW = Van der Waals interaction

Prospective studies

1. Preparation of new polydentate ligands with different substituents.
2. Synthesis of polymeric complexes employing different bridging systems. These complexes may have potential applications in photochemistry, molecular magnetism, catalysis, optoelectronic devices and clean energy.
3. Determination of the magnetic behaviour of complexes using variable temperature magnetic studies.

REFERENCES

References

1. T. Tanase, J. W. Yun, S. J. Lippard, ***Inorg. Chem***., 35, 3585, (1996).
2. M. Melnik, M. Koman, D. Hudecov, J. Moncol, B. Dudov, T. Glowiak, J. Mrozinski, C. E. Holloway, ***Inorg. Chem. Acta***, 308, (2000)
3. V. Zelenak, K. Gyoryov, D. Mlynar, ***Met. Based Drugs***, 8, 269, (2002).
4. P. Koczo, J. Piekut, M. Borawska, R. Swisłocka, W. Lewandowski, ***Spectrochim. Acta***, Part A: Mol. Biomol. Struct. 61, 1917, (2005).
5. P. Koczo, J. Piekut, M. Borawska, R. Swisłocka, W. ewandowski, ***J. Mol. Struct***., 651–653 (2003).
6. D. Aiello, R. Aiello, F. Testa, T. Martino, I. Aiello, M. L. Deda, M. Ghedini, ***J. Photochem. Photobio***. A. 201, 81-86, (2009).
7. K. Yu, Z. C. Gu, R. N. Ji, L. L. Lou, S. X. Liu, ***Tetrahedron***, 65, 305-311, (2009).
8. B. J .Jung, N. J. Tremblay, M. L. Yeh, H. E. Katz, ***Chem. Mater***. 23, 568-582, (2011).
9. V. K. Garripelli, J. K. Kim, S. Son, W. J. Kim, M. A. Repka, S. Jo, ***Acta Biomater***., 7, 1984-1992, (2011).
10. J. S. Pap, B. Kripli, T. Varadi, M. Giorgi, J. Kaizer, G. Speier, ***J. Inorg. Biochem***., 105, 911-918, (2011).
11. D. M. Griffith, B. Szocs, T. Keogh, K. Y. Suponitsky, E. Farkas, P. Buglyo, C. J. Marmion, ***J. Inorg. Biochem***., 105, 763-769, (2011).
12. A. L. Pochodylo, R. L. LaDuca, ***Inorg. Chem. Comm***., 14, 722-726, (2011).
13. Q. Ma, M. L. Zhu, L. P. Lu, S. S. Feng, J. Z. Yan, ***Inorg. Chem. Acta***, 370, 102-107, (2011).
14. S. Losse, J. G. Vos, S. Rau, ***Coord. Chem. Rev***. 254, 492-.14 2504, (2010).
15. S. R. Batten, R. Robson, ***Angew. Chem., Int. Ed***., 37, 1460, (1998).
16. L. Carlucci, G. Ciani, D. M. Proserpio, ***Coord. Chem. Rev***., 246-247, (2003).

17. S. R. Batten, ***Cryst Eng Comm***., 3, 67, (2001).

18. X-J Kong, X-J Long., L-S Long ., Z-P Zheng., R-B Huang, L-S Zheng, ***Acc. Chem .Res***., 43, 201-209, (2009).

19. E-Q Gao, Y- F Yue , S-Q Bai , Z-Yan He.. ***J. Am. Chem. Soc***., 126, 1419, (2004).

20. P. P Liu, A. L. Cheng, N. Liu, W. W. Sun, E. Q. Gao, ***Chem. Mater***., 19, 2724, (2007).

21. X. Y. Wang, L. Wang, Z. M. Wang, S. Gao, ***J. Am. Chem. Soc***., 128, 674, (2006).

22. Y. Z. Zhang, H. Y. Wei, F. Pan, Z. M. Wang, Z. D. Chen, S. Gao, ***Angew. Chem. Int. Ed***., 44, 5841, (2005).

23. S. R. Caskey, A. J. Matzger***, Inorg. Chem***., 47, 7942, (2008).

24. P. Ren, W. Shi, P. Cheng, ***Cryst. Growth Des***., 8, 1097, (2008).

25. J. W. Cheng, J. Zhang, S. T. Zheng, E. Ma, G. Y. Yang, ***Inorg. Chem***., 46, 10534, (2007).

26. Y. Ouyang, W. Zhang, N. Xu, G. F. Xu, D. Z. Liao, S. P. Yan, P. Cheng, ***Inorg. Chem***., 46, 8454, (2007).

27. X. Q. Zhao, B. Y. Ma, W. Shi, P. Cheng, Z. H. Jiang, D. Z. Liao, S. P. Yan, ***Inorg. Chem***., 46, 5832, (2007).

28. M. Du, X. H. Bu, Y. M. Guo, J. Ribas, ***J. Chem.-Eur. J***., 10, 1345, (2004).

29. X. Y. Wang, Z. M. Wang, S. Gao, ***Chem. Comm***., 281, (2008).

30. S. C. Chen, Z. H. Zhang, K. L. Huang, Q. Chen, M. Y. He, A. J. Cui, C. Li, Q. Liu, M. Du. ***Cryst. Growth Des***., 8, 3437, (2008).

31. B. R. Manzano, F. A. Jalon, M. L. Soriano, M. C. Carrion, M. P. Carranza, K. Mereiter, A. M. Rodriguez, A. dela Hoz, A. Sanchez-Migallon, ***Inorg. Chem***., 47, 8957, (2008).

32. T. K. Prasad, M. V. Rajasekharan. ***Cryst. Growth Des***., 8, 1346, (2008).

33. T. Enoki, A. Miyazaki, ***Chem. Rev***., 104, 5449–5477, (2004).

34. P. Amo-Ochoa, O. Castillo, S. S. AlexandreL. Welte, L.; P. J. de Pablo, M. I. Rodriguez-Tapiador, J. Gomez- Herrero, F. Zamora, ***Inorg. Chem***., 48, 7931–7936, (2009).

35. D. Gatteschi, R. Sessoli, ***Angew. Chem., Int. Ed***., 42, 268, (2003).

36. R. Lescouezec, L. M. Toma, J. Vaissermann, M. Verdaguer, F. S. Delgado, C. Ruiz-Perez, F. Lloret, M. Julve, ***Coord. Chem. Rev***., 249, 2691, (2005).

37. G. Aromi, D. Aguila, P. Gamez, F. Luis, O. Roubeau, ***Chem. Soc. Rev***., 41, 537, (2012).

38. A. Escuer, G. Aromı, ***Eur. J. Inorg. Chem***., 4721, (2006).

39. Y. F. Zeng, X. Hu, F. C. Liu, X. H. Bu, ***Chem. Soc. Rev***., 38, 469, (2009).

40. C. H. Ge, A. L. Cui, Z. H. Ni, Y.-B. Jiang, L.-F. Zhang, J. Ribas, H. Z. Kou, ***Inorg. Chem***., 45, 4883, (2006).

41. X.-Y. Wang, L. Wang, Z. M. Wang, G. Su, S. Gao, ***Chem. Mater***., 17, 6369, (2005).

42. T. F. Liu, D Fu, S. Gao, Y. Z. Zhang, H. L. Sun, G. Su, Y. J. Liu, ***J. Am. Chem. Soc***., 125, 13976, (2003).

43. Y. F. Yue, E. Q. Gao, C. J. Fang, T. Zheng, J. Liang, C. H. Yan, ***Inorg. Chem***., 8, 3295, (2008).

44. X. T. Liu, X.-Y. Wang, W.-X. Zhang, P. Cui, S. Gao, ***Adv. Mater***., 18, 2852, (2006).

45. P. S. Mukherjee, T. K. Maji, G. Mostafa, T. Mallah, N. R. Chaudhuri, ***Inorg. Chem***., 39, 5147, (2000).

46. R. Y. Li, X. Y. Wang, T. Liu, H.-B. Xu, F. Zhao, Z.-M. Wang, S. Gao, ***Inorg. Chem***., 47, 8134, (2008).

47. H. Li, M. Eddaoud, M. Okeeffe, O.M. Yaghi, ***Nature***, 402, 276, (1999).

48. A. Escuer, R. Vicente, F. A. Mautner, M. A. Goher, M. A. M. Abu-Youssef **,** ***Chem. Comm***., 64, 2002.

49. T. Liu, Y. J. Zhang, Z. M. Wang, S. Gao, ***Inorg. Chem***., 45, 2782, (2006).

50. X. T. Wang, X. H. Wang, Z. M. Wang, S. Gao, ***Inorg. Chem***., 48, 1301, (2009).

51. F. C. Liu, Y. F. Zeng, J. R. Li, X. H. Bu, H.-J. Zhang, ***J. Inorg. Chem***., 44, 7298, (2005).

52. G. Aromi, E. K. Brechin, ***Struct. Bond***. 122, 1–67, (2006).

53. Y. Q. Wang, J. Y. Zhang, Q. X. Jia, E. Q. Gao, C. M. Liu, ***Inorg. Chem.***, 48, 789, (2009).

54. J. Xia, B. Zhao, H. S. Wang, P. Cheng. ***Inorg. Chem***., 46, 3450 (2007).

55. X. H. Zhou, Y. H. Peng, X. D. Du, C. F. Wang, J. L. Zuo, X. Z. You. ***Cryst. Growth Des***., 9, 1028, (2009).

56. P. King, R. Clerac, C. E. Anson, A. K. Powell. ***Dalton Trans***., 6, 852, (2004).

57. J. C. Bayon, P. Esteban, G. Net, P.G. Rasmussen, K. N. Baker, C. W. Hahn, M. M. Gumz. ***Inorg. Chem***., 30, 2572, (1991).

58. J. L. Tian, S. P. Yan, D. Z. Liao, Z. H. Jiang, P. Cheng. ***Inorg. Chem. Comm***., 6, 1025, (2003).

59. S. Y. Zhang, Y. H. Li, W. Li. ***Inorg. Chem. Acta***, 362, 2247 (2009).

60. P. King, R. Clerac, C. E. Anson, C. Coulon, A. K. Powell. ***Inorg. Chem***., 42, 3492, (2003).

61. L. F. Chen, X. Y. Cao, Z. J. Li, J. K. Cheng, Q. P. Lin, Y. G. Yao. ***Inorg. Chem. Comm***., 11, 961, (2008).

62. J. J. Wang, B. Zhang, H. M.Shu, C. Q. Du, H. M. Hu. ***Acta Cryst***., 63, 2190, (2007).

63. Y. Wang, Y. Song, Z. R. Pan, Y. Z. Shen, Z. Hu, Z. J. Guo, H. G. Zheng., ***Dalton Trans***., 41, 5588, (2008).

64. D. G. Branzea, A. Guerri, O. Fabelo, C. Ruiz-Perez, L.M. Chamoreau, C. Sangregorio, A. Caneschi, M. Andruh. ***Cryst. Growth Des***., 8, 941, (2008).

65. M. Frisch, C. L. Cahill., ***Dalton Trans***., 8, 1518, (2005).

66. T. C. Stamatatos, K. A. Abboud, W. Wernsdorfer, G. Christou, ***Angew. Chem., Int. Ed***., 46, 844, (2007).

67. C. I. Yang, W. Wernsdorfer, G. H. Lee, H. L. Tsai, ***J. Am. Chem. Soc***., 129, 456, (2007).

68. S. Kitagawa, R. Kitaura, S. Noro, ***Angew. Chem., Int. Ed***., 43, 2334, (2004).

69. G. Ferey, ***Chem. Soc. Rev***., 37, 191, (2008).

70. J. R. Li, R. J. Kuppler, H. C. Zhou. ***Chem. Soc. Rev***., 38, 1477, (2009).

71. L. Q. Ma, C. Abney, W. B. Lin. ***Chem. Soc. Rev***., 38, 1248, (2009).

72. D. J. Tranchemontagne, J. L. Mendoza-Cortes, M. O. Keeffe, O. M. Yaghi. ***Chem. Soc. Rev***., 38, 1257, (2009).

73. J. B. Goodenough, ***Prog. Solid State Chem***., 5, 149, (1971).

74. D. Gatteschi and R. Sessoli, ***Angew. Chem. Int. Ed***., 42, 268, (2003).

75. J. Veciana, ***Struct. Bonding***, 100, 1, (2001).

76. J. M. Baik and J. L. Lee ***Adv. Mater***., 17, 2745, (2005).

77. S. K. Pati and C. N. Rao***, Chem. Comm***., 4683, (2008).

78. D. Grohol, K. Matan, J. H. Cho, S. H. Lee, J. W. Lynn, D. G. Nocera and Y. S. Lee, ***Nat. Mater***., 4, 323, (2005).

79. A. B. Gaspar, V. Ksenofontov, M. Seredyuk and P. Gütlich, ***Coord. Chem. Rev***., 249, 2661, (2005).

80. S. W. Cheong and M. Mostovoy, ***Nat. Mater***., 6, 13, (2007).

81. E. Coronado, J. R. Galan-Mascaros, M. Monrabal-Capilla, J. Garcia-Martiand P. P. Pardo-Ibanez, ***Adv. Mater***., 19, 1359-1361, (2007).

82. C. N. Rao, S. Natarajan and R. Vaidhyanathan, ***Angew. Chem. Int. Ed***., 43, 1466, (2004).

83. S. Natarajan and P. Mahata, ***J. Ind. Ins. Sci***., 88, 179, (2008).

84. D. Maspoch , D. Ruiz-Molina and B. Veciana ***J***. ***Chem. Soc. Rev***., 36, 770, (2007).

85. L. J. Smith , H. Eckert and A. K. Cheetham, ***J. Am.Chem. Soc***., 122, 1700, (2000).

86. S. Cobo, G. Molnar, J. A. Real and A. Bousseksou, ***Angew. Chem***., 45**,** 5786, (2006).

87. E. Freysz, S. Montant, S. Letard and J. F. Letard, ***Chem. Phys. Lett***. **3**94, 318-232, (2005).

88. J. F. Letard, P. Guionneau and L. Goux-Capes, ***Top. Curr. Chem***. 235, 221-49, (2004).

89. O. Kahn and C. J. Martinez, ***Science***, 279**,** 44-8, (1998).

90. P. Gutlich, A. Hauser and H. Spiering, ***Angew. Chem. Int. Ed. Engl***. 33 2024-54, (1994).

91. P. Gutlich and H.A. Goodwin, ***Top. Curr. Chem***., Spin Cross in Transition Metal Compounds I-III, 233-235, (2004).

92. P. Gutlich, Y. Garcia and H. A. Goodwin, ***Chem. Soc. Rev***., 29, 419, (2000).

93. Malcolm A. Halcrow, ***Chem. Soc. Rev***., 37, 278-289, (2008).

94. R. Pritchard, C. A. Kilner and M. A. Halcrow, ***Chem. Comm***., 577, (2007).

95. B. A. Leita, B. Moubaraki, K. S. Murray, J. P. Smith and J. D. Cashion, ***Chem. Comm***., 156, (2004).

96. A. B. Gasper, V. Ksenofontov, S. Reiman, P. Gutlich, A. L. Thompson, A. E. Goeta, M. C. Munoz and J. A. Real, ***Chem.-Eur. J***., 12, 9289, (2006).

97. J. A. Real, I. Castro, A. Bousseksou, M. Verdaguer, R. Burriel, J. Linares and F. Varret, ***Inorg. Chem***., 36, 455, (1997).

98. F. Volatron, L. Catala, E. Riviere, A. Gloter, O. Stephan and T. Mallah, ***Inorg. Chem***., 47, 6584-6586, (2008).

99. T. Fujigaya, D. L. Jiang and T. Aida, ***Chem.-Asian J***., 2, 106-113, (2007).

100. J. F. Letard, P. Guionneau, and L. Goux-Capes, in Spin Crossover in Transition Metal Compounds III, springer-Berlin, vol.235, pp.221-249, (2004).

101. D. F. Shriver and P. W. Atkins, ***Inorg. Chem***., Oxford University Press, Oxford, (1999).

102. A. Hauser, in Spin Crossover in Transition Metal Compounds I, Springer-Berlin, vol. 233, pp. 49-58, (2004).

103. Y. Tanabe and S. Sugano, ***J, Phys. Soc. Jpn***., 9, 766-779, (1954).

104. M. Sorai and S. Seki, ***J. Phys. Chem. Solids***, 35, 555-570, (1974).

105. T. Forestier, S. Mornet, N. Daro, T. Nishihara, S. Mouri, K. Tanaka, O. Fouche, E. Freysz and J. F. Letard, ***Chem. Comm***., 4327-4329, (2008).

106. Xue-Ting Liu, Xin-Yi, Wei-Xin Zhang, Peng Cui, and Song Gao, ***Adv. Mater***, 18, 2852-2856, (2006).

107. G. Lazari, T. Stamatatos, C. Raptopoulou, Va. Psycharis, M. Pissas, S. Perlepes and A. Boudalis, ***Daltom Trans***., 3215-3221, (2009).

108. T. C. Stamatatos, J. C. Vlahopoulou, V. S. Tangoulis, C. P. Raptopoulou, A. Terzis, G. S. Papaefstathiou, and S. P. Perlepes, ***Polyhedron***, 28, 1656-1663, (2009).

109. Q. Yang, J.-P. Zhao, B.-W. Hu, X.-F. Zhang and X.-H. Bu, ***Inorg.Chem***., 49, 3746-3751, (2010).

110. S. Saha, D. Biswas, P. P. Chakrabarty, A. D. Jana, A. Boudalis, S K. Seth and T. Kar, ***Polyhedron***, 29, 3342-3348, (2010).

111. Oindrila Sengupta, Bappaditya Gole, Sandip Mukherjee and Partha Sarathi Mukherjee, ***Dalton Trans***., 39, 7451-7465, (2010).

112. Yang Fu, Hua Li, Xingguo Chen and Jingui Qin, ***Inorg. Chem.. Comm.***, 14, 268-270, (2011).

113. Feng Luan, Ling Xu, Yuan Gao and Bing Liu, ***Bull. Korean Chem. Soc.*** Vol. 32, No.5, (2011).

114. Noelia De La Pinta, M. Luz Fidalgo, Luis Lezama, Gotzon Madariga, Lorena Callejo and Roberto Cortes, ***Cryst. Growth Des***., 11, 1310-1317, (2011).

115. Ken-ichi Sakai, Tomoyuki Akutagawa, and Takayoshi Nakamura**,** ***Eur. J. Inorg. Chem***., 116–120, **(**2011)**.**

116. Yan-Qin Wang, Qian Sun and En-Qing Gao, ***Inorg. Chem. Comm.***, 15, 8-11, (2012).

117. J. B. Goodenough, Magnetism and the chemical bond (New York: Wiley), (1963).

118. Partha Mahata, Debajit Sarma and Sriniv Asan Natarajan, ***J. Chem. Soc***., vol. 122, No.1, 19-35, (2010).

119. Jin-Zhong Gu, Wen-Guan Lu, Long Jiang, Hong-Cai Zhou, and Tong-Bu Lu, ***Inorg. Chem***., 46, 5835-5837, (2007).

120. J. –F. Song, R.-S. Zhouy, T.-P. Huy, Z. Cheny and B.-B. Wang, ***J. Coord. Chem.***, Vol. 63, No. 24, , 4201–4214, (2010).

121. T. Okubo, N. Tanaka, K. H. Kim, H. Yone, M. Maekawa, and T. Kuroda-Sowa, ***Inorg. Chem***., 49, 3700–3702, (2010).

122. Ming-Hua Zeng, Yan-Ling Zhou, Mei-Chun Wu, Hao-Ling Sun and Miao Du, ***Inorg. Chem***., 49, 6436–6442, (2010).

123. Dong-Yu Lv, Zhu-Qing Gao, Jin-Zhong Gu, Ren Ren, Wei Dou, ***Transition Met Chem,*** 36, 313–318, (2011).

124. Tarak Nath Mandal, Somnath Roy, Samik Gupta, Kinsuk Das, Rajat Saha, Golam Mostafa, Ray J. Butcher, Cai-Ming Liu, Susanta Kumar Kar, ***Polyhedron,*** 30 , 1571–1578, (2011).

125. Hong-Lin Zhu, Jian-Lin, Wei Xu, Jie Zhang and Yue-Qing Zhang, ***J. Coord. Chem.***, Vol. 64, No. 12, 2088-2100, (2011).

126. Xin Zhang, Zhao-Ji Li, Ye-Yan Qin and Yuan-Gen Yao, ***Inorg. Chem. Comm.***, 15, 1-4, (2012).

127. Sarvendra Kumar and Fabio Doctorovich, ***Inorg. Chem. Comm.***, 15, 33-36, (2012).

128. Guo-Jie Yin, Bao-Ming Ji and Chen-Xia Du, ***Inorg.Chem. Comm.***, 15, 21-24, (2012).

129. Cui-huan Jiao, Cui-hong He, Jian-chen Geng and Guang-hua Cui, ***Transition Met Chem***, 37, 17-23, (2012).

130. Balasubramanian Murugesapandian and Peter W. Roesky, ***Eur. J. Chem***., 292-297, (2012).

131. Veronica Gomez, Montserrat corbella, Gema Fernandez, Oliver Roubeau, Simon J. Teat and Miguel A. Maestro, ***Eur. J. Inorg. Chem***. 2359-2367, (2012).

132. A. K. Gupta and M. Gupta, ***Biomaterials***, 26, 3995, (2005).

133. R. Weissleder and M. J. Pittet, ***Nature***, 452, 580, (2008).

134. Y. W. Jun, J. H. Lee and J. W. Cheon, ***Angew. Chem., Int. Ed***., 47, 5122, (2008).

135. Chenjie Xu and Shouheng Sun, ***Dalton Trans***., 5583-5591, (2009).

136. Y. Hu, J. Xie, Y. W. Tong and C. H. Wang, ***J. Controlled Release***, 7, 118, (2007).

137. Y. M. Huh, Y. W. Jun, H. T. Song, S. Kim, J. S. Choi, J. H. Lee, S. Yoon, K. S. Kim, J. S. Shin, J. S. Suh and J. Cheon, ***J. Am. Chem. Soc***., 127, 12387, (2005).

138. R. Hao, R. Xing, Z. Xu, Y. Hou, S. Gao and S. Sun, ***Adv. Mater***., 22, 2729, (2010).

139. S. Laurent, D. Forge, M. Port, A. Roch, C. Robic, L. Vander Elst and R. N. Muller, ***Chem. Rev***., 108, 2064, (2008).

140. Nohyun Lee and Taeghwan Hyeon, ***Chem. Soc. Rev***., 41, 2575–2589, (2012).

141. B. Wang, C. J. Xu, J. Xie, Z. Yang and S. H. Sun, ***J. Am. Chem. Soc***., 130, 14436, (2008).

142. T. K. Jian, M. A. Moralles, S. K. Sahoo, D. L. Lesllie-Pellecky and V. Labhasetwar, ***Mol. Pharm***., 2, 194, (2005).

143. K. E. Uhrich, S. M. Cannizzaro, R. S. Langer and K. M. Shakesheff, ***Chem. Rev***., 99, 3181, (1999).

144. N. Kohler, C. Sun, J. Wang and M. Q. Zhang, **Langmuir**, 21, 8858, (2005).

145. G. Timco, T. B. Faust, F. Tuna, R.E. P. Winpenny**, *Chem. Soc. Rev***., 40, 3067, (2011).

146. J. Ashley, M. P. Bernal,G. W. Burr, H. Coufal, H. Guenther, J. A. Hoffnagle, C. M. Jefferson, B. Marcus, R. M. Macfarlane, R. M. Shely and G. T. Sincerbox, ***IBM J. Res. Dev***.,44, 341-368, (2000).

147. L. Hesselink, S. S. Orlov and M. C. Bashaw, **Proc. IEEE**, 92, 1231-1280, (2004).

148. J. Kusz, P. Gutlich and H. Spiering, in Spin Crossover in Transition Metal Compounds II, Springer- Berlin, vol. 234, pp. 129-153, (2004).

149. A. Hauser, ***Coord. Chem. Rev***., 111, 275-290, (1991).

150. P. Gutlich, Y. Garcia and T. Woike, ***Coord. Chem. Rev***., 219, 839-879, (2001).

151. Roberta Sessoli, ***Angew. Chem. Int. Ed***. 51, 43-45, (2012).

152. C. S. Smith and K. R. Mann, ***Chem. Mater***., 21, 5042–5049, (2009).

153. O. Oter, K. Ertekin and S. Derinkuyu, ***Mater. Chem. Phys***., 113, 322–328, (2009).

154. N. J. Hinks, A. C. Mckinlay, B. Xiao, P. S. Wheatley, R. E. Morris, ***Microporous, Mesoporous Mater***., 129, 330, (2010).

155. L. H. Williams, ***Acc. Chem. Res***., 32, 869, (1999).

156. Jacqueline L. Harding and Melissa M. Reynolds, ***J. Am. Chem. Soc***., 134, 3330−3333, (2012).

157. A. R. Hirst, B. Escuder, J. F. Miravet and D. K. Smith, ***Angew. Chem., Int. Ed***., 47, 8002–8018, (2008).

158. J. W. Steed, ***Chem. Comm***., 47, 1379–1383, (2011).

159. Prakash Kanoo, R. Sambhu andTapas Kumar Maji, ***Inorg. Chem***., 50, 400-402, (2011).

160. CS Chem 3D Ultra Molecular Modelling and Analysis, Cambridge, www. cambridgesoft.com.

161. R. C. Maurya, S. Rajput, ***J. Molecular Structure***, 794 24-34, (2006) (molecular modelling).

162. *A.* Jiang-Gao Mao, Hong-Jie Zhang, Jia-Zuan Ni, Shu-Bin Wang, Thomas C. W. Mak, ***Polyhedron***, 18, 1519-1525, (1999). 162.*B.* A. D. Philips, Z. Fei, W. H. Ang, R.S. Scopelliti and P. J. Dyson, Cry. Growth & Design, 9(4), 1966-1978, (2009)

163. Yu Ma, Yan-Qing Wen, Jian-Yong Zhang, En-Qing Gao and Cai-Ming Liu, ***Dalton Trans***., 39, 1846-1854, 2010.).

164. Masayuki Nara, Hajem Torri and Mitsuo Tasumi, ***J. Phs.Chem***., 100, 51, (1996).

165. V. Zelenak, Z. Vargova, K. Gyoryova, ***Spectrochemica Acta***, 66, 262-272, (2007).

166. Li-Fang Song, Chun-Hong Jiang, Cheng-Li Jiao, Jian Zhang, Li-Xian Sun, Fen Xu, Wan-Sheng You, Zhong-Gang Wang and Ji-Jun Zhao, ***Crystal Growth& Design***. Vol. 10, No. 12, (2010).

167. Guang-Xiang Liu, Kun Zhu, Huan-Min Xu, Sadafumi Nishihara, Rong-Yi Huang and Xiao-Ming Ren, ***Cryst. Eng.Comm.***, 12, 1175-1185, (2010).

168. Robert M. Silverstein, **Spectrometric identification of organic compounds** 7th edition, John Willey and Son, inc., p 174, (2005).

169. Mikhail A. Kiskin, Grygory G. Aleksandrov, Artem S. Bogomyakov, Vladimir M. Novotortsev and Igor L. Eremenko, ***Inorg. Chem. Comm.***, 11, 1015-1018, (2008).

170. Feng-Mei Nie, Zhi-Yun Dong, Fei Lu, and Guo-Xing Li, ***J. Coord. Chem.***, 63, 24, 4259-4270, (2010).

171. Yu Pang, Dan Tian, Yuhui Luo, Xiao Fei Zhu and Hong Zhang, ***J. Coord.Chem***., No. 11, 2002-2009, (2011).

172. Qi Ma, Miaoli Zhu, Liping LuSisi Feng and Juanzhi Yan, ***Inorg. Chem. Acta***, 370, 102-107, (2011).

173. Sandip Mukherjee, Bappaditya Gole, Yo Song and Partha Sarathi Mukherjee, ***Inorg .Chem***., 50, 3621-3631, (2011).

174. N. Raman, S. Esther, C. Thangaraj, ***J. Chem. Soc***, 116(4),209, (2004).

175. Krzysztof Drabent, Zbigniew Ciunik and Andrzej Ozarowski, ***Inorg. Chem***, 47, 3358-3365, (2008).

176. Oindrila Sengupta, Bappaditya Gole, Sandip Mukherjee and Partha Xiao Sarathi Mukherjee, ***Dalton Trans***., 39, 7451-7465, (2010).

177. -Ning Cheng, Wei Xue and Xiao-Ming Chen, ***Eur. J. Inorg. Chem***. 3850–3855, (2010).

178. K. Nakamato Infrared spectra of inorganic and coordination compounds, 4th edn. Wiley, New York, (1996).

179. N. Chkaku, K. Nakamato, ***Inorg. Chem***, 10, 768, (1971)

180. Choong-Sun Lim, Jennifer K. Schnobrich, Antek G. Wong-Foy and Adam J. Matzger, ***Inorg. Chem***., 49, 5271-5275, (2010).

181. Dong-Yu Lv, Zhu-Qing Gao, Jin-Zhong Gu, Jian-Zhao Liu and Wei Dou, ***Transition Met Chem.***, 36, 275-281, (2011).

182. E. Hamed, M. Attia and K. Bassiouny, ***Bioinorg. Chem. and Appli.***, 10:1155, 979680, (2009).

183. M. A. Mesubi, (An infrared study of zinc, cadmium, and lead salts of some fatty acids), ***J. Molecular Structure***, vol. 81, no. 1-2, pp. 61-71, (1982).

184. A. Escuer, M. A. Goher, F. A. Mautner, R. Vicente, ***Inorg. Chem***., 39, 2107, (2000).

185. Theocharis C. Stamatatos, Giannis S. Papaefstathiou, Leonard R. MacGillivray, Albert Escuer, Ramon Vicente, Eliseo Ruiz and Spyros P. Perlepes, ***Inorg. Chem***., 46, 21, (2007).

186. En-Cui Yang, Wen Feng, Jing-Yi Wang and Xiao-Jun Zhao, ***Inorg. Chem. Acta***, 363, 308-316, (2010).

187. Mohamad Jaber Al-Jeboori, Ahlam Jamil Abdul-Ghani and Ahmed Jassim Al-Karawi, ***Transition Met. Chem.***, 33, 925-930, (2008).

188. S. Chandra, M. Pundir, ***Spectrochem Acta***, Part A, 69, 1, (2007).

189. Mohamad Jaber Al-Jeboori, Amar H. Al-Dujaili and Alyaa E. Al-Janabi, ***Transition Met. Chem***., 34, 109-113, (2009).

190. A. Z. El-Sonbati, A. S. Al-Shihri and A. A. El-Bindary, ***Spectrochemica Acta*** Part A., 60, 1763, (2004).

191. Kemal Sancak, Mustafa Er, Yasemin Unver, Melike Yildirim and Ismail Degirmencioglu, ***Transition Metal Chemistry***, 32, 16-22, (2007).

192. Ahlam Jamil Abdul-Ghani, Mohamad Jaber Al-Jeboori, Ahmed Jasim M. Al-Karawi, ***J. Coord. Chem.***, Vol. 62, No. 16, 2736–2744, (2009).

193. Modi CK ***Spectrochim Acta*** Part A., 71, 1741, (2009) .

194. Jin Suk Kwag, Hanyoung Park, Alan J. Lough and Ju Chang Kim, ***Bull. Korean Chem. Soc***. Vol. 31, No. 1, (2010).

195. Mohamad Jaber Al-Jeboori, Hassan Ahmed Hassan, Worood A. Jaafer Al-Sa'idy, ***Transition Met Chem***, 34, 593-598, (2009).

196. Himanshu Arora, Francesc Lloret and Rabindranath Mukherjee, ***Eur. J. Inorg. Chem***., 3317-3325, (2009).

197. Qing Chen, Ming-Hua Zeng, Lian-Qiang Wei and Mohamedally Kurmoo, ***Chem. Mater***, 22, 4328-4334, (2010).

198. H. C. Zhang, L. N. Zakharov, S. K. Das, M. M. Hetu, A. L. Rheingold, ***Inorg.Chim. Acta***, 360, 1691–1701, (2007).

199. O. Kahn, ***Adv. Inorg. Chem***., 43, 179–259, **(**1995) .

200. V. Tangoluis, G. Psomas, C. Dendrinou-Samara, C. P. Raptopoulou, A. Terzis, D. P. Kessissoglou, ***Inorg. Chem***., 35, (1996) .

201. M. Kato, Y. Muto, ***Coord. Chem. Rev***., 92, 45–83, **(**1988**).**

202. Z. Guo, G. Li, L. Zhou, S. Su, Y. Li, S. Dang, H. Zhang., ***Inorg. Chem.***, 48, 8069, (2009).

203. Pablo Albores and Eva Rentschler, ***Inorg. Chem***., 49, 8953-8961, (2010).

204. T. Cauchy, E. Ruiz, S. Alvarez, ***J. Am. chem. Soc***., 128, 15722, (2006).

205. A. Tsohos, S. Dionyssopoulou, C. P. Raptopoulou, A. Terzis, E. G. Bakalbassis, S. P. Perlepes, ***Angew. Chem. Int. Ed***.,38, 983–985, **(**1999**)**.

206. C. V. Wullen, ***J. Phys. Chem.***, 113, 1535–1540, **(**2009).

207. T. Tohyama, T. Saito, M. Mizumaki, A. Agui, Y. Shimakawa, ***Inorg. Chem***., 49, 2492–2495, (2010).

208. S. H. Zhang, Y. Song, H. Liang, M. H. Zeng, ***Cryst. Eng. Comm.,*** 11, 865–872, (2009).

209. S. H. Zhang, Y. L. Zhou, X. J. Sun, L. Q. Wei, M. H. Zeng, H. Liang, ***J. Solid State Chem***., 182, 2991–2996, (2009).

210. Gordon A. Bain and John F. Berry, ***J. Chem.Education***, vol. 85, No.4, (2008).

211. D. Martini, M. Pellei, C. Pettinari, B. W. Skelton, A. H. White, ***Inorg. Chem. Acta***, 72, 333, (2002).

212. W. Lewandowski, M. Kalinowska, H. Lewandowska, ***Inorg. Chem. Acta***, 358, 2155, (2005).

213. D. Czakis-Sulikowska, A. Czylkowska, ***J. Therm. Anal. Cal***. 71, 395, (2003).

214. G.B. Deacon, R. J. Philip, ***Coord. Chem. Rev***., 33, 227, (1980).

215. W. Lewandowski, M. Kalinowska, H. Lewandowska, ***J. Inorg. Biochem***., 99, 1407, (2005).

216. M. W. Wong, M. J. Frisch, K. B. Wiberg, ***J. Am. Chem. Soc***., 113, 4776, (1991).

217. M. W. Wong, K. B. Wiberg, M. J. Frisch, ***J.***

218. ***Chem. Phys***., 95, 8991, (1991).

219. W. J. Geary, ***Coord Chem. Rev***., 7, 81, (1971)

220. A P. Mishra, R. K. Mishra, S.P. Shrivastava, **J.** ***of the Serbian Chem. Soc.***, 74, 523-535, (2009).

221. P. Børsting and P.J. Steel, ***Eur. J. Inorg. Chem***., 376-380, (2004).